ISSN 1018-5593

European Commission

Institute FOR Transuranium Elements

Annual Report 1994

EUR 16152 EN

EUROPEAN COMMISSION

Directorate-General
Science, Research and Development
Joint Research Centre

INSTITUTE FOR TRANSURANIUM ELEMENTS KARLSRUHE

Annual Report 1994

TUAR-94

1995

EUR 16152 EN

Published by the
EUROPEAN COMMISSION

Directorate-General XII
Research and Development
Joint Research Centre

D-76125 Karlsruhe

LEGAL NOTICE

Cataloguing data can be found at the end of this publication

This report was compiled and edited by R. Schenkel, J. Richter, D. Pel, R. Wellum

Inquiries for more details should be addressed to the Programme Office,
Institute for Transuranium Elements, P.O. Box 2340, D-76125 Karlsruhe,
Phone 07247-951-386, FAX 07247-591

For further information concerning JRC programmes please contact the
Directorate-General Science, Research and Development of the European Commission
Rue de la Loi 200, B-1049 Brussels, Belgium.

Luxembourg: Office for Official Publications of the European Communities, 1995

ISBN 92-827-0171-9

Printed in Germany

Abstract

Safety of Actinides in the Fuel Cycle concentrated in 1994 on the study of effects which could influence the safety of nuclear fuel materials at extended burn-ups, under variable load conditions and extended operation periods.

Progress was achieved by performing in parallel work on i) simulated high burn-up UO_2-based fuel, so-called SIMFUEL, ii) evaluating and modelling the large data base on post-irradiation examination of high burn-up fuel iii) continuing the tailormade irradiation of different UO_2-based fuels to 100 000 MWD/t burn-up and iv) studying radiation damage effects by using fission products with high energies in various accelerators. Emphasis in these activities was placed on the "grain-subdivision process" producing the so-called "Rim" structure in high burn-up UO_2.
High temperature thermophysical properties of UO_2 were measured, analysed and critically reviewed.

The fuel performance code TRANSURANUS was further improved and applied in cooperation with an increasing number of organisations and licensing bodies.

The work on partitioning of actinides from waste solutions was continued with genuine high level waste. Potential extractants were tested in centrifugal contactors. Actinides, apart from neptunium, were extracted from high level waste with very high yields.

Preparatory work was done on fuel targets for the transmutation of minor actinides in a fast reactor. The irradiation of 3 technetium samples, fabricated at ITU and of 6 iodine samples, fabricated at ECN started in 1994 in the High Flux Reactor in Petten.

For different transmutation recycling schemes, radiation dose levels have been calculated during fabrication and after reactor discharge. The extension of the minor actinide laboratory progressed with the development of powder preparation equipment based on the sol-gel process.

Fuel behaviour under accident conditions concentrated on the delivery of ultrasonic thermometers for the PHEBUS reactor safety project and on source term studies on radionuclide release from irradiated fuel.

Characterization of Nuclear Waste Forms continued with the characterization of the properties of nuclear waste forms including high burn-up fuels relevant to their behaviour under irradiation or under conditions of long term storage. Electrochemical techniques were used to investigate the dissolution and corrosion behaviour of these materials. Electrochemical experiments were carried out on sintered UO_2 and single crystal UO_2.

Possible high temperature reactions during a reactor accident between fuel and structural materials were examined. The results show the effect of structural materials on fuel at temperatures that are below those of the melting points of the main components and how material interaction can create liquid mixtures at low temperatures (1200 °C) with rapid attack on irradiated UO_2.

UO_2 power reactor fuels irradiated to a burn-up of over 50 000 MWd/t display new aspects of the fuel chemistry. A reaction between Cs and UO_2 at the cladding-fuel interface was found resulting in a modification of the fuel-cladding mechanical interaction and thermal properties of the fuel pellet periphery.

The chemical interaction between sodium and fuels used in the Superfact experiment was analysed by means of thermogravimetry and differential thermal analysis.

Basic Actinide Research concentrated on the preparation and characterization of actinide metals and compounds. An improved "mineralisation" technique allowed the production of large single crystals of U_2Pt_2Sn and U_2Ru_2Sn which are needed for the determination of their physical properties.

Examples of highlights can be taken from such varied topics as the study of Np diluted into the now "famous" heavy-fermion superconductor $NpPd_2Al_3$, to the production and study of uranium overlayers on graphite, to the use of resonant magnetic X-ray scattering to examine magnetism, to the unusual properties of NpAs under pressure, and, finally, to the drawing together of many experiments (on uranium sulphide) and understanding them with one theory.

The Actinide Group was also involved in a large number of collaborations with outside organisations. These collaborations take a number of forms. Some 50 samples were provided in 1994 to about 20 different organisations. Another, relatively new, venture is to create a so-called "user laboratory" in which scientists from outside the Institute can come for short visits to perform measurements. There were about 10 such visitors last year. This operation recognizes the increasing difficulty of working on actinides in many places, and provides a central European laboratory for such an endeavour. New equipment (in some cases brought from other institutions) is being added to the laboratory to increase its utility.

Under **Exploratory Research** work was performed in the area of aerosol agglomeration studies with ultrasonic and infrasound waves, the study of magnetic anisotropy of rare earth-transition metal magnets, alternative fuel cycles, partitioning of actinides from molten salt media, property studies with uranium-aluminium cermets, two dimensional heat transfer mapping and on the feasibility of manufacturing a new high density fuel for Material Test Reactors.

The majority of the Institute's **Scientific-Technical Support to Community Policies** concerned work for the safeguarding of fissile materials. Major progress was achieved in the preparation for the installation and operation of on-site analytical laboratories in Sellafield and Cap la Hague. New nondestructive measurement equipment was tested and the internal staff training programme continued. The Institute provided scientific-technical assistance in the area of analyses and characterization of vagabonding nuclear materials seized by Member State authorities.

As a new activity, a laboratory for the Analysis of Radioisotope Traces for the Identification of Nuclear Activities (ARTINA) is being established.

Under **Work for Third Parties** work was pursued along several lines: alpha-radioimmunotherapy, fabrication of minor actinide bearing multi-component alloys as targets for transmutation, and the assessment of spent fuel behaviour under interim dry storage. Major work was performed in the area of examination of commercial high burn-up fuel and fuel cladding performance. Contract work also covered electron microscope investigations on irradiated zircaloy cladding materials.

European Commission
Joint Research Centre

TUAR 94

Institute for Transuranium Elements

Annual Report

January – December 1994

Table of Contents

Foreword

by J. van Geel, Director

The Annual Report for 1994 provides an account of the activities performed and the progress achieved in the various scientific and technical disciplines covered by the Institute's mission, the work schedules and the most significant tasks performed under contracts with third parties.

From the large amount of data and results presented and from discussions and requests from our customers, the major trends and orientation for our future work are perceived as described below.

In the area of safety of nuclear fuels, the Institute concentrates on the measurement and the modelling of thermodynamic and mechanical properties of high burn-up uranium and mixed oxide fuels and their interaction with the fuel cladding. A high portion of work performed is on request or under contract from nuclear authorities or nuclear industry.

A further important area is the contribution of the Institute to the efforts to minimise the radiotoxicity of spent fuel and highly active waste. The activities in this area concentrate on:

- the test of suitable partitioning and transmutation schemes, including fabrication techniques and post-irradiation examinations of actinide and long-lived-fission product containing fuels. This work is performed in close collaboration with European and other international partners

- the design, construction and operation of a minor actinide laboratory

In the area of spent fuel characterization, in view of long-term storage and final disposal the Institute continues to concentrate its activities on the following major subjects:

- improvements of destructive and non-destructive measurement technology for the determination of important fuel parameters like burn-up, actinide content as well as data affecting the physical integrity of spent fuel under long-term storage conditions

- improvement of the basic understanding of the mechanisms of leaching and its kinetics

- the evolution of radiotoxicity of spent fuels and different waste forms

An essential asset for the scientific and technical vitality of the Institute remains the expertise and know-how in basic and applied actinide research. The Institute is extending its role as the leading Actinide User Laboratory and as a European Actinide Information Center in line with the requests and recommendations from its customers and advisory bodies.

In the area of nuclear safeguards, the Institute concentrates the available resources on the following major tasks:

- analytical support to the Euratom Safeguards Directorate has been and will continue to be a major operational task for the Institute's staff. A high degree of accompanying development will be needed to further improve and robotise the applied analytical technology

- improvement and implementation of new measurement technology for nuclide trace analysis. This capability is required for forensic analysis of seized materials from illicit trade and, even more important, for environmental monitoring

The Institute for Transuranium Elements will continue to adjust its activities to the changing requirements, in line and in collaboration with its European and international partners and customers from authorities, industry and research organisations. It will thus continue to provide major and highly relevant contributions to the improvement of the safety of the nuclear fuel cycle.

Executive Summary

Introduction

The major task of the Institute in 1994 was the execution of the European Commission's third framework programme in its last year.

The most important area of activity was the specific research programme, now called institutional research, which accounted in 1994 for about 58% of the Institute's resources. The activities covered predominantly safety of actinides in the nuclear fuel cycle, fuel behaviour under accident conditions, characterization of nuclear waste forms and exploratory research.

Another important area was scientific and technical support to other Directorates General of the Commission to support the formulation and implementation of policies of the European Union. These activities accounted in 1994 for about 34% of the Institute's resources. The activities covered assistance and support to the Euratom Safeguards Directorate in Luxembourg, assistance and support to the International Atomic Energy Agency (IAEA) through the Directorate General for External Relations and activities related to technology transfer and utilisation of research results in collaboration with the Directorate General for Telecommunication, Information Market and Utilisation of Research Results.

Finally the Institute has continued to offer its scientific/technical expertise to external customers. During 1994, the Institute has carried out and invoiced work corresponding to about 2.5 MEcu. This corresponds to about 8% of the Institute's resources.

1. Safety of Actinides in the Fuel Cycle

1.1 Safety of nuclear fuel at high burn-up

The research activities aimed at improving the safety of nuclear fuels were continued along the lines of the previous reporting period. Emphasis was placed on modelling and understanding the physical and chemical processes and mechanisms of importance for the behaviour of LWR oxide fuels up to very long operation periods, i.e. up to high burn-ups of ~ 60 000 MWd/t and above. Progress was achieved by performing in parallel work on i) simulated high burn-up UO_2-based fuel, so-called SIMFUEL, ii) evaluating and modelling the large data base on post-irradiation examination of high burn-up fuel iii) continuing the tailormade irradiation of different UO_2-based fuels to 100 000 MWD/t burn-up and iv) studying radiation damage effects by using fission products with high energies in different accelerators. Emphasis in these activities was placed on the "grain-subdivision process" producing the so-called "Rim" structure in high burn-up UO_2.

As in previous years important results were obtained, evaluated and published within the reporting period. These include the following:

- an electron microscope study of the Rim structure in a fuel with a very wide Rim zone, and modelling of these zones
- oxygen potential measurements on high burn-up UO_2 fuel
- modelling of the high temperature λ-transition in UO_2 and of the thermal conductivity of molten UO_2
- further theoretical and experimental work on the thermal conductivity of SIMFUEL, extended to oxidized fuel
- measurements of creep and hot hardness of SIMFUEL
- further theoretical and experimental work on fission gas release and on the behaviour of bubbles containing volatile fission products other than the rare gases.

Studies of the high temperature properties of UO_2 were continued. In particular the heat capacity and diffusitivity data for UO_2 were critically reviewed and evaluated.

The fuel performance code TRANSURANUS was further improved and applied in cooperation with an increasing number of organisations and licensing bodies.

The laser flash device for measurement of the thermal diffusivity of irradiated fuel was tested with several standard samples and with semi-transparent materials which presented particular difficulties. The apparatus constructed in our laboratory proved to give an outstanding performance, thanks to the very sophisticated optical and mechanical alignment system.

1.2 Partitioning and transmutation

The work on partitioning of actinides from waste solutions was continued with genuine high level waste. Potential extractants were tested in centrifugal contactors. Actinides, apart from neptunium, were initially extracted from high level waste with very high yields. By changing the process conditions, the decontamination factors for Am, Cm and Np could be improved to better than 99.9%.

In relation with the project CAPRA (Consommation Accrue de Plutonium dans les Rapides) fuel pins for the irradiation experiment TRABANT (TRAnsmutation and Burning of ActiNides in TRIOX) are fabricated. Due to the unusual composition and the high specific radioactivity it was necessary to develop special fabrication procedures for the new fuel materials.

Preparatory work was done on fuel targets for the transmutation of minor actinides in a fast reactor. (Experimental Feasibility of Targets for TRAnsmutation - EFTTRA). It has been decided to focus efforts on technetium-99 (metal), iodine-129 (compound) and to americium-241 (in an inert matrix).

The irradiation of 3 technetium samples, fabricated at ITU and of 6 iodine samples, fabricated at ECN started in 1994 in the High Flux Reactor in Petten.

For different transmutation recycling schemes, radiation dose levels have been calculated during fabrication and after reactor discharge. In order to assess the accuracy of these predictions, measured radiation doses of irradiated fuel, for example from the SUPERFACT programme, have been compared with those calculated.

The extension of the minor actinides laboratory progressed, with the development of powder preparation equipment based on the sol-gel process. First fuel powder specimens were prepared. In parallel, the design of a new fabrication chain for the preparation of fuel pins containing minor actinides was continued.

In the frame of the PADIT project (Particle Agglomeration and Deposition in Turbulence), experiments were carried out to study the influence of turbulence on the agglomeration of particles. It was observed that transport in a highly turbulent flow strongly increases the agglomeration of uranium oxide particles. Direct observation of particles smaller than the original size on the filters indicates that the turbulence can also have the opposite effect and agglomerates can be broken up.

2. Fuel Behaviour under Accident Conditions

2.1 Studies of problems related to reactor safety

A total of 16 multi-section ultrasonic thermometers and the thermometer control and evaluation unit were transferred to CEA-CEN Cadarache for use in the PHEBUS reactor safety project.

2.2 Source term studies on radionuclide release from irradiated fuel

Laboratory measurements were carried out on vaporization/effusion effects of irradiated nuclear fuels at high temperature. The aim of these experiments was twofold; first, to collect data on the release of fission gas and less volatile fission products enabling their diffusion coefficients in the fuel as well as their respective release pathways to be identified. Second, to analyse the vaporization rate of the various species in order to reconstruct the thermochemical properties of the system fuel plus fission products including reaction products, and fuel stoichiometry.

3. Characterization of Nuclear Waste Forms

The studies on radioactive waste carried out at the Institute are centred on the characterization of the properties of nuclear waste forms including high burn-up fuels relevant to their behaviour under irradiation or under conditions of long-term storage.

Electrochemical studies of UO_2 and nuclear fuels in aqueous solutions are essential to understand the dissolution and corrosion behaviour of these materials in groundwaters. The knowledge of the mechanisms (e.g. rate determining steps, intermediate species involved, precipitates, etc.) is important in assessing the stability of nuclear fuels in final or intermediate storage.

In the current electrochemical experiments, sintered UO_2 and single crystal UO_2 were used as electrodes of non-irradiated fuels. Electrodes from irradiated UO_2 with 26.4 and 68 GWd/t burn-up, UO_2 from a failed fuel rod with abnormal grain size (20 - 25 GWd/t) and MOX fuels (21.1 GWd/t) with Pu particles containing 25% Pu were used for the studies on irradiated fuels. Measurements were carried out in aerated and deaerated 3 w/o Na_2CO_3 solution at room temperature (25 $\pm$ 2 °C). For measurements in the hot cells the electrolyte was deaerated by N_2 bubbling to about 0.1 ppm O_2 and kept under a N_2 - 5% O_2 atmosphere during the course of the experiment.

Because of their high resistivity, UO_2 samples are subject to pitting attack at grain boundaries or inclusions. Irradiated fuels display a more heterogeneous behaviour and suffer about 50 times higher corrosion than non irradiated UO_2.

High temperature reactions are possible during a reactor accident between fuel and structural materials as the fuel bundle degrades. The investigation of these interactions and their kinetics is important as they can result in low melting point eutectics or mixtures which are liquid at temperatures substantially below those of the individual melting points and can cause a severe and accelerated degradation of the reactor core even below the UO_2 melting point.

The results show the effect of structural materials on fuel at temperatures that are below those of the melting points of the main components and how material interaction can create liquid mixtures at low temperatures (~ 1200 °C) with rapid attack on irradiated UO_2. The zirconium penetration into UO_2 was about 10 - 20 microns after 30 mins. at 1500 °C. The comparison of results between non-irradiated and irradiated UO_2 fuels indicate significant differences, both structural and compositional.

UO_2 power reactor fuels irradiated to a burn-up of over 50 000 MWd/t display new aspects of the fuel chemistry. A reaction between Cs and UO_2 at the cladding-fuel interface was found resulting in a modification of the fuel-cladding mechanical interaction and thermal properties of the fuel pellet periphery. UCs_2O_4 was synthesised and its thermal conductivity was measured by means of the comparison method in the temperature range of 100 to 600 °C. Initial determinations of the micro-hardness of high burn-up fuel were carried out at room temperature concentrating in particular at the pellet periphery.

Cladding rupture during irradiation in a Fast Breeder Reactor could lead to a chemical interaction between sodium and mixed oxide fuels containing Am and Np used for transmutation. The chemical interaction between sodium and fuels used in the Superfact experiment was analysed by means of thermogravimetry and differential thermal analysis.

4. Actinide Research

Actinide research is basic, and therefore long term, in nature. It has definite goals aimed at understanding the behaviour of the 5f electrons in actinide compounds; a subject of much current interest in condensed-matter science, but also it aims to develop and sustain the expertise needed to work on actinide systems.

Examples of highlights can be taken from such varied topics as the study of Np diluted into the now "famous" heavy-fermion superconductor $NpPd_2Al_3$, to the production and study of uranium overlayers on graphite, to the use of resonant magnetic X-ray scattering to examine magnetism, to the unusual properties of NpAs under pressure, and, finally, to the drawing together of many experiments (on uranium sulphide) and understanding them with one theory.

In the area of preparation and characterization of actinide metals and compounds, an improved "mineralisation" technique allowed the production of large single crystals of U_2Pt_2Sn and U_2Ru_2Sn which are needed for the determination of their physical properties.

In the area of solid state physics and high pressure studies, the investigation of the physical and structural properties of the heavy-fermion superconductor UPd_2Al_3 and its isostructural compounds $NpPd_2Al_3$ and $NpNi_2Al_3$ was continued, including solid solutions between the first two compounds with two different Np/U ratios.

Theoretical work on the optical and magnetic properties of actinide materials was continued. In particular, a newly developed program for calculating circular dichroism was applied to various materials, e.g. US. The pressure dependences of the Curie temperatures of Cm and Gd were calculated and compared.

Another group of materials on which experimental effort was concentrated (Mößbauer study, structural and electrical properties) were the uranium and neptunium compounds of the $AuCu_3$ structure type. All of the uranium compounds exhibit anomalous compression without any structural change which is not the case for the neptunium compounds. The origin of this phenomenon is not yet clear, but may indicate pressure-induced electron transfer in uranium.

Other interesting effects of pressure observed were the enhancement of superconductivity in amercium and the strong increase followed by a decrease of the magnetic ordering temperatures in some uranium, neptunium and plutonium compounds.

The Actinide Group is also involved in a large number of collaborations with outside organisations. These collaborations take a number of forms. In many cases they involve providing samples upon which work is done. Some 50 samples were provided in 1994, to about 20 different organisations. In addition in 1994, a major programme funded from Japan used much of the expertise of the Actinide Group in producing materials containing minor actinides for irradiation. Another, relatively new, venture is to create a so-called "user laboratory" in which scientists from outside the Institute can come for short visits to perform measurements. There were about 10 such visitors last year. This operation recognizes the increasing difficulty of working on actinides in many places, and provides a central European laboratory for such an endeavour. New equipment (in some cases brought from other institutions) is being added to the laboratory to increase its utility.

5. Exploratory Research

The Institute has pursued exploratory research in the areas of aerosol agglomeration with ultrasonic and infrasound waves, the study of magnetic anisotropy of rare earth transition metal magnets, alternative fuel cycles, property studies with uranium-aluminium cermets and two dimensional heat transfer mapping.

The feasibility of manufacturing a new high density fuel for Material Test Reactors was demonstrated in collaboration with the industry. These developments support non-proliferation objectives to convert high enriched uranium fuel to lower enrichments.

The acoustic agglomeration rate of aerosols has been shown to depend linearly on the applied acoustic power. This result has important implications for acoustic agglomeration models and for the design of effective agglomeration cavities.

6. Scientific-Technical Support to Community Policies

6.1 Support to DGI

The field test of a robotised system for the chemical treatment of diluted spent fuel solutions at the Gatchina reprocessing facility south of St. Petersburg in Russia was concluded. The robot system worked well under the conditions experienced at this reprocessing plant.

In the framework of safeguards monitoring for detection of undeclared activities, ITU has been requested to analyse radioisotopes at trace levels in environmental type samples. A series of experiments and improvements

of instruments were carried out in this field including the preparations for the construction of the ARTINA laboratory (Analysis of Radioisotope Traces for the Identification of Nuclear Activities).

6.2 Support to DG XIII

The development of a process using acoustic waves to treat airborne particles so, that they can be separated with high efficiency in conventional gas cleaning devices was continued. Experimental work performed demonstrates that the acoustic agglomeration of titanium dioxide can be enhanced by the addition of inertial droplets of glycol fog.

6.3 Support to DG XVII

Important steps forward have been taken concerning the design and implementation of the on-site laboratory (OSL) in Sellafield. Major progress was achieved in the following areas:

- completion of the Hazards of Procedures Study
- finalisation of the Precommencement Safety Report
- introduction of a quality assurance system in accordance with ISO 9001 (EU 29000)
- start of purchasing of instruments and glove-boxes
- testing of new non-destructive measurement equipment
- training of ITU analysts for operation of OSL

Concerning the on-site laboratory in Cap la Hague, technical discussions continued to define in more detail the scope of the project.

Routine analyses of safeguards samples for the Euratom Safeguards Directorate in Luxembourg continued: About 500 chemical analysis were performed in 1994.

A portable compact K-edge absorptiometer for uranium solutions and a neutron-gamma counter for plutonium oxide samples was built for use by inspectors. A hybrid K-edge apparatus, installed at La Hague for routine measurements of input samples was maintained and used for routine inspection measurements by Institute staff.

Also in support of DG XVII the ICP/MS technique has been combined with a high pressure liquid separation (HPLC) column for the on-line measurement of actinides and fission products. A high sensitive glow-discharge mass-spectrometer (GDMS) has been installed in a glovebox and calibrated for a wide range of materials.

The scientific and technical assistance of the Institute for Transuranium Elements in the area of analysis and characterization of nuclear materials seized by German authorities reached a culmination point during 1994. The number of samples transported to and analysed in the Institute was higher than in previous years, and the quality of the material found was remarkably variable.

The work carried out by the Institute can be considered as an example on how the facilities and expertise of the Joint Research Centre can be of benefit to authorities and institutions in Member States of the European Union.

7. Work for Third Parties

Under contract work for Alphamedical Holdings BV a breakthrough was achieved in the preparation of 10mCi amounts of α-emitting agents for a new radioimmuno-therapy. The chemical separation scheme for Ac-225 from U-233/Th-229 feed, based on sorption on titanium phosphate followed by cation exchange, was brought to a routine stage. First charges of Ac-225 were shipped to New York, where clinical studies are being performed in the Memorial Sloan Kettering Cancer Center.

Contractual work for the Central Research Institute of the Electric Power Research Institute (CRIEPI) in Japan continued. The fabrication of minor actinide bearing multi-component alloys to be used as targets for a transmu-

tation experiment in the Phenix fast reactor was successfully finished. The fuel is presently being characterized. The characterization of UO_2 and MOX spent fuel with burn-ups of about 60 GWd/tHM and 45 GWd/tHM was continued. Destructive and non-destructive examinations are necessary for the assessment of the spent fuel behaviour under conditions of interim dry storage.

Contractual work for CRIEPI also included experiments on in-situ monitoring of the dissolution of spent fuel.

A passive neutron interrogation device for spent fuel measurements is being tested in the ITU hot cells under contract from the Gesellschaft für Nuklearservice, Hannover (GNS).

In the Institute's hot-cells major work on the assessment of commercial fuels and cladding performance of fuel under high burn-up continued in cooperation with Siemens-KWU. Transmission electron microscopy investigations of irradiated zircaloy cladding materials are performed for Siemens and the Paul Scherrer Institute, in Würenlingen. Fuel cladding chemical and mechanical interactions are the focal point of research performed in cooperation with Électricité de France.

Non-destructive and destructive testing was performed on a further 28 BR3 fuel rods . These rods will be used for the Phebus reactor safety experiment, coordinated by the Commissariat à l'Énergie Atomique. Post-test analysis of aerosol deposits from coupons coming from the first Phebus PF experiment FPTO was also carried out under third party work.

The total volume of third party work performed and invoiced in 1994 amounted to about 2.5 MECU.

8. Scientific Infrastructure

Work performed at the Institute in 1994 resulted in 60 publications in books, periodicals or in the from of reports (published or submitted) and in 82 contributions to conferences, workshops or seminars held during the reporting period. 6 patents were granted; 6 patent applications & proposals have been submitted.

During 1994, twenty-seven new doctoral grantees, post doctoral grantees and visiting scientists were welcomed at the Institute. Close collaborative contacts were maintained in 1994 with some 80 scientific and industrial institutions in 20 countries in Europe and overseas.

The stepwise introduction of a quality management system was pursued in 1994. Quality plans and procedures have been introduced for the post-irradiation examination of fuel rods, for the installation of on-site laboratories, for the production of α-sources for cancer treatment and for the treatment of vagabonding materials.

MAIN ACHIEVEMENTS AND MILESTONES

1. Safety of Actinides in the Nuclear Fuel Cycle

1.1 Safety of Nuclear Fuels at High Burnup

1.1.1 Introduction

The research activities aimed at improving the safety of nuclear fuels were continued along the lines of the previous reporting period. Emphasis was placed on modelling and understanding the physical and chemical processes and mechanisms of importance for the behaviour of LWR oxide fuels up to very long operation periods, i.e. up to high burnups of ~60 000 MWd/tM and above. Progress was achieved by performing in parallel work on i) simulated high burnup UO_2-based fuel, so-called SIMFUEL, ii) evaluating and modelling the large data base on post-irradiation examination of high burnup fuel iii) continuing the tailor-made irradiation of different UO_2-based fuels to 100 000 MWd/tM burnup and iv) studying radiation damage effects by using fission products with high energies in different accelerators. Emphasis of these activities was placed on the "grain-subdivision process" producing the so-called "Rim" structure in high burnup UO_2.

As in previous years important results were obtained, evaluated and published within the reporting period. These include the following:

- an electron microscope study of the Rim structure in a fuel with a very wide Rim-zone, and modelling of these zones
- oxygen potential measurements on high burnup UO_2 fuel
- modelling of the high temperature λ-transition in UO_2 and of the thermal conductivity of molten UO_2
- further theoretical and experimental work on the thermal conductivity of SIMFUEL, extended to oxidized fuel
- measurements of creep and hot hardness of SIMFUEL
- further theoretical and experimental work on fission gas release and on the behaviour of bubbles containing volatile fission products other than the rare gases

Studies of the high temperature properties of UO_2 were continued. In particular the heat capacity and diffusitivity data for UO_2 were critically reviewed and evaluated. Finally, the fuel performance code TRANSURANUS was further improved and applied in cooperation with an increasing number of organisations and licensing bodies.

1.1.2 Structural investigations and basic studies on fuels

A scanning electron microscope investigation of the variations in fuel structure at the rim of high burnup LWR fuel

It has been known for some years that important changes occur in the microstructure at the periphery of LWR UO_2 pellets when the average cross-sectional burnup exceeds 40000 MWd/tU [1]. These microstructural changes lead to a "cauliflower structure" caused by a grain subdivision process, each grain of the original sintered structure transforming into some 10000 new subgrains, and this is usually referred to as the "Rim effect". The possible consequences of this process on the thermal behaviour and gas release and the possible mechanism have been described before [2,3].

Often this structural change is confined to a shallow zone of 150 - 200 μm at the Rim of the pellet. In this zone the burn up is locally increased due to fission of Pu-239, formed by resonance capture of neutrons by U-238. The question of to what extent this grain subdivision process can extend into the interior of the fuel is at present of great interest. The fact that it is not restricted to this shallow zone at high burnup has also been recognised for some time. An irradiation experiment (TUAR-93, p. 227) in cooperation with CRIEPI, Tokyo, and the OECD Halden project, Norway, will provide results on the dependence of the onset of grain subdivision on parameters like burnup, fuel temperature and applied pressure.

The results of this irradiation will not be available before 1996. Therefore we have extended our previous transmission electron microscope (TEM) and scanning electron microscope (SEM) study obtained on very small pieces of fuel taken from the outermost periphery of a high burnup fuel which was irradiated to an average burnup of 7.6%, but with a local peripheral burnup approaching 20%. The investigation of the fuel structure

was continued with a SEM examination of larger residual pieces of this fuel in the Institute hot cells, extending the radial depth of the investigation to nearly 2 mm. These pieces were too active to have been examined in the Hitachi STEM, used for the previous electron microscopy investigations (TUAR-92, p. 17; and reference [4]). The scanning electron microscope used was the JEOL 35C mounted in the hot cells and controlled remotely.

Pieces chosen for examination were those where the outer pellet surface could be clearly defined, as shown for example in Fig. 1.1. A full cross section of the pellet was also examined, but this had previously been mounted and polished for optical metallography and the microstructure could only be revealed within the pores.

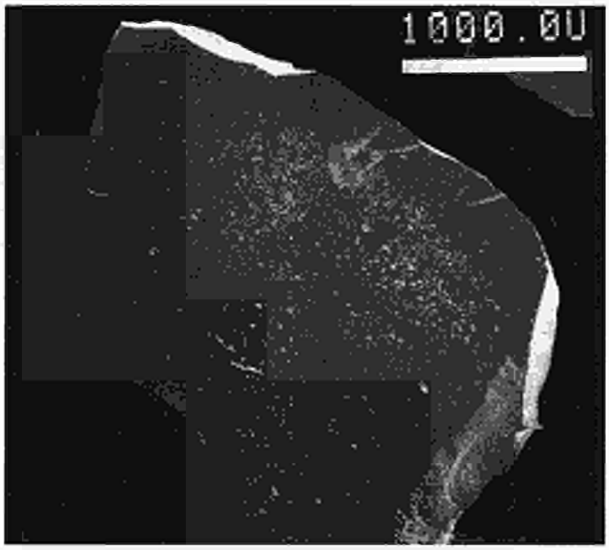

Fig.1.1 Scanning electron micrograph showing a typical fuel fragment chosen for the analysis.

The typical "Rim" structure of very small subgrains could be found locally up to a depth of 1650 µm from the fuel surface, but the proportion of grains showing the effect decreased with depth. At 1700 µm the structure was no longer found at all, this thus can be taken to represent the limit for this particular fuel. Subgrain size histograms were constructed for various depths, based on up to 200 grain size measurements, and examples of these from 50 µm depth to 1570 µm are shown in Figs. 1.2a to 1.2e. Fig. 1.3 shows a typical example of the subgrain structure at a depth of 1250 µm.

It is interesting to note that the grain size histograms do not vary very significantly with depth into the fuel, and always show a peak between 0.3 and 0.4 µm. The main variation with depth is the decreasing proportion of regions showing this structure as opposed to the normal grain structure of the fuel, from 100% at the very Rim to a very small proportion at depths > 1 mm (< 5% of the area examined).

Figs. 1.4 and 1.5 show examples of the normal and the fine-grained structure at a depth of 1570 µm from the

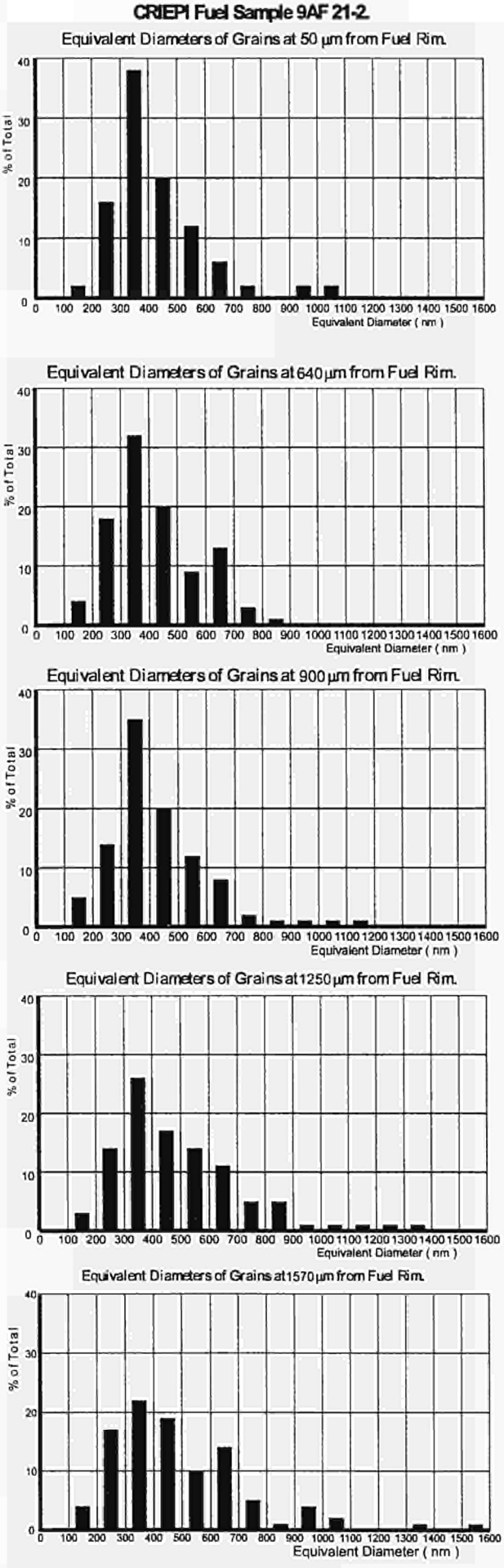

Fig. 1.2 a-e Subgrain size histograms for the various depths indicated from the fuel surface.

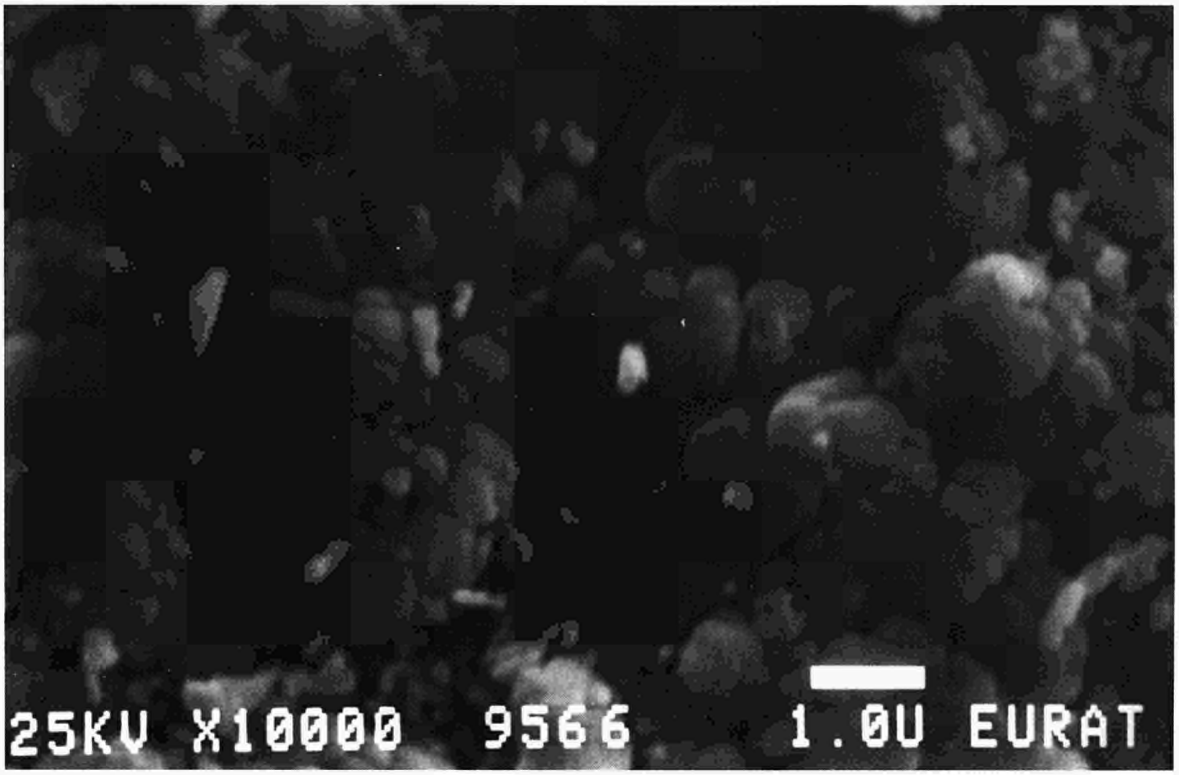

Fig. 1.3 Scanning electron micrograph of the typical subgrain structure found at a depth of 1250 μm from the fuel surface.

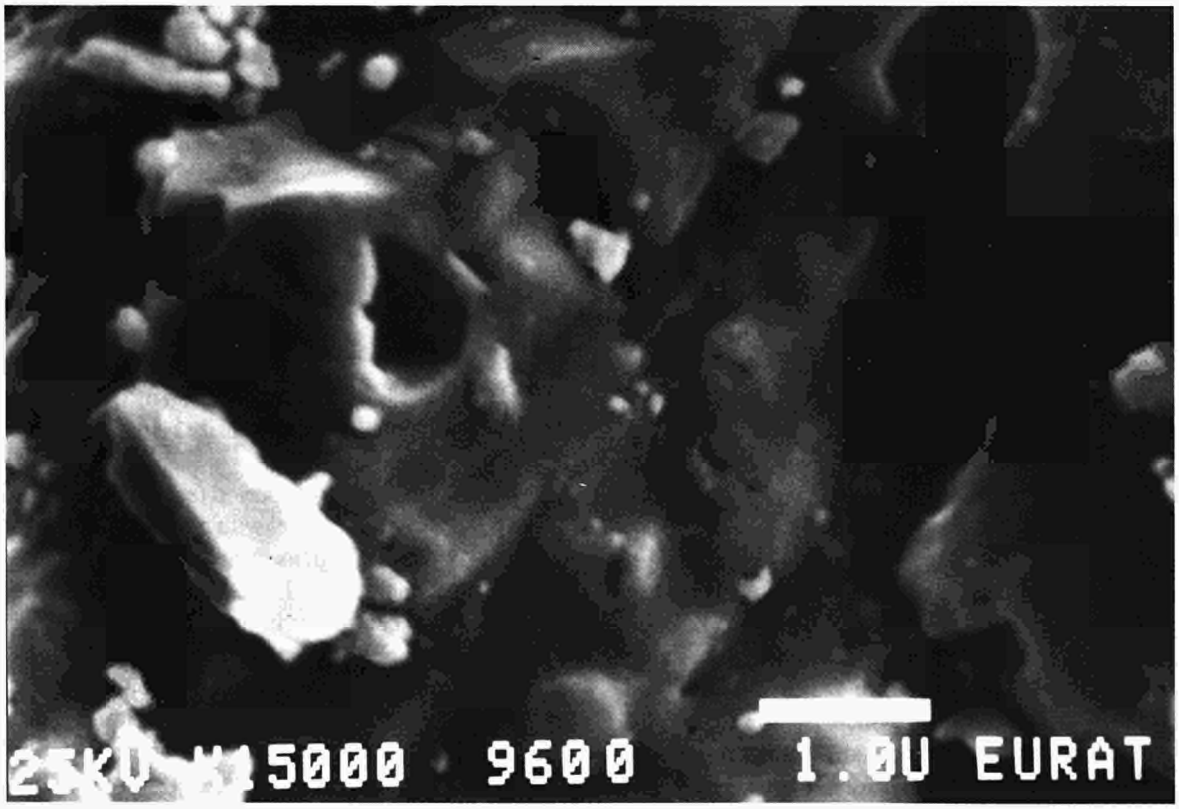

Fig. 1.4 Scanning electron micrograph showing the "normal" fuel structure found at a depth of 1570 μm from the fuel surface.

fuel surface. The SEM results show convincingly that the grain subdivision can occur up to a depth of 1.6 mm from the fuel surface, but at this depth only apparently at very few preferential sites or within pores. The examination of these samples is continuing with the aim of correlating the structure seen by SEM with other measurements made on the fuel cross sections.

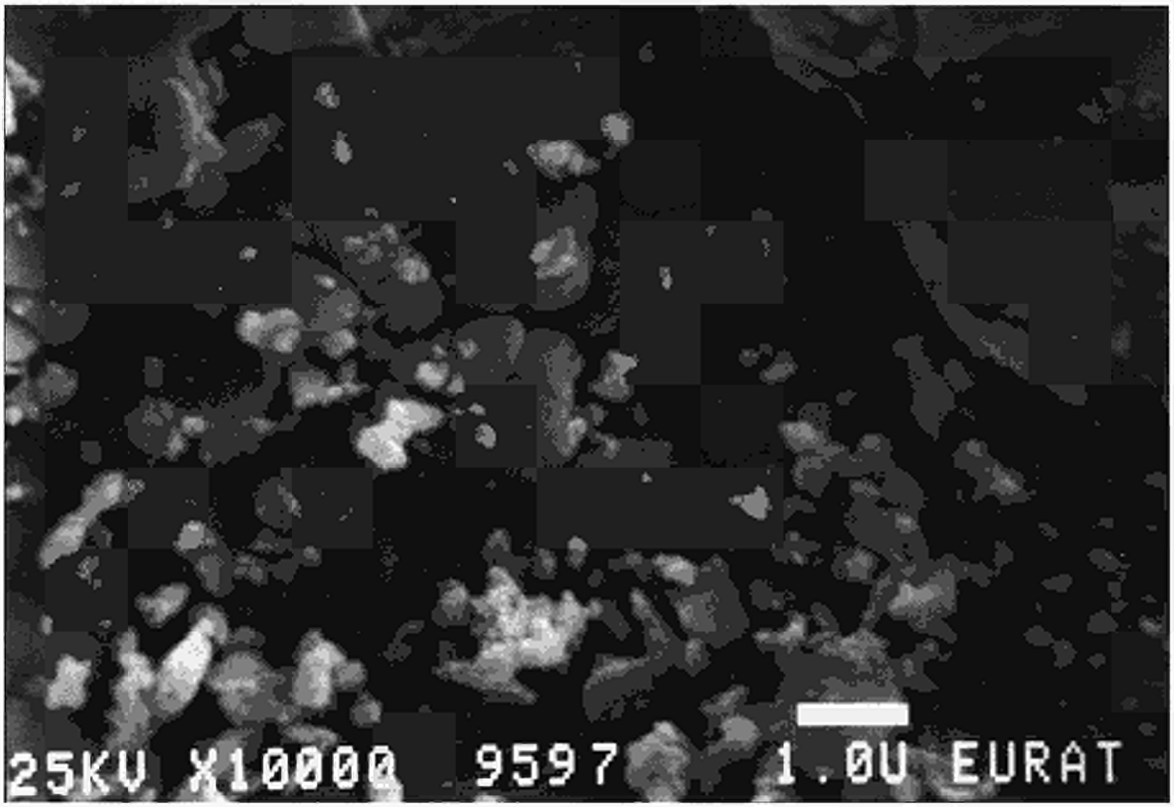

Fig. 1.5 Scanning electron micrograph showing the subgrain structure found along with the normal fuel structure at a depth of 1570 μm from the fuel surface.

References

[1] Hj. Matzke, I. L. F. Ray et al.; J. Nucl. Mater. **166** (1989) 165
[2] Hj. Matzke; J. Nucl. Mater. **189** (1992) 141
[3] Hj. Matzke; Proc. 8th World Conference on Ceramics, CIMTEC, Firenze (1994), Ed. P. Vincencini
[4] I. L. F. Ray, H. Thiele and Hj. Matzke; J. Nucl. Mater. **188** (1992) 90

Oxygen potential of high burnup UO_2

UO_2 fuel is commonly assumed to oxidize with increasing burnup, in particular for Pu-fission, since the fission products consume less oxygen than is liberated by fission of (tetravalent) U and Pu. Though two fission products are formed from each U (or Pu) atom, many of the fission products are metals (Mo, Tc, Ru, Rh and Pd, with particularly high yields for fission of Pu) or rare gases (Kr, Xe) and many of them are trivalent (lanthanides). Also, dissolution of trivalent rare earth ions (and also of Pu) in UO_2 causes the oxygen potential, $\Delta\overline{G}(O_2)$ to increase (to become less negative) at constant oxygen-to-metal, O/M, ratio. Changes in $\Delta\overline{G}(O_2)$ and in the oxidation state of the fuel (its O/M-ratio) affect many important properties and significantly influence the irradiation behaviour of the fuel; examples are clad inside corrosion, fuel thermal conductivity and hence operating temperatures, diffusion and gas release rates, creep and plasticity of the fuel. A knowledge of the development of $\Delta\overline{G}(O_2)$ and of the O/M-ratio of the fuel with burnup is therefore of great scientific and technological interest. A miniature solid state galvanic cell has been previously developed to measure $\Delta\overline{G}(O_2)$ of unirradiated and irradiated fast breeder (U, Pu)O_{2-x} fuel up to high burnups of 11 a/o [1]. This cell was modified to allow measurements on UO_{2+x} in the range of higher oxygen potentials, which means that a large range of $\Delta\overline{G}(O_2)$ values between about -650 and -150 kJ/mol can now be reliably measured, even for very high burnups up to 200 GWd/tM in the Rim region of UO_2 fuel (TUAR-91, p. 33 and [2]). Any possibly existing oxidation of UO_2 arising from high burnup could therefore easily be measured.

In the previous reporting period (see TUAR-93, p. 24), it was shown that a UO_2 fuel with a low enrichment of only 1.46 %, but with a high average burnup of 75 GWd/tM in the section analysed did not oxidize during irradiation, neither at the centre nor in the Rim zone which showed clear grain subdivision and experienced burnups up to 200 GWd/tM. This previous report contained also a literature review of the effect of fission products on $\Delta\overline{G}(O_2)$ and of the previous work on irradiated fuel.

The modified miniaturized galvanic cell was used for measurements on further fuels in the reporting period. The main features of the fuels used are summarized in Tab. 1.1.

The fuels studied were selected on the basis of their burnups and their enrichments. Together with the fuel with

Tab. 1.1 Some details of the investigated fuels

Fuel	initial enrichment %	burnup GWd/tM	inner surface clad oxidation,
1	6.85	28.9	very thin, no gap closure
2	5.0	34.5	very thin, no gap closure
3	8.25	58	up to 10 µm only local patches
4a	1.46	75	15 to 20 µm
4b	1.46	up to 200, RIM-area of fuel 4a	
Fuel 4 is the one described in TUAR 93, p. 24 and is included here for completeness.			

1.46 % U-235, they had very different contributions of Pu-fission to the total burnup. Small pieces of these fuels of a few mg weight were introduced into the cell and repeatedly measured in the temperature range of about 900 to 1350 K. These repeated measurements (called 1st, 2nd or 3rd run in Figs. 1.6-1.8) consisted in raising and lowering the temperature. Between the different measurements with the high burnup UO_2, measurements with unirradiated UO_2 or UO_{2+x} with known O/U-ratios were made to verify the reliable operation of the cell.

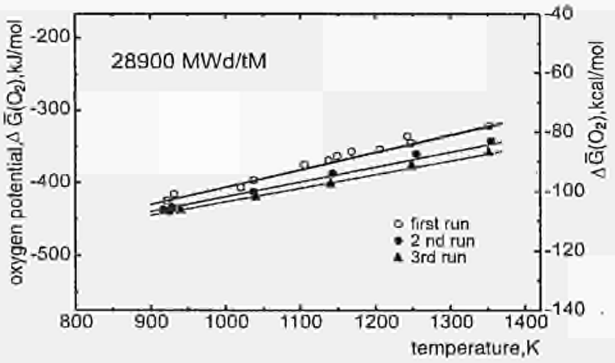

Fig. 1.6 Oxygen potential measurements of UO_2 fuel at 28900 MWd/tM burnup as a function of temperature.

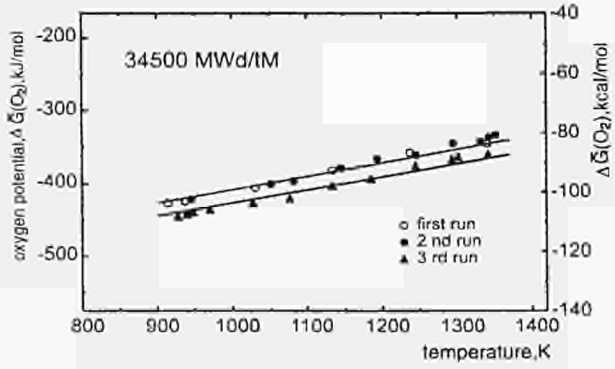

Fig. 1.7 Oxygen potential measurements of UO_2 fuel at 34500 MWd/tM burnup as a function of temperature.

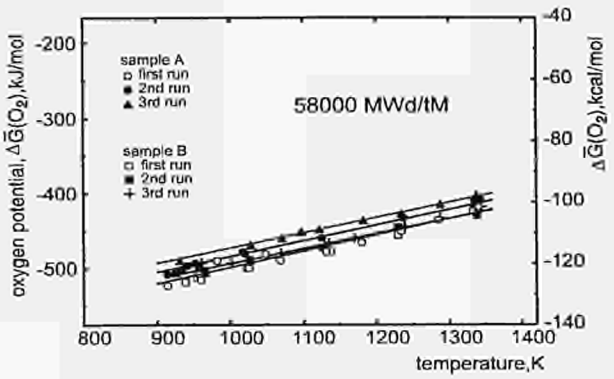

Fig. 1.8 Oxygen potential measurements of UO_2 fuel at 58000 MWd/tM burnup as a function of temperature. Two different pieces (samples A and B) were used.

Results

Figs. 1.6 to 1.8 show the results for the fuels with 28.9, 34.5 and 58 GWd/tM burnup. The fuel of 58 GWd/tM yielded the lowest $\Delta\overline{G}(O_2)$-values, and for this reason and to confirm the results on the first fuel piece, two pieces were measured. A possible explanation of the low $\Delta\overline{G}(O_2)$-values for this fuel may be its power history. This fuel experienced an unusual power history, with a high rating in the first cycle, a low rating in the second cycle and a high rating in the third cycle.

The small changes between different runs shown in Figs. 1.6 to 1.8 may be due to either a slight surface oxidation of the fuel pieces between preparation of these pieces in the hot cells and the emf-measurements, or to a certain rearrangement, precipitation or compound formation of some fission products during the 1st or 2nd annealing. For the present purpose, however, these small changes are of little importance. The important point is that all values measured are very low. In contrast to still existing ideas about fission (and in particular Pu-fission) oxidizing the fuel, none of the fuels investigated showed any oxidation above the level of O/M = 2.00. The measured values correspond rather to those of unirradiated stoichiometric UO_2 or, at the most, to those of unirradiated UO_{2+x} with $x \leq 0.001$ (see Fig. 1.9 in TUAR-93, p. 26). If due allowance is made for the ingrowth of Pu and of rare earths during irradiation, the results prove a very slight *substoichiometry* of the order of O/M = 1.995 for the higher burnups. Also, rather importantly, all data points are at or below the value for Mo oxidation, hence the reaction $Mo + O_2 \rightarrow MoO_2$ (see Fig. 1.9).

Any conclusive treatment of the development of O/M-ratio with burnup must include a realistic description of the chemical state and of the mobility of the fission products in the temperature gradient of the operating fuel. Also, chemical reactions occurring on the inner surface of the clad must be known and included, hence the chemical state of the Zr in the cladding must be properly modelled. The present results show that the decisive fission product in the fuel is Mo. Mo can be present in the well known 5-

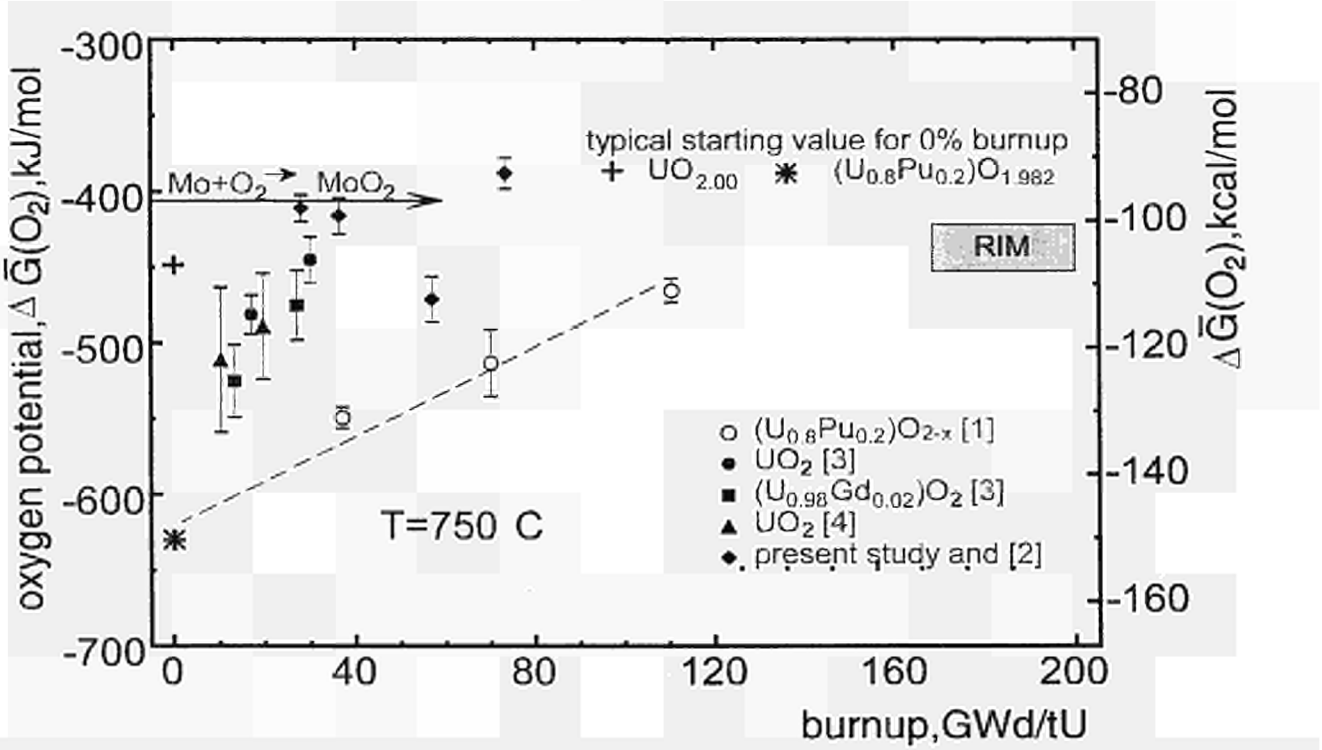

Fig. 1.9 Burnup dependence of the oxygen potential at 750 °C for different irradiated oxide fuels (UO_2, (U, Gd)O_2 and (U, Pu)O_2) [1-4]. The threshold of Mo oxidation ($Mo + O_2 \rightarrow MoO_2$) is also shown. The square labelled Rim shows the results obtained in the last reporting period with 3 fuel pieces from the Rim region of the fuel with up to 200 GWd/tM burnup.

metal particles, or it can be present as oxide. Recent work on SIMFUEL has indeed shown that Mo oxidizes before the UO_2 matrix does [5]. We thus can conclude that oxygen buffering by the oxidation of Mo, aided by the formation of the interaction layer between clad and fuel, causes the oxygen potential to increase only in the first irradiation period and then to remain quasi-constant (at e.g. about -400 kJ/mol at 750 °C). At such an oxygen potential, and depending on the kinetics, Cs-zirconates, -uranates and -molybdates can form besides MoO_2, ZrO_2, CsI, Cs_2Te etc.

The implications are manifold. We can conclude that:

- the needles sometimes observed in (intact) irradiated fuels are not U_4O_9
- high temperature matter transport processes (e.g. fission gas release, creep) in the fuel matrix are not enhanced due to excess oxygen (excess oxygen is known to enhance these processes)
- the technologically important Rim structure is not caused by Pu-fission and oxidation of the fuel matrix, but it is due to the inherent properties of the UO_2 lattice.

References

[1] Hj. Matzke, J. Ottaviani, D. Pellottiero, J. Rouault; J. Nucl. Mater. **166** (1988) 142

[2] Hj. Matzke; J. Nucl. Mater. **208** (1994) 18

[3] K. Une, Y. Tominaga, S. Kashibe; J. Nucl. Sci. Techn. (Japan) **28** (1988) 142

[4] M. G. Adamson, E. A. Aitken, S. K. Evans, J. H. Davies; in Thermodynamics of Nuclear Materials 1974, vol. I (IAEA, Vienna, 1975) 79

[5] Unpublished cooperative work Hj. Matzke, P.G. Lucuta; (AECL Chalk River, Canada)

Coulometric titration of simulated fuel (SIMFUEL) and UO_2

The emf cell previously used for oxygen potential measurements on LWR fuels [1-3] has been modified by attaching a constant current source to the cell. Predetermined quantities of oxygen can be moved between the specimen and the reference electrode (Fe/FeO) through the solid electrolyte (Y_2O_3 doped ThO_2). Knowing the mass of the specimen, and the time and intensity of the applied current, the transfer of oxygen corresponds to a change of the composition of the sample, i.e. the oxygen/metal ratio, according to the following equation:

$$\frac{\Delta x \cdot W \cdot F \cdot z}{W_{mol}} = I \cdot t$$

where:
Δx = change of composition
W = weight of the specimen (g)
F = 96485.31 Coulomb.mol (Faraday constant)
z = 2 (valence of oxygen)

W_{mol} = molar weight of the oxide (g)
I = current intensity (A)
t = time (s)

The changes of composition are verified by measuring the emf potential after each current insertion. Quite long equilibration times (hours, or even days) are often necessary before obtaining a stable reading of the emf potential: these times decrease with increasing temperature and decreasing intensity of the insertion current (larger oxygen diffusion coefficient and smaller amounts of oxygen to diffuse into the specimen). Oxidation and reduction were performed on unirradiated UO_{2+x} by varying the oxygen/metal ratio between 2.03 and 2.09, at constant temperatures (in the interval between 800 °C and 1050 °C) in order to calibrate the device. The results obtained show good reproducibility and are in good agreement with the expected values, particularly those obtained at higher temperature. Oxygen to metal ratios around stoichiometry are currently being tested. SIMFUEL specimens will be analyzed in the next reporting period.

The apparatus currently in use is in a contaminated glove box; a second apparatus is being set up in a non-contaminated laboratory, in order to be able to perform surface characterisation analysis on the specimens after the current insertions.

References

[1] Institute for Transuranium Elements, report EUR 14493 (1992), Annual Report 1991, p. 33
[2] Hj. Matzke, V. Tebaldi; Technical Note K 0293170, Institute for Transuranium Elements, Karlsruhe, June 1993
[3] Hj. Matzke, J. Nucl. Mater. **208** (1994) 18

Thermal conductivity of simulated high burnup UO_2 fuel (SIMFUEL)

Measurements of the thermal conductivity λ of UO_2 and 1.5, 3 and 8 a/o simulated burnup UO_2 (SIMFUEL, [1]) were reported previously (TUAR-91 p. 26 and TUAR-92, p. 24). A modelling activity of these results was reported in TUAR-93, p. 30. The results included a correction for precipitated phases and the evaluation of the intrinsic thermal conductivity of the UO_2-based fluorite matrix. Also, the strength of phonon scattering by dissolved fission products (f.p.) could be evaluated, based on two approaches: i) considering the effect of the fission products on the phonon heat current and ii) considering the effect of the mass difference between the host U atoms and the dissolved fission products.

These theoretical approaches described and explained the important degradation of λ of UO_2 due to dissolved f.p. The work, performed in cooperation with Chalk River, AECL, Canada, was extended and concluded in the reporting period. The final results were published [2]. The analysis revealed the following features of the thermal conductivity of near-stoichiometric SIMFUEL

- the effect of the solid precipitated phases in SIMFUEL and irradiated high-burnup fuel can be accounted for in the same manner as spherical porosity, using a combined porosity-precipitates correction factor (gas bubbles were not considered here);

- the effect of the phonon scattering by the dissolved fission products explains the reduction in the matrix thermal conductivity for various burnup compositions; and

- the linear parametric dependence of thermal resistivity with burnup could describe the overall burnup effect (dissolved and precipitated fission products), or only the burnup effect on the fluorite matrix (dissolved fission products) for computer code modelling.

The experimental work was extended in the reporting period towards measurements of λ in hyperstoichiometric UO_{2+x} and in slightly oxidized SIMFUEL, again in cooperation with Chalk River, AECL, Canada.

Though our oxygen potential measurements have shown that normal LWR fuels do not oxidize during irradiation (see contribution above), excess oxygen strongly affects fuel properties and behaviour in defected fuels. Also, fuel with graphite inside coating of the clad (CANLUB concept) may possibly oxidize slightly during irradiation. There are limited data available for UO_{2+x} [3, 4], but no results exist for high burnup UO_{2+x}. We have therefore measured the thermal diffusivity of UO_2 and 3% SIMFUEL preheated in different atmospheres and at different temperatures. Annealing in Ar+4 % H_2 at 1700 °C ($\Delta\overline{G}(O_2) = -530\,kJ/mol$) yielded stoichiometric specimens for comparison, annealing in $CO_2/CO = 9$ at 1310 °C ($\Delta\overline{G}(O_2) = -232\,kJ/mol$) yielded $UO_{2.007}$. Two further anneals in $CO_2/CO = 99$ at 1220 and 1380 °C yielded $UO_{2.035}$ and $UO_{2.084}$, respectively.

Thermal diffusivity was measured by the laser-flash method from room temperature to 1500 °C. The thermal diffusivity was determined from the rear-surface temperature rise, after the front surface of the sample was heated by the laser beam at various temperatures obtained by heating the sample in a graphite furnace, and the results were checked during the cooling cycle. The measurements were performed in vacuum (10^{-6} torr). No major changes in the oxidation state (O/U ratio) of the specimens were detected after the thermal diffusivity.

The specific heat of SIMFUEL was also measured between 25 and 1500 °C using a differential scanning calo-

rimeter (DSC) with sapphire as a reference material. The standard and sample, both placed in pans, were heated, and the differential power required to achieve the same temperature in both samples was recorded. The specific heat of SIMFUEL specimens was computed from the mass of the sapphire standard, the differential power and the known specific heat of the sapphire.

Results

The thermal conductivity λ was calculated from the thermal diffusivity α, specific heat c_p and density ρ, using the standard expression

$$\lambda = \alpha \cdot c_p \cdot \rho$$

The density was corrected for temperature using the thermal expansion coefficient of UO_2 [5] for both hyperstoichiometric UO_{2+x} and SIMFUEL specimens. The thermal conductivity results were normalized to 95% and 100% of the theoretical density (TD), applying corrections for the porosity using the Loeb equation [6]:

$$\lambda = \lambda_{TD} \cdot (1 - \beta \cdot P)$$

where P is the pore volume fraction ($P = 1 - \rho/\rho_{TD}$), β is a constant, and the subscript TD refers to a 100% theoretical density sample. The value for β, including its temperature dependence, reported by Notley and McEwan [7] ($2.58 - 0.58\ 10^{-3} \cdot T$), was used. (T is the temperature in degree Kelvin).

The λ-values obtained in this way are shown in Fig. 1.10 for UO_2 and UO_{2+x} and in Fig. 1.11 for 3% SIMFUEL at different oxidation levels. The thermal conductivity of UO_{2+x} is seen to decrease with increasing O/U ratio: a reduction of 13%, 37% and 56% at 600 °C and 11%, 23% and 33% at 1500 °C was found for O/U ratios of 2.007, 2.035 and 2.084, respectively.

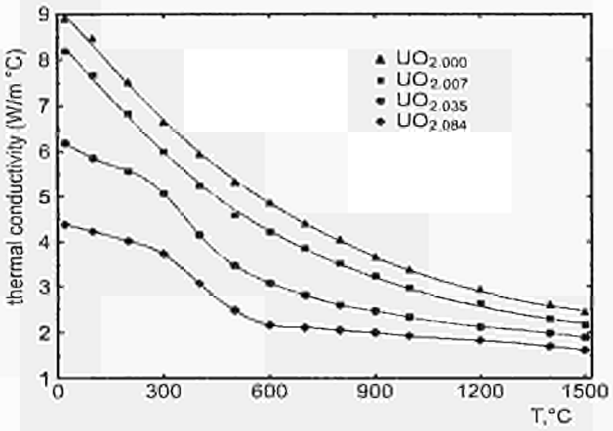

Fig. 1.10 Thermal conductivity (normalized to 100% of TD) of stoichiometric UO_2 and of hyperstoichiometric UO_{2+x} as a function of temperature.

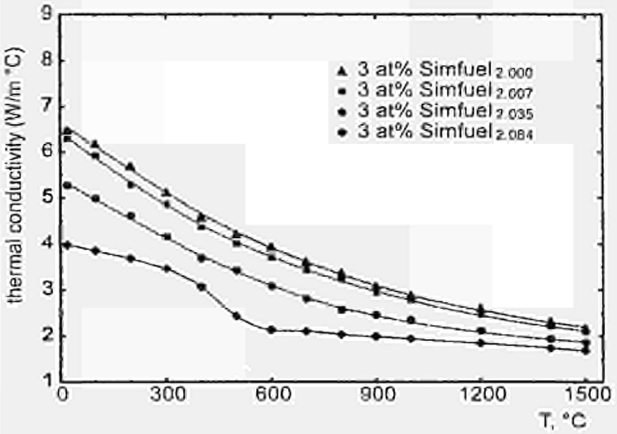

Fig. 1.11 Thermal conductivity of 3 a/o burnup SIMFUEL at various oxygen potentials ($\Delta\overline{G}(O_2)$ = -550, -245, -205 and -160 kJ/mol (see text); 100 % TD) as a function of temperature. The label indicates the equivalent deviation from stoichiometry measured in the reference UO_2.

Below 600 °C, a change in the slope of the thermal conductivity curve of UO_{2+x} occurred for deviations from stoichiometry of 0.035 and 0.084. This anomaly in the thermal conductivity variation with the temperature is associated with the phase change from U_4O_9 to UO_{2+x}. Precipitation of the U_4O_9 phase, identified by X-ray diffraction (XRD) could not be avoided, despite the careful preparation of the UO_{2+x} specimens. Hence, below 600 °C, the measured thermal conductivity values are not valid for UO_{2+x}, for $x \geq 0.035$. The reduction measured by us in the thermal conductivity of hyperstoichiometric UO_{2+x} is in good agreement with the previously reported results; for example, our values for $UO_{2.035}$ match well those obtained by Goldsmith and Douglas [3] for $UO_{2.04}$ between 600 °C and 1000 °C.

The thermal conductivity values obtained from hyperstoichiometric 3 a/o SIMFUEL also decreases with temperature for each oxygen potential. The thermal conductivities of hyperstoichiometric SIMFUEL were lower than those measured on the specimens annealed under reducing conditions (-540 kJ/mol). For an oxygen potential of -245 kJ/mol (x=0.007 in UO_{2+x}), the change in thermal conductivity for 3 a/o SIMFUEL was very small. At higher oxygen potential, a similar reduction to that observed for UO_{2+x} was found for SIMFUEL. The anomaly due to U_4O_9 formation was only seen at highest oxidation state.

The measurements will in future be extended to 8 a/o SIMFUEL, and a careful modelling evaluation will be performed. The results obtained so far lead to the following conclusions:

- Thermal conductivities of hyperstoichiometric UO_{2+x} are lower than those of stoichiometric UO_2, in the temperature range of 600 to 1500 °C where U_4O_9 does not form.

- The thermal conductivity of hyperstoichiometric SIMFUEL at high oxygen potentials is also reduced compared with the samples annealed in reducing conditions.

- Simulated burnup does not play any major role at high oxygen potentials, or alternately, excess oxygen is the dominant factor contributing to thermal conductivity degradation at high oxygen potentials.

References

[1] P. G. Lucuta, R. A. Verrall, Hj. Matzke, B. Palmer; J. Nucl. Mater. **178** (1991) 48

[2] P. G. Lucuta, Hj. Matzke, R. A. Verrall; J. Nucl. Mater. **217** (1994) 279

[3] L. A. Goldsmith, J.A.M. Douglas; "Measurements on Thermal Conductivity of Uranium Dioxide at 670 - 1270 K," UKAEA report TGR 2103 (w) (1971)

[4] I. C. Hobson, R. Taylor, J. B. Ainscough; J. Phys. D: Appl. Phys. **7** (1974) 1003

[5] MATPRO - A Handbook of Materials Properties for Use in the Analysis of Light Water Reactor Fuel Rod Behaviour, TREE-NUREG-1005, EG&G Idaho, Inc (1989)

[6] A. L. Loeb; J. Am. Ceram. Soc. **37** (1954) 96

[7] M. J. F. Notley, J. R. McEwan; Nucl. Appl. Technol. **2** (1966) 117

Mechanical properties of SIMFUEL

Very little knowledge exists on the mechanical properties of high burnup UO_2 fuel though these properties are of utmost importance for fuel performance. As shown before for other thermophysical properties (e.g. melting behaviour, gas release, etc.) SIMFUEL is a good stand-in for fully active reactor irradiated UO_2 to perform high temperature property measurements. For instance, creep machines are not available in any hot cell at present whereas SIMFUEL can be investigated in an actinide laboratory. To fill this important gap in the present knowledge, creep measurements were started on SIMFUEL and the hot hardness was measured, both relative to UO_2.

Creep measurements

Experimental

An existing Tinius-Olsen testing machine was to be used to measure the thermal creep of UO_2 and of SIMFUEL under compression. In first preliminary tests, SIMFUEL showed very low creep rates. A number of improvements had to be carried out on the testing machine before the very low creep rates of SIMFUEL could be reliably measured. Such experiments need high precision in displacement measurements which have to be stable for long times (a few days at the set temperature).

Effects of the day/night temperature variations produced by the laboratory ventilation system had to be eliminated by heating the four structural columns of the testing machine and operating the ventilation system during the full duration of the test. The creep machine operated with SiC pistons contacting the sample. At the experimental temperature of 1350 °C and the stresses used (15 to 200 MPa), the UO_2 showed a slight reaction with SiC and a deformation on the SiC piston occurred which was larger than the deformation of the UO_2 specimen. In order to simultaneously reduce the tension, and so the deformation, on the SiC-piston, it was decided to use discs of a refractory metal or metal alloy with a very low creep rate and a diameter about 3 times greater than the sample, giving a stress reduction factor of almost one order of magnitude. The tungsten alloy with 2% ThO_2 was selected because of its availability and very low creep rate [1,2].

With these improvements, very low creep rates of $d\varepsilon/dt$ $\sim 10^{-5}$ h^{-1} could be measured. This limit is identical with the lowest creep data reported in the literature and is due to some remaining deformation of SiC. The modified and improved machine uses three displacement gauges, both mechanical and electrical. As an example, all gauges showed displacements of about 20 μm after 50 h in an experiment with 8 a/o SIMFUEL at 20 MPa, although the SIMFUEL was not measurably deformed (measurement error ± 2 μm). To extend the creep detection range down to rates of 10^{-6} h^{-1}, the SiC-pistons will be replaced by tungsten alloy pistons.

Results

In the present first series of experiments, the temperature was kept constant at 1350 °C and the stress was varied between σ = 15 and 200 MPa. UO_2 pellets from different batches were used to compare the results with those for SIMFUEL with 8 a/o simulated burnup. A typical example for an intermediate stress of 80 MPa is shown in Fig. 1.12. It is evident that SIMFUEL creeps much less than UO_2; its creep rate is lower by about a factor of 50 (at σ = 80 MPa) than that of UO_2 (a small displacement within the test machine caused the step of 5 μm after 2 h). The results obtained so far are given in Fig. 1.13. The present values for UO_2 are in good agreement with existing values [1, 3, 4]. All creep rates for 8 a/o SIMFUEL are lower than those for UO_2 and are all at the conventional detection limit for creep at 1350 °C. Because of the reasons described above, and because of the low creep rates, the experimental scatter is rather large. Note that the two higher points were obtained in shorter experiments (as in Fig. 1.12). Therefore, there might have been a contribution of primary creep to the very small total strain. The lower points are thus thought to be the most representative.

Hot hardness

Experimental and results

Vickers indentations (16.8 or 21 N, 15 sec) were made in UO_2 and SIMFUEL for 3, 6 and 8 a/o burnup between

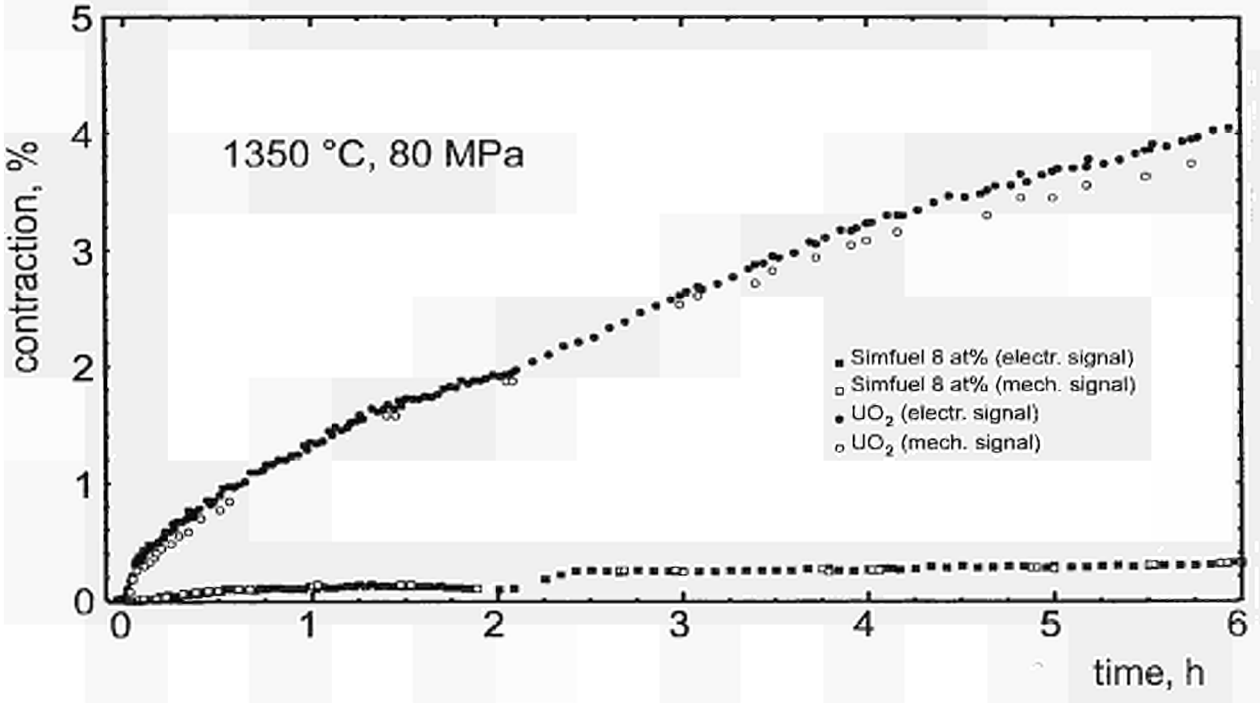

Fig. 1.12 Creep experiment at 1350 °C, 80 MPa, comparing the behaviour of UO_2 with that of 8 a/o burnup SIMFUEL.

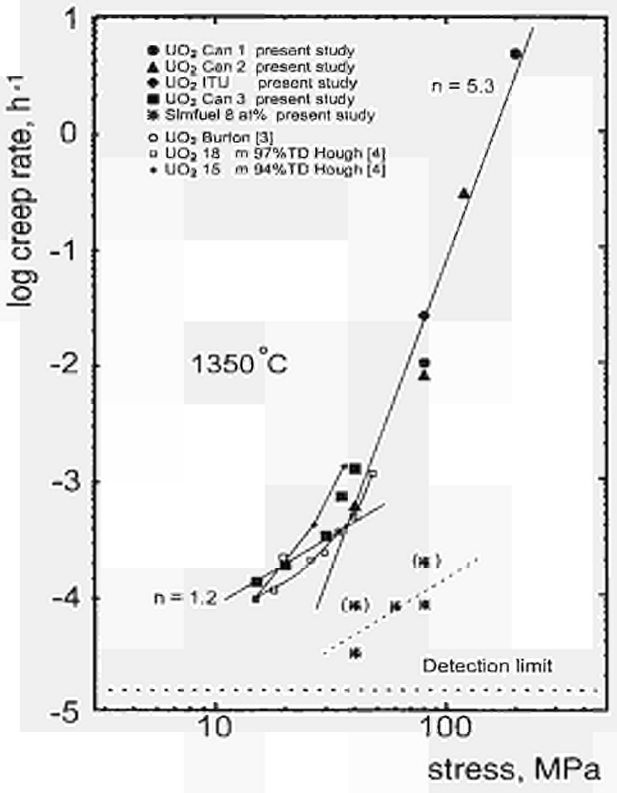

Fig. 1.13 Stress dependence of creep, comparing UO_2 with 8 a/o burnup SIMFUEL. For UO_2, literature data are included. For SIMFUEL, the short time experiments are given in brackets.

room temperature and 900 °C. Both specimen and indentor were preheated such that no temperature gradient existed between indentor and specimen. The hardness of UO_2 decreased from 530 to 100 kp/mm^2 (5.2 to 0.98 GPa) in this temperature range, in good agreement with literature data [5]. All SIMFUEL specimens were consistently harder than those of UO_2 at all temperatures, e.g., the hot hardness of 8 a/o burnup SIMFUEL at 500°C, a typical temperature of the fuel in contact with the clad, was higher than that of UO_2 by about 150 kp/m^2 (1.47 GPa); 3 and 6 a/o SIMFUEL results fall in between these values, as shown in Fig. 1.14.

Conclusions

The present results on creep and hot hardness are the first data on the effect of fission products dissolved and/or precipitated in SIMFUEL on thermomechanical proper-

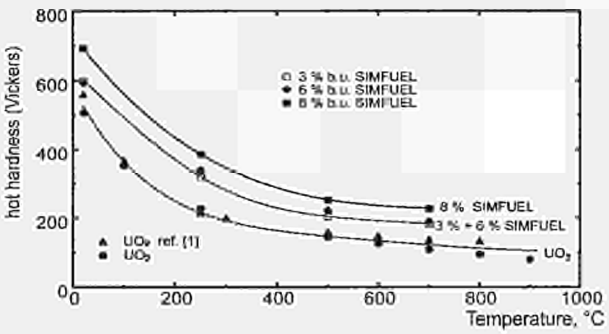

Fig. 1.14 Vickers hardness of UO_2 and of 3, 6 and 8 a/o SIMFUEL as a function of temperature.

ties. Just as the thermal conductivity (see above), hardness and creep rates become less favorable with burnup: UO_2 shows reduced thermal conductivity, reduced creep rates and increased hardness with increasing burnup. Whereas the present hot hardness results indicate a continuous degradation with burnup up to 8 a/o as observed for the thermal conductivity, there are not enough data available so far for a similar conclusion for creep to be reached. Such data will be measured in the next reporting period with the modified, improved machine.

Whenever deformations are produced at constant stress, at elevated temperature, and over an extended period of time, a creep curve is obtained, i.e. a curve of the change of strain with time. Following an initial elastic extension, usually two types of creep behaviour can be distinguished: primary (or transient) creep in which the creep rate $d\varepsilon/dt$ decreases with time, followed by a period of a (smaller) constant creep rate (secondary or steady-state creep). Only the latter type is discussed here. Primary creep can be clearly seen in about the first hour in Fig. 1.12. Both types of creep were much slower in SIMFUEL.

It is known for UO_2 [1,3,4] that there is a transition point in the stress dependence. Plots of creep rate $d\varepsilon/dt$ versus σ (at constant temperature) show a slope $n \approx 1$ to 1.4 at low stresses and a slope of $n \approx 4.5$ to 6 for high stresses. The relation used to describe the creep rate is

$$d\varepsilon/dt = A \cdot d^{-m} \cdot \sigma^{n} \cdot e^{-(Q/RT)}$$

where A is a constant, d is the grain size and Q is the activation energy. Diffusion controlled creep has a stress exponent n = 1, whereas creep rate-controlled by dislocation climb has a stress exponent of n = 5 [6]. Thus a change of creep mechanism from rate control by U-diffusion to dislocation climb is expected for UO_2 and is indeed indicated in the present results for UO_2 as well (see Fig. 1.13), where slopes of n = 1.2 and n = 5.3 are represented by the two lines through the data points for UO_2. The transition occurs between 30 and 40 MPa, again in agreement with literature data. For SIMFUEL 8 a/o, much lower rates are found. Also, though only three stresses were used, the expected stress exponent of $n \approx 1$ is indicated to be valid to higher stresses than for UO_2. Future experiments with higher stresses up to 200 MPa will be carried out to define more satisfactorily the transition stress for SIMFUEL.

References

[1] M. S. Seltzer, A. H. Clauer and B. A. Wilcox; J. Nucl. Mater. **44** (1972) 43

[2] H. E. Boyer; (ed.), Atlas of Creep and Stress-Rupture Curves, Metals Park Ohio, ASM International (1988)

[3] B. Burton; Diffusional Creep of Polycrystalline Materials, Trans tech Publications, Switzerland (1977)

[4] A. Hough; Compressive Creep in Nuclear Oxides; report AERE R 13232 (1988)

[5] G. Engelhardt and H. Hoffmann; Mechanische Eigenschaften von UO_2, report KfK-729 / EUR 3729 d (1968)

[6] Hj. Matzke; Science of Advanced LMFBR Fuels, A Monograph on Solid State Physics, Chemistry and Technology of Carbides, Nitrides and Carbonitrides of Uranium and Plutonium, North-Holland, Amsterdam (1986), Appendix 5

Behaviour of volatile fission products in UO_2

The theoretical model developed to study the evolution of fission gas bubbles in UO_2 [1, 2], which had been used to analyse the size distribution of fission gas bubbles in reactor-irradiated UO_2 following furnace anneals (see TUAR-92, p. 27, and [3]), has now been applied to analyse experimental data [4] on bubbles containing Rb, Cs, I or Te as fission products. Despite the considerable effort devoted to studying the behaviour of volatile fission products (VFPs) in oxide nuclear fuel, the rate-controlling processes of VFP release are still not completely understood. A reduction of the gap in our knowledge of VFP release mechanisms is very important for the correct estimation of the rates of VFP release under steady-state, transient or accident irradiation conditions. The behaviour of the volatiles Rb, Cs, I and Te is of special interest in fuel chemistry because of their radiotoxicity. So far only few well-characterized data exist for the release of VFPs other than fission rare gases (Xe and Kr).

Taking into account the complexity of the matter transport processes in irradiated nuclear fuels, separate effect studies are needed to reduce the existing uncertainties. Ion implantation has been shown to be a very valuable experimental approach for this purpose: Ion implantation data are ideally suited for the theoretical modelling of the development of fission product porosity because the type and concentration of VFPs can easily be varied and controlled.

Transmission electron microscopy (TEM) studies of UO_2 specimens ion-implanted with Kr, Rb, Cs, and Te [4, 5] and subjected to annealing treatments were used for comparison with model predictions. Ion implantation was performed at energies of about 40 keV and total doses of 5×10^{15} (Rb, Te and I), 1×10^{16} (Kr, Cs and I) and 2×10^{16} (Te) ions/cm^2. All implantations were done at ambient temperature. Following implantation, the specimens were annealed for one hour in the temperature range from 773 to 1773 K. Available TEM data of matrix bubble size distributions for Rb and I for different annealing temperatures were chosen for the comparison with model predictions. Fig. 1.15 shows a typical example of the available micrographs. These careful TEM studies allowed size distributions for spherical bubbles, for faceted bubbles in the UO_2 matrix as well as for bubbles linked to dislocations to be determined. Only the first of these three classes is considered in the following.

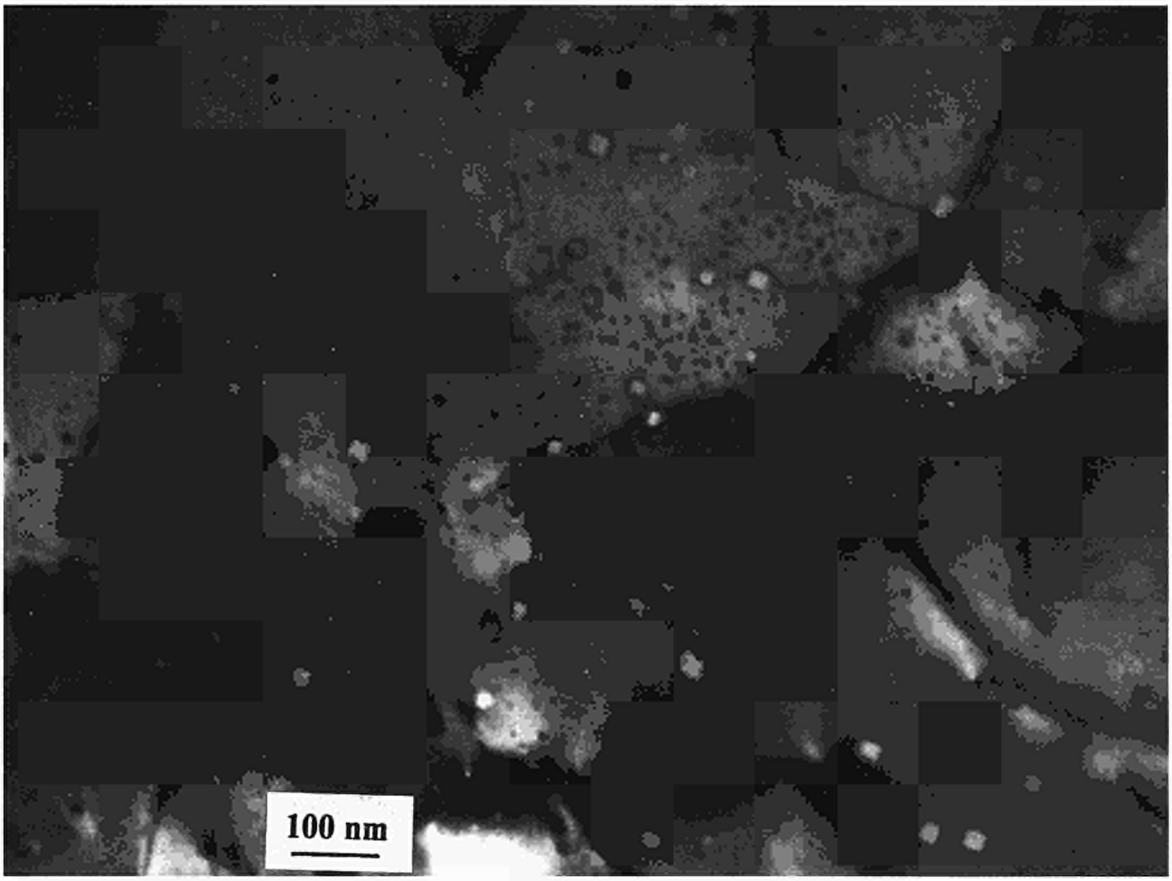

Fig. 1.15 Transmission electron micrograph of UO_2 implanted with Te-ions and annealed upto 1372 K.

Physical model

As in the previous work [3], it was assumed that random bubble migration and coalescence of bubbles are the main mechanisms of their growth. Bubbles are taken to be spherical and in equilibrium. The equation of state (EOS) chosen for the description of the VFP gaseous state in the bubbles was the reduced Van der Vaals EOS. Appropriate EOS constants were defined on basis of the critical parameters of the VFPs. It is also assumed that VFPs are largely insoluble [6, 7] in the fuel matrix and therefore Ostwald ripening is not considered as a bubble growth mechanism. Diffusion and trapping of VFPs and bubble population development are considered in the framework of the rate-theory approach.

For the case of annealing, a system of coupled equations for $F_i^{(1)}$, the density of matrix bubbles ($\alpha = 1$), is given by [2, 3]

$$\frac{dF_i^{(1)}}{dt} = \sum_{j=1}^{J} W_{j,i-j}^{(1,1)} - \sum_{\alpha=1}^{4} \left\{ \sum_{j=1}^{N} W_{ij}^{(1,\alpha)} + (1-\delta_{\alpha,1})\Phi_i^{(1,\alpha)} \right\}$$

where $W_{ij}^{(1,\alpha)} = 4\pi(r_i + r_j)(D_i + D_j) F_i^{(1)} F_j^{(\alpha=1,2,3,4)}$ is the rate of collisions between matrix bubbles with radii r_i and bubbles with radii r_j in the matrix, at dislocations ($\alpha = 2$), grain faces ($\alpha = 3$), or grain edges ($\alpha = 4$) and D_i and D_j are the diffusion coefficients, respectively. $\Phi_i^{(1,\alpha)}$ is the rate of matrix bubble trapping by the bubble-free parts of the dislocations or grain boundaries.

The equations for the bubbles at dislocations, grain faces or grain edges are given in [3] and are not reproduced here. Bubble migration is assumed to be caused by mass transport both on the bubble surface and through the matrix around the bubble. Therefore, the bubble diffusion coefficient is given by $D_i = D_i^{(s)} + D_i^{(v)}$,

where $D_i^{(s)} = \frac{3}{2\pi} D_s(r_i) \left(\frac{\Omega^{1/3}}{r_i}\right)^4 \left(1 - \frac{q}{4\pi r_i^3/3}\right)^{m_i}$

for the surface diffusion mechanism and

$$D_i^{(v)} = \frac{3}{4\pi} D_v \left(\frac{\Omega^{1/3}}{r_i}\right)^3$$

for the volume diffusion mechanism. Ω is the atomic volume, q is the bubble diffusion suppression parameter or the adatom interaction zone, m_i is the number of gas atoms in the bubble and D_v is the volume diffusion coefficient. The surface diffusion coefficient on the bubble sur-

face is $D_s(r_i) = D_{s0} \exp\left(-\frac{2\gamma\Omega}{r_i kT}\right)$

where D_{s0} is the surface diffusion coefficient on the flat surface and γ is the surface energy.

The model calculations were performed with the parameters (Ω, D_v, D_{s0}, γ) as in TUAR-92, p. 28. During test model calculations, it become obvious that there is a very weak dependence only of the model results on the values of VFP atomic diffusion coefficients. Therefore, the diffusion coefficient of the fission rare gas Xe was chosen for all types of VFPs.

Results

Experimental and predicted bubble size distributions as a function of annealing temperature for Rb and I are shown in Figs. 1.16 and 1.17. The model predictions for the Cs and Te bubbles are not shown since, with the above model assumptions they did not differ appreciably from those for the Rb and I bubbles. The dependencies of VFP total bubble densities and mean radii on the annealing temperature are shown in Fig. 1.18. Predicted and experimental data for the fission rare gas (Kr) are also shown for comparison.

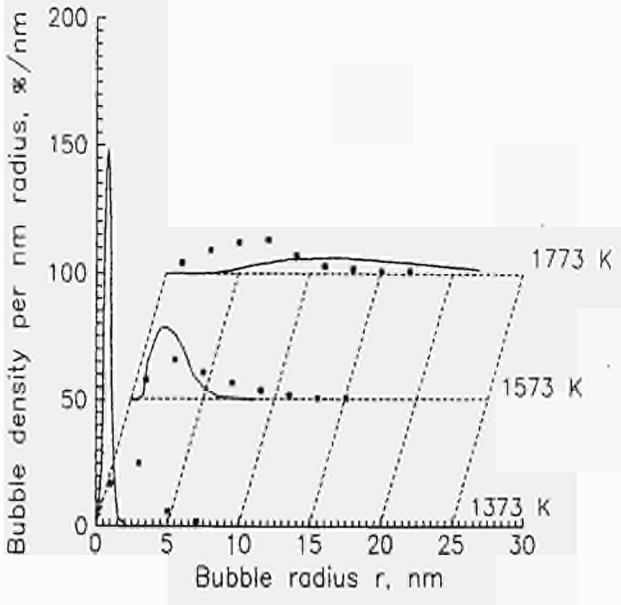

Fig. 1.16 Calculated and experimental (black squares) [4] size distributions of rubidium bubbles in UO_2 after annealing for 1 h as a function of annealing temperature. Each bubble size distribution is normalized to the total number of bubbles.

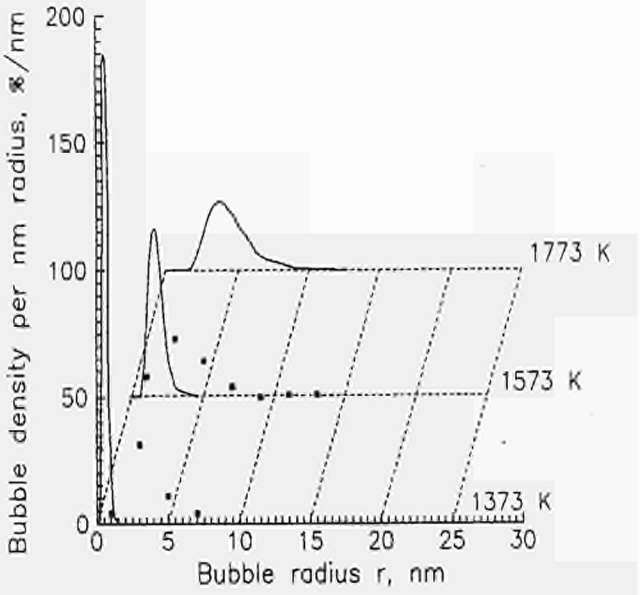

Fig. 1.17 Calculated and experimental (black squares) [4] size distributions of iodine bubbles in UO_2 after annealing for 1 h as a function of annealing temperature. Each bubble size distribution is normalized to the total number of bubbles.

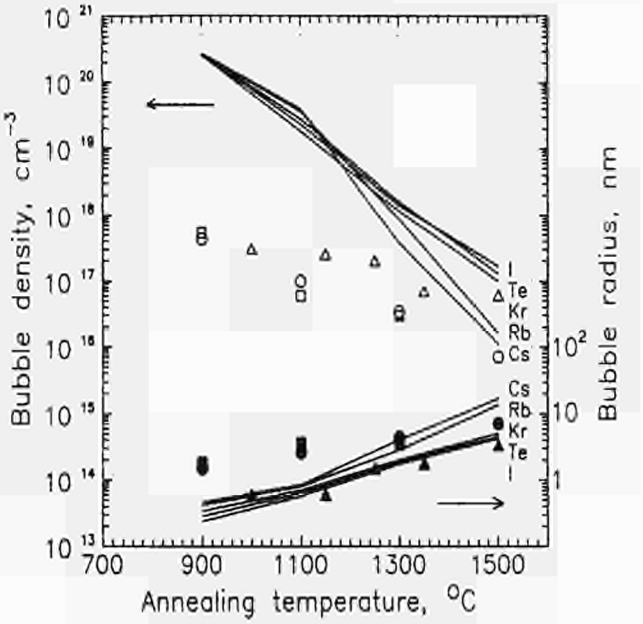

Fig. 1.18 Calculated (solid lines) and experimental (circles, squares and triangles) volatile fission product bubble densities (open symbols) and mean radii in UO_2 after annealing for 1 h as a function of annealing temperature.(circle-Rb, square-I and triangle-Kr)

Discussion

The ion implantation data have undoubtedly advantages over data from measurements on reactor irradiated specimens because the type of VFP implanted into the fuel

matrix can be controlled and only one VFP is implanted into a given specimen. This allows a separate study of the influence of different VFPs on bubble evolution which is completely impossible under reactor irradiation when bubbles are filled with the mixture of different VFPs. The composition of this mixture is not constant and depends on burnup and temperature.

The model predictions show that for the condition of insolubility of VFP in the fuel matrix, the development of bubble size distributions is practically insensitive to the VFP diffusion properties. This is evident because after a relatively short time (its value depends on the VFP diffusion coefficient in the fuel matrix), the majority of VFP atoms will be precipitated into bubbles. Due to their low solubility, thermal resolution of VFPs back into fuel matrix is unlikely and bubbles grow only due to the migration and coalescence mechanism (mass transport due to only the diffusion of fuel matrix atoms).

It is seen from Figs. 1.16 - 1.18, that at low temperatures there is some difference between model predictions and experiment. Bubble migration due to the volume diffusion mechanism for T = 1373 K alone is insufficient to completely explain the experimental data. However, the specimens were preannealed at a number of lower temperatures (773 K, 1023 K, 1173 K), where recovery of excess defects, in addition to radiation-enhanced diffusion during implantation, could have contributed to bubble growth. In fact, large concentrations of bubbles with radii between 1 and 4 nm were already seen at 1023 and 1173 K. In Fig. 1.18 it can also be seen that the volatiles can be divided into two groups (Cs with Rb and I with Te). Reasoning from the model assumptions, this is connected with the form of the EOS. For the reduced Van der Vaals EOS used in the model, a relatively weak dependence on Van der Vaals constants was obtained. In spite of great uncertainties in using such a form of EOS for the VFPs other than fission rare gases, the predicted tendency does not contradict the available experimental data (Fig. 1.18). Reasons for the fact that at the lower temperatures the experimental bubble density is smaller and the bubble radii are larger than expected have been given above.

Generally, a reasonable good agreement was found between model predictions and experiments at higher temperatures. The bubble migration concept is most useful just in this temperature range for which the observed bubble size distributions can be better reproduced by model calculations. The model shows that the surface diffusion mechanism has only a minor influence under the conditions considered.

It is interesting to note that three of the four main reasons for suppression of surface diffusion in reactor-irradiated UO_2 are not applicable in the present study on ion-implanted UO_2. This is the case for

i) contamination of the bubble surface with other fission products and
ii) pinning of bubbles on metallic precipitates (so-called five metal particles consisting of the fission products Pd, Ru, Rh, Tc and Mo). Such fission products were not present in the ion-implanted specimens.
iii) a further well documented mechanism reducing surface diffusion is that of faceting of bubbles. Faceted bubbles were excluded by careful TEM analysis as were bubbles pinned at dislocations.

This leaves the suppression due to the inhibition of the mobility of surface adatoms by the space required for the jump-step being occupied by VFP atoms as likely reason.

Conclusions

The main conclusions of the present study are as follows:

(1) The behaviour of different volatile fission product bubbles in UO_2 has many similar features regardless of the type of fission product (including fission rare gases).

(2) Bubble migration and coalescence can be considered as the main mechanism of VFP bubble growth in ion-implanted UO_2 at annealing temperatures higher than 1373 K.

(3) Migration of volatile fission product bubbles is caused mainly by the volume diffusion mechanism.

It should be emphasized that a better knowledge of the solubilities, of the equation of state in the gaseous phase of VFPs and their diffusion properties will probably influence to some extent the conclusions made. Therefore, a study of these quantities would be extremely useful to obtain a more reliable basis for model predictions.

References

[1] E. Ya. Mikhlin, V. F. Chkuaseli; J. Nucl. Mater. **105** (1982) 230
[2] V. F. Chkuaseli; J. Nucl. Mater. **188** (1992) 258
[3] V. F. Chkuaseli, Hj. Matzke; J. Nucl. Mater. **201** (1993) 96
[4] Hj. Matzke, I. L. F. Ray and R.A. Verrall; Proc. Int. Working Group on Water Reactor Performance and Technology, IWGFPT/27, IAEA, Vienna (1987) p.183
[5] Hj. Matzke, I. L. F. Ray; European Institute for Transuranium Elements, Annual Report 1987, EUR 11783 EN (1988) p. 88
[6] H. Kleykamp; J. Nucl. Mater. **131** (1985) 221
[7] R. W. Grimes, C. R. A. Catlow; Phil. Trans. R. Soc. Lond. **A335** (1991) 609

The effect of gas concentration on the behaviour of Xe in UO_2

Atomistic computer simulation in combination with a simple statistical mechanics treatment was used to investi-

gate the importance of gas concentration for the behaviour of Xe in UO_2. As one of the major fission products, the behaviour of Xe in uranium dioxide has been a focus of considerable experimental and theoretical attention since the early days of the nuclear industry. Concern has particularly centred on its important role in fuel swelling and this has accordingly led to a desire to obtain a greater understanding of the basic processes governing its migration and trapping within the fuel.

There are many factors which determine the behaviour of Xe in nuclear fuels. A review of the most important points has been published previously [1]. In the present activity, we confined ourselves, in the main, to an investigation of the behaviour of single isolated atoms of Xe in stoichiometric UO_2. It became apparent that in the process of doing this, some insights into the experimental work on non-stoichiometric UO_{2+x} can also be obtained.

It is well known [e.g. 1], that trapping of Xe occurs rather fast during irradiation due to Xe atom interaction with fission induced radiation damage. It is also well known, that Xe diffuses faster in UO_{2+x} than in stoichiometric UO_2 - at least as long as no bubbles are formed [e.g. 1-3]. Experimental [4] and computational work [5] lead to the conclusion that isolated Xe atoms are located in trivacancies (that is, bound Schottky trios consisting of a uranium vacancy and two oxygen vacancies), whereas in UO_{2+x}, Xe would be most likely to occupy single uranium vacancy sites.

Computational procedure

The formation energies of defects in uranium dioxide (such as the energies required to form vacancies, vacancy clusters, and interstitials etc.) were calculated based on the well-documented Mott-Littleton method for the computation of defect energies. The essential approach is to divide the host crystal into two regions. In the inner region, surrounding the defect, all the displacements and forces of interaction between the ions are calculated explicitly (in the present work, this region contains about 800 ions). Surrounding this inner region, the crystal is assumed to extend to infinity and interactions with ions of the inner region are assumed to be purely Coulombic in nature. The ionic displacements here are calculated by assuming that this outer region can be modelled as a dielectric continuum which may be polarised by any effective charge due to the defect centre. For these calculations, the computer program CASCADE has been used [6].

To calculate interactions between ions of the Xe-UO_2 system, a set of empirical potentials developed for the UO_2 system [7] was used. A set of potentials for the Xe interactions was then derived in a way aiming at compatibility with these. The approach used was to employ the electron gas method [8] to calculate Xe-U, Xe-O and U-O interactions. Essentially, the differences between these Xe-host and U-O interactions were used to modify the empirical U-O potential to give the "empiricised" Xe-U and Xe-O interionic potentials. Van der Vaals type forces were calculated separately using the formula of [9]. In this way, potentials were obtained for the short range part of the interaction potentials. For the long range Coulombic interactions, full formal ion charges are assumed. Ionic polarizabilities were handled via a shell model [10].

Results and discussion

The basic defect energies derived from the computer simulations are summarized in Tab. 1.2. In UO_2, the trivacancy site is found to be slightly more favourable than the divacancy. The tetravacancy consists of two U and two O vacancies bound together. It was not found to be an important Xe-site. For UO_{2-x}, Xe atoms were found to be positioned in trivacancies, and for UO_{2+x}, Xe was found to be located at uranium vacancies. The interesting point arises, when we consider the predicted concentrations of Xe at each particular site. By introducing stoichiometry and gas concentration, we can investigate the effect of continually varying these parameters upon the behaviour of Xe.

Tab. 1.2 Basic defect energies of the system Xe-stoichiometric UO_2 calculated via computer simulation. The calculated lattice energy for UO_2 was -103.1 eV.

Defect	Energy (eV)
O interstitial	-12.26
O vacancy	17.09
U vacancy	80.22
Divacancy	94.87
Trivacancy	110.47
Tetravacancy	187.69
Xe interstitial	18.67
Xe at O vacancy	32.23
Xe at U vacancy	86.05
Xe at divacancy	99.26
Xe at trivacancy	113.77
Xe at tetravacancy	191.12

In Fig. 1.19, the proportion of Xe occupying divacancy sites is plotted against the gas concentration at 1400 °C in stoichiometric UO_2. Above a certain gas concentration there is a sharp decrease in the amount of Xe in divacancies, virtually all the Xe atoms are then found at trivacancy sites. This transition coincides with the experimental data showing a pronounced decrease in the diffusion coefficient for Xe with increased gas concen-

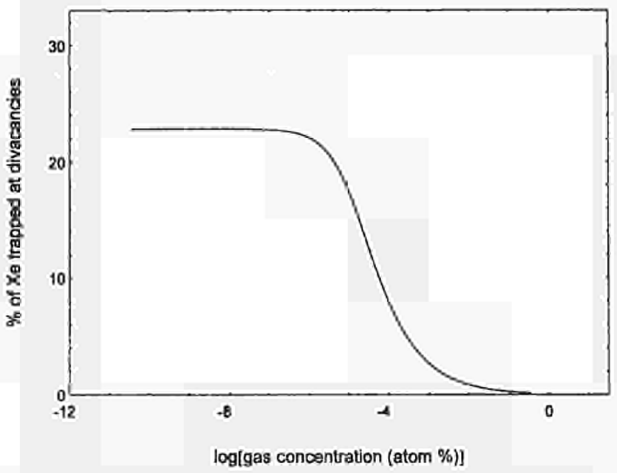

Fig. 1.19 Calculated proportion of Xe trapped at divacancy sites in stoichiometric UO_2 as a function of the gas concentration at 1400 °C. The remaining proportion of the gas is calculated to be at trivacancy sites.

tration [e.g. 1, 11]. The situation is different for small oxygen excess, as shown in Fig. 1.20. Here, divacancies may actually form the majority Xe sites for low Xe concentrations.

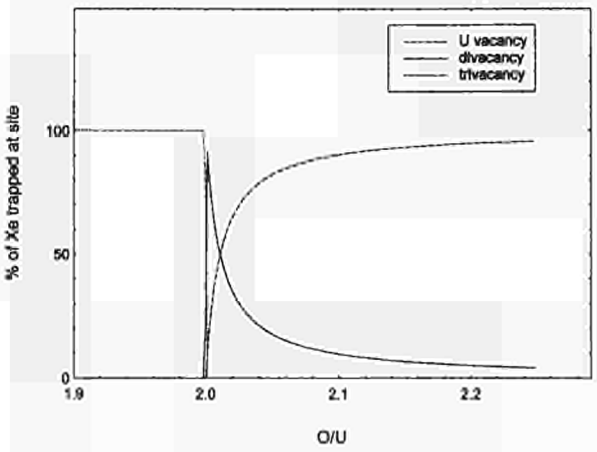

Fig. 1.20 Calculated proportion of Xe trapped at U, di-, and trivacancy sites in uranium dioxide as a function of stoichiometry. Gas concentration = 10^{-7}a/o and T = 1400 °C.

Atomic diffusion is, of course, not only a function of atom location, but also of the migration mechanism, i.e. both site and mobility are decisive. The migration mechanism of Xe in $UO_{2\pm x}$ is still not completely understood. However, if Xe in divacancies is more mobile that Xe in trivacancies we may suggest that any change in the diffusion coefficient, D_{Xe}, on going from UO_2 to UO_{2-x} reflects the transition in the Xe *location*, in a manner similar to that seen in Fig. 1.19, i.e. a reduction in D_{Xe} with increasing gas concentration. In both cases, a transition occurs from conditions where both di- and trivacancies are important Xe sites to those where Xe is located in trivacancies only.

Similarly, we expect a change in D_{Xe} when going from UO_2 to UO_{2+x} because even at very small x-values Xe is not located in trivacancies anymore, but rather in divacancies or in single U-vacancies. Such a change (increase in D_{Xe}) has been measured experimentally [2,3]. We also see in Fig. 1.20 that even very small deviations from the exact stoichiometric composition $UO_{2.000}$ cause a complete change of Xe location. Such small changes may often not have been noted in experimental work thus explaining part of the scatter in reported results.

Summary

We have calculated the effect of increasing gas concentration upon the equilibrium site of single atoms of Xe in stoichiometric UO_2. At low gas concentrations, the calculations demonstrate the importance of divacancy sites. Although these may not necessarily constitute the majority site (more Xe is to be found in trivacancies) we suggest that divacancies are an important factor in the diffusion of Xe atoms in the stoichiometric material. As gas concentration is increased, the importance of divacancy sites is diminished until most of the single Xe atoms are located in trivacancies. The transition is fairly sharp and is calculated to occur at a gas concentration of about 10^{-6} a/o. Although the actual migration mechanisms of Xe atom diffusion are beyond the intended scope of the calculations, experimental data gathered at different stoichiometries suggest that a reduction in the proportion of Xe at divacancies, would result in a lowering of D_{Xe}. As the transition mentioned above is calculated to coincide with the observed decrease in D_{Xe} [11], it is suggested that in addition to being induced by radiation damage as has been suggested, the decrease in D_{Xe} may also contain a contribution originating from a change in the site of single Xe atoms. Although our results in no way deny the importance of bubble formation and radiation damage on the behaviour of fission gases in nuclear fuels, they add an important new aspect to the atomistic picture of Xe in UO_2. Similar conclusions can be made, based on the present calculations, for the diffusion of Xe in UO_{2+x}.

References

[1] Hj. Matzke; Radiation Effects **53** (1980) 219
[2] R. Lindner and Hj. Matzke; Z. Naturforschg. **14a** (1959) 582
[3] W. Miekeley and F.W. Felix; J. Nucl. Mater. **42** (1972) 297
[4] Hj. Matzke and J. A. Davies; J. Appl. Phys. **38** (1967) 805
[5] C. R. A. Catlow; Proc. R. Soc. Lond. A. **364** (1978) 473

[6] M. Leslie; S.E.R.C. Daresbury Laboratory Report DL/SCI/TM31T (1982)
[7] R. A. Jackson, A.D. Murray, J. H. Harding, C. R. A. Catlow; Phil. Mag. A **53** (1986) 27
[8] R. G. Gordon and Y. S. Kim; J. Chem. Phys. **56** (1972) 3122
[9] J. C. Slater and J. G. Kirkwood; Phys. Rev. **37** (1931) 682
[10] B. G. Dick, Jr. and A. W. Overhauser; Phys. Rev. **112** (1958) 90
[11] R. MacEwan and W. H. Stevens; J. Nucl. Mater. **11** (1964) 77

Studies on the mechanism of damage creation in UO_2 induced by fast heavy ions

Introduction

In nuclear reactors, heat is produced by slowing down high energy heavy ions (fission products) in the fuel matrix. A thorough understanding of the physics of this process is helpful to understand the performance and behaviour of UO_2 at long operation times.

In order to extend the available knowledge on radiation damage in UO_2 [1], the damage produced by ions of an energy up to several MeV per nucleon has been studied.

Irradiation by fast heavy ions is a good tool to create microscopic defects. The defects created in the wake of a single ion, i.e. point defects, clusters, amorphisation of a crystal, may give rise to a latent track. The first step is to examine the latent tracks by TEM and to measure their radii, and also to etch them chemically. The aim of these examinations is to relate the damage mechanism to measurable parameters like ion energy, velocity and mass, and to determine the threshold energy for track formation. The specimens of Tab. 1.3 were implanted in the reporting period and the techniques to investigate the damage state have been developed. The experimental results will be communicated in the next annual report.

Experimental

Specimens to be implanted were UO_2 polished cylinders, or thin TEM disks transparent for electrons, annealed for 2 hours in Ar/H_2, at 1400 °C. Irradiations were performed at GSI (Gesellschaft für Schwerionenforschung), Darmstadt. Various types of heavy ions have been used at different doses and energies (see Tab. 1.3). Some of the samples were covered with 30m polycarbonate foils. The chemical etching of these foils permits the exact irradiation dose to be calculated. In Fig. 1.21 the tracks of Au-ions of 2.6 GeV energy in the etched foils are shown. Each black dot shows the track of one individual ion. Chemical etching can be done with maximal doses of about 10^8 ion/cm^2 because at higher dose, the risk of overlapping of the etched tracks increases. At 10^8 ions/cm^2, there is on average one track/m^2.

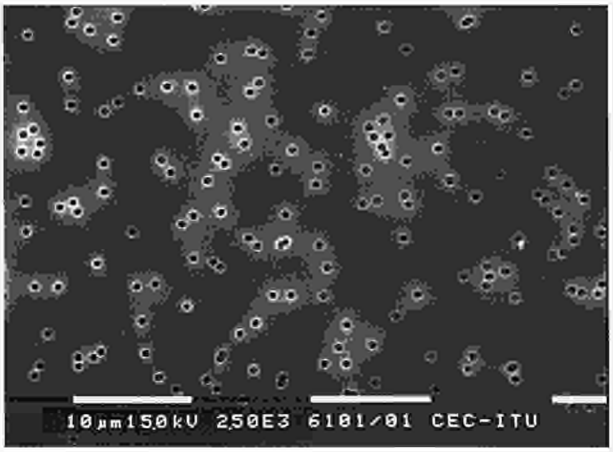

Fig. 1.21 Image of Au implanted polycarbonate foil, etched in a 6M NaOH solution, at 60 °C, for 1h.

Tab. 1.3 Conditions for some of the samples irradiated at GSI.

Target	Ion implanted	Energy (MeV/amu)	Dose (ion/cm^2)	Projected range (µm)	Beam (deg.)
UO_2 TEM disk	^{100}Mo	14	10^{10}	63	45+90
UO_2 Cylinder	^{238}U	11.4	2.10^9	52	90
UO_2 TEM disk	^{238}U	11.4	10^{10}	52	45
UO_2 TEM disk	^{120}Sn	14	10^{10}	59	45+90
UO_2 TEM disk	$^{197}Au^{25+}$	13.39	5.10^9	58	45+90
UO_2 Cylinder	$^{197}Au^{25+}$	13.39	5.10^7	58	90

Several TEM specimen preparation techniques were used in order to obtain samples which showed ion tracks along longitudinal directions. These paths have a length of several tens of micrometers at the studied energies. The best results were obtained by adopting cross-sectional TEM preparation methods. Depending on the shape of the irradiated specimens, we have developed two techniques to produce cross-sectioned UO_2 TEM disks.

In the first one, the specimen is cut vertical to the surface and the two pieces are glued together by their previous front faces, using epoxy M-bond 610, heated for 2 hours at 150 °C under pressure. It is very important that the width of the glued region between faces of the ceramic specimen is thin enough to prevent loss of the near-surface region during ion milling. A cross-sectioned slice is then ground and dimpled before being ion milled (Fig. 1.22).

For smaller specimens, thin slices have been positioned into the slit of a copper cylinder. This cylinder is glued inside a tube providing the necessary mechanical stability (Fig. 1.23). The assembly is glued together using M-bond AE15, which needs a lower hardening temperature than the M-bond 610 used to glue the specimens. Subsequently the tube is sectioned into 3 mm diameter rings which are then ground, dimpled and ion milled.

A second aim of this work is to etch the latent tracks. The etching of these tracks is based on the fact that the etch rate along the damaged zone is higher than the etch rate for the virgin bulk material and is a function of the damage density. The differential etching rate determines the geometry of the etched pores [2]. The choice of the etching acids and of the etching conditions (temperature, time, concentration of the acids) has to be optimised to obtain good results. The best conditions will be communicated in the next annual report.

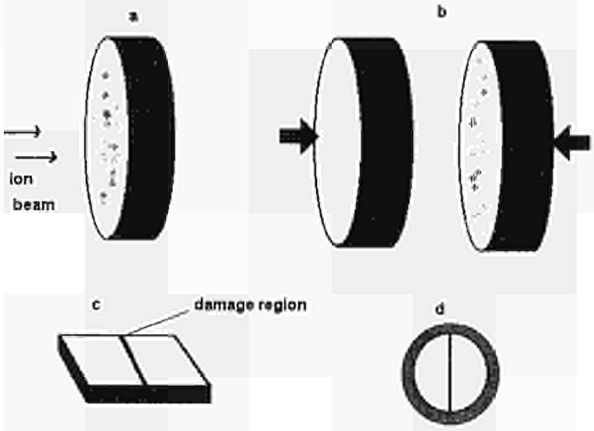

Fig 1.22 Schematic of procedure used to prepare TEM cross-section UO_2 specimens from implanted cylinders. (a) ion irradiation. (b) glued under pressure. (c) sliced, mechanically ground and dimpled. (d) mounted on support ring and ion milled.

The slowing down of energetic ions in matter

The main energy loss mechanism of fast heavy ions passing through matter is ionisation of the atoms surrounding the incoming ion path. It is well known that this mechanism can induce latent tracks in insulators [3].

At very high velocities (in excess of the orbital velocities of its electrons) all the electrons of the ion will be stripped off. The incoming nucleus suffers Coulomb collisions with the target electrons and gradually loses energy until it becomes able to capture an electron. Then the projectile continues to interact with the target electrons as a particle of charge $(Z-1)+$, until it captures a second electron, and so forth until it reaches velocities smaller than the orbital velocity of the least tightly bound electron.

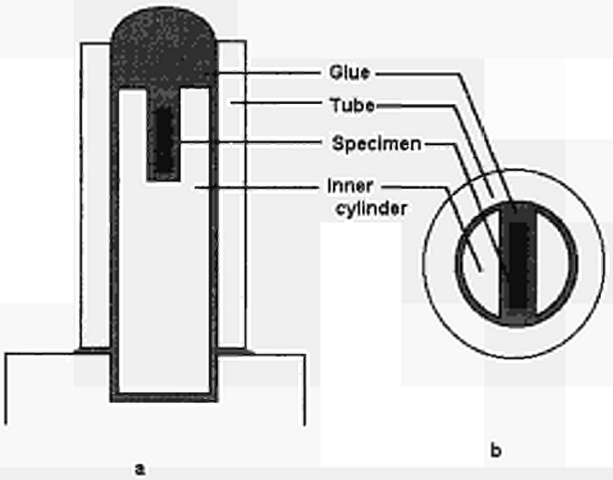

Fig. 1.23 Schematic of procedure used to prepare TEM cross-section from thin pieces of material. (a) specimen assembly. (b) schematic cross-section after gluing the thin film into the holder.

Three points should be stressed in this simple approach to the energy loss process:

- The key parameter which characterises the state of the projectile in a given material is not its energy, but its velocity.
- Due to the statistic nature of collisions, the charge state is not a well defined function of velocity.
- Energy loss due to electronic collisions comes about not only by energy transfer to target electrons, but also by loss of own electrons (stripping), and by electron exchange with the target atoms.

In the special case of fast heavy ions, the main theoretical treatments can be outlined as follows :

- The energy loss per collision is a function of the instantaneous velocity, v_i of the projectile rather than of its kinetic energy (E).
- Since electrons have a very small mass, the energy loss per collision is always very small in terms of the

projectile's energy, E_i, thus giving rise to a continuous slowing down resembling a friction-type stopping.
The momentum transfer to the electrons is small resulting in a very small angular deflection of the ion. At high velocities we can assume that the stopping power of a heavy ion can be given by the BETHE-BLOCH formula:

$$\frac{dE_i}{dx} = -N_v Z_t \frac{(\gamma_i Z_i)^2 \cdot e^4}{8 \cdot \pi \cdot \varepsilon_0^2 \cdot m_e \cdot v_i^2} \ln \frac{2 \cdot m_e \cdot v_i^2}{I}$$

E_i : ion energy (MeV)
v_i : ion velocity (cm.s^{-1})
Z_i : atomic number of incoming ion
Z_t : atomic number of target atom
m_e : mass of the electron
I : mean excitation energy of target atom
N_v : atomic density (atoms.cm^{-3})
γ_i : shell coefficient
ε_0: dielectric constant

Damage mechanisms

Although the number of investigations on damage produced by fast heavy ions in ceramics has increased, the damage mechanisms are still unclear. Various models have been proposed, such as thermal spikes, ionic spikes, etc [1, 4].

Up to now the damage creation has been linked to the linear energy transfer, but so far the lateral distribution of the energy deposition has not been taken into account. As it can be seen on Fig. 1.24, the energy loss, *dE/dx*, can be identical for a given ion at two different incident energies, or for different ions at various incident energies. This is the case of our study, where for Mo and Sn the specimens implanted at GSI have approximatively the same *dE/dx* as at fission energy, but different velocity. It has been shown that for a given projectile ion, the damage is higher at low velocity than at high velocity at constant *dE/dx*. Thus, it can be assumed that the electronic stopping power is not the only key parameter to account for the creation of the ion tracks. Part of our experiments are aimed at answering this question, for the specific case of UO_2.

References

[1] Hj. Matzke; Radiat. Eff., **64** (1982) 3
[2] R. L. Fleischer, P. B. Price, R. M. Walker, Nuclear Tracks in Solids, University of California Press (1975)
[3] Chr. Lehmann; Interaction of Radiation with Solids, North-Holland Publishing Company (1977)
[4] M. Toulemonde, E. Paumier, C. Dufour; Radiat. Eff. Def. Sol., **126** (1993) 201
[5] J. Biersack; Ion Modification of Insulators, eds. P. Mazzoldi and G. Arnold (Elsevier, Amsterdam, 1987) chap. 1

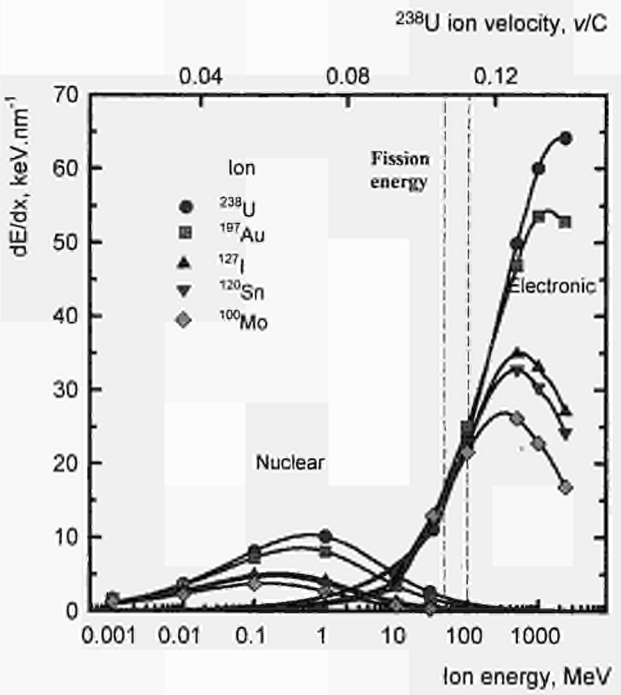

Fig. 1.24 UO_2 stopping power for different ions, calculated with the TRIM92 code [5]. The figure shows nuclear and electronic energy losses separately.

Leaching Experiments on SIMFUEL

Leaching experiments under static conditions were performed on SIMFUEL [1] to evaluate the behaviour of spent fuel (UO_2 at different burn-up) in contact with water in a granitic repository. Unirradiated UO_2 specimens were also used as reference. In particular, these experiments consider the effect of an anoxic atmosphere and of granite in contact with the fuel. Small cups made of granite hold the SIMFUEL specimens. The granite and the specimens are immersed in water, inside leaching containers sealed in autoclaves. SIMFUEL is used because it simulates different levels of burn-up (in our case, 3, 6, and 8 a/o are considered) [1] without the corresponding high levels of activity of the spent fuel. Since SIMFUEL can be manipulated in a normal glove box, instead of a hot cell, a more thorough characterisation of the specimen is possible. Moreover, the disturbing effects due to radiolysis, which are unavoidable when working with reactor-irradiated fuel, are avoided.

The early stage of the study has been devoted to set up the apparatus and to define the experimental parameters. In particular, a glove-box has been built and tested to maintain an Ar atmosphere during the preparation of the leachant solutions and the measurement of pH and redox conditions before and after the test. An important element under study was the leachant formulation (granitic water). To equilibrate the water with the granite sample holders prior to the actual leaching experiment, deionized

water was mixed with crushed granite from the same block as the sample holders, and stored for several months. Early analysis (4 weeks after mixing) showed that the ion concentrations in this water were significantly below the minimum reported values for granitic groundwaters.[2] Therefore, a well known granitic water already used by several authors (Volvic mineral water) is also used [3-5], together with deionized water, as a reference. The effect of using containers made of different materials, namely titanium and teflon, is also an important issue when comparing results from SIMFUEL to spent fuel tests. Titanium containers must be used for leaching tests involving spent fuel, because ordinary (and less expensive) teflon containers cannot withstand high radiation levels. Preliminary results of ICP-MS analysis of leaching solutions, after leaching UO_2 for 2.5 hours at 200 °C, indicate higher concentration of uranium in solution in the case of titanium containers.

For the first tests, a temperature of 200 °C has been chosen. In later experiments, lower leaching temperatures will be used, down to room temperature. High temperatures are considered as a starting point in order to obtain significant (i.e., measurable) amounts of altered surface layers and of dissolved ions [6]. Several characterisation techniques are involved in the analysis of the samples and the solutions (electrochemical methods, Inductively Coupled Plasma Mass Spectrometry (ICP-MS), Rutherford Backscattering Spectroscopy (RBS), Auger Electron Spectroscopy (AES), and Scanning Electron Microscopy (SEM)). In parallel with the RBS experiments, computer simulations of the surface modifications are performed (RUMP code). The final aim is to correlate these experimental results with those obtained on reactor irradiated fuel in the hot cells.

References

[1] P. G. Lucuta, R. A. Verrall, Hj. Matzke, B.J. Palmer; J. Nucl. Mater. **178** (1991) 48

[2] B. Allard; Mat. Res. Symp. Proc. **26** (1984) 219

[3] P. Franco, P. Trocellier and F. Menes; Mat. Res. Symp. Proc. **127** (1989) 343

[4] M.P. Lahalle, P.Franco, P. Trocellier, J.C. Krupa, M. Genet, G.C. Allen, N.R. Holmes; C.R. Acad. Sci. Paris **307**, Série II (1988) 1163.

[5] M. P. Lahalle, J. C. Krupa, R. Guillamont, M. Genet, G. C. Allen, N. R. Holmes; Mat. Res. Symp. Proc. **127** (1989) 351

[6] Hj. Matzke, A. Turos; Solid State Ionics **49** (1991) 189

Zr-diffusion in α-Ti measured by Rutherford Backscattering Spectroscopy (RBS) and Heavy Ion Rutherford Backscattering Spectroscopy (HIRBS)

Both Ti and Zr occur in α hcp (a) structure at low temperatures. The transformation temperature to the bcc (ß) high temperature structure is higher for Ti (1155 K, or 0.68 $T_{m\alpha}$) than for Zr (1136 K, or 0.62 $T_{m\alpha}$). Here, $T_{m\alpha}$ is the hypothetical melting point of the α-phase, calculated following the procedure given by Ardell [1]. Therefore, a wider temperature range is available for measurements in α-Ti. Though both Ti and Zr are widely used in industry, diffusion phenomena in the α-phase are not well understood.

The diffusion of Zr in α-Ti in the temperature range of 823-1133 K has been measured, using the ion beam analysis techniques of conventional Rutherford backscattering spectroscopy (RBS) with 2 MeV He-ions of the van de Graaff accelerator at the Kernforschungszentrum Karlsruhe, Institut für Nukleare Festkörperphysik (INFP) and of Heavy Ion Rutherford backscattering spectroscopy (HIRBS) using the 38 MeV F-19 ion beams of the TANDAR accelerator at Buenos Aires, Argentina.

Penetration profiles are shown in Fig. 1.25 plotted as log Zr-concentration C (in arbitrary units to show the individual profiles separately) versus penetration depth squared, x^2, for the HIRBS experiments. The expected straight lines are found for penetrations of between about 500 to 1000 nm. It is likely that the influence of dislocations is small as these penetrations are smaller than the average dislocation spacing, considering up to $10^{12}/m^2$ a reasonable dislocation density of very well annealed sam-

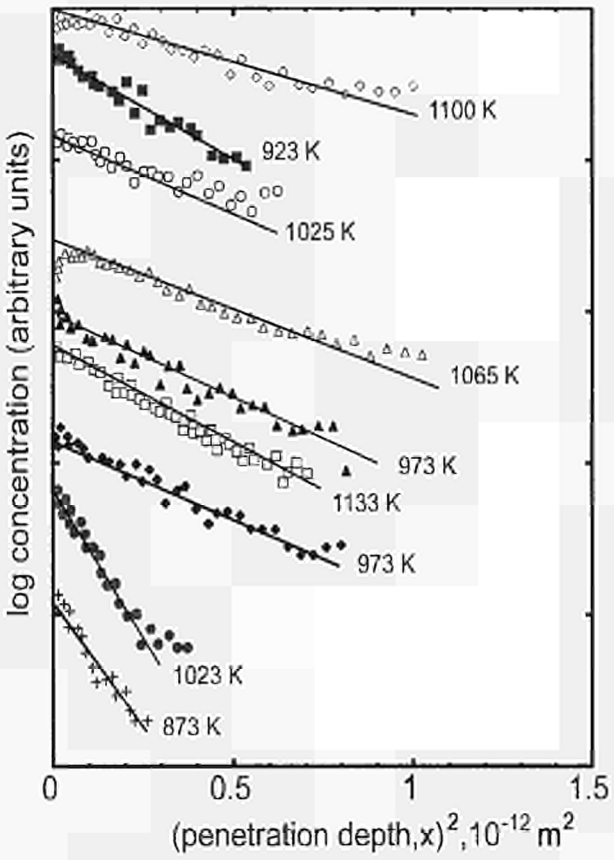

Fig. 1.25 Diffusion profiles of all the HIRBS experiences

ples. The penetration depths for the RBS specimens is even smaller; the argument holds thus for both techniques. Grain boundaries did not affect the measurements either because of the large grain size of the Ti samples. An Arrhenius plot for Zr diffusion in Ti, compared with the results for self-diffusion of Ti [2] is shown in Fig. 1.26.

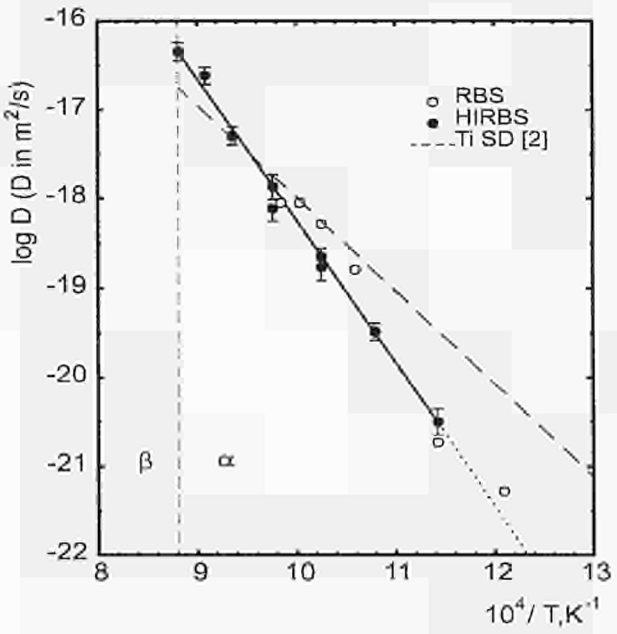

Fig. 1.26 Arrhenius plot for diffusion in α-Ti. Full line: mean squares fit of Zr diffusion; dashed line: -Ti self-diffusion [2].

The temperature dependence of Zr diffusion in -Ti between 873 and 1133 K, using only HIRBS data, is expressed as:

$$D = (4.3 \pm 3.1) \cdot 10^{-3} \exp\left[-\frac{304 \pm 30 \text{kJ} \cdot \text{mol}^{-1}}{RT}\right] \text{m}^2\text{s}^{-1}$$

The present diffusion parameters, the pre-exponential D_0 and the activation energy Q, are slightly higher than those obtained applying the known empirical rules for self-diffusion. Given the higher mass, the larger ionic radius and thus the larger atomic volume of Zr with respect to Ti, lower diffusion coefficients for Zr in Ti than for Ti self-diffusion would be expected. This behaviour is only observed below 1065 K. At higher temperatures, the trend is reversed. The most probable explanation of this result is that Zr forms a complex with one or more impurities in the Ti (particularly Fe and/or O) and then migrates [3].

References

[1] A. Ardell; Acta Met. **11** (1963) 591

[2] Chr. Herzig, R. Willecke, K. Vieregge; Phil. Mag. **A 63** (1991) 949

[3] R. A. Perez, F. Dyment, Hj. Matzke, G. Linker, H. Dhers; J. Nucl. Mater. **217** (1994) 48

Small Angle X-ray Scattering (SAXS) and Transmission Electron Microscopy (TEM) studies of ion-implanted waste glasses

During their storage, waste glasses are subjected to -decay of actinides and large amounts of He are produced in the glasses. The aim of the present study was to verify if and to what extent the nondestructive technique of SAXS (small-angle X-ray scattering) can be used to obtain reliable information on microstructural damage and gas bubble formation in waste glasses. Such bubbles are expected to be formed by to the accumulation of He produced by the α-decay of the actinides in the waste glass. A non-destructive technique to measure the formation of such bubbles would be very helpful.

The glass GP 98/12 [1] was implanted with 200 and 320 keV He-ions at fluences and 3 or 4×10^{16} ions/cm^2, and with 225 keV Kr- and Xe-ions at fluences of 4×10^{16} ions/cm^2 to simulate α-decay damage (α-particles and recoil atoms). Damage characteristics in each target were investigated first by SAXS. Following this non-destructive determination, the target was investigated by TEM (transmission electron microscopy). The absence of microstructural damage in the as-prepared glass foil was carefully verified by a detailed SAXS measurement before irradiation, which also provided the sample background SAXS intensity. Precipitates of the rare metal fission products contributed to this background intensity. The metal particles were clearly observed by TEM in unirradiated portions of GP 98/12 foils, which served as control samples for the TEM analyses. These metal particles were also clearly resolved from all post-irradiation damage features. Ion irradiations were performed at GSI, Darmstadt, and at Technion, Haifa. SAXS measurements were carried out at Technion, utilizing the CuK_α X-ray beam. The TEM analyses were conducted at ITU, employing a 200 kV Hitachi TEM.

Two distinct radiation effects were observed by SAXS and confirmed by TEM. The He-irradiated foils show an increased SAXS intensity with little angular dependence, as shown in Fig. 1.27 for one of three He-irradiated targets. This behaviour suggests the importance of enhanced density fluctuations, that may be attributed to radiation-induced material distortions having atomic to molecular sizes (similar to point defects in a crystalline matrix). The TEM measurements on these targets revealed only featureless material. The absence of a TEM signal is fully consistent with the above interpretation of the SAXS results, because detection of point defects by TEM is impossible due to their very small geometrical dimensions. The foils irradiated by Kr^+ and Xe^+ ions have clearly shown, in contrast to the above results, a rise in the SAXS intensity with decreasing angle at small angles. The meas-

urements on the Xe-irradiated GP 98/12 foil are displayed in Fig 1.27c. Nearly similar SAXS results were obtained for the Kr-irradiated GP 98/12 target. The analyses of the SAXS data are fully consistent with TEM measurements. All TEM data are well represented by the micrograph in Fig. 1.28 taken on the Xe-irradiated GP 98/12 foil. The microstructure in Fig. 1.28 is characterized by a high density of small bubbles in the size range 5 to 50 nm. In addition, there is a much less frequent population of larger features, resembling bubbles or cavities with largely irregular shapes, in the size range up to 400 nm. The majority of the features of the latter group are too large to be detected by SAXS. The average size of the bubbles of the first group was found to be approximately 18 nm. This value is in excellent agreement with the SAXS analysis described above.

Point defects in ion-irradiated glass originate primarily from dissipation of the ion energy via nuclear stopping. The process occurs via a series of atomic collision cascades that involve many neighbouring atoms of the glass matrix. For the He^+ beam, each projectile is expected to displace ~ 130 atoms, mainly near the end of the ion trajectory (computations by TRIM [2]). The mean projected ranges of 200 and 320 keV He^+ ions in GP 98/12 are estimated to be 0.89±0.12 and 1.2±0.12 mm, respectively. The uncertainty represents the straggling of the ions along the range). Apparently, with the He-ion fluences of the present experiments, the above point defects remained largely isolated, as is evident from the observed isotropic X-ray scattering intensity. With Kr and Xe ions, the atomic displacement damage is relatively dense essentially along the entire length of any single particle trajectory (the mean projected ranges of 225 keV Kr^+ and Xe^+ ions in GP 98/12 are 0.11±0.03 and 0.07±0.02 mm, respectively. The average atomic displacement yields are approximately 2300 to 2400 matrix atoms per ion). Accumulation of significant amounts of damage is associated with accumulation of stress, and stress release may lead to the formation of extended defects such as pores. In addition, point and extended defects serve as efficient traps for inert gas species, which in turn may control the pore growth and lead to the formation of gas bubbles. In addition, Kr and Xe are not soluble in glass, in contrast to He. These argu-

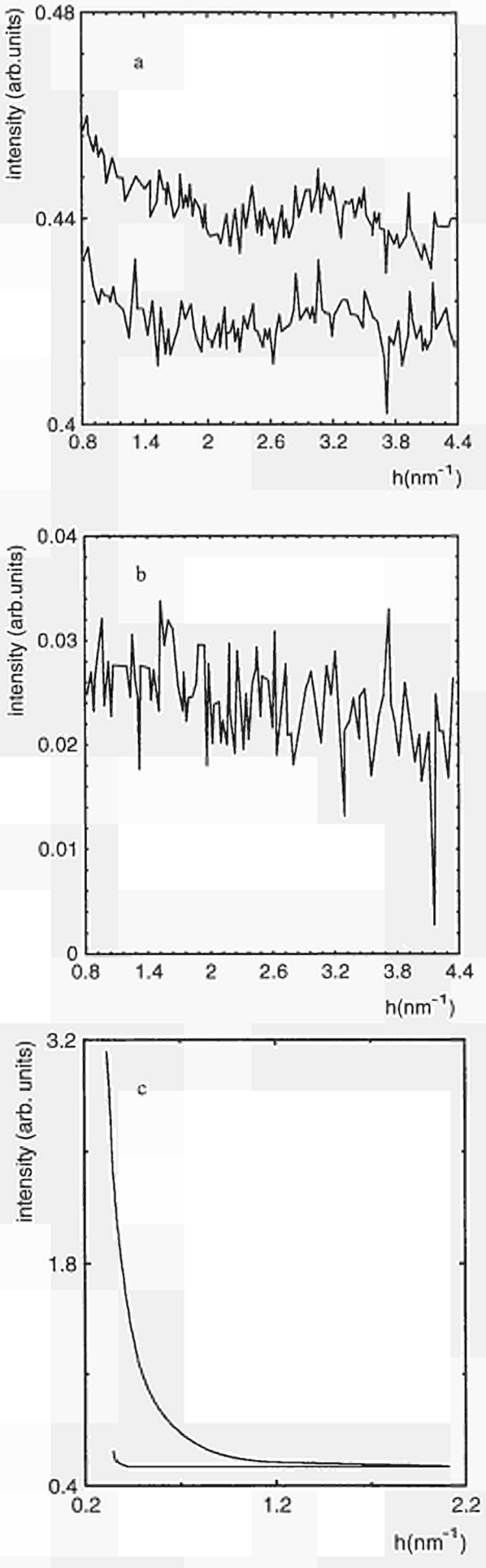

Fig. 1.27 a) Measured SAXS intensities (in arbitrary units) of GP 98/12 glass before irradiation (lower curve) and after irradiation by 200 keV He^+ ions at a fluence of $3.1x10^{16}$ cm^{-2}. b) Net increase of scattering intensity after irradiation. The quantity $h = (4p/l)\sin q$, where l is the wavelength of the X-ray radiation, is essentially proportional to the scattering angle 2q. c) Measured SAXS intensities from a foil of GP 98/12 glass before irradiation (lower curve), and after irradiation by 225 keV Xe^+ ions at a fluence of $4x10^{16}$ cm^{-2}.

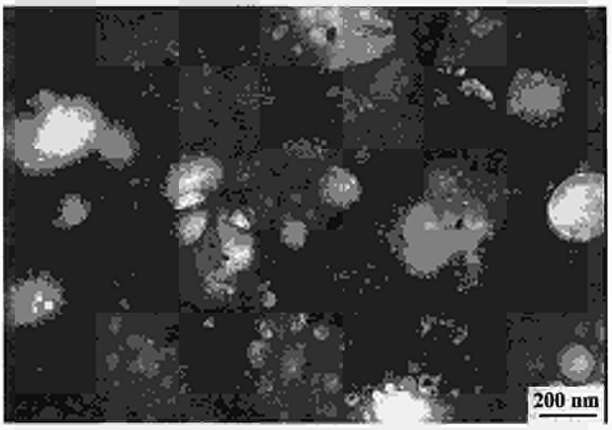

Fig. 1.28 TEM micrograph showing pore/bubble formation in a GP 98/12 foil after irradiation by 225 keV Xe^+ ions at a fluence of $4x10^{15}$ cm^{-2}. The area shown is 2000 x 1500 nm^2.

ments may explain the nature of the microstructural damage observed in the GP 98/12 samples after their irradiation with Kr and Xe beams.

In summary, employing SAXS, this study has provided first experimental evidence for the accumulation of point defects in He-irradiated nuclear waste glass. In addition, pore and bubble formation by low-energy heavy ions has been verified by two independent experimental techniques (TEM and SAXS). This approach is highly justified because the glass microstructure observed by TEM is known to be sensitive to the microscope electron beam. The relevance of the present research for predicting the behaviour of a nuclear waste glass under self-irradiation by alpha particles and alpha recoil atoms is obvious. The interaction of displacement character of alpha particles (typical kinetic energy ± 5 MeV) with glass is largely similar to that of 200 or 320 keV He^+ ions, taking into account that the excessive energy of the former particles is dissipated primarily via electronic stopping. A similar equivalence is approximately true for heavy alpha-recoil atoms (typical kinetic energy ± 100 keV) and low-energy Kr^+ and Xe^+ ions, although the alpha-recoil atoms are not inert gas atoms. This assessment is supported by the significant porosity that was produced in the PNL 75-68 glass by low-energy Pb^+ ions [3]. Thus, the two types of radiation from alpha decay will produce microstructural damage, and possibly extended defects as well, in common types of nuclear waste glass, and SAXS is a promising non-destructive technique for analyzing these damage effects.

References

[1] L. Kahl, M. C. Ruiz-Lopez, J. Saidl, Th. Dippel; "Fabrication and characterization of an improved borosilicate glass to solidify high level waste solutions", Kernforschungszentrum Karlsruhe, report KfK-3251 (1982) (in german)

[2] J. F. Ziegler, J. P. Biersack, O. Littmark; "The Stopping and Range of Ions in Solids", ed. J.F. Ziegler (Pergamon, New York, 1985) Vol. 1, Chap. 40

[3] J. F. DeNatale, D. G. Howitt, G. W. Arnold; Radiation Effects **28** (1986) 63

1.1.3 Studies of high temperature properties

High temperature thermophysical properties of UO_2

The recent investigations in our laboratory on the heat capacity λ-transition in stochiometric and non stoichiometric uranium dioxide at temperatures around 0.8 T_m are progressively leading to a unitary view of the high temperature thermophysical properties of this material. The order-disorder transition which the UO_2 anion sublattice undergoes was in fact well described by a mean field model of Debye-Hückel (DH) kind. This model is based on the assumption that the electric polarization in the crystal is sufficiently isotropic and homogeneous for the atomic interactions to be calculated from the macroscopic dielectric constant. It is well known in statistical thermodynamics that DH models provide a correct description of weakly interacting systems (e.g. very diluted solutions), whilst systematic deviations of the predictions from reality may or may not be found in the case where close interactions are involved. Anion defects in UO_2 at high temperatures do certainly constitute a strongly interacting system, a proof being given by the calculated distance of closest approach, which, in the DH formalism, is of the same order of magnitude as the defect ionic radius. Though this condition does not justify the use of the limiting formula of Debye for the interaction free energy, upon which the Hückel formalism is based, the groundwork of the main field approach is secured if the real electric induction is continuous across the boundary of the defect radius and the surrounding medium, and the Poisson-Boltzmann equation for the interatomic potential is soluble. The Debye approximation of the "average" defect free energy as well as the truncation at the linear term of the series representing the charge density function do not entail any further restriction on the properties of the system.

We have therefore first taken for granted that the DH model provides sufficiently a realistic description of the system, and, consequently that the mean field hypothesis could be extended to explain the behaviour of other thermophysical properties in UO_2.

A tentative model of the d.c electrical conductivity, σ, was reported in TUAR-93, p. 51. Previous investigations showed that the principal electrical carriers in UO_2 at high temperatures consist of small polarons, i.e. of electron-

hole pairs associated to local lattice strains. Thermodynamically, these defect are described as reaction products of the disproportioning of U(4+) into U(3+)+ U(5+). This pair is essentially analogous to a vacancy-interstitial pair, whereby the electrical field and the complementary defect interactions occur, in this case, within the electronic shell. Since the main assumption in the main field approach is that the polarization is continuous across the ionic radius, we also applied a cooperative model of DH type to small polaron formation.

A first application led to the positive result that the dielectric constant which provides a fitting of the resistivity data is not far from the value used to describe the intersite interaction in Frenkel pairs, which is in turn near to the empirically measured macroscopic dielectric constant.

A problem was, however, faced in the analysis of the conductivity of UO_2.The only existing data at temperatures above 2500K, obtained (almost twenty years ago) by Bates [1] corroborate the conclusion issued by the analysis of measurements at lower temperatures, that the Arrhenius plot of $\sigma=\sigma(1/T)$ exhibits an inflective structure at high temperature which cannot be explained in terms of single-energy activated carrier migration mechanism. This was directly interpreted as due to a pronounced increase in the defect interaction, and, hence, as a confirmation of the validity of the DH approach. Unfortunately, Bates' data are not fully consistent: whilst a set of measurements (on sintered pellets) gave relatively low conductivities, others, mostly obtained from single crystals, and published in a separate report, are approximately twice as large. The whole set of measurements is shown in Fig. 1.29. It is clear that, in view of studying the transition which is expected to be behind the conductivity inflection point, a crucial point is to decide whether one of the two datasets can be discarded as erroneous or not representative. In a recent personal communication, Bates [2] confirmed that all measurements on sintered pellets and single crystals were experimentally reliable. On the other hand, in the given experimental context, it is hardly conceivable that single crystals exhibit an exceedingly high electrical conductivity; on the contrary, sintered samples (with initially 92% th.d.) undergo at high temperatures restructuring processes which do not necessarily result into densification. Actually, high temperature annealings are often inducing void agglomeration processes which can negatively affect the effective electrical conductivity.

We have therefore assumed that the single crystal measurements of provide a better representation of the UO_2 electrical conductivity above 2500K.

Fitting of the DH model parameters was therefore repeated on a less scattered empirical dataset. The results are reported in Tab. 1.4

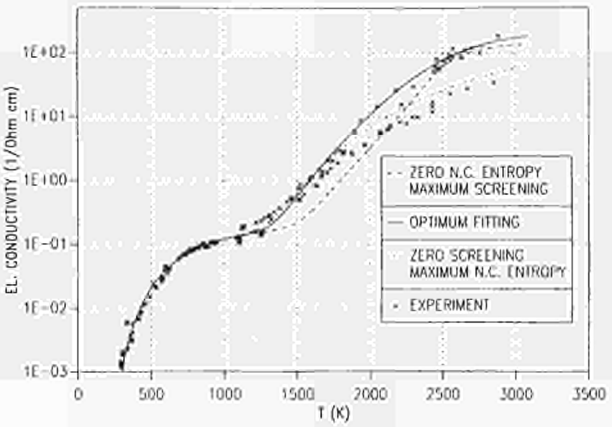

Fig. 1.29 Experimental electrical conductivity data compared with the Debye-Hückel model predictions. The dashed and dotted curves represent the model calculation at the extremity of the viable parameter range.

The fixed parameters are the defect free energy in a perfect lattice, W_0, and the defect enthalpy of migration. The former was obtained from the $\sigma(1/T)$ slope in the temperature range corresponding to a defect intrinsic concentration at values, where interaction is negligible and can, therefore, be expressed as:

$$\sigma = \sigma_o T^{3/2} exp(-2.34\ \text{eV}/kT) \quad (\text{ohm m})^{-1}$$

where $\sigma_o = 1.6 \cdot 10^{11}$

The charge mobility parameters were deduced from hole mobility measurements [3] in the extrinsic concentration range (T<1300K), obtaining:

$$\mu_{hole} = \mu_{electron} = \mu_o T^{3/2} exp(-0.25\ \text{eV}/kT)\ (m^2/volt \cdot s) \quad (1)$$

where: $\mu_o = 3.3$

The non-configurational defect entropy can be straightforwardly obtained from the relationship:

$$\Delta S/2R = ln\ (\sigma_o / 2eN^U \mu_o) = 1.88 \quad (2)$$

where N^U is the uranium atom concentration and e the electron charge.

Finally, the intrasite screening constant can be estimated from the approximate formula:

$$\lambda^2 = 2N^U e^2 d^2 / (10^3 k \varepsilon_0 \varepsilon_s) = 1.85 \quad (3)$$

where ε_s is the solid dielectric constant and d the average closest approach distance of two electrons whose separation give rise to the disproportioning transition. This distance can be approximately expressed as:

Tab. 1.4 Cooperative small polaron formation: free energy and entropy

EXPERIMENTAL DATA	
Free energy of formation of defects at zero concentration	2.34 eV (from low temperature σ(1/T) slope)
Activation enthalpy for charge migration	0.25 eV (From charge mobility data)

MODEL VARIABLE PARAMETERS		
	FITTING	EXPERIMENT
Intrasite potential screening factor	2.0	-
Non-configurational defect entropy	(2±0.2)R	(3.6±0.5)R

$$d = \int \rho(r)|r - r'|\rho(r')drdr' \qquad (4)$$

(where ρ is the electron density function in the disproportioning U^{4+} atom).

The sixfold integral in eq.(4) was calculated numerically for the *5-f* ^{2} configuration, obtaining a value of *d* of approximately 0.103 nm.

At this point, by substituting for λ the value calculated from eq. (3) in the expression of the on-site Coulomb repulsion:

$$U = W_0 \exp(-\lambda(n/t)^{1/2}) \qquad (5)$$

with *t*=T/1000 and *n* = small polaron concentration,

and by assuming the value of the non-configurational entropy calculated from eq.(2), the unknown model variables, λ and ΔS, are determined, and the small-polaron concentration, *n*, can be calculated as a function of temperature, the d.c. electrical conductivity is then expressed as:

$$\sigma = 2ne\mu \qquad (6)$$

Alternatively, a numerical Least Square Fitting (LSQ) of the experimental conductivity measurements was carried out using both the parameters λ and ΔS as variables, so that, for a given ΔS, a corresponding value of λ is found which provides the *one-parameter* best fitting of the data. The solution pairs constitute a function which is plotted in Fig. 1.30 over the relevant variable interval. The *absolute* best fitting, within the experimental error, is obtained in the segment of the curve contained within the framed area, where the value of is found to be more stationary against the variation of ΔS. For values of λ comprised

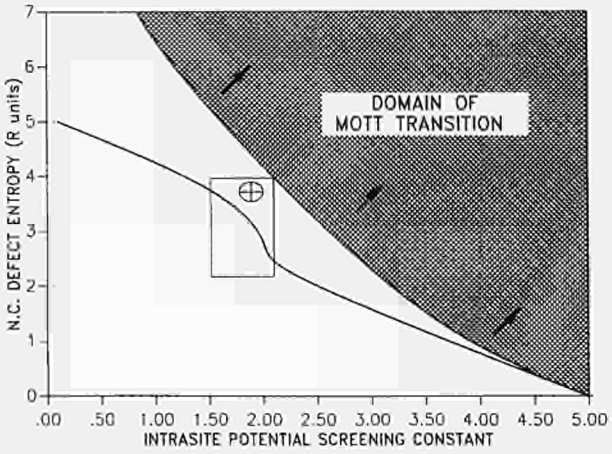

Fig. 1.30 Solutions of the underdetermined model by fitting the data of Fig. 1.29 with both defect entropy and potential screening factor. The LSQ residual is minimum in the framed range. The crossed circle represents the theoretically estimated solution pair. By increasing defect entropy and/or screening factor an insulator-metal transition is predicted by the Debye-Hückel model (full line), and an upper limit for the permissible model parameter is established.

between 1.5 and 2.2, the model predicts a pronounced inflection of σ (T) around 2500 K, in good agreement with the experimental observation. This inflection becomes smoother for screening constants below the optimum range and, obviously, disappears if no screening is applied to the potential (λ=0); on the other side, at the maximum calculated value of λ=5 the inflection becomes an almost vertical step.

From the curve plotted in Fig. 1.30 one can get an insight into the properties of the system described by the DH model: in fact, the curve represents systems of constant free energy and variable potential screening (the loss in internal energy due to a decrease in λ, is compensated by an increase in entropy). In systems whose parameters lie in the unshaded area of Fig. 1.30 the defect concentration increases *continuously* with temperature. On the other hand, if, starting from one of these systems, λ and/or ΔS is gradually increased, conditions are eventually met at which the system shows a discontinuity in the curve $n=n(T)$ at a distinct temperature (Mott transition). The line corresponding to this transition, as predicted by the adopted model, is plotted in Fig. 1.30 (full line at the top); the shadowed semiplane above this line corresponds to system parameters giving rise to an insulator-metal transition at a certain temperature. Since UO_2 does not exhibit any insulator-metal transition, this line represents the upper boundary for admissible (λ,ΔS) pairs.
Two remarks are in order here: First, in the „optimum" fitting range, the resulting system parameters are not too far from the Mott transition line. Practically, this represents a positive aspect of the model, because a large sensitivity with respect to the parameter variation is entailed. On the other side, the theoretically calculated model parameters, λ=1.85, ΔS=3.6, are represented by a point, indicated in Fig. 1.30 by a crossed circle, lying rather close to the optimum fitting domain.

From the above mentioned arguments one is induced to conclude that both anion (Frenkel pairs) and electronic defects (small polarons) in UO_2 are suitably described by the DH model in the same mean-field context. However, the validity of the model is to be confirmed by comparison of the theoretical predictions with other independent thermophysical data.

a) The small polaron contribution to the heat capacity can be obtained from the temperature derivative of the electron-hole pair equilibrium concentration. The plot of $C_v^{s.p.}$ versus T is shown in Fig. 1.31. The curve has a maximum at circa 2500 K, and decreases with lower slope at high temperatures. The contribution to the total heat capacity, dominated in this temperature range by lattice harmonic vibrations and by Frenkel defect formation, is smaller than the experimental uncertainty of C_v, so that a validation of the model based on the analysis of the heat capacity has to be excluded. However,

b) the small polaron contribution to thermal conductivity, expressed as:

$$K^{s.p.}(T) = k\, e^{-1} \mu T C_v^{s.p.} \quad \text{(W/mK)} \qquad (7)$$

represents in UO_2 an important property.

This function, plotted in Fig. 1.31, has a trend similar to that of the heat capacity, with the maximum at approximately 2650 K, i.e. at 150 K higher. Interestingly, the temperature of the maximum small polaron conductivity is only a few tens of degrees lower than that corresponding to the λ-transition of the anion defects.

The analysis of the main contributions to the thermal conductivity of UO_2 in this temperature range is still in progress: in the following section some aspects concerning the influence of the lattice defects on the effective thermal diffusivity are illustrated.

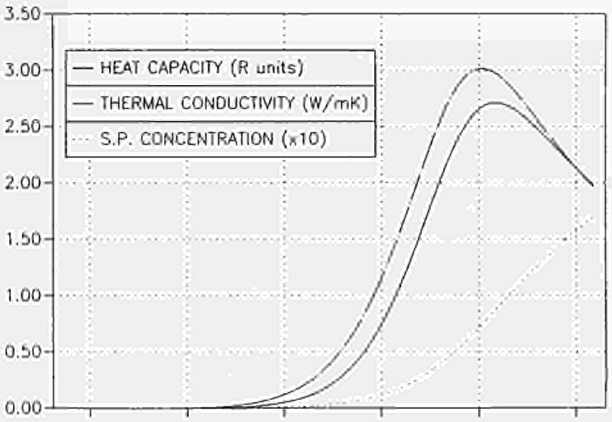

Fig. 1.31 Calculated small polaron concentration with the entailed heat capacity and thermal conductivity contributions as functions of temperature.

A preliminary remark can, however, be made here:
The increase of the small polaron contribution to thermal conductivity above 1500 K, as predicted by the DH model, is in agreement with the experiment. However, the value of the total conductivity, k by approaching the anion disorder transition is likely affected by the marked increase of the phonon scattering centres with temperature. This effect on the lattice vibration contribution to k has not been properly accounted for so far. For instance, customary empirical extrapolations of the lattice vibration conductivity at 2500 K give approximately:

k^{lv} = 1.6 W/mK ,

which, summed to the small polaron contribution, would give a total conductivity of approximately 4.3 W/mK, that is too high compared with the experimental value of 2.7-2.9 W/mK. An agreement of the model with the experi-

ment would imply that the lattice conductivity at this temperature is by a factor ten lower than the extrapolated value. In the light of the considerations reported in the following sections, this could be justified. The same can be anticipated for the total conductivity between 2500 K and the melting point: the slight decrease of the small polaron contribution is likely compensated by an increase with temperature of the vibrational contribution in disordered lattice above the λ-transition.

References

[1] J. L. Bates, C. A. Hinman, T. Kawada; J. Amer. Ceram. Soc. **50** (1967) 12
J. L. Bates, C. A. Hinman, T. Kawada; Battelle Northwest (USA), report BNWL-296 (1966)

[2] J. L. Bates, Battelle Northwest (USA); Personal communication (1994)

[3] N. J. Dudney, R. L. Coble, H. L. Tuller; J. Amer. Ceram.Soc. **64** (1981) 627

On the thermal conductivity and diffusivity of solid and liquid UO_2

For a long time in the past the large discrepancy between the various measurements of the thermal conductivity k of liquid UO_2 has represented an insoluble difficulty. The stand of the controversy is summarized in Tab. 1.5 and Fig. 1.32.

The recent experimental determination of the heat capacity of this material at temperatures from 2500 K to above the melting point. makes it possible to evaluate the heat diffusivity, α, in this temperature range.

This section shows that the dependence of α on temperature indicates that the lowest measured value of k, measured in the Institute [3,5], is probably the right one.

Tab. 1.5 Thermal conductivity of liquid UO_2.

Ref.	k W/mK	Method	Sample
[1]	11	Periodic heat flow	Tungsten-encapsulated 0.8-1.2 mm thick sample: "three -layers" mounting.
[2]	8.5	Flash	Tungsten-encapsulated 0.7 mm thick sample: "three-layers" mounting.
[3]	2.5	Melting front penetration under surface laser-heating.	Self crucible: partly molten sample.
[4]	5.5 [1] 6.7 [2] 4.5 [3]	Re-evaluation of experiments of refs. [1,2,3] using a 3-D transient heat transfer computer code.	-
[5]	2.5	Melting front penetration under surface laser heating; 2-D scanning of the temperature field top and bottom. F.e.m. analysis under unsteady conditions.	Self-crucible: partly molten sample.

Analysis of the data

The properties of the heat capacity of UO_2 between 2000 K and the melting point have been recently measured and analyzed [8, 9]. The empirical function $Cp = C_p(T)$ in the solid is characterised by:

1) a pronounced increase with temperature due to creation of lattice and electronic defects,
2) the appearance of a -transition at 2670 K, caused by cooperative defect formation in the oxygen sub-lattice. The experiment shows that this transition is absent in hyperstoichiometric UO_{2+x}, whilst in the hypo-stoichiometric oxide the transition is of the first order, that is to say, the oxygen Frenkel-pair concentration increases continuously in the former case, whereas in the latter a transition occurs at a temperature $T_t = T_t(x)$ from an "ordered-oxygen" phase to a disordered one, with a sudden increase in defect concentration of nearly one order of magnitude [9].

Between these two behaviours, the stoichiometric oxide is found to undergo a second-order transition at $T_c = 2670$ K: the defect concentration $n = n(T)$ is continuous across the transition temperature, but $dn/dT = \infty$ at T_c. The measured heat capacity in the stoichiometric oxide is shown in Fig. 1.33 as a function of temperature in an interval around the λ-transition.

The data of the liquid heat capacity, taken from ref. [7] are shown in Fig. 1.34 from the measured solidus temperature up to 4500 K. A sharp drop in C_p is observed from the experimental point nearest to the solidus (640

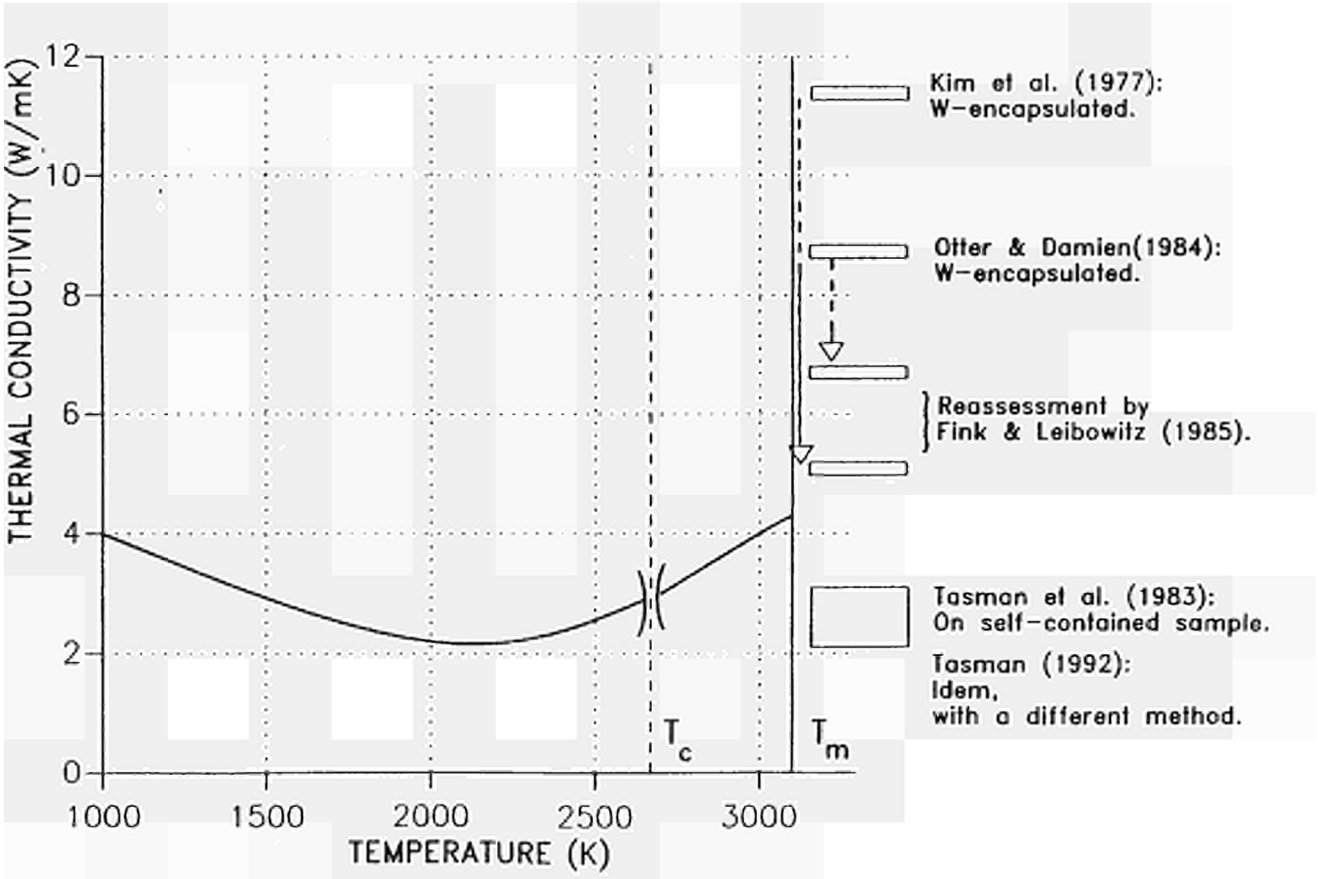

Fig. 1.32 Measured thermal conductivity in solid and liquid UO_2. The temperature T_c corresponds to the observed λ-transition. No discontinuity in k is measured across this temperature.

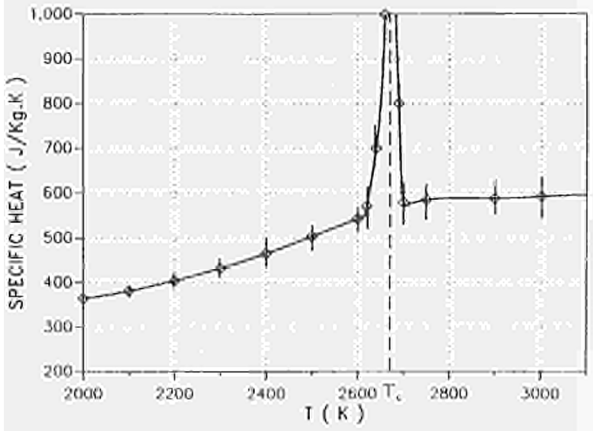

Fig. 1.33 Heat capacity in solid UO_2 in the region of the λ-transition.

J/KgK) to that nearest to the liquidus (448 J/KgK): at higher temperatures, the less pronounced decrease of $C_p(T)$ with T can be approximated by a parabolic dependence of C_p on $1/T$.

Around 4500 K the heat capacity of UO_2 approaches the value 9R, appropriate to the harmonic vibration in a triatomic lattice (as observed, for instance, in the case of H_2O).

The values of C_p plotted in Figs. 1.33 and 1.34 have been used to calculate the heat diffusivity,α, from the thermal conductivity. The liquid data are those measured by Tasman et al. [3,5]. Since they have been obtained, within a first approximation in the absence of any assumption on the value of C_p in the liquid, the defining formula (1) can be used to deduce α.

$$\alpha = k / (C_p \rho) \qquad (1)$$

(where: ρ = density)

Unfortunately this procedure could not be applied to the data of refs. [2] and [4] because k was obtained in these cases by assuming an estimate of C_p in the liquid which substantially differs from the experimental value. If one applies the initial one-dimensional analysis of [6] (which, however, was proved to be inadequate), one realizes that the correction of $C_p(liq.)$ leads to a decrease in the resulting α(liq.) of approximately 50%. On the other hand we were not able to repeat the computer code calculations of Fink and Leibowitz with the correct heat capacity assessment.

For comparison, two sets of values of k have been adopted to calculate α in the solid: those from the MATPRO

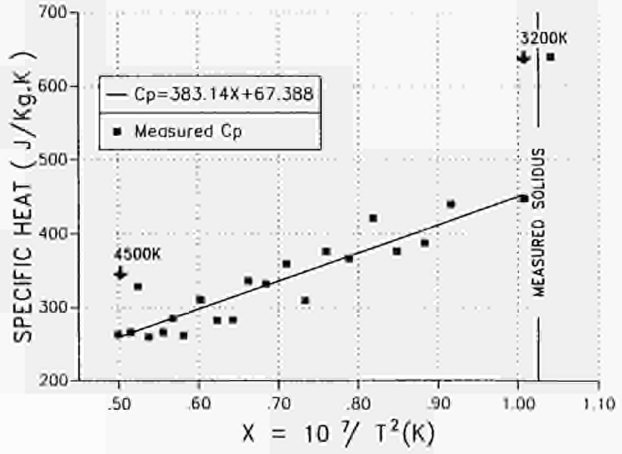

Fig. 1.34 Heat capacity of liquid UO_2.

databank [10] and those used at ITU [11]. Fig. 1.35 shows the thermal diffusivity obtained from eq. (1) in the liquid and in the solid as a function of temperature. Two features immediately catch the attention:

1) The diffusivity value calculated from Tasman's data is on the extrapolated line of the solid indicating no effective discontinuity across the melting temperature.

2) The diffusivity curve in the solid is split into two segments respectively decreasing and increasing with temperature, separated by a "pit" corresponding to the λ-transition; which, being formally similar to a thermodynamical critical point, entails that $\alpha \rightarrow 0$ for $T \rightarrow T_c$.

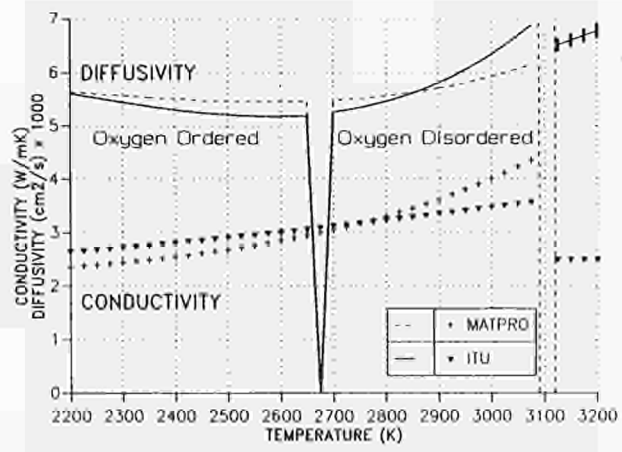

Fig. 1.35 Thermal conductivity (recommended empirical fitting) and deduced diffusivity in UO_2. The conductivity data labelled MATPRO (crosses) are taken from [10]. Those labelled ITU (triangles) are taken from [11] for the solid and from [5] for the liquid.

Discussion

The dependence of the thermal conductivity in solid UO_2 on temperature between 2000 K and T_m has been criticaliy scrutinized (see e.g. [11]) because the presence of a minimum in this temperature interval indicates that a distinct heat transport mechanism is activated at high temperatures. However: the complexity of the dependence of k on T makes this analysis very difficult. If the heat diffusivity α(T) is examined instead, a clearer insight is obtained.

Diffusivity in crystals decreases with temperature due to increasing anharmonic vibrations (caused by lattice strains, impurities and defects): in this sense the regular decrease of α in UO_2; between RT and 2500 K can be qualitatively explained.

By approaching the λ-transition the number of phonon scattering centers dramatically increases. The zero of the dynamic quantity at T_c = 2670 K is attributable to the slowness to which fluctuations decay at the critical point.

Above the λ-transition, in the oxygen sublattice the concentration of Frenkel pairs approaches 0.2 [10], hence the lattice displays a high degree of disorder.

Making comparisons between thermal diffusivity of crystalline and glassy forms of the same substance, it is realized that the dependence on temperature is opposite in the two cases, k in the glassy phase displaying an increase with rising temperature (a typical example is provided by crystalline and fused SiO_2).

Furthermore, an analogous behaviour of α(T) is also observed in systems where electrons carry a significant part of the heat current: in fact, in a number of metals and binary alloys undergoing magnetic transitions around the Curie point (e.g. Fe, Ni, Co), a sharp minimum, located at the transition temperature, defines two branches of the curve α = α(T) respectively descending (ordered) and ascending (disordered phase) with increasing T.

On the other hand, in systems which do not exhibit premelting order/disorder transitions, the reversal of the slope of α(T) normally occurs at the melting point.

Furthermore, these materials often exhibit a discontinuity (in several cases a significant drop) in thermal diffusivity at T_m (e.g. alkali metals: Cu, Au); whereas in those which previously undergo a premelting order/disorder transition the thermal diffusivity mostly increases continuously across the melting point.

A full discussion of these phenomena is outside the scope of this contribution, however some conclusions can be drawn concerning the observed behaviour of α(T) in UO_2 at temperatures above the λ-transition. Actually, this tran-

sition appears to be an important discriminating feature for several physical properties, which, in the interval between T_c and T_m, are affected by the anion-sublattice disorder to an extent which has not been fully appreciated. For instance, there is experimental evidence that in UO_2 also cation mass transport coefficients and mechanical properties are affected by the λ-transition [12].

It is therefore not surprising that thermal diffusivity is so much affected by oxygen lattice defects that under conditions of pronounced oxygen disorder created by the λ-transition this quantity exhibits a temperature dependence which is typical for most glassy structures, whose passage from solid to liquid state occurs without solution of continuity in their dynamical properties.

In this context. the thermal diffusivity value obtained by Tasman et al. [3,5] and plotted in Fig. 1.33, is conform with the observed behaviour of a set of analogous solid and fluid systems and, therefore, appears to be the correct one.

References

[1] C. S. Kim, R. A. Haley, J. Fischer, M. G. Chasanov. L. Leibowitz; Proceedings of the 7th Symposium on Thermophysical Properties. Editor: A.Cezairliyan, Publ.: American Soc. of Mechanical Engineers, New York. (1977), p. 338-343

[2] C. Otter, D. Damien; High Temp.-High Pressures **16** (1984) 1-6

[3] H. A. Tasman, D. Pel, J. Richter, H.-E. Schmidt; High Temp.-High Pressures **15** (1983) 419-431

[4] J. K. Fink, L. Leibowitz; High Temp.-High Pressures **17** (1985) 17-26

[5] H. A. Tasman, European Institute for Transuranium Elements, Karlsruhe, Annual Report 1988, EUR 12385 EN, p. 80-91

[6] C. Otter, J. Vandevelde; Rev. Int. Hautes Temp. Refr. (FR) **19** (1982) 41-53

[7] C. Ronchi, J.P. Hiernaut, R. Selfslag; G.J. Hyland, Nucl. Sci. Eng. **113** (1993) 1-19

[8] J. P. Hiernaut, G. J. Hyland, C. Ronchi; Int. J. Thermophys. **14** (1993) 259-283

[9] C. Ronchi, G. J. Hyland; J. Alloys Comp. **213/214** (1994) 159-168

[10] O. L. Hagrman; US Department of Energy, Idaho Operation Office. Idaho National Engineering Laboratory, report EG&G-CDAP 3029 (1979)

[11] G. J. Hyland; J. Nucl. Mater. **113** (1983) 125

[12] Hj. Matzke; Adv. Ceram. **17** (1986) 1-54

1.1.4 Modelling work

Fuel performance code development (TRANSURANUS)

TRANSURANUS is a computer program for the thermal and mechanical analysis of fuel rods in nuclear reactors which was developed at the Institute [1]. The TRANSURANUS code is fully described in the literature and was outlined in previous Annual Reports. The code is in use in several European organisations, both research and private industry. Preparatory work to release TRANSURANUS and the related know-how to several Eastern countries has been initiated.

The TRANSURANUS code consists of approximately 200 subprograms which have their own test programs. The total number of files to be maintained is more than 3000. In 1994 many subroutines have been carefully checked, revised and documented. The work on the TRANSURANUS handbook which contains at present 400 pages continued. A specific Windows-type user interface is under development.

A first step towards the development of a specific TRANSURANUS-VVER version has been made by introducing WWER cladding data and a specific WWER correlation for the thermal conductivity of the fuel. Several WWER fuel rod analyses have been performed [2], however, further verification is needed.

Probabilistic analyses

After more than 25 years of research of fuel rod modelling, the basic concepts are well established and the limitations of the specific approaches are known. However, the widely used mechanistic approach leads in many cases to discrepancies between theoretical predictions and experimental evidence indicating that many of the physical processes encountered are not sufficiently understood and are too complex to be modelled exactly. Some of these processes may even be of a stochastic nature. Generally, the material behaviour is far too complex to be characterised by models or correlations consisting of a few parameters. Therefore, for a better understanding of the uncertainties involved and their technological consequences, the influence of the various parameters needs to be investigated which is best done by probabilistic methods.

Probabilistic methods have not been used frequently until now and there are only a few publications in the area of modelling the fuel rod behaviour. However, with the advent of cheap and fast workstations, the situation will certainly change. Probabilistic standard techniques are sensitivity methodologies, response surface techniques and Monte Carlo methods.The fuel rod performance code TRANSURANUS includes two such probabilistic approaches: the Monte Carlo method and the further developed Numerical Noise Analysis. The Monte Carlo method must be considered as a very flexible, general approach whereas the Numerical Noise Analysis is more specific and limited. At present this method is applied within the TRANSURANUS code to three relevant parameters which dominate the fuel rod behaviour: linear rating, gap conductance and thermal conductivity of the fuel. The

analyses provide the uncertainty of the centre line temperature, the integral fission gas release, and the inner pin pressure. The main advantage of the Numerical Noise Analysis is that by considering these relevant parameters as random variables a fairly good probabilistic analysis can be performed at the expense of approximately only one single deterministic analysis. Fig. 1.36 shows the good agreement between the Monte Carlo Technique and the Numerical Noise Analysis: the details are given in Reference [3].

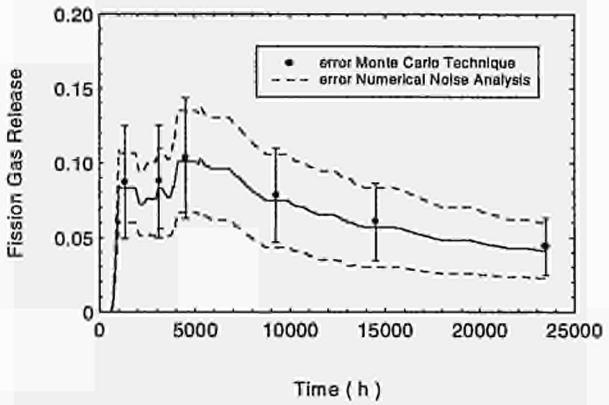

Fig. 1.36 Fission gas release as a function of time: Comparison between the Monte Carlo technique and the Numerical Noise Analysis according to the TRANSURANUS code; the linear rating, the thermal conductivity of the fuel and the gap conductance were treated as continuous random variables.

Fumex blind predictions

The ITU modelling group participated in the international blind FUMEX (FUel Modelling at EXtended) burnup exercise [4] organised by the IAEA (Co-ordinated Research on „Fuel Modelling at Extended Burnup"). The FUMEX irradiations were provided by the OECD Halden Reactor Project. The different rod designs are given in Tab. 1.6, the six tests are summarized in Tab. 1.7 and characteristic temperatures of all tests are shown in Fig. 1.37.

The blind predictions employing the TRANSURANUS code were in very good agreement with experimental evidence and the TRANSURANUS code can be considered as a well validated, mature code [5]. In order to give an overall impression of the predictability of the TRANSURANUS code some predicted temperatures are compared with measured ones in Fig. 1.38. The temperatures were selected in such a way that all different conditions of the tests (burn-up, gas pressure and composition, steady-state and ramp) are represented. It can clearly be seen that the deviations of the TRANSURANUS code are significantly less than the deviations of all other codes.

The following conclusions were drawn:

1. A satisfactory overall agreement was found
2. Fuel swelling was overpredicted, consequently, gap closure occured too early
3. The gap conductance under contact conditions seems to be underpredicted. At high burn-up the concept of surface roughness needs revision.

Tab. 1.6 Design characteristics of the FUMEX Cases 1-6

	Diametral gap (μm)	Filling Gas	Pin Pressure (bar)	^{235}U enrichm. (w/o)	Grain Size (μm)	Fuel Density (%TD)	Fuel Diameter (mm)	Fuel Length (mm)
Fumex 1	130	He	10	3.5	10	94.1	8.09	810
Fumex 2	130	He	10	13.0	7-10	94.3	5.92	443
Fumex 3	100	Xe	1	10.0	3.4	95.0	10.70	140
Rod 2	100	Xe	1	6.0	20.0	95.0	10.70	140
Rod 3	50	He	1	10.0	3.4	95.0	10.75	140
Fumex Rod A	220	He	3	9.9	12.0	95.0	10.68	781
Rod B	220	He 92 % Xe 8 %	1	9.9	12.0	95.0	10.68	781
Fumex 5	210	He	1	3.93	14.5	95.0	10.60	457
Fumex 6	260	He	1 (50)	9.88	16.0	94.7	10.50	466

Tab. 1.7 Description of the six FUMEX cases

FUMEX 1	This dataset represents the irradiation of production line PWR fuel type under benign conditions. Temperatures remained low but increased slightly with burn-up.
FUMEX 2	This was a small diameter rod designed to achieve rapid accumulation of burn-up. Assessment of fission gas release by measurement of internal pressure and puncturing.
FUMEX 3	This case consisted of 3 short rods equipped with centreline thermocouples each with a different gap and fill gas composition. After steady-state irradiation to approximately 30 MWd/kg UO_2, they were given a severe increase in power.
FUMEX 4	Two rods filled with 0.3 MPa He and 0.1 MPa He/Xe mixture were irradiated to approximately 33 MWd/kg UO_2. Both rods experienced a period of increased power during part of the irradiation.
FUMEX 5	This test comprised a single rod base irradiated at low power with a ramp and hold period at the end of life. The main purpose of this case was to assess PCMI and fission gas release under ramp conditions.
FUMEX 6	Two rods were base irradiated at low power. The rods were refabricated to include pressure transducers. Rod internal pressure was monitored during power ramps, one fast, one slow.

Specific model development

The model TUBRNP (TransUranus BuRNuP Model) predicts the radial power density distribution as a function of burnup (and hence the radial burnup profile as a function of time) together with the radial profile of uranium and plutonium isotopes [6]. This model has been utilised to make significant advances to the understanding of both MOX and UO_2 fuel behaviour [7, 8].

Plutonium Isotopic Composition of MOX fuel

A collaboration with the Paul Scherrer Institute (PSI) and access to Belgonucleaire data, see Tab. 1.8, has led to the development of an improved version of the TUBRNP model for the prediction of the total plutonium and radial isotopic composition [7]. It is well known that neutron capture in the resonances of ^{238}U (with a high absorption cross-section) leads to a large build-up of plutonium near the fuel pellet surface (neutronic rim effect). TUBRNP includes this effect with the result that it models accurately the total plutonium radial profile. The crucial factor for describing the isotopic radial distribution was recognising that there is also significant neutron capture in the resonances of ^{240}Pu which leads to a build-up of ^{241}Pu near the edge of the fuel, see Fig. 1.39. It can be seen that calculated profiles are in reasonable agreement with the Secondary Ion Mass Spectometry (SIMS) measurements done at the PSI.

Tab. 1.8 Range of relevant pellet and pin design characteristics

pellet radius (mm)	4.00 - 5.53
pellet density (%TD)	94.0 - 95.6
^{235}U (wt%)	0.23 - 0.72
Pu/(U+Pu) (wt%)	2.8 - 11.5
burnup (GWd/tM)	15 - 55

The predicted burnup profiles are in good agreement with the SIMS results, for example see Fig. 1.40. Details of the TUBRNP results compare favourably with the results of radiochemical analysis and with those of ORIGEN2 [9] and KORIGEN [10] calculations (Tabs. 1.9, 1.10).

Work on improving the model by using better values for the cross-sections and treating the flux depression is in progress. Given the complexity of MOX fuels, the model, even in its present form, is a valuable tool for the analysis of mixed oxide fuel data.

High burnup effects

Change in the structure of high burnup fuels (average burnup greater than 40 GWd/t) is a complex phenomenon which results in the formation of subgrains, the loss of matrix fission gas and an increase in porosity. The ba-

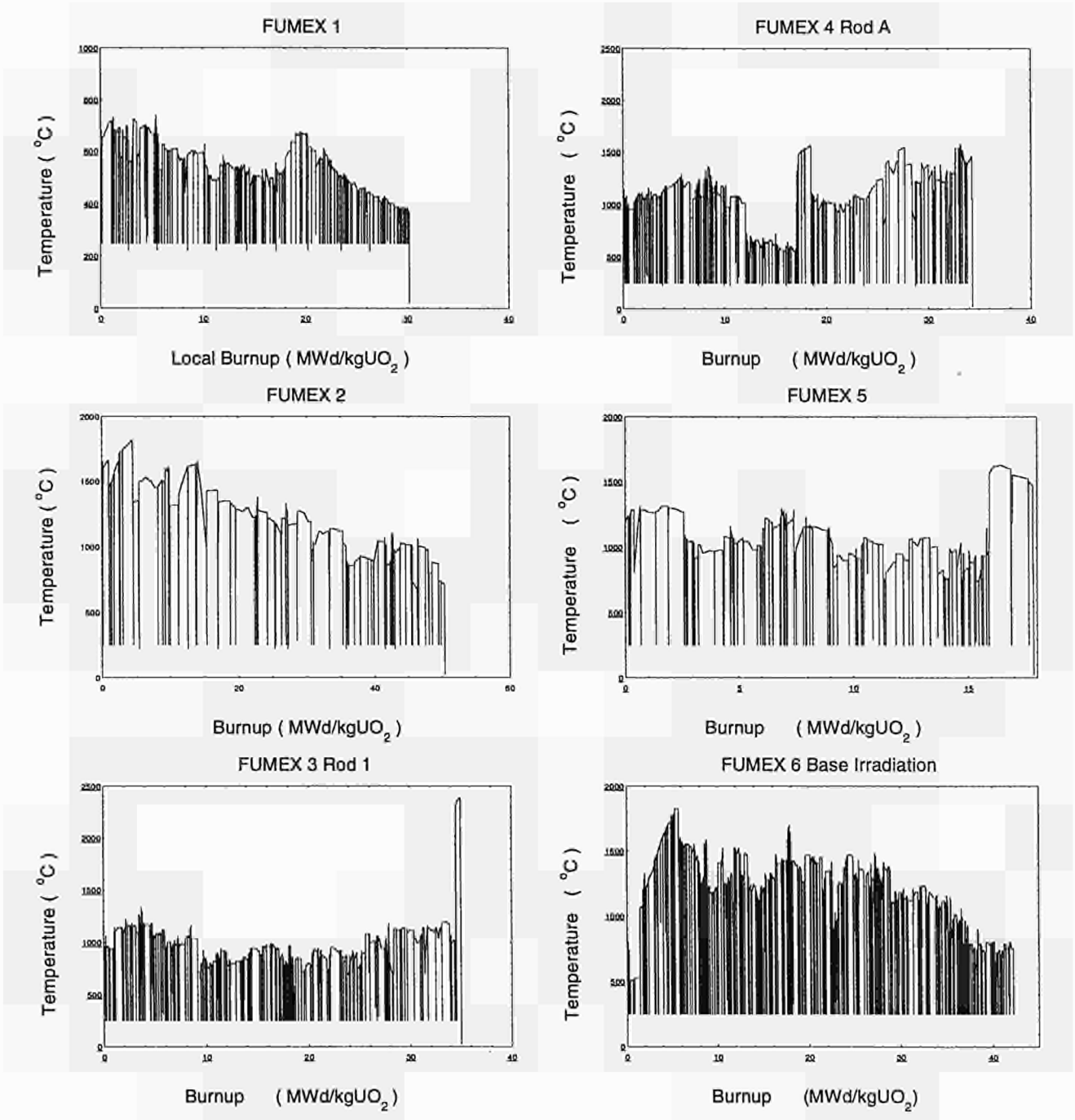

Fig. 1.37 Characteristic temperatures of the six FUMEX tests.

sic process that causes this to occur is the high value of local burnup at the fuel edge due to increased production of ^{239}Pu from resonance capture in ^{238}U. The TUBRNP model was developed to describe this phenomenon in UO_2. It has been noted experimentally that the restructuring (Xe depletion and changes in grain structure) has an onset threshold local burnup in the region of 70 to 80 GWd/t; a specific value was taken for use in the model. For a given fuel TUBRNP predicts the local burnup profile, and the depth corresponding to the threshold value is taken to be the thickness of the Xe depleted region. The results of calculations are displayed in Figs. 1.41 and 1.42. Its predictions for the depth of the Xe depleted zone, as derived from Electron Probe Micro-Analysis (EPMA) measurements done in-house, are in reasonable agreement with experiment even though such other parameters like temperature are not included: this is in progress.

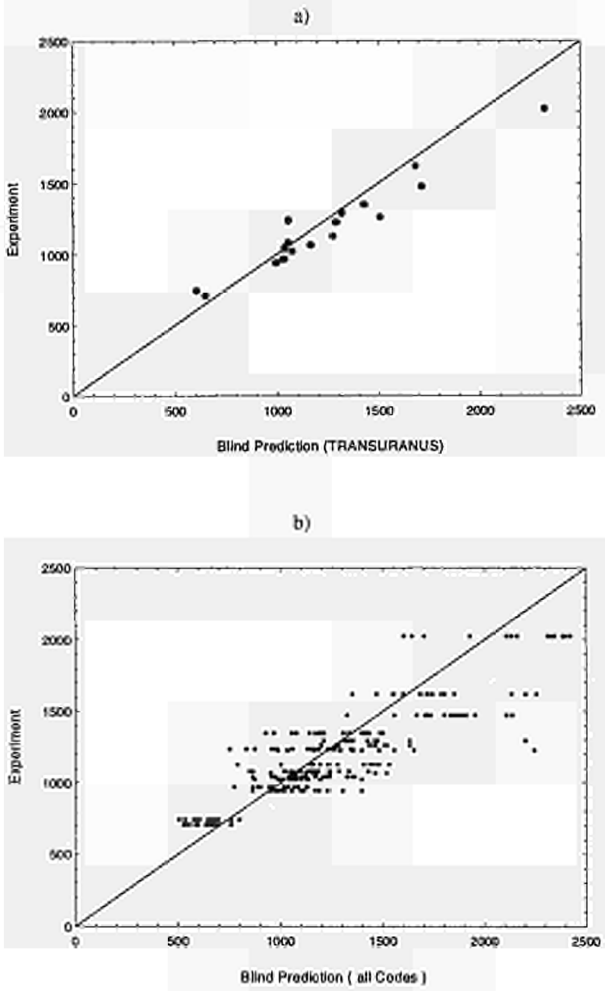

Fig. 1.38 Comparison between selected temperatures from FUMEX 1, 3.1, 3.2, 3.3, 4a and 4b as predicted and thermocouple measurements; Fig a) shows the results of the TRANSURANUS code and b) the results of all 19 participating groups.

Tab. 1.9 Percentage deviation of the predictions of TUBRNP and ORIGEN from the results of radiochemical analysis for two PWR samples (note that the ± indicate over and under prediction). The ORIGEN calculations were done with the latest ORIGEN 2.1 PC version.

	Example 1		Example 2	
	TUBRNP	ORIGEN	TUBRNP	ORIGEN
Total Pu	-11.98	-7.69	+7.45	+11.63
^{239}Pu	-0.59	-1.61	+1.84	+3.42
^{240}Pu	+11.7	-0.99	+9.95	-3.06
^{241}Pu	-40.7	+32.6	-13.46	+17.78
^{242}Pu	-20.8	-5.0	-9.28	-7.23

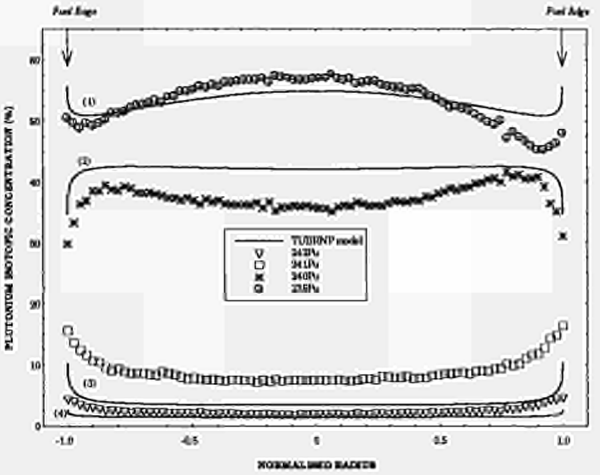

Fig. 1.39 The isotopic plutonium composition plotted as a function of fuel radius as determined by SIMS (PWR MOX pin) and predicted by TUBRNP. The curves labelled 1 to 4 correspond to the predictions for the isotopes 239 to 242.

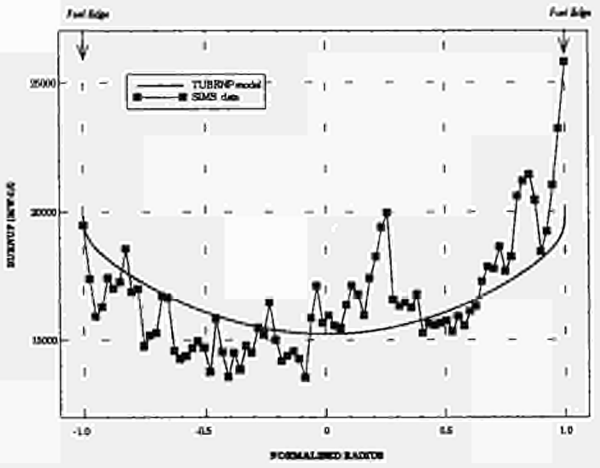

Fig. 1.40 The burnup (MWd/t) plotted as a function of radius as determined from SIMS ^{148}Nd measurements (BWR MOX pin) and the TUBRNP prediction.

Tab. 1.10 Percentage deviation of the predictions of TUBRNP and ORIGEN from the results of radiochemical analysis for two BWR samples (note that the ± indicate over and under prediction). The ORIGEN calculations were done with the latest ORIGEN 2.1 PC version.

	Example 1		Example 2	
	TUBRNP	ORIGEN	TUBRNP	ORIGEN
Total Pu	-2.38	+10.59	-5.05	+4.17
^{239}Pu	+10.1	-2.05	+6.71	+5.71
^{240}Pu	+11.75	-10.81	+13.2	+0.74
^{241}Pu	-38.69	+58.6	-31.9	+4.16
^{242}Pu	-28.32	+16.77	-23.0	-10.34

References

[1] K. Lassmann; J. Nucl. Mater. **188** (1992) 295-302

[2] S. Stefanova, et al., K. Lassmann; IAEA Seminar on WWER Reactors Fuel Performance, Modelling and Experimental Support, Varna, St. Constantine, Bulgaria, 7-11 November 1994

[3] K. Lassmann, C. O'Carroll, J. van de Laar; IAEA Technical Committee Meeting on Water Reactor Fuel Element Modelling at High Burnup and Experimental Support, Bowness-on-Windermere, England, 19-23 September 1994

[4] IAEA Co-ordinated Research Programme on „Fuel Modelling at Extended Burnup" (FUMEX)

[5] C. O'Carroll, J. van de Laar, K. Lassmann; Report on ITU FUMEX Results, Paper presented at the Research Co-ordination Meeting on Fuel Element Modelling at Extended Burnup (FUMEX), International Atomic Energy Agency, Bowness-on-Windermere, England, 15-16 September 1994

[6] K. Lassmann, C. O'Carroll, J. van de Laar, C. T. Walker; J. Nucl. Mater. **208** (1994) 223

[7] C. O'Carroll, J. van de Laar, C. T. Walker, C. Ott, R. Restani; IAEA Technical Committee Meeting on Water Reactor Fuel Element Modelling at High Burnup and Experimental Support, Bowness-on-Windermere, England, September 19-23, 1994

[8] C. O'Carroll, K. Lassmann, J. van de Laar, C.T. Walker; IAEA Technical Committee Meeting on Water Reactor Fuel Element Modelling at High Burnup and Experimental Support, Bowness-on-Windermere, England, September 19-23, 1994

[9] Oak Ridge National Laboratory, internal report CCC-371 (1991)

[10] U. Fischer, H. W. Wiese; Kernforschungszentrum Karlsruhe, report KFK-3014 (1983)

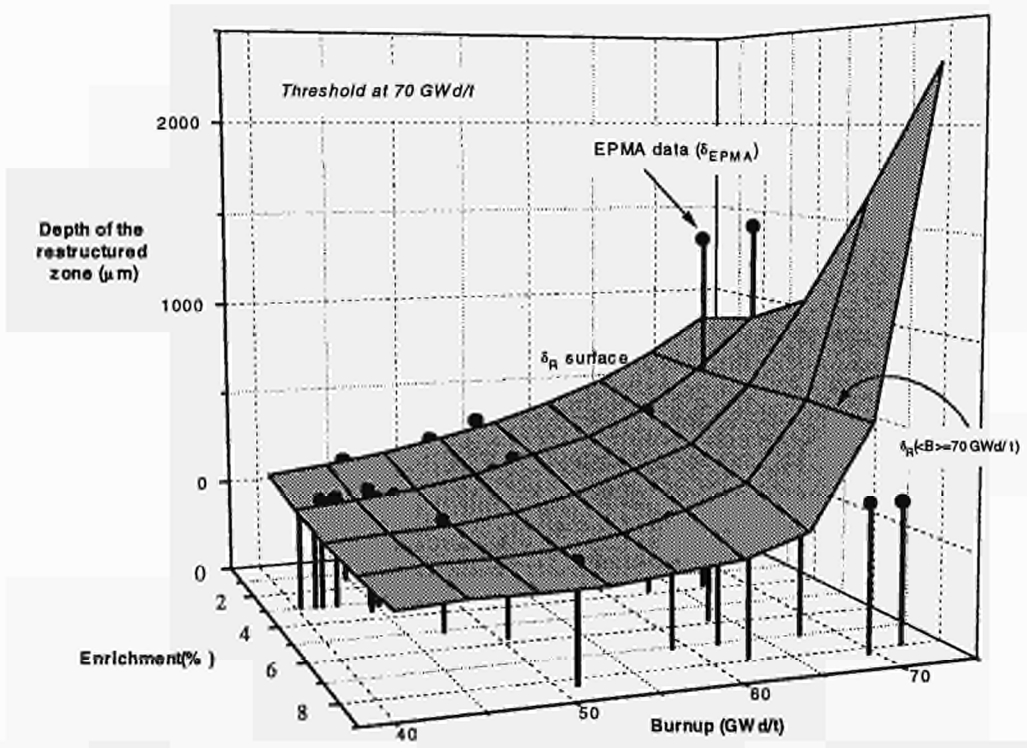

Fig. 1.41 The depth of the restructured zone as a function of enrichment and average burnup. The surface is the prediction (δR) of the TUBRNP model for the standard case with a threshold value of τ_b=70 GWd/t. The points are the values of the depth of this zone derived from the Xe profiles (δ_{EPMA}).

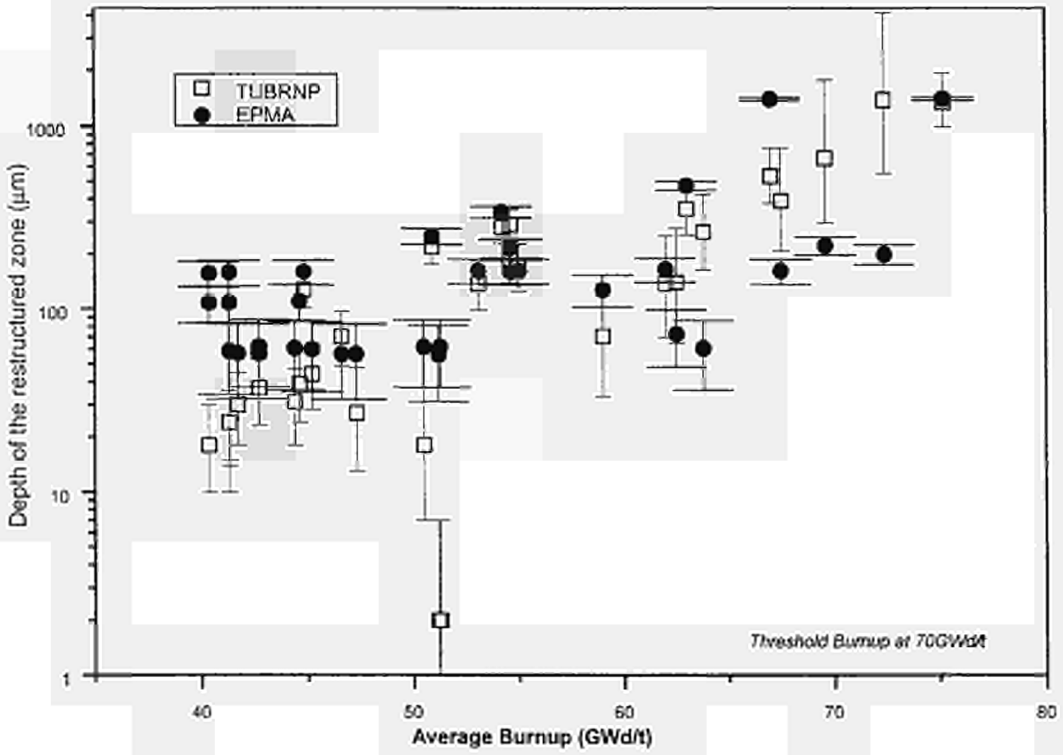

Fig. 1.42 Log-log plot of the depth of the restructured zone as a function of the average burnup. The predicted values are calculated at the nominal burnup <B> and at <B>±5% for a threshold burnup of 70 GWd/t. The upper and lower values of δR (<B>±5%) are plotted at <B> for convenience. The points are the values of the depth (with errors) of this zone derived from the Xe profiles (δ_{EIMA}).

1.2 Partitioning and Transmutation

1.2.1 Actinide partitioning from HLW in a continuous diisodecylphosphoric acid (DIDPA) extraction process by means of centrifugal extractors

A series of comparative experiments is being carried out at the Institute to select a suitable partitioning process for the reprocessing of dissolved spent fuel stored in the chemical hot cell facility and especially also for the separation and recovery of non-transmuted radiotoxic elements from SUPERFACT dissolver solutions. It is evident, that the transmutation of these nuclides achieved in a single irradiation cannot sufficiently reduce (e.g. by a factor of 100) the radiotoxicity. Hence recycling of the remaining minor actinides becomes necessary [1,2,3]. In case of homogeneous, self-generated recycling, the same partitioning process can be applied as was used for the original separation from the HLW.

After the Chinese (TRPO) and the American CMPO (TRUEX) process (TUAR-92, p. 80, TUAR-93, p. 76), the Japanese extractant diisodecylphosphoric acid (DIDPA) was tested using the centrifugal extractor installation. The process was developed at the Japan Atomic Energy Research Institute (JAERI) [4,5]. DIDPA is an acidic extractant similar to hexyl di(2-ethyl)phosphoric acid (HDEHP), but in contrast to this solvent it can extract trivalent actinides from solution at higher HNO_3 concentrations (0.5 M).

During 1993, the partitioning process developed had been tested on a genuine HLW (1.2 l, 200 Ci) using mixer-settler equipment [6] with very satisfactory results for the recovery of Am and Cm. In the DIDPA process, the Np extraction is determined by the rate of the extraction process, not as for most other extractants by the distribution ratio at equilibrium. This rate can be increased by the addition of H_2O_2 [7,8] leading to good extraction results for Np. It was thus interesting to see whether in centrifugal extractors (under conditions similar to those used for TRPO and CMPO) the shorter contact time between acqeous and organic phase would still be sufficient to obtain the same results.

The HLW used in the experiment was similar to that of the previous experiments, originating from a HLW concentrate from the reprocessing of different LWR fuels. After separation of the fines by centrifugation, the solution was diluted about 11 times to adjust the HNO_3 concentration to 0.5 M and the specific volume to ca. 3000 l/t U. The HLW feed was stored 4 days prior to the experiment to let Np reach equilibrium.

The extractant, DIDPA, produced by the Daihachi Chemical Industry Co., Ltd. in Japan was used without further purification. The composition of the solvent was 0.5 M DIDPA - 0.1 M TBP in n-dodecane.

The centrifugal extractors used in the present experiment were developed at the Institute of Nuclear Energy and Technology in Beijing, China and modified for hot-cell operation at the Institute. The characteristics of the extractors were described previously [9]. The operating conditions of the centrifugal extractors are shown in Fig. 1.43. Similar to the previous experiments, the 12 extractors were used twice. After cleaning the equipment, Am and Cm were stripped from the loaded solvent in the first stripping step with 4 M HNO_3 followed by Np and Pu stripping with 0.8 M oxalic acid ($H_2C_2O_4$) after 3 hours when the process had reached equilibrium. Samples were prepared and analysed by ICP-MS from each outlet stream and from each stage.

Results and Discussions

The concentration profiles of the actinides in the aqueous phase of the extraction section are shown in Fig. 1.44. Apart from Np, actinides (as shown from the concentration decrease in Fig. 1.44 from stage 8 to 1), were extracted with a very high yield. Their concentration in the raffinate fraction reached the detection limit by ICP-MS. Decontamination factors of actinides from the raffinate are given in Tab. 1.11.

The low DF value for Np can be explained by the short contact time between the aqueous and organic phase in the centrifugal extractors. As mentioned above, the Np extraction is determined by the reaction rate and thus a recovery of only 84 % was achieved after 8 stages at room temperature. Experiments carried out in JAERI using mixer-settlers gave 99.95 % recovery of Np in 12-stages extraction at 45 °C.

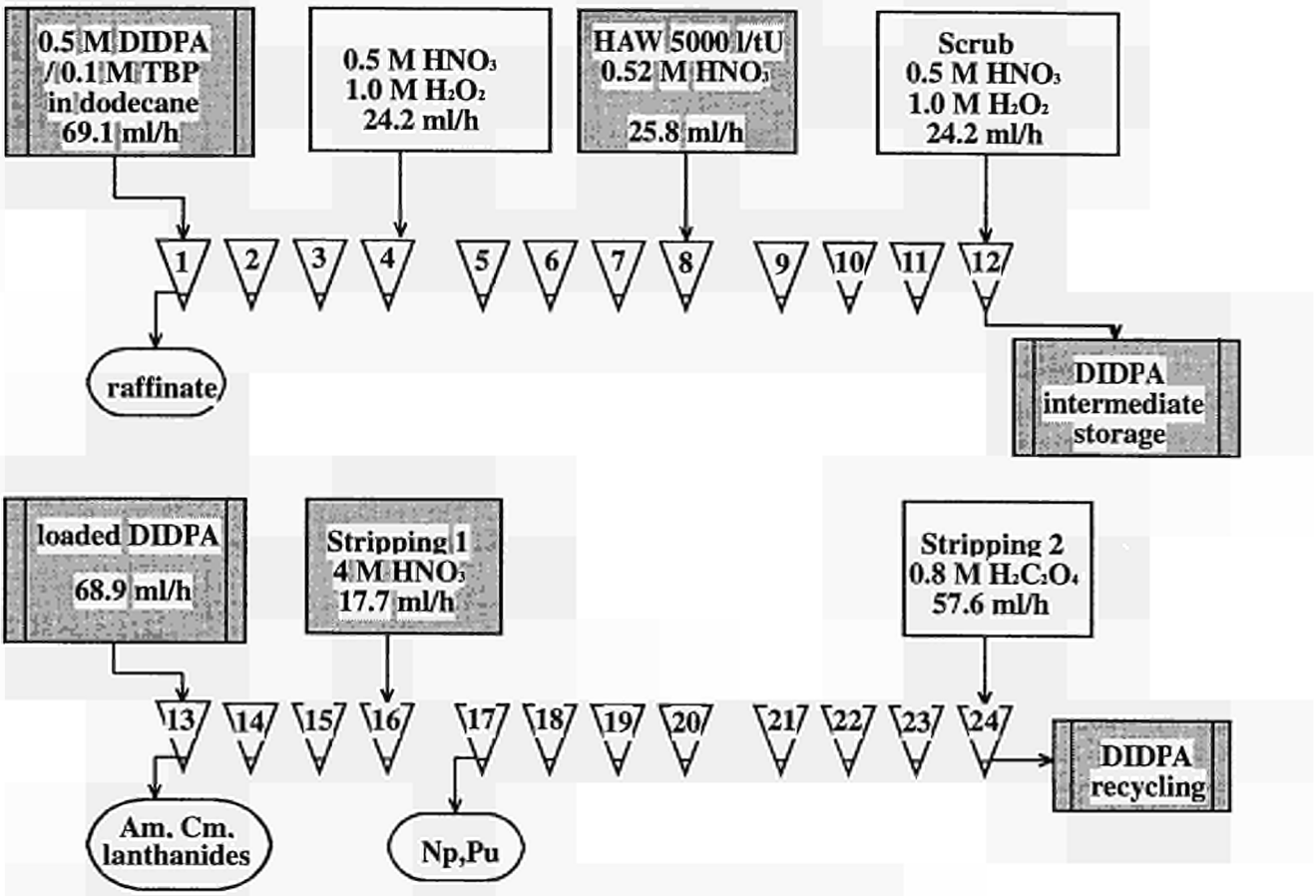

Fig. 1.43 Operating conditions of the centrifugal extractors in the DIDPA process.

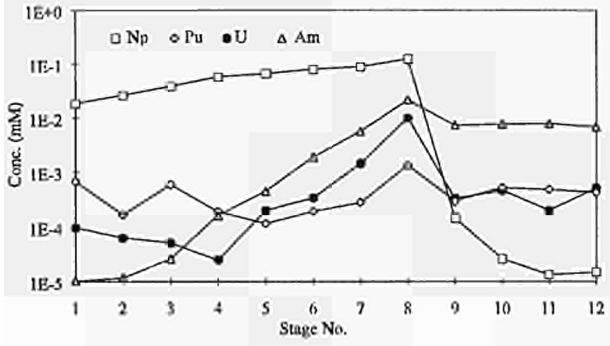

Fig. 1.44 Concentration profiles of main actinides in the aqueous phase of the extraction section.

Tab. 1.11 Decontamination factors (DF) determined for the main actinides and Nd.

Isotope	Concentration in the feed (g/l)	DF
^{144}Nd	0.47	> 4000
^{237}Np	0.05	>5
^{238}U	0.86	>20000
^{239}Pu	0.02	> 150
^{243}Am	0.06	> 10000
^{244}Cm	0.007	> 1500

On the other hand the short contact times in centrifugal extractors has the advantage that the decomposition of H_2O_2 is negligible in the present experiment. In Fig. 1.45 a linear decrease of the Np concentration in the aqueous phases from stage 8 to stage 1 is shown, compared to the feed solution. The second addition of H_2O_2 at stage 4 further increased the extraction rate of Np. In the experiments in JAERI with the mixer-settler, a gradual decomposition of H_2O_2 caused by the long residence time in the extractors, particularly in the settling zone, was observed.

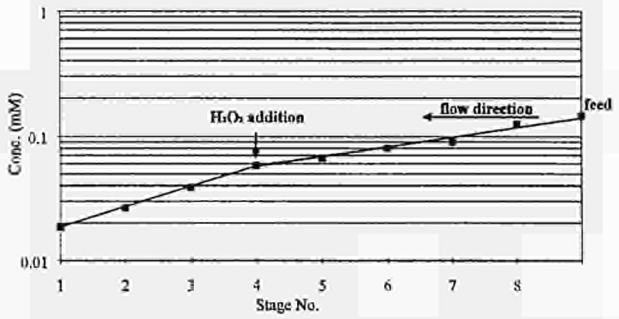

Fig. 1.45 Concentration profiles of Np in the aqueous phase of the extraction section.

The extraction rate of Np per stage as a function of the H_2O_2 concentration can be calculated from the slope of the straight line in Fig. 1.43 according to:

$C_n = C_{n+1}\exp(-k)$ C_n : Np concentration at stage n

$k = K[H_2O_2]^{1/2}$ $[H_2O_2]$: H_2O_2 concentration

From the rate constant K in [stage^{-1}M$^{-1/2}$] in the present experiment and the rate constant in [stage^{-1}M$^{-1/2}$] obtained in the mixer-settler run at 25 °C, an effective contact time of 10 s was calculated for the centrifugal extractors. However this value could be an underestimate because it was found in the mixer-settler experiment that the extraction rate of Np depends on the concentration of elements with catalytic properties such as Pd and in the present study the concentrations of these elements in the feed solution were lower.

The Np extraction could be improved if the temperature were raised and the number of extraction stages increased; a calculation showed that for instance 99.6% recovery would be achieved with 16 extraction stages at 45 °C and 2 M H_2O_2 in the scrubbing solution without further addition of H_2O_2 . With a H_2O_2 concentration of 4 M in the scrubbing solution a recovery of 99.96% would be possible. Also centrifugal extractors with longer contact time in the mixing zone would give a higher recovery of Np.

The concentration profiles of some relevant fission products in the extraction section are shown in Fig. 1.46. Lanthanides and actinides are extracted together. As observed in the experiment with mixer-settlers, Fe was extracted with a yield of 92%. Tc, which has a long-lived isotope, and Cs were not extracted and thus separated from the actinides. For certain elements there was a difference between the genuine HLW used in the present experiment and the simulated HLW used for the mixer-settler test: For Rh only 0.08% (instead of 12%), for Pd 6% (instead of 0.5%) were extracted in the present experiment. More important were the differences observed for Mo. Although batch experiments [10] in JAERI showed that Mo would be extracted with DIDPA with a high yield,

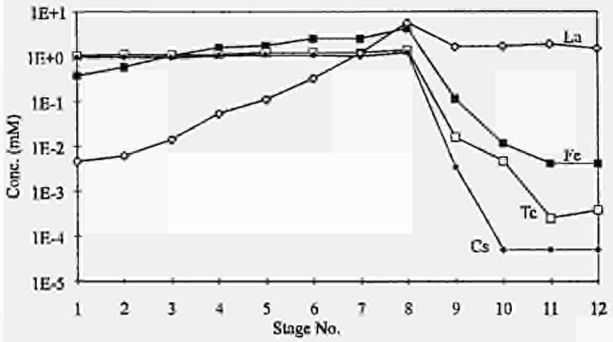

Fig. 1.46 Concentration profiles of main fission and corrosion products in the aqueous phase of the extraction section.

only about 0.5% of Mo was extracted in the present work, which is rather favourable. These differences show again that especially for elements with a complex chemical behaviour it is very important to use real HLW.

The concentration profiles of the actinides in the aqueous and the organic phases in the two stripping sections are shown in Fig. 1.47. The recoveries of the two actinides needs to be further improved as can be seen from Tab. 1.12 where the relative distribution of the elements in the different process streams is given.

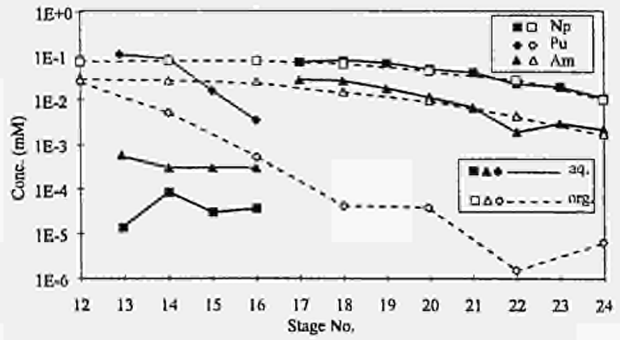

Fig. 1.47 Concentration profiles of main actinides in the aqueous and the organic phases of the stripping section.

97.9% of Am was recovered during the stripping with 4 stages. The extrapolation of the present result would lead to a recovery of 99.2% with 5 stripping stages and 99.9% with 7-stages. Higher temperatures should improve the recovery of Am as well. In the cold experiments with mixer-settlers, the recovery of Nd in 5 stages increased from 99.43% to 99.996% when the temperature was raised from 25 °C to 45 °C.

In the case of Np an increase of the recovery rate from 72.6 to 99.9% would require 27 back-extraction stages. It is known that stripping of elements from the loaded DIDPA solvent with $H_2C_2O_4$ proceeds a little more slowly than stripping with HNO_3. Radiolysis of DIDPA caused by longer storage of the loaded solvent might have an

Tab. 1.12 Fractional distribution of elements into different process streams.

	Raffinate	Strip 1 (Am,Cm)	Strip 2 (Np,Pu)	Used DIDPA (U)
Cr	96.9	0.043	0.24	2.8
Fe	8	0.46	41	50
Ni	> 99.1	< 0.9	< 0.009	< 0.009
Rb	> 99.99	< 0.01	< 0.0001	< 0.0001
Sr	99.79	0.21	< 0.0021	< 0.0021
Y	0.01	7.9	0.66	91.4
Zr	< 0.7	< 0.5	7	93
Mo	99.47	0.017	0.31	0.20
Tc	99.99	0.01	< 0.0001	< 0.0001
Ru	98.5	0.32	0.19	1.0
Rh	99.92	0.028	0.031	0.021
Pd	93.8	0.74	0.48	5.0
Cd	96.4	0.43	2.5	0.63
Sb-Te	> 98.4	< 1.6	-	-
Te	> 99.81	< 0.17	< 0.02	< 0.02
Cs	> 99.993	< 0.007	< 0.00007	< 0.00007
Ba	99.5	0.5	< 0.005	< 0.005
La	0.17	99.2	0.47	0.13
Ce-Nd	0.025	97.0	2.5	0.54
Sm-Gd	0.023	91.4	5.3	3.3
Ln Total	0.042	96.9	2.4	0.68
U	0.005	< 0.04	0.72	> 99.2
Np	15.8	< 0.0025	72.6	11.6
Pu	< 0.6	< 0.44	91.9	8.1
Am	< 0.01	97.9	2.1	< 0.002
Cm	< 0.13	98.4	1.5	< 0.1

influence on the stripping as one of the degradation products, monoisodecylphosphoric acid (MIDPA), makes the stripping difficult [11]. To improve the Np stripping, it is necessary to decrease the flow rate ratio, to raise the temperature and/or to modify the extractors to increase the contact time. The first approach increases the volume of the solutions to be treated. Raising the temperature exerts two positive effects: the distribution ratio of Np decreases and the stage efficiency increases. The use of extractors with longer mixing time seems to be the most practical approach, because the radiation level is very low in this section.

The decontamination factors of corrosion and fission products in the three actinide fractions are given in Tab. 1.13. Since the U stripping was not included in the present experiment, the used solvent was regarded as the U fraction in this table.

Yttrium and lanthanides were quantitatively found in the Am-Cm fraction. The main contaminating elements in the Np-Pu fraction were Fe, Zr, Pd and Cd. From cold experiments Zr was expected to be quantitatively stripped with $H_2C_2O_4$ [10]; in the present study only 7% was back-extracted, probably due to a different chemical form. The modification of this step for the quantitative recovery of Np and Pu would decrease the DF values of Fe and Zr. Therefore, an additional separation of Fe - Zr from Np - Pu would be required. A possible solution for instance would be an oxalate precipitation of Np and Pu with the additional benefit of converting these two elements into a solid form.

Conclusions

Actinides, apart from Np, were extracted from HLW with very high yields. Although only 84% of Np was recovered in the present experiment because of the short contact time, the recovery would be improved to 99.6% or

Tab. 1.13 Decontamination factors of elements from the three actinide fractions.
** : DFs that will be improved by the optimisation of the preceding step*

	Am, Cm (Strip 1)	Np, Pu (Strip 2)	U (Used DIDPA)
Cr	2300	410	35
Fe	200	2.4	2*
Ni	> 110	> 11000	> 11000
Rb	> 1000	> 1000000	> 1000000
Sr	470	> 47000	> 47000
Y	12	150	1
Zr	> 200	14	1*
Mo	5800	320	500
Tc	10000	> 1000000	> 1000000
Ru	310	520	100
Rh	3500	3200	4700
Pd	130	200	20
Cd	230	40	150
Te	> 580	> 5000	> 5000
Cs	> 14000	> 1400000	> 1400000
Ba	200	> 20000	> 20000
La	1	210*	760*
Ce-Nd	1	40*	180*
Sm-Gd	1	18*	30*
Ln Total	1	41*	140*
U	2500	130	-
Np	> 33000	-	8.6*
Pu	> 220	-	12*
Am	-	47*	> 50000
Cm	-	66*	> 1000

further to 99.96% by increasing the number of stages and the H_2O_2 concentration and by raising the temperature. About 98% of Am and Cm were recovered from the loaded solvent in the first stripping step with 4 M HNO_3. The recovery would be also improved to more than 99.9% by changing the process conditions. The situation of the second stripping step for Np and Pu with 0.8 M $H_2C_2O_4$ was similar to that of the first stripping. Tc and heat-generating Cs and Sr were not extracted and were separated from the actinides with high decontamination factors. The present results show that the centrifugal extractors are applicable also to the DIDPA extraction process, but that a small modification of the extractors seems to be required.

References

[1] L. Koch, G. Nicolaou; Comparison of Possible Partitioning and Transmutation Schemes When Added to the Existing Nuclear Fuel Cycle, Proc.of the IAEA Technical Committee Meeting on Safety and Environmental Aspects of Partitioning and Transmutation of Actinides, 29.11-2.12, 1993, Vienna, (in press)

[2] J. O. Blomeke, A. G. Croff; „Nuclear Waste Partitioning and Transmutation", Nucl. Technol. **56** (1982) 361

[3] L. Koch; „Minor Actinide Transmutation - A Waste Management Option", J. Less-Common Met. **122** (1987) 371

[4] M. Kubota, S. Dojiri, I. Yamaguchi, Y. Morita, I. Yamagishi, T. Kobayashi, S. Tani; Development of a Partitioning Method for the Management of High-Level Liquid Waste", High-Level Radioactive Waste and Spent Fuel Management Vol II, Slate, S.C., Kohout, R., Suzuki, A., Eds, The American Society of Mechanical Engineers (1989) 537

[5] M. Kubota, I. Yamaguchi, Y. Morita, Y. Kondo, K. Shirahashi, I. Yamagishi, T. Fujiwara, „Development of a Partitioning Process for the Management of High-Level Waste", Proc. of GLOBAL'93, p. 588 (1993)

[6] M. Kubota, I. Yamaguchi, K. Okada, Y. Morita, K. Nakano, H. Nakamura; „Partitioning of High-Level Waste as Pretreatment in Waste Management", Mat. Res. Soc. Symp. Proc. **26** (1984) 551

[7] Y. Morita, M. Kubota, J. Nucl. Sci. Technol. **24** (1987) 227

[8] Y. Morita, M. Kubota, Solvent Extr. Ion Exch. **6** (1988) 233

[9] J.-P. Glatz, C. Song, He, X., H. Bokelund, L. Koch; „Partitioning of Actinides form HAW in a Continuous Process by Means of Centrifugal Extractors", Proc. of I&EC Special Symp., Am. Chem. Soc., Atlanta, USA, Sep 27-29, (1993)

[10] K. Shirahashi, Y. Morita, M. Kubota; J. Radioanal. Nucl. Chem. **185** (1994) 173

[11] Y. Morita, M. Kubota, M.Yoneya, O. Tochiyama; Y. Inoue, J. Nucl. Sci. Technol. **26** (1989) 698

1.2.2 Fabrication of fuel pins for the HFR irradiation experiment TRABANT (TRAnsmutation and Burning of Acti-Nides in TRIOX)

In the frame of the project CAPRA (Consommation Accrue de Plutonium dans les RApides), irradiation experiments are planned to study the transmutation of actinides and long-lived fission products and the behaviour of the new fuel types, which are either defined by a very high content of plutonium (> 40 wt%), uranium and minor actinides (MA) or by the complete absence of uranium (in order to avoid additional breeding).

The irradiation experiment TRABANT is planned and executed in a trilateral cooperation with CEA and KfK. The Institute activities are concentrated in the fabrication of fuel pins to be irradiated in a TRIOX capsule in the HFR reactor at Petten. The purpose of the irradiation is to study the behaviour of the new materials under neutron irradiation in order to get information on such parameters as Pu- and MA-distribution, separation processes and solubility behaviour in nitric acid.

The TRIOX capsule allows the simultaneous irradiation of 3 pins under comparable flux and temperature conditions. Based on that, 4 fuel columns were designed containing the following different fuel types. The fuel types a) and d) are fabricated by CEA Cadarache, the fuel types b) and c) by ITU.

a) mixed $(U,Pu)O_2$ with a Pu-content of 45 wt%
b) mixed $(U,Pu,Np)O_2$ with 40 wt% Pu and 5wt% Np
c) mixed $(Pu,Ce)O_2$ with 41 wt% PuO_2 and 59 wt% CeO_2
d) mixed PuO_2-MgO with 52 wt% PuO_2 and 48 wt% MgO

Fuel and fuel pin specifications have been established.

For all TRABANT pins an austenitic cladding material (15/15 Ti) is used; the main geometrical data are:

outer cladding diameter:	6.55 mm
inner cladding diameter:	5.65 mm
total pin length:	632.00 mm
fuel column length:	340.00 mm

The fuel columns consist of fuel pellets, either in annular or in a solid form. In case of one pin (pin No. 3) two half-columns are used, one half consisting of $(Pu,Ce)O_2$ fuel pellets, the other having the PuO_2-MgO fuel type.

It was necessary to develop special fabrication procedures for the new fuel materials, both because of their unusual composition and the high specific radioactivity. Problems arose with the handling of the Np-containing mixed oxide in a Pu-glove box line from the radiation of the Np; and in case of the $(Pu,Ce)O_2$ where no fuel experience existed before.

After additional shielding of the glove boxes fuel preparation was started. In order to assure a solid solution of

the $(Pu,Ce)O_2$ and the $(Pu,U,Np)O_2$ fuel the starting oxide powders were prepared by a „Sol-Gel" technique. This technique also minimizes the formation of dust during the fabrication steps. The other mixed oxide fuel pellets are under fabrication by pressing and sintering techniques.

1.2.3 POMPEI mixed nitrides and technetium irradiation experiment

The investigations of operational limits for future fuels were continued. The high burn-up irradiation experiment POMPEI (POM PEtten Irradiation) in HFR-Petten has achieved the goal burn-up (27.8 a/o) and was unloaded from the reactor for post irradiation examination (PIE).

The transport of the irradiated pins of the NILOC 3 and NILOC 4 experiment in HFR-Petten to ITU-Karlsruhe was postponed to 1995.

The additional destructive examination of selected fuel section of the 19 carbide-pin bundle, irradiated to 7 a/o burn-up in the KNK reactor was started at the end of this reporting period.

The high burn-up irradiation experiment POMPEI, containing targets loaded with mixed nitride fuel and technetium has reached its goal burn-up > 20 a/o after 270 days of irradiation in HFR Petten. The aim of this experiment is to obtain data on the evolution of structure, fission products and the chemical behaviour at high burn-up.

9 mixed nitride fuel discs, with an oxygen content varying from 500 ppm to 7000 ppm and prepared by two different fabrication processes were individually sealed in small capsules and assembled together with 3 encapsuled discs of technetium and technetium-ruthenium alloys (TUAR-92, p. 56-57). The (U,Pu)N fuel irradiation is complementary to the joint investigation on mixed nitride fuels of the French Commissariat à l'Énergie Atomique (CEA) and the Institute. The technetium specimens were later included to obtain information on the irradiation behaviour which will be needed for future transmutation.

The temperature of each specimen was individually measured on the capsule surface with thermocouples. The calculated surface temperature of the nitride fuels was 800 - 900 °C and 400 - 420 °C for the technetium specimens at the beginning of the irradiation. The peak fissile power was 954 W/g. The burn-up for the nitride fuels varies from 21.3 to 27.8 a/o and the transmutation for the technetium specimens between 6 and 7.5 a/o. The experiment was unloaded from the reactor in August 1994. After the non-destructive examination to be done in Petten, the capsule will be transported to ITU Karlsruhe for destructive postirradiation analysis.

1.2.4 Experimental feasibility of targets for transmutation (EFTTRA)

In the field of research on nuclear waste management, the possibility of separating and transmuting the long-lived radioactive nuclides, with the aim of reducing the radiotoxicity of the final waste, is being investigated. In order to contribute efficiently to the development of materials for the transmutation, the Institute is collaborating with CEA (France), ECN (The Netherlands), EDF (France), and KfK (Germany), with the aim of setting up joint experiments. The group was named "Experimental Feasibility of Targets for TRAnsmutation" (EFTTRA) [1]. Following a series of meetings, held regularly since September 1992, a contract has finally been signed, and support from the Human Capital and Mobility programme of the European Commission is under consideration. In November 1994, the extension of the collaboration to a further partner, namely the Institute for Advanced Materials in Petten (JRC), was agreed upon.

The goal of the EFTTRA collaboration is the study of materials for transmutation, including the fabrication and characterization of fuels and samples, their irradiation, and test of their in-pile behaviour. The work should be limited to the basic study of fundamental aspects of the problem. Being the subject of other programmes, the reprocessing and the partitioning as such are not considered in EFTTRA, but their interrelation with transmutation should of course be taken into consideration. This applies to strategies, where the type of reactor to be used for transmutation is, among others, an important parameter.

It has been decided to focus efforts on the study of materials for the transmutation of ^{99}Tc (metal), of ^{129}I (compound), and of Am (in an inert matrix); the homogeneous recycling of Am is the field of other international collaborative efforts, as illustrated for example by the irradiation experiments SUPERFACT 1 [2] and SUPERFACT 2 (in preparation). The first phase of the EFTTRA collaboration was defined as the irradiation of Tc samples, I compounds, and "empty" (without Am, but partially using U to simulate Am) inert matrices, and the related post-irradiation examinations.

The irradiation of 3 Tc samples, fabricated at ITU [3], and of 6 iodine compounds, fabricated at ECN, started in April 1994 in the HFR in Petten. The irradiation will be stopped by the mid of January 1995, after 8 cycles. The objective of the irradiation of Tc is the knowledge of its behaviour under irradiation, the determination of the importance of the self-shielding effect, and a first estimation of the transmutation rate. The expected transmutation for Tc is of the order of 5%. The irradiation of samples of PbI_2, CeI_3, and NaI (replacing the initially foreseen YI_3) aims at the verification of the transmutation rate, and at the investigation of the chemical interaction

with the cladding. After the transportation of the irradiated samples to the different laboratories, the post-irradiation examination (PIE), will take place: non-destructive (metrology, X-radiography, gamma scanning), and destructive (gas analysis, chemical analysis, micrography, microprobe analysis).

A second experiment, called MATINA (MATrices pour INcinération d'Actinides) [4], will supply information on the irradiation effects on inert matrices. The MATINA capsule, containing the candidate inert matrices for Am transmutation (heterogeneous recycling mode), has been mounted in the Phenix reactor for irradiation. For the MATINA experiment, the matrices are „empty", i.e. they contain no americium, but some of them contain uranium to simulate americium. After 2 cycles in Phenix (MATINA 1), 3 pins will be removed for a destructive analysis, and replaced by new samples. The rest of the pins will undergo a non-destructive examination. The irradiation will then be pursued for 2 more cycles (MATINA 1 bis). The nature of the new matrix samples to be irradiated will be discussed among the EFTTRA partners.

New matrices, not yet included in the MATINA experiment, have been proposed as candidates for the fabrication of Am targets. For these matrices, a lack of knowledge of their properties hindered a straightforward irradiation in Phenix; preliminary out-of-pile studies are required, and have been started. A bibliographic study let to a first selection of these new matrices; ion implantation experiments have been started for a better understanding of possible irradiation damages both in matrices already selected for MATINA (like spinel), and in new matrices. At a later stage, compounds of these matrices with Am will be examined for defects after 1 year storage.

A long-term irradiation of 3 Tc samples, identical to the samples of the HFR irradiation will be performed in Phenix from 1995 to 1998 (ANTICORP 1 irradiation). The fabrication of these 3 samples will be carried out by ITU.

References

[1] J.-F. Babelot , H. Gruppelaar , G. Mühling , C. Prunier , M. Rome , M. Salvatores; EFTTRA, A European collaboration for the development of fuels and targets for the transmutation, 3rd NEA International Information Exchange Meeting, Cadarache, December 12-14, 1994

[2] C. Prunier, F. Boussard, L. Koch, M. Coquerelle; in GLOBAL'93: Future Nuclear Systems: Emerging Fuel Cycles and Waste Disposal Options, Seattle, Washington, September 12-17, 1993, Proceedings pp. 158-163

[3] J.-F. Babelot, J.-F. Gueugnon, J. McGinley, K. Richter, J.-C. Spirlet; Projet EFTTRA, Fabrication de 3 capsules de Technétium pour irradiation dans HFR, Rapport de fabrication Cera-Met 1/94, Note Technique K 02 94 182, Commission Européenne, Centre Commun de Recherche, Institut des Transuraniens, Karlsruhe, Germany, Avril 1994

[4] N. Chauvin; Dossier technique de l'expérience MATINA (CEA), private communication, 1993

1.2.5 Radiation dose aspects of fuels used for the transmutation of minor actinides (MA)

Introduction

Nuclear waste, either in the form of spent fuel or high level waste from fuel reprocessing, is associated with a radiotoxicity potential due to minor actinides (MA) and fission products (FP). The possibility of partitioning minor actinides out of the waste and transmuting them into less hazardous nuclides has been proposed and its technical feasibility is being studied [1]. Several concepts of MA transmutation, relying on existing nuclear power stations, are being studied theoretically and experimentally. In one, the recycling of MA with plutonium in the "self-generated mode" is being studied either in thermal (PWR) or fast reactors (FR) [2,3]. Another concept, the transmutaion of minor actinides in a fast reactor has been investigated in practise in the irradiation in the fast reactor PHENIX [4].

Radiation dose levels have to be calculated at fabrication and discharge for the different recycling schemes. In order to assess the accuracy of these predictions, measured radiation doses of minor-actinide-containing fuel irradiated during, e.g. the SUPERFACT programme, can then be compared wth those calculated.

Fuel cycles under consideration

Nuclear fuel cycles for the self-generated recycling of Pu and minor actinides

Several concepts, relying on existing nuclear power stations, have been proposed for the self-generated recycling of the nuclides of Np, Pu, Am, Cm and Tc [5]:

1. PWR and Fast Reactor reference fuel cycles (R1)

A BIBLIS type PWR reactor is considered, fuelled with UOX or MOX (U, Pu) and enriched by either 4 wt % in ^{235}U or by 3.7 wt % fissile Pu. The inventory of the spent fuel was calculated after a burnup of 50 and 33 GWd/t respectively and a cooling time of 7 years [2]. As fast reactor, a PHENIX type, fuelled with 25% first generation Pu and burnt to 60 GWd/t is considered.

2. PWR self-generated transuranium (TU) recycle (R2)

All self-generated transuranium nuclides together with ^{99}Tc are recycled in the same reactor and under the same conditions as above.

3. FR self-generated transuranium recycle (R3)

The inventory of spent fuel, having a burnup of 80 GWd/t, was calculated after the 16th cycle of transuranium nuclide recycling in the fast reactor SUPERPHENIX [3]. An out-of-pile-time of 2 years was considered in this case.
The fuel compositions corresponding to the above nuclear fuel cycles are given in Tab. 1.14 [5].

Tab. 1.14 Fuel compositions of different reference nuclear fuel cycles.

PWR-UOX and -MOX, FR reference cycles (R1)	UO_2, $(U_{0.95}Pu_{0.05})O_{2-x}$, $(U_{0.75},Pu_{0.25})O_{2-x}$
PWR self-generated TU recycle (R2)	$(U_{0.95}Pu_{0.04}Np_{0.004}Am_{0.002}Cm_{0.001}Tc_{0.003})O_{2-x}$
FR self-generated TU recycle (R3)	$(U_{0.8}Pu_{0.186}Np_{0.001}Am_{0.007}Cm_{0.006})O_{2-x}$

Minor actinide containing fuel for fast reactors: a case study (experiment SUPERFACT)

Minor actinide recycling in a Fast Reactor has been studied on a series of oxide fuels containing ^{237}Np and ^{241}Am at low and high concentrations [4]. Four types of mixed actinide oxide fuels (Tab. 1.15) were prepared at the Institute in accordance with the homogeneous (SF13, SF16) and heterogeneous (SF14, SF15) fuel concepts. The fuels have been irradiated in the PHENIX power station and are currently undergoing post-irradiation examinations at the Institute [4].

Tab. 1.15 Fuel compositions of the SUPERFACT irradiation experiment.

Fuel	Fuel composition	burnup
SF13	$(U_{0.74}Pu_{0.24}Np_{0.02})O_{2-x}$	6.4 a/o
SF14	$(U_{0.60}Am_{0.20}Np_{0.20})O_2$	4.1 a/o
SF15	$(U_{0.55}Np_{0.45})O_2$	4.5 a/o
SF16	$(U_{0.74}Pu_{0.24}Am_{0.02})O_{2-x}$	6.4 a/o

Methodology

Experimental

The gamma dose rates of the four SUPERFACT pins were measured during *fabrication* using a portable ionisation chamber. *After discharge* (cooling time 57 months), the gamma and neutron dose rates were measured using a passive neutron-gamma interrogation unit developed for the characterization of spent fuel inside a hot cell at the Institute [4]. The experimental arrangement comprises a shielding for the detectors made of 25 mm polyethylene and 60 mm lead.

Theoretical calculations

The computer code KORIGEN [6] was used to calculate the evolution of the fuel during irradiation for each of the recycling concepts and minor-actinide-containing fuels. Appropriate burnup-dependent fission and capture cross-sections were used for the studies in PWR. The cross-section libraries were adjusted to those for the PHENIX reactor in the case of the SUPERFACT fuels. The neutron and gamma dose rates were calculated for the different fuels using the computer program PUDOL [7]. The calculations were performed on the basis of the fuel composition and the physical properties of the fuel and cladding. The spent fuel compositions obtained by KORIGEN were used as input to PUDOL for the dosimetry calculations. The program considers self-shielding effects in the fuel itself and attenuation in the cladding. Furthermore, it allows the use of a range of shielding materials for radiation protection purposes.

Results and discussion

Comparison of the nuclear fuel cycles

In the present study, it is assumed that the fuels are fabricated one year after reprocessing. Thus, the buildup of large amounts of ^{208}Tl (2.6 MeV gamma) from the decay of ^{236}Pu (half-life 2.6 years) is avoided.

The dose rates per unit mass of the fresh fuel material corresponding to the recycling schemes for Pu and MA are compared to the PWR and FR MOX reference cycles (Tab. 1.16). The distance of 50 cm corresponds to the working conditions when pellets are handled manually inside a glove-box. An dose rate limit for a radiation worker of 2 μSv/h is considered. The results confirm the expected increase in dose rates at fabrication due to the inclusion of Pu and minor actinides.

The difference between PWR MOX and self-generated Pu recycling schemes is due to the change in the Pu isotopic

Tab. 1.16 Dose rates at 50 cm for one gram of fresh fuel material.

Material	Gamma dose rate (mSv/h)	Neutron dose rate (mSv/h)
PWR-UOX	2.0 E-7	4.0 E-11
PWR-MOX	3.5 E-4	5.0 E-7
FR-MOX	2.0 E-3	3.0 E-6
R2	3.0 E-3	1.5 E-4
R3	9.3 E-3	7.5 E-4

composition. Multiple recycling of self-generated Pu in PWR results in a Pu composition with a significant increase in the even isotopes. The ^{238}Pu, increased by 3-4 times, contributes greatly to both gamma and neutron dose rates. The inclusion of minor actinides contributes to a further increase of the dose rates of the fuels R2 and R3 over the corresponding reference MOX fuels. The soft gamma spectrum from Pu and ^{241}Am which is important to the dose rate, can however be easily shielded by 1-2 mm of lead. In normal industrial practice, remote handling may be necessary when a large number of pellets are present inside the box.

The handling of a single PWR or FR fuel pin at fabrication involves dose rates which exceed the working limit by factors of up to twenty (Tab. 1.17). Although the soft gamma spectrum is again easily shielded by thin Pb, the neutron dose rate demands up to 150 mm polyethylene. The above analyses have been performed for one year after reprocessing. At longer times, ^{208}Tl builds up and may eventually require the use of further Pb shielding. In the case of the R2 recycling scheme, the dose rate for one pin due to ^{208}Tl is just below (1 mSv/h) the working limit. At discharge, the gamma dose rate is determined by the burn-up, i.e. the fission product content of the fuel. Dose rates comparable to the PWR- UOX and MOX fuels are observed at 1m from the fuel, requiring 100-150 mm Pb of shielding. However, the inclusion of minor actinides in the charge composition of the fuels results in an increase of the neutron emission after irradiation. Polyethylene shielding of 200 mm is now required.

Tab. 1.17 Dose rates at 1 m and necessary shielding for fresh fuel.

Fuel	Gamma emission		Neutron emission	
	Dose rate (mSv/h)	Pb shielding (mm)	Dose rate (mSv/h)	polyethylene shielding (mm)
PWR-UOX	2.0 E-5	-	1.0 E-7	-
PWR-MOX	4.0 E-3	1	2.0 E-4	-
FR-MOX	6.5 E-3	1	1.8 E-4	-
R2	4.0 E-2	2.5	6.7 E-2	150
R3		2.5	4.6 E-2	130

Verification of dosimetry predictions

The availability of computer programs enabling the prediction of dose rates is essential to estimate possible hazards in a given fuel cycle. Future industrial scale fabrication of minor actinides fuels will be planned according to calculations using computer programs. Verification of such predictions is therefore needed using the minor-actinide fuels available from small-scale irradiation experiments.

In order to assess the reliability of the dosimetry computer codes, measured radiation doses from fresh and spent fuels are compared to the calculated ones. The gamma dose rates during fabrication are given in Tab. 1.18 for the minor-actinide fuels used in the SUPERFACT program. The calculations were performed on the basis of the fresh fuel compositions obtained by chemical analyses. The level of agreement is within 30%, which is an acceptable accuracy for radiation protection purposes. The high radiation doses from the mixtures containing americium can be seen in the results. The increased concentration of ^{241}Am in the SUPERFACT fuels causes an increased gamma dose of 40 times for SF14 and 7 times for SF16. The former exceeds the dose limit by two and the latter by one order of magnitude. However, the soft gamma spectrum emitted by the fuels can be easily shielded by 1-2 mm Pb.

Tab. 1.18 Predicted and measured dose rates at 1 m from a fresh fuel.

Fuel	Gamma dose rate (mSv/h)	
	Measured	Predicted
SF13	7.0 E-3	8.0 E-3
SF14	2.6 E-1	2.5 E-1
SF15	< 1.0 E-2	2.0 E-4
SF16	4.0 E-2	5.6 E-2

The presence of PWR and MA spent fuels in the hot-cells at ITU, provided the opportunity to study their dosimetry. Furthermore, it allowed an assessment of the accuracy in predicting these rates by a computer code on the basis of the fuel compositions obtained by KORIGEN. The experimental and theoretical neutron and gamma dose rates for the spent fuels are shown in Tab. 1.19. The corresponding final burnup and cooling times are included since they determine the radiation emissions at measurement.

The increase in the dose rate following the inclusion of MA in the charge composition of fuels is demonstrated in Tab. 1.19. The total radiation dose is dominated by the gamma dose rate. This is due to the large cooling times, particularly for the SUPERFACT fuels, and the conse-

Tab. 1.19 Predicted and measured dose rates from spent fuel

Fuel	Burnup (a/o)	Cooling time (a)	Gamma dose rate (mSv/h)		Neutron dose rate (mSv/h)	
			Predicted	Measured	Predicted	Measured
SF13	6.4	5	3.0 E2	2.7 E2	2.2 E-2	4.3 E-2
SF14	4.1	5	1.0 E2	1.5 E2	5.5 E-2	9.0 E-2
SF15	4.5	5	1.0 E2	1.5 E2	3.0 E-2	4.2 E-2
SF16	6.4	5	3.0 E2	2.5 E2	2.4 E-2	4.0 E-2
PWR-MOX	4.7	3	4.2 E2	7.0 E2	3.0 E-1	8.4 E-1

quent decay of ^{242}Cm and ^{244}Cm. Even for the SF14 fuel which contains 20% ^{241}Am and for which most of the curium isotopes are expected to be produced, the gamma dose dominates. Nevertheless, at discharge the neutron dose rate is considerable, although still lower than the gamma dose rate. A shielding of 100-150 mm polyethylene would be required to reduce the occupational exposure at 1 m from SF14 and SF16 during unloading. In order to assess the PUDOL predictions, the experimental and theoretical dose rates have been compared (Tab. 1.19). An agreement within 50% is observed. The discrepancy can be attributed to different sources including the reproducibility of the experimental setup and the fuel compositions obtained from KORIGEN predictions. The reliability of KORIGEN, for the source term nuclides, has been checked by the comparison of its predictions with chemical analyses [4]. The agreement is within 25% for the actinides and 50% for the fission products. This agreement, although sufficient for dose-rate calculations indicates limitations in its basic nuclear data libraries. The latter should be considered when neutron-physics calculations are performed.

References

[1] L. Koch; J. Less Common Met. **122** (1986) 371

[2] H. W. Wiese; Nucl. Technol. **102** (1993) 68

[3] J. P. Grouiller; DRN/ CEA: Recyclage des actinides mineurs dans un réacteur type SPX1, Work performed under ITU contract (unpublished), 1986

[4] G. Nicolaou, K. Richter, C. Prunier, L. Koch; IAEA Technical Committee Meeting on Safety and Environmental Aspects of Partitioning and Transmutation of Actinides and Fission Products, Vienna, 1993

[5] L. Koch, G. Nicolaou; IAEA Technical Committee Meeting on Safety and Environmental Aspects of Partitioning and Transmutation of Actinides and Fission Products, Vienna, 1993

[6] U. Fischer, H. W. Wiese; 'Verbesserte konsistente Berechnung des nuklearen Inventars abgebrannter DWR-Brennstoffe auf der Basis von Zell-Abbrand-Verfahren mit KORIGEN, Kernforschungszentrum Karlsruhe, report KfK-3014 (1983)

[7] M. Schmid, W. Benz PUDOL 8.4 Dosimetry Computer Program, Siemens A 99, KWU, BW Hanau 1993

1.2.6 Transmutation of long-lived radionuclides: Requirements for and review of technical possibilities

Public acceptance

Accelerator-Driven Transmutation Technology (ADTT) is presently being discussed in a situation where nuclear energy generation in some countries faces an acceptance problem. The intention of expanding this technology for future nuclear energy generation would, therefore, have to give answers to the three main acceptance problems:

1. reactor safety, which is under discussion since the accident in Three-Mile-Island and the catastrophe of Chernobyl

2. fissile material safeguards, now in the focus of interest because of increasingly observed vagabonding of nuclear material

3. disposal of nuclear waste, of which the on-going search for geological disposal sites initiated a debate on long-term radiotoxic hazards.

In the public opinion, there is a distinct ranking order on the possibilities of waste treatment in general:

Most welcome would be a technique that produces less waste. In the case of nuclear fission, energy is always generated together with fission products, the yields of which vary slightly with the fission source. Only the build-up of radiotoxic actinides changes, and it is obvious that ^{232}Th-based fuel produces by far less transuranium elements than ^{238}U-containing fuel.

The second best choice is the possible re-use and recycling of waste back to the process where it was produced. One would expect Pu recycling to fall under this category.

Because of its potential misuse for military purposes, the extraction of pure plutonium from the less attractive (in the sense of diversion) spent fuel, the recycling (and breeding) of plutonium is questioned in some states. Moreover, the re-use of plutonium in nuclear power stations leads to a further build-up of transplutonium elements, which - in the case of the light water reactor - would convert one third into americium and curium. Hence, only recycling of all other radiotoxic nuclides together with plutonium would reduce the toxicity of nuclear waste. Partitioning and Transmutation - as explained below - could achieve this.

A waste burner is, of course, generally welcomed, but heavily disputed by the communities neighbouring its installation site. Any dedicated nuclear reactor for the transmutation of long-lived radionuclides collected from other power stations will find itself in such a situation. Geological disposal is the last accepted solution. Any release back to the biosphere would endanger the surrounding population for generations to come. The present international legislation demands a geological repository in the state where the waste has been generated. Therefore, disposal in uninhabited areas - a certainly more accepted solution - is sometimes not possible. It has to be pointed out that all the transmutation technologies studied now could reduce the radiotoxicity of long-lived radionuclides but not completely eliminate it. Consequently, a geological repository will be needed in any case, however, reduced radiotoxicity would have a reduced associated hazard.

The nuclear hazard

Radiotoxicity and misuse as nuclear explosives are the imminent dangers of anthropogenic radionuclides. Presently, the worldwide installed nuclear energy generating capacity of 60,000 GWe leads to annual discharges of 10,000 t of spent fuel containing about 80 t of Pu and 40 t of long-lived radiotoxic nuclides. So far, ca. 100,000 t of spent fuel have accumulated, from which in some states, plutonium will be recovered. The amount of recovered plutonium, when all plants under construction have been commissioned, will reach between 40 and 50 t per year [1]. Although the plutonium primarily stems from light water reactors, containing about 60% ^{239}Pu, it can still be misused as nuclear explosives - but not as easily as the plutonium dismantled from nuclear warheads. Nuclear disarmament foresees a gradual reduction of the several hundred tons of stockpiled Pu at a rate of about 10 t/a. The proposed accelerator-driven concepts show how one could avoid plutonium production, transmute plutonium into other elements, or use it in a denaturated state, where it cannot be readily used for a nuclear explosive.

The time-dependence of the radiotoxicity resulting from energy generation in a typical light water reactor is given in Fig. 1.48. The radiotoxicity of fission products decreases within a few hundred years below that of the uranium ore mined to produce the fresh fuel [2] .

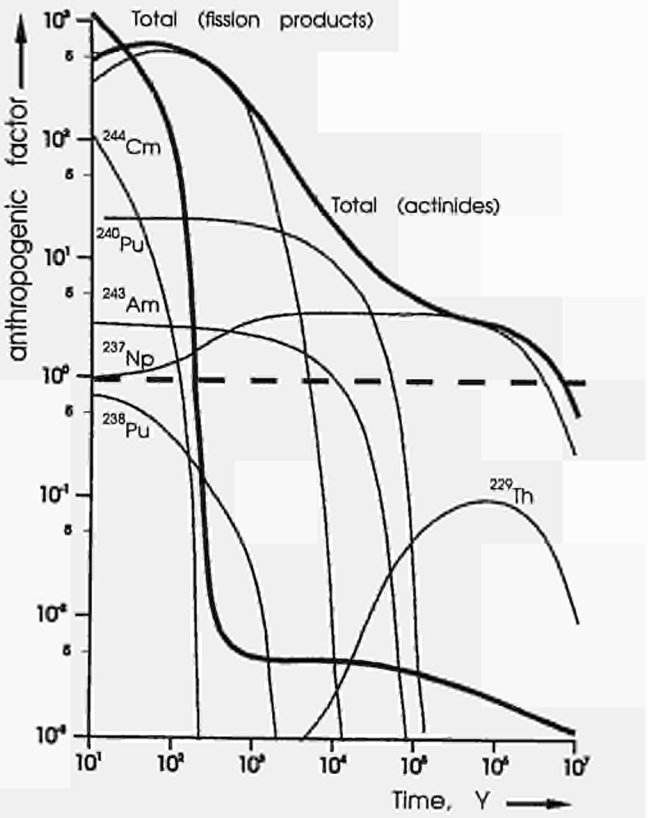

Fig. 1.48 Time-dependence of radiotoxicity in a spent LWR fuel of 33 GWd/t normalised to the radiotoxicity of the uranium ore (dashed line) mined to produce the fuel.

The accumulated transuranium elements would decay over much longer periods. Hence, their transmutation into short-lived or stable nuclides would reduce the radiotoxic hazard for future generations. This consideration takes only into account the source of the radiotoxic hazard as it is posed by the spent fuel. If stored in a geological repository, the leaching of the fuel and the eventual migration of nuclides back to the biosphere is a more relevant description of the imminent danger. Also fission-product nuclides, even if of lower quantities, could pose a problem if they accumulate in the biosphere.

So far, no common criteria have been accepted which would allow the identification of those nuclides and the extent to which they ought to be partitioned and transmuted. To close this knowledge gap, the IAEA has started a co-ordinated research programme on Evaluation of the Safety, Environmental and Non-Proliferation Aspects of Partitioning and Transmutation of Actinides and Fission Products aimed at the definition of criteria to determine the radiological hazard posed by the numerous anthropogenic radionuclides (Tab. 1.20). Not yet knowing the outcome of this co-ordinated research programme, one can assume that the largest hazard is posed by such

Tab. 1.20 List of long-lived radionuclides considered candidates for nuclear transmutation.

nuclide	$T^1/_2$ [a]	
^{14}C	5.7 E3	
^{36}Cl	3.0 E5	Nuclides forming monovalent ions with natural isotopic diluent
^{129}I	1.6 E7	
^{135}Cs	20 E6	
^{79}Se	6.5 E4	Nuclides forming no monovalent ions
^{93}Zr	1.5 E6	
^{90}Sr	28.5	
^{121}Sn	50	Nuclides with half-lives below 100a decaying into stable nuclides
^{126}Sn	10.5	
^{137}Cs	30.17	
^{99}Tc	21 E5	
^{237}Np	2.1 E6	
^{238}Pu	87.7	
^{239}Pu	2.4 E4	
^{240}Pu	6.5 E3	
^{241}Pu	14.4	
^{242}Pu	3.7 E5	Nuclides and their parents forming monovalent ions with no natural diluent
^{241}Am	432	
^{242}Am	141	
^{243}Am	7.3 E3	
^{245}Cm	8.5 E3	
^{246}Cm	4.7 E3	
^{247}Cm	1.5 E7	
^{248}Cm	3.4 E5	

radionuclides which have no natural diluent, i.e. unlike ^{135}Cs, which will be diluted by natural caesium. Hence, the transuranium nuclides as well as ^{99}Tc, should be the first target in studying a partitioning and transmutation scheme (IAEA Specialists' Meeting on Use of FBRs for Actinide Transmutation, Obninsk, 22.-24.9.1992).

Reducing the nuclear hazard

A radiotoxic or fissile nuclide can be transmuted by nuclear reactions into a short-lived or stable non-fissile one. Several possibilities exist and the major ones are presented in Fig. 1.49. The transmutation by photon-induced reactions or by charged particles appears to have technical difficulties. The most promising, therefore, would be transmutation by neutron capture or neutron-induced fission. For this purpose, existing power stations could be used, but also newly-developed dedicated burner reactors which are driven by accelerators.

The concept of partitioning of radiotoxic nuclides was introduced by Claiborne in 1972 [3]. The transmutation of transuranium elements was successfully demonstrated in an irradiation experiment in the PHENIX fast reactor in 1985 [4]. The use of accelerators to destroy hazardous radionuclides was described already 1974 by J.R. Harries [5]. Since then, several research programmes have started implying the use of existing nuclear reactors or advanced burner reactors in Russia, Japan, USA and Europe.

To define a reduction of the nuclear hazard, the direct storage of spent light water reactor fuel is taken as a reference point. This concept can be compared with the concept of plutonium recycling in LWR and recycling of Np, Pu, Am, Cm, Tc in fast reactors. In the latter case, the radionuclides which are self-generated by the nuclear reactor are recycled. Instead of slow decay in a geological repository, they will be transmuted faster when stored in the nuclear reactor. The equilibrium concentration given for each reactor fuel corresponds to such a partitioning and transmutation cycle loss that the overall hazard reduction will be 100 times [6]. Such a target is also aimed at in some of the accelerator driven transmutation technique (ADTT) options.

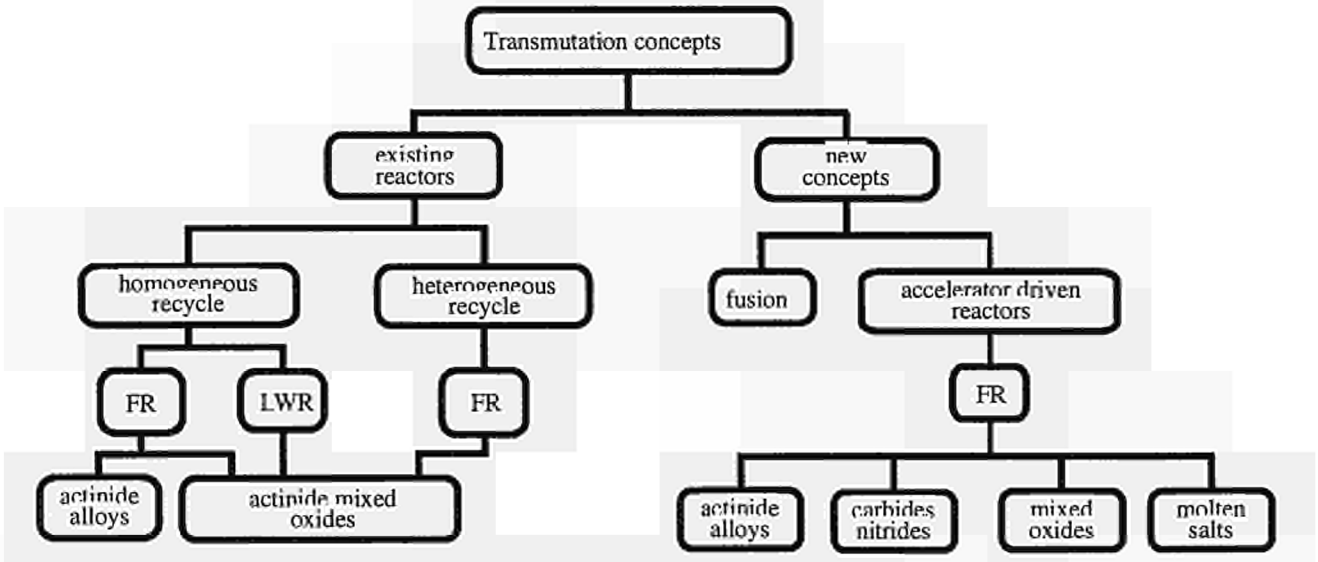

Fig. 1.49 Transmutation possibilities in existing reactors and new concepts.

Accelerator-driven reactors (ADR)

The breeding of plutonium from ^{238}U or ^{233}U from ^{232}Th by accelerator-driven reactors is, of course, a well-known concept. Earlier, there was the need to enhance the breeding of the reactor, but now the situation is reversed leading to the need to have a purposely subcritical reactor operating as will be explained below.

The main feature of the concept is a neutron-spallation-source: accelerated charged particles of about 1 GeV hit an initially non-radioactive target of heavy elements (e.g. Pb). The spallated nuclei produce a neutron shower, i.e. for each incident particle up to 50 neutrons are produced. In an appropriate set-up, a dense neutron flux is induced in the surrounding, previously subcritical fission reactor (Fig. 1.50). This is the unique safety feature of an accelerator-driven reactor (ADR) compared to existing ones: as soon as the accelerator beam is turned off, the reactor shuts down, which copes e.g. with the so-called void effect observed for reactors fuelled with transuranium nuclides. (In the event of coolant loss, however, the hardened neutron energy spectrum would surpass the fission energy threshold of higher actinides to such an extent that this eventually would lead to an uncontrolled reactivity increase of the reactor). There are, of course, measures to cope with this phenomenon for existing reactors (mainly by changing the geometry of the reactor core), but only accelerator-driven reactors can take very high concentrations of transplutonium nuclides.

Since ADTT is a technology still to be developed, additional safety features are foreseen, which have been also considered for future fission reactors not driven by accelerators. Instead of Na, the chemically less reactive Pb or Pb/Bi will serve as coolant. It is obvious that an ADR will feed less electricity to the external power net than a conventional power station of the same size, because elec-

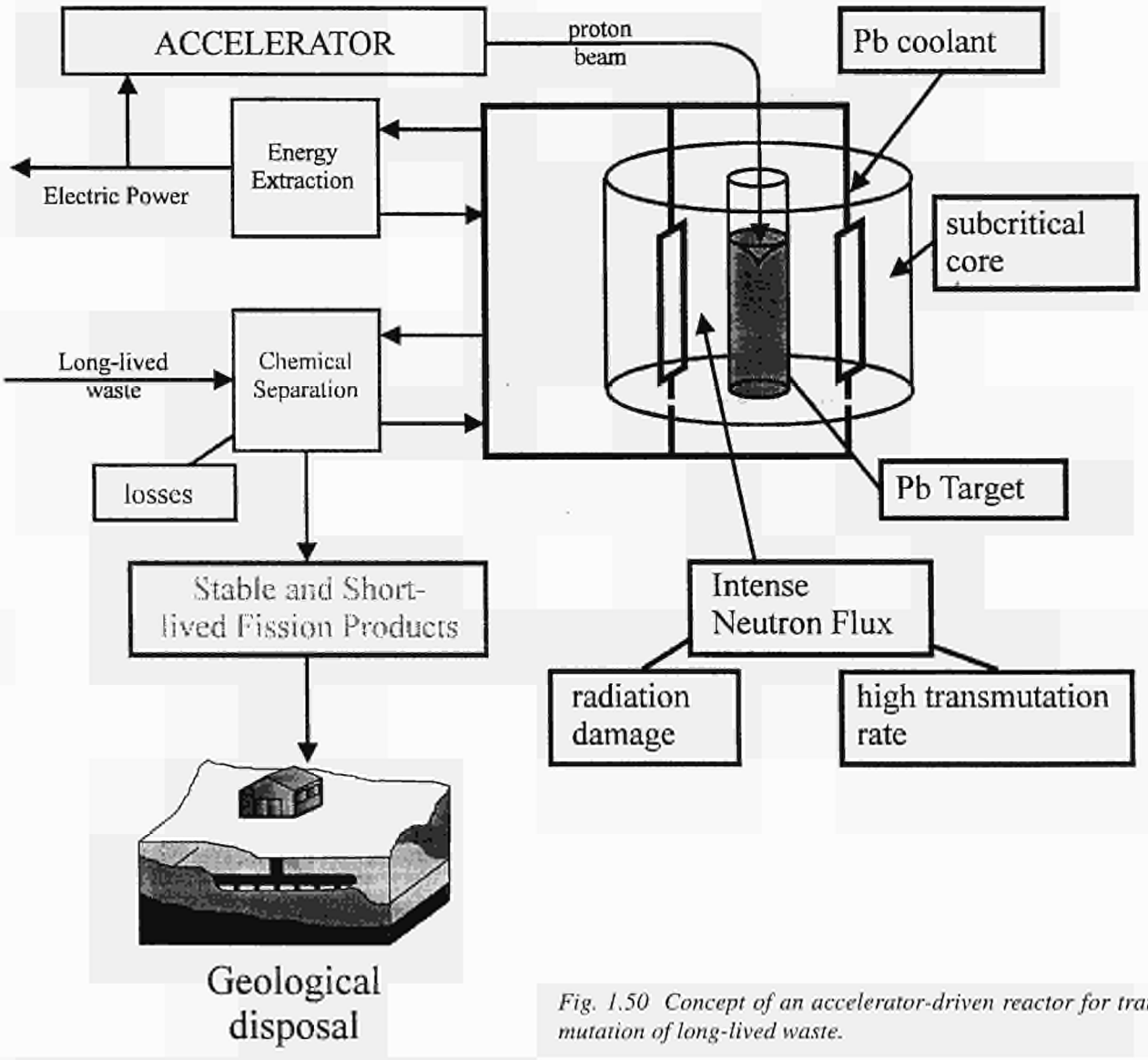

Fig. 1.50 Concept of an accelerator-driven reactor for transmutation of long-lived waste.

tricity is needed to drive the accelerator itself. Though the ADTT can rely to some extent on existing technology: accelerator, fission reactors, nuclear fuel reprocessing, there are still considerable tasks ahead to be accomplished, such as the construction of high current accelerators (ca. 100 mA), cooling and replacement of spallation targets and of structure material damaged by irradiation, etc.

The neutron fluxes expected in accelerator-driven reactors are up to 100 times higher compared to corresponding thermal or fast reactors. Consequently, the transmutation rate is higher, and waste (including weapons plutonium) will be transmuted faster. One ADR could transmute the same amount of waste as tens of nuclear power stations that are operated on the self-generated waste recycling mode.

Concluding remarks

Since worldwide research on partitioning and transmutation has just begun, it would be premature to draw conclusions on technical feasibility and cost/benefit of the different concepts. Moreover, the development status of the various approaches does not yet allow a meaningful comparison. It should be pointed out that spent nuclear fuel has to be stored for tens of years. Also decades will be needed to disassemble nuclear warheads and the recovered Pu has to be stored intermediately, because of the lack of facilities in the US and Russia to feed the Pu into the commercial fuel cycle. Partitioning and transmutation, including the accelerator-driven transmutation technology - if feasible -, could offer the next generation an option to solve a waste problem being generated now.

References

[1] IAEA Yearbook 1993, ISBN 92-0-102493-2 (1993)

[2] L. Koch; „Formation and Recycling of Minor Actinides in Nuclear Power Stations", Handbook on the Physics and Chemistry of the Actinides, vol.4, p. 457-490; Eds.: A. J. Freeman, C. Keller (1986), ISBN 0-444-86983-2

[3] H.C. Claiborne; Oak Ridge National Laboratory, report ORNL/TM-3964 (1972)

[4] C. Prunier, A. Chalony, M. Boidron, J. P. Pagès, M. Coquerelle, J. F. Gueugnon, L. Koch, K. Richter; „Transmutation of Minor Actinides: Behaviour under Irradiation of Americium and Neptunium Based Fuels" (1991) Internat. conference on Fast Reactors and Related Fuel Cycles (FR '91), 28.10-1.11 1991, Kyoto (Japan)

[5] J. R. Harries; AAEC/E326, ISBN 0642996390 (1974)

[6] L. Koch, G. Nicolaou; „Comparison of Possible Partitioning and Transmutation Schemes when Added to the Existing Nuclear Fuel Cycle" Proceedings of the Technical Committee Meeting on Safety and Environmental Aspects of Partitioning and Transmutation of Actinides and Fission products, Vienna 29.11-2.12 1993, IAEA, TECDOC-783, p. 195, Jan. 1995

1.2.7 Working group meeting on minor actinide containing targets and fuels, ITU Karlsruhe, 28-29 June 1994

This was the fourth in the series of meetings of the Working Group on Targets and Fuels initiated following the Workshop on Partitioning and Transmutation of Minor Actinides held in the Institute in October 1989 (TUAR-90, p. 71). The meeting was attended by 32 participants, including representatives from national organisations, IAEA, EC, OECD/ NEA, and 9 from the Institute. The following countries were represented: Belgium, Canada, Germany, France, Japan, S. Korea, Netherlands, Spain, Switzerland and UK.

These meetings provide an international forum for the discussion of technical problems associated with all aspects of partitioning and transmutation. Presentations included national programmes, international co-operation and conceptual studies on different transmutation schemes, partitioning studies, post-irradiation examinations of minor actinides targets and fuels and different matrices containing minor actinides.

A major issue still to be resolved is that of determining the target nuclides to be transmuted. This compilation will influence the choice of partitioning techniques and transmutation schemes. It was clear that in the field of partitioning one of the main goals remaining is the separation of actinides and lanthanides. Two aspects of the fabrication of minor actinide targets and fuels were considered: losses, which can be as little as 0.1% using the *sol-gel* process, and dosimetry aspects, which indicate the need of remote handling. A fuel type that would not produce any plutonium and americium during irradiation, was proposed in the form of an inert matrix. Basic structural studies on such material are in progress.

The working group, set up in 1990, has evidently served the scientific community in offering a platform to arrange joint studies. Studies on a network level have already been set up, e.g. EFTTRA, and ITU - EDF. Outcomes of these studies are regularly discussed in dedicated meetings between the partners involved. As a consequence of this and in view of the many meetings taking place nowadays in the field of partitioning and transmutation (e.g. Global '95), it has been decided not to hold a working group meeting in 1995.

1.3 Minor Actinides Laboratory

The Minor Actinides (MA) laboratory has been extended to include equipment for powder preparation based on the sol-gel process; first fuel powder material was prepared.

In parallel, the design of a new fabrication chain for the making of fuel pins containing minor actinides work has continued on. The arrangement of the different working stations was based on the model of the existing water-shielded cells. The new chain will be installed in a specially constructed caisson. The glove-boxes, with the equipment for the different fabrication steps, will be placed in the centre of the caisson, and surrounded by protecting walls of water and lead. After an estimation of the quantities of radioactive nuclides to be handled in the frame of the foreseeable fabrication campaigns in the coming years, the required biological protection was calculated to be 50 cm water, covered with 5 cm lead. Windows having an equivalent protecting factor will be installed at the front of each box. Normal operations will be performed using manipulators or through automatic remote devices. For maintenance of the equipment, or for special reasons, direct access to the glove boxes will be possible for short periods of time after the removal of the highly radioactive material from the boxes. It was decided to equip each box -even those with remote control devices- with at least one manipulator, which should allow the removal of the material from outside in case of a failure of the automatic devices. Wells, protected with lead and water, will be installed for storage of the radioactive material during rear operations.

At present, the decommissioning of the equipment to be removed from the future site of the caisson is underway. Six glove-boxes will first be installed in the caisson: for special preparations, pressing, sintering, pellet control, pin filling and welding and pin control. Two further stations are planned for a later stage, for machining of the pellets, and for waste storage and conditioning. The installation of equipment in the first glove-box, for special preparations, has also been postponed; the box will initially serve for introducing material (normally sol-gel powder) into the chain. The microscope equipment, with image processing and archiving system, is presently being tested for later implementation in the pellet control box. The connection between the boxes will be through stainless steel cylinders of 250 mm diameter, with double-cap apertures at both ends.

The conceptual study of the fabrication chain is well advanced, and should be completed by the beginning of 1995. A powder container for the feeding of the press has to be transferred from box 1 (entry) to box 2 (pressing), and back. After pressing, the pellets, individually identified, will be checked and sorted; the pellets in accordance with the specifications will be arranged on a tray, and transferred to box 3 for sintering (the discarded pellets will be pushed in a waste container). The pellets to be produced, and consequently the related handling devices, are classified into 3 categories according to their diameter: 5-8 mm, 9-12 mm, and larger than 12 mm. The final control of the pellets, and their preparation for pin filling, will occur after sintering. For pin filling, welding and control, two stations are foreseen; the pellets will be handled in the first glove-box, while the second box will be kept as a non-contaminated zone for final control of the closed pins before shipment. A detailed description of the various stations, with technical specifications, is under preparation.

1.4 Particle Agglomeration and Deposition In Turbulence (PADIT)

Introduction

Turbulence is a phenomenom present in most industrial and environmental flows. From a review of the literature, it appears that a few studies, mostly theoretical, show that micron or sub-micron size aerosols agglomerate under these conditions so that the initial size distribution is modified. This effect will have a significant influence on the conditions of deposition of particles at the boundaries of the flow. Experimental data are needed on this agglomeration process, particularly in order to model the deposition process during accidental release of radioactive aerosols and to manipulate aerosols in restricted spaces where turbulence takes place (e.g. duct flows).

The earlier experimental study of Duct Transport of Big Particles (TRABI) (see TUAR-93, p. 64) done with non-active bismuth oxide particles confirmed the importance of the agglomeration process for the transport of big particles (30-40 μm) in a highly, but well controlled, turbulent flow (Re>100,000). More than 25% of the particles counted on the sampling filters were significantly larger than those originally injected.

In the frame of the present PADIT project, it was planned to verify the occurrence of this agglomeration process during the transport of nuclear aerosols, under the same turbulent conditions as in the TRABI experiments. As plutonium was excluded for safety considerations, polydisperse aerosols from natural uranium oxide were used as a substitute.

Experimental

For these experiments, the TRABI test facility was modified. Parts of the wind channel (sections A, B, C and D, see Fig. 2.1 in TUAR-91, p. 62) and the analytical equipment were mounted inside a conventional steel glove box as described in TUAR-93, p. 64. As in the previous TRABI experiments (see description and results in TUAR-92, p. 59) the sampling Nuclepore 10 μm porosity filter was located along the axis of the plexiglass section located at the downstream end of the test duct.

Loss of large particles is avoided by minimizing the transport of the filter samples to the analysis station. For this purpose, a special construction permitted in-situ examination of the Nuclepore sampling filters, using a microscope located outside the glove box. The microscope was connected to a color-video copy processor system (QUANTIMET). A quantimetric evaluation of the micrographs was carried out with a GALAI CIS-1 Macro-Viewer. In this way, the particles could be characterized as a function of the Ferret diameter (TUAR-93, p. 64).

Sintered natural uranium oxide was ground and particles were divided by ultrasonic sieving into two size fractions: 25-30 μm and 30-65 μm. These particles are similar in size to those generated in the fabrication of nuclear fuel materials. Aerosol injection into the wind channel was achieved by means of a spray bulb. The aerodynamic data and the particle collection system were the same as that described in TUAR-91, p. 61 and TUAR-92, p. 58.

Results and discussion

In spite of attempts to vary the optical contrast with the background, the GALAI Macro-Viewer does not allow small uranium oxide particles and the perforations of the Nuclepore filter itself to be distinguished. In fact, there is a significant percentage of irregular or adjoining perforations which are much greater than the nominal size (10 μm). Nevertheless, direct observation of the loaded filters with the microscope shows clearly that UO_2 particles, recognizable by their colour and shape, smaller than 30 μm are always present in significant but variable quantities. This suggests that the fraction resulting from sieving consists of aggregates of poor mechanical stability which are broken up during the injection and/or in the turbulent flow.

Numerous duct transport experiments were carried out during the reporting period with both size fractions. In each run, a 100 mg sample of test powder of the given size range was injected into the turbulent flow, so that after complete dispersion of the sample, the particle number concentration of the transported aerosol may be estimated at between 1.5 and 2.5×10^6 particles m^{-3} in an air volume of about 0.3 m^3. Nevertheless only in a few experiments were sufficiently well loaded filter samples obtained for valid quantimetric evaluation (at least 50 objects). The results are given in Tab.1.21 for the size fractions (A) 25-30 μm and (B) 30-65 μm. For the reasons discussed above, the particles smaller than the original size range were not counted. Fig. 1.51 shows micrographs of the UO_2 particles collected on a Nuclepore 10 m porosity filter for (A) an original test sample of the size fraction 30-65 μm and (B) a sample of the same size fraction after transport in the turbulent flow.

These data are in agreement with those obtained from TRABI with bismuth oxide powder. Transport in a highly turbulent flow strongly increases the agglomeration of uranium oxide particles. Direct observation of particles

smaller than the original size on the filters indicates that the turbulence can also have the opposite effect and agglomerates can be broken up. The further study of these counteracting processes requires the use of monodispersive spherical UO_2 particles generated by the sol-gel process and suitable equipment for direct *in situ* measurement of the particle size and characterization of the turbulence within the duct (e.g. a laser phase doppler anemometer).

Tab. 1.21 Quantimetric evaluation of the particles collected on the sampling filter. Original size ranges of the test aerosol were: (A) experiments 1 to 5 : 25-30 µm, (B) experiments 6 to 9 : 30-65 µm.

	Number of particles present on the collecting filter		
(A) Size range (µm)	25-30	30 - 60	> 60
Experiment			
1	80	75	19
2	26	27	0
3	43	32	10
4	121	94	25
5	49	21	0
(B) Size range (µm)	30 - 65	65 - 90	> 90
Experiment			
6	48	13	3
7	141	42	28
8	78	11	7
9	67	6	5

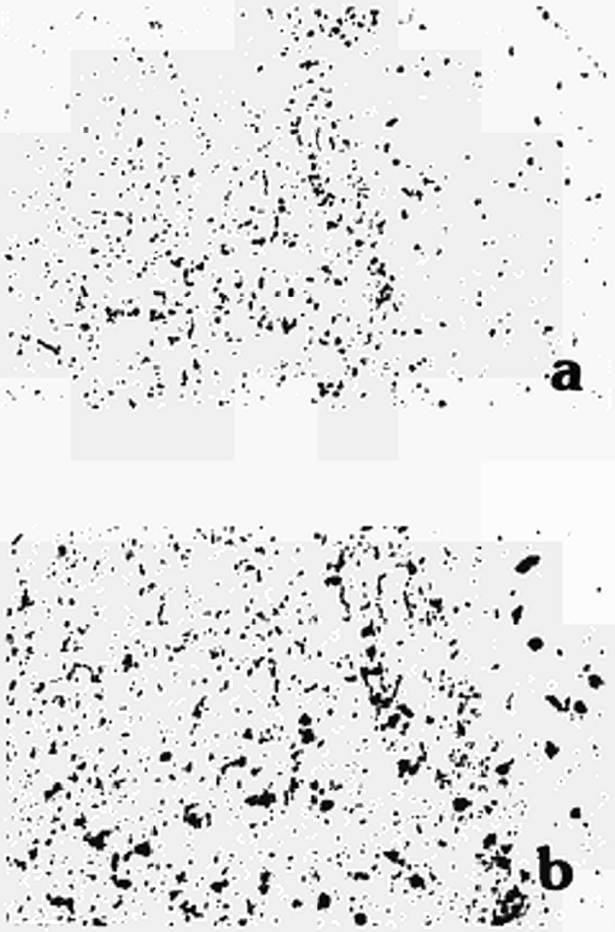

Fig. 1.51 Micrographs of the UO_2 particles collected on a Nuclepore 10 m porosity filter for:
(A) an original test sample of the size fraction 30-65 µm,
(B) a sample of the same size fraction after transport in the turbulent flow. (magnification 20x)

2. Fuel Behaviour under Accident Conditions

2.1 Studies of Problems related to Reactor Safety

2.1.1 Ultrasonic thermometer sensors for Phebus

A total of 16 7-section ultrasonic thermometer sensors were fabricated and calibrated [1,2] and delivered to CEA-Saclay for use in the Phebus experiments FPT1 through FPT5.

Technology transfer

The Black Box Mark 3 (ultrasonic thermometer control and evaluation electronics) and the corresponding operating software [3,4] were transferred to CEA-CEN-Cadarache for use in the PHEBUS project. The software runs under WINDOWS on a standard 486DX33 computer, which is equipped with a commercial 100 MHz digital-to-analogue converter card and a second parallel port LPT2.

References

[1] H. A. Tasman, Ultrasonic thermometer sensors for PHEBUS FPT1 through FPT5. Technical Note K0294180 (April 1980)

[2] The cooperation is acknowledged of Mr. G. Lemaitre, CEA-CEN-Saclay/SETIC/LIFT

[3] H. A. Tasman, Black Box Mark 3: Control and evaluation electronics and software (version 2.3) for ultrasonic thermometry (revised edition). Technical Note K0294181 (1994)

[4] H. A. Tasman, Thin wire ultrasonic thermometry for measuring axial temperature profiles. EUR 15870 EN (1994).

2.1.2 Source term studies on radionuclide release from irradiated fuel

Laboratory measurements were carried out on transpiration/effusion effects in irradiated nuclear fuels at high temperature. The aim of these experiments was twofold: first, collection of data on release of fission gas and less volatile fission products, enabling their diffusion coefficients in the fuel as well as their respective release pathways to be identified. Second, the analysis of the vaporization rate of the various species makes it possible to reconstruct the thermochemical properties of the system *fuel+fission product (F.P)*, including reaction products and fuel stoichiometry.

Experimental method

A Knudsen cell effusion method was adopted. This consists of heating the sample in a cell provided with a small aperture through which the vapors escape as a molecular beam which is analyzed by a mass spectrometer. In our apparature, the cell is located in a tungsten resistance furnace surrounded by five thermal cylindrical screens. To align the effusing molecular beam the furnace is installed on a micrometric x-y table. At the top of the furnace housing, 5 cm above the outer screen, an externally adjustable diaphragm separates the furnace from the mass-spectrometer chamber.

A window at the top of the spectrometer enables the alignment of 1) spectrometer head, 2) diaphragm, 3) screen holes-Knudsen cell aperture to be adjusted by sequentially focussing a TV camera on these items; the axis position of the cell is controlled by using a vertically fixed He-Ne laser beam.

The mass-spectrometer is a quadrupole with a mass range 1-500. This can be operated both with a continuous scanning of a mass interval, or with sequential measurements of a set of selected masses. The shortest measurement time per mass is 0.5 ms, however, in our experiments, where most signals are low, this time is normally chosen to lie between 1s and 10 s.

The temperature is measured through a lateral window by using a linear pyrometer. This window is internally protected by optical glasses mounted on a revolving disk, so that only one glass is permanently exposed to acci-

dental vapor deposition, whilst the other ones are kept in a sheltered position for temperature measurement purpose; one is never exposed during heating, and maintained clean for calibration purposes of the pyrometer at room temperature.

The system is evacuated by three turbomolecular pumps attaining a vacuum of better than 10^{-8} torr.

In the primary vacuum stage, a beta-counter is installed for measuring the flow rate of radioactive gases (mostly ^{85}Kr); furthermore, the evacuated gas of the furnace before reaching the dry rotary pump passes through a flow counter and, finally, through a liquid nitrogen cooled trap where ^{85}Kr is retained and measured to obtain the integral release value. This furnishes an additional check for the calibration factor of the mass-spectrometer (it is known that in effusion experiments the calibration of the concentration of gaseous species has to be carried out independently of that of condensable species).

Since in most cases the annealing of the sample is protracted until complete evaporation, the fractional vaporization of the various components is measured with good accuracy as a function of temperature and time.

The annealing times are chosen according to the measured vaporization rates and to the required accuracy. At temperatures below 1500 K a mass-spectrum measurement was made within a few minutes, whilst above 2000 K the scanning times are of the order of a few tens of seconds. The main features of the apparature are listed in Tab. 2.1.

Tab. 2.1 Features of the shielded "Knudsen" cell.

Knudsen Cell	ThO_2-coated tungsten Cylindrical 10x10 mm Hole: 0.5 mm Hole distance from the MS: 82 mm
Temperature range	1000-2800 K
Vacuum	10^{-8} torr
Pyrometer	Monochromatic (700 nm) 1000-3000 K
Counters	Two Plastic Scintillators beta (flow counter): 1-10000 /s gamma (LN trap): 100-10000/s
Mass spectrometer	Balzers QMA 420 Quadrupole Counter: electron multiplier Used E-Energy: 20 eV Counter: electron multiplier E-Current: 0.5 mAmp V SEV: 1800 V Resolution: 20 Threshold: 0.01% Range of Mass: 1-500 Used Range of Mass: 80-290 Maximum Noise level: at 2300 K: 10^{-13} Amp at 2600 K: 10^{-9} Amp Counting time per mass: 1 to 10 s

Samples

The irradiated fuel samples were obtained from cross-sections of BR3 fuel rods similar to those to be used in the PHEBUS experiments (Tab. 2.2).

Their weight varied between 10 and 30 mg and their measured gamma-activity was less than 30 mSv at 8 cm distance. At this radioactivity levels the operators are allowed to remove the eventual contamination in the vessel by using normal glove box procedures, whereas during the measurements the box containing the apparatus is completely surrounded by a biological shielding of 5cm lead, and all operations are automated and remotely controlled.

With a Knudsen cell hole diameter of 0.5 mm the samples vaporize at variable rates up to 2500-2600 K. Above this temperature a nearly complete depletion in fission products is attained, accompanied by marked changes in the stoichiometric composition of UO_2. At these temperatures total evaporation is achieved within 10-20 min.

In the experiments it is difficult to predict under which conditions thermodynamic equilibrium is effectively attained, since these may be different from species to species; actually, strictly speaking, the chemical composition of the fuel varies continuously during annealing. The analysis of the data is too complex to be carried out on line, and is therefore conducted in the following subsequent steps. In the first, to which this report refers, the gross release spectrum at different temperatures is measured, and the distinct stages are identified. In a second set of measurements only a few selected masses will be

Tab. 2.2 Characteristics of the examined fuel.

Reactor cycles	2 (4D1,4D2)
Linear power	140 to 180 W/cm
Irradiation time at full power	593 days
Burnup	23-30 GWd/t
Cooling time	7 years in June 1994
U-235 enrichment	6.85%
Fuel composition	$UO_{2.00}$
Fuel form	Sintered pellets; 8mm diam. 85% th. d.
Rod	Pressurized with 23 bar He

tracked with greater accuracy, and empirical data will be used to calculate kinetics and/or thermodynamic quantities of the pertaining evaporating species. Finally, in the end stage, these quantities will be compared with theoretical predictions deduced from thermochemical models of the investigated system.

Sample stoichiometry

Preliminary experiments were dedicated to the check of the stoichiometric stability of the irradiated fuel during Knudsen effusion experiments. The first question regards the compatibility of the sample with the cell. Tungsten crucibles are customarily used for high temperature treatments of UO_2. Normally, sufficiently large bulk samples do weakly react with tungsten up to temperatures near the melting point, however, an interaction layer is observed at the W-UO_2 interface, whose thickness may correspond, in our small samples, to a significant fraction of their volume.

Irradiated fuel fragments of approximately 1 mm size and 10 mg total weight were first tested. The vapour species containing U could be clearly measured above 2000 K, temperatures at which the solid-solid interaction with tungsten is appreciable. Astonishingly, the dominant vapour species detected was U(g), followed by UO(g), whilst UO_2(g) was by far the smallest (Fig. 2.1). This vapour composition corresponds to the equilibrium conditions on a markedly *substoichiometric* oxide. This is in disagreement with the post-irradiation examinations of the fuel which do not reveal any presence of uranium in metallic phases. The reduction of the sample is, therefore, to be ascribed to a chemical reaction with the tungsten cell. This conjecture is corroborated by the variation of the effusion rates with temperature: that of U(g) is in accord with the expected Arrhenius line, whilst the oxide vapours exhibit a dramatic decrease at temperatures above 2200 K.

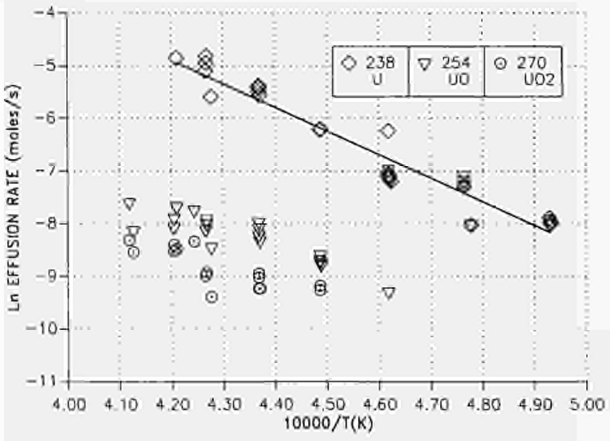

Fig. 2.1 Effusion rate vs. temperature of the U-bearing species for the case of the reaction between irradiated fuel (U627LOT2) with the W-crucible.

If larger samples are used, the vapour compositions and the partial pressures approach more and more the equilibrium values over stoichiometric UO_2. Fig. 2.2 shows the results obtained with a single fuel fragment of approximately 30 mg weight. The major species is here UO_2(g) followed, in the order, by UO(g) and U(g).

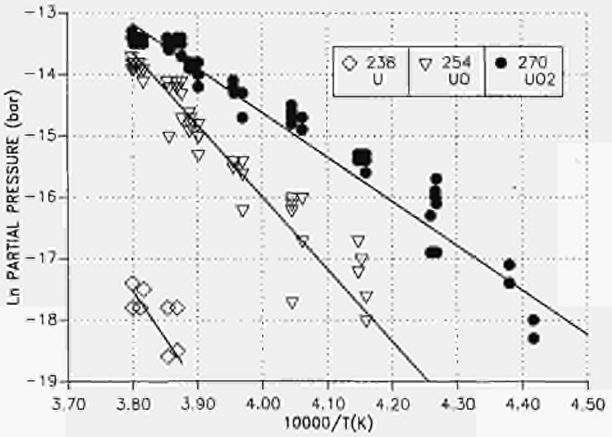

Fig. 2.2 Partial pressures of the U-bearing species as functions of temperature for the irradiated fuel (U627LOT2).

Fuel-tungsten interaction may therefore result in a substantial perturbation of the analysis, and, very likely, affected the recent mass spectrometric results on BR3 irradiated fuel obtained at Battelle [1]. Actually these analyses, carried out in the characterization context of the candidate fuel for the PHEBUS experiments, were initialy interpreted as an "anomalous" chemical state of this BR3 rod, and, consequently, gave rise to concerns on the representativity of this fuel with respect to modern PWR's.

In order to prevent this kind of disturbances a new cell was developed made of tungsten with an internal ThO_2 shroud. This cell provides the same thermal performance as the standard cell (especially with regard to temperature homogeneity) and, at the same time, the internal walls are effectively passive with respect to UO_2.

Fission product effusion

a) Gas

The experiments presently in progress are aimed at defining the various fission product perspiration and release stages under thermal conditions near to those of the first PHEBUS FP test. Generally, 15 temperature steps were applied starting from a conditioning temperature of 1200 K. In order to keep the mass spectrometric measurements within acceptable precision limits and, on the other side, to prevent too high vaporization losses in the sample, the duration of annealing steps was 10-20 min at low tem-

peratures, and was progressively shortened down to a few minutes at 2500 K.

In these first experiments, where a wide mass range was scanned, the step duration was chosen according to the effusion behaviour of Xe and UO_2. This entails that some nuclides could have been measured under non-optimal annealing conditions. The theoretical analysis of the fission product behaviour during this type of transient was made by using our codes FUTURE-MITRA-CHEMIF, and the results are reported in TUAR-93, p. 42. These codes are mechanistically based, so that they can be better validated by this type of laboratory release experiments than by large scale in-pile tests.

The first question to be answered is whether the assumed diffusion coefficients and intra- and intergranular trapping models (including formation of less volatile phases) are in agreement with the experimental observations.

An important difference between the laboratory and reactor release conditions is that in the former case the process takes place in vacuo, whilst in the latter a flow of pressurized gas/steam is generally present. This may entail a) a diversity in the chemical state of the fuel, and b) an essential inequality of the vaporization rate of the matrix in the two cases. The first difficulty will be removed by repeating the laboratory experiments under controlled $\Delta G(O2)$ by means of the available gas inlet system. As for point b), laboratory measurements have to be elaborated by applying a mass convection model to extrapolate reactor release rates. In this context it is necessary that thermodynamic equilibrium constants are obtained from Knudsen effusion raw data.

A great advantage of vacuum effusion experiments is that the whole sample can be vaporized at the end, and hence the vaporization rates of the different species can be calibrated with great accuracy, making it possible to perform a reliable diffusion analysis. The measured rates and the integral fractional release curves enable the various release stages to be identified, although, the detection limit at low temperatures is obviously limited by the incubation time during which the release pathways on the fuel grain boundaries are created (in the absence of thermal shocks for bulk samples this can be as long as several days).

Good tracers for identifying these events are rare gases, since they escape as soon as venting conditions are attained, whilst release of other elements may be influenced, in addition, by their volatility. Fig. 2.3 shows a typical release evolution (sample U6272 LOT2) of ^{85}Kr during a transient up to 2600 K of 2 h durations, made in small temperature steps. In this timescale release is first detected at approximately 1700 K. The release rate as a function of time is observed in the form of distinct peaks which normally start immediately after a temperature rise. However, even at constant temperature release may suddenly occur after a long incubation time. These release stages involve only a few percent of the gas inventory.

At temperatures between 1900 and 2000 K a much more important release stage is observed during which about one half of the gas inventory escapes. This stage comes to completion within 10-15 minutes, after which no release is observed up to temperatures of the order of 2500 K, at which UO_2 vaporizes at a comparable rate to the gas.

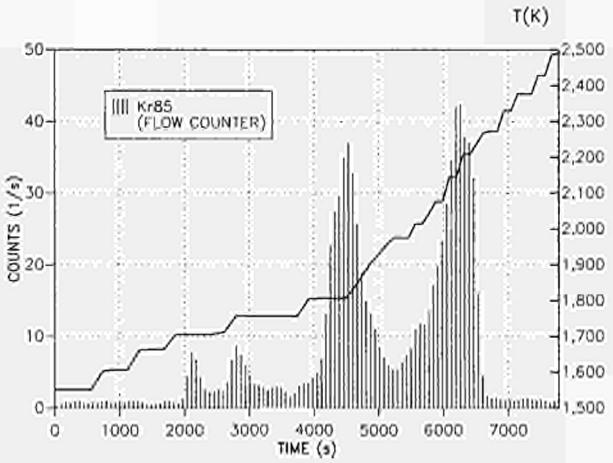

Fig. 2.3 Release curve of ^{85}Kr during a transient up to 2600 K of 2h duration (U627LOT2).

b) Volatile species

The elements which constitute the beta-decay chain to which rare gases belong (e.g Te-I-Xe-Cs-Ba) are expected to have quite different chemical activities in the fuel matrix. However, their diffusion may display a mutual correlation, for location and state, both in the physical and chemical sense, of a daughter element at its birth time may essentially depend on the previous behaviour of its mother. This correlation is more relevant for short-lived than for long-lived isotopes. Whenever the lifetime of the mother is sufficiently long with respect to the occurring diffusion rate, ambiguity is always faced in analyzing the release parameters of the daughter, that can only be removed by a complex mathematical treatment [2].

In Fig. 2.4 the mass-spectrometer measurements of ^{137}Cs compared with that of ^{136}Xe are shown. It can be seen that there is a close correspondence in the release stages of the two nuclides. However, the fractional release curve (Fig. 2.4a) shows that Xe release is appreciably delayed

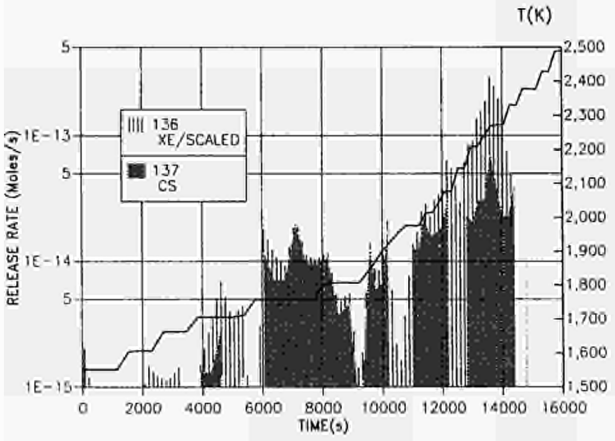

Fig. 2.4 Mass-spectrometer measurements of the effusion curves of ^{136}Xe and ^{137}Cs as functions of time and temperature (U627LOT2).

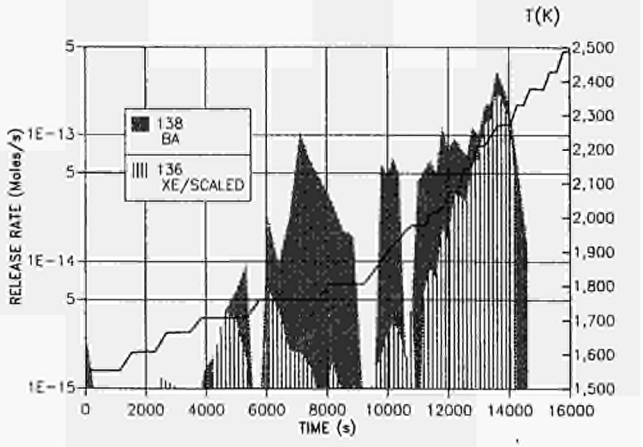

Fig. 2.5 Compared measurements of the effusion curves of ^{136}Xe and ^{138}Ba as a function of time and temperature (U627LOT2).

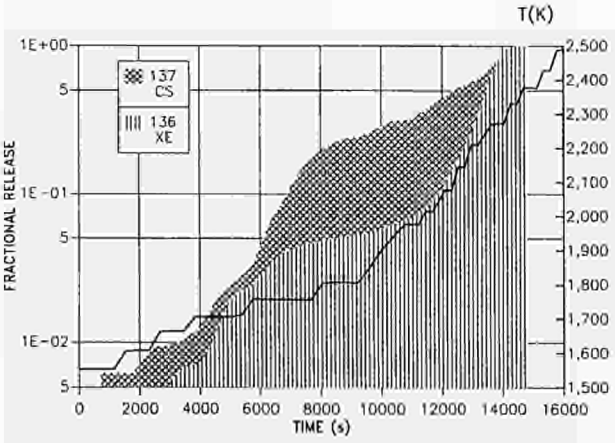

Fig. 2.4a Fractional release curve of ^{136}Xe and ^{137}Cs as a function of time and temperature (U627LOT2).

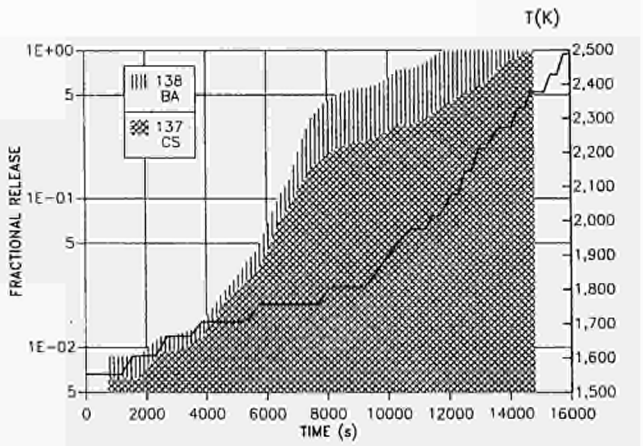

Fig. 2.5a Fractional release of ^{136}Xe and ^{138}Ba (U627LOT2).

relative to Cs. The difference is particularly relevant at high temperatures where a significant amount of Xe is retained (in bubbles), whilst Cs is to a large extent released. This difference relative to Xe is even more pronounced for ^{138}Ba (Figs. 2.5 and 2.5A), whose continuous release curve up to 2300 K indicates a preferential precipitation of this element on the grain boundaries, with almost no intragranular precipitation. For instance, during the transient annealing indicated in Fig. 2.5, approximately 95% of Xe is released after precipitation into intragranular bubbles (stage III), whereas only 50% Ba (and 70% Cs) seems to be trapped in closed phases (Fig. 2.5c).

Marked barium grain boundary precipitation followed by release at relatively low temperatures was confirmed by the results of ad hoc experiments. The mass spectrometer signal from a sample kept at 1560K for several hours is shown in Fig. 2.5b. During this time no significant sig-

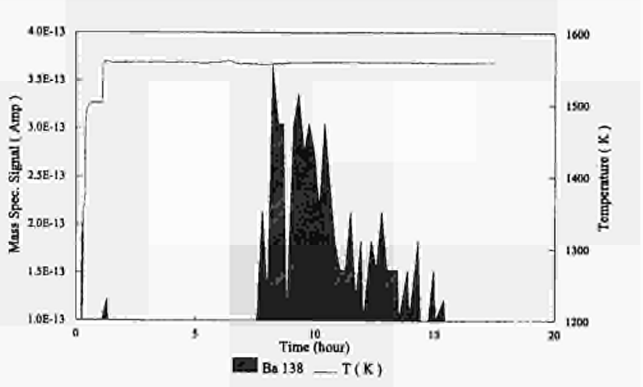

Fig. 2.5b Comparison of fractional release of ^{138}Ba and ^{137}Cs (U627LOT2).

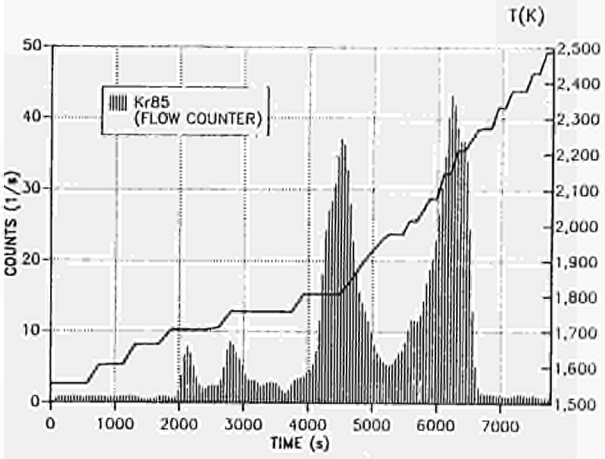

Fig. 2.5c Mass spectrometer signal of ^{138}Ba when the sample is kept at 1560 K for 20 hours (U627LOT2).

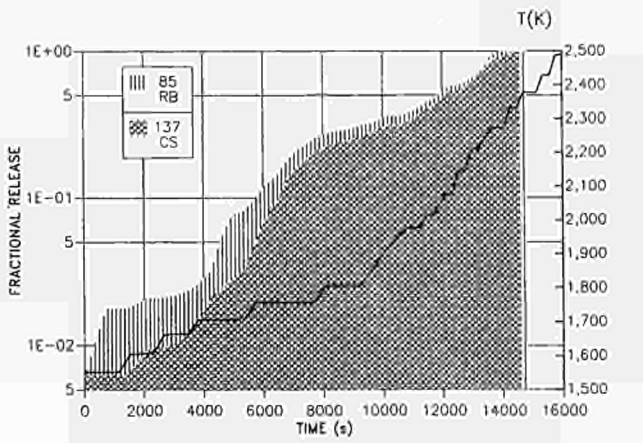

Fig. 2.6 Comparison of fractional release of ^{85}Rb and ^{137}Cs (U627LOT2).

nals were detected by the spectrometer. After approximately 10 hours at constant temperature ^{138}Ba suddenly appeared with effusion rate increasing with time, until a maximum was reached, followed by a slow decrease. After 7 hours the release episode terminated, and the sample did not display any other effect in the next ten hours. Together with Ba also Cs, Te and, in smaller amounts, Ru and Xe escaped. It should be noted that at 1560 K the vapor pressure of Ba(l) is sufficiently high to explain this release event. Had barium been present as an oxide, it could not have vaporized at the observed rate. The concomitant escape of tellurium is an indication for the probable presence of caesium and barium tellurides on grain boundaries, whereas rather puzzling is the presence of ruthenium, which in the metallic form has a very low vapor partial pressure at 1560 K, and whose oxidized state would entail a larger oxygen potential than that of stoichiometric UO_2.

By comparing the release behaviour of fission products of the heavy group with that of their chemical correspondents of the light group one realizes that, whilst for ^{85}Kr and ^{136}Xe one cannot detect any significant difference, Rb exhibits a higher mobility than Cs (Fig. 2.6). However, both ^{88}Sr and ^{90}Sr (Figs. 2.7a and 2.7b) have a lower mobility than Ba, and are effectively released only at temperatures above 1800 K.

Data evaluation

Data analysis on these experimental data is presently in progress. Additionally, new samples are being prepared from better localized radial positions on fuel rod cross-sections.
The aim of this second stage of the work is to correlate the measured release to suitable algorithms enabling the different diffusion/release stages as well as the respective coefficients to be obtained.

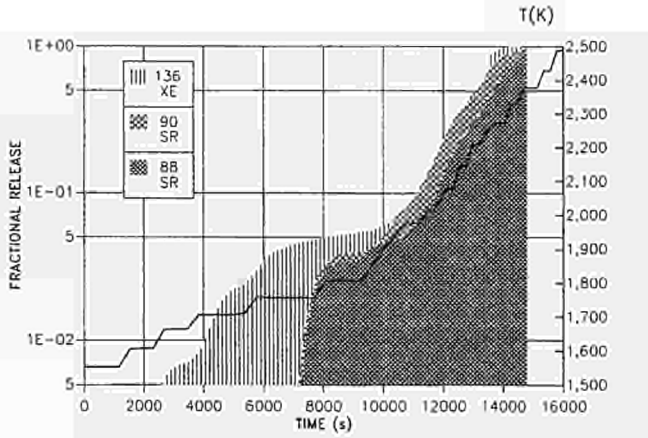

Fig. 2.7a Release rate of ^{136}Xe, ^{88}Sr and ^{90}Sr (U627LOT2).

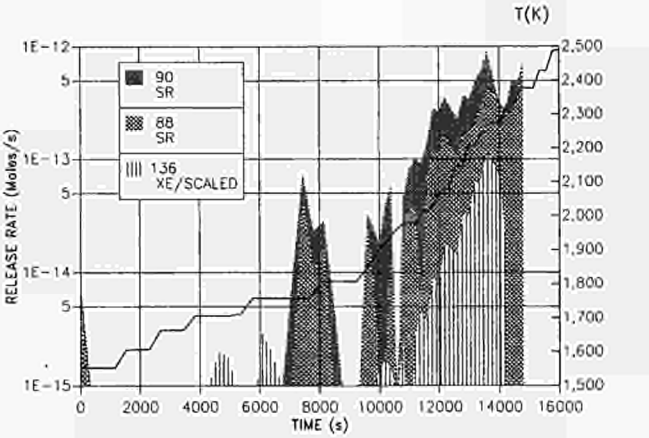

Fig. 2.7b Fractional release of ^{136}Xe, ^{88}Sr and ^{90}Sr (U627LOT2).

One of the salient points of the analysis is the identification of the low temperature release stage. Since the fuel samples were taken from zones with in-pile temperatures of less than 1000K, most of the fission products in the spent fuel are frozen in the UO_2 lattice as point defects or small clusters, which are not in thermodynamic equilibrium. Only very small fractions of the most mobile elements could diffuse to the fuel grain boundaries. Therefore, the principal effect of annealing consists of short-range redistributions of both inert and chemically active species, with simultaneous growth of the intergranular fission product concentration (in gas-filled pores and condensed phases). Since interconnection and/or microcrack venting of these phases, with creation of new free surfaces is a necessary condition for low temperature release, this phenomenon will be investigated by parallel scanning electron microscopy (SEM) investigation of the annealed samples.

Finally, at higher temperatures, equilibrium partial pressure of several fission product elements can be measured in a reasonably extended temperature range, and be directly compared with those of the UO_2 vapours, enabling a first tentative of fission product speciation to be carried out.

References

[1] C. Alexander; Battelle, Columbus, OH, (USA), private communication

[2] M. Gardani; C. Ronchi, Nucl. Sci. Eng. **107** (1991) 315

3. Characterization of Nuclear Waste Forms

3.1 Introduction

The studies on radioactive waste carried out at the Institute are centred on the characterization of nuclear waste forms including high burn up fuels with respect to properties relevant to their behaviour under irradiation or under conditions of long term storage.

Properties to investigate include thermal conductivity, chemical and mechanical stability, redistribution of actinides and fission products within the waste materials, resistance to corrosive agents and investigation of the leaching behaviour with various leachant compositions.

1. Electrochemical studies of UO_2 and MOX fuels in aqueous solutions are essential for the understanding of the dissolution and corrosion behaviour of these materials in groundwaters. The knowledge of the mechanisms (e.g. rate determining steps, intermediate species involved, precipitates, etc.) is important in assessing the stability of nuclear fuels in final or intermediate storage.

   Electrochemical testing has been continued and potentio-dynamic experiments (cyclic voltammetry) were used for an overview of the redox behaviour and to estimate the corrosion current densities of the materials investigated. Additional impedance measurements under potentiostatic conditions gave information about electric conductivity, corrosion rate and the inner resistance of the sample, which is used to correct the potential drop across the sample. In the future potentiostatic long term experiments will be suitable to compare electrochemical and analytical dissolution rates.

   In the current study sintered UO_2, and single crystal UO_2 were used as electrodes of non-irradiated fuels. Electrodes from irradiated UO_2 with 26.4 and 68 GWd/t burn-up, UO_2 from a failed fuel rod with abnormal grain size (20 - 25 GWd/t) and MOX fuels (21.1 GWd/t) with Pu particles containing 25% Pu were used for the studies on irradiated fuels. Measurements were carried out in aerated and deaerated 3 w/o Na_2CO_3 solution at room temperature (25 ± 2 °C). For measurements in the hot-cell the electrolyte was deaerated with N_2 bubbling to about 0.1 ppm O_2 and kept during the course of the experiment under a N_2 - 5% O_2 atmosphere.

2. A leaching test on UO_2 powder in an autoclave at 200 °C for a short duration (one month) was repeated using Ti containers because this material is expected to display a neutral behaviour.

   The goal of this experiment was to quantify the influence of oxidation conditions on the leaching rate. A clear difference was seen: in presence of Fe (reducing conditions) the lowest values were observed and an increase of the amounts leached was noted when the tests were carried out under oxidizing conditions in H_2O or H_2O_2.

3. High temperature reactions are possible during a reactor accident between fuel and structural materials as the bundle degrades. The investigation of these interactions and their kinetics is important as they result in low melting point eutectics or mixtures which are liquid at temperatures substantially below those of the individual melting points. This can cause a severe and accelerated degradation of the reactor core even below the UO_2 melting point.

   This study was done in two parts:

   - structural material interactions with natural UO_2
   - structural material interaction with irradiated UO_2.

   The structural materials tested were 304L stainless steel, zircaloy 4 cladding and Ag-In-Cd from absorber control rods.

   The techniques used were annealing, differential thermal analysis (DTA), dilatometry, optical and electron scanning microscopy.

   The results show the effect of structural materials on fuel at temperatures that are below those of the melting points of the main components and how material interaction can create liquid mixtures at low temperatures (~ 1200 °C) with rapid attack on irradiated UO_2.

Further work should be carried out together with that on natural UO_2 to clarify the influence of certain mixtures and to identify the critical liquefaction temperatures and the effective threshold of attack both for natural UO_2 and for irradiated UO_2. The influence of the enlarged grain boundaries and secondary precipitates on liquefied mixture penetration between the grains should also be measured (e.g. testing with lower burn-up fuel).

4. UO_2 power reactor fuels irradiated up to a burnup of 50.000 GWd/t and more display new aspects of fuel-clad interaction. A reaction between Cs and UO_2 at cladding-fuel interface was found resulting in a modification of the fuel cladding mechanical interaction and thermal properties of the fuel pellet periphery.

   UO_4Cs_2 was synthesised and its thermal conductivity was measured by means of the comparison method in the temperature range 100 to 600 °C. The experimental data indicate that this compound has a poorer conductivity than that of UO_2 by a factor 2.

5. Initial determinations of the micro-hardness of high burn-up fuel in particular at the pellet periphery were carried out at room temperature. The results are of the same order of magnitude to those obtained on simulated fuels. This suggests that the deleterious effect of porosity on hardness might have been compensated by Hall-Petch strengthening due to the smaller grain size in this region.

6. The determination of the porosity distribution of various irradiated UO_2 fuels up to 80.000 GWd/t indicate the existence of at least three modes of restructuring:

   - in-pile sintering during the first irradiation phase with progressive decrease of the initial porosity.
   - two further restructuring modes are associated with the formation of fission gas pores with two strong local increases as the burn-up increases.
     a. at the pellet periphery (100 - 200 μm depth). The local increase of the pore concentration can reach a factor 2 to 3 and seems to be very sensitive to the burn-up profile in this thin zone.
     b. in the central part of the fuel the formation of intergranular porosity results from gas diffusion to the grain boundary and coalescence mechanism on the grain boundary.

7. Cladding rupture during irradiation in a FBR could lead to a chemical interaction between Na and mixed oxide fuels containing Am, Np used for transmutation (SUPERFACT experiment). These interactions were analysed by means of thermogravimetry and differential thermal analysis.

   The extent of this reaction was studied in the temperature range of 600 - 700 °C and the reaction product characterization was carried out by X-ray diffraction. Although equilibrium conditions were not completely achieved the results suggest that after total disappearance of Na_2O_2, the compound formed is $Na_{11}M_5O_{16}$ (M = U; $U_{0.8}Pu_{0.2}$; $U_{0,74}Pu_{0.24}Am_{0.02}$; $U_{0.74}Pu_{0.24}$ $Np_{0.02}$; $U_{0.6}Np_{0.2}Am_{0.2}$; $U_{0.55}Np_{0.45}$).

   The reaction temperature (684 to 692 °C) increases as actinide content increases.

3.2 Characterization of Spent Fuel in View of Long Term Storage

3.2.1 Study of natural UO_2 and spent fuel in aqueous carbonate solutions by electrochemical techniques

Electrochemical studies of UO_2 and nuclear fuels in aqueous solutions are essential to understand the dissolution/ corrosion behaviour of these materials in ground waters. Knowledge of the mechanisms (e.g. rate determining steps, intermediate species involved, precipitates ...) are important in assessing the stability of nuclear fuels in final storage.

Potentiodynamic experiments (cyclic voltammetry) were used to get an overview about the redox behaviour and an estimation of corrosion current densities of the materials under investigation. Additional impedance measurements under potentiostatic conditions gave information about electric conductivity, corrosion rate and the inner resistance of the sample, which must be used for correction of the potential drop across the sample. Potentiostatic long term experiments are suitable to compare electrochemical and analytical dissolution rates.

For electrochemical measurements with irradiated nuclear fuels it was necessary to develop a sample holder for remote handling in the hot cells. Fig. 3.1 shows the resulting working electrode assembly. Pieces (0.2 - 0.5 g; Ø = 2 - 4 mm) from the fuel edge were mounted on a flat brass screw in the head of the electrode using nickel conductive glue. Then the samples were embedded in epoxy resin and polished down to 1 µm. After preparation the head could be mounted on the electrode holder and placed in the electrochemical cell. Measurements were started after ~5 minutes immersion.

The following electrode materials were used:

non-irradiated:
- natural UO_2, sintered (95% density)
- natural UO_2- single crystal (JRC Ispra)

irradiated:
- commercial UO_2 fuel, 6.85% ^{235}U (burnup 26.4 GWd/tU)
- UO_2 fuel from defective pin with abnormal grain size (burnup 20/25 GWd/tU)
- high burnup commercial UO_2 fuel (burnup 68 GWd/tU)
- commercial MOX fuel, approximately 7.5% Pu; Pu-rich particles 25% PuO_2 (burnup 21.1 GWd/tU)

Measurements were carried out both in aerated and deaerated 3 w/o Na_2CO_3 solution at room temperature (25 ± 2 °C). For use in the hot cells the electrolyte was deaerated with N_2 bubbling to ~0.1 ppm O_2 and kept during the experiment under N_2 - 5% O_2 atmosphere.

Cyclovoltammograms (CV) were recorded with a maximum potential scan of 0.3 mV/s. Resulting polarization curves (i.e. potential (E) versus logarithmic current density (log i) diagrams) for commercial UO_2 (26.4 GWd/ tU) and MOX (21.1 GWd/tU) fuel are shown in Figs. 3.2 and 3.3. The polarisation potential E is corrected for the ohmic resistance of the circuit; the so-called 'iR' drop. In the case of semi-conducting UO_2 its substantial resistance causes a large potential drop across the electrode itself. The general form of the irradiated UO_2 curve is similar to that of the non-irradiated UO_2 curve (see also TUAR-93, p. 90). It could be seen that UO_2 has an anodic curve rising in two stages; this shows it oxidises in a 2 stage oxidation process. The first stage seems to be irreversible and is followed by a second reversible step. At high anodic potentials O_2 evolution is possible.

Characteristic parameters of these polarisation curves (loglil vs. E) are the zero current or corrosion potentials (E at the points i=0) and the exchange current densities i_o at the zero current potential (E(i=0)). The latter can be obtained by extrapolation of the tangents of the anodic and cathodic curves (Tafel lines) to the zero current potential. The slopes of the tangents or Tafel lines b_a and b_c, can be used to calculate the correlation factor B between the reciprocal polarisation resistance $1/R_p$ (determined from ac impedance measurements of the UO_2 electrodes) and the corrosion current density i_{corr} (determined from the exchange current density above). This will give an indication of the rate-determining step at the electrode surface. Values of these parameters for various experiments are collected in Tab. 3.1.

The potential E(i=0) in the cathodic range that is reached first with rising anodic polarisation seems to be strongly dependent on oxygen concentration. The most negative potential (-800 / -900 mV_{SHE}) is reached for the single crystal electrode and approaches the true UO_2 E_{corr} potential (no hidden oxygen in pores and cracks). E(i=0) downward, that is with decreasing anodic polarisation, is more constant at +200 mV_{SHE} to +350 mV_{SHE} and is related to the free corrosion potential at long term measurements.

The values of the correlation factor B are for most experiments between 20 mV and 36 mV except for MOX

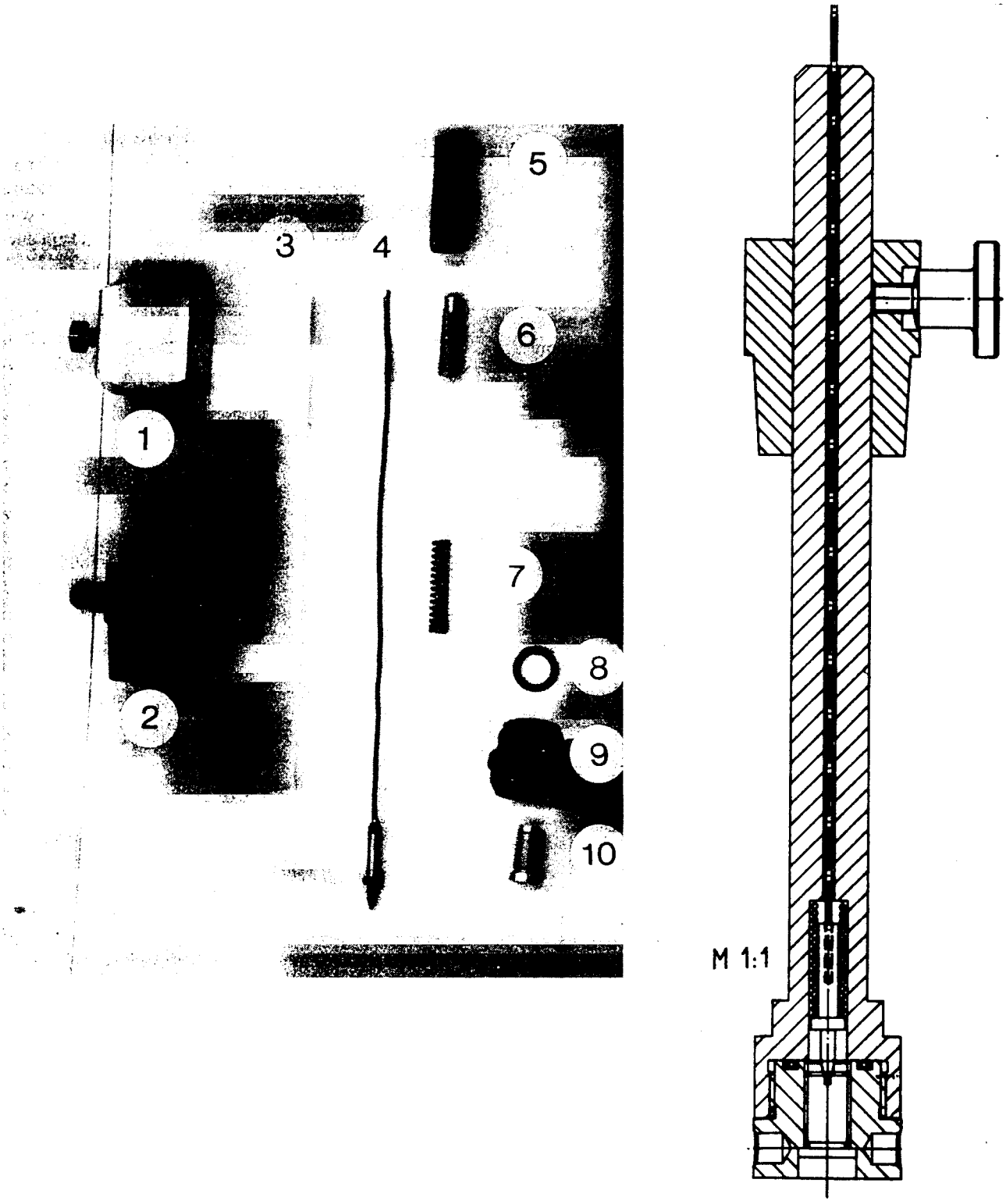

Fig. 3.1 Working electrode assembly for electrochemical experiments performed on spent fuel. 1) grip for manipulator, 2) flange fitting adapter for holder, 3) electrode holder, 4) Cu wire with contact head, 5) banana plug, 6) plug connector, 7) spring, 8) O-ring, 9) electrode head, 10) brass sample holder

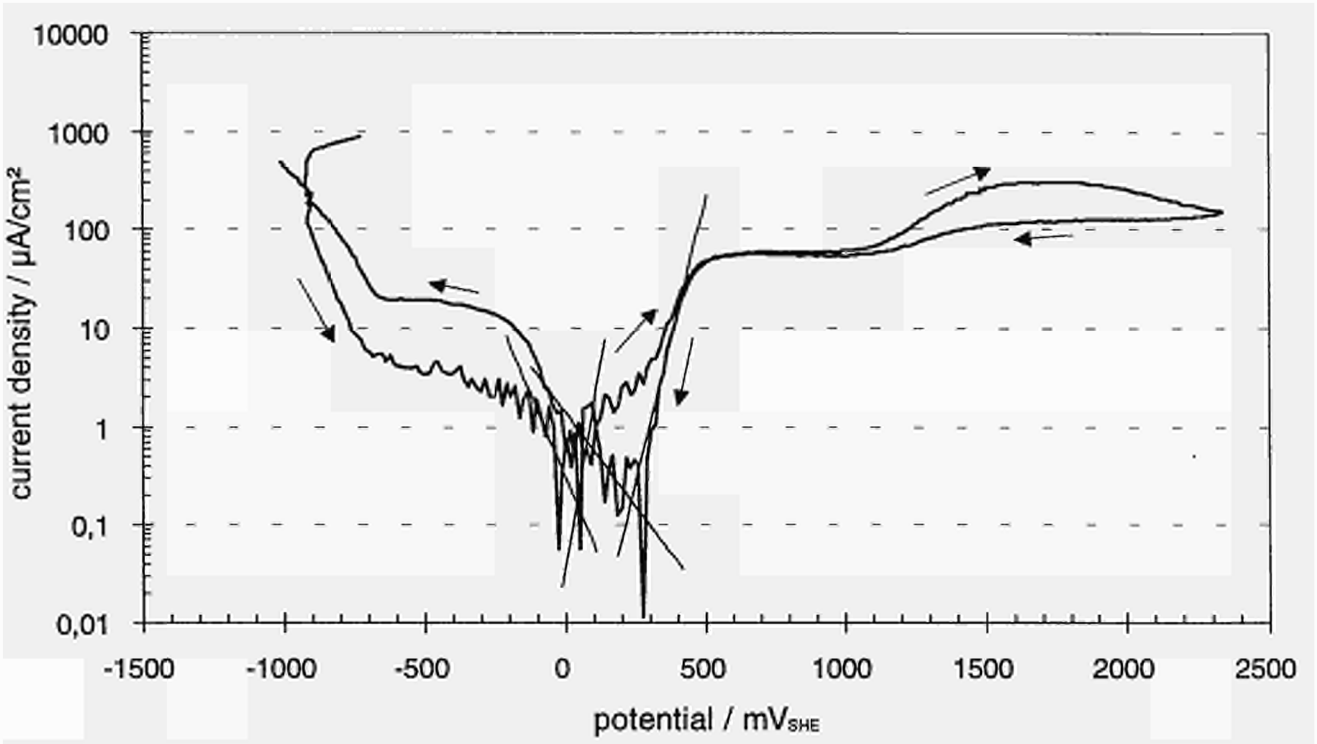

Fig. 3.2 Polarisation curve (log|i| vs. E) of polished commercial UO_2 fuel (6.85% ^{235}U; burn-up 26.4 GWd/tU) in 3 w/o Na_2CO_3 solution (max. scan 0.3 mV/s; pH 11.2; $[O_2]$ ~2 ppm; 25 °C; vacuum impregnated sample).

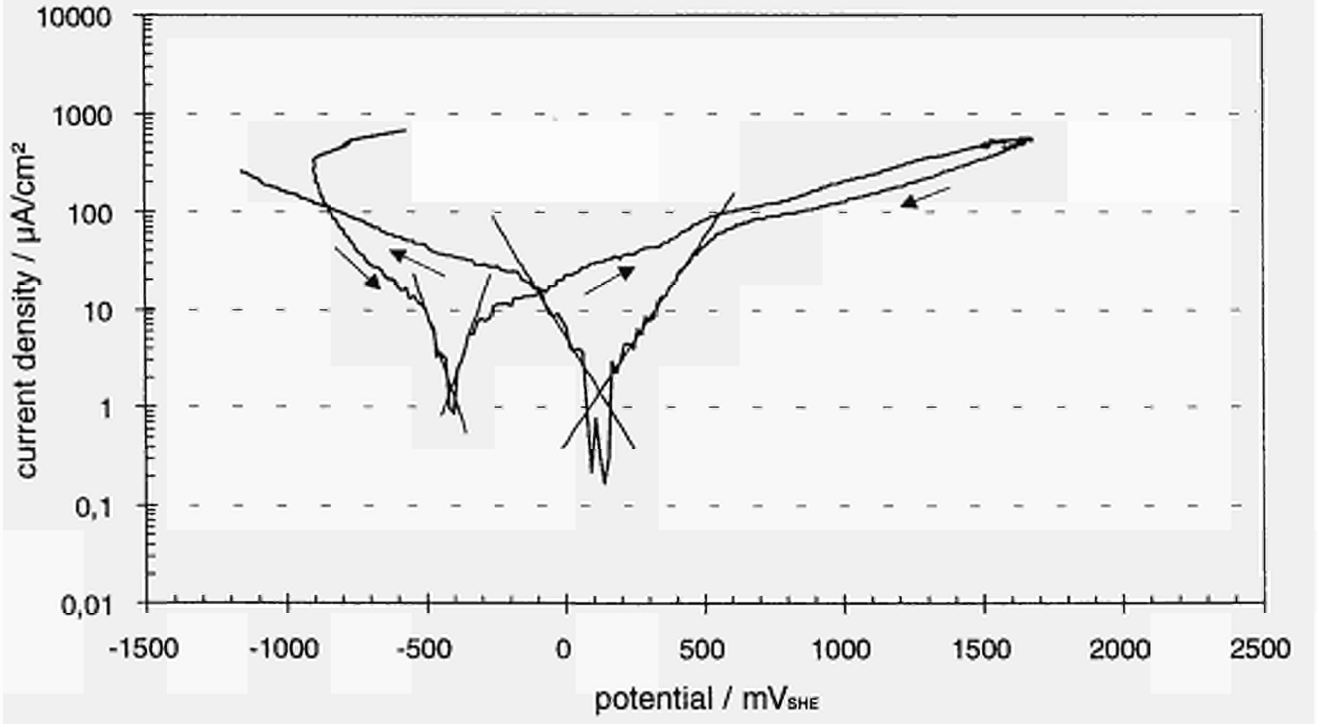

Fig. 3.3 Polarisation curve (log|i| vs. E) of polished commercial MOX fuel (approx. 7.5% Pu, Pu-rich particles 25% Pu; burnup 21.1 GWd/tU) in 3 w/o Na_2CO_3 solution (max. scan 0.3 mV/s; pH 11.2; $[O_2]$ ~2 ppm; 25 °C; vacuum impregnated sample).

Tab. 3.1 Corrosion currents and potentials from cyclic voltammetry performed on natural UO_2 and spent fuel in 3 w/o Na_2CO_3 solution at room temperature.

sample	$C(O_2)$ ppm	cycle No.	upward $E(i=0)$ mV_{SHE}	upward i_o $\mu A/cm^2$	downward $E(i=0)$ mV_{SHE}	downward B mV	downward i_{corr} $\mu A/cm^2$	remarks
nat. UO_2	6	1	-30	0,2	200	28	0,1	
pellet		5	-180	0,2	240	20	0,2	
nat. UO_2	0,01	1	-320	0,05	210	26	0,1	
pellet		2	-400	0,1	240	35	0,15	stirred
UO_2 single	0,1	1	-780	1	310	36	1	
crystal		2	(-900)	(1)	(320)		(3)	stirred, pitting
UO_2 fuel	≈2	1	40	0,2	235	28	0,2	vacuum impregnated,
(26.4 GWd/tU)								pitting
		2	-180	0,2	281	26	0,5	vacuum impregnated,
								pitting
high burn up	≈2	1	-	-	340	47	-5	vacuum impregnated,
UO_2 fuel								heavy pitting
(68 GWd/tU)		2	-	-	350		-4	vacuum impregnated,
								heavy pitting
UO_2 fuel	≈2	1	-580	4	300		6	pitting
defective pin		2	-620	7	350	66	22	pitting
(20/25 GWd/tU)		3	-750	15	340		20	
		1	-350	2	305	35	2	vacuum impregnated
MOX fuel	≈2	1	-500	6	80	53	5	pitting
(21.1 GWd/tU)		2	-530	5	140	76	7	pitting
		1	-410	2	125	49	2	vacuum impregnated

fuel and non-vacuum impregnated UO_2 fuel from a defective pin. As well the MOX fuel polarisation curve (Fig. 3.3) shows in the anodic range Tafel lines with slopes that are not so steep as in the case of pure UO_2. The coefficient b_a is for UO_2 about 120 mV/dec and for MOX about 260 mV/dec. The corrosion potentials of MOX fuel are also more negative than for UO_2 fuel. The electrochemical behaviour of MOX fuel is affected by the PuO_2 content.

The influence of PuO_2 is as well seen on the surface of a MOX sample after measuring 2 cyclovoltammograms (exposure time approximately 6 days) (Fig. 3.4). The material around the MOX particles is attacked and the Pu-rich particles still remain. Local corrosion elements are formed on the surface where Pu-rich particles are cathodically corrosion protected and anodic sites of bulk UO_2 material are dissolved.

The corrosion behaviour can furthermore be influenced by the structure (grain boundaries, cracks, pores) of the fuel. For testing UO_2 fuel from a defective pin the sample was first embedded in epoxy resin under atmospheric pressure and then polished down to 1 µm. The current during the cyclic voltammogram (CV) experiment (Fig. 3.5) was very 'noisy' even in the region of the free corrosion potential (-500 to +500 mV_{SHE}). This unstable current behaviour indicates pit initiation and/or secondary phase dissolution may occur.

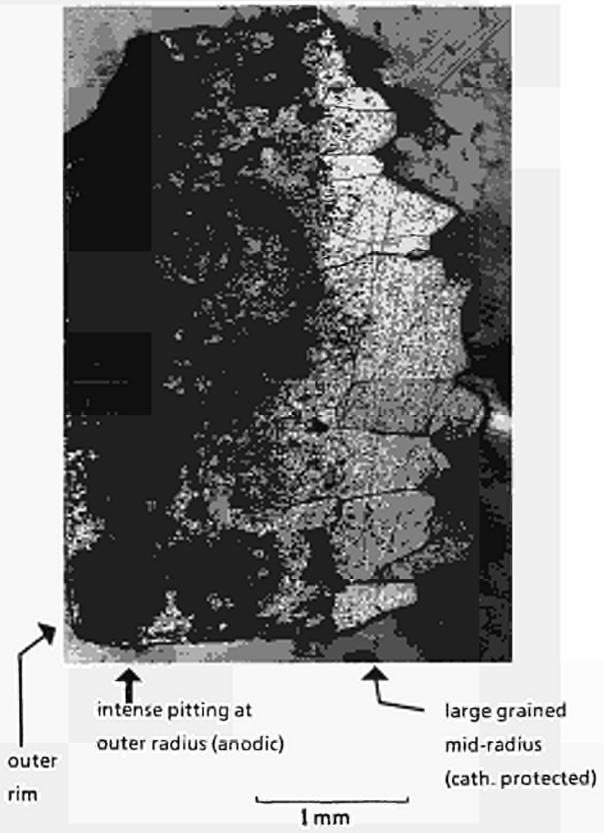

Fig. 3.4 UO_2 fuel from defective pin (burnup 20/25 GWd/tU) after 3 cyclic voltammograms (cath./anodic/cath.)-12 days in 3 w/o Na_2CO_3 solution. Intense pitting is seen at outer radius (left side)(38x).

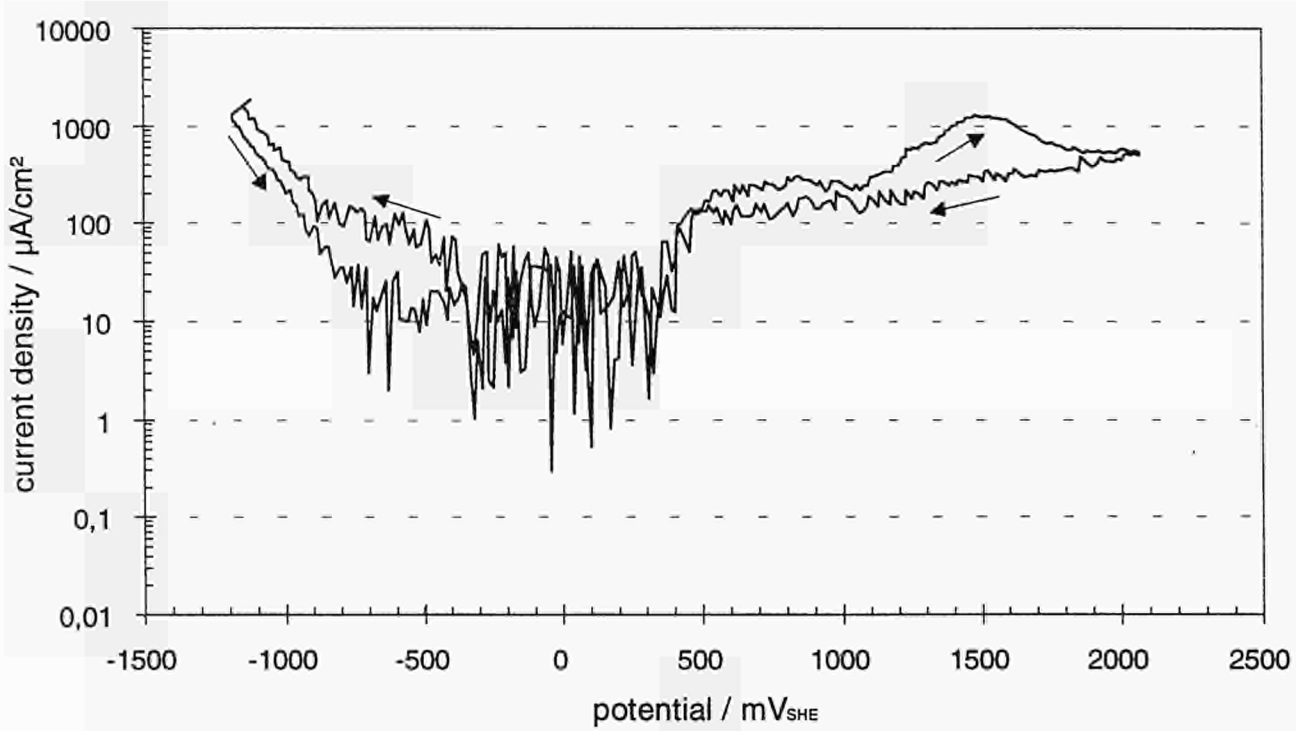

Fig. 3.5 Polarisation curve (log|i| vs. E) of polished UO_2 fuel from defective pin (burnup 20/25 GWd/tU) in 3 w/o Na_2CO_3 solution (max. scan 0.3 mV/s; pH 11.2; $[O_2]$ ~2 ppm; 25 °C).

A micrograph from this sample was taken after 3 CVs (14 days exposure time) (Fig. 3.6). It shows clearly a heavily attacked zone in the region of small grains. In the case of large grains the onset appears mostly at the grain boundaries. Reimpregnation of the sample was done under vacuum after these measurements to fill the structural defects with resin. In the resulting polarisation curve of polished and reimpregnated UO_2 fuel all current fluctuations have vanished indicating that no intense pitting corrosion occurs (Fig. 3.7).

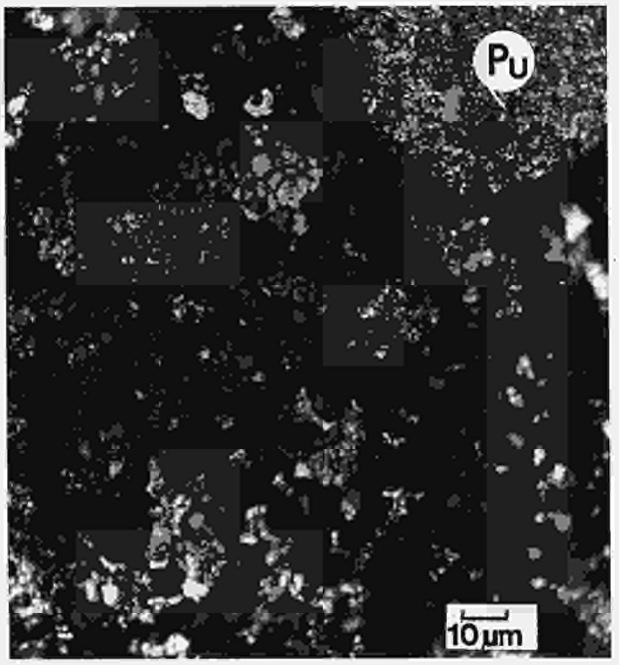

Fig. 3.6 Irradiated MOX electrode after 2 cyclic voltammograms (cath./anodic/cath.)- 6 days in 3 w/o Na_2CO_3 solution. Heavily attacked zone with PuO_2 rich particle protruding (noble compared to UO_2 matrix) (591x).

Corrosion current densities i_{corr} obtained from potentiodynamic experiments (Tab. 3.1) are least for sintered pure UO_2 samples (natural and irradiated) ($i_{corr} < 1\ \mu A/cm^2$). Medium range values ($1 < i_{corr} < 10\ \mu A/cm^2$) are found for single crystal UO_2, vacuum reimpregnated fuel (defective pin), MOX and high burnup fuel. Heaviest corrosion attack takes place at structural defects of UO_2 fuel from the defective pin ($i_{corr} > 10\ \mu A/cm^2$).

In comparison the resulting corrosion current densities from potentiostatic impedance and current measurements are mainly one order of magnitude lower (see Tab. 3.2). The highest values were found for MOX fuel but however the large errors for this fuel must be also taken into consideration.

From these measurements anodic Tafel slopes in the range of 80 mV/dec to 143 mV/dec were calculated. A slope of about 120 mV/dec implies a charge transfer of 2 electrons/molecule. This assumption was made to compare the amount of total uranium in solution calculated from the total charge flowing during 15 h potentiostatic electrode treatment with direct solution analysis by ICP-MS. The results are in very good agreement (see Tab. 3.3).

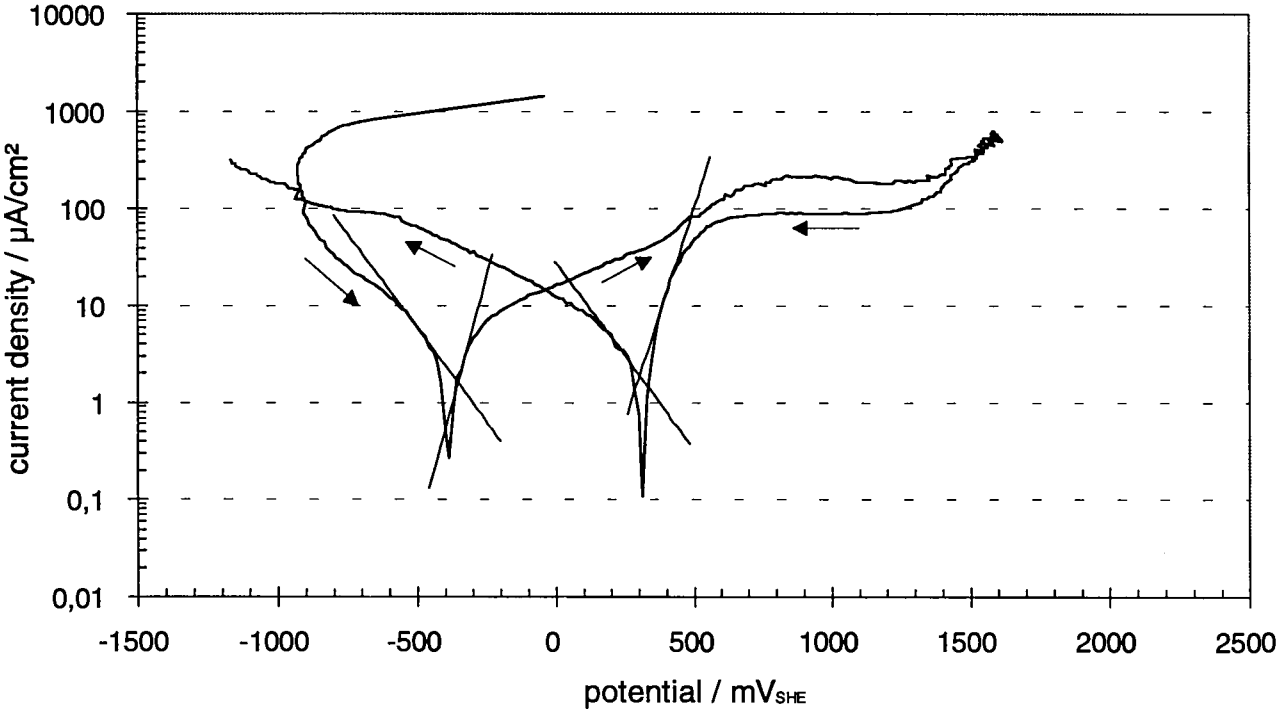

Fig. 3.7 Polarisation curve (log|i| vs. E) of polished UO_2 fuel from defective pin (burnup 20/25 GWd/tU) in 3 w/o Na_2CO_3 solution (max. scan 0.3 mV/s; pH 11.2; $[O_2]$ ~2 ppm; 25 °C; after vacuum reimpregnation of the sample).

sample	$C(O_2)$	impedance measurement				current measurement			
		b_a	B	E_{corr}	i_{corr}	b_a	B	E_{corr}	i_{corr}
	ppm	mV/dec	mV	mV_{SHE}	$\mu A/cm^2$	mV/dec	mV	mV_{SHE}	$\mu A/cm^2$
nat. UO_2	6	135±10	40± 4	140±50	0.16±0.06	85± 2	29± 5	185±25	0.07±0.03
pellet	0,01	101± 4		150±50	0.04±0.05	80± 3		150±50	0.01±0.01
stirred ->	0,02	127±11		150±50	0.3 ±0.3	81± 1		150±50	0.02±0.02
UO_2 single crystal	0,3	122±40		80±50	0.06±0.08	91± 9		180±50	0.3 ±0.3
UO_2 fuel (26.4 GWd/tU)	≈2 #	100±13	35± 9	259±35	0.4 ±0.5	89±10	26± 5	240±26	0.2 ±0.2
high burn up UO_2 fuel (68 GWd/tU)	≈2 #	142±41	50±28	175±45	0.4 ±0.5	80± 3	31± 3	272±13	0.3 ±0.1
UO_2 fuel defective pin (20/25 GWd/tU)	≈2 #	143± 8		160±30	0.8 ±0.5	131± 4		160±30	0.9 ±0.3
MOX fuel	≈2	233±28		150±50	2 ±2	281±50		150±50	5 ±5
(21.1 GWd/tU)	≈2 #	212±40		- 8±20	0.4 ±0.2	282±50		- 8±20	1.4 ±8

#: vacuum impregnated samples

Tab. 3.2 Corrosion currents, potentials and Tafel parameters from potentiostatic impedance and current measurements performed on natural UO_2 and spent fuel in 3 w/o Na_2CO_3 solution at room temperature.

Tab. 3.3 Comparison of corrosion rates of natural UO_2 in aqueous 3 w/o Na_2CO_3 solution obtained from electrochemical techniques and direct solution analysis (15 h exposure time, 100 ml electrolyte volume, room temperature).

	electrochemical analysis			solution analysis ICP-MS		
E	Q	$C_U(Q)$	w_{int}	$C_U(sol)$	w_{int}	$\delta(C_U(Q)-C_U(sol))$
mV_{SHE}	mAs	ppm	mm/a	ppm	mm/a	%
416 ± 20	18,3	0,23	0,031	0,21	0,028	8,7
400 ± 10	382,8	4,72	0,64	4,65	0,63	1,5
445 ± 200	3151,5	38,9	5,3	37,55	5,1	3,5
1100 ± 300	7154,9	88,2	12,0	82,1	11,2	6,9

Micrographs of these natural UO_2 electrodes show formation of localised corrosion cells with cathodically protected surface areas and on the other hand the onset of preferential dissolution at grain boundaries (Fig. 3.8). At the bottom of pores in heavily attacked zones brownish uranium oxides (UO_3?) were observed. XPS analysis also showed the surface to be hyperstoichiometric $UO_{2.13}$ (as averaged over the surface area).

Finally from analysis of impedance spectra and the related geometric parameters of the samples under investigation electrical resistivities of the various fuels could be obtained. A comparison of these values with literature data for non-irradiated materials is shown in Fig. 3.9.

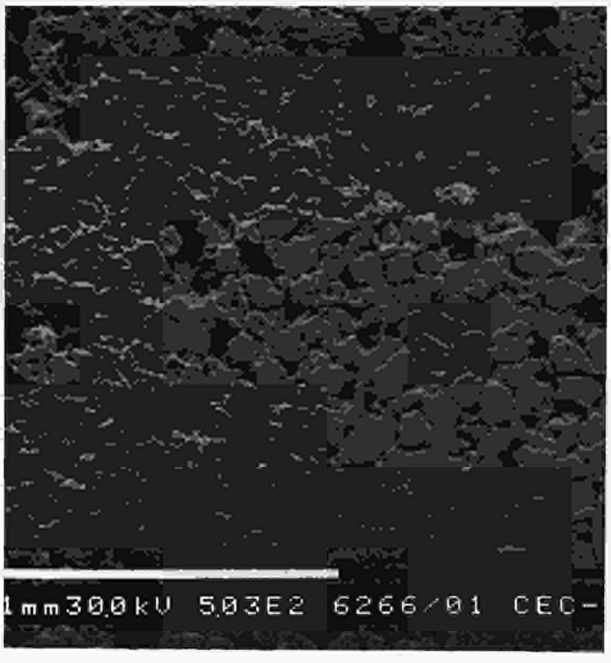

Fig. 3.8 Natural UO_2 electrode polished to 1 μm with diamond paste after 15 h potentiostatic treatment at +400 mV_{SHE} in 3 w/o Na_2CO_3 solution showing localised attack at grain boundaries (lower right side) and heavily corroded surface (upper left side)(500x).

Preliminary conclusions relevant to spent fuel behaviour during oxidation by groundwater

From these studies it can be concluded that:

a) because of its high resistivity, UO_2 is subject to pitting attack at grain boundaries or inclusions. Pits propagate into the specimen depth with locally increased polarisation.

b) irradiated fuels display a more heterogeneous behaviour and suffer higher corrosion. There is more intense pitting in some zones which protect adjacent zones (large grain sizes are more protected).

c) UO_2 undergoes a two stage oxidation, the first stage is irreversible. This higher oxide layer then dissolves at higher anodic potentials. Higher oxides (e.g. UO_3) and $CO_3^=$ anions are observed in pits.

d) at rest potential oxide filming occurs on the surface with time (electrode bulk resistance increases).

e) the presence of $(U,Pu)O_2$ particles in irradiated MOX fuels causes the E_{corr} values to shift towards each other compared to UO_2.

3.2.2 Leaching studies

Modified leaching test in autoclaves

The leaching experiments carried out with Teflon containers as described in TUAR-92, p.101 and the follow-up experiment presented in TUAR-93, p. 95 had as main drawback, the poor radiation resistance of the Teflon container material. Furthermore it has been shown (TUAR-91, p.102) that Ti has highly neutral behaviour in leach-

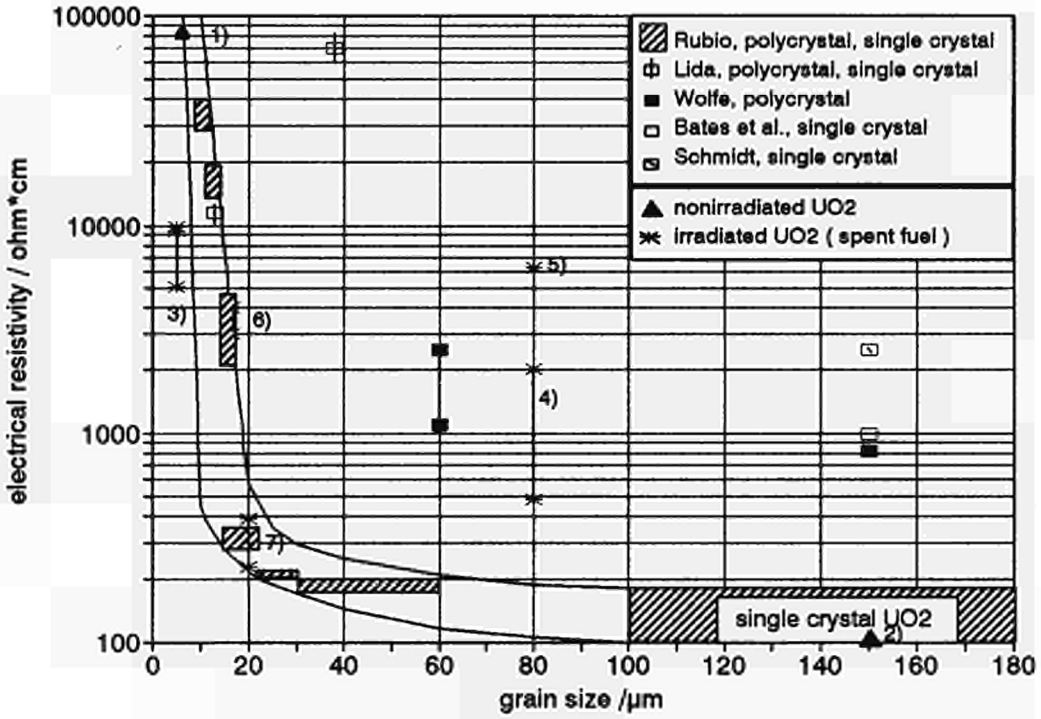

Literature data: Gmelin Handbook, U Suppl. Vol. C5, (1986), 207/23

Data measured in 3%(wt) Na2CO3 sol.(RT) using impedance spectroscopy:

nonirradiated UO2:
1) natural UO2 pellet (KWU)
2) single crystal (Ispra)

irradiated UO2 (spent fuel):
3) MOX fuel; approx. 7.5% Pu; burn up: 21.1 GWd/tU
4) UO2 fuel; defective pin; abnormal grain size; oxidised UO2; burn up: 20/25 GWd/tU
5) UO2 fuel; defective pin; abnormal grain size; oxidised UO2; burn up: 20/25 GWd/tU; vacuum reimpregnated sample
6) UO2 fuel, 6.85% U-235; burn up: 26.4 GWd/tU
7) high burn up UO2 fuel; burn up: 68 GWd/tU

Fig. 3.9 Electrical resistivities of natural UO_2 and spent fuel obtained from impedance measurements in comparison with literature data.

ing experiments of real vitrified waste and also very good radiation properties, a result confirmed elsewhere [1]. The fuel oxidation experiment has been therefore repeated using Ti containers. As in the previous experiments, spent fuel (burn-up: 51 GWd/t U) in powder form (125-250 µm) was treated at 200 °C for 5 weeks under various conditions (Fig. 3.10).

Three different conditions were tested: in addition to H_2O and H_2O_2, Fe powder was added in one case; Fe should provide reducing conditions typical of containment corrosion during storage. The experimental conditions for the 3 cases are summarised in Tab. 3.4.

After 1 week the solutions from the bottom of the Ti containers were collected, the containers without the sample holders were washed with 0.1 M HNO_3 and the solutions were analysed by ICP-MS. The result of the qualitative analysis of the leachates by ICP-MS is shown in Fig. 3.11.

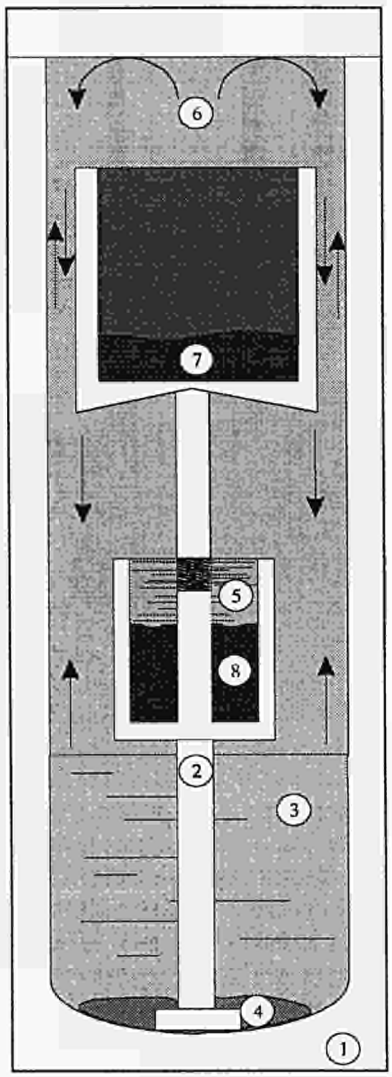

Fig.3.10 Experimental set-up for the leaching of oxidised spent fuel (test duration 1 week) 1. autoclave liner (Ti), 2. sample holder (Ti), 3. solution (H_2O or H_2O_2) in equilibrium with the vapour phase, 4. Fe powder, 5. leachant (H_2O) in equilibrium with the vapour phase, 6. vapour phase, 7. fuel powder in contact with the vapour phase, 8. fuel powder in contact with the leachant.

Tab.3.4 Experimental conditions for the oxidizing spent fuel powder at 200 °C (test duration 5 weeks).

solution in equilibrium with the vapour phase	H_2O_2	H_2O	H_2O + Fe powder
amount, g	6.019	5.956	5.945 + 13.104
fuel amount, g upper sample holder	0.279	0.249	0.298
fuel amount, g lower sample holder	0.372	0.239	0.283

There is a strong influence of the redox conditions on the leaching of spent nuclear fuel. In all cases the lowest values were observed in the presence of Fe. The leached amounts increase with water vapour and especially if the vapour is in equilibrium with H_2O_2. The increase is the highest for elements sensitive to the redox potential such as Tc, U and Np. An exception is Mo, where a leaching decrease in the presence of Fe is evident, but also in the presence of H_2O_2 the leached Mo amount is lower compared to that of H_2O. These results are confirmed by the quantitative analysis (Tab. 3.5).

Tab. 3.5 Composition of the leachates and the increase of the leaching under oxidising (H_2O_2 and H_2O) in comparison to reducing (H_2O +Fe) conditions

	total amount in the leachate, µg			increase factor compared to H_2O + Fe	
	H_2O + Fe	H_2O	H_2O_2	H_2O	H_2O_2
Rb	0.204	0.259	5.089	1	25
Sr	0.097	0.032	0.187	0	2
Y	0.001	0.000	0.003	1	4
Zr	0.013	0.155	0.015	12	1
Mo	0.431	8.885	1.341	21	3
Tc	0.157	0.365	3.315	2	21
Ru	0.002	0.024	0.513	15	317
Rh	0.007	0.009	0.492	1	75
Pd	0.003	0.065	0.913	20	279
I	1.719	2.374	1.928	1	1
Te	0.001	0.005	0.001	5	1
Cs	3.783	9.277	42.313	2	11
Ba	0.031	0.042	0.037	1	1
La	0.001	0.002	0.006	3	10
Ce	0.001	0.007	0.010	6	9
Np	0.000	0.007	0.186	39	967
U	0.479	3.819	49.682	8	104
Pu	0.020	0.028	0.026	1	1
Am	0.000	0.000	0.000	0	0

The relative increase of leaching under oxidising (H_2O) and strongly oxidising (H_2O_2) conditions were calculated and are given in Tab. 3.6. It is evident that big differences are observed for the redox sensitive elements, mainly U and Np, but also for the noble metals Ru, Rh and Pd. From the fraction of inventory in the aqueous phase (FIAP) values it becomes however evident, that besides Np mainly Cs, Rb and I show high leaching values, the latter almost independent of the redox conditions. At the present time this observation cannot be explained.

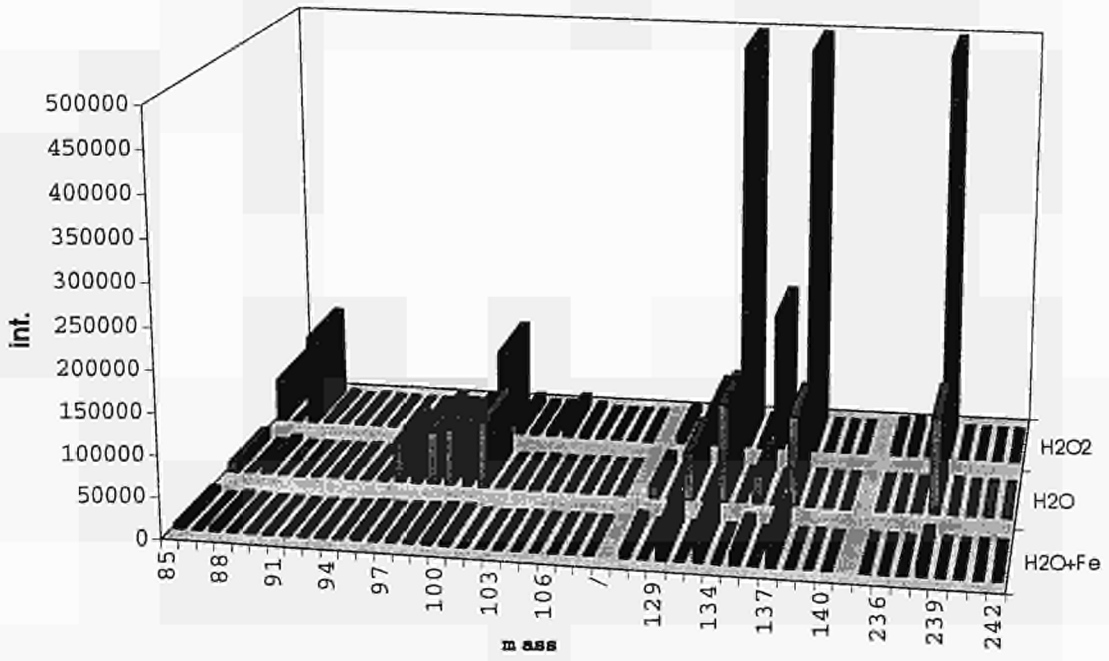

Fig. 3.11 Qualitative composition of the leachates.

Tab. 3.6 Fractions of inventory in the aqueous phase (FIAP) for the different leachates.

	content in the fuel, µg/g	H_2O + Fe	H_2O	H_2O_2
Rb	505	1.7E-03	2.1E-03	2.7E-02
Sr	1045	3.9E-04	1.3E-04	4.8E-04
Y	630	5.1E-06	3.2E-06	1.5E-05
Zr	5395	1.0E-05	1.2E-04	7.3E-06
Mo	5273	3.4E-04	7.0E-03	6.8E-04
Tc	1262	5.2E-04	1.2E-03	7.1E-03
Ru	3752	1.8E-06	2.7E-05	3.7E-04
Rh	562	4.9E-05	6.4E-05	2.4E-03
Pd	5778	2.4E-06	4.7E-05	4.2E-04
I	392	1.8E-02	2.5E-02	1.3E-02
Te	760	5.5E-06	2.6E-05	2.9E-06
Cs	3375	4.7E-03	1.2E-02	3.4E-02
Ba	3191	4.0E-05	5.6E-05	3.1E-05
La	1875	1.3E-06	4.3E-06	8.5E-06
Ce	3730	1.2E-06	7.9E-06	6.9E-06
U	934129	8.6E-10	3.3E-08	5.3E-07
Np	745	2.7E-03	2.1E-02	1.8E-01
Pu	9373	9.1E-06	1.3E-05	7.4E-06
Am	919	2.0E-06	0.0E+00	0.0E+00

The absolute leaching values given in Tabs. 3.5 and 3.6 are considerably lower compared with the previous experiment with Teflon containers (TUAR-92, p. 102). Whether this discrepancy is due to the different container material or to a changed S/V ratio, cannot be decided, because the reflux rate in the experimental set-up (Fig. 3.10) cannot be measured in the closed system. For the present experiment however, the relative values show the large influence of the oxidizing atmosphere on the leaching of spent fuel especially for redox sensitive elements but also for the matrix itself.

More information is expected from the leaching experiment with 4 weeks duration time and the SEM examination of the fuel samples.

Reference

[1] E. Smailos;.Kernforschungszentrum Karlsruhe, report KfK-3953 (1985)

3.2.3 Oxidation of irradiated UO_2 at low temperatures (< 500 °C)

Development of a shielded glove box for X-ray diffraction and thermogravimetry

Results of a literature survey was reported in the last Annual Report (TUAR-93, p. 99-104) and differences in the oxidation between unrirradiated and irradiated UO_2 were mentioned. It was concluded that a systematic study of the oxidation of irradiated UO_2 at temperatures lower

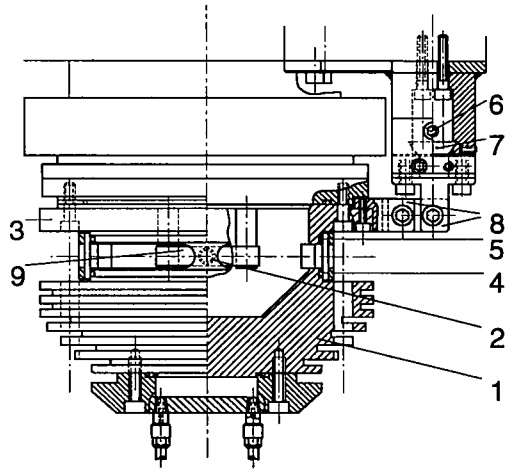

Fig. 3.12 Design of a Densimet-18 furnace chamber with a parallel closing hinge and vertical adjustment. (1) furnace chamber, (2) sample holder, (3) stainless steel disk, (4) Kevlar foil, (5) O-ring, (6) setting screw, (7) dovetail guide, (8) double-hinge, (9) platinum tape-heater

than 500 °C was necessary. Such a study includes oxidation tests under controlled atmosphere on well characterised specimen, thermogravimetric analysis, characterization of the oxidized specimens by means of microstructure examinations and *in situ* X-ray diffraction analysis. The present equipment in the hot cells, particularly in the fields of X-ray diffraction and thermogravimetry has to be updated. For this purpose a lead-shielded glove box has been designed (TUAR-93, Fig. 4.11, 4.12) and measurements on irradiated specimens are planned for spring 1995. During this year a goniometer and a thermobalance have been installed in the glove box, while further developments concern the shielding of the high temperature chamber of the goniometer and sample holders for both devices permitting the safe transport of samples between the hot-cells and the shielded glove-box.

Shielding of the high temperature chamber

Most oxidation tests will be long-term experiments, conducted in a specially constructed furnace chamber (Fig. 3.12), manufactured in Densimet-18, a high density alloy with a γ-ray shielding equivalent to 50 mm lead. The sample is held in a α-tight holder designed in such a way that appreciable X-ray absorption is avoided and the oxidizing gas flow to the sample is ensured by using porous materials.

The furnace chamber (1) is screwed on a water-cooled stainless steel disc which acts as a heat sink.

The X-ray beam from the tube to the sample and the diffracted beam to the detector pass through a slit 12 mm wide and 200° angle located in the upper half of the furnace; the vacuum tightness of the sample is assured by a Kevlar foil (4) which allows the transmission of the incident and diffracted X-ray beam. The correction in the zero-straight-line between X-ray beam, sample surface and detector slit, is achieved firstly with a micrometer which moves the stainless steel disc (3) of the diffractometer and secondly by a setting screw (6) which adjusts the level of the furnace chamber (1) with the aid of the dovetail guide (7). The use of the parallel-acting double hinge (8) ensures the vacuum tightness of the furnace chamber (1). This is designed for temperatures up to 500 °C, although inner furnace temperatures up to 1000 °C can be accepted. However a water-cooled aluminium flange has been already designed and can be additionally fitted on the front-side of furnace chamber (1) with a screw attachment, to reach sample temperatures of about 1400 °C.

The heating system of the sample consists of a platinum tape-heater (9) on which the sample-holder (2) is placed. The desired temperature is controlled by a thermocouple, directly welded on the heater, and by a thermocontroller.

Thermobalance sample holders

The shielding previously foreseen for the thermobalance oven, in order to reduce the high γ-activity background on the X-ray goniometer from samples used for the thermogravimetric analysis, appears not necessary as expected, because a) the sample weight is about 5-10 mg (lower limit) and consequently its γ-dose rate is quite low (< 100 mrem per hour), b) the goniometer detector is well protected by its own shielding and c) such a shielding does not protect the sensitive parts of the thermobalance. Damage to these can be avoided by using a special sample holder, as illustrated in Fig. 3.13. This holder consists of a Densimet-18 cylinder (1) 30 mm high, whose 20 mm thick base provides γ-shielding for the thermobalance. The potential oxidation of the holder material (W-Cu alloy) above 400 °C is prevented by a gold coating. The samples are positioned in a small cavity (2) at the top of the cylinder and kept in position by a screwed cap (4) equipped with a 150 mm stainless steel sintered filter (5) which allows the contact between the sample and the surrounding atmosphere.

Goniometer sample holder

Another closed stainless steel specimen holder is shown in Fig. 3.14. It consists of two parallel semicircular discs (3), one of them made of sintered stainless steel, mounted on an horizontal base plate (4). The sample is put in a cavity located in the middle of the base plate as illustrated in Fig. 3.14. A cylinder (1) can be screwed downwards through a nut fixed at the top between the two disks to keep the sample in position. After transfer to the glove box, the cylinder is screwed upwards and the sample holder is placed for measurement in the high temperature chamber. In order to reduce the contamination possibili-

Fig. 3.13 Thermobalance sample holder: (1) densimet cylinder covered with gold, (2) samposition, (3) hollow for the thermobalance thermoelement positioning, (4) threaded cap, (5) sintered stainless steel filter.

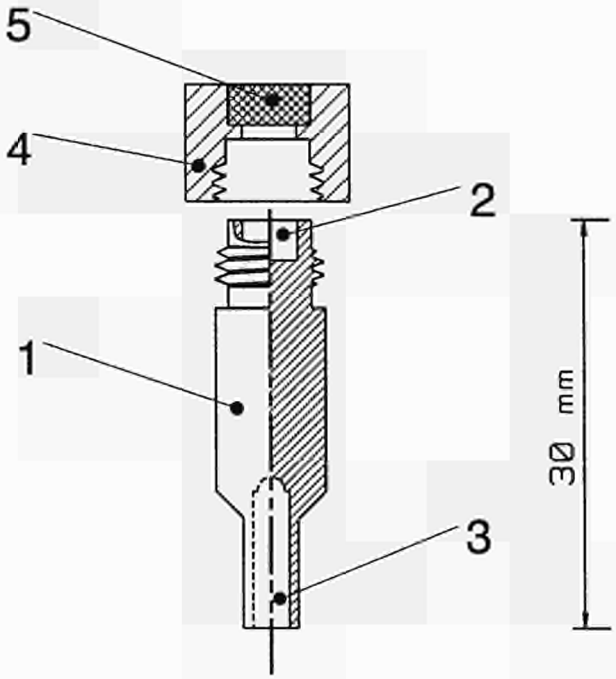

ties, the window between the two parallel semicircular discs is closed by a 0.1 mm thin Beryllium foil, while the oxidizing atmosphere comes into contact with the sample through the porous disk. The semicircular form of the parallel discs insures the X-rays transmission through the Beryllium foil for all angles. After the measurement the cylinder can be screwed downwards again and the holder can be stored.

3.2.4 Long term oxidation tests of irradiated UO_2

Apparatus and measurements

An autoclave (Fig. 3.15) has been designed to perform oxidation tests on irradiated UO_2 fragments, aiming to measure oxidation rates up to a maximum of 270 °C. Twelve probes can be simultaneously oxidized under various oxidizing atmospheres in small preweighed ceramic crucibles. As shown in Fig. 3.15, two ceramic crucibles (3) are positioned in each of the six bores of the heating block (12) by means of a stainless steel holder (11). A Chromel-Alumel thermocouple (7) close to the two crucibles controls the furnace temperature and the oxidizing gas flows continuously. By opening the furnace and interrupting the oxidation for 5-10 min, the probes can be removed at several time intervals for weighing and ceramographic examination.

A series of long-term oxidation tests has been started and aims for an improved determination of the influence of fuel microstructure characteristics (porosity, grain size, burn-up) on oxidation at temperatures ranging between 170 and 270 °C. Although the first samples are still under oxidation, the preliminary experimental results of oxidation of UO_2 fuel irradiated to 53.1 GWd/t burn-up in dry air are given in this report. The fragments are selected, from the outer rim and the central region of the fuel pellets where according to grain size and porosity features different oxidation kinetics would be expected. Most of the fuel particles have an intitial weight of 50-100 mg and 2 or 3 of them are put together in the same crucible. The operating temperature was 268±1 °C and

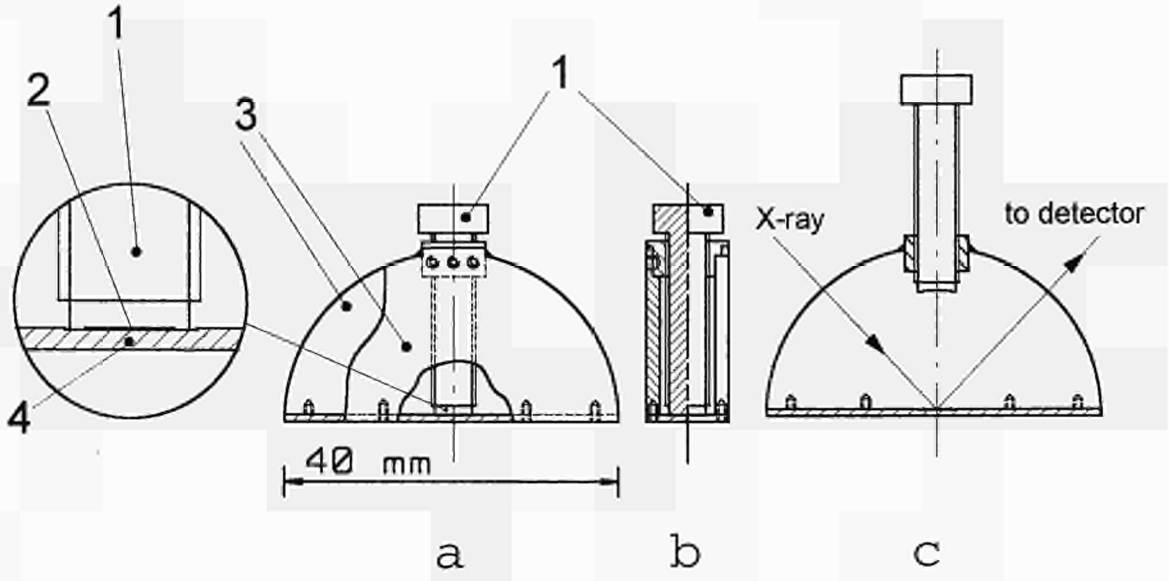

Fig. 3.14 Goniometer sample holder. a. front view b. side view c. measuring state (1) cylinder, (2) powder sample, (3) parallel semicircular disks, (4) base plate

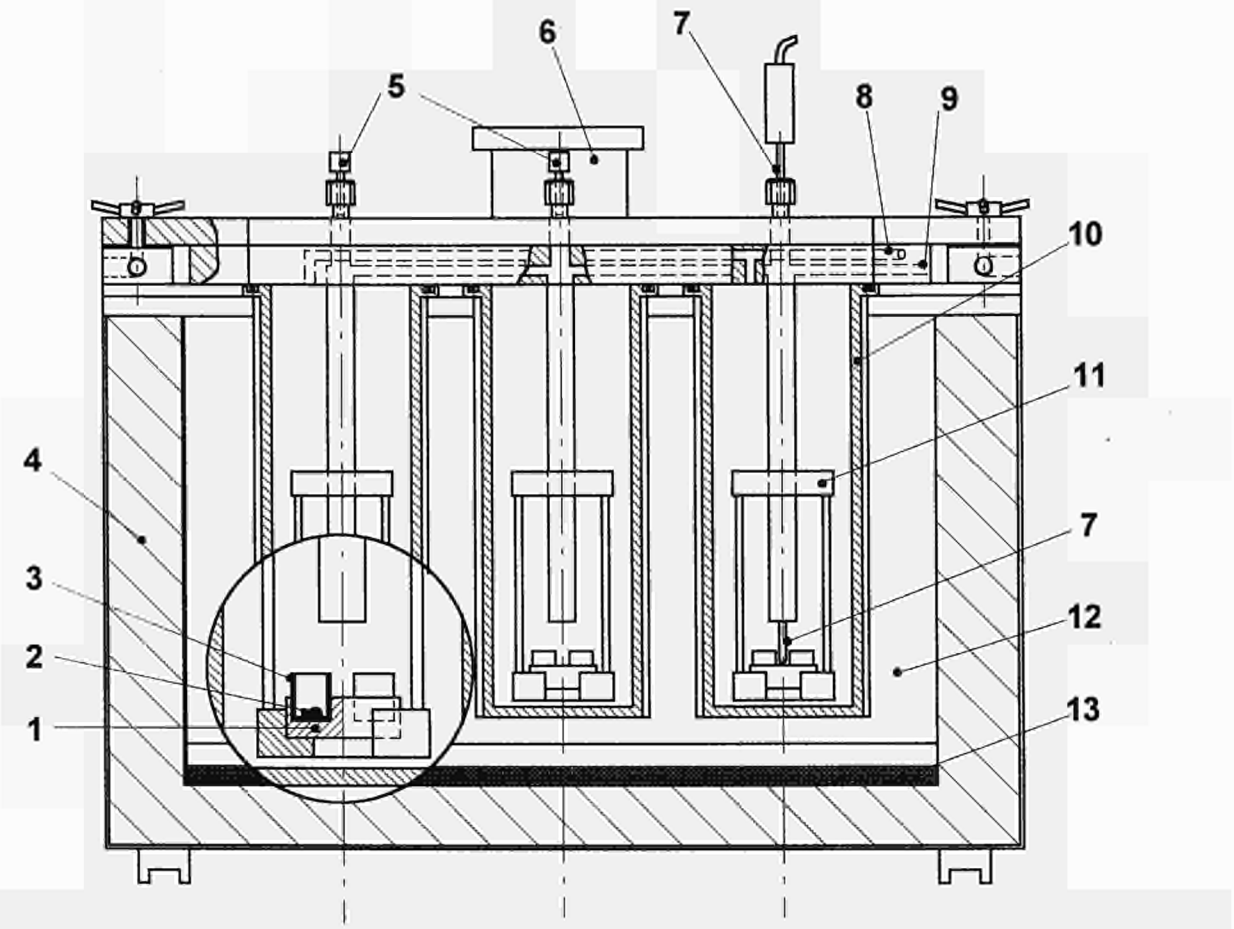

Fig.3.15 Autoclave for long term oxidation tests: (1) aluminium crucible carrier, (2) sample, (3) ceramic crucible, (4) insulation, (5) plugs, (6) plate holder, (7) thermocouple, (8) oxidizing gas inlet, (9) oxidising gas outlet, (10) crucible well, (11) sample system stainless steel holder, (12) aluminium block, (13) heating plate.

the oxidising dry air flowing through each block borehole at 34 cm^3/min.

Discussion

The weight gain due to the oxidation carried out at 268± 1 °C is plotted in Fig. 3.16 as a function of time. No differences in oxidation behaviour between samples from the outer rim and the center of the pellet were noted; although the samples showed very different porosity and grain size, the reaction kinetics is apparently not influenced by these parameters. Both sets of experimental results are treated here as one group of data.

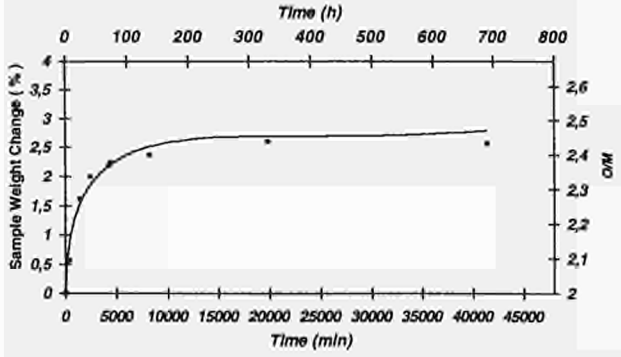

Fig. 3.16 KWU B4 fragment oxidation at 268±1 °C. Weight gain and bulk oxygen to metal ratio (O/M) as a function of time. squares: experimental data. Solid line: best fitting curve by Eq.(2).

The weight change in percent as a function of time displays a rapid initial oxidation followed by a plateau slightly above an oxygen to metal ratio (O/M) of 2.4. According to previous reports [1,2] U_4O_9 is the only phase detected by X-ray diffraction at a bulk O/M ratio of 2.4 so that additional oxygen is accomodated compared to the expected value of 2.25 and it should be noted that oxidation to higher stoichiometry, less dense states (e.g. U_3O_8) may be continued, but at temperatures lower than 250 °C a long time is required. As can be seen in Fig. 3.16, after 700 h at 270 °C the O/M ratio is still steady. In oxidation studies [3] at higher temperatures, between 280 and 360 °C a O/M 2.59 was reached and substantial amounts of U_3O_8 were detected. The necessary weight gain for the complete conversion of the UO_2 to U_3O_8 is greater than the minimum necessary of 3.98%, which indicates a higher phase. A better understanding of our

weight gain data, will require information on the microstructure and density of the oxidised samples. The samples will be analysed by optical, and scanning electron microscopy and X-ray diffraction. Weight change data of UO_2 samples will be compared for samples of various burn-ups, and for LWR MOX fuels.

Based on the assumption that the oxidation of UO_2 to U_4O_9 is controlled by O_2 diffusion through a U_4O_9 layer, then the layer thickness y increases with time t according to a parabolic law : $y^2 = C \cdot t$ (where C is a constant).

Assuming that the grains are spherical, the final reaction rate equation can be expressed as:

$$\left[1-(1-a)^{1/3}\right]^2 = k \cdot \exp(-E/R \cdot T) \cdot t$$

a = fraction of UO_2 converted to U_4O_9
k = rate constant
E = reaction activation energy
T = temperature
R = ideal gas constant

By fitting the experimental data of Fig. 3.16 to this equation a value of 124 kJ/mol is obtained for the activation energy E and $4x10^7$ (min^{-1}) for the coefficient k. The activation energy E = 124 kJ/mol is in the expected range of 100-130 KJ/mol found by other authors and comparable with reported activation energies for O_2 diffusion in U_4O_9 [4,5].

References

[1] R. E. Einziger, L. E. Thomas, H. C. Buchanan, R. B. Stout; J. Nucl. Mater., **190** (1992) 53-60
[2] L. E. Thomas, R. E. Einziger, H. C. Buchanan; J. Nucl. Mater. **201** (1993) 310-319
[3] R. E. Einziger; Nucl. Technol. **75** (1986) 82-95
[4] S. R. Teixeira, K. Imakuma; J. Nucl. Mater. **178** (1991) 33-39
[5] R. E. Woodley, R.. E. Einziger, H. C. Buchanan; Nuclear Fuel, **85** (1989), 74-87

3.3 Fuel Chemistry

3.3.1 Chemistry of the UO_2 fuel pellet periphery: Properties of Cs-U-O compounds

Introduction

The investigations on U-Cs-O compounds reported in TUAR-92, p. 124 and TUAR-93, p. 117, were continued and aimed at the determination of the thermal conductivity of Cs_2UO_4. The study of the chemical interaction between Mo and ZrO_2 was also started.

Thermal conductivity

The comparison method was used for the determination of the thermal conductivity of Cs_2UO_4 by means of an apparatus (ANTER) which allows the measurements in the temperature range 20 to 900 °C.

Basically the measurement is carried out by setting the specimen to be analysed between two specimens of identical chemical composition and known thermal conductivity. These latter specimen constitute the reference material. A scheme of the thermal conductivity apparatus is shown in Fig. 3.17. A major point in this technique is the preparation of the specimen for measurement.

Cs_2UO_4 as powder is first pressed in order to obtain a disc with 10 mm diameter and a few millimeters thickness. On the disc face two grooves with 0.8 mm depth and 0.8 mm width have to be prepared. Direct grinding of the grooves on the Cs_2UO_4 discs was not possible and moulding was the only satisfactory way to prepare the grooves. The tungsten carbide mould used for this operation was fabricated by spark erosion.

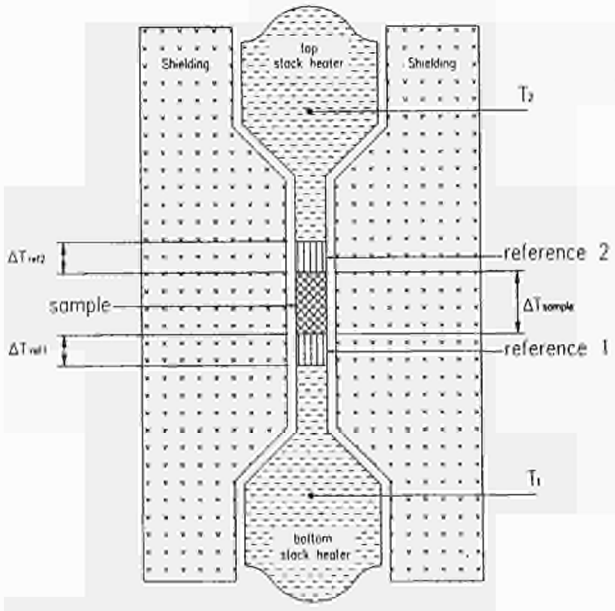

Fig. 3.17 Thermal conductivity - Apparatus.

Before measurement, the specimen is coated with a nickel paste and covered with a 6 m thick Ni foil; during measurement the specimen is inserted between the two Fe discs as reference specimen. The thermocouples are mounted in the grooves and a pressure of 1 to 2 kg/cm^2 is applied on the discs by means of a piston. The measurement is carried out under argon atmosphere and a programme controls the rate of temperature increase, the duration of annealing at constant temperature and the temperature gradient through the pellet.

The thermal conductivity of the material analysed is calculated according the following equation:

$$\lambda_{specimen}=\frac{1}{2}\lambda_{reference}\left[\frac{\Delta T_1}{\Delta x_1}+\frac{\Delta T_2}{\Delta x_2}\right]\cdot\frac{\Delta x_{specimen}}{\Delta T_{specimen}}$$

$\Delta T_1, \Delta T_2, \Delta x_1, \Delta x_2$ are defined in Fig. 3.17

The thermal conductivity calculated according to the preceeding equation for a specimen of given density is corrected for a 100% dense material by using the following corrections:

$$\lambda_p=\lambda_0\cdot 2\left(\frac{1-p}{2+p}\right) \quad (1)$$

and

$$\lambda_p=\lambda_0(1-p)^{1.5} \quad (2)$$

where

p = porosity of the specimen
λ_0 = thermal conductivity of the specimen with 100% theoretical density
λ_p = thermal conductivity of the porous specimen as used for the measurement.

Measurements have been carried out on specimens with densities ranging between 75 and 95% of the theoretical density after checking the method by measuring the thermal conductivity of UO_2. The experimental data and corrected values are given in Fig. 3.18

The first results indicate a lower thermal conductivity of Cs_2UO_4 in the temperature range 100 to 600 °C com-

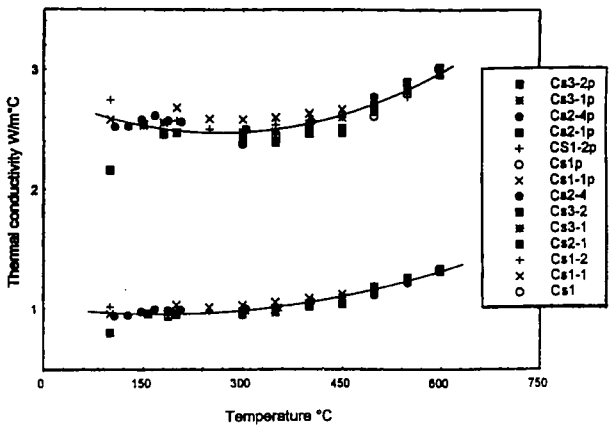

Fig. 3.18 Thermal conductivity measurements of Cs_2UO_4.

pared to UO_2 (at least a factor 2). The reproducibility of the measurements is relatively good at temperatures > 500 °C with a few percent scatter and worse between 100 and 300 °C where the scatter rises up to 20%.

Chemical Interaction between Cs_2UO_4 and molybdenum and zirconium oxide

This study is aimed at determining possible interactions between phases which are formed during the last irradiation period in a thermal reactor.

During the irradiation ZrO_2 results from the interaction between UO_2 and zircaloy and a possible reaction at the inner side of the cladding between ZrO_2 and Cs_2UO_4 can be envisaged. Furthermore, an interaction between metallic Mo and Cs_2UO_4 can be expected as well as long as oxygen potential is not high. The following experiments were carried out:

a) Annealing at 600 °C for 48 hours under He flow of a pressed mixture of UO_2 and metallic Mo in contact with Cs_2CO_3. In microstructure examinations and EDX analysis, Cs_2UO_4 as well as small amounts of Cs_2MoO_4 were determined.

b) Annealing (U, Zr)$_3O_8$ in contact with Cs_2CO_3 at 600 °C for 30 hours under He flow. (U, Zr)$_3O_8$ was obtained by oxidation under air of a mixture of metallic U and 10% Zr. The characterisation of the compounds formed is presently being determined; first results indicate the formation of (U, Cs, Zr)O.

c) Introducing Cs_2CO_3 in a cavity drilled into a UO_2 pellet. The mixture was annealed at 600 °C under He flow for a week. The microstructure of the interaction zone supposes a mechanism based on intergranular attack. The compound built up was analysed by EDX and appears to be Cs_2UO_4.

The major information from these tests is the evidence of intergranular attack of UO_2 by Cs and the formation of Cs uranate at the grain boundary level, which could modify the mechanical properties of the fuel. The chemical interaction tests between Cs uranate and MoO_2 or ZrO_2 need more detailed experiments before drawing conclusions.

3.3.2 Na-Superfact-fuel compatibility tests

Introduction

Laboratory tests were designed to simulate the conditions and analyse the consequences of the potential contact of Na with fuels of the Superfact experiment - (U, Pu, Am)O_2, (U, Pu, Am, Np)O_2, (U, Pu, Np)O_2 - in the case of cladding failure during the irradiation in a fast breeder reactor.

The aim of the measurements is to determine principally the extent of reaction between liquid Na and irradiated Superfact fuel samples, in the temperature range 600-700 °C, and to characterize chemically and crystallographically the reaction products formed at different exposure times. Since the reaction can occur via intermediate formation of sodium oxides at the contact interface, it is also of interest to study the reaction between Na_2O_2 and the Superfact fuel for comparison. Besides, the use of Na_2O_2 allows the characterization of the reaction under conditions of maximum oxygen availability.

In order to check the experimental set up, a preliminary series of tests was performed with unirradiated fuel-material in glove-boxes in an α-laboratory. Once the test parameters are settled a final test series will be performed with irradiated fuel samples in hot-cell laboratories.

Experiments with liquid Na were performed in gas-tight steel capsules under an inert atmosphere containing an oxygen getter (Zr-foil) to reduce the oxygen content of Na to 5 ppm, and the experiments with Na_2O_2 were performed in a thermobalance equipped for differential thermal analysis (DTA).

Materials

Materials used were Na and Na_2O_2 (Fluka), and fuel pellets of the type MO_2 (with M= $U_{1-x-y-z}$, Pu_x, Am_y, Np_z), which were prepared using the standard cold pressing and sintering route. The O/M ratio was determined from lattice parameter measurements; all analysed fuels were slightly hypostoichiometric except UO_2 which has a stoichiometry of 2.05 [1].

Characterization of the fuels

Fuels were characterized by X-ray diffraction and the lattice parameters measured are given in Tab. 3.7.

Tab. 3.7 Lattice parameters of the fuel used for the interaction study with Na.

Fuel	Parameter [Å]
$(U_{0.74}Pu_{0.24}Am_{0.02})O_2$	5.4735 (3)
$(U_{0.74}Pu_{0.24}Np_{0.02})O_2$	5.4716 (4)
$(U_{0.55}Np_{0.45})O_2$	5.4554 (3)
$(U_{0.8}Pu_{0.2})O_2$	5.4706 (6)
UO_2	5.4639 (11)

Experimental

The chemical interaction between Na and the fuels mentioned here above was analysed by means of thermogravimetry (TG) and differential thermal analysis (DTA). These methods yielded information about the temperature of the reaction. The reaction products were identified by X-ray diffraction using a Siemens 500 diffractometer with a Cu tube.

A special furnace was developed for the study of the reaction between liquid Na and the fuel (Fig. 3.19). This furnace has two tubes which can be heated independently, one is used for the purification of liquid sodium at 700 °C in presence of an oxygen getter (Zr-foil), the other heats the fuel at the planned working temperature in the range 600 - 700 °C. Once purification of Na is achieved, molten sodium is poured into the tube containing the fuel, where the reaction proceeds under isothermal conditions.

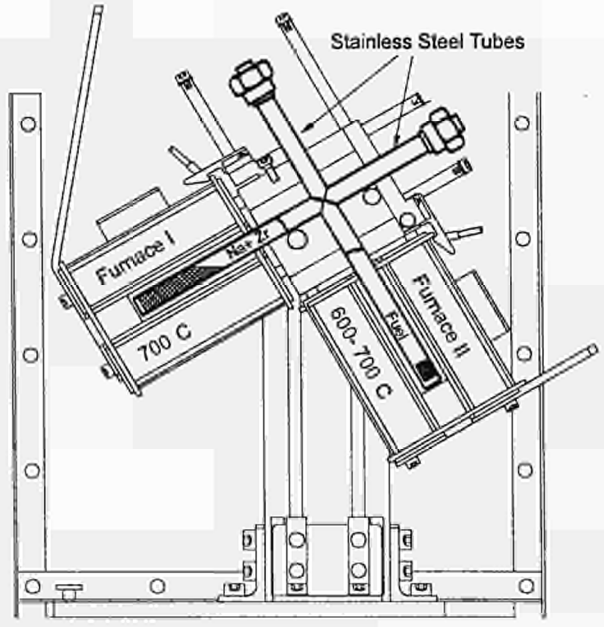

Fig. 3.19 Diagram of the furnace.

The fuel pellets were cut to the same size, 5 mm height and 5.7 mm diameter. Changes of the initial geometry after reaction provided information of the reaction extent at given temperature-time conditions.

System Na_2O_2 - fuel. Analysis of the reaction

TG-DTA experiments were performed in Al_2O_3 crucibles under inert atmosphere at a heating ramp of 10 °C/min. from room temperature to 750 °C, followed by a hold time of 1 hour at the highest temperature.

Fig. 3.20 shows the TG/DTA of Na_2O_2 thermal decomposition curves (a) and the curves obtained for the reaction $Na_2O_2 + UO_2$ (b).

In all cases, before any reaction with the fuel could be observed, the phase transition of Na_2O_2 (from hexagonal-phase I- to the non-cubic phase II) at 512 °C, the onset of the decomposition of Na_2O_2 to Na_2O (with the corresponding oxygen release) at 650 °C, and the melting of Na_2O_2 at 670 °C, was invariably observed [2]. The reaction temperature between Na_2O_2(l)/Na_2O(s) mixture and the fuel was determined; generally this temperature increases slightly as the actinide content increases. Results are shown in Tab. 3.8.

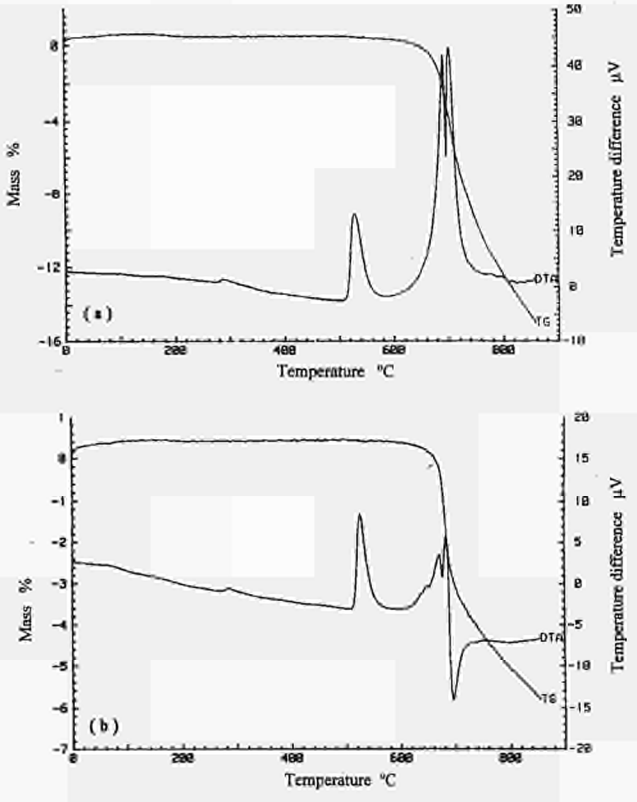

Fig. 3.20 TG/DTA curves of the reaction with the temperature of Na_2O_2 (a) and $Na_2O_2 + UO_2$ (b).

Tab 3.8 Temperature of the reaction between Superfact fuel and sodium oxide.

Composition	(Pu+Act.) / U	Reaction Temp. °C
O_2	0	684
$(U_{0.8}\,Pu_{0.2})O_2$	0.25	688
$(U_{0.74}\,Pu_{0.24}\,Am_{0.02})O_2$	0.35	689
$(U_{0.74}\,Pu_{0.24}\,Np_{0.02})O_2$	0.35	690
$(U_{0.6}\,Np_{0.21}\,Am_{0.19})O_2$	0.67	693
$(U_{0.55}\,Np_{0.45})O_2$	0.82	692

After completion of the reaction (i.e. after complete disappeareance of the initial Na_2O_2), the X-ray diffraction results show that traces of the phases UO_{2+x} and Na still coexist with the reaction product phase, which was identified as a compound of the type $Na_{3-x}M_{1+x}O_4$. Under these conditions, the system analysed corresponds to the triangle A illustrated in Fig. 3.21.

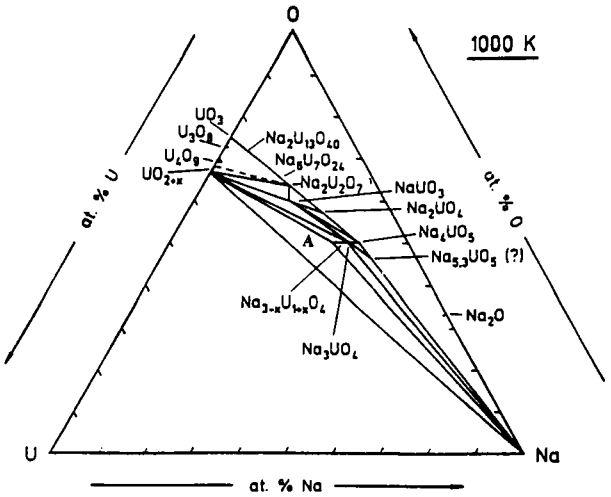

Fig. 3.21 Isothermal section of the ternary Na-U-O system at 1000 K [2].

Final structure assessment and lattice parameter determination of the reaction products, as well as determination of the reaction kinetics are on the way.

References

[1] Gmelin Handbook of Inorganic Chemistry, Uranium Dioxide, Supplement C 4 (1984). 112

[2] T. B. Massalski; Binary Alloy Phase Diagrams, 2nd Ed., ASM International (1990)

[3] H. Kleykamp; Kernforschungszentrum Karlsruhe,. report KFK-4701 (1990)

3.3.3 High temperature interactions of structural material with fuel

Introduction

These reactions are possible during a reactor accident as the bundle degrades and structural materials make contact with the fuel. The investigation of these interactions and their kinetics is important as they result in low melting point eutectics or mixtures which are liquid at temperatures substantially below those of the individual melting points, and result in severe and accelerated degradation of the reactor core even below the UO_2 melting point (~ 2600 °C).

This study in the reactor safety programme was done in two parts:

1) Interactions of various materials with natural (non-irradiated) UO_2.
2) Interactions of various materials with irradiated UO_2.

Another part of this study that examined the fission gas release during structural material interaction with irradiated UO_2 was reported in the previous Annual Report (TUAR-93, p. 104-112). A description and diagram of the apparatus and oven used for this work was given there.

Interactions of various materials with non-irradiated UO_2

Materials and methods

The structural materials used were:

i) 304L austenitic stainless steel which is used as the cladding for the Ag-In-Cd absorber control rods.
ii) Silver-based (Ag-15In-5Cd) alloy.
iii) Zircaloy4 fuel cladding.

The composition and melting points of these materials is given in Tab. 3.9a. These materials were machined in the form of either 1 mm thick discs (5 mm dia.) or 5 mm high cylinders (also 5 mm dia.). Natural UO_2 pellets (95% density) of approx. 5 mm diameter and 6 mm length were also used.

The materials were placed in an alumina crucible in a dilatometer. In the first series of experiments (INT 1-6: see Tab. 3.9b) the materials were examined in pairs using 2 cylinders of materials one placed on top of the other in the crucible with the tip of the dilatometer probe resting on the upper surface. In the second set of 3 experiments (INT 7-9) 3 materials arranged as one cylinder of the first material then a disc of the second material and then a

Tab 3.9a Structural material composition.

Abbreviation	Material	composition	melting point
zry4	Zircaloy4	Zr-1.6Sn - 0.2Fe - 0.13Cr - 0.1O - 0.012C	1760 °C
304ss	304 stainless steel (austenitic)	Fe-19Cr - 9Ni - 2Mn - 1Si - 0.08Co - 0.08C	1450 °C
AIC	Absorber rod	Ag-15In-5Cd	800 °C

Tab 3.9b Material interaction results.

Exp. No.	Materials	melting/ interaction Temp. °C	T_{max} °C	Interaction	melting point (material with lowest T_m) °C
INT1	zry-304ss	1030	1230	strong	1450
2	zry-AIC	790	900	some	800
3	304ss-AIC	790	1210	v. slight	800
4	UO_2-304ss	1415	1450	v. slight (not wetting)	1450
5	UO_2-AIC	770	915	v. slight (not wetting)	800
6	UO_2-zry	1380	1540	slight attack of UO_2	1760
7	UO_2-AIC-zry	810	890	slight AIC-zry interaction	800
8	UO_2-AIC-304ss	835	910	AIC wets UO_2, v. sl. AIC-zry interaction	800
9	UO_2-304ss-zry	1030	1270	v. strong zry/ss reaction and some UO_2 interaction	1450

cylinder of the third material on top in a sandwich arrangement were examined: (Fig. 3.22). The materials were heated under a constant argon gas flow at 10 °C.min^{-1} until a sharp change in the thermal expansion indicated that a phase change, interaction or melting had occurred, and then cooled at 20 °C.min^{-1} to room temperature. The samples were then removed for metallographic examination and subsequent scanning electron microscopy - energy dispersive X-ray analysis (SEM-EDX). In Tab. 3.9b the results are summarised showing the material interaction temperatures, and the maximum temperatures actually reached compared with the lowest melting point of the materials present as well as the extent of interaction observed visually.

Experimental results

The 2 material experiments containing AIC absorber (INT 2, 3, 5) showed the lowest interaction temperature at 770 °C - 790 °C which is only slightly below the absorber alloy melting point of 800 °C. The corresponding 3 material experiments show 810 °C as the interaction temperature. The maximum temperatures are usually about 900 °C and although the silver alloy has melted the stainless steel has only very slightly interacted with the liquid

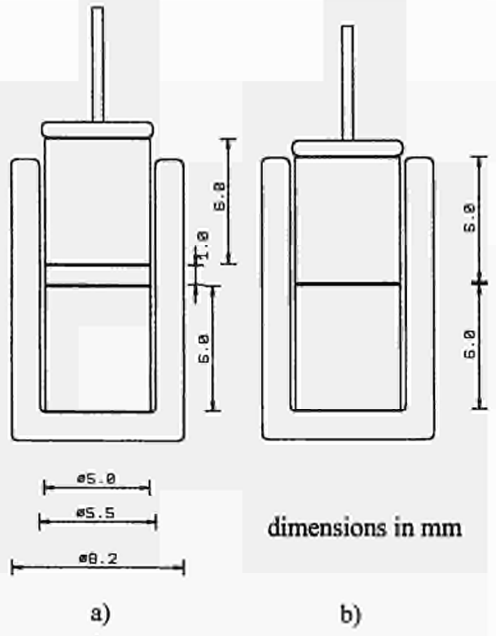

Fig. 3.22 Schematic diagram of materials in a) 3-material and b) 2-material interaction experiment. Structural materials: zircaloy-4, 304 stainless steel, Ag-15In-5Cd (AIC) absorber; fuels: natural UO_2 (sintered, 95% theo. density).

absorber alloy in the form of a diffusion layer of approx. 20 µm thick. By contrast the zircaloy/ stainless steel interaction is very marked at 1030 °C which is more than 400 °C below the melting point of the stainless steel (~ 1450 °C) and this interaction dominates in both the 2 material (INT 1) and 3 material (INT 9) experiments. The stainless - zircaloy interaction test (INT 1) was repeated in a differential thermal analysis (DTA) device. The result is given in Fig. 3.23. It shows a very slight change of slope at ~ 880 °C which may be the α-β phase change of

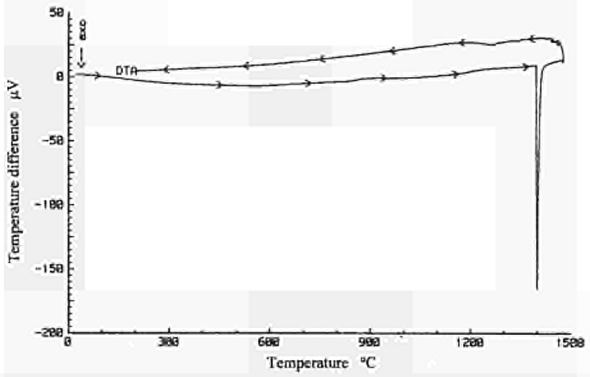

Fig. 3.23 Differential Thermal Analysis (DTA) of a zircaloy4 - 304 stainless steel couple heated at 10 °C. min^{-1} upto 1400 °C and back under a flow of argon.

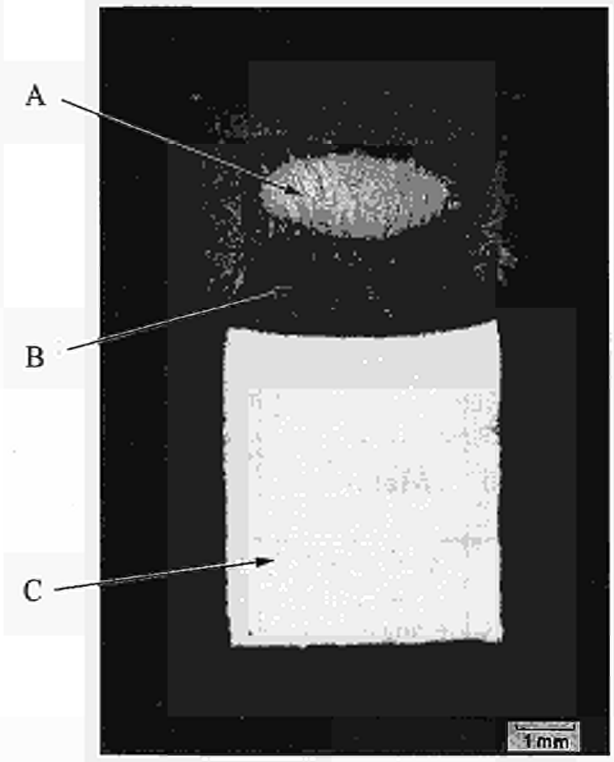

Fig. 3.24 Zircaloy4 - 304 stainless steel interaction (INT 1) after heating at 10 °C.min^{-1} upto 1230 °C and back under flowing argon (Macrograph 12.5x). A) unreacted zry (α+β); B) zircaloy/304 ss interaction zone; C) 304 ss

zircaloy since it appears to be reversible; however at 1380 °C there is a large exothermic interaction so that although the reaction is delayed to within 70 °C of the melting point, it appears to have gone to completion since only small traces of this reaction are seen on cooling. The macrograph of INT 1 (Fig. 3.24) shows that even at 1030 °C to 1230 °C the interaction zone has penetrated slightly (15-18 µm depth) into the stainless steel while the zircaloy disc has liquified and collapsed from 5 mm to ~ 3.7 mm or 74% of its original height and has flowed around the stainless steel cylinder into the crucible. The upper surface and sides of the zircaloy appear to have an interaction zone with the Al_2O_3 ceramic of the crucible walls and lid, with only a central oval zone that would be pure zircaloy. This central zone has large needles in a matrix; the needles may be the retained β-phase after cooling. The interaction zone between the central zircaloy zone and the stainless steel has several phases, with some crystalline geometrical forms. Initial EDX indicates one phase is a Fe-rich Zr alloy (e.g. Fe_2Zr). Greater magnification (Fig. 3.25) shows that the interaction zone/stainless steel interface is very rough, indicating a continuing reaction between the 2 phases.

The zircaloy-AIC interaction (INT 2) is slight but still distinct, although this occurred at lower temperatures: 790 - 900 °C and for a shorter time (16.5 mins) compared to the zircaloy/stainless interaction (INT 1): 1030-1230 °C for 30 mins. At the molten silver/zircaloy interface (Fig. 3.26) a 40 µm broad intermediate layer is seen by microscopy (presumably a mixed Zr-Ag layer). However the most interesting result is INT 6: the UO_2-zircaloy interaction. An interaction was observed at 1380 °C although zircaloy melts at 1760 °C (and natural UO_2 at 2580 °C). The maximum temperature reached was 1540 °C;

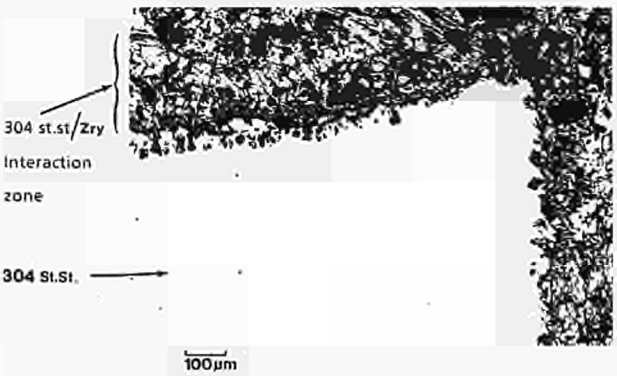

Fig. 3.25 Zircaloy4 - 304 stainless steel interaction (INT 1) Micrograph 100x - showing the interaction zone and its interface with the steel.

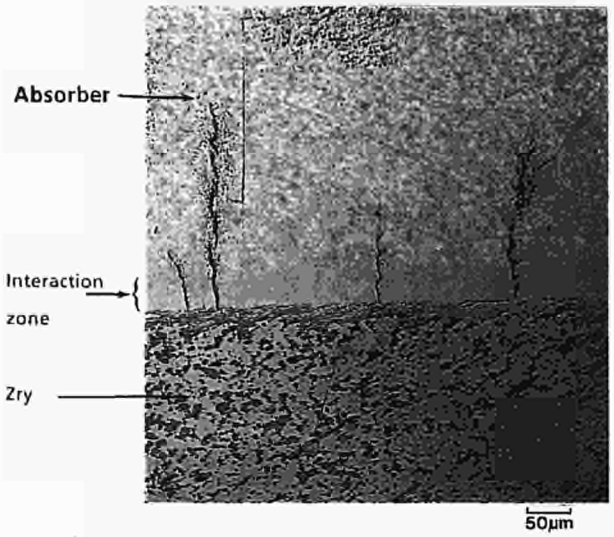

Fig. 3.26 Zircaloy4 - AIC absorber interaction (INT 2) Micrograph 200x - showing the small (~ 40 µm) interaction zone between the 2 components.

the material was held for 24 minutes between these temperatures. The zircaloy clearly interacted with the UO_2. A convoluted interface boundary and precipitates of Zr (or Zr(O)) in the UO_2 are shown in Fig 3.27. These had diffused upto 10 µm into the material before precipitating out during the cooling.

The interaction as well as the very strong stainless steel/ zircaloy interaction was seen again in the sandwich INT 9 experiment: UO_2 (cyl.) - 340 ss (disc) - zry (cyl.). This displayed an interaction temperature of 1030 °C similar to that of INT 1 (stainless-zircaloy). The micrograph (Fig. 3.28) confirms that the zircaloy cylinder has become liquefied by interaction with the 304 stainless and has flowed around the stainless disc and up the sides of the upper UO_2 cylinder. The stainless steel disc became deformed but did not liquefy. However the liquefied zircaloy/stainless mixture (Fe_2Zr or $ZrNi_2$) in contact with the UO_2 pellet at 1030 °C to 1270 °C for 21 mins. displays an interaction with the pellet (Fig. 3.29). There is a 10 µm deep interaction layer in which UO_2 had diffused into the zircaloy/stainless liquefied mix and precipitated on cooling. Similarly the zircaloy/stainless mix appeared to have diffused to a 10 µm depth into the UO_2 fuel before precipitating during cooling. This proves that a second stage interaction can occur even within the short time periods and at the lower eutectic temperatures of liquid zircaloy/ stainless steels, since this reaction was not seen in INT 4 with only UO_2 and stainless steel: here a melting/interaction only occurred at 1415 °C (practically the 304 ss melting point).

The dissolution or liquefaction of UO_2 fuel by liquid zircaloy or zirconium is already known [1, 2, 3] and the

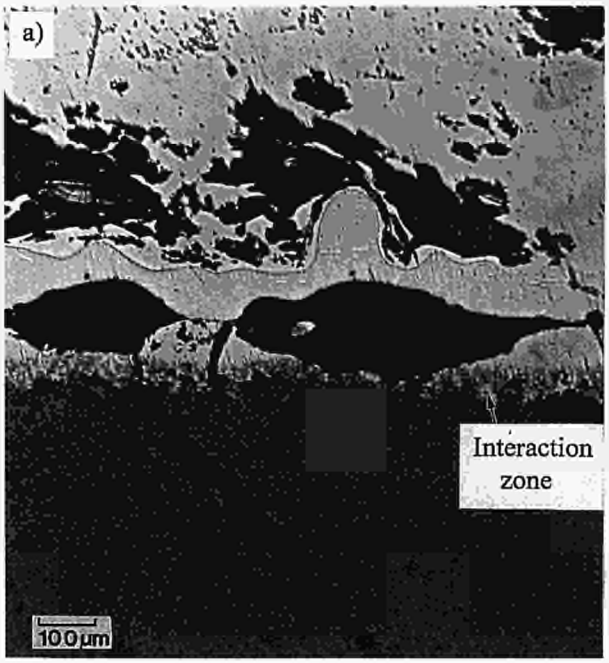

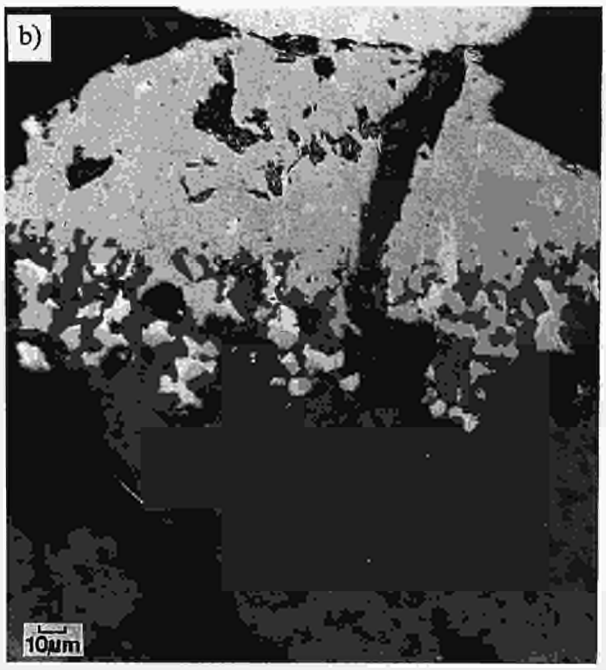

Fig. 3.27 UO_2 - zircaloy4 interaction (INT 6) Micrograph a) 100x ; b) 500x - showing the interfacial diffusion zone between the two components.

interaction of the 304 stainless steel and zircaloy system has already been described and its kinetics measured by Hofmann et. al. [4]. Nevertheless that these two interactions can concatenate to produce a rapid liquid metal-ceramic interaction (i.e. Fe-Zr/Ni-Zr vs. UO_2) at 1030 - 1250 °C is a less well-researched, but very important fact for reactor accident studies.

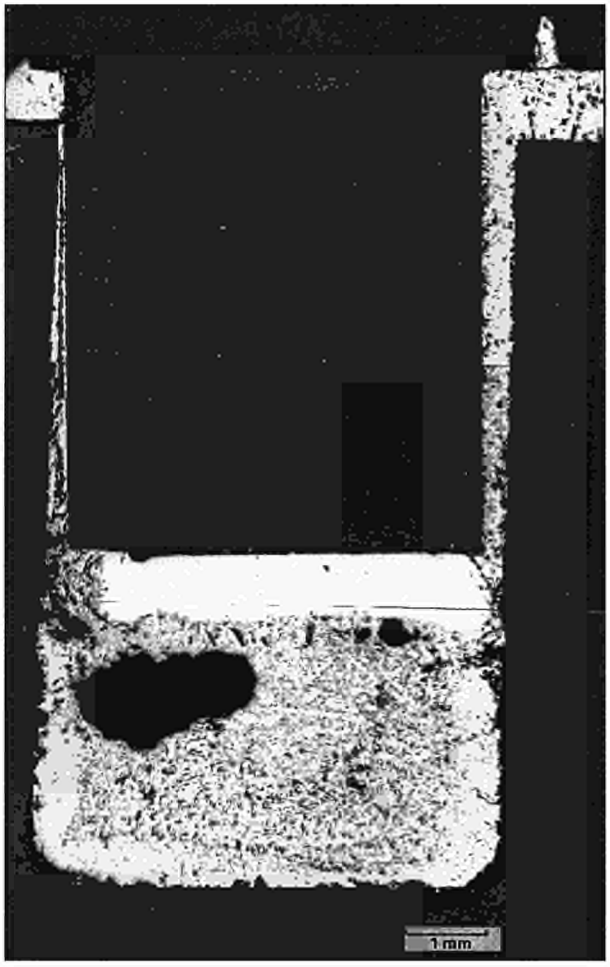

Fig. 3.28 UO_2 - 304 stainless - zircaloy4 interaction (INT 9) Macrograph 12.5x - showing the stainless-zircaloy interaction that has considerably deformed the steel and has liquefied the zircaloy.

Concluding remarks and future work

Further experiments will be carried out to examine the zircaloy α/β transition and its influence on any subsequent reactions as well as repeating the experiments with zircaloy/iron, zircaloy/nickel and zircaloy/chromium combinations to see the influence of the individual components on the strong zircaloy/stainless steel interaction. The existing samples (especially INT 6 and INT 9) will be further examined by (SEM) and the various phases analysed by EDX to determine the phases that have been formed.

The initial reactions such as those between stainless steel and zircaloy are strong and will be important in determining penetration depths. Furthermore, at these low interaction temperatures second-order interactions of structural materials with UO_2 fuel can occur subsequently and can result in a more rapid, but also more complex, fuel

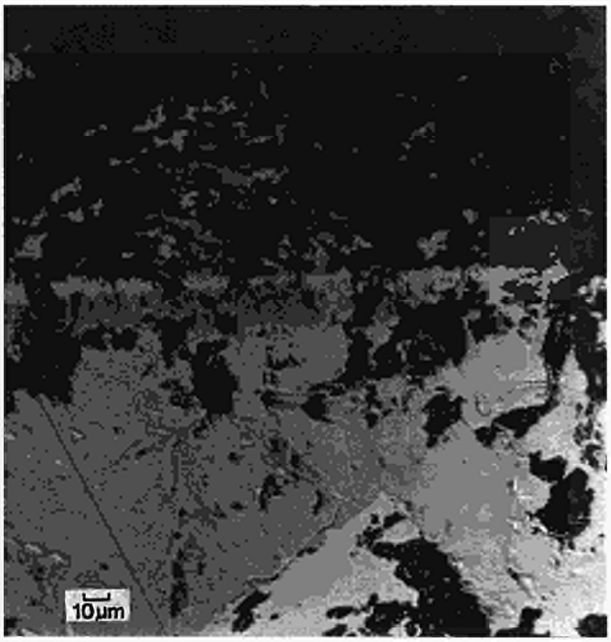

Fig. 3.29 UO_2 - 304stainless - zircaloy4 interaction (INT 9) Micrograph 200x - showing the subsequent interaction of the liquefied zircaloy/stainless steel and the UO_2 with which it has come into contact.

degradation. These interaction sequences and effects on overall bundle geometry and its degradation will also be difficult to model.

Interactions of various materials with irradiated UO_2

Materials and methods

In the second part of the study the same reactor structural materials: 304L stainless steel, silver-based (AIC) absorber alloy and zircaloy4 were studied in contact with irradiated UO_2 fuel under a slow heating ramp of approximately 4-5 °C/min. from 20 to 1500 °C (~ 6 hours) before rapid cooling by cutting the power under a constant (550 $ml.min^{-1}$) flow of a reducing $N_2/H_2O/H_2$ gas (H_2O:H_2 = 1:10 vol.), or N_2-2% H_2. The sample fuel was a high burn-up 58 GWd/tU UO_2 fuel from Belgonucleaire (BN 3-241). The structural materials were machined into small filings while the irradiated fuel was introduced as a single piece of approx. 0.1 g weight.

The fuel sample was placed in a ZrO_2 crucible in a W susceptor. Equal quantities of filings of each of the chosen components were added successively, and then pressed lightly down. The crucible was then placed in the induction furnace. Experiments performed with the following combinations of materials given in Tab. 3.10 below were selected for further examination.

Tab. 3.10 Material combinations for interaction experiments with irradiated fuel.

Fuel	Weight of fuel	Material added	Gas mixture
BN 3-241	0.04 g	AIC / 304 ss / Zr	$H_2O / H_2 = 1:10$
BN 3-241	0.06 g	AIC / 304 ss / Zr	$H_2O / H_2 = 1:10$

The gas release results of these annealing tests were reported in TUAR-93, p.104-112 but no scanning electron microscopy (SEM) or energy dispersive X-ray analysis (EDX) results were then available. It is these results that will be reported below.

Scanning Electron Microscopy (SEM) - Energy Dispersive X-ray (EDX) results

The SEM-EDX results showed that the samples had often broken into pieces of fused metal and fuel as it was necessary to break the crucible (Fig. 3.30), to retrieve the sample. The pieces were mounted on the specimen holder and gold coated before SEM examination.

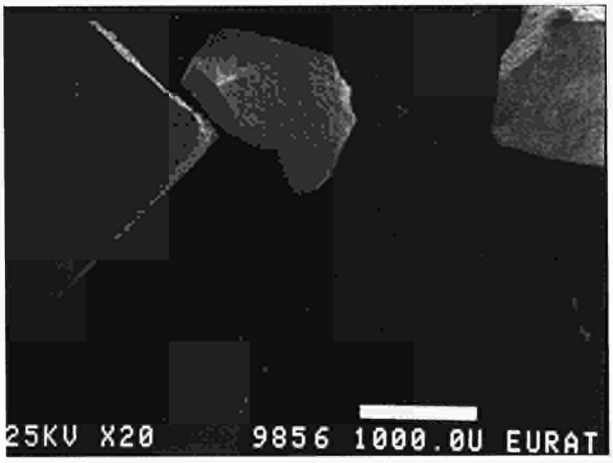

Fig. 3.30 Low power macrograph of pieces of BN 3-241 and structural materials after thermal annealing under a reducing H_2O/H_2 atmosphere.

Irradiated fuel (BN 3-241) and 3 material (AIC / 304 ss / zry) test

For the BN 3-241 fuel in the H_2O/H_2 atmosphere with all three additives the fracture surface of the fuel reveals considerable intergranular porosity that has coalesced to form networks of grain boundary tunnels that are filled with spherical precipitates (these are metallic fission products such as Mo, Tc and Ru, see Fig. 3.31). However a more remarkable feature is the fine porosity (Fig. 3.32)

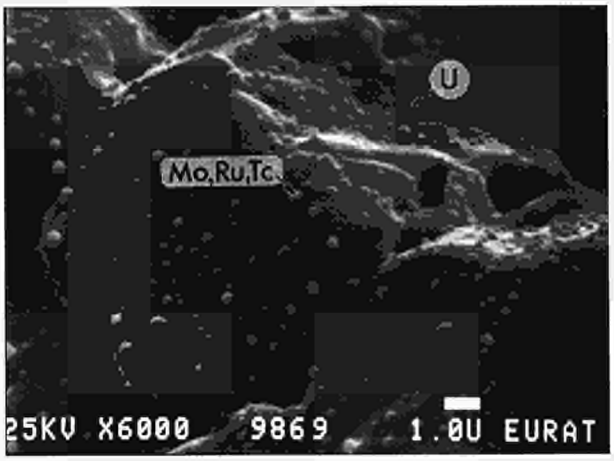

Fig. 3.31 Micrograph of BN fuel after interaction with structural materials (AIC/304ss/zry) in a reducing atmosphere H_2O/H_2 = 1:10, showing rounded contours and droplets of material on the surface (some of these have fission products).

around the edge of the grains and in the case of some grains fine porosity through the entire volume of the grain. Previous work with fission gas release (TUAR-92, p. 115-123) has shown that this is not due to the reducing atmosphere and therefore it is assumed that the structural materials that diffused into the grain have increased the bubble growth or the fission gas diffusivity. Zr-rich grains were also noted occasionally on the fracture surface. The external surface of the fuel shows many fine spherical precipitates (Fig. 3.31) some of which are metallic fission products. The grains have much more rounded edges and have a dissolved appearance which suggests an interaction between the liquid mixture and solid UO_2.

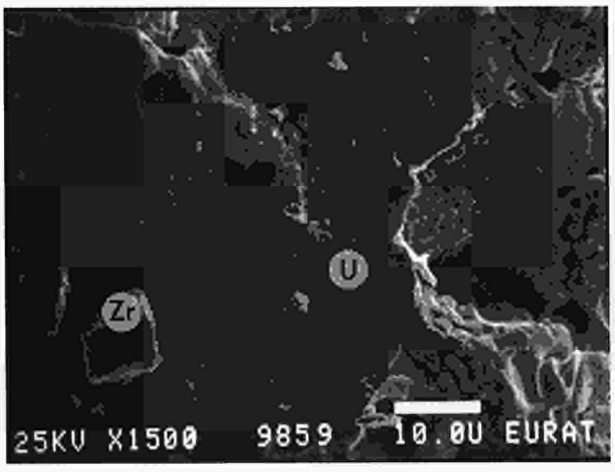

Fig. 3.32 Fracture surface of BN fuel after annealing with structural materials under H_2O/H_2 showing considerable porosity at the grain boundaries.

Irradiated fuel (BN 3-241) and 2 material (AIC / zry) test

At low magnification the sample has a rounded form with an inner surface where a scale has cracked off (Fig. 3.33).

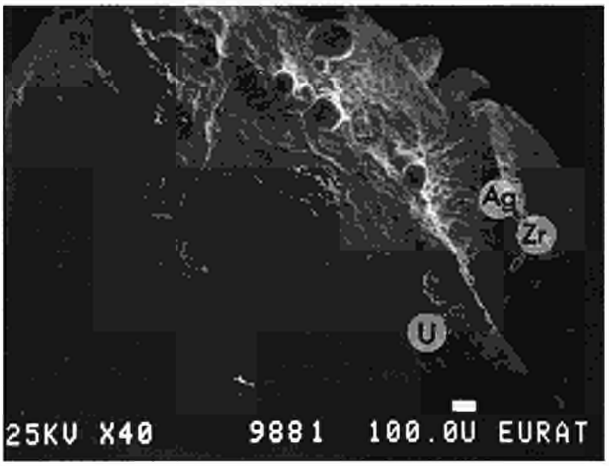

Fig. 3.33 SEM micrograph of fuel and two component AIC /zry interaction material after annealing in a reducing atmosphere H_2O/H_2 = 1:10.

EDX analysis shows that the various parts of the outer scale are either Zr-rich and have a very fine grained structure (2-4 µm dia.) and had melted (despite not reaching the zircaloy melting point of 1760 °C) or was rich in Ag and displayed a large lobular surface that had clearly liquified and contained large crystals (~ 20 µm dia.) (Fig. 3.34). No large-scale alloying of zirconium and silver was noted although the Zr-Ag phase diagram indicates the existence of AgZr and $AgZr_2$ intermetallics [5] and previous work [6] has demonstrated (and modelled) the liquid Ag-In-Cd dissolution of zircaloy4.

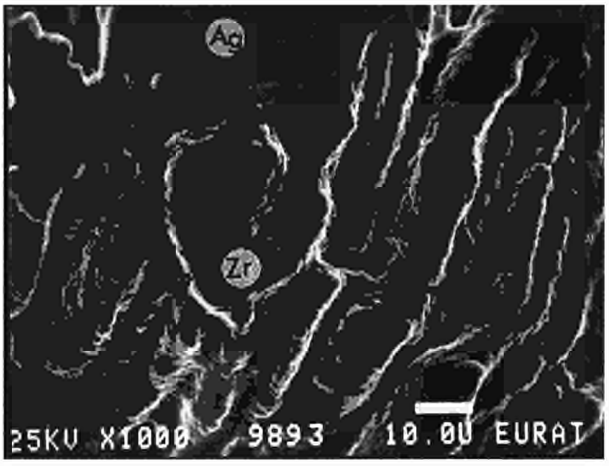

Fig. 3.34 Micrograph of zirconium rich coating on BN fuel (zone with small crystallites) after annealing in a reducing atmosphere.

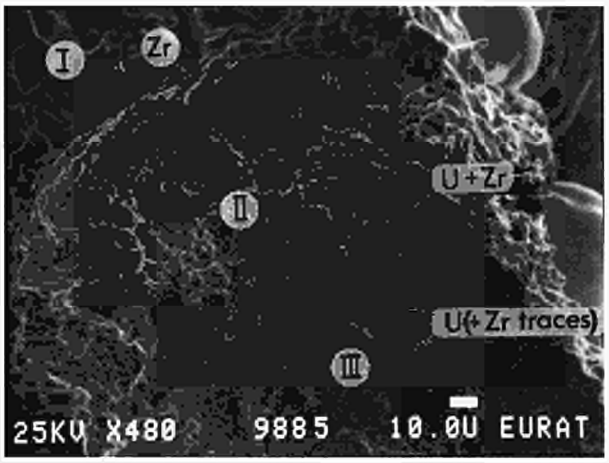

Fig. 3.35 Micrograph of zirconium crust on fuel after thermal annealing under H_2O/H_2 of irradiated BN fuel with AIC/zry showing three zones: I. Zr rich outer layer, II. mixed uranium and zirconium middle layer, III. inner UO_2 fuel surface with low Zr content.

However at the outer crust (Fig. 3.35) three different layers could be analysed: i) an outer Zr-rich layer, ii) an intermediate U- and Zr-containing layer, and finally iii) an inner U-rich layer in which some traces of Zr could be detected. The inner layer showed the UO_2 fuel grain structure, but at higher magnification (Fig. 3.36) it could be seen that some grains had a dense centre with fine porosity at the edge, while other grains appeared to be filled with large pores that often contained spherical precipitates probably of structural material (such as the detected Zr) and / or fission products. The presence of Zr in the UO_2 fuel shows that even at temperatures below the zircaloy melting point there is considerable interaction and diffusion of zirconium into UO_2. It was also notable

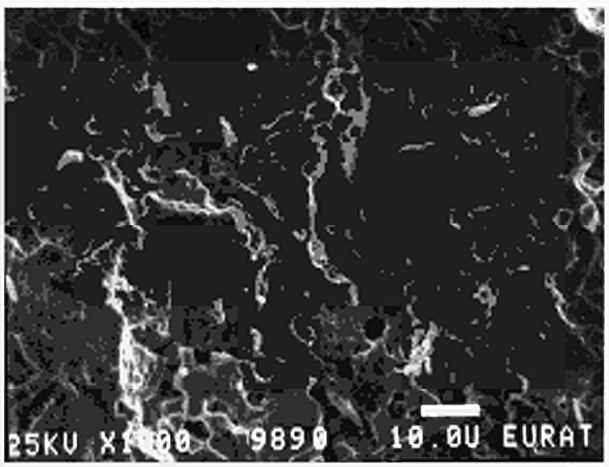

Fig. 3.36 Close-up of inner UO_2 fuel surface from Fig. 3.35 showing very broad porous zones between the UO_2 grains as a result of the AIC/zry interaction at high temperature. Only the grain centres remain dense.

in the intermediate Zr and U layer that both UO_2 grains and other smaller grains were visible, the latter being probably ZrO_2, as well as spheres of lower-melting silver absorber alloy. Again the UO_2 grains had a rounded appearance indicating a dissolution of the UO_2 by the zircaloy and absorber.

Concluding comments

These results show the effect of structural materials on fuel at temperatures that are below those of the melting points of the main components and how material interaction can create liquid mixtures at low temperatures (~ 1200 °C) with rapid attack on irradiated UO_2. The above example showed zirconium penetration into the UO_2 of 10-20 microns after approximately 30 mins. at 1500 °C.

Comparison of results with non-irradiated and irradiated UO_2 fuels.

There are results of the very significant differences (both structural and compositional) between the irradiated and non-irradiated fuels: thus the grain boundary and intragranular porosity is higher after irradiation, and there is the presence of many secondary phases (principally metallic fission products: e.g. Ru/Rh, Tc, Nb, Zr) in the irradiated fuel. The fission products are also present in solid solution along with higher lattice defect densities compared with non-irradiated fuels. Of these differences the presence of Zr in the UO_2 fuel grains implies that Zr volume diffusion is enhanced in irradiated material. (The increased porosity at the fuel grain edges also implies that fission gas volume diffusion may also be enhanced in the irradiated UO_2 lattice).

However the greatest difference appears to be the penetration depth by the structural material down the grain boundaries as a consequence of the increased grain boundary porosity. A rough comparison (since there are differences in temperature, duration, and atmosphere) implies a doubling of penetration in the irradiated compared to the non-irradiated UO_2. A further factor is the metallic fission product precipitates at the grain boundaries which also interact or are dissolved by the molten structural material and hence aid the grain boundary penetration (TUAR-93, p. 104-112).

Further work should be carried out to clarify the influence of particular mixtures and to identify the critical liquefaction temperatures and the effective thresholds of attack both for natural UO_2 and for irradiated UO_2 and to quantify the influence of the enlarged grain boundaries and secondary precipitates on liquefied mixture penetration between the grains (e.g. by testing with lower burn-up fuel).

References

[1] P. J. Hayward, I. M. George; J. Nucl. Mater. **208** (1994) Part I 35-42; Part II 43-52

[2] M. S. Veshchunov, P. Hofmann; J. Nucl. Mater. **209** (1994) 27-40

[3] S. Hagen, P. Hofmann; Physical and chemical behaviour of LWR fuel elements upto very high temperatures, Kernforschungszentrum Karlsruhe, report KfK-4104 (June 1987)

[4] P. Hofmann, M. Markiewicz; KfK report, KfK 5106 (1994)

[5] T. B. Massalski, H. Okamoto, P. R. Subramanian and L. Kacprzak; Binary Alloy Phase Diagrams, 2nd Ed., Eds. T. B. Massalski, et al., ASM International, Ohio, (1990)

[6] P. Hofmann, M. Markiewicz; J. Nucl. Mater. **209** (1994) 92-106

3.4 Characterization of High Burn-up Fuels

3.4.1 Porosity of UO_2 irradiated to high burn-up

Introduction

High internal fuel rod pressure due to excessive fission gas release is one of the limiting factors of the lifetime of fuel rods. This aspect could be particularly relevant when high burn-up is a technological target. Key parameters in fission gas release are the fuel temperature, the fuel restructuring, and the irradiation time. In order to quantify the influence of the burn-up and the irradiation conditions on the fuel restructuring the radial distribution of the porosity was studied by means of optical microscopy. The selected fuels came from fuel rods irradiated in power reactors at two and five cycles under steady conditions (samples A and B) and from a fuel rod irradiated under follow-up conditions (sample C). The linear power during the irradiations and the burn-up reached are listed in Tab. 3.11.

Tab. 3.11 Linear power and burn-up of the samples studied by optical microscopy. The subsequent numbers for the linear power refer to successive reactor operation cycles.

Sample	Cycle	Cycle Average L H G R W/cm	Cycle Average Burn-up GWd/Kg U	Cumulative Average Burn-up GWd/Kg U
A	1 2	180 - 160 160 - 140		 25.2
B			16.5-15.0 14.5-13.0 12.5-11.5 11.0-10.5 10.5-9.5	16.5-15.0 30.0-29.5 43.0-41.5 54.5-51.5 64.0-60.5
C	1 2 3	384-320 75 170-100		 64.1

Polished cross-sections were examined by optical microscopy at magnification 500x. Photographs illustrating the fuel microstructure at different radial positions were analysed by means of an image analyser (Quantimet). From this analysis the porosity area, porosity distribution, the number of pores per mm^2, and the mean pore area on the radial position were obtained.

Experimental results

The radial distribution of the porosity area, the pore number per mm^2 and the mean pore size are displayed for each sample in Figs. 3.37a-c.

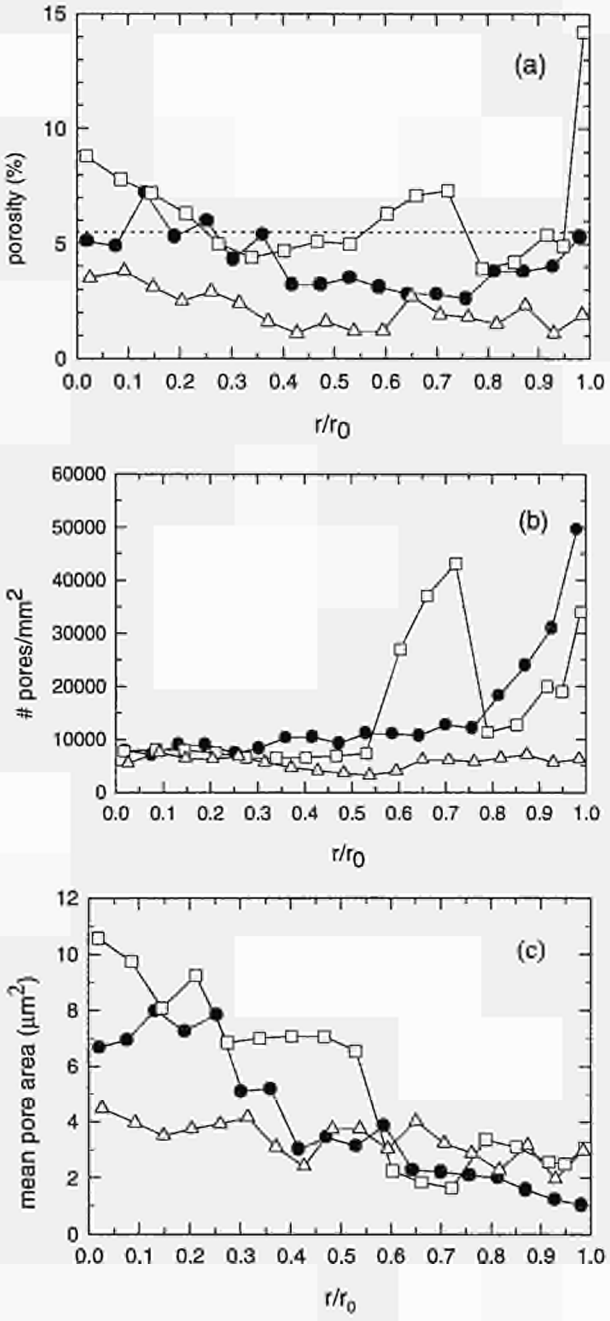

Fig. 3.37 Radial distribution of (a) porosity, (b) pore number, and (c) mean pore size for the samples A (white triangles), B (black circles), and C (white squares). The dashed line indicates the value of the porosity before irradiation.

a) UO_2 irradiated under steady conditions (samples A and B)

For both samples the porosity of the fuel as fabricated amounted to about 5.5%. A clear influence of the burn-up can be seen (see Figs. 3.38a and 3.38b). The fuel irradiated at 25.2 GWd/t (sample A) indicated porosity values lower than that of the unirradiated fuel independent of the radial position.

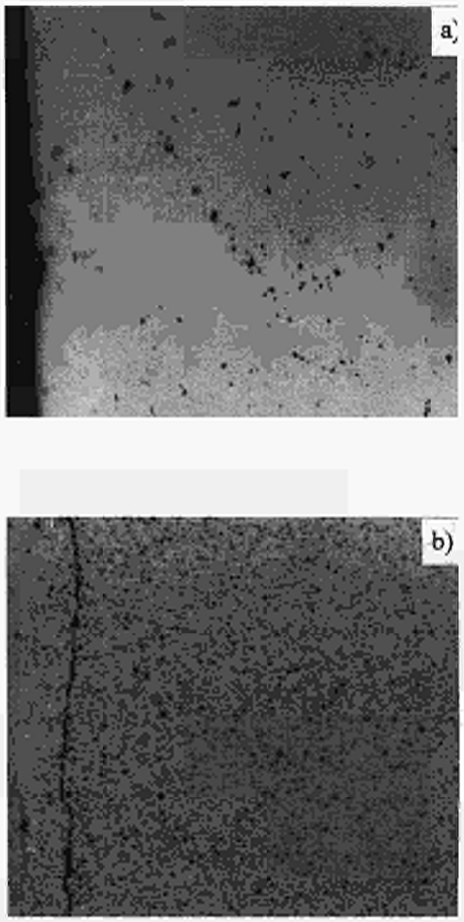

Fig. 3.38 Optical microscope photographs (magnification 500x) of the outer rim of the samples (a) A and (b) B. The outer edge of the sample is on the left side of the photos.

This variation can be considered to be the result of an in-pile sintering process associated with a progressive disappearance of the porosity of the fuel as fabricated during the first step of the irradiation.

As the burn-up rises to 66.7 GWd/t after 5 reactor cycles (sample B) an increase of the porosity was determined compared with the sample A which was only irradiated for two reactor cycles. In particular, the measurements corresponding to the central point ($r/r_0 < 0.4$) showed a strong continuous porosity increase as the fuel temperature increases and reached values of the unirradiated fuel. The data collected in Figs. 3.37b and 3.37c showed that the determining factor of the porosity increase at high burn-up is the increase of pore size and pore number per mm^2 for the position $r/r_0 > 0.4$. In the central zone ($r/r_0 < 0.4$) mechanisms such as atomic diffusion to the grain boundary and pore coalescence explain the formation and concentration of intergranular porosity.

A further influence of the burn-up is the formation of a very porous zone over the first 200 microns at the fuel pellet periphery with a higher pore density (by about a factor 3) and shows the influence of the greater fission gas concentration which is, in turn, a consequence of neutron resonance capture (i.e. increased burn-up) at the periphery.

b) Fuel irradiated under follow-up conditions (sample C)

The characteristics of the porosity evolution mentioned for sample B are found again in sample C (64.1 GWd/t, 3 cycles). One major new feature is the presence of a pore concentration peak at $r/r_0 = 0.7$ in the zone $0.59 < r/r_0 < 0.74$ which corresponds to a ring with a high pore number (diameter ≤ 0.5 µm) in both intra- and intergranular modes. Presumably this ring results from pore redistribution occurring during the second and third power cycles. This aspect has to be analysed by means of replica electron microscopy and the results will be reported in the next annual report.

Preliminary conclusions

The radial distribution of porosity shows a clear influence of the burn-up and different mechanisms explain the progressive evolution. At low burn-up the predominating mechanism is fuel densification due to in-pile sintering associated with the disappearance of the porosity of the unirradiated fuel. As the burn-up increases the fuel swells due to the precipitation of fission gas as pores; this swelling proceeds at different rates and is more important at the fuel periphery and in the central part of the fuel. The latter aspect results from gas diffusion to the grain boundary and progressive coalescence of the intergranular porosity.

At the fuel periphery in the range $0.8 < r/r_0 < 1$ the pore concentration and pore number decrease as the fuel temperature increases; the local burn-up variation determined by neutron resonance seems to be the determining factor.

Further work

Extension of the image analysis to photographs with higher magnification, in particular from replicas examined by scanning electron microscopy (SEM), is the first objective of future research. All results presented above are valid for the particular magnification of 500x. Pictures at higher magnification can give a better insight on

a submicron scale and on the separate contributions of inter- and intragranular pores to the total porosity. A point of concern is the preparation of samples to obtain SEM photographs from replicas which are suitable for analysis with the image analyser.

3.4.2 Micromechanical testing of high burnup fuels at room and high temperatures

Mechanical behaviour and microstructure of high burnup fuels.

Phenomena like fuel swelling, fission gas release, degradation of the fuel thermal conductivity, oxidation of zircaloy cladding and its associated embrittlement due to H_2 pick-up are limiting factors of the time of life in reactor for fuel rods irradiated under normal conditions. Also during local peak power transients, which in a number of cases can occur accidentally under normal irradiation conditions (i.e. **ATWS** (**A**nticipated **T**ransient **W**ithout **S**cram) and **RIA** (**R**eactivity **I**nitiated **A**ccident) transients), the possibility of rupture during the power excursion will depend on the mechanical behaviour of the fuel material itself.

During such fast transients, the excess of power rapidly results in an expansion of the fuel column, giving rise to the so-called **PCMI** (**P**ellet-**C**ladding-**M**echanical-**I**nteraction) effects, when the fuel-cladding gap is closed. If the fuel behaves rigidly, almost the whole interaction is absorbed by the cladding by developing high tensile hoop stresses, with the risk of failures by pure rupture or by **SCC** (**S**tress **C**orrosion **C**racking) if the resulting stresses are too high [1]. During the change, if the fuel is able to exhibit some plasticity, partial relaxation of the interaction stresses can occur via material flow (i.e. into the free space available at the interpellet dishings and shoulders, etc.), diminishing the possibility of failures when the cladding stresses fall below the threshold value needed for rupture [1].

Very recent results of in-pile transient tests performed under RIA conditions have shown that contrary to unirradiated and low burnup fuels (Bu < 20 GWd/tU), high burnup fuels (Bu ≈ 39 GWd/tU) can exhibit a rapid PCMI relaxation during the course of a power excursion, apparently due to creep and thermal annealing effects of UO_2 in the vicinity of the dish shoulder areas [2]. However, other recent RIA tests performed at CEA-Cadarache with a high burnup fuel rod, resulted in the sudden rupture of the cladding. An explanation would be that no relevant relaxation mechanism could operate during the transient [3] as a consequence of the high power ramp rate exercised in this case.

PIE results obtained in our hot cell laboratory on LWR UO_2 fuels irradiated at burnups higher than 40 - 50 GWd/t brought evidence of some material flow at the pellet periphery, as inferred from the unambiguous crack healing and the disappearance of the pellet interface. In addition, micrographs of the corresponding pellet rim zones, together with that of the interaction layer which is frequently formed at those burnups between the fuel and the oxidized cladding (Fig. 3.39), suggest that both external layers (rim and interaction) may exhibit a plastic or superplastic behaviour under irradiation, because of their fine grain size (<0.2 µm for the rim), and the relatively large size of pressurised pores that they can admit (pore size to grain size ratio >20) (Figs. 3.39, 3.40, 3.41) [4,5]. It is worth mentioning that the microstructure of the interaction layer according to SEM examination of freshly fractured samples appears either as a glassy phase or a crystalline compound with an extremely small grain size (Figs. 3.41, 3.42).

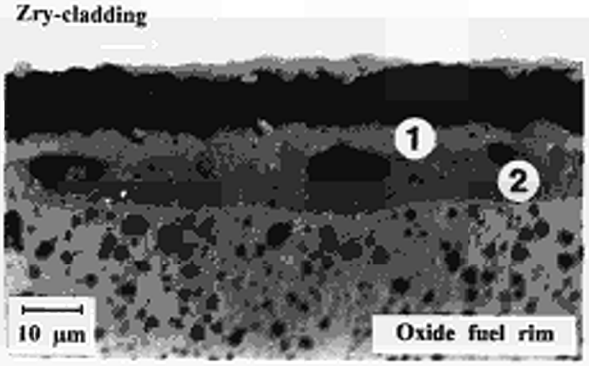

Composition of interaction layers according to EMPA in normalised at %.

Layer compound	Zr	U	Pu	Cs	Mo	Nd	O (1)
1	33.34	0.03	0.02	-------	0.04	0.03	66.54
2	28.32	1.14	0.06	3.56	0.11	0.11	66.75

(1) obtained by difference

Fig. 3.39 Double fuel-cladding interaction layer in a high burnup LWR-fuel.

Because of its technological importance, a new experimental programme has been therefore started in our hot-cell laboratories aiming for a detailed characterisation of the mechanical behaviour of high burnup fuels, with special attention payed to the influence of the new structures formed at the pellet periphery.

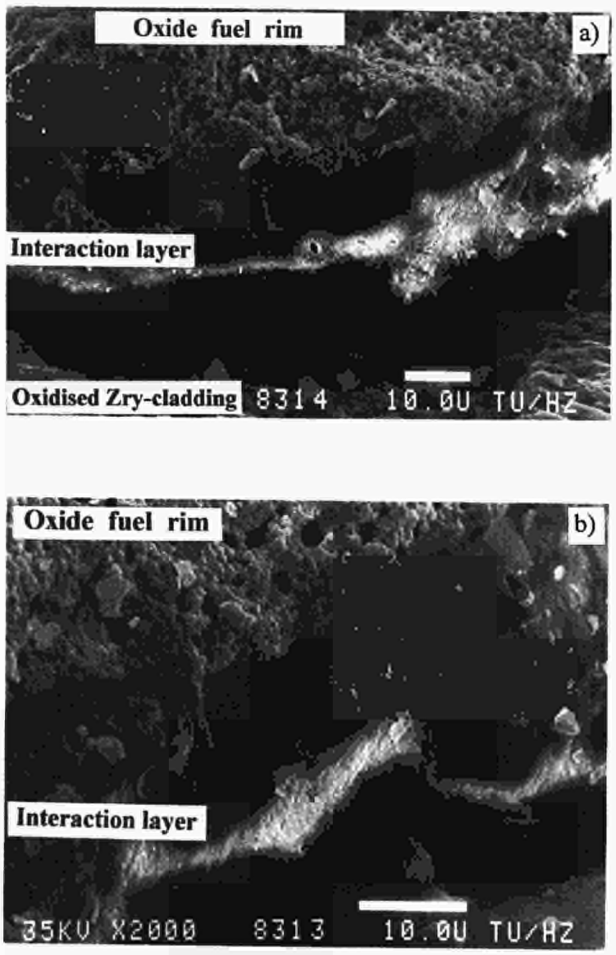

Fig. 3.40 Fresh fracture surface appearance of a high burnup LWR-fuel in the pellet rim region. magnification a) 1200x; b) 2000x

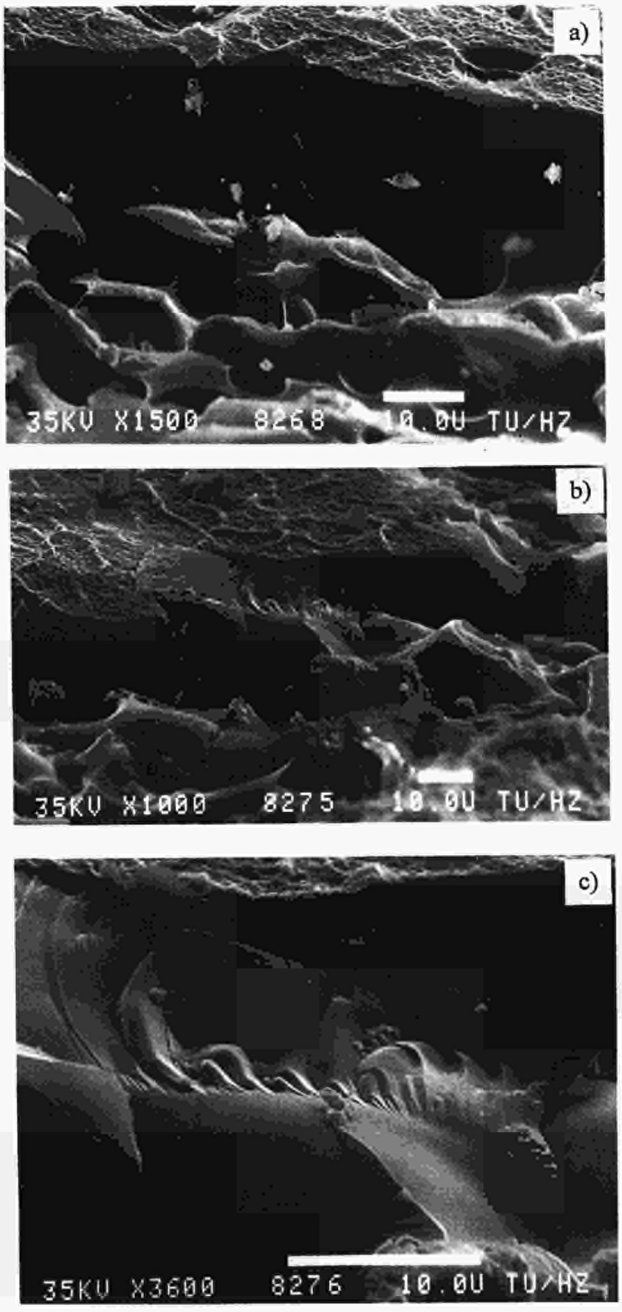

Fig. 3.41 Appearance of a Type 2-interaction layer (Fig. 3.39) after impact fracture. magnification a) 1500x; b) 1000x; c) 3600x

Experimental approach.

Due to the heterogeneity of the irradiated fuel, the determination of the mechanical properties of the different zones formed across the pellet radius would only be possible by performing local micromechanical tests, like those newly derived from the microindentation technique. In fact, by using the so-called dynamic load micro-indentation tests, where the applied load and the penetration depth of the indentator are controlled and measured at any time, properties like the stress-strain dependence [$\sigma(\varepsilon)$], creep [$\varepsilon(t)$], and stress relaxation [$\sigma(t)$] can be determined, in addition to the usual microhardness parameters (Hv , KIC, E) which are normally derived from indentation tests [6].

For such purposes, special remote-controlled equipment is under development, with the requirements that fuel areas of about 1 mm^2 can be tested under compression at a maximum stress of 100 MPa, under controlled atmosphere (Ar/H_2 or CO/CO_2) , and at temperatures up to 1200 °C.

In parallel, microhardness tests at room temperature are being performed with a separate device in a microscopy cell, the first experimental results of which are reported here.

Room temperature microhardness of high burnup fuels. Preliminary results.

First microhardness characterisation on UO_2 fuel irradiated at very high burnup has been performed at room temperature under N_2 atmosphere with the indentation device of a hot-cell microscope, which is able to work only in the range of small indentation loads (0-200 g-force). Fig. 3.42 shows the microhardness values obtained for the different phases of interest as function of the applied load, together with other own results at higher loads with unirradiated material (zry-4 and SIMFUEL 8%). (Each data point of Fig. 3.42 corresponds to the average of 8 measurements).

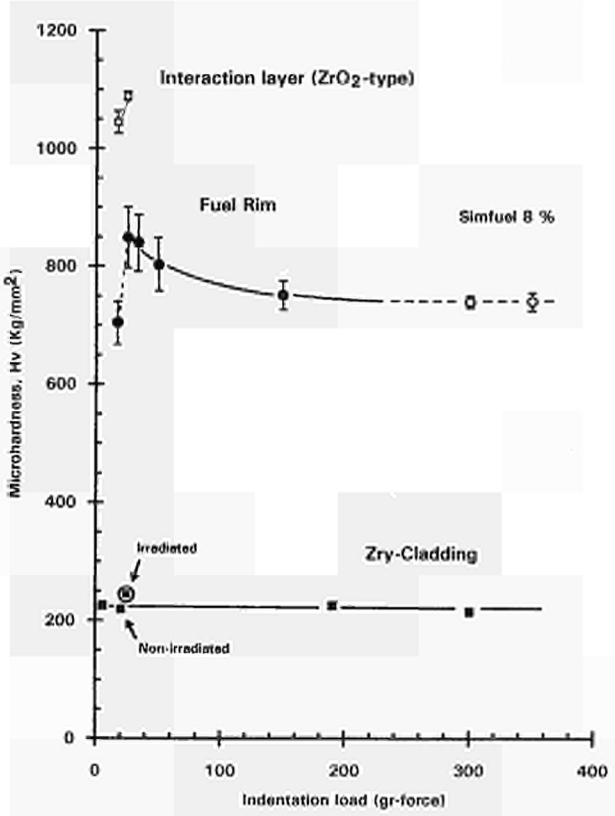

Fig. 3.42 Results of microhardness tests in the pellet rim region of a high burnup fuel, as function of the indentation load.

The microhardness curve corresponding to the fuel rim region extrapolate rather consistently towards the values measured for the simulated fuel (Fig. 3.42). However, it must be noted that the porosity of the rim material examined was at least 3-4 times higher than that of the simulated sample. This suggests therefore that the deleterious effect of porosity on hardness may have been compensated by Hall-Petch strengthening due to the smaller grain size of this region [6, 7]. The reduced grain size is expected also to be responsible for creep acceleration at high temperatures.

The high microhardness values obtained at the interaction layer are consistent with a structure of the type ZrO_2. The values of both unirradiated and irradiated zircaloy cladding materials agree well with existing literature data [8].

References

[1] P. Hofmann, J. Spino; Stress corrosion cracking of Zircaloy-4 cladding at elevated temperatures and its relevance to transient LWR fuel rod behaviour. J. Nucl. Mater. **125** (1984) 85-95

[2] K. Yanagisawa et al.; Pellet Cladding Mechanical Interaction of PWR fuel rods under rapid power transients. J. Nucl. Sci. Technol. **31** (7) (1994) 671-676

[3] D. Baron; EDF-France, private communication (Dec. 1994)

[4] A. H. Choski; Superplasticity in fine grained ceramics and ceramic composites: current understanding and future prospects. Mater. Sci. Eng. **A 166** (1993) 119-133

[5] Y. Ma, T. Langdon; An examination of the implications of void growth in submicrometer and nanocrystalline structures. Mater. Sci. Eng. **A 166** (1993) 225-230

[6] P. J. Blau and B. R. Lawn; Microindentation Techniques in Material Science and Engineering. Eds. ASTM STP **889**. American Society for Testing Materials (1986)

[7] A. S. Wagh et. al.; Dependence of ceramic fracture properties on porosity. J. Mater. Sci. **28** (1993) 3589-3593

[8] H. Sakurai et al.; Application of advanced PIE techniques to Irradiated BWR fuels. IAEA Technical Committee Meeting on Recent Developments on Post Irradiation Examination Techniques for Water Reactor Fuels. Cadarache, France (1994)

4. Actinide Research

4.1 Introduction

The central objective of actinide research in ITU and in its numerous collaborations is the elucidation of the electronic structure of actinide metals and actinide compounds, in particular of the behaviour of the 5f electrons. The dualism between localized and itinerant characteristics as it is particularly clearly demonstrated in the actinide series, is a key problem in these studies.

These goals are approached by experiment and theory. Experimental studies are either selective investigations on the basis of theoretical or other experimental information which indicates that a particular material and method are promising, or they can involve a systematic approach to a whole class of compounds. Theoretical calculations can indicate to the experimentalist where he can expect to find important results, and theory can on the other hand try to combine experimental evidence from different sources into a general picture. An important basis for the experimental study is the preparation of polycrystalline and single crystal samples of actinides of high specific activity, and their careful characterization by X-ray diffraction, chemical, and electron microprobe analysis. As far as possible, study of physical properties concentrates on the most interesting of the available actinide compounds, and an attempt is made to study them by several different methods to obtain a maximum of information on their physical behaviour. Many of the experimental investigations take place at the special facilities in ITU, but we also make use of unique large facilities, such as neutron, X-ray synchrotron, and muon sources, in other locations.

4.2 Preparation and Characterisation of Actinide Metals and Compounds

4.2.1 Methods for preparation of americium and curium metal

As part of our actinide metals preparation activity, as well as on request of outside contracts, we made a considerable effort in 1994 to prepare Am and Cm metal.

The preferred method for the preparation of high purity americium and curium metal is the metallothermic reduction of the oxide by lanthanum or thorium in a high vacuum.

$$An_2O_3 + 2La \rightarrow La_2O_3 + 2An^{\uparrow}$$
$$2An_2O_3 + 3Th \rightarrow 3ThO_2 + 4An^{\uparrow}$$

The actinide metal is separated from the reaction products and from the excess of reductant by selective evaporation and condensation. During the reporting period, 0.85 g of ^{244}Cm metal, 10 g of ^{241}Am metal and 8.65 g of ^{243}Am metal were prepared and refined for contractual work.

Americium and curium are emitters producing considerable self-heat. The produced heat is 0.11 Watt/g for americium-241 and 2.8 Watt/g for curium-244. The temperature of a small piece of curium metal can reach several hundred degrees if it is not cooled. Self heating considerably increases the reactivity of the samples. The corrosion risk by the surrounding atmosphere and self-ignition of exothermic reactions in mixtures must be avoided.

Americium and curium are also γ emitters. The emitted dose rates measured on the americium and curium purchased for this work are shown in Tab. 4.1. In addition, curium-244 is a neutron emitter. The measured neutron dose is of 6 mSv/h for 1 g of curium at a distance of about 10 cm. The handling of those isotopes in the quantities needed for this work requires water- and lead-shielded glove-boxes with telemanipulators. The shielded glove-box is equipped with a device for mixing powders, with a balance (Fig. 4.1), and with a press to pelletize the powder mixtures. The reduction and distillation take place in a vacuum chamber. The tantalum crucible and distillation column are heated by electron bombardment and the temperature is monitored by optical pyrometry.

Tab. 4.1 γ and neutron dose rates measured on 1 g at 10 cm (mSv/h).

	γ	neutron
Pa 231	10	-
Am 241	20	-
Am 243	30	-
Cm 244	20	6

Metallothermic distillation procedure

Two different types of distillation columns were used. The distillation column shown in Fig. 4.2 was used for the preparation and refining of americium metal.

To prepare americium and curium metal, a pelletized mixture of americium or curium sesquioxide with lanthanum or thorium is heated under a high vacuum (10^{-6} Torr) at temperatures above 1000 °C. At these temperatures the vapour pressure of americium and curium metal is high enough and the metal evaporates out of the reaction products with an acceptable speed (greater than 1 g/h for americium and greater than 100 mg/h for curium). The americium and curium metal vapour is condensed on the coldest part of the distillation column: the condensor.

It is preferable to condense the metal as a solid to avoid its contamination by the reaction of the liquid actinide metal with the tantalum. The melting point and vapour pressure of americium metal are high enough to be prepared in the distillation column (Fig. 4.2). For curium, a reaction temperature of 1700°C is required. It is more difficult to keep the temperature of the condensor lower than the melting point. If the condensed metal melts on the condensor, the condensor welds to the distillation column and the recovery of the metal is impossible. To decrease the temperature of the condensor, a water-cooled support was installed in the electron beam furnace.

Preparation of ^{241}Am and ^{243}Am

Three runs were made with americium-241 oxide as starting material. The first two runs were made with about 5 g

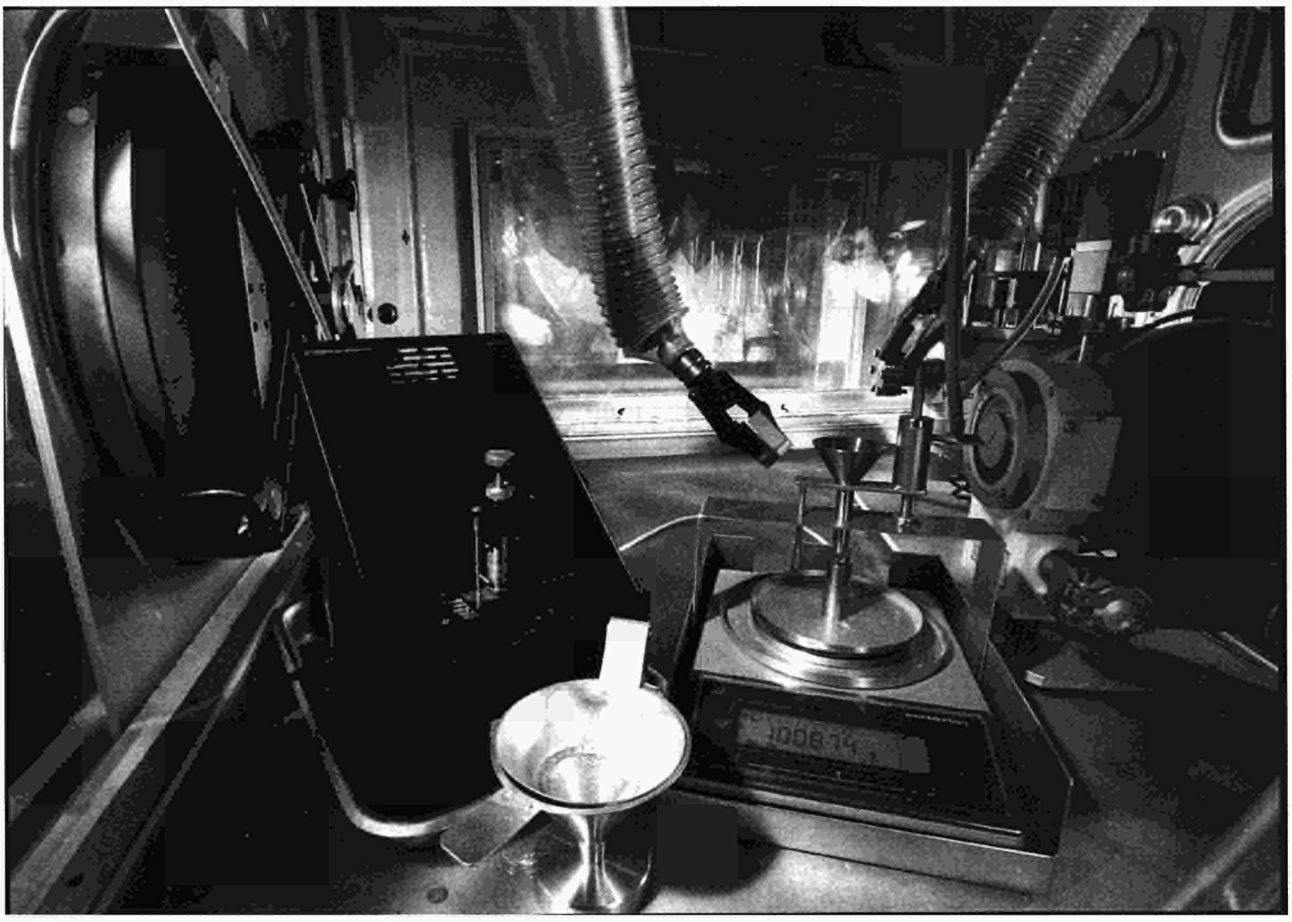

Fig. 4.1 Inside view of the shielded glove-box with the device for mixing powders and with the balance.

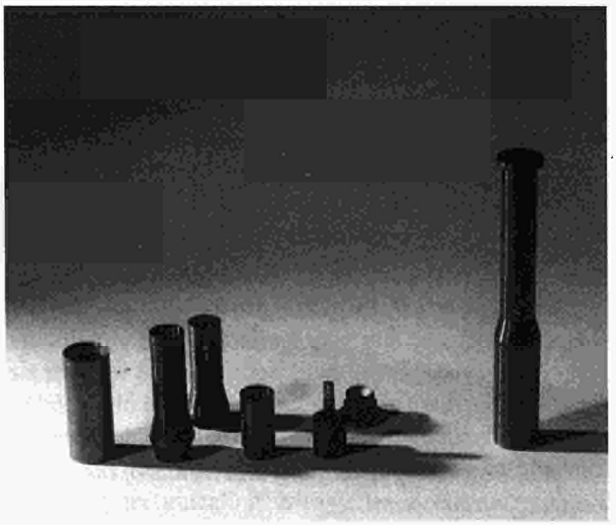

Fig. 4.2 Tantalum column for the preparation of americium metal.

of AmO_2 each, the last with 9 g of oxide. The oxide is a mixture containing 65 to 70% of americium. The impurities are plutonium (5%), Np (1%), Fe, N, Cu, Zn, Pb, also present at the % level. After distillation the impurities are reduced to the ppm level, except for lead.
To prepare americium-243 metal, two runs with about 5 g of oxide each were carried out. The preparation conditions and results are summarised in Tab. 4.2. The third run was carried out with the pellets of americium-243 oxide and the lanthanum remaining from the first two runs. 0.25 g of americium metal could be extracted. A total quantity of 8.65 g of americium-243 was produced with a yield of 95%. The americium metal (Fig. 4.3) was transformed into turnings and sealed for storage under vacuum in quartz tubes, containing each about 1 g of americium metal.

Preparation of ^{244}Cm

To prepare curium metal, the stock of curium oxide (2.235 g) was first heated under vacuum at 800°C to obtain Cm_2O_3. After the heating, 1.66 g of Cm_2O_3 were recov

Tab. 4.2 Processing conditions and results of the 5 americium metal preparation runs.

		Quantities of starting materials g		Temperature °C		processing time h	distilled quantities g
	Run no.	Am_2O_3	La	Crucible	Condenser		
Am 241	1	6.498	4.322	1070 1170 1200	950 950 1000	6 3 5	0.06 0.5 1.6
	2	6.700	8.100	1200 1200 1200	1000 1000 1000	5 4 6	2 1.3 0.3
	3	9.054	13.600	1200 1200	1000 1000	4 6	4.04 0.157
Am 243	1	6.000	6.1	1200 1200 1200	1000 1000 1000	6 4 5	3.869 1.124 0.23
	2	4.38	4.45	1200 1200 1200	1000 1000 1000	3 5 5	0.400 2.279 0.73
		Pellets from Run 1 and 2		1200 1200	1000 1000	8 8	0.25 0.2

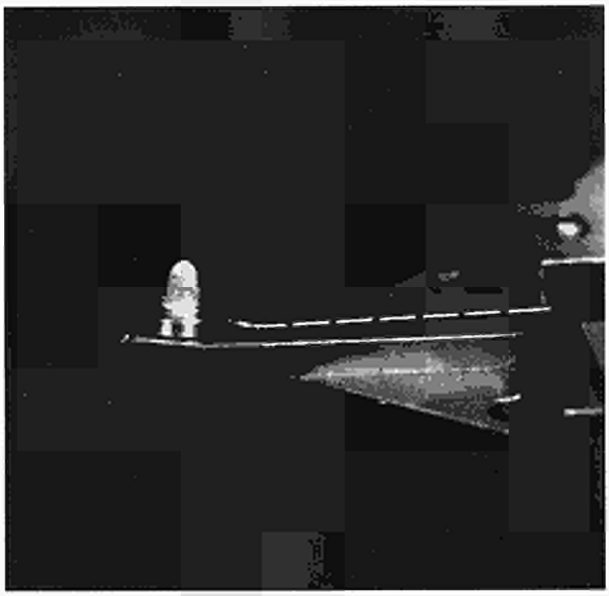

Fig. 4.3 2 g of americium metal condensed on a tantalum condenser.

ered. The large weight decrease can be explained by the presence of oxalate or carbonate in the purchased curium oxide. 1.114 g of Cm_2O_3 was mixed with 1.25 g of thorium metal. The processing conditions and results are summarised in Tab. 4.3. After five hours at 1700°C, 0.853 g of curium metal was condensed, giving a yield of 85 %.

Tab. 4.3 Processing conditions and results of the preparation of curium metal.

Quantities of starting materials g		Temperature °C		processing time h	distilled quantities g
Cm_2O_3	Th	Crucible	Condenser		
1.114	1.253	1700	1200	5	0.853

4.2.2 Preparation and characterization of actinide compounds and alloys

During the reporting period, more than 77 samples were prepared, characterised and encapsulated for different studies in collaboration with external organizations. The samples are listed in Tab. 4.4.

Progress in the following groups of materials is reported:

- Synthesis and characterisation of LaAm alloys
- Preparation of compounds with the AnT_2X_3 composition
- Preparation of $NpBe_{13}$
- Preparation of uranium compounds with $AuCu_3$ structure
- Compounds with the An_2T_2X composition

4.2.3 Synthesis and characterization of La-Am alloys

Am exists in a pivotal position in the actinide series of elements in that it lies at the transition point for elements normally displaying either itinerant (delocalized) or localized 5f electron states. Although its f electrons are localized, Am is non-magnetic and even displays superconducting properties [1]. Recently, a new interesting aspect on the superconductivity of Am was given by Link et al. [2], who studied its superconductivity under pressure. To further understand the properties of pure Am, we have extended our collaborative studies to La-Am alloys. Hill et al. [3] reported previously the synthesis of dilute La-Am alloys. In order to perform electrical resistivity measurements under pressure of these alloys, new samples of LaAm with 1 and 2 $^{a}/_{o}$ Am were synthesized by arc-melting the constituent metals in stoichiometric ratio under Ar atmosphere. Both samples were analyzed by metallography, autoradiography and microprobe analysis in order to check their homogeneity, and were found to be single phase. Both alloys were cold-worked into a shape suitable for the experiments, then annealed at 200°C and 400°C for one week to stabilize the dhcp and fcc phases. After annealing, X-ray characterisation revealed single-phase samples with the following lattice parameters: $La_{0.99}Am_{0.01}$ annealed 200°C: dhcp a= 376.7 (2) pm c= 1218 (1) pm; $La_{0.98}Am_{0.02}$ annealed 200°C: dhcp a= 377 (1) pm c= 1214 (4) pm; $La_{0.99}Am_{0.01}$ annealed 400°C: fcc. a= 530.9 (1) pm and $La_{0.98}Am_{0.02}$ annealed 400°C: fcc. a= 530.3 (1) pm. A slight difference of crystallographic parameters of fcc phases is observed, compared with previous reported values [3]. The dilatation of the lattice in our samples may be a self-irradiation effect. Further experiments are under way to analyse this fact. The electrical resistivity of the fcc $La_{0.98}Am_{0.02}$ sample was measured and a superconducting transition observed at around 5 K. Further experiments will be reported later.

References

[1] J.L Smith, R. G. Haire; Science **200** (1978) 535

[2] P. Link, D. Braithwaite, J. Wittig, U. Benedict and R. G. Haire; J. Alloys Comp. **213/214** (1994) 148-152

[3] H. H. Hill, J. D. G. Lindsay, R. W. White, L. B. Asprey, V. O. Struebing and B. T. Matthias; Physica **55** (1971) 615
H. H. Hill, F. H. Ellinger; J. Less Comm. Met. **23** (1971) 92

4.2.4 Preparation of compounds with the AnT_2X_3 composition

Since the discovery of the two heavy fermion superconductors UPd_2Al_3 and UNi_2Al_3 [1] many investigations have already been carried out on these compounds, and a consistent scheme of their properties is beginning to emerge [2]. In order to extend our understanding of these systems, we have investigated the isostructural Np and Pu compounds [3]. Syntheses of samples of $NpPd_2Al_3$, $NpNi_2Al_3$, $PuPd_2Al_3$ and of the solid solution $U_{1-x}Np_xPd_2Al_3$ with x = 0.5 and 0.3 were already reported (TUAR-92, p. 151 and TUAR-93, p. 145). We continued our efforts and prepared $U_{1-x}Np_xPd_2Al_3$ with x = 0, 0.01, 0.1 and 0.8. The results of the crystallographic characterisation of the full series are summarised in Tab. 4.5. The c parameter is equal to the shortest interactinide distance. A slight contraction of the cell is observed from $NpPd_2Al_3$ to UPd_2Al_3. The cell parameters of the solid solutions $U_{1-x}Np_xPd_2Al_3$ follow Vegard's law (Fig. 4.4). The compounds were encapsulated for resistivity measurements, Mössbauer spectroscopy, magnetic susceptibility and neutron diffraction studies. The results are reported below (4.3.3).

References

[1] C. Geibel, C. Schank, S. Thies, H. Kitazawa, C.D. Bredl, A. Böhm, M. Rau, A. Grauel, R. Caspary, R. Helfrich, U. Ahlheim, G. Weber, F. Steglich; Z. Phys. B **84** (1991) 1.

[2] C. Geibel,, A. Böhm, R. Caspary, K. Gloos, A. Grauel, P. Hellmann, R. Modler, C. Schank G. Weber, F. Steglich; Physica B **186-188** (1993)188-194.

[3] A. Seret, F. Wastin, J. C. Waerenborgh, S. Zwirner, J. C. Spirlet, J. Rebizant; to be published in Physica B.

Tab. 4.4 Samples prepared, characterized and encapsulated in 1994 for the indicated measurements (77 samples).

Measurements	Laboratories	Compounds	Form
Resistivity	ITU-Karlsruhe	Tc_4Al_{11} U_2Ni_2Sn Np_2T_2Sn (T = Ni, Co, Ru, Rh, Pd, Pt) Np_2T_2In (T= Pd, Pt) $U_{1-x}Np_xPd_2Al_3$ (x = 0, 0.01, 0.1, 0.3, 0.5, 0.8, 1) $PuPd_2Al_3$ $NpNi_2Al_3$ $La_{0.98}Am_{0.02}$ NpX (X = As, Sb, Bi) $NpGa_3$	AcM Cz-SC AcM AcM AcM AcM AcM AcM M-SC AcM
Mössbauer Spectroscopy	CEN Grenoble	Np_2T_2Sn (T = Ni, Co, Ru, Rh, Pd, Pt) Np_2T_2In (T = Co, Rh)	AcM AcM
	TU-München	$U_{1-x}Np_xPd_2Al_3$ (x = 0.1, 0.8) $NpBe_{13}$ NpX_3 (X = Ga, In)	AcM M AcM
Neutron Scattering	CEN Grenoble	$NpPd_2Al_3$ $NpBe_{13}$	AcM and SC AcM and SC
	Hahn-Meitner Inst. -Berlin	U_2Pt_2Sn	AcM
Magnetic properties	CEN Grenoble	Tc_4Al_{11} Np_2T_2Sn (T= Ni, Pd, Pt) $NpPd_2Al_3$ $NpBe_{13}$ $Y_{1-x}Np_xPd_3$ (x= 0.25, 0.5, 0.75)	AcM AcM AcM M AcM
	ITC-KfK Karlsruhe	NpT_2Al_3 (T= Ni, Pd) $PuPd_2Al_3$ Pu_2T_2Sn (T= Ni, Pd, Pt) Pu_2T_2In (T= Ni, Pd, Pt)	AcM AcM AcM AcM
PAC	Univ. Leuven	$U(In_xSn_{1-x})_3$ (x= 0, 0.01, 0.02, 0.1, 0.3, 0.45, 0.5, 0.7, 0.8, 0.9, 1)	AcM
m-Sr	TU-München	$U(Ga_{0.8}Ge_{0.2})_3$ $U(Ga_{0.9}Ge_{0.1})_3$	AcM AcM
HPXRD	DESY-Hamburg	UX_3 (X= Ga, Ge, In, Si, Al)	AcM
Irradiation	High Flux Reactor Petten	Tc metal	Casting

AcM = arc melting M = mineralisation SC = single crystal P = powders, polycrystalline sample
Cz = Czochralsky method PAC = perturbed angular correlation μ-Sr = muon spectroscopy
HPXRD = high-pressure X-ray diffraction

Tab. 4.5 Lattice parameters of AnT_2Al_3 compounds.

Compound	Structure Type	Lattice Parameters	
		a (pm)	c (pm)
UPd_2Al_3	$PrNi_2Al_3$	537.1 (1)	419.1 (1)
$U_{0.99}Np_{0.01}Pd_2Al_3$	$PrNi_2Al_3$	536.7 (1)	419.0 (1)
$U_{0.9}Np_{0.1}Pd_2Al_3$	$PrNi_2Al_3$	536.9 (1)	418.8 (1)
$U_{0.7}Np_{0.3}Pd_2Al_3$	$PrNi_2Al_3$	537.4 (1)	418.9 (1)
$U_{0.5}Np_{0.5}Pd_2Al_3$	$PrNi_2Al_3$	537.9 (1)	419.0 (1)
$U_{0.2}Np_{0.8}Pd_2Al_3$	$PrNi_2Al_3$	538.8 (1)	419.3 (1)
$NpPd_2Al_3$	$PrNi_2Al_3$	539.1 (1)	419.6 (1)
$NpNi_2Al_3$	$PrNi_2Al_3$	522.2 (1)	399.5 (1)
$PuPd_2Al_3$	$PrNi_2Al_3$	540.2 (1)	419.4 (1)

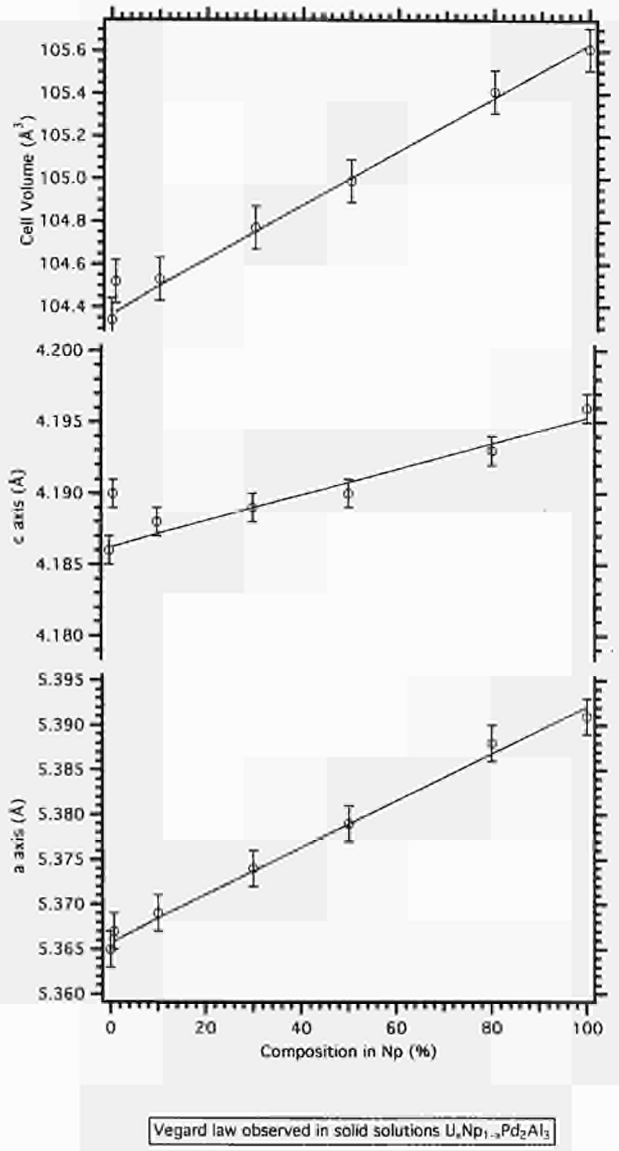

Fig. 4.4 Vegard's law in solid solutions $U_{1-x}Np_xPd_2Al_3$.

4.2.5 Preparation of $NpBe_{13}$

$NpBe_{13}$ is a compound of great interest in the study of heavy fermion 5f-materials. Preliminary studies have shown that its magnetic properties were sensitive to the Be content [1]. Mössbauer study of samples from two different syntheses has revealed different magnetic properties, one sample being magnetic at 4 K and the other remaining non-magnetic (original sample was provided by LANL). As reported previously (TUAR-93, p. 129), we investigated the sensitivity of the magnetic behaviour to the Be content on samples of composition $NpBe_{12}$ and $NpBe_{14}$ and no difference in magnetic behaviór was observed, both being similar to the magnetic $NpBe_{13}$ sample. Annealing the non-magnetic sample at 1500°C for 175h leads to a well crystallized sample whose magnetic properties were similar to all previous samples. Part of this new sample was encapsulated for neutron diffraction on powder and magnetic susceptibility measurements (results are reported below, 4.3.6). Single crystals were selected for neutron diffraction.

In conclusion, we suggest that the difference in the magnetic properties observed previously is much more due to the crystallization of the samples than to stoichiometric discrepancies. A good sample is now available for the measurements of physical properties, and there is some indication that single crystals can be prepared by mineralisation.

References

[1] J. Gal, F. J. Litterst, W. Potzel, J. Moser, U. Potzel, G. M. Kalvius, S. Fredo, S. Tapuchi; Phys. Rev. B36 (1987) 2457

4.2.6 Preparation of uranium compounds with $AuCu_3$ structure for perturbed angular correlation study

The compounds UIn_3 and USn_3 with the $AuCu_3$-type structure have almost the same cell parameter and U-U spacing. As the magnetic behaviour of 5f compounds is determined mainly by the distance of 5f atoms and the f-spd hybridization, the $U(In_xSn_{1-x})_3$ solid solutions provide an opportunity to study the influence of the hybridization. Solid solutions with x = 0, 0.1, 0.2, 0.3, 0.5, 0.55, 0.7, 0.9, 0.98, 0.99, 1 have been synthesized by arc-melting. All the samples are X-ray single phases, showing that UIn_3 and USn_3 form a continuous solid solution. Our calculated cell parameters are in good agreement with literature [1]; for instance, 460.8(1) pm for USn_3, 459.9(2)

for UIn_3 and 460.1(2) for $U(In_{0.5}Sn_{0.5})_3$.
The study of the $U(In_xSn_{1-x})_3$ compounds is in progress at the Institut voor Kern en Stralingsfysica (University of Leuven) using the perturbed angular correlation method.

For temperatures above the magnetic ordering temperature, the electric quadrupole hyperfine interaction strength follows a linear temperature dependence, whereas the magnitude reveals a reduced electronic enhancement. In the pseudo-binary compounds, we conclude that the valence difference between In and Sn is small. The low-temperature perturbed angular correlation spectra for the indium-rich compounds are understood in terms of a two-site model with temperature-dependent relative populations and confirm the triple-k antiferromagnetic ordering earlier suggested to reconcile Mössbauer and neutron scattering data. In the pure UIn_3 a spin reorientation is observed [2].

Another interesting system could be $U(Pb_xSn_{1-x})_3$. The preparation of these solid solutions is in progress.

References

[1] Pearson Handbook of Crystallographic Data, A.S.M. International, 1991.

[2] S. Cottenier, A. Toye, M. Rots, J. C. Spirlet, J. M. Winand; Physica B (in press).

4.2.7 Compounds with the An_2T_2X composition

During the reporting period, the main effort was to determine the stability domain of the 2:2:1. family of compounds by extending our investigation to Pu and Am and in growing single crystals of some well selected compounds. Their synthesis and the crystal structure were described in detail previously (TUAR-93, p. 130).

Uranium compounds

A superstructure derived from the tetragonal U_3Si_2 type-structure, with doubling of the *c* axis, was found in two compounds, U_2Pt_2Sn and U_2Ir_2Sn. These compounds are isotypic with the tetragonal Zr_3Al_2-type structure (space group $P4_2/mnm$, Z=4) and the atomic positions are the following: U_1 in 4g(x_1, $-x_1$, 0) U_2 in 4f(x_2, x_2, 0) T in 8j(x_3, x_3, z) and Sn in 4d(0, 1/2, 1/4). The main differences between the two structures are:

- The shift of the Pt and Ir atoms from the ab plane, in contrast to their positions in the U_3Si_2-like structure.
- In the superstructure, the U atoms occupy two different crystallographic positions and are not in a straight line along the c axis.

In the solid solution $U_2Pt_2Sn_xIn_{1-x}$ (x = 0.25, 0.5, 0.75), the intensities of the superstructure peaks decrease regularly with x, leading to the hypothesis that the superstructure could exist in other 2:2:1. compounds, even if the additional peaks are not intense enough to be detected. The lattice parameters (pm) are:

x	a	c
1	766.8(1)	738.9(1)
0.50	768.9(2)	738.1(3)
0.75	768.3(2)	737.8(3)
0.25	769.8(3)	736.4(4)

Two methods have been used to obtain single crystals: Czochralski and mineralization. By the first method, crystalline blocks (possibly single crystals) of U_2Pt_2Sn, U_2Pd_2Sn, U_2Co_2Sn and U_2Rh_2Sn with a length of 3-4 cm and diameters of 0.2-0.4 cm were obtained. Crystals of U_2Pd_2In and U_2Co_2Sn were obtained by the classical mineralization method. A modified radiofrequency heated crucible, allowing the determination of the melting point of the material in situ during the crystal growth process, led to single crystals of good quality in a much shorter time (5 hours of mineralisation). Good quality crystals of U_2Ru_2Sn, U_2Ir_2Sn and U_2Pt_2In of sizes (2-6 mm^3) were obtained. The single crystals are characterised by the X-ray Laue diffraction technique taking the Laue photographs from various points of the sample.

Progress in the study of the bulk magnetic properties and heavy-fermion behaviour in the U_2T_2X compounds were made with polycrystalline samples [1,2]. For further progress, measurements on single crystals are required.

References

[1] H. Nakotte, K. Proke_, E. Bruck, N. Tang, F.R. de Boer, P. Svoboda, V. Sechovsky, L. Havela, J.M. Winand, A. Seret, J. Rebizant, J. C.Spirlet; The 6th Joint MMM-International Magnetism Conference, Albuquerque, New Mexico, June 20-23, 1994

[2] A. Purwanto, R. A. Robinson, L. Havela, V. Sechovsky, P. Svoboda, H. Nakotte, K. Proke_, F. R. de Boer, A. Seret, J. M. Winand, J. Rebizant, J. C.Spirlet; Physical Review B **50** (1994) 6792-6801

Plutonium and americium compounds

Attempts were made to synthesize Pu_2T_2X compounds with the same compositions which were easily obtained with U and Np: T=Fe, Ru, Co, Rh, Ir, Ni, Pd, Pt and X=Sn, In. It was only possible to prepare the 2:2:1 compounds (see Tab. 4.6) with T=Ni, Pd, Pt; X=Sn, In. This shows that the degree of stability of this family decreases with the substitution of the actinide element in the order U → Np → Pu, probably due to the increasing degree of localization of the 5f-states. Indeed, for most of the U and Np compounds studied up to now, the 5f localization increases within each T metal series towards the heavier end of the

Tab. 4.6 Lattice parameters of Pu_2T_2X intermetallics compounds.

Compounds	Lattice Parameters	
	a (pm)	c (pm)
Pu_2Ni_2In	733.6(3)	369.0(2)
Pu_2Pd_2In	765.7(2)	381.8(1)
Pu_2Pt_2In	766.3(4)	389.5(1)
Pu_2Rh_2In	744.4(6)	373.7(2)
Pu_2Ni_2Sn	727.2(2)	374.5(1)
Pu_2Pd_2Sn	760.7(2)	386.7(1)
Pu_2Pt_2Sn	762.9(2)	380.6(1)

periodic table and Sn-containing compounds have a stronger tendency to order magnetically than the corresponding In compounds.

The new Pu_2T_2X compounds have the tetragonal U_3Si_2-type structure (space group P4/mbm, Z=2). The atomic positions are: An in 4h(x_1, x_1+0.5, 0.5), T in 4g(x_2, x_2+0.5, 0) and X in 2a(0, 0, 0) with the average values of x_1 = 0.17 and x_2 = 0.37. No superstructure such as found in U_2Pt_2Sn was detected in Pu_2Pt_2Sn.
Americium compounds with the Ni group were synthetised, using Sn as *p*-element: Am_2Ni_2Sn, Am_2Pd_2Sn, and Am_2Pt_2Sn. Their investigation by single crystal X-ray diffraction is in progress.

4.3 Solid State Physics Studies on Actinide Systems

4.3.1 Electrical resistivity measurements of 1:2:3 compounds

Above their superconducting transition, the two heavy-fermion superconductors UT_2Al_3 (T = Ni, Pd) behave as Kondo lattice systems [1]. In UPd_2Al_3 an antiferromagnetic ordering at 14 K suppresses the spin disorder contribution to the resistivity leading to an increase in |d/dT| just below the Néel temperature. In UNi_2Al_3 no anomaly is apparent in the resistivity curve around the Néel temperature. For the $U_{1-x}Th_xPd_2Al_3$ series the resistivity evolves smoothly when increasing x from a Kondo lattice regime to a single impurity Kondo behaviour [2]. The substitution of U by Th finally leads to a loss of the heavy-fermion properties due to the lack of 5f-electrons. Here we have chosen to increase the number of 5f-electrons by substituting Np or Pu for U. We report resistivity data of new compounds (presented above) isostructural to the UT_2Al_3, namely $NpNi_2Al_3$, $U_{1-x}Np_xPd_2Al_3$ (x = 1, 0.8, 0.5, 0.3, 0.1, 0.01, 0) and $PuPd_2Al_3$.

The resistivity was measured between 1.2 and 295 K by a standard 4-point AC lock-in technique.
The resistivity versus temperature curves of all the compounds studied here are presented in Fig. 4.5. Down to 1.2 K no superconducting transition could be observed for any compound. The magnetic ordering temperatures (T_{ord}) have been determined by Mössbauer spectroscopy and are reported in the section on Mössbauer studies of this report (4.5.3). At T_{ord} the resistivity curve always shows a change of sign of the curvature, which is therefore the anomaly associated with the magnetic ordering.

All the curves of the $U_{1-x}Np_xPd_2Al_3$ series display a maximum in the paramagnetic domain. From x = 0.1 to x = 0.3, both the temperatures of this maximum (T_M) and T_{ord} decrease. For x > 0.3, T_M and T_{ord} increase (Fig. 4.6). Finally, for $NpPd_2Al_3$ they greatly exceed the values recorded for UPd_2Al_3. This parallel behaviour indicates that the same mechanism causes the variation of T_M and T_{ord} with x. In the case of $PuPd_2Al_3$, neither an anomaly nor a maximum appears in the resistivity. A linear increase of the resistivity from 1.2 to 100 K is observed and a flattening of the curve becomes obvious above 200 K. Similarly to UNi_2Al_3 [1] no hint of magnetic order is observed in the resistivity curve of $PuPd_2Al_3$ down to 1.2 K.

In $NpPd_2Al_3$, the appearance of the magnetic ordered phase is followed by a decrease of |dρ/dT|. For x = 0.5, the onset of the magnetic order causes an increase in the resistivity. For the lower x values (x = 0.3 and 0.1) or UPd_2Al_3 [1], an increase in |dρ/dT| is observed below T_{ord}. Remembering the change of the magnetic structure with x evidenced by Mössbauer spectroscopy [3,4], it can be concluded that from x = 0 to x = 0.3 the magnetic contribution to the resistivity is decreased below T_{ord} whereas for the higher x values the magnetic contribution is increased. In the same way, in UNi_2Al_3 the magnetic ordering leaves dρ/dT unchanged [1] whereas in $NpNi_2Al_3$ [5] a drastic reduction of the conductivity is observed with the onset of the magnetic ordering. Furthermore in $NpPd_2Al_3$ an increase in dρ/dT is observed below 23 K. Mössbauer studies highlight a change in the magnetic structure [4] below this temperature that is probably the reason for the change in electrical conductivity.

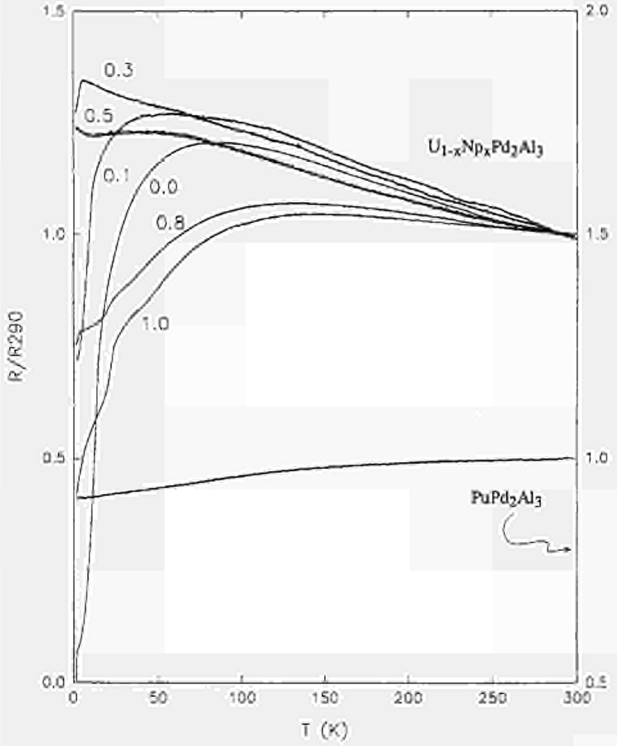

Fig. 4.5 Temperature dependence of the resistivity of $U_{1-x}Np_xPd_2Al_3$ (x = 1, 0.8, 0.5, 0.3, 0.1, 0) and $PuPd_2Al_3$ between 1.2 and 295 K.

The resistivity curves of $U_{1-x}Np_xPd_2Al_3$ (x= 1, 0.8, 0.1) (Fig. 4.5) show the characteristic shape of Kondo lattice systems already found in UPd_2Al_3 and UNi_2Al_3 [1]. For x= 0.3 and 0.5 flatter curves are observed. Nevertheless they look like curves of a dilute Kondo impurity system.

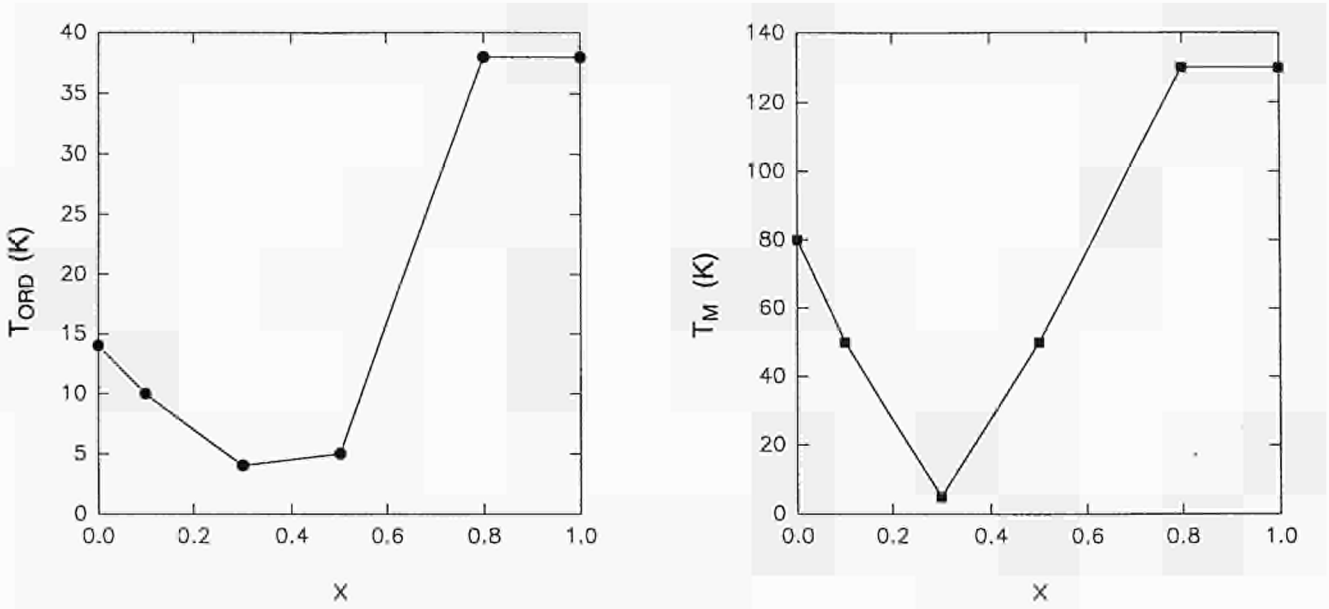

Fig. 4.6 Variation of T_{ord} and T_M as a function of x in $U_{1-x}Np_xPd_2Al_3$.

Kondo behaviour is common to many heavy-fermion systems and is observed in most of the compounds studied here. All changes in the magnetic structure of the NpT_2Al_3 compounds are reflected by anomalies in the resistivity curve. This contrasts with the UT_2Al_3 systems where, for example, the antiferromagnetic transition of UNi_2Al_3 is not detected in the resistivity curve [1]. Another difference to the U-compounds is the absence of a superconducting transition at least down to 1.2 K even for very diluted Np alloys.

References

[1] C. Geibel, A. Böhm, R. Caspary, K. Gloos, A. Grauel, P. Hellmann, R. Modler, C. Schank, G. Weber, F. Steglich; Physica B **186-188** (1993) 188-194 and references therein

[2] Y. Dalichaouch, M. B. Maple; Abstracts of International Conference on Strongly Correlated Electronic Systems, San Diego, 15-19 August 1993

[3] S. Zwirner, J. C. Spirlet, J. Rebizant, W. Potzel, G.M. Kalvius, Ch. Geibel, F. Steglich; Physica B **186-188** (1993) 681-683

[4] S. Zwirner, J. C. Waerenborgh, W. Potzel, G.M. Kalvius, J. Rebizant, J. C. Spirlet, Ch. Geibel, F. Steglich; to be published

[5] A. Seret, F. Wastin, J. C. Waerenborgh, S. Zwirner, J. C. Spirlet, J. Rebizant; to be published in Physica B

4.3.2 Measurement of the electrical resistivity up to 1000 K

The extension of the measurement of some actinide compounds up to 1000 K allows a better understanding of the measurements carried out from 0 to 300 K. In particular, the Kondo systems with a high characteristic Kondo temperature transition as well as semiconductor behaviour can be better identified. Equipment for measuring high-temperature resistivity was designed, constructed and installed in a glove-box in co-operation with the Joseph Fourier University, Grenoble.

The equipment consists of a sample holder which can be evacuated (turbomolecular pumping system) and then filled with an inert gas (helium or argon). The sample holder is heated in a resistance furnace ($T_{max.}$ = 1500 K). The temperature of the sample is measured with a Ni-Cr thermocouple. The resistivity is measured with two lock-in amplifiers. The measurement and data acquisition are controlled using a personal computer program developed for this equipment.

The sample holder is shown in Fig. 4.7. It consists of a vacuum chamber which can be filled with argon or helium, a flange at the back end provided with vacuum tight

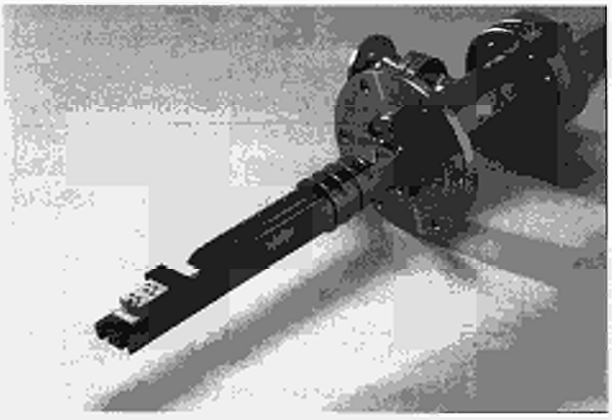

Fig. 4.7 Sample holder for the high temperature resistivity measurements.

connectors for the electrical signals, a water refrigerator for cooling of the flask, four tungsten wires to assure the electrical contacts on the sample using the four point configuration, and a thermoelement.

The equipment has been tested by measuring the resistivity of Ni metal with temperature, which shows a ferromagnetic transition at 630 K. The curve obtained is in good agreement with the literature data [1].

References

[1] M. J. Laubitz, T. Matsumara, P. J. Kelly; Can. J. Phys. **54** (1976) 92

Resistivity of neptunium compounds

The electrical resistivity of four compounds of neptunium was measured between 1.4 and 295 K (Fig. 4.8). The resistivity data show anomalies at temperatures which correspond to the magnetic ordering already detected by ^{237}Np Mössbauer spectroscopy: 55 K for Np_2Ni_2Sn, 32 K for Np_2Pt_2Sn, 18 K for Np_2Pd_2Sn, and 15 K for Np_2Pd_2In. The increase of the resistivity below the magnetic ordering temperature for both Pd compounds is unexpected and remains unexplained.

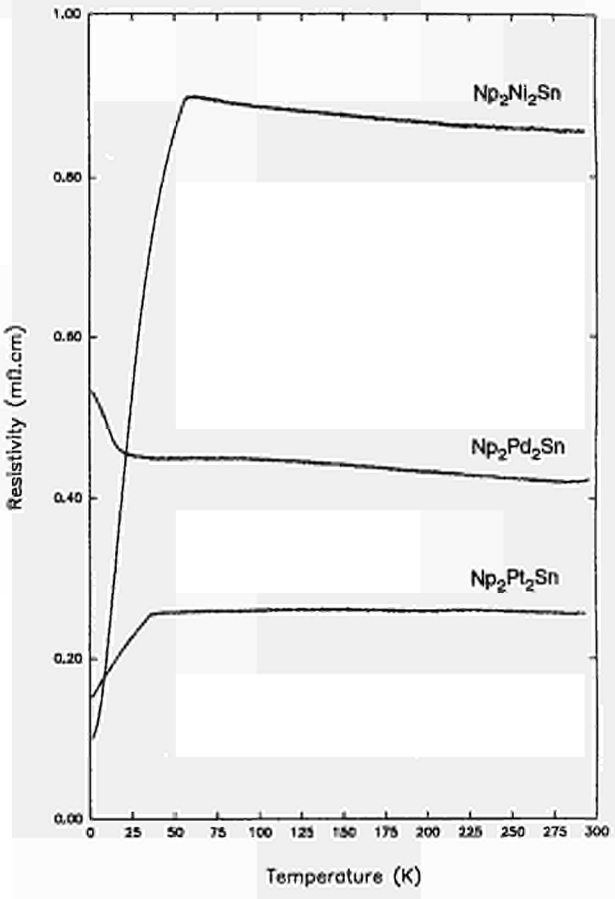

Fig. 4.8 Temperature dependence of electrical resistivity for Np_2Ni_2Sn, Np_2Pd_2Sn and Np_2Pt_2Sn.

Further work to characterise these materials with magnetisation measurements is in progress.

4.3.3 Mössbauer studies

The ^{237}Np Mössbauer spectroscopy studies, which are mainly concentrated on the study of hybridization between the 5f and ligand orbitals in the magnetic properties of Np intermetallic compounds, have progressed in cooperation with the Physik Department E15, Technische Universität München.

Investigation of $Np_xU_{1-x}Pd_2Al_3$ $(0.1 \leq x \leq 1)$

$NpPd_2Al_3$ is the Np analogue of the isostructural heavy fermion superconductor UPd_2Al_3 [1,2]. The previous studies on the x = 1 [3], 0.5 and 0.3 compounds were completed this year with the measurement of the x = 0.1 and 0.8 solid solutions.

The isomer shifts and quadrupole splittings are the same within the experimental error for all members of the series suggesting that neither the electronic state of Np (Np^{3+}, $^5I_4$) nor the electric field gradient are affected by the substitution of Np for U. However both the magnetic ordering temperatures T_{ord} and the saturated Np magnetic moments μ_{Np} similar in x = 0.8 and $NpPd_2Al_3$ were found to decrease for x < 0.8 as shown in Fig. 4.9 and in Fig. 4.6.

On the other hand the values of the quadrupole coupling constants measured below the T_{ord} of each compound

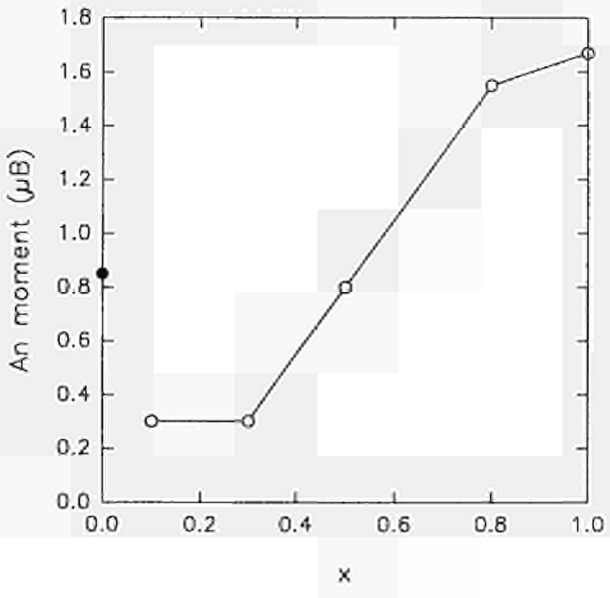

Fig. 4.9 U (closed circle) and Np (open circles) magnetic moments in the $U_{1-x}Np_xPd_2Al_3$ compounds.

suggest that the μ_{Np} are aligned along the c-axis for x = 1, 0.8 and 0.5 but are strongly deviated from this axis for the other compounds, probably lying on the ab-plane as was found for the U magnetic moments in UPd_2Al_3 [2]. Preliminary results of a neutron powder diffraction study on $NpPd_2Al_3$ seem to confirm the results deduced from the Mössbauer spectra of this compound particularly the alignment of the μ_{Np} along the c axis, see below.

The strong suppression of magnetic properties observed in the x = 0.1, 0.3 and 0.5 in comparison to the pure U- and Np- compounds may thus be related to the different anisotropic coupling of the magnetic moments in $NpPd_2Al_3$ and UPd_2Al_3.

References

[1] C. Geibel, S. Thies, S. Kaczorowski, D. Mehner, A. Grauel, B. Seidel, U. Ahlheim, R. Helfrich, K. Petersen, C. D. Bredl, F. Steglich; Z. Phys. B **83** (1991) 305

[2] C. Geibel, C. Schank, S. Thies, H. Kitazawa, C. D. Bredl, A. Böhm, M. Rau, A. Grauel, R. Caspary, R. Helfrich, U. Ahlheim, G. Weber, F. Steglich; Z. Phys. B **84** (1991) 1

[3] S. Zwirner, J. C. Spirlet, J. Rebizant, W. Potzel, G. M. Kalvius, C. Geibel, F. Steglich; Physica B **186-188** (1993) 681

Study of the $Np(Sn_xGe_{1-x})_3$ compounds with x = 0.95, 0.9, 0.8 and 0.5

In the literature the effects of the "chemical pressure" on the physical properties of actinide compounds are often compared with the effects resulting from the application of external pressure (e.g. [1]). $NpSn_3$ and $NpGe_3$ are isostructural compounds (cubic $AuCu_3$ structure type) with different cell parameters, 4.627 Å and 4.212 Å, respectively. The Np ligands, Sn and Ge, have the same external electron configurations.

The observed unit cell parameters of the $Np(Sn_xGe_{1-x})_3$ compounds follow the Vegard law, decreasing linearly with increasing x. According to the measured isomer shifts, the electron densities at the Np nuclei were found to increase with decreasing unit cell volume, as expected. However, pressure measurements of the $Np(Sn_xGe_{1-x})_3$ alloys showed that both the magnetic ordering temperature and the Np magnetic moments decreased with the decreasing unit cell volume in contrast to what was found for $NpSn_3$ under pressure up to 6 GPa [2].

These results emphasize the importance of Mössbauer measurements under pressure which cannot be replaced by the study of the effects of "chemical pressure". As far as the present study is concerned the difference in the energy- and space-distribution of the valence p electrons of Sn and Ge may have a much stronger influence on the hybridization of the 5f electrons with the conduction band than the volume reduction due to the application of external pressure. In the latter case the decrease of the isomer shifts with the unit cell volume might rather be due to the increase of conduction-band electron density at the Np nuclei rather than due to the increasing hybridization of the 5f electrons. The experimental results further suggest that $NpSn_3$ and $NpGe_3$ behave like highly correlated 5f electronic systems.

In agreement with the Mössbauer results the variation with temperature of the magnetic susceptibilities of these compounds (Curie-Weiss behaviour at high temperatures, followed by a decrease at low temperatures [3]), point to mainly localised 5f electrons, whose magnetic moments are reduced at low temperatures probably due to a Kondo mechanism or $a1_1$ electronic ground state [4]. The high value of the paramagnetic electronic specific-heat coefficient found for $NpSn_3$ [5] is consistent with a strong 5f - conduction band exchange interaction which could lead to the establishment of a Kondo resonance. High pressure resistivity measurements on this compound may show if the increase in the magnetic ordering temperature coincides with a suppression of the Kondo behaviour as was found for $NpGa_3$ [6].

References

[1] J. M. Fournier; Physica B **190** (1993) 50

[2] G. M. Kalvius, S. Zwirner, U. Potzel, J. Moser, W. Potzel, F. J. Litterst, J. Gal, S. Fredo, I. Yaar, J. C. Spirlet; Phys. Rev. Lett. **65** (1993) 2290

[3] J. P. Sanchez, M. N. Bouillet, E. Colineau, A. Blaise, M. Amanowicz, P. Burlet, J. M. Fournier, T. Charvolin, J. Larroque; Physica B **186-188** (1993) 675

[4] S. Zwirner; PhD Thesis, TU München (1994).

[5] D. D. Koelling, B. D. Dunlap, G. W. Crabtree; Phys. Rev. B **31** (1985) 4966

[6] V. Ichas, D. Braithwaite, U. Benedict, F. Wastin, A. Moens, J. C. Spirlet; 24^{ièmes} Journées des Actinides (1994)

4.3.4 Synthesis and spectroscopic studies of actinide layers

Introduction

The study of layers of actinides and actinide compounds is interesting both from a practical and a fundamental point of view. Even though they contain only a minute amount of actinide material, many of the chemical and solid-state physical properties of layers are already representative for the bulk. As such, they allow the chemical interaction of solid actinide compounds (e.g. metals, alloys, oxides, carbides) with surrounding materials such as fuel claddings or waste containers to be investigated. Because of the small thickness of overlayers, from below one monolayer to several micrometers, surface spectroscopy can penetrate them and give detailed information on the interface between the actinide phase and the substrate. Interface stability and dissolution, surface corrosion and bulk diffusion of actinides and fission products may be investigated on such systems [1]. From a more funda-

mental point of view, layers allow those solid state properties which are related to the high correlation of the 5f-electrons to be accentuated. The lowered coordination in layers (ranging from two dimensional bonding to quantum isolation) generally results in a narrowing of valence bands, and for the 5f bands, which are already narrow in bulk compounds, this may even result in breakdown of the delocalization. Heavy-fermion properties or the Kondo effect, both related to the 5f electrons at the threshold of localization-delocalization, can thus be investigated in layers.

Future projects associated with layer research include synthesis of multilayers, ion beam mixing for preparation of non-stoichiometric compounds, replicate preparation for surface spectroscopy studies of materials with poor mechanical properties or relatively low chemical purity.

Study of layers of uranium on graphite

X-ray and Ultra-Violet Photoelectron Spectroscopy (XPS and UPS) have been used to study layers of U from below one monolayer to several monolayers deposited on graphite. Graphite was chosen because it is an inert material and it was hoped that U would not interact strongly with it. It was the intention to investigate band-narrowing effects in U layers and eventually U clusters. In addition, the high-temperature reaction between U and graphite was studied. In Fig. 4.10, U4f spectra of U below and above monolayer coverage are compared. The U4f emission of a U layer of 3.5 monolayers thickness is typical for bulk U. It is sharp and asymmetrical with a binding energy (BE) of 388.7 eV. Below monolayer coverage the U4f lines broaden, developing small peaks on their high BE side, which is typical for emissions from small surface clusters. The peak at 6 eV higher BE is attributed to a correlation satellite, as typically observed in U systems with highly correlated 5f electrons [2]. These findings suggest that at very low coverage the U5f electrons at least approach the localization threshold. UPS data corroborate this view. The He^{II} spectrum of a 3.5 monolayer coverage (Fig. 4.11) shows the sharp U5f peak right at the Fermi-level (E_F). At low coverage the maximum is shifted to higher BE and a small satellite appears as 0.5 eV BE. Both features have been observed on $U(PdPt)_3$ ternary alloys where the 5f correlation could be gradually enhanced by increasing the Pd concentration [3].

Above 550 K, U layers react with graphite to form UC. This is indicated by the appearance of a strong C1s signal at 282 eV BE (not shown), which is characteristic for carbidic carbon. The U4f (Fig. 4.12) shifts to 0.5 eV higher BE, becomes symmetrical and develops shake-up satellites at 6 eV higher BE. All these features are characteristic for UC [4]. UPS spectra do not agree with published values [5]. It can be agreed that these latter values were

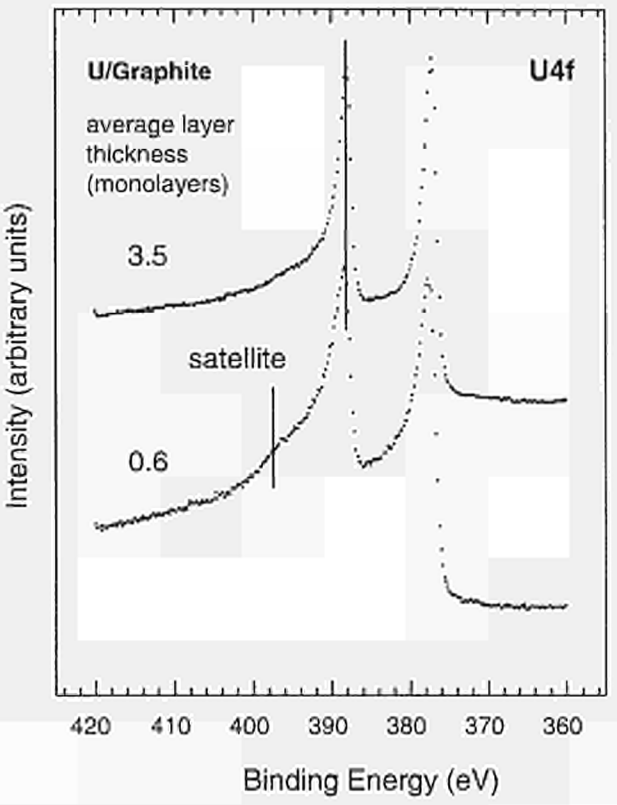

Fig. 4.10 U4f spectra of U layers on graphite.

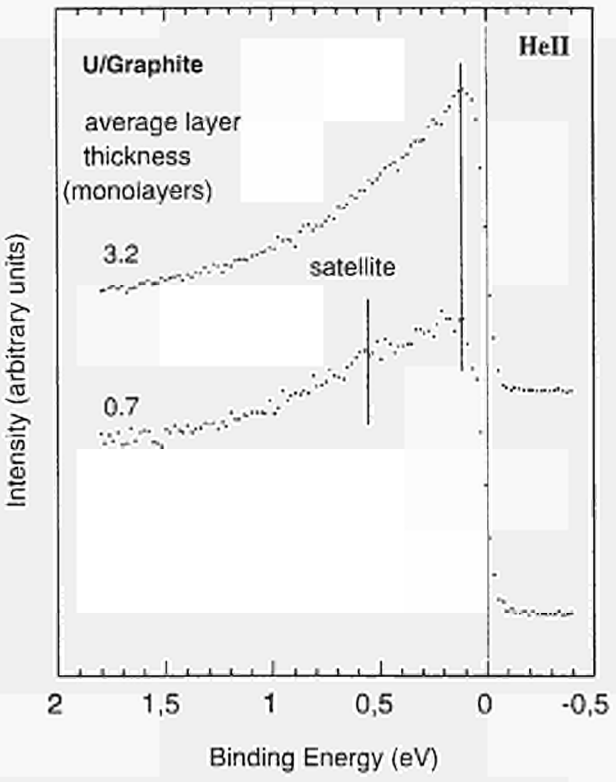

Fig. 4.11 UPS-HeII spectrum of U layers on graphite.

derived from surfaces contaminated with UO_2. Our data confirm band structure calculations of UC [6] and show U to have metallic character with the U5f level lying close at E_F. In addition they reproduce well published XPS valence band spectra of UC [4].

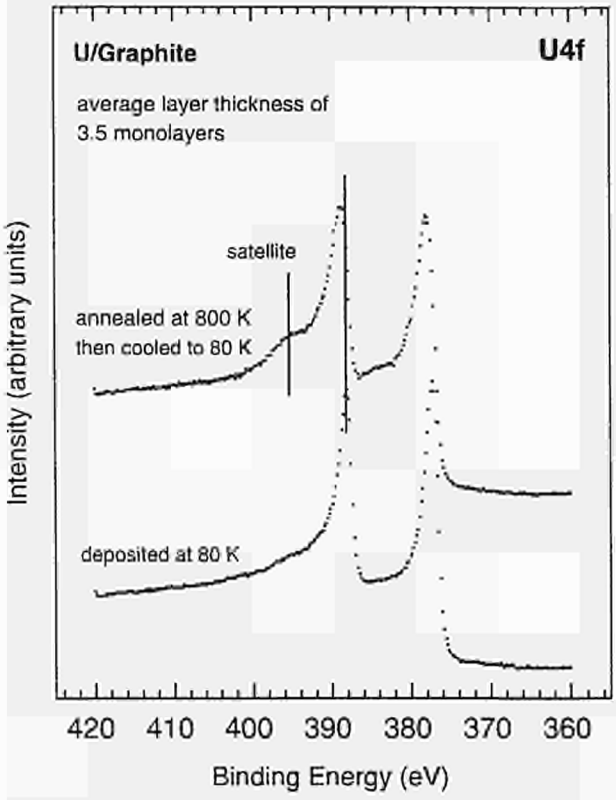

Fig. 4.12 U4f spectra of U layers on graphite before and after annealing at 800 K.

Other activities

- Layers of UO_2 have been prepared for Rutherford Back Scattering (RBS) studies of fission-product diffusion at the "Centre de spectrométrie nucléaire et de spectrométrie de masse" in Orsay. This activity is part of a collaboration with the group of applied physics. In contrast to conventional UO_2 bulk samples, layers allow RBS to detect light elements even at very small concentrations, because the multiple scattering loss tail associated with the U edge is missing. Samples of 400 Å to 1000 Å thickness were prepared by sputter deposition. Their purity was checked by XPS and Auger Electron Spectroscopy (AES). Subsequent annealing in a CO/CO_2 atmosphere yielded stoichiometric UO_2 layers.

- AES have been started on SIMFUEL pellets (97 % UO_2, 3 % simulated burn-up elements) as part of a study on the leaching of fission products. This activity is part of a collaboration with the group of applied physics. Measurements were first made on an unleached sample to determine whether the AES facility on our instrument is sensitive enough to detect the relevant elements at 0.1 to 1 at % concentrations. While not all fission products may be detected by AES, either because of small signal intensities or because of signal overlap with U, many of the fission products could be seen, e.g. Ba, La, Ce and Nd with 0.147, 0.106, 0.285 and 0.460 at%, respectively. Measurements of leached samples are planned for the future.

- XPS was used to study the surface oxidation of sintered UO_2 pellets by anodic polarization. These measurements are part of a collaborative study on the dissolution of nuclear waste in ground water. The process is accelerated for laboratory studies by polarizing UO_2 samples to a positive potential in various electrolytic environments (chlorides, carbonates). We used XPS to detect possible surface oxidation, averaged over the analysis spot of our spectrometer (2 by 8 mm). Samples were sputtered slightly to remove most of the chemisorbed surface impurities (water, CO_2, etc.) while avoiding, however, damaging the UO_2 surface itself (a safe amount of impurities was left at the surface). Fig. 4.13 shows an ex-

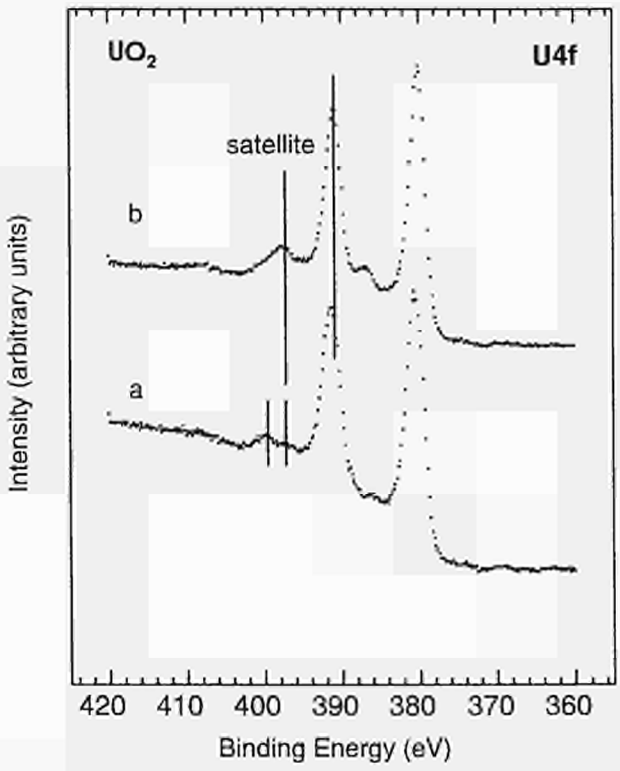

Fig. 4.13 XPS U4f spectrum of UO_2 pellets: a) slight sputtering leaving the surface intact; b) heavy sputtering reducing the surface to UO_2.

ample of a UO_2 pellet polarized at 842 mV for 17 hours in 3% Na_2CO_3 after slight (Fig. 4.13a) and after heavy (Fig. 4.13b) sputtering. After heavy sputtering the $U4f_{7/2}$ level lies at 391.4 eV, which is typical for stoichiometric UO_2. After slight sputtering the peak is shifted to 0.4 eV higher BE indicating further oxidation of UO_2 to hyperstoichiometric UO_{2+x} ($x \cong 0.13$). Surface oxidation is also shown by the satellite at high BE , which after slight sputtering consists of two small peaks (Fig. 4.13a) [7] typical for hyperstoichiometric UO_{2+x}, and after heavy sputtering has BE and shape characteristic for stoichiometric UO_2.

References

[1] T. Gouder and C.A. Colmenares; UCRL report 10-118664, Oct. 27 1994

[2] A. Grassmann; Physica B **163** (1990) 547

[3] A. J. Arko, D. D. Koelling, B. D. Dunlap, A. W. Mitchell, C. Capasso, M. del Giudice; J. Appl. Phys. **63** (1988) 3680

[4] J. G. Dillard, H. Moers, H. Klewe-Nebenius, G. Kirch, G. Pfennig , H. J. Ache; J. Phys. Chem. **88** (1984) 5345

[5] M. Erbudak and J. Keller; Z. Physik B **32** (1979) 281

[6] M. S. S. Brooks; J. Phys. F **14** (1984) 639

[7] Yu. A. Teterin, V. M. Kulakov, A. S. Baev, N. B. Nevzorov, I. V. Melnikov, V. A. Strelsov, L. G. Mashirov, D. N. Suglobov, A. G. Zelenkov; Phys. Chem. Minerals **7** (1981) 151

4.3.5 Calculated bulk, magnetic and spectroscopic properties of uranium sulphide as a function of lattice constant: seven experiments, one theory

US has a relatively small lattice constant of 5.47 Å and a correspondingly high bulk modulus [1]. We have used self-consistent, ab initio, energy band calculations [2] to calculate the zero temperature equation of state for US and the results are shown in Fig. 4.14a. For a paramagnetic ground state the calculated lattice constant is 5.35 Å whereas for a magnetic ground state it increases to 5.43 Å, the difference being a magnetovolume effect.
Not only is the calculated lattice constant within 1% of the measurements but the bulk modulus is accurate to better than 10%.

US becomes ferromagnetic below 177 K with a zero temperature moment of 1.55 μ_B [3]. Under pressure, the Curie temperature decreases by -0.23 K/kbar [4]. The calculated spin moment as a function of lattice constant is shown in Fig. 4.14b, which is the magnetic equation of state with spin-orbit interaction absent. The sizeable drop in the moment as the lattice constant is reduced to 5.2 Å is responsible for the reduction of the magnetovolume effect at high pressures seen in Fig. 4.14a.

There is ample evidence that US has, although it is cubic, enormous magnetic anisotropy at low temperatures [5]. The anisotropy is due to a relativistic effect - a large spin-orbit interaction which couples the spin, via an orbital moment, to the lattice. In light actinides the orbital moment is antiparallel to the 5f spin moment. The conduction electron moment is known to be antiparallel to the total moment from a comparison of the measured relative magnitudes of 5f and total moments in neutron scattering and magnetization experiments [3,6], from the interpretation of spin polarized photoemission experiments on uranium chalcogenides [7] and deduced from magneto-optical spectroscopy [8].

We have calculated the magnetic equation of state including spin-orbit coupling and interaction between the orbital moments ab initio and the results are shown in Fig. 4.14c. In the presence of both spin polarization and spin-orbit interaction there is a net current, and it is from this current that the orbital moment arises. We calculate a spin moment of $\mu_S = -2.10\ \mu_B$ and an orbital moment of $\mu_L = 3.60\ \mu_B$ at ambient pressure leading to a total moment of 1.5 μ_B in excellent agreement with measurements [3].

In addition to the above mentioned integrated bulk properties the theory produces the actual spin and orbital moment densities in the solid. These densities are measured in neutron diffraction experiments and the normalized Fourier transform of the total magnetization density is the magnetic form factor.

The calculated magnetic form factor of US is shown in Fig. 4.14d where it is also separated into its spin and orbital contributions. Again, agreement with measurements [6] is excellent and the difference between the spin and total contributions demonstrates the importance of the orbital moment.

We have calculated the interband reflectivity of US up to 12 eV and compared with the measurements [9]. The results are shown in Fig. 4.15. The calculated results are shown for two values of lifetime broadening (0.27 and 0.4 eV). The overall agreement between theory and experiment is good. The reflectivity decreases from about 60 per cent at 1 eV to about 20 per cent at 4.5 eV with a shoulder (marked B in Fig. 4.15a) at about 3 eV. The calculated reflectivity has this shoulder in the same place in Fig. 4.15c whereas it is a peak in the less broadened Fig. 4.15b. The measured reflectivity subsequently rises to about 35 per cent with several features between 5 and 9 eV. The calculated reflectivity is too high, but not by much, at 4.5 eV and some of the features around 7 eV are missing but the shoulder (labelled C,D) in Fig. 4.15a) is obtained. Finally the calculated reflectivity is too large at high energies, rising to 60 % at 10 eV compared with a measured 40 %. The change in reflectivity as a function of lattice constant is also shown in Fig. 4.15d,e. The low energy peak diminishes with decreasing lattice constant and the low reflectivity at 4 eV is increased.

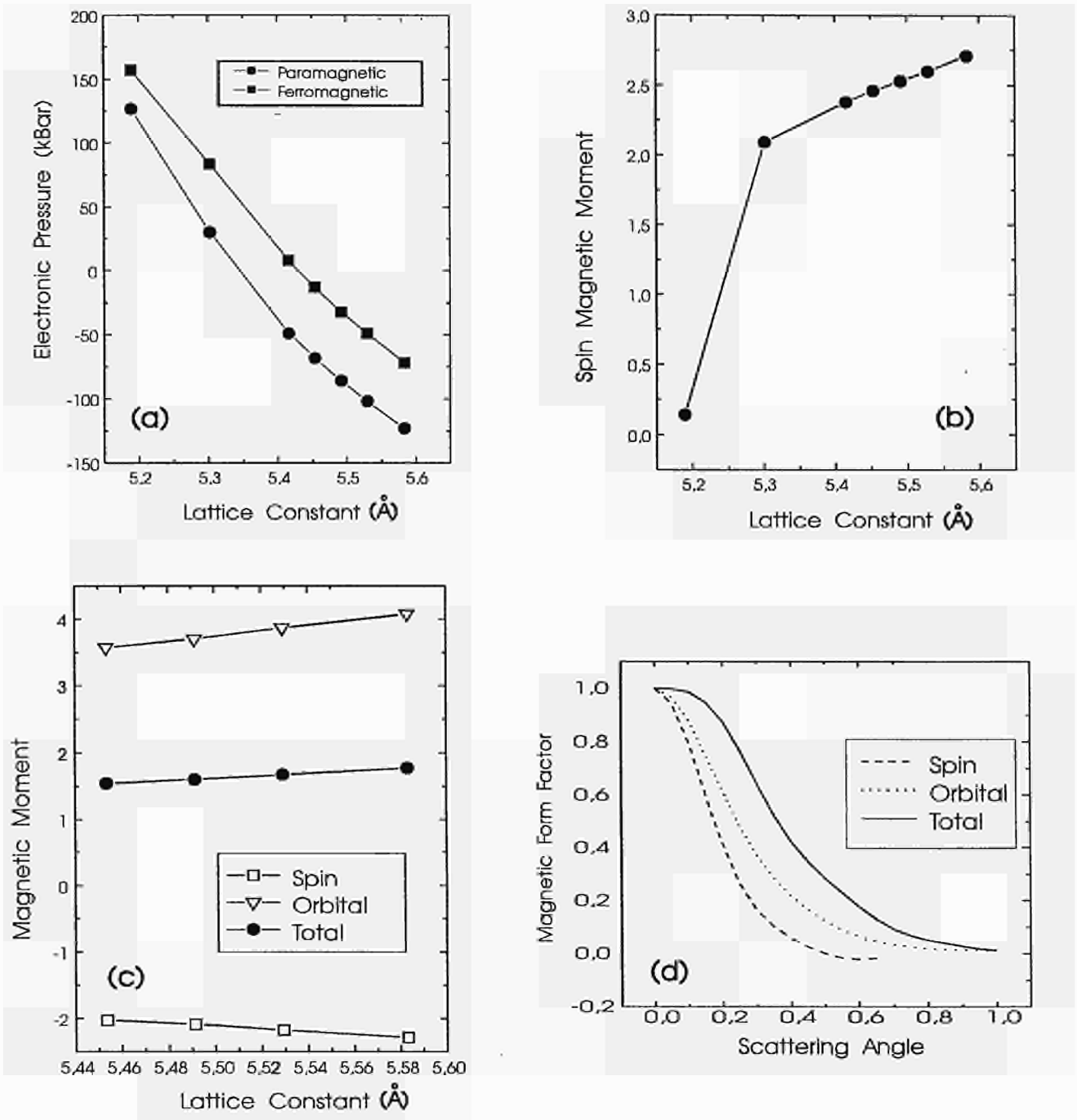

Fig. 4.14 Calculated Ground State Properties of US. (a) Electronic equation of state, (b) Magnetic equation of state with spin-orbit interaction omitted, (c) Magnetic equation of state with spin-orbit interaction included, (d) calculated magnetic form factor.

The magneto-optical Kerr effect, or complex rotation of plane polarized light upon reflection, has been measured by Reim and Schoenes [8] for US and is shown in Fig. 4.16a. The most noticeable feature of the energy dependence of both real and imaginary parts of the Kerr angle is its simplicity. There is a pronounced broad resonance at just under 2 eV with a shoulder at about 3 eV. Measurements [8] for the other uranium chalcogenides USe and UTe are similar, with the shoulder closer to the main resonance. The imaginary part of the Kerr angle, or ellipticity, has the energy dependence of the imaginary part of a double resonance with resonant energies at about 2 and 3 eV. In fact we can reproduce both parts of the Kerr angle by modelling the system with two broadened oscillators at 2 and 3 eV. US is an extremely hard magnet at low temperatures [5], so hard that it is impossible in realizeable applied fields to move the magnetic moment from the ‹111› easy direction. Since crystals of US can only be

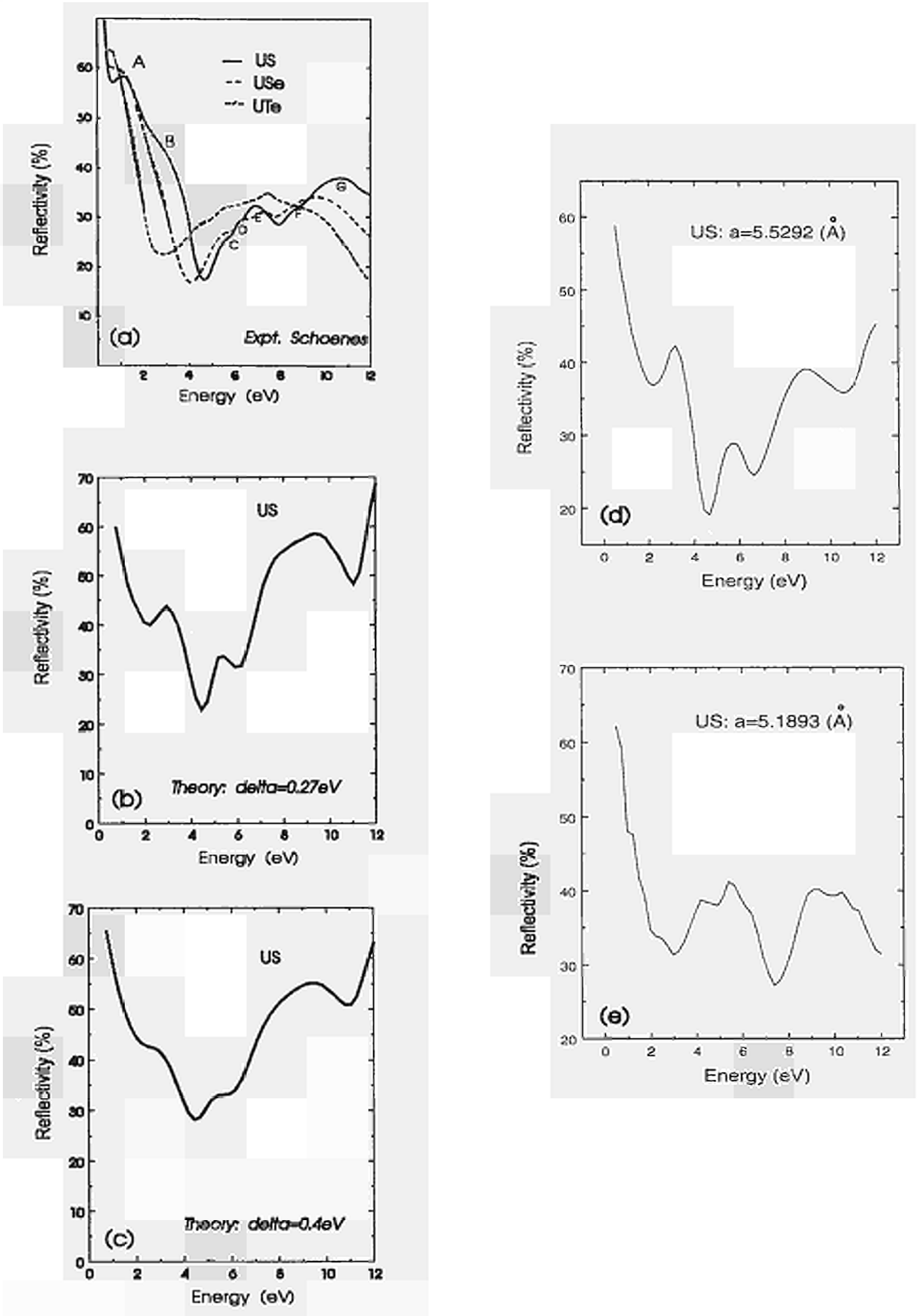

Fig. 4.15 Reflectivity of US: (a) Measurements, (b) and (c) Calculated using different lifetime broadening, delta (d) and (e) the effect of reducing the lattice constant.

cleaved along ‹100› and symmetry related faces, it is actually impossible to measure the polar Kerr effect at low temperatures. The Kerr effect from a [100] face with the moment along a [111] direction was measured, but theorists have programmed for the polar Kerr effect which corresponds to a [111] face. Despite this discrepancy in geometry, the general features of the Kerr rotation in uranium compounds remain universal enough for us attempt a direct comparison with experiment. The results of Kerr rotation calculations for two different values of lifetime broadening (delta = 0.4 eV and 0.5 eV) are shown in Fig. 4.16b and Fig. 4.16c.

The wavelength of light used in the magnetic Kerr effect is in the eV range and the electronic transitions are between valence electron states. This energy range is particularly convenient for modern lasers which is why the Kerr effect is used to read in magneto-optic recording. The difference in absorption between left and right circularly polarized light is called magnetic circular dichroism. The incident radiation normally used in dichroism experiments is in the X-ray region and the electronic transitions are from core states. The interpretation of recent magnetic circular dichroism experiments at synchrotron light sources is that there should be a relationship between the orbital magnetic moment and the magnitude of the dichroism. In Fig. 4.17 is shown the calculated dichroism spectrum for transitions from the 3d M4 and M5 edges in US. The vertical line at 9eV represents the position of the Fermi energy and transitions are only allowed into the empty states above this energy. In experiments, therefore, only the region to the right of the vertical line is observed. Inspection shows that the sum of the M4 and M5 edge contributions is indeed similar to minus the calculated orbital state density. In experiments the integrated intensity summed over both edges therefore yields the total orbital magnetic moment.

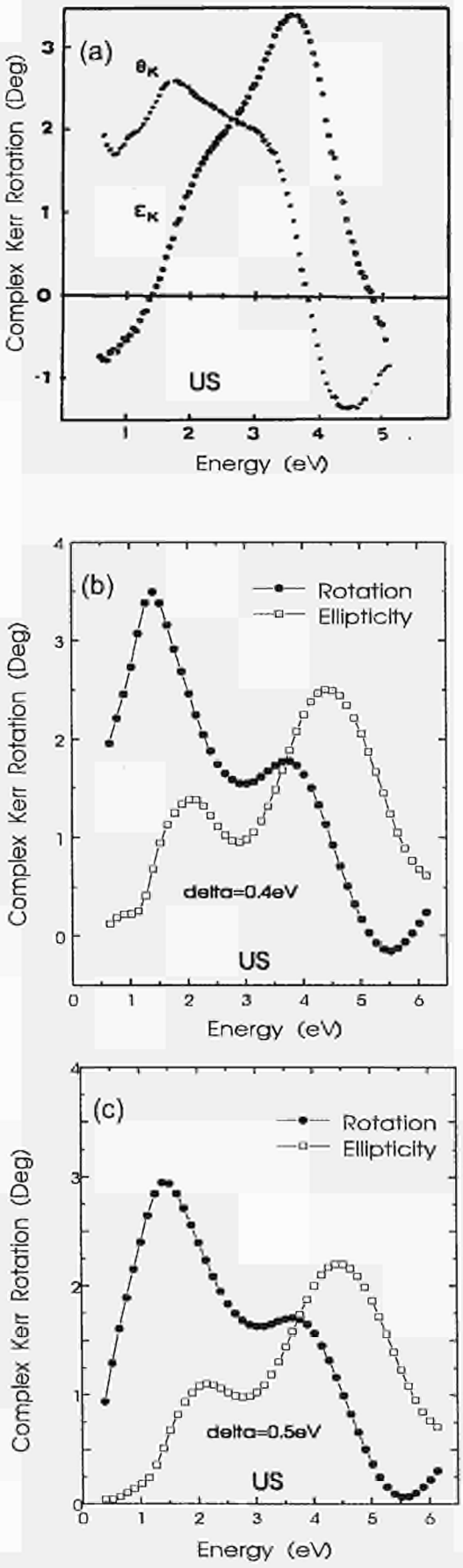

Fig. 4.16 Magneto-optical Kerr Rotation in US: (a) Measurements (b) and (c) calculated using different lifetime broadening, delta.

References

[1] L. Gerward, S.J. Olsen, U. Benedict, S. Dabos, O. Vogt; High Pressure Res. 1 (1989) 235

[2] O.K. Andersen; Phys. Rev. bf B**12** (1975) 3060; H. L. Skriver, in Muffin Tin Orbitals and Electronic Structure, Springer Verlag, Heidelberg, 1983

[3] W. E. Gardner and T. F. Smith; in D.M. Finlayson , D. M. McCall (eds.), Proc. 11'th Int. Conf. on Low Temp. Phys., vol. **2** (1968) 1377

[4] C. Y. Huang, R.J. Laskowski, C.E. Olsen, J.L. Smith; J. de Physique **40** (1979) C4-26

[5] G. H. Lander, M. S. S. Brooks, B. Lebech, P. J. Brown, O. Vogt, K. Mattenberger; J. Appl. Phys. **69** (1991) 4803

[6] F.A. Wedgwood; J.Phys **C5** (1972) 2427; F.A. Wedgwood and M. Kuznietz; J.Phys **C5** (1972) 3012

[7] W. Eib, M. Erbudak, F. Greuter, B. Reihl; Phys. Letts. **68A** (1978) 391; M. Erbudak, F. Meier; Physica **102B** (1980) 134

[8] W. Reim, J. Schoenes; in E.P. Wohlfarth and K.H.J. Buschow (eds.), Ferromagnetic Materials (North Holland 1990) vol. **5**

[9] J. Schoenes; Physica **102B+C** (1980) 45

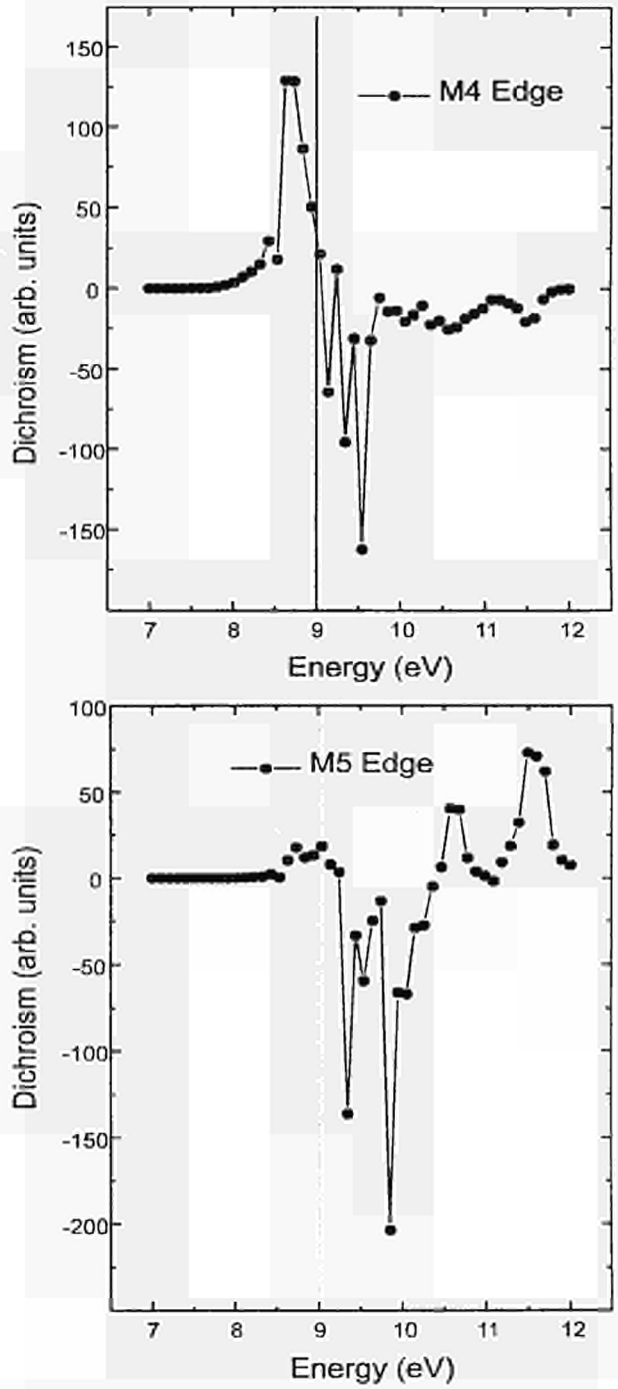

Fig. 4.17 The calculated magnetic circular dichroism for US for transitions from the M4 and M5 edges.

4.3.6 Neutron and X-ray magnetic scattering

Introduction

Neutron experiments were performed this year in the reactors at Siloë (Grenoble), Risø (Denmark) and Saclay (Paris), and at the ISIS (UK) spallation source. Major progress was made in understanding the magnetic response in UFe_2. In connection with our research on heavy-fermion and related materials, we have continued our work on single crystals of UPd_2Al_3, and succeeded in performing neutron experiments on polycrystalline samples of $NpBe_{13}$ and $NpPd_2Al_3$.

The magnetic X-ray scattering continued at the Brookhaven synchrotron with experiments on USb and $USb_{0.8}Te_{0.2}$. The installation of a more elaborate security system will, we hope, allow work on Pu compounds to be performed in 1995. New experiments using the M_{IV} resonance of uranium were successful in seeing scattering from an antiferromagnetic surface (of UO_2) for the first time. Our first experiments at the European Synchrotron Radiation Facility (ESRF) succeeded in observing non-resonance magnetic scattering, and this is a promising area for further effort.

Neutron studies of intermetallic compounds

Structural studies

Our studies of UPd_2Al_3 single crystals, which were produced at the University of Tohoku, Sendai, Japan, have continued with a number of both neutron and X-ray experiments. This is a heavy-fermion material that becomes antiferromagnetic at ~15 K and superconducting at ~1.5 K, so that there is much topical interest in its properties. In a series of experiments to measure the AC susceptibility of this material (carried out at the University of Ancona, Italy) we have discovered a large anomaly at ~240 K. This is shown in Fig. 4.18. The effect is dependent on frequency, and has been found on two samples of different nominal stoichiometry. No anomaly occurs in the AC resistivity. Efforts to understand the microscopic cause of this anomaly have included neutron experiments at the ISIS spallation source (UK) and X-ray Laue experiments at both LURE (Orsay) and the ESRF (Grenoble) synchrotrons, as well as a number of laboratory X-ray experiments. No evidence for a microscopic phase transition involving the lattice structure has been found, but diffuse X-ray scattering does suggest that defects (or interstitials) are present in this hexagonal layer structure, and it is these that are giving rise to the anomalies in the AC susceptibility. A similar effect has been postulated for the isostructural cerium compound.

The critical magnetic scattering from UPd_2Al_3 has been examined at the Siloë reactor (CEN, Grenoble). Because of the co-existence of superconductivity and antiferromagnetism at low temperature, there is interest in the precise form of the magnetic interactions. In the critical regime just above the ordering temperature ($T_N = 15.5$ K), the remaining short-range correlations give valuable information on these interactions. For example, in Fig. 4.19, it may be seen that the transverse ($k \perp c$) scattering

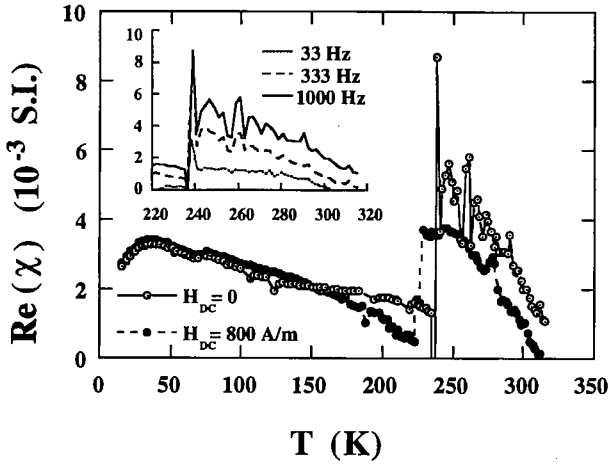

Fig. 4.18 The real component of the susceptibility χ' measured (at Ancona) during heating from 15 K for a single crystal of composition $UPd_2Al_{3.06}$ oriented with the hexagonal c axis perpendicular to the field of H_{ac} = 800 A/m (10 Oe) for two different applied DC fields. The frequency of the AC field f=667 Hz. The insert shows χ' above 200 K for different frequencies of the AC field at H_{dc}=0.

is much wider in spatial extent than the longitudinal scattering (k || c). This means that the magnetic correlations are weaker in the planes perpendicular to the unique c hexagonal axis than they are parallel to the c axis. Since the crystal structure is planar, this is an unexpected result; the assumption being that the transverse correlations are the stronger. Measuring these interactions more completely may allow a better understanding of why the superconductivity and magnetism can co-exist in this material.

To extend our research into the transuranium materials that are related to heavy-fermion uranium compounds, we have performed neutron diffraction (at the Siloë reactor, CEN, Grenoble) on polycrystalline samples of $NpBe_{13}$ and $NpPd_2Al_3$, both of which were prepared at ITU. Magnetic order has been found in both compounds; we shall describe here the results of the study on $NpBe_{13}$. The powder-diffraction spectra, and their difference, are shown in Fig. 4.20. The ordering temperature, T_N = 4.2 K, is in good agreement with the results of the Mössbauer studies performed at ITU. The magnetic peaks can be indexed on a commensurate unit cell 3 times larger than the chemical unit cell, thus k = (0, 0, 1/3). The presence of the first peak shows that there is a component of the spin direction transverse to the propagation direction. With the statistics of the present experiment, it is difficult to say if the magnetic arrangement is a square-wave (which would involve weak 3rd-order harmonics) or a simple sine-wave modulation. However, the Mössbauer results show that there are at least two different hyperfine fields present, suggesting that the modulation is not a square wave even at the lowest temperature. The amplitude of the modulation determined from the neutron data is 1.5(2) μ_B, which is slightly larger than that determined from the Mössbauer experiments. Interestingly, the rare-earth Be_{13} compounds also exhibit the k = (0, 0, 1/3) magnetic structure, but with a different arrangement of the individual moments than found in $NpBe_{13}$. This suggests that there is a definite maximum in the conduction-electron susceptibility at this position, and that this is a property of the crystal structure and the Be conduction electrons. This information will be useful for further experiments on UBe_{13}. We are hopeful that experiments on single crystals of $NpBe_{13}$ can also be performed.

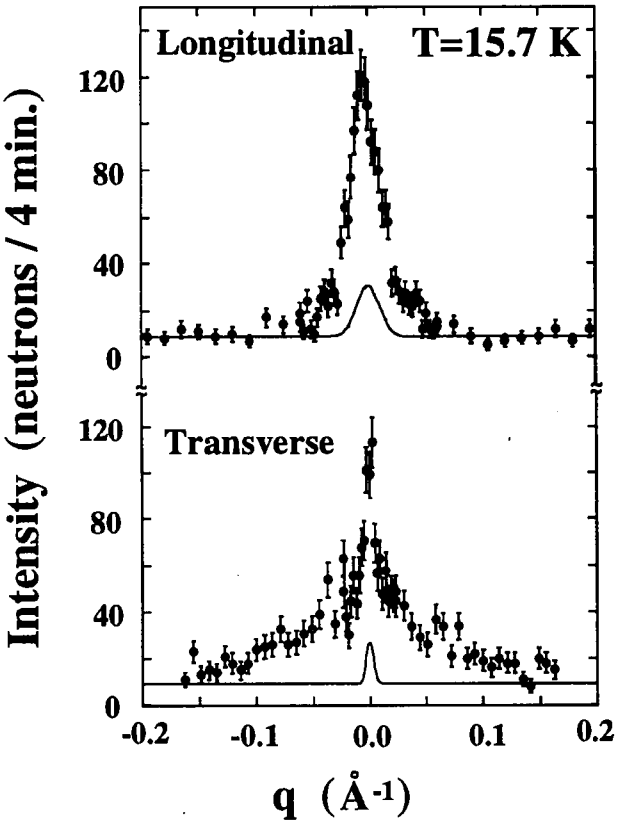

Fig. 4.19 The critical magnetic scattering around the point (0, 0, 1/2) just above the ordering temperature (T_N = 15.5 K) from a single crystal of UPd_2Al_3 in two perpendicular directions. The upper graph shows the longitudinal scan (k || c) and the lower one the transverse scan (k ⊥ c). In each case the solid line is the high-temperature background, the small resolution-limited peak arising from second-order scattering from the strong (001) nuclear reflection. Data taken at the Siloë reactor, CEN, Grenoble.

Dynamical studies

UFe_2 is a ferromagnet with T_C = 165 K, and a strong interaction occurs between the uranium 5f and iron 3d electrons. To understand this interaction we have been

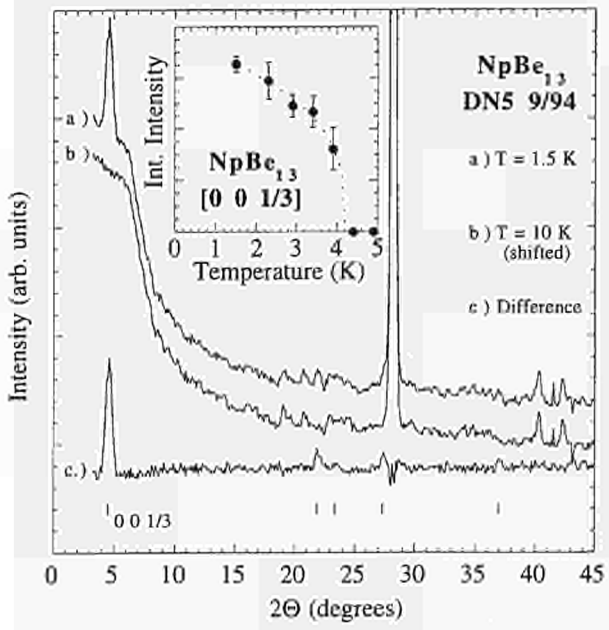

Fig. 4.20 Neutron-diffraction spectra from a polycrystalline sample of $NpBe_{13}$ taken at the Siloë reactor, CEN, Grenoble. The sharp rise in the scattering at low angle in the raw data is because of background from the forward beam. This is eliminated by taking the difference spectra (c). The temperature dependence of the first peak is shown in the inset, giving a T_N = 4.2 K.

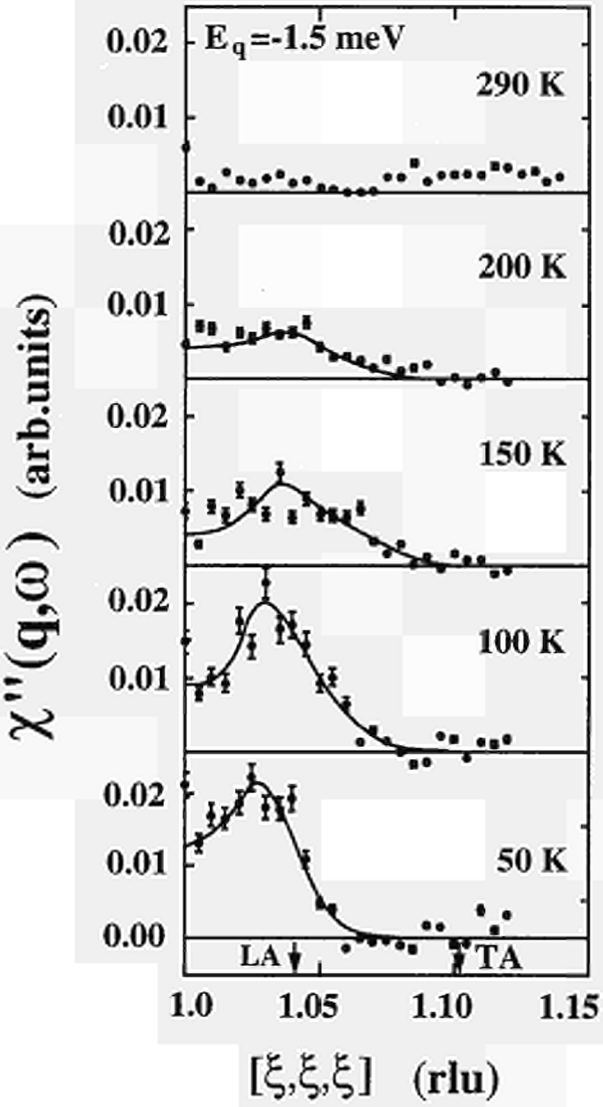

Fig. 4.21 Evolution of the magnetic response associated with the iron spins in the compound UFe_2 as a function of temperature. Experiments performed on triple-axes spectrometers at Risø National Laboratory, Denmark and CEN, Grenoble reactors. Notice how the response changes its form near T_C (=165 K), but does not completely disappear. The function plotted $\chi'(q, \omega)$ takes account of the thermal population of the states.

engaged in experiments to characterize the dynamic (inelastic) response of both the phonons and magnons in a large single crystal of this material. We reported on the phonons in the TUAR-93, p. 139. We show in Fig. 4.21 the magnetic response associated with the precession of the Fe spins. The dispersion curve at T=100 K is shown in Fig. 4.22. These studies show that the iron sublattice is little changed from that in pure iron. Apart from the small gap of 0.7(1) meV due to the anisotropy, the dispersion curve is similar in its curvature to that found in pure iron. In addition, the positive response shown above T_C in Fig. 4.21 is an indication of the itinerant nature of these d electrons. However, we have not yet succeeded in characterizing completely the response from the uranium f electrons. First, there is no 'local' mode, equivalent to a crystal-field excitation, as seen in the isostructural rare-earth compounds. This is not surprising. More interesting is the acoustic spin wave, which is at low energy and apparently interacts strongly with the transverse acoustic phonons. Our results appear capable of explaining the important magneto-elastic interactions that have been observed in a number of measurements, e.g. the elastic constants, on this material. To separate the phonon and magnon response at low energy we need polarized neutrons, and the higher intensity available at the ILL, Grenoble, which is operating again.

X-ray magnetic scattering

Studies of the critical magnetic scattering

The studies of the critical scattering using resonant magnetic scattering that were reported last year on NpAs have now been extended to USb and $USb_{0.8}Te_{0.2}$. We shall describe some features of the latter study. One important aspect of the X-ray experiments is that the instrumental resolution is considerably better, by a factor of five or

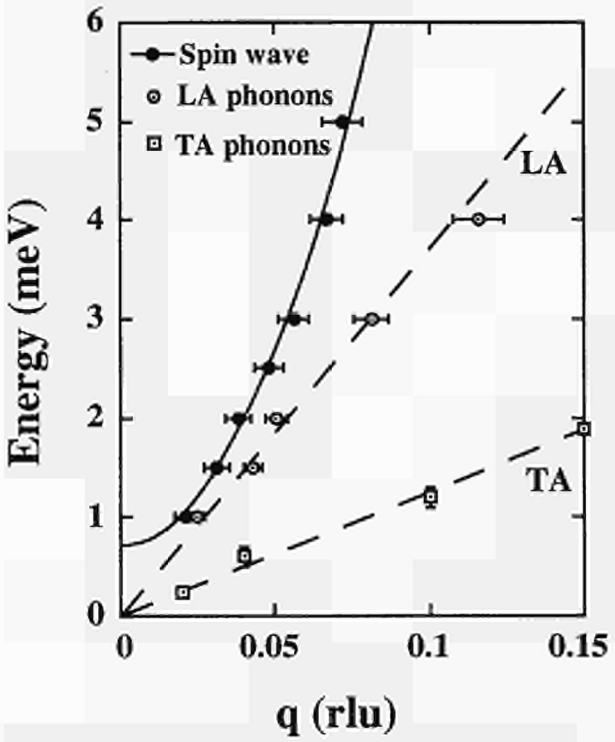

Fig. 4.22 Dispersion curves for UFe_2 at T=100K. The solid line corresponds to the magnetic optic Fe mode, with a dispersion close to that observed in elemental iron. The dashed lines correspond to phonons. The lower-energy magnetic mode is close in energy, and probably mixed with, the transverse acoustic (TA) phonon.

more, than that available in conventional neutron experiments. Frequently, this allows new information to be obtained. An example is given in Fig. 4.23. Here we show the full-width at half maximum for the critical scattering peaks as a function of temperature. The ordering temperature T_N, where on warming the widths suddenly increase, is about 207 K. However, note that the narrowest widths are actually observed at T_N and that these are significantly wider than the X-ray resolution. Furthermore, below T_N the widths of the magnetic peaks actually increase. Neither of these latter two points can be seen with neutron experiments (performed on the same material at Risø National Laboratory, Denmark) because the resolution is not sufficient. An understanding of why the peaks increase below T_N requires a consideration of the coupling between the magnetic moments and the underlying lattice. A more complete study of these effects is being undertaken on USb. An analysis of the critical magnetic scattering in $USb_{0.8}Te_{0.2}$ has now been completed, and shows reasonable agreement between the neutron and X-ray investigations. There is, surprisingly, no sign of a sharp extra component in the X-ray data, such as was found for NpAs, Ho, Tb, etc. We believe this is related to the lack of complete long-range order in the antiferromagnetic structure. Although the atomic sizes of Sb and Te are very similar (they are neighbouring elements in the periodic table), their valence-band structures are quite different. This implies that the disturbance caused by a Te "impurity" in the magnetic exchange is considerable, and leads to a lack of long-range coherence, whereas this is not the case in the atomic structure, which is governed simply by size effects.

Non-resonant magnetic scattering

The non-resonant magnetic scattering of X-rays has a small cross-section, but it contains valuable information, particular if the polarization of the scattering can be measured. Our main goal in trying to develop this technique is to use the fact that the magnetic scattering can probe the spin and orbital contributions to the magnetism independently. This is a problem of considerable current interest in research on 5f materials. However, in the case of uranium-based materials the non-resonant scattering is about 10^{-5} of the resonant scattering, so it is only at the third-generation X-ray synchrotrons, such as the ESRF in Grenoble, that we can contemplate such measurements. Fig. 4.24 gives the results of our first measurements in April 1994. Non-resonant scattering was observed. Because of the absence of a mirror to remove higher-order contamination (now installed) we had to work with an incommensurate system, and chose the same one as examined at Brookhaven, $USb_{0.8}Te_{0.2}$, although the magnetic structure of this is rather complicated. Satellite peaks were seen about the (0,0,4) reflection and are shown in panel (a). In panel (b) the results of polarization analysis of the (0,0,4+τ) satellite peak are shown. Most of the signal is in the $\pi \rightarrow \pi$ channel, which is a puzzling result.

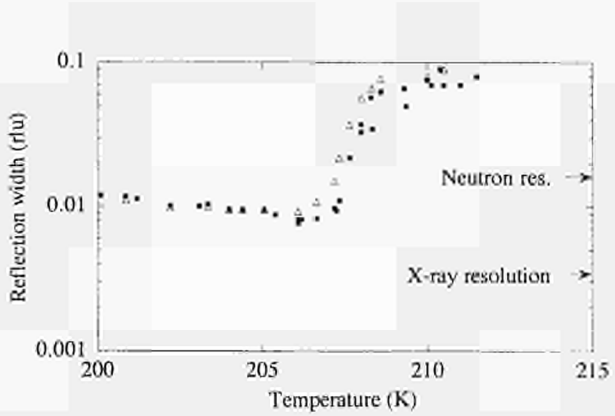

Fig. 4.23 The experimental data for the full-width at half maximum of the magnetic peaks as a function of temperature for a single crystal of $USb_{0.8}Te_{0.2}$ as measured on the X22C spectrometer at the Brookhaven synchrotron with photons at the uranium M_{IV} resonance of 3.73 keV. The different symbols refer to measurements on different satellite peaks. Notice the substantial difference between the X-ray and neutron resolutions, and the fact that the peaks are always wider than the X-ray resolution.

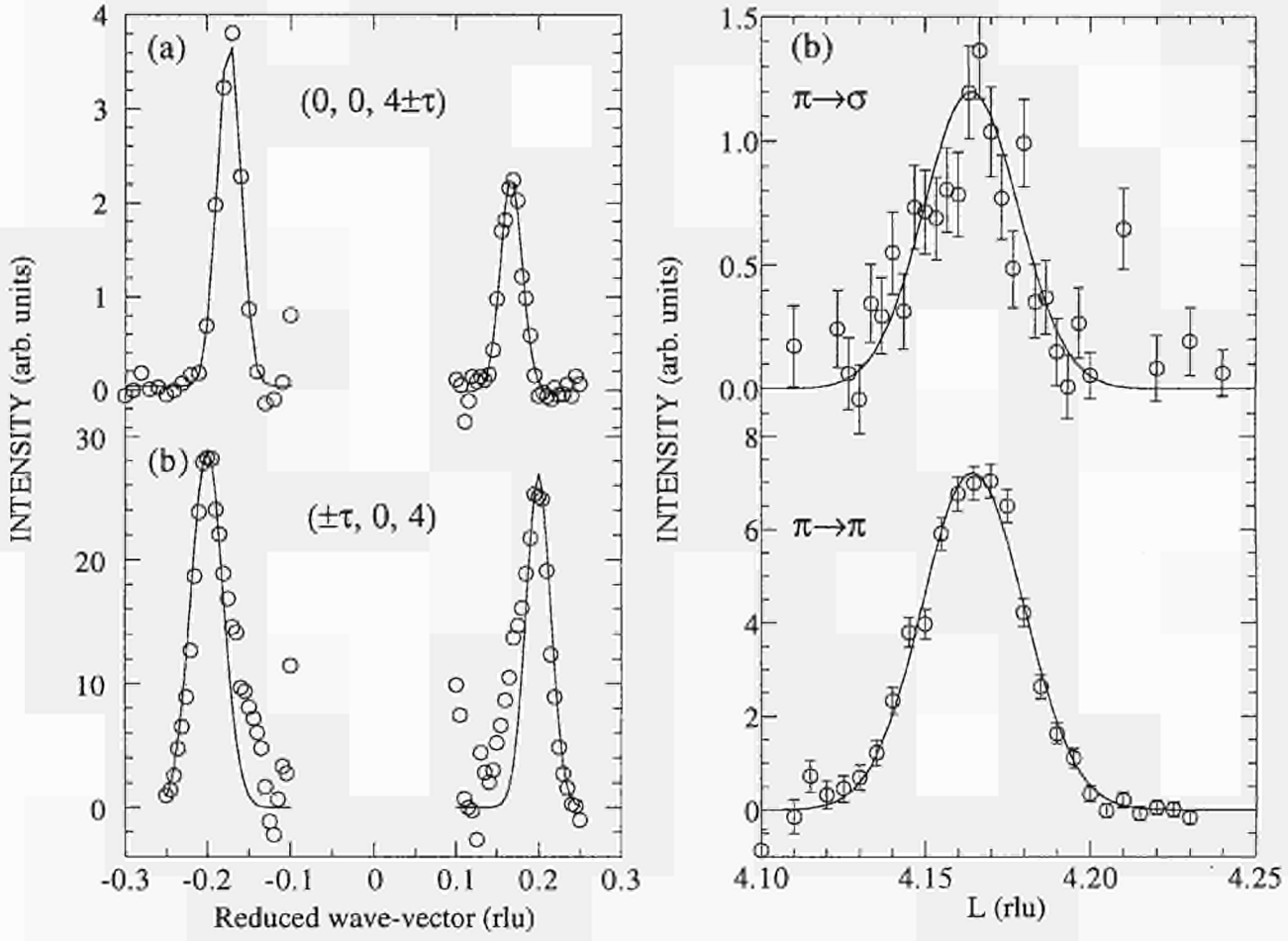

Fig. 4.24 Panel (a) shows the non-resonant symmetric satellites around the (0,0,4) charge peak in $USb_{0.8}Te_{0.2}$ without any polarization analysis at T=175K. Panel (b) presents the scattering in the two polarization channels at the (0,0,4+τ) position at T=175K and an incident photon energy of 8.1 keV. Measurements taken at the Troika beamline at the European Synchrotron Radiation Facility, Grenoble.

According to theory, and if we correctly understand the magnetic structure, the signal should be totally in the π→σ channel, which is clearly not the case. This difficulty can be overcome only with more measurements, and we are planning experiments early in 1995 on more than one compound.

X-ray scattering from magnetic surfaces

The large intensities observed in resonant magnetic scattering from actinide compounds implies that measurable signals can be obtained from small samples. This fact will hopefully allow studies of the magnetic properties of heavier actinides, which are available only in small quantities, and of magnetic surfaces. This year we have performed the first experiment on this last topic - X-ray scattering from a magnetic surface. The experiments, at Brookhaven, were performed on a specially prepared UO_2 crystal, and have shown that a surface "peak" can be measured from the antiferromagnetic ordering developing at the surface, see Fig. 4.25. The signal in Fig. 4.25(a) is about 3 times wider that the normal reflection from the material, showing that the surface order is somewhat less than long range. This may be due to the intrinsic "roughness" of the surface layer. We are making efforts to improve the quality of the crystal surface, and also the experiments will be performed on the more intense wiggler beam line at BNL. Note that these intensities are small, less than 1 count/sec. They represent a signal that is less than 10^{-7} of the conventional "charge" scattering in UO_2, and open the way to more experiments of this sort; a completely new field of investigation.

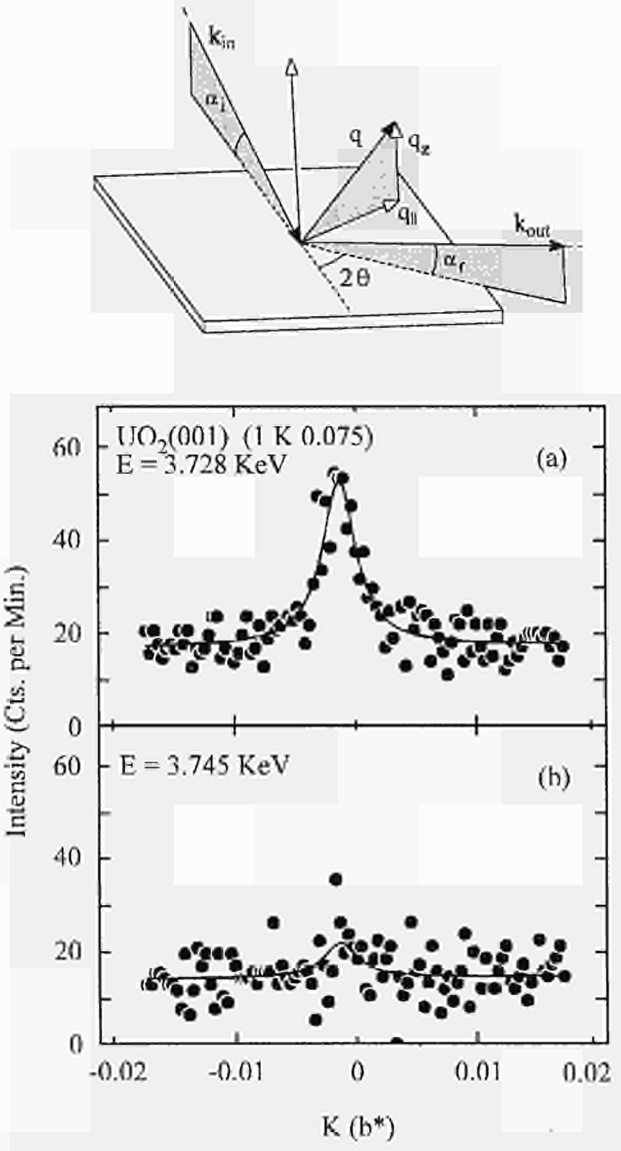

Fig. 4.25 Top: Schematic figure of how the grazing incident is performed on the surface of a highly polished UO_2 crystal. The angles $\alpha_i = \alpha_f = 1.3°$, which implies a penetration of ~20 Å into the crystal. Diagram (a) shows the intensity as the diffractometer passes through the so-called truncation rod on the surface and the scattering conditions are fulfilled. The X-ray energy corresponds to the M_{IV} resonance. Diagram (b) is the same scan as (a) but performed at 17 eV away from the resonance energy.

4.4 High-Pressure Studies on Actinide Systems

Pressure effects in optical reflectivity, electrical resistance and crystal structure were investigated. Attempts will be made to correlate the effects observed to obtain a more complete picture of what happens to the electrons in actinides under pressure.

4.4.1 Optical reflectivity of neptunium and plutonium monochalcogenides under high pressure

The near normal incidence optical reflectivity of cubic AnX - compounds (An = Np, Pu; X = S, Se, Te) has been measured in the energy range 0.5 eV to 5 eV at room temperature as a function of pressure. By comparison with results on corresponding uranium-analogs the two main contributions could be identified as transitions from hybridized 4p-5f - and 4p - valence band to crystal field split 6d -conduction band states.

The spectra of NpX and PuX at low pressures are shown in Fig. 4.26 a and b.

Monosulfides

The reflectivity of NpS (Fig. 4.26) at 1.6 GPa has a definite maximum (A) at low energies, dropping rapidly to a minimum (B) at about 4 eV, and rising again at the end of the measuring interval (C), indicating the onset of an unresolved transition at higher energies. With increasing pressure the initial maximum becomes more pronounced, shifting towards higher energies with a slope of ~6 meV/GPa, while the minimum (B) at the same time flattens progressively and lowers its energetic position.

The reflectivity of PuS (Fig. 4.27) shows more fine structure in comparison with NpS. Peak (A) of the NpS - sample is now split into three distinct features, here labeled (A1), (A2) and (A3), which all shift towards higher energies with pressure while broadening at the same time. The pressure coefficients are 9 meV/GPa, 13 meV/GPa and 12 meV/GPa, respectively. The rest of the spectrum is very similar to NpS.

No indication of phase transitions up to a maximum pressure of ~45 GPa could be found for either sulphide compound, since no sudden change of the spectra was observed. It would be interesting to compare this with X-ray results, since phase transitions are not always visible

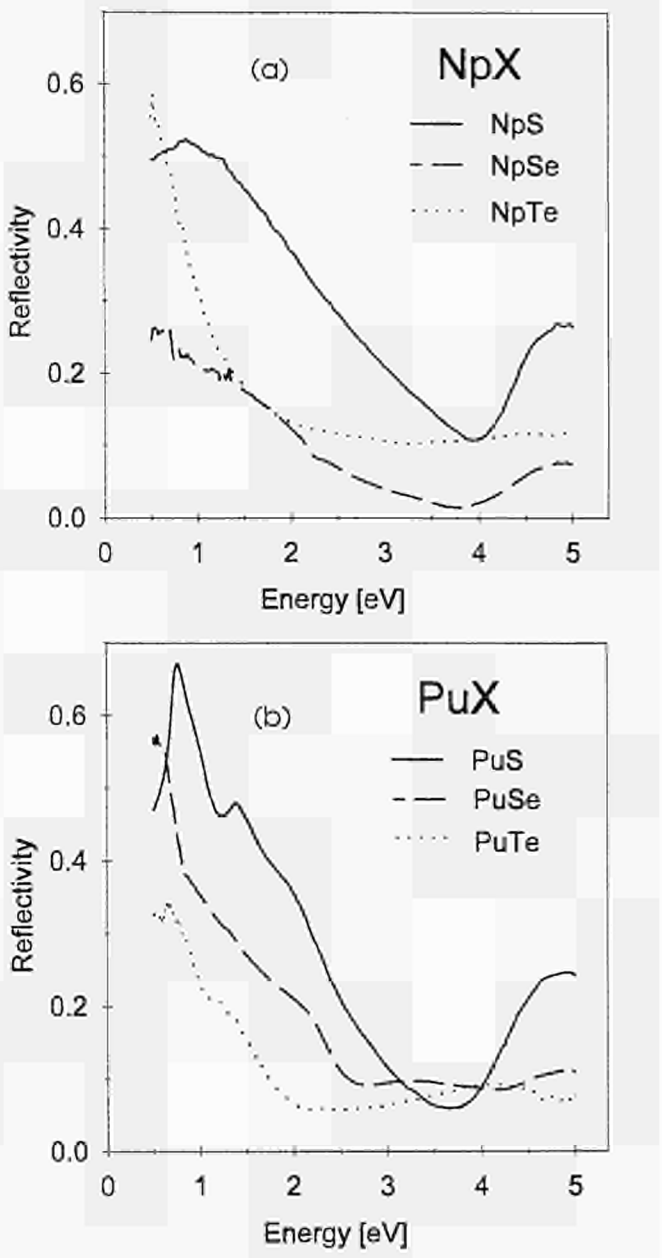

Fig. 4.26 Reflectivity of NpX (a) and PuX (b) (X = S, Se, Te) for low pressures at 300 K.

in reflectivity spectra, but there is no structural information for high pressures available up to now.

Monoselenides

NpSe appears very similar to NpS and PuS, having a strong reflectivity at low energies (A), a steep drop to a

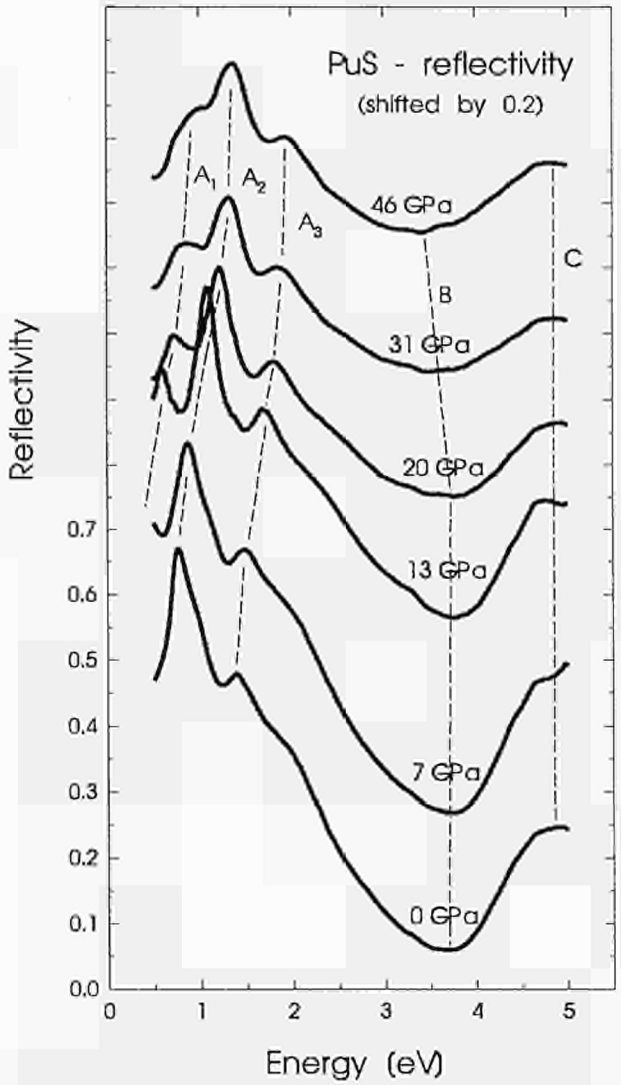

Fig. 4.27 Reflectivity of PuS for different pressures at 300 K.
The vertical scale applies to the curve for the lowest pressure. To avoid overlapping, all successive spectra have been shifted upwards as noted in the figure (dashed lines are only as a visual guide).

minimum (B) with increasing energy and a final increase at the end of the measuring interval (C), but the overall reflectivity has decreased to about half relative to that of NpS. Applying pressure has little effect on the reflectivity. PuSe is similar to the already presented spectra, but reveals a change at elevated pressures which can be attributed to a structural phase change. At low pressure, peak (A) is split into two distinct substructures (A_1) and (A_2). The minimum (B) is reached at lower energies (~2.3 eV). The overall reflectivity is comparable with that of PuS. With increasing pressure, features (A_1), (A_2) and (B) shift towards higher energies. The disappearance of these peaks at about 12 to 16 GPa indicates the phase transformation into the rhombohedral high pressure structure, while with X-rays it is observed at ~20 GPa.

Monotellurides

The low pressure spectrum of NpTe (Fig. 4.26) is dominated by a steep drop of the reflectivity, falling from ~0.4 at 0.5 eV to ~0.05 in less than 1.5 eV. The higher energy part has only a weak oscillator strength and is relatively flat except for a small and very broad peak at ~4.1 eV. PuTe is very similar to PuSe. An indication for the crystallographic phase transition, as derived from the reflectivity spectra, is found at ~16 GPa, which is the same transition pressure as observed with X-rays.

Discussion

Three general trends can be observed in the low pressure reflectivity of NpX - and PuX - compounds shown in Fig. 4.26. First, all investigated samples share a collection of common structures, starting at low energies with a Drude - like edge typical for materials with partly free electrons, superimposed by an optical transition (A), a reflectivity minimum at intermediate energies and an increase in reflectivity towards 5 eV. Second, with the exception of NpTe (Fig. 4.26), the overall reflectivity decreases in the chalcogenide series S - Se - Te. A possible explanation for this behaviour might be the reduced overlap of the electron wavefunctions with the increasing lattice constant in this series which leads to a reduction of the oscillator strength. Correspondingly the plasma frequencies of the compounds decrease within the series, as shown by the shift of the minimum (B) towards lower energies with increasing lattice constant. Finally, the Pu-compounds contain more fine structures in their reflectivity spectra than their Np-analogs.

Based on a comparison with uranium results [1-4], we expect dipole-allowed transitions from the hybridized p-f valence band to conduction band 6d states formed predominantly by the actinide atoms at low energies (peaks labeled A), and transitions from anion p to 6d states at higher energies (C). This interpretation is supported by recent band structure calculations of PuX (X = S, Se, Te) by a relativistic Augmented Plane Wave (APW) method [5].

In the conductivity curves for the NpX and the PuX compounds, except for NpTe, the two main transitions can be easily observed at low pressures. The blue shift of the fine structures (A) of the PuS-spectra with pressure is obvious, demonstrating, that the final state of the f-d transition has to be the upper level e_{2g} of the crystal field split energy levels, since transitions into the lower level would have a negative pressure derivative [6].

The reflectivity of NpTe seems to be an exception to the general behaviour. It is not possible to observe the two main transitions, and NpTe has only a small effective car-

rier density, as shown by the steep ascent of the Drude - edge. Instead, it has a small and broad high-energy peak. A possible interpretation of this abnormal behaviour may be that the conduction-band e_{2g} states are closer to the valence-band states than for the other compounds, leading to an optical transition below the lowest energy measured.

Finally, it can be concluded that structural phase transitions of the actinide compounds can be quite well observed with reflection techniques as long as the electronic states involved in the optical transitions are somehow connected to the instability of the crystal lattice. In general, the phase transition pressure in reflection precedes the structural phase transition detected by X-ray measurements.

References

[1] J. Schoenes, J. Vogt; Sol. Stat. Comm. **28** (1978) 261
[2] J. Schoenes; Physica B **102** (1980) 45
[3] J. Schoenes; Phys. Rep. **5** (1980) 187
[4] J. Schoenes; J. Less-Common Met. **121** (1986) 87
[5] A. Hasegawa, H. Yamagami; J. Magn. Magn. Mater. **104-107** (1992) 65
[6] K. Syassen; J. Phys. (Les Ulis) **C8** (1984) 123

4.4.2 Effects of pressure on electrical and magnetic properties

High-pressure resistance study of NpSb

A selection of resistance of NpSb curves with temperature for pressures up to 23.8 GPa is shown in Fig. 4.28. The curve for the data measured at the lowest pressure (0.7 GPa) agrees well with the previous measurement for the high temperature part where the resistivity exhibits a Kondo-like increase with decreasing temperature. The sharp increase in the resistance below T_N is also well reproduced. NpSb exhibits a semi-metallic or semiconductor-like resistivity at low temperature which tends to be suppressed by the application of pressure.

The other effect which can be clearly seen in the lower pressure curves of Fig. 4.28 is the decrease of T_N with increasing pressure, and a slight reduction in the high temperature resistivity. Between two successive pressure steps at 2.3 and 2.7 GPa, the behaviour has changed quite dramatically: the presumed magnetic ordering now appears as a sharp decrease in the resistance while the behaviour above the ordering temperature has changed very little. Further increasing the pressure leads to a clear decrease in the high temperature resistivity, a flattering of the curve, and a progressive trend from the high temperature Kondo-like resistivity to a typical metallic behaviour.

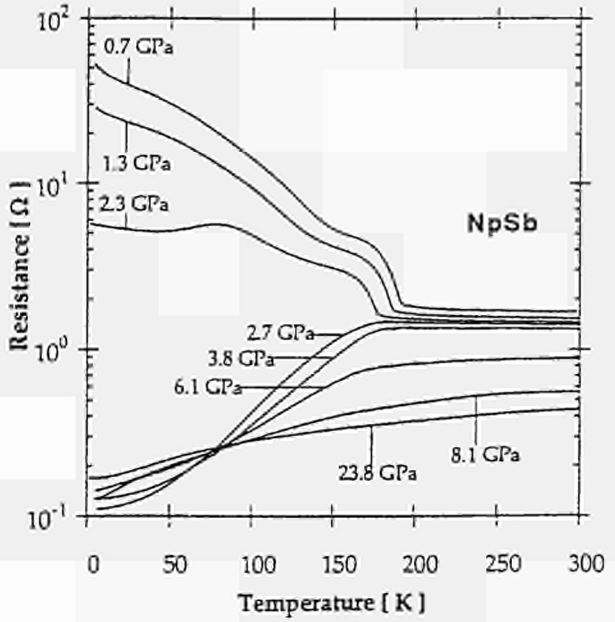

Fig. 4.28 Resistance versus temperature curves of NpSb at pressures up to 23.8 GPa (note the logarithmic scale for the resistance).

The ordering temperature can be extracted from the resistance versus temperature curve from the maximum in the derivative |dR/dT|. For the lower pressure range T_N appears as a sharp negative peak. The temperatures at which peaks in the derivative are observed are plotted as a function of pressure in Fig. 4.29. Above about 8 GPa

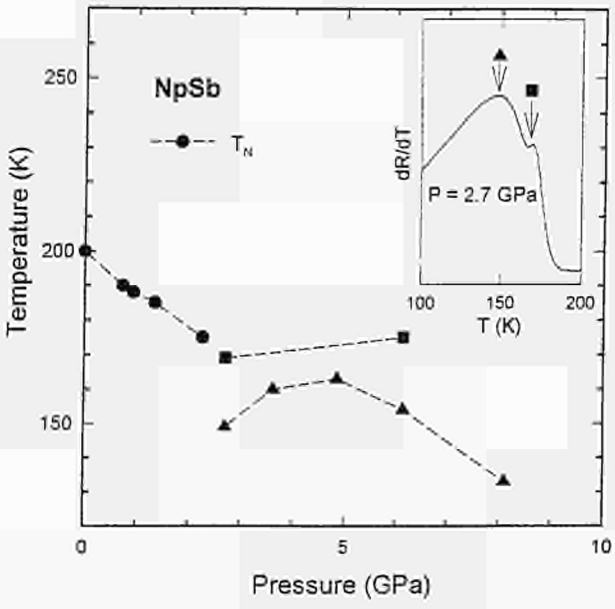

Fig. 4.29 Variation of the Néel temperature and other anomalies in the |dR/dT| curves versus pressure. Circles represent the Néel temperature as determined in analogy to the ambient pressure measurement. The inset shows the derivative dR/dT for P=2.7 GPa and explains the significance of the other symbols (the connecting lines are intended only as visual aids).

very little change is observed over the whole temperature range and the signature of magnetic ordering in the derivative completely disappears.

Electrical resistivity of NpAs under pressure up to 25GPa

Among the family of the Np monopnictides, NpAs has a particularly complex magnetic phase diagram at ambient pressure [1]. Similar to NpSb and NpBi, this compound is semi-metallic and exhibits a triple k magnetic structure at low temperature.

We measured the electrical resistance of NpAs (using a single crystal of NaCl structure) up to 27 GPa and from room temperature down to 1.5 K. At 0.2 GPa (Fig. 4.30), the curve reproduces all the features found at ambient pressure by Pleska et al. [2]:

- from 300 K a slight increase of the resistance when the temperature decreases,
- at T_N=173 K, a small decrease corresponding to the ordering temperature (AF incommensurate structure),
- at T_{ic}=158 K, a small anomaly when the AF structure changes from incommensurate to commensurate.

Similar to the curve at ambient pressure, the most striking feature is the big increase of the resistance occurring at 136 K (T_o of Fig. 4.30) and corresponding to the onset of the triple k magnetic structure. This behaviour suggests that the triple k phase strongly affects the electronic properties of NpAs.

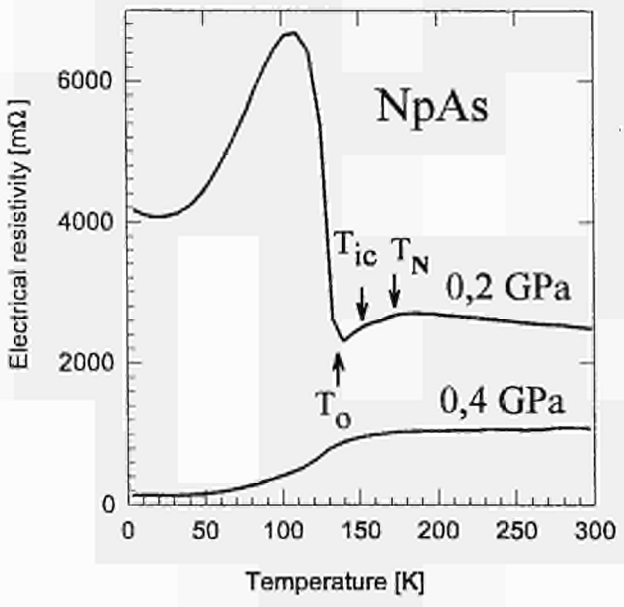

Fig. 4.30 The electrical resistance of NpAs at lower pressures: 0.2 GPa and 0.4 GPa.

As the pressure is increased, a dramatic change is observed even by 0.4 GPa, when the signature of the triple k phase totally disappears. According to the Mössbauer data [3] the value of the magnetic moment does not exhibit any particular change in this range of pressure. However, the magnetic structure could be different. A similar behaviour was observed in NpSb around 2.5 GPa but for this compound only the resistivity data exist [4].

There are a number of complex effects happening in NpAs at higher pressures, none of which are easy to interpret. A comparison with the Mössbauer data does allow the identification of the ordering temperature (T_N) and the values obtained by the two techniques are shown in Fig. 4.31.

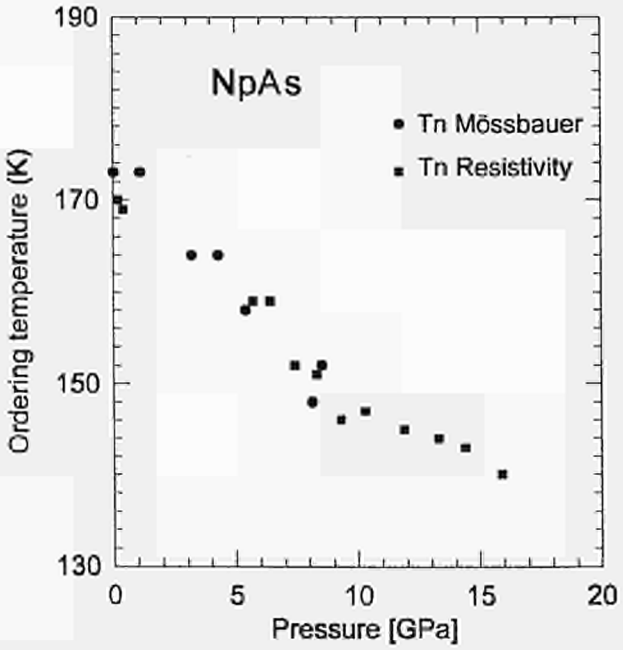

Fig. 4.31 Variation of the magnetic ordering temperature of NpAs with pressure given by two techniques (Resistivity and Mössbauer data).

References

[1] P.Burlet, D. Bonnisseau, S. Quezel, J. Rossat-Mignot, J. C. Spirlet, J. Rebizant, O. Vogt; J. Magn. Magn. Mater. **63 & 64** (1987) 151

[2] E. Pleska; Thèse de Doctorat, Université Joseph Fourier, Grenoble (1990)

[3] U. Potzel, J. Moser, W. Potzel, S. Zwirner, F. J. Litterst, G. M. Kalvius, J. Gal, S. Fredo, S. Tapuchi, J. C. Spirlet; Hyperfine Interact. **47** (1989) 399

[4] M. Amanowicz, D. Braithwaite, V. Ichas, U. Benedict, J. Rebizant, J. C. Spirlet; Phys. Rev. B **50** (1994) 6577

The Curie temperature T_C of USe and UTe under pressure

The variation of T_C of USe with pressure was derived from resistance measurements by Link et al. [1]. Recently, collaborative work [2] confirmed this variation by direct determination of the AC susceptibility under pressure. It can be seen in Fig. 4.32 that with both methods, T_C is observed first to increase and then decrease with pressure. A steep decrease of T_C is indicated from 10 to 12 GPa, by both methods, and no sign of magnetic order is detected any longer above 12 GPa.

Very similar results were also obtained by both methods for UTe.

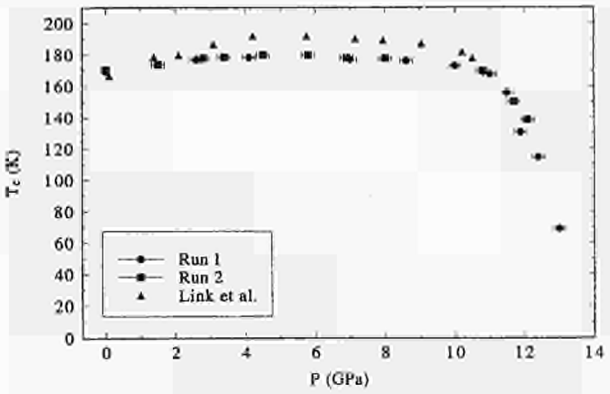

Fig. 4.32 Effect of pressure on the ferromagnetic transition temperature T_C of USe.

The high pressure phase can be indexed in a tetragonal structure (isostructural with CeSb at high pressure). The phase transition was accompanied by a 11.6 % volume collapse representing a first order transition. The tetragonal phase of AmBi was conserved up to the highest pressure attained of 53 GPa where the relative volume was found to be 62 % of the initial volume of AmBi at ambient pressure.

The bulk modulus and its pressure derivative was determined for the low pressure phase, by fitting the V(p) data to the Birch and Murnaghan equations of state (Fig. 4.33). The results were Birch B_0 = 74.4(0.2) GPa with B_0' = 4.6(0.2) and Murnaghan B_0 = 74.8(0.2) with B_0' = 4.4(0.2).

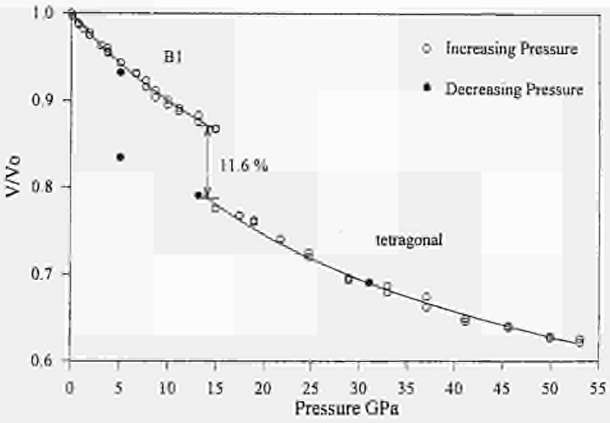

Fig. 4.33 Relative volume of AmBi as a function of pressure.

References

[1] P. Link, U. Benedict, J. Wittig, H. Wühl; Physica B **190** (1993) 68-71

[2] A.L. Cornelius, J.S. Schilling, O. Vogt, K. Mattenberger, U. Benedict; Spring Meeting of the Am. Phys. Soc., San José, CA, March 1995

4.4.3 Structural studies under pressure

Energy dispersive X-ray diffraction analysis of AmBi under pressure

The relative volume of AmBi as a part of pressure is shown in Fig. 4.33. As can be seen, the start of a phase transformation was observed at 13 GPa and was complete at 15 GPa. Upon releasing the pressure, the inverse transformation showed a strong hysteresis down to 5 GPa where the low pressure phase starts to reappear and is pure again at ambient pressure.

High-pressure X-ray diffraction studies of USi_3 and $NpGa_3$

In continuation of our study of AnX_3 (X = Ga, Ge, Sn), USi_3 was studied up to 45 GPa. As with the other UX_3 (TUAR-93, 162-163), USi_3 shows the same anomalous type of compression curve (Fig. 4.34). No crystallographic phase transition was observed over the pressure range studied. A similar behaviour had been noted in pressure studies of YbTe which has been attributed to a 4f-5d electronic collapse, and in the samarium monochalcogenides (see following section). For the neptunium compound of the same $AuCu_3$ structure type, the compressibility data were determined as K_0 = 73(3)GPa, K_0' = 7(1).

Interestingly, no anomalies were seen in the compressibility of the Np compounds.

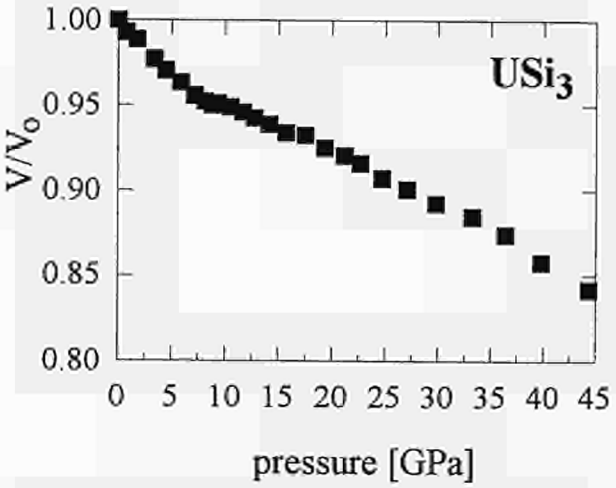

Fig. 4.34 Relative volume of USi_3 as a function of pressure.

Phase transformation of the monochalcogenides SmX (X = S, Se, Te) under high pressure

We have checked and extended to much higher pressure the investigations [1] on the compressibility of the monochalcogenides of samarium.

SmS (Fig. 4.35a) underwent a phase transformation at 1.24 GPa retaining the initial NaCl-type of structure but undergoing a considerable volume collapse (13.8%). At 1.8 GPa this transformation was completed and the sample changed from blue/black to a golden color. This phenomenon can be attributed to a valence transition of the Sm^{2+} ion to the trivalent state. A relatively normal compression curve was obtained from this point until 32 GPa when a previously unobserved phase transition to a CsCl type structure started to occur. This transformation, accompanied with a 10% change in the relative volume, was almost complete at the highest pressure obtained, i.e. 54 GPa. At this pressure the sample had undergone a 42% decrease in volume. All these transformations were found to be reversible upon reducing the pressure.

SmSe (Fig. 4.35b) gave rise to an extremely anomalous compression curve which is attributed to a 4f-5d electronic collapse. This transition was complete at 9 GPa and, like in SmS, a change of the color (from black to gold) was observed. Above this pressure a normal compression curve was obtained until another change from the NaCl to CsCl type structure occurred starting at 25 GPa and completed at 35 GPa. The CsCl type structure remained until the highest pressure of 50 GPa. Upon releasing the pressure the CsCl phase was observed down to about 8 GPa before changing completely back to the collapsed, and then expanded, NaCl type structure. This represents a significant hysteresis effect for the B2 Π B1 transition. Like SmS, this sample underwent a 45% change in volume over the pressure range studied.

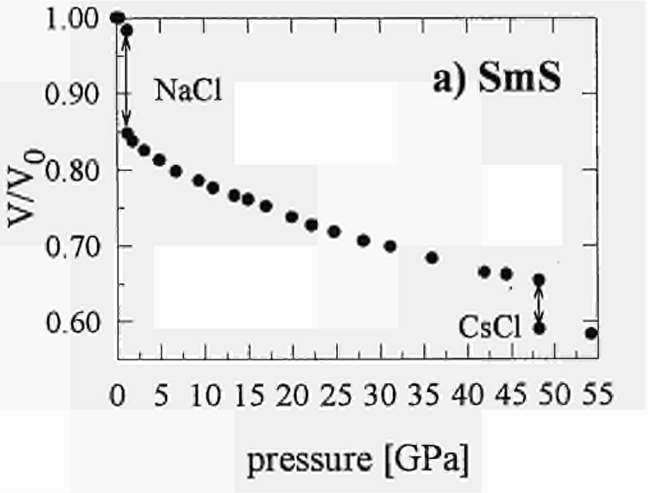

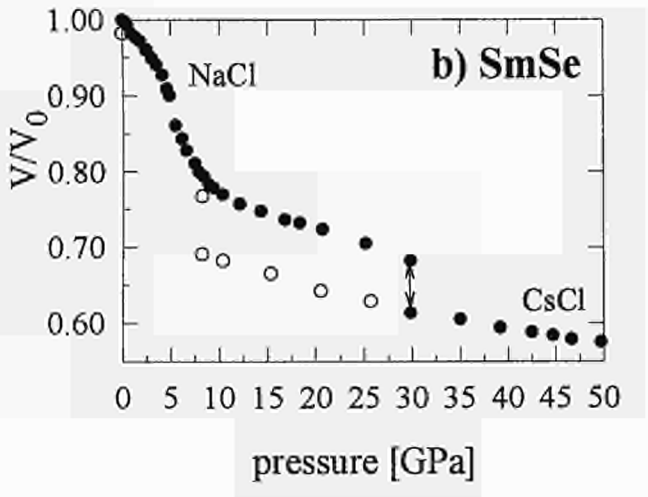

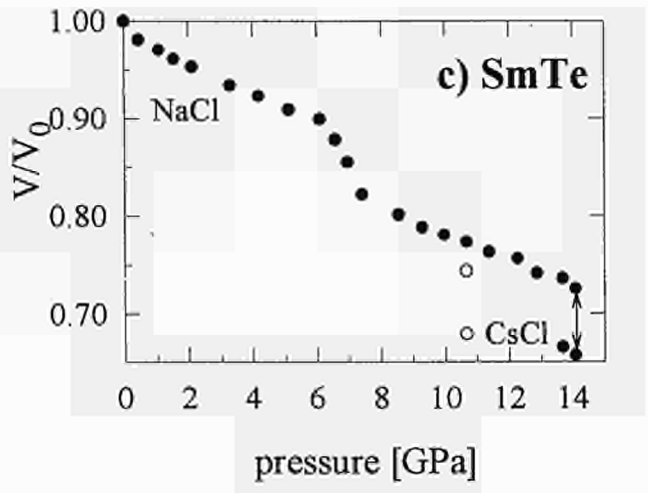

Fig. 4.35 Relative volume as a function of pressure for SmS (a), SmSe (b), SmTe (c).

SmTe (Fig. 4.35c) showed, as SmSe, an extremely anomalous compression curve similar to those of the UX_3 type compounds. Again this transformation is believed to be due to the promotion of a 4f electron of the rare earth ion into the 5d conduction band states. This transformation occurred between 6 and 8 GPa and was followed at 12.9 GPa by a further change to a CsCl type structure which was complete at 14 GPa.

References

[1] A. Chatterjee, A. K. Singh; Phys. Rev. B **6** (1972) 2285

Megabar study of the Ce-Th system

Ce-Th alloys were fabricated at ITU by arc melting the constituent elements. The alloy compositions were calculated from the measured lattice parameters and using the calibration curve obtained by Waber, Harris and Raynor [1]. The following three compositions were studied:

$Ce_{0.2}Th_{0.8}$ (lattice parameter a = 507.76 pm)
$Ce_{0.43}Th_{0.57}$ (a = 508.94 pm)
$Ce_{0.76}Th_{0.24}$ (a = 512.83 pm)

Energy dispersive X-ray diffraction studies were carried out at pressures of up to 253 GPa at the Cornell High Energy Synchrotron Source (CHESS) and the National Synchrotron Light Source (NSLS), Brookhaven. Copper and platinum were employed to provide in situ pressure calibration for the Ce-Th alloy samples in the diamond anvil cells.

We observed a first order volume collapse (γ-α transformation) in the $Ce_{0.76}Th_{0.24}$ alloy with increasing pressure.

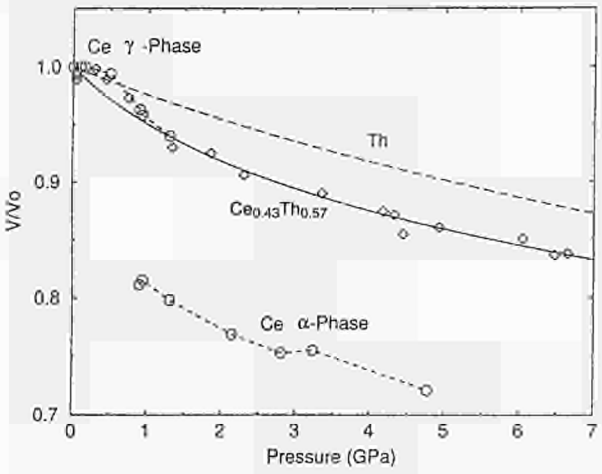

Fig. 4.36 Comparison of pressure-volume data for $Ce_{0.43}Th_{0.57}$ (0) and its constituent metals Ce (o) and Th (- - -) in the pressure range 0-7 GPa. Ce shows a collapse of 16 % at the $\gamma \rightarrow \alpha$ transition. No such collapse was observed in Th metal and the Ce-Th alloy.

In the $Ce_{0.43}Th_{0.57}$ alloy, only a residual compression anomaly around 1 GPa is indicative of the $\gamma \rightarrow \alpha$ volume collapse (Fig. 4.36). In the alloy with thorium concentration greater than 57 %, only a smooth decrease of the fcc lattice parameter with pressure is observed. On further increasing the pressure beyond the stability limit of the α-phase, the transformation to the bct (body centered tetragonal) phase is observed in all alloy samples.

The structural data for all the alloy samples is summarised in Fig. 4.37, where we show the measured c/a ratio for the bct phase as a function of pressure for the three alloy samples and pure thorium. The intrinsic germanium x-ray detector in Energy Dispersive X-ray Diffraction (EDXD) studies has limited energy resolution and the closely spaced diffraction lines at the phase transformation cannot be resolved. The transformation pressure was therefore calculated by extrapolating the c/a ratio to the fcc value.

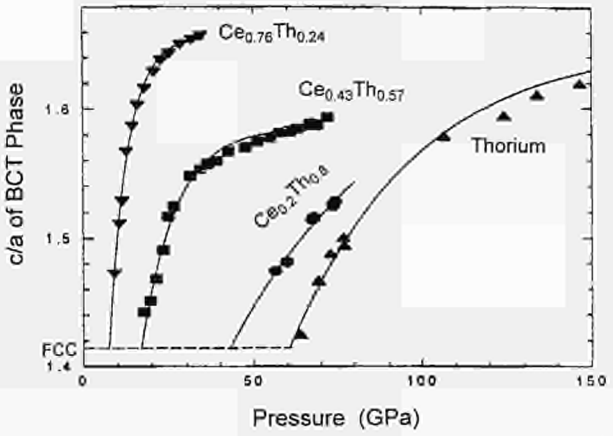

Fig. 4.37 The c/a ratio for the high pressure bct phase of various Ce-Th alloys and pure thorium. The ideal value ($\sqrt{2} = 1.4142$) for the fcc phase (dashed line) is indicated. The solid curves are the fits to equation (1) and are used to determine the transformation pressures.

The c/a ratio increases with increasing pressure from the undistorted fcc value of $\sqrt{2}$ and then saturates at higher pressures. The fcc to bct transformation pressures are obtained by fitting the c/a (y parameter) to the following function:

$$y = y_0 + \left(\sqrt{2} - y_0\right) \times \exp\left(\left(P_0 - P\right) / d\right) \qquad (1)$$

where y_0 is the saturated c/a ratio, P_0 is the transformation pressure, and d is a constant. The transformation pressure is determined to be the point where the bct phase c/a ratio becomes $\sqrt{2}$ (i.e. when $P=P_0$ in equation (1)).

References

[1] J. T. Waber, I. R. Harris, G. V. Raynor; Trans. Metall. Soc. AIME **230** (1964) 148

Comparison of high-pressure phase transitions in B1 type compounds of Th, U, Np, Pu and Ce

The main aim is to compare Ce and Th on one side, and the shifted homologues Ce-Pu on the other. Since the three light actinides U, Np and Pu resemble each other in several respects, uranium and neptunium compounds will be included in the comparison with cerium.

In Fig. 4.38 the high-pressure phases and the phase-transition pressures obtained on increasing the pressure of the CeX compounds, on one side, and in Th, U, Np and Pu monopnictides and monochalcogenides on the other. To facilitate comparison according to f-count homologues as well as for shifted homologues, Pu and Th compounds are presented on either side of the Ce compounds (Pu compounds appear a second time in the increasing-Z sequence after Np).

The following restriction applies to this comparison: While the actinide compounds have been studied up to pressures between 45 and 60 GPa, the upper pressure limit was 23-25 GPa (32 GPa in the case of CeAs) for the cerium compounds. This means that structural evolution at 25 GPa and higher is in general not known for CeX, and that e.g. phase transitions that might occur at higher pressure remain undetected. In particular, no structural phase transition was detected to 25 GPa in CeS; the transformation to a hexagonal phase observed at 23-33 GPa in the f-count homolog ThS might suggest that CeS transforms also somewhere below 60 GPa.

Comparison between Ce and Th compounds (f-count homologues)

For Ce as well as for Th compounds, B2 is the preferred structure type for the high-pressure phases. There are two exceptions among the 13 known compounds of these two elements: 1) CeSb has no B2 type phase, but instead becomes tetragonal under pressure. 2) ThS has a hexagonal high-pressure phase. The general tendency in transition pressures is: for the light anion P, ThX transforms at higher pressure than CeX; for the medium-heavy anions As, Se and Sb, transformation of CeX starts at about the same pressure as for ThX; for the heaviest anions implied, Te and Bi, the pressure for transition to the high-pressure phase is much lower, (i.e. at ambient, or if one likes even "negative" pressure,) for ThX than for CeX.

Comparison between Ce and Pu compounds (shifted homologues)

This comparison is limited to the arsenides, selenides, antimonides and tellurides.

It is obvious from the two leftmost columns of Fig. 4.38 that the plutonium compounds need higher pressure to destabilize the B1 type structure than the cerium compounds. The latter, in contrast, were seen to transform at about the same pressure as the corresponding thorium compounds, with the exception of ThTe which is already B2 type at ambient pressure.

The B2 type appears as high-pressure structure in 7 of these 8 compounds. CeSb has a tetragonal high-pressure structure which also appears in the homologue PuSb as the second high-pressure phase. The latter is formed when pressure is further increased on the first-appearing (B2 type) high-pressure phase.

References

[1] U. Benedict, W. B. Holzapfel; Chapter 113 of Handbook on the Physics and Chemistry of Rare Earths, Vol. **17**; K.A. Gschneidner, Jr., L. Eyring, G. H. Lander,G. R. Choppin (eds.), Elsevier (1993) 245-300

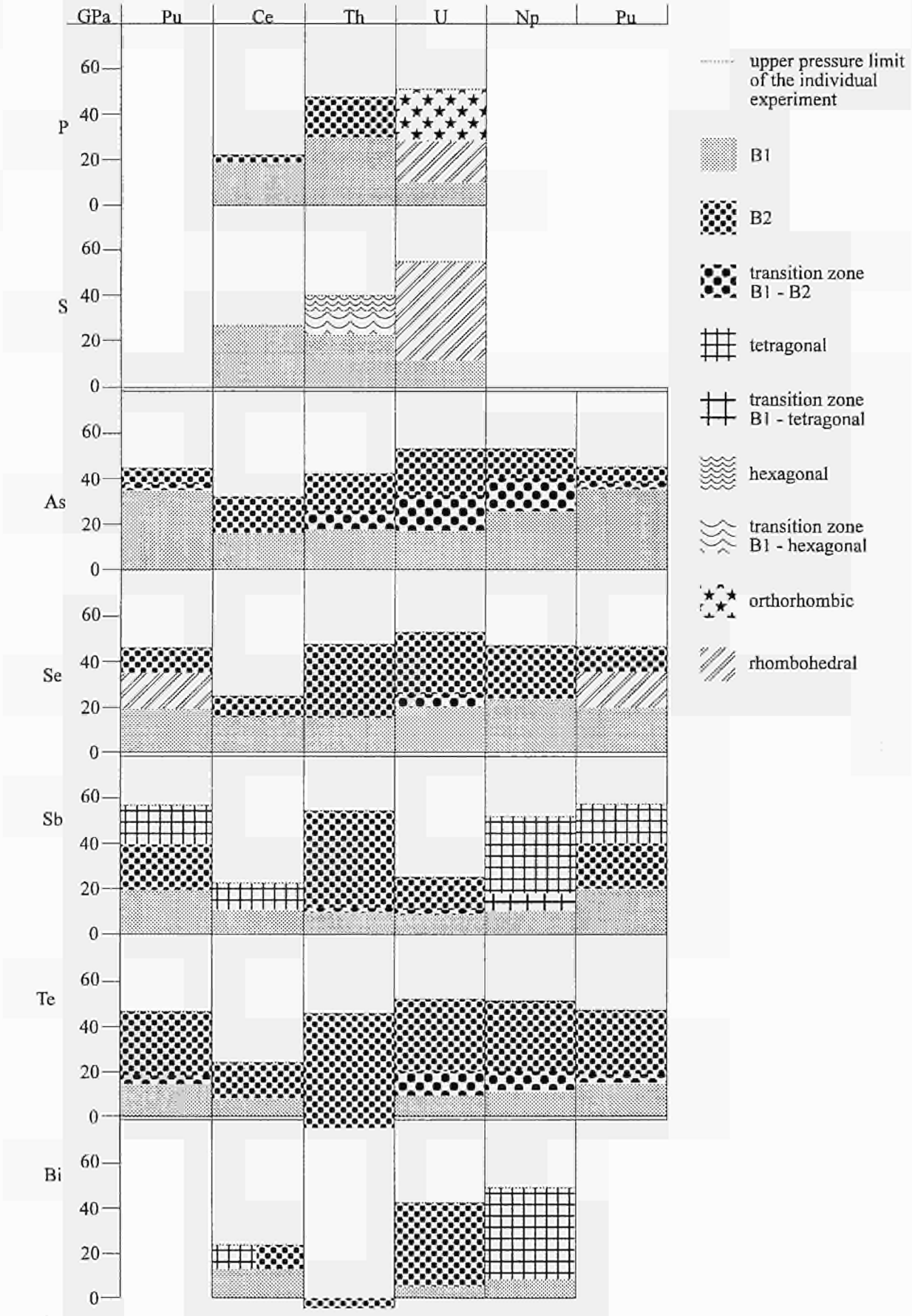

Fig. 4.38 Graphical comparison of high-pressure phases and upstroke phase transition pressures for monopnictides and monochalcogenides of Ce with those of the light actinides Th, U, Np and Pu. Data are taken from a recent review [1].

5. Exploratory Research

5.1 Acoustic Aerosol Agglomeration Studies

5.1.1 Ultrasonic aerosol agglomeration in standing and progressive waves

Introduction

The results presented here deal with the global parameters in the acoustic agglomeration process. This approach was spurred on by the need for the determination of the relationship between power consumption and acoustic agglomeration efficiency. The first objective of this work was the evaluation of the dependence of the agglomeration rate on the wave amplitude U_w. The second objective was the characterization of the influence of the initial particle concentration on the initial agglomeration rate. A model has been devised which permits a full interpretation of the experimental results obtained with two frequencies under standing or progressive wave conditions. This model provides the basis for the design of future acoustic agglomeration chambers.

Installation for agglomeration tests

Acoustic aerosol agglomeration measurements were performed in a facility described in detail elsewhere [1,2]. In an earlier experimental arrangement [3], the walls parallel to the acoustic source were not covered with sound absorbing material, and an uncontrolled build up of standing waves in the cavity was possible. The newer experimental chamber [1,2] was fitted with such material and improved control of the wave, which was approximately progressive, was achieved. The glycol fog used in these agglomeration experiments has the same characteristics as previously reported [2].

The sound sources (10 and 21 kHz), are described in detail elsewhere , and their efficiency, η_s, for conversion of electrical to acoustic energy is about 75% [4]. The linearity of the acoustic power P_{ac} with respect to the input electrical power, P_{el}, was checked before all sets of experiments. The distribution of acoustic energy within the chamber is not homogeneous because the near field of the acoustic sources comprises the entire chamber volume [5, pp 294-300] and because the oscillation amplitude of the acoustic plate is not radially homogeneous. A fan located near the top of the chamber provided efficient mixing of the aerosol so that all particles were treated in an identical manner in the sound field. The fan also guarantees uniformity of the aerosol size distribution within the cavity.

Scaling of the agglomeration rate as a function of acoustic energy

The influence of the input electrical power, P_{el}, of the source on the acoustic agglomeration rate at 10 and 21 kHz was investigated systematically, by keeping the initial total particle concentration, N_T^0, constant, and varying the electrical power in the linearity range of the acoustic sources. Agglomeration experiments were performed at five different electrical powers at both frequencies. The total particle concentrations during the course of an agglomeration experiment are plotted in Figs. 5.1a and 5.1b as a function of time, t. The data at 0 W corresponding to Brownian agglomeration and particle losses to the walls are shown for comparison. The effect of acoustic agglomeration increases with the applied power as expected. Consideration of the models of the agglomeration process permits a more detailed analysis of the data and testing of the models themselves.

The orthokinetic model [6] is based on the impaction of small particles, entrained in the wave, onto inertial particles which are stationary or near stationary in the acoustic flow. It predicts a linear dependence of the agglomeration rate $K = d N_T / (N_T dt)$ on the velocity amplitude, U_w, of the wave and thus on the square root of the acoustic power, $\sqrt{P_{ac}}$. Models based on hydrodynamic interactions [7], which could arise between particles of the same or different sizes, predict a dependence of K on U_w^2 and thus on P_{ac}. As the agglomeration time, τ_a , is proportional to K^{-1}, the scaling of the time of evolution in Figs. 5.1a and 5.1b can be investigated simply by multiplying t by $\sqrt{P_{ac}}$ or by P_{ac}.

In Figs. 5.1c and 5.1d, the total particle concentrations are plotted as a function of $\sqrt{P_{el}} \times t$ (which is proportional to $U_w \times t$), while in Figs. 5.1e and 5.1f, they are plotted as a function of $P_{el} \times t$ (which is proportional to $U_w^2 \times t$). The latter scaling gives best results, as all the curves corresponding to measurements made at different powers, P_{el}, collapse on each other. Thus, these experimental observations support the hydrodynamic model of acoustic agglomeration. It is also worth noting that the instantaneous efficiency is given by the consumed energy, irrespective of the applied power.

Model of acoustic agglomeration in a chamber

The model presented here includes the tuning of the acoustic cavity and attenuation of the wave due to the presence of the aerosol. The aim is to find an expression describing the initial agglomeration rate as a function of the total number of particles, provided that the initial size distributions are in similitude. The following assumptions have been invoked:

- The acoustic wave in the cavity is treated as a plane wave.
- Effective agglomeration takes place within a cylindrical volume of cross-sectional area, S_p, which depends on the geometry of the plate.
- Attenuation of the wave by the aerosol is included, but its dispersion by the aerosol is neglected.
- In the case of a standing wave, perfect reflection of the wave is considered.

The equation modelling the agglomeration process at initial times is given by:

$$K = \frac{dN_T}{N_T dt} = \frac{d\ln(N_T)}{dt} = A|U_w|^{\delta} N_T \qquad (1)$$

where K is a logarithmic acoustic agglomeration coefficient which characterizes the agglomeration at a given point, and A is an integral parameter that characterizes the efficiency of agglomeration at a given frequency f. In expression (1), δ characterizes the dependence of the agglomeration process on the velocity amplitude of the wave, U_w, and, $|U_w|$ is the root mean square of the acoustic velocity U at point x. As in the experimental situation, the fan ensures that variations in the aerosol size distribution and concentration are small throughout the chamber, the spatial variation of K is due only to the velocity amplitude of the wave, U_w. The determination of the average rate of agglomeration, $\overline{K}_p$, in the volume, V, in which agglomeration occurs, is given by:

$$\overline{K}_p = \left\langle \frac{dN_T}{N_T dt} \right\rangle = \frac{1}{V}\int_V \frac{dN_T}{N_T dt} dv \qquad (2)$$

Within the simplifications introduced earlier, the agglomeration rate, $\overline{K}_p$, in the central active agglomeration region, is expressed as:

$$\overline{K}_p = \frac{1}{\overline{\tau}_a} = \left\langle \frac{dN_T}{N_T dt} \right\rangle = \frac{1}{L} A N_T \int_0^L |U_w|^{\delta} dz \qquad (3)$$

where $\overline{\tau}_a$ is a characteristic agglomeration time and L the chamber length. This expression of the agglomeration rate applies in the effective volume of agglomeration, and can be extended, by means of the particle concentration balance, to the global agglomeration rate in the entire chamber volume, $\overline{K}_C$. Thus

$$\overline{K}_c = \frac{\text{reduction in the number of particles}}{\text{total number of particles}} = \overline{K}_p \times \frac{S_p}{S_C} \qquad (4)$$

where S_C is the cross sectional area of the agglomeration chamber.

The attenuation coefficient, α, of a plane wave propagating through an aerosol is determined by the shape of the aerosol size distribution and the total particle concentration [8]. When the size distribution functions are in similitude, this coefficient α is directly proportional to N_T. Thus,

$$U_w = U_0 \mathcal{R}e\left(e^{kz - i\omega t}\right) = U_0 e^{-\alpha z} \cdot \cos(kz - \omega t) = U_0 e^{-\gamma N_T z}\cos(kz - \omega t) \qquad (5)$$

where $\gamma = \alpha / N_T$ is the attenuation coefficient per particle for an aerosol with a given size distribution, $K = k + \imath\alpha = 2\pi/\lambda + i\gamma N_T$ is the complex wave number based on the wave length, $\lambda = c/f$(where c is the velocity of sound in air and $i^2 = -1$) and $\mathcal{R}e$ signifies the real part of the argument. In the case of a progressive wave,

$$|U_w| = U_0 e^{-\gamma N_T z}/\sqrt{2} \qquad (6)$$

In the following, the model is developed for progressive and standing waves and comparison with experimental data is made, for the case when all initial size distributions are in similitude.

Model for progressive waves

Introduction of expression (6) in equation (2) and integrating gives:

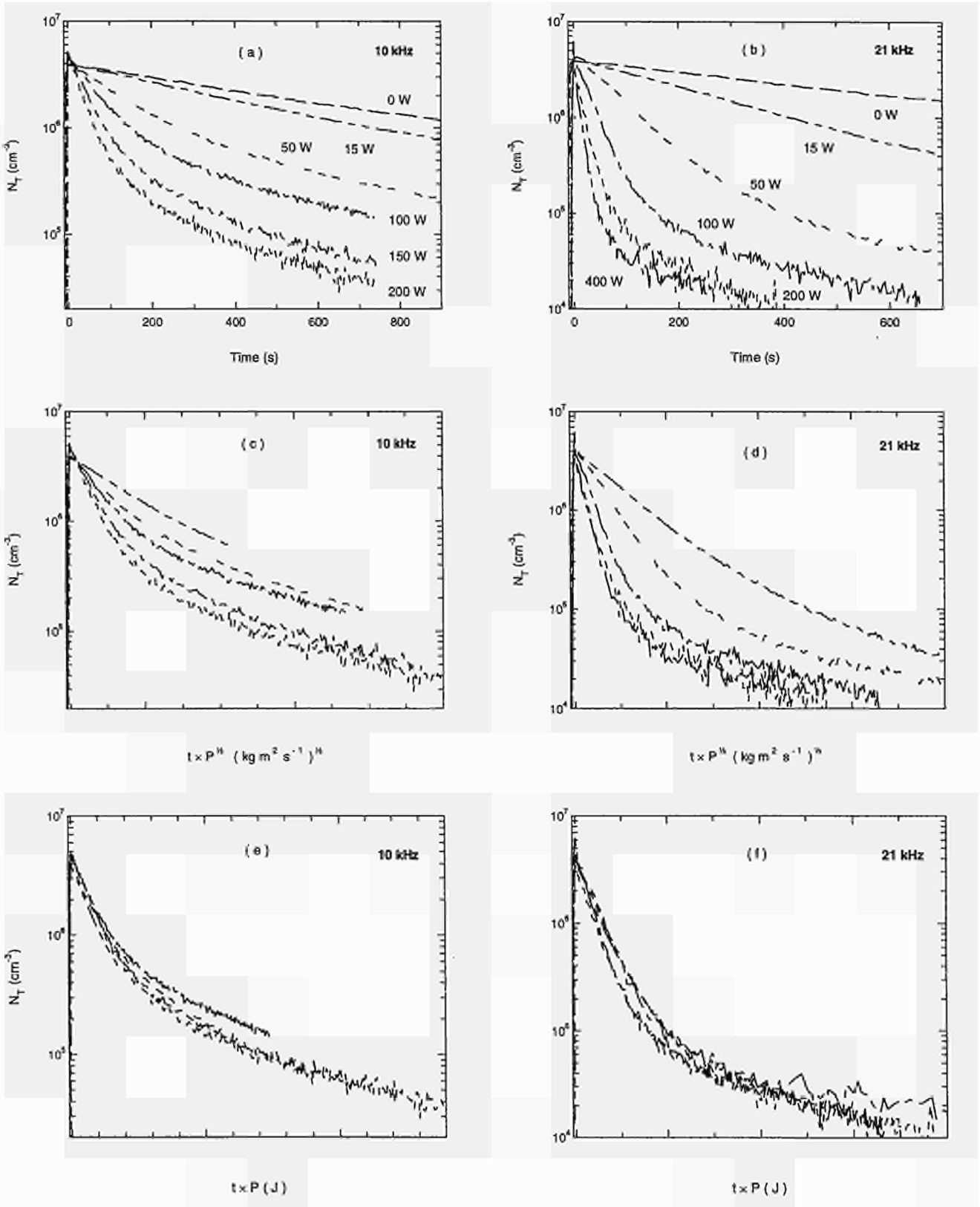

Fig. 5.1 Evolution of the total particle concentration as a function of time for 10 kHz (a) and 21 kHz (b) for various electrical powers, P_{el}. Evolution of the total concentration with $\sqrt{P_{el}} \cdot t$ for 10 kHz (c) and 21 kHz (d). Evolution of the total concentration with the energy $P_{el} \cdot t$ for 10 kHz (e) and 21 kHz (f).

$$\overline{K}_p^o = \frac{1}{\overline{\tau}_a} = \frac{1}{\overline{\tau}_{sat}}\left(1 - e^{-N_T^o/N_{sat}}\right) \quad (7)$$

where

$$\frac{\overline{K}_p}{\overline{K}_{sat}}\left(n, X_\lambda\right) = \frac{\sinh(n)}{\cosh(n) - \cos\left(2\pi X_\lambda\right)} \quad (8)$$

Increasing the particle concentration favours the agglomeration process, but it is counterbalanced at high N_T^o (i.e. $N_T^o >> N_{sat}$) by the attenuation of the sound wave by the aerosol. Increasing the length of the chamber (thus the volume to be treated) also increases $\overline{\tau}_{sat}$ and thereby decreases the effectiveness of the sound treatment.

The expression for $\overline{K}_c^o$, corresponding to the entire volume of the chamber is analogous to expression (7), except that $\overline{\tau}_{sat}$ needs to be replaced by $\overline{\tau}_c$, i.e.:

$$\overline{\tau}_c = \frac{S_C}{S_p}\,\overline{\tau}_{sat} = \frac{2^{\delta/2}\delta\gamma}{AU_0{}^{\delta}}\frac{LS_C}{S_p} \quad (9)$$

Model for standing waves

The expression for the velocity amplitude of the standing wave is obtained directly from the boundary conditions at each end of the chamber [5] such that

at the source $(z=0)$: $U_w = U_0 e^{-i2\pi ft}$

at the perfect reflector $(z=L)$: $U_w = 0$

Thus the velocity amplitude of the standing wave is given by:

$$U_w(z,t) = U_0 u_w(z,t) =$$

$$\mathcal{R}e\left(U_0 e^{-i2\pi ft}\frac{\sin\left(k(z-L)\right)}{\sin(kL)}\right) \quad (10)$$

where u_w is the non dimensional velocity. The following non dimensional parameters are now introduced:

$$X_\lambda = kL/\pi = 2L/\lambda \quad n = N_T^o/N_{sat} = \delta\alpha L$$

$$\zeta = z/L \quad (11)$$

Of these parameters, X_λ expresses the number of half wave-lengths in the chamber, it characterizes not only the length of the chamber, but also its tuning (which occurs every $\lambda/2$). The parameter n, being the ratio of the chamber length to the characteristic attenuation length, $|U_w| = f\int_0^{1/f} U_w(x,t)dt$, characterises the amplitude of the reflected wave.

When $\delta=2$, equation 3, in which expression (10) has been incorporated, can be integrated to give

$$\frac{\overline{K}_p}{\overline{K}_{sat}}\left(n, X_\lambda\right) = \frac{2\pi X_\lambda \sinh(n) - n\sin(2\pi X_\lambda)}{2\pi X_\lambda\left(\cosh(n) - \cos(2\pi X_\lambda)\right)} \quad (12)$$

Thus in this model, $\overline{K}_p/\overline{K}_{sat}$ depends on $n = N_T^o/N_{sat}$ and X_λ. When n is large, $\overline{K}_p/\overline{K}_{sat}$ tends to unity and the standing wave system in the cavity is similar to a progressive wave system, since the amplitude of the reflected wave is negligible. The only physical difference lies in the geometrical locking of the wave, which occurs due to the boundary conditions. Thus for high values of n, the standing or progressive wave cases are equivalent. In the experimental arrangement considered here, $X_\lambda >> 4$, and:

$$\frac{\sinh(n)}{n} >> \frac{\sin(2\pi X_\lambda)}{2\pi X_\lambda} \quad (13)$$

Expression (12) then simplifies to:

$$\frac{\overline{K}_p}{\overline{K}_{sat}}\left(n, X_\lambda\right) = \frac{\sinh(n)}{\cosh(n) - \cos\left(2\pi X_\lambda\right)} \quad (14)$$

In this case $\overline{K}p/\overline{K}sat$ is only influenced by the fractional part, ΔX_λ, of X_λ, which characterizes the degree of tuning of the cavity, and by n, which characterizes the attenuation of the wave.

The non-dimensional agglomeration rate $\overline{K}p/\overline{K}sat$ has been plotted as a function of n in Fig. 5.2a, for values of ΔX_λ ranging from 0 to 1/2 (which corresponds to /4). The limiting cases of perfect tuning ($\Delta X_\lambda = 0$) and of perfect detuning ($\Delta X_\lambda = 1/2$) correspond to the curves which maximise and minimise $\overline{K}p/\overline{K}sat$ for all values of n. When $0 \le \Delta X_\lambda < 1/4$, the agglomeration rate reaches a maximum, before decreasing to its asymptotic value, $\overline{K}_{sat}$, at high values of n. When $1/4 < \Delta X_\lambda \le 1/2$, which corresponds to a negatively tuned cavity, $\overline{K}p/\overline{K}sat$ is never greater than unity.

The infinite value of $\overline{K}_p$ at n=0, when the cavity is perfectly tuned ($\Delta X_\lambda = 0$), is merely due to inclusion of perfect reflection at the boundaries in the model. This obviously does not correspond to practical conditions, but it will be shown that this model, although idealised, is able to describe the experimental results.

When $\delta=1$, the presence of $|U_w|$ in expression (3) hinders any easy analytical integration of this equation. A numerical integration procedure has been used to perform this task. The results shown in Fig. 5.2b indicate that $\overline{K}p/\overline{K}sat$ increases monotonically to unity for all values ΔX_λ.

The structure of the solution to equation (3) depends on the value of , thus this model combined with comparison to experimental data provides a means to discriminate between the dependence of the agglomeration rate on $|U_w|$ or $|U_w|^2$.

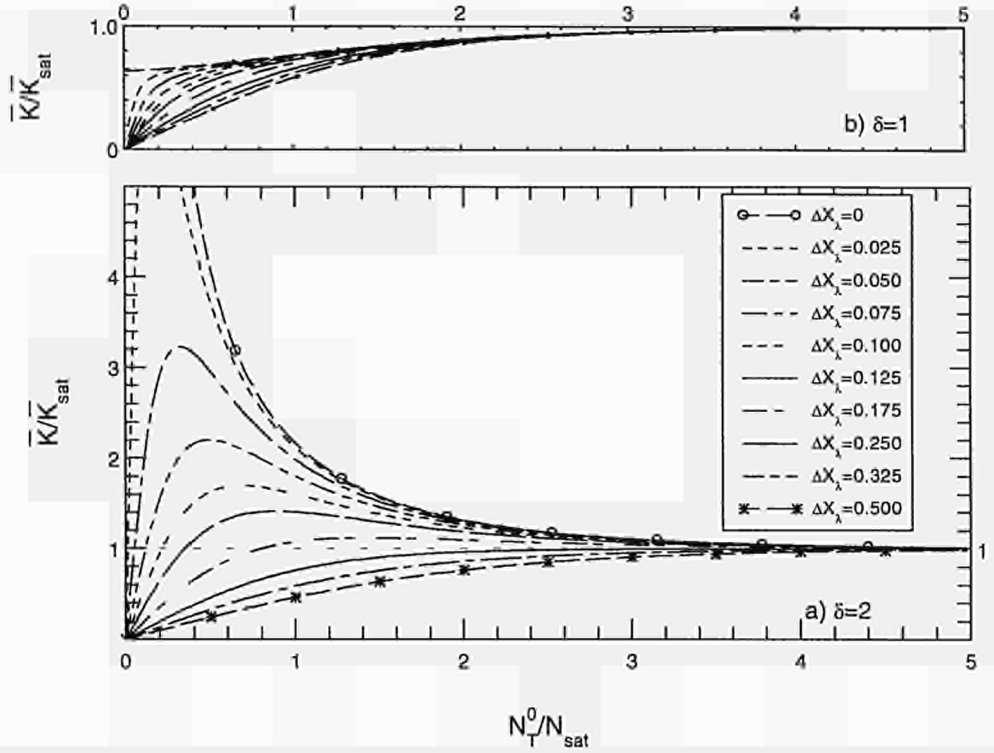

Fig. 5.2 Model calculations of the aerosol agglomeration rate in a standing wave: the normalised agglomeration rate $(\overline{K}_c^o/\overline{K}_{sat})$ *is shown as a function of normalised initial particle concentration* $(n = N_T^o/N_{sat})$ *for various values of the tuning condition of the cavity* (ΔX_λ)*, and two values of the coefficient* δ *(*δ *= 1 and 2) which characterize the dependence of* $\overline{K}_c^o$ *on* U_w $(\overline{K}_c^o \equiv U_w^{\delta})$

Comparison of the model with experimental data

The behaviour of the initial agglomeration rate, $\overline{K}_c^o$, as a function of the initial particle concentration, N_T^o, has been investigated at a constant electrical power of 100 Watts, at both frequencies. The experiments were performed in two different acoustic cavities (in length and diameter), and under different boundary conditions (with or without attenuation material at the ends of the cavity). Using equations (4) and (8) scaling of different geometrical configurations has been made, and the transformed experimental values are shown in Fig. 5.3.

The experimental results at 10 kHz made without attenuation material in the agglomeration chamber (filled circles in Fig. 5.3a) [3] are very similar to the behaviour predicted by the model for a positively tuned cavity, when δ=2. Indeed, one can fit equation (14) to the experimental points, as shown in Fig. 5.3a. The corresponding measurements made at 21 kHz (Fig. 5.3b, filled circles) correspond to a detuned cavity.

When sound absorption material is fitted, progressive waves prevail. The measurements (open circles) in Figs. 5.3a and 5.3b have been fitted to the adapted expression for a progressive wave (7). The parameters derived from these fitting procedures are summarised in Tab. 5.1. Of particular interest is the derived value of the acoustic energy attenuation coefficient, $2\gamma = 2\alpha/N_T^o = (LN_{sat})^{-1}$. This coefficient can be compared to reference measurements, γ_{ref}, made in an independent experiment [9,10], which was specially designed for attenuation measurements. The agreement between γ_{ref} and the value deduced from the fitting is quite good, especially when one considers the simplifications incorporated in the model.

Conclusions

The results of these experiments and model calculations highlight two effects. First, the global agglomeration rate depends on U_w^2. This means that the acoustic agglomeration efficiency is directly proportional to the energy input. This result appears to favour the hydrodynamic interaction mechanism, nevertheless, it could be linked to the combination of aerosol size distributions and applied frequencies in this particular investigation. Further studies are needed to verify this result over a wider range of parameters (frequency and size distribution). Secondly, the role of attenuation has been highlighted in this experiment. Indeed, the agglomeration rate is constant at high particle concentrations. It has been shown, however, that an increased acoustic agglomeration rate can be obtained in a limited range of particle concentrations if a

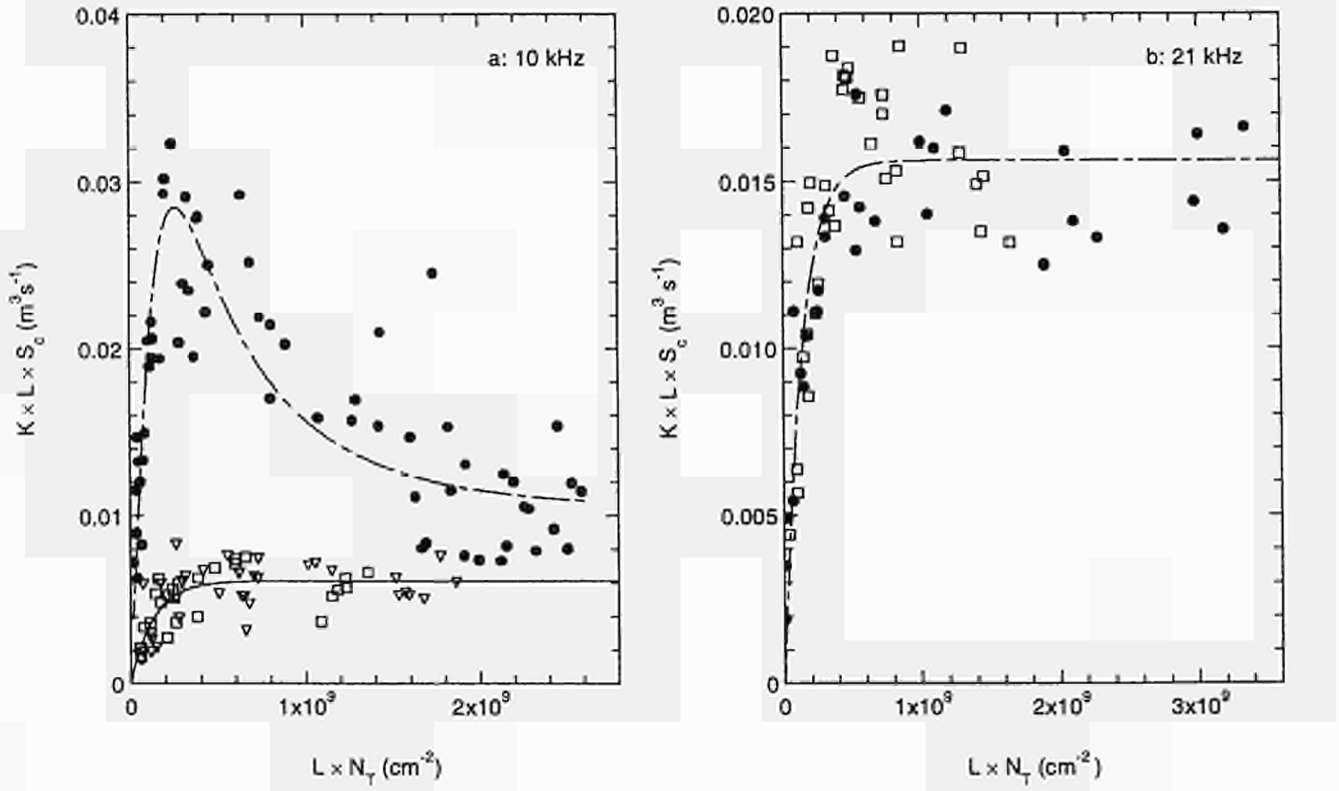

Fig. 5.3 Measurements of the initial rate of agglomeration as a function of particle concentration, which are scaled to the dimensions of the agglomeration chambers (see equations 4 and 8). Open and filled symbols correspond to progressive [2] and standing [3] wave conditions, respectively.

Tab. 5.1 Values of 2 γ obtained by fitting the model to the two sets of experimental measurements of the agglomeration rate. An independent measurement gives $2\gamma_{ref} = 1.35 \cdot 10^{-9}$ cm² *at 10 kHz, and* $2\gamma_{ref} = 2 \cdot 10^{-9}$ cm² *at 21 kHz. Under standing wave conditions, the fitted value of* $X\lambda$ *corresponds to positive (10 kHz) and negative (21 kHz) tuning of the cavity.*

Frequency	Wave situation	Length L (cm)	Volume V_c (m^3)	$\bar{\tau}_{sat}$ (s)	N_{sat} (cm^{-3})	X_λ	2γ (cm^2) from fit	γ/γ_{ref}
10 kHz	standing	130	0.4	37.4	$5.15 \cdot 10^6$	76,06	$1.49 \cdot 10^{-9}$	1.1
10 kHz	progressive	140	0.54	78	$1.3 \cdot 10^6$		$5.5 \cdot 10^{-9}$	4.1
21 kHz	standing	115	0.38	30.8	$1.05 \cdot 10^6$	140.32	$8.28 \cdot 10^{-9}$	4.14
21 kHz	progressive	140	0.54	42	10^6		$7.1 \cdot 10^{-9}$	3.55

standing wave persists in the cavity. These results can be used to optimise the design and running costs of an acoustic agglomeration installation.

5.1.2 Influence of infrasound on aerosols

Previous investigations on the interaction of high intensity sound waves with aerosols in the Institute have concentrated on sound frequencies of 10 and 21 kHz and aerosols with particle diameters of about 1 µm and geometric standard deviations of about 1.4. Under these conditions, the combination of particle size distribution and acoustic frequency is such that the differential velocity of particles, provoked by the wave, is sufficient to induce their agglomeration [2,6]. Under these conditions, however, the attenuation of the wave by the aerosol is not negligible [8]. At infrasound frequencies of 20 Hz, all particles are fully entrained in the wave and attenuation by the aerosol is negligible. If agglomeration occurs at this frequency, the mechanisms must be different to those at 10 and 21 kHz. The results of the first preliminary investigations on the interaction between aerosols and infrasound are presented in the following.

Experimental installation

The infrasound generator consists of a tube within which a piston is mounted. The tube (Ø =150 mm) emanating from the pulsator was connected directly to a chamber consisting of seven tubes (Ø = 500 mm) bolted together. The total length of this chamber (7.2 m) was such that the resonance frequency of the whole system was 21 Hz. Infrasound was generated in this system by driving the piston at the desired frequency. Aerosol injection and ventilation of the chamber were achieved through valves installed on the sealing flanges of branched tubes which were located nearest and furthest away from the pulsator. The sound pressure was monitored by a Bruel and Kjaer microphone protected by a Milar film attached to the 150 mm tubing close to the pulsator.

The aerosol used in these investigations was generated by the evaporation and condensation of a low vapour pressure oil (Optronix GmbH). Because of the large chamber volume, aerosol generation was achieved reproducibly by injecting the aerosol into the cavity for 5 minutes, and then waiting a further 7 minutes to permit its ageing and mixing by fans located within the cavity. Thereafter the aerosol was treated with infrasound for 30 s. An aerodynamic particle sizer (APS) was used to monitor the aerosol size distribution continuously (20 s sampling time) during its generation and after treatment by the infrasound. Due to the relatively high wave pressures, continuous measurement was not possible when the infrasound source was in operation.

Characterization of the sound pressure within the cavity

The sound pressure level within the cavity was monitored as a function of the driving frequency applied to the pulsator. The results are shown in Fig. 5.4. The sound pressure level reaches 177 dB (14.2 kPa) at 21 Hz which is the fundamental resonance frequency of the cavity. At a driving frequency of 10.5 Hz, a resonance is also observed, which reveals that the piston does not generate a pure frequency without harmonics.

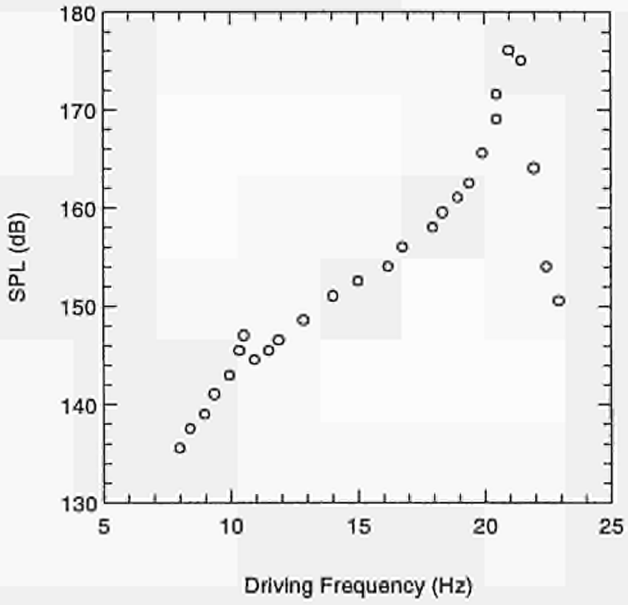

Fig. 5.4 Sound pressure level (SPL) as a function of the driving frequency of the piston.

Effect of aerosol agglomeration on the aerosol size distribution

The effect of Brownian agglomeration and infrasound on the aerosol (d_g = 1.3 µm, σ_g = 1.46) prepared in the way described above is compared in Fig. 5.5. In the case of Brownian agglomeration, the particle concentration decreases steadily while application of infrasound for 30 s causes a sharp decrease in particle concentration. The elapsed time between aerosol samples before and after application of infrasound was greater than 30 s due to the time required to initiate the pulsator, and to achieve a representative aerosol sample after the APS was reconnected to the cavity.

The particle size distributions before and after treatment using infrasound are shown in Fig. 5.6. The decrease in particle concentration caused by infrasound is most significant at particle diameters greater than 1 µm. In contrast to other measurements [2], no creation of new particles with larger diameters than that present initially could be detected directly. However, these results need to be corrected for particle loss to the walls, which are significant.

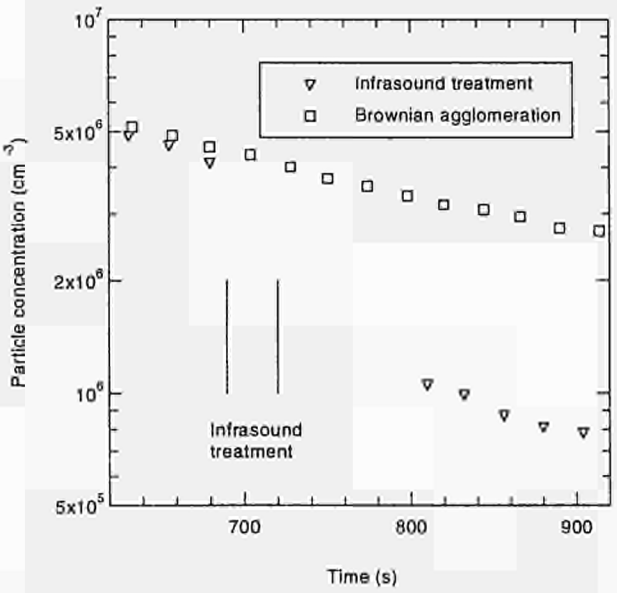

Fig. 5.5 Particle concentration as a function of time. Zero in time corresponds to the initiation of the aerosol generation process. In the measurements denoted ∇ the aerosol was treated with infrasound for 30 s, as indicated. In the measurements denoted □ no infrasound was applied.

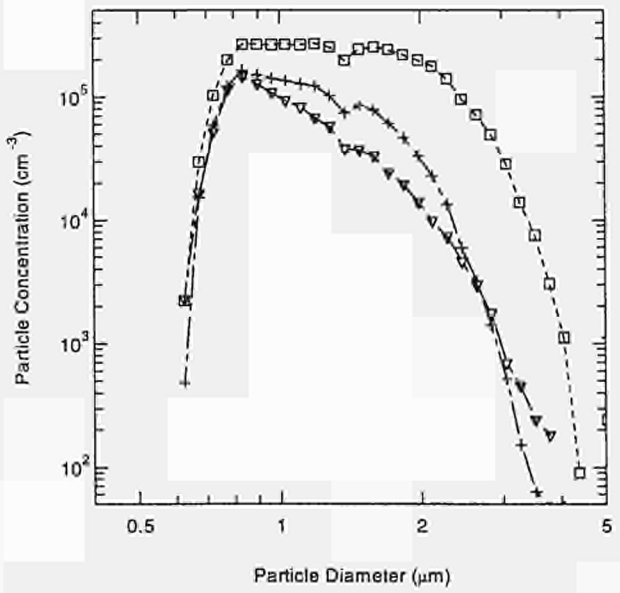

Fig. 5.6 Size distribution of the aerosol before (□) and after (∇) 30 s treatment by Infrasound. The data marked + correspond to an evaluation of the effect on the initial size distribution due to wall losses induced by infrasound (30 s) followed by Brownian agglomeration in the remaining 100 s before the final size distribution was measured.

Wall losses have been characterised as a function of particle diameter in independent measurements made at low particle concentrations ($N_T \approx 10^3$ cm^{-3}) so that particle agglomeration was hindered. Utilising these data, the effect on the initial aerosol size distribution from wall losses, while infrasound was applied to the aerosol and subsequent Brownian agglomeration thereafter can be evaluated. The results, also shown in Fig. 5.6, indicate that the effect of wall losses and Brownian agglomeration can account for the decrease in concentration of particles with diameters less than about 0.9 μm. Particles with diameters between 1 and 2.8 μm are removed more effectively than would be expected for wall losses and Brownian agglomeration alone. In contrast, however, particles with diameters greater than 2.8 μm are removed less effectively than expected. These results indicate that at higher particle concentration, agglomeration of particles with diameters less than 2.8 μm occurs and particles with larger diameters are produced. Due to their larger diameter, however, these particles impact on the walls with high efficiency and their direct observation is not possible.

As discussed above, all aerosol particles should be entrained in an acoustic wave with a frequency of 21 Hz. Given the high sound pressure levels (≈ 177 dB) the most likely effect which could give rise to agglomeration is that of acoustically induced turbulence [6,11]. This may also be responsible for the particle losses to the chamber walls. A complete investigation of the interaction between infrasound and aerosol particles requires a detailed study of the turbulence itself, particle impaction on the walls, and *in situ* characterisation of the particle size distribution.

Conclusions

These first preliminary investigations on the influence of high intensity infrasound on aerosols indicate that particle agglomeration occurs. The high rate of particle deposition onto the chamber walls inhibits the direct detection of larger particles which are produced. It is most likely that turbulence is the main cause of the observed agglomeration. Further investigations will concentrate on the effect of sound intensity on the agglomeration process. An additional measurement device such as a Phase Doppler Anemometer is required for *in situ* particle classification and characterisation of the turbulence.

References

[1] TUAR-94, p. 173
[2] Ph. Capéran, J. Somers, K. Richter, S. Fourcaudot; J.Aerosol Sci, in press
[3] J. Magill, Ph. Capéran, J. Somers, K. Richter, G. Rodriguez-Corral, E. Riera-Franco de Sarabia, J. A. Gallego-Juarez; J. Aerosol Sci. **22** (1991) S27-S30
[4] G. Rodriguez-Corral, J. A. Gallego-Juarez, E. Riera-Franco de Sarabia, F. Montoya; Ultrasonic International '81 (1981) 77-82

[5] S. Temkin; Elements of Acoustics, John Wiley & Sons (1981)
[6] E. P. Mednikov; Acoustic coagulation and precipitation of aerosols, translated from the Russian by Larrick, C. V., Consultants Bureau, New York (1965)
[7] N. L. Shirokova; Aerosol coagulation, in L.D. Rozenberg (ed), Physical principles of ultrasonic technology, translated from the Russian by J.S.Wood, Plenum, New-York (1970) 477-541
[8] S. Temkin, R. Dobbins; J. Acoust. Soc. Am. **40** (1966) 1016-1024
[9] Ph. Capéran, J. Somers, J. Magill, K. Richter, S. Fourcaudot, P. Barraux, P. Lajarge, G. Rodriguez-Corral, E. Riera-Franco de Sarabia, J. A. Gallego-Juarez, Proceedings of the 7th Annual Conference of the Aerosol Society (1993) 117-122
[10] Ph. Capéran; Institute for Transuranium Elements, Karlsruhe (Germany), Internal Report K0293167, 1993
[11] M. Barbe-Le Borgne, D. Boulaud, C. Malherbe, A. Renoux, A. Boutier; J. Aerosol Sci. **19** (1988) 3-10

5.2 Computation of Curie Temperature and Magnetic Anisotropy of Rare Earth - Transition Metal Magnets using Density Functional Theory

We have shown that the interaction between the rare earth magnetic moment and the transition metal magnetic moments can be derived from a variational principle. The magnitude of the interaction depends on the induced R-5d spin and local 5d-4f exchange integrals. Comparison with experiment for rare earth intermetallics is excellent and the theory is being extended to actinides, in particular the anti-ferromagnet, uranium dioxide.

Molecular field theory and the Onsager cavity field theory have been implemented. The first principles molecular field theory, based upon density functional theory, involves subtraction - from the calculated susceptibility - of the self-interaction of conduction electrons at a given site since this plays no role in long range ordering , hence phase transitions. The results are very promising with a calculated paramagnetic Curie temperature for Gd metal of 430 K compared with the experimental value of 319 K.

Calculations of the non-spherical spin and charge densities at the R-sites in rare earths have been started. Full potential calculations were made for the Pr chalcogenides and pnictides, including the non-spherical 4f charge density in the ground and excited crystal field states. The total energies of the compounds in each of the crystal field states was then calculated. The crystal field excitation energies, measured in inelastic neutron scattering experiments, were then computed as differences between these total energies.

5.3 Evaluation of Potentialities of Alternative Nuclear Fuel Cycles

Introduction

In present day studies of nuclear fuels one of the main concerns is the long term radiotoxic effects of spent fuel. The possibility of reducing the toxic hazard by altering the charge isotopic composition of the fuel itself for use in existing LWRs is investigated. The radiotoxicities of spent fuels of different charge compositions are calculated: the fuels studies are standard LWR uranium dioxide (UO_2), mixed oxide (MOX), thorium-uranium (Th-U) and thorium-plutonium (Th-Pu) fuels. The study focused on the potential radiotoxicity of the spent fuel (once through) without considering any specific accident scenarios or treatment of the mobility and migration of nuclides in the geosphere and biosphere.

The characterization in terms of radiotoxicity potential is based on the inventory of actinides and fission products in the spent fuel and the means to calculate the radiotoxicity. Inventory data found in the literature or specifically calculated for the purpose of this work were used for the radiotoxicity predictions. The code KORIGEN [1] has been used: it is a zero dimension code predicting, for a given charge composition and neutron spectrum, the evolution of a fuel under irradiation and cooling. Consequently, the nuclide inventory as a function of irradiation and cooling times is obtained (1 year up to 10 million years after discharge). This is a version of the ORIGEN [2] code adapted for use with German reactors and employed for the in-house calculations. The data banks on reaction cross-sections used with the KORIGEN code are coupled with three spectral indices which characterize the thermal, resonance and fast components of the neutron spectrum. The application of KORIGEN to UO_2 and Th-U cycles has been shown to be in agreement with the results of the Japanese code SRAC [3].

The radiotoxicity is calculated using the Annual Limits of Intake (ALI) values for both ingestion and inhalation, for the various nuclides, set by the International Committee for Radiological Protection (ICRP-61, 1991) [4]. It is important to note that these values can change with new information about how a particular isotope behaves in the body. For example, the ALI values for plutonium were increased by a factor of ten and those of americium, curium and californium by a factor of two while that of neptunium was decreased by a factor of ten [5]. Thus it is always possible that the values used here may be changed in the future.

The radiotoxicity is calculated in relation to the maximum permissible dose of 0.1 Sv over a five year period for occupational exposure with a limit of 0.02 Sv in any single year [4]. The radiotoxicity is defined by,

$$\text{Radiotoxicity} = 0.02A/ALI \text{ Sv/g}$$

where A is the specific activity (Bq). Of course there are other definitions of radiotoxicity but these will only give different absolute results: the relative differences will remain the same since they are all based on the same ALI values.

Results

Extensive calculations were done on the uranium and thorium cycles. The final results are given in terms of the radiotoxicity created in order to produce 1 GWe.yr of energy. All data were compared to the radiotoxicity of the natural uranium required to produce 1 tonne of 3.5% enriched uranium (7.6 tonnes nat.U). There is a difference in the inventory of fission products produced in UO_2 and ^{233}U-Th fuels due to the slight differences in mass between the fissile ^{233}U and ^{235}U (on average the fragments for ^{233}U are one atomic mass smaller than those for ^{235}U). However the total radiotoxicities hardly differ.

UO_2 Fuels

In Fig. 5.7 the total radiotoxicity as a function of time is given along with the significant contributions of the various isotopes and fission products for ingestion and inhalation. In both cases, up to 10^4 years $^{238\text{-}241}$Pu, ^{241}Am and ^{244}Cm are the major factors in the radiotoxicity. Note that fission products are significant for ingestion. Between 10^4 and 10^7 years these are superseded by ^{210}Pb, ^{229}Th, ^{226}Ra, ^{227}Ac, ^{231}Pa, ^{237}Np, ^{242}Pu for ingestion and ^{229,230}Th, ^{227}Ac, ^{231}Pa, ^{238}U, ^{237}Np, ^{242}Pu for inhalation. It was found that for the standard LWR UO_2 fuels the variation of enrichment and burnup does not significantly alter the radiotoxicity. The presence of Pu, Am, Cm, Np and their decay products are the major contributors to the radiotoxicity. These isotopes when combined produce a cocktail of long-lived highly radiotoxic material: the same is true for MOX fuels.

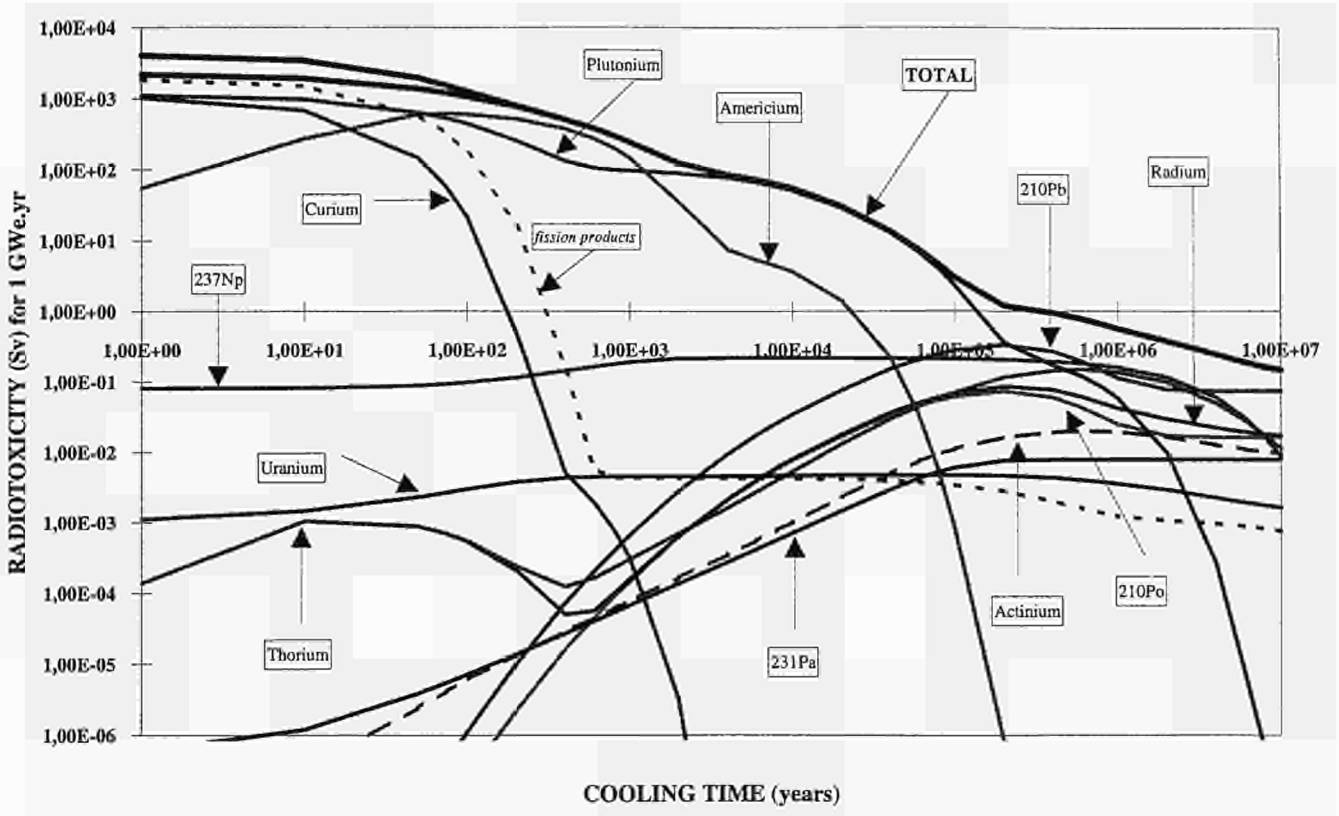

Fig. 5.7(a) The radiotoxicity as a function of cooling time for ingestion: UO_2 fuel (3.5% enrichment, 50 GWd/t). The contribution of the various actinides and fission products are displayed.

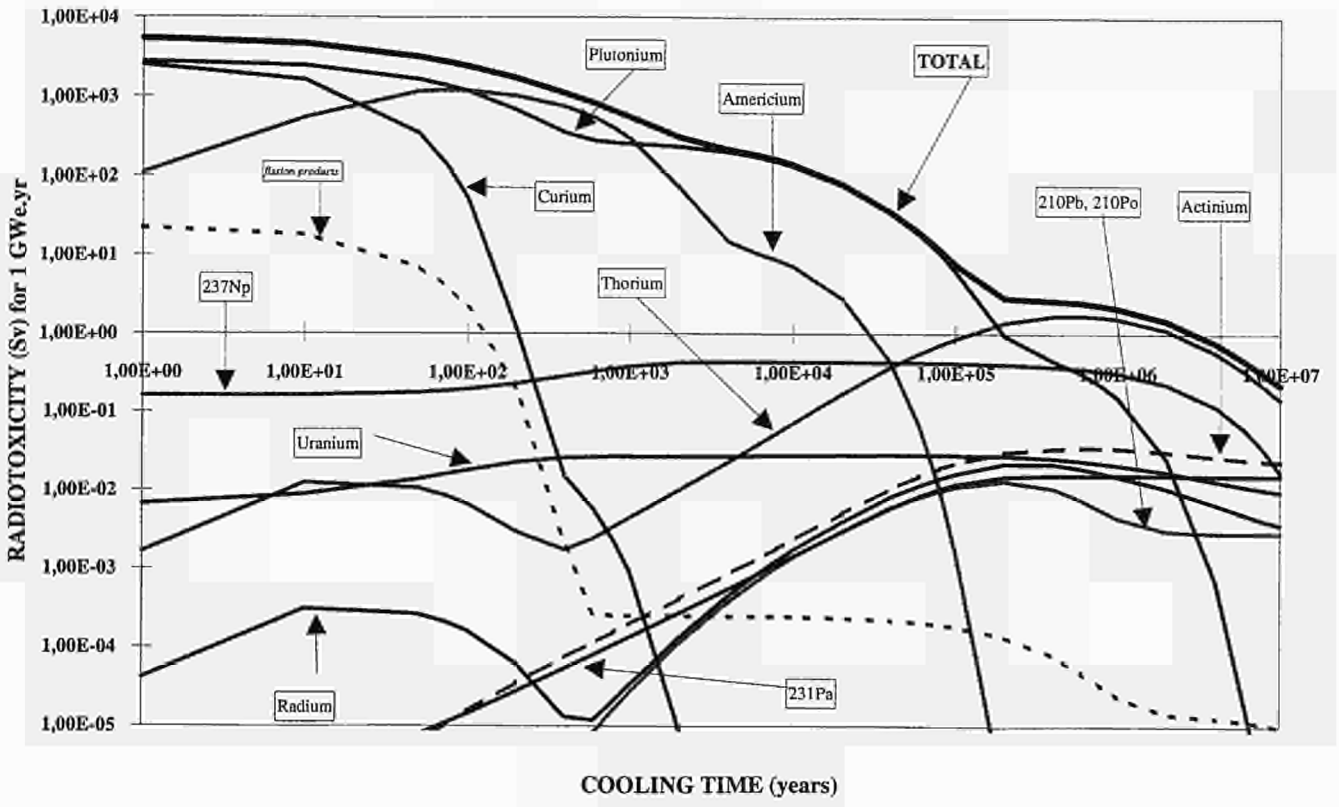

Fig. 5.7(b) The radiotoxicity as a function of cooling time for inhalation: UO_2 fuel (3.5% enrichment, 50 GWd/t). The contribution of the various actinides and fission products are displayed.

Thorium-uranium fuels

The presence of ^{238}U, the major component of UO_2 fuels, leads to the formation of plutonium, americium and curium. In order to suppress the production of these highly radiotoxic isotopes one must look to a different fuel cycle. The obvious candidate is the thorium fuel cycle: this can be substituted for UO_2 fuel in existing LWR reactors. There are two possibilities that may be considered. First, is the simple substitution of the ^{238}U by ^{232}Th in standard fuels and second is the fuel cycle using ^{233}U and ^{232}Th.

For the ^{233}U-^{232}Th cycle, up to 1000 years the radiotoxicity for ingestion is dominated by fission products, ^{228}Th, ^{224}Ra, ^{238}Pu, ^{231}Pa, ^{227}Ac, $^{232,233}U$ and $^{232,233}U$, ^{228}Th, ^{238}Pu for inhalation. From 10^3 to 10^7 years ^{229}Th (on the decay chain of ^{233}U) is the major contributor for ingestion and almost the sole factor for inhalation. In the case of UO_2 fuels the total radiotoxicity steadily decreases with time. In this case the toxicity at first decreases and then rises to a maximum at about 10^5 years after which it once more decreases (Fig. 5.8). This is due to the decay of ^{233}U which gives rise to the isotope ^{229}Th, the main factor after 10^3 years. The results for the Th-U fuels using ^{235}U instead of ^{233}U are similar. Thorium-plutonium fuels also give similar results with far higher values in the first 10^4 years due to the presence of plutonium. As in the previous case the variation of enrichment and burn-up does not significantly alter the radiotoxicity of Th-U fuels.

Comparison between UO_2 and Th-U fuel

The results show that plutonium, americium and curium dominate the radiotoxicity of UO_2 fuels while uranium and protactinium dominate that of Th-U fuels. In Fig. 5.9 the radiotoxicity for ingestion of these fuels is compared. Neglecting the contribution of fission products the radiotoxicity of Th-U fuels can be as much as two orders of magnitude less than that of UO_2 fuels up to 10^4 years [6] . There is then a period, from 10^4 to 10^6 years, where the radiotoxicity of Th-U spent fuels exceeds that of UO_2. After that time the radiotoxicity of Th-U falls sharply below that of UO_2. This is unchanged for inhalation when the fission products are included. However, for ingestion, the inclusion of the fission products means that the radiotoxicities of both fuels is almost the same for the first five hundred years.

In Fig. 5.10 the radiotoxicity of the Th-U fuel after the removal of 99% uranium is displayed. The uranium must be recovered in order to provide fissile ^{233}U for the next cycle. The case when 99% protactinium is removed is also displayed. As can be seen it is well below that for the standard UO_2 fuel. Moreover it falls below the value of the natural uranium required for 1 tonne of 3.5% enriched fuel after 5000 years.

Energy Amplifier

The Energy Amplifier (EA) has been proposed as new type of reactor which would form part of a safer less radiotoxic fuel cycle [7] . Detailed calculations have been carried out in order to assess the radiotoxic impact of such a system [8].

References

[1] U. Fischer, H. W. Wiese; Kernforschungszentrum Karlsruhe, report KFK-3014 (1983)

[2] M. J. Bell; ORNL-4628 (1973)

[3] T. Naka, T. Takeda, Proceedings of the Indo-Japanese Seminar on Thorium Utilisation, Dec 10-13, Bombay, India (1990) 177

[4] ICRP Publication 61 (1991)

[5] A. G. Elayi, J. P. Shapira; Radioactive Waste Management and the Nuclear Fuel Cycle, 8 (1987) 327

[6] J. van Geel, H. E. Schmidt, Hj. Matzke, G. Nicolaou and C. O'Carroll; Global '93, ANS Topical Meeting, Seattle, September 12-17 (1993)

[7] F. Carminati, R. Klapisch, J. P. Revol, C. Roche, J. A. Rubio and C. Rubbia; CERN/AT/93-47, (1993)

[8] J. Magill, C. O'Carroll, P. Gerontopoulos, K. Richter and J. van Geel; Obninsk, Russia, November 7-11 (1994)

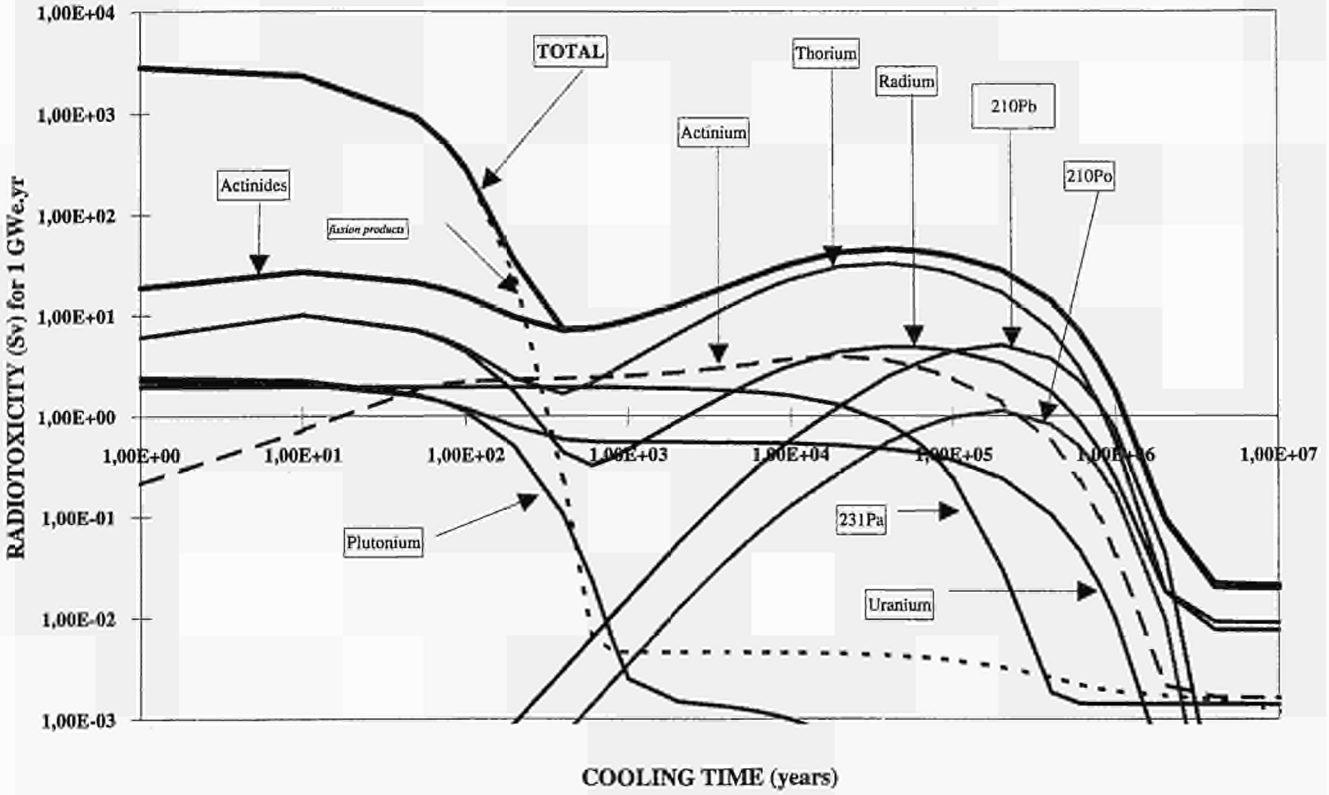

Fig. 5.8(a) The radiotoxicity as a function of cooling time for ingestion: Th-U fuel (3.52% ^{233}U, 60 GWd/t). The contribution of the various actinides and fission products are displayed.

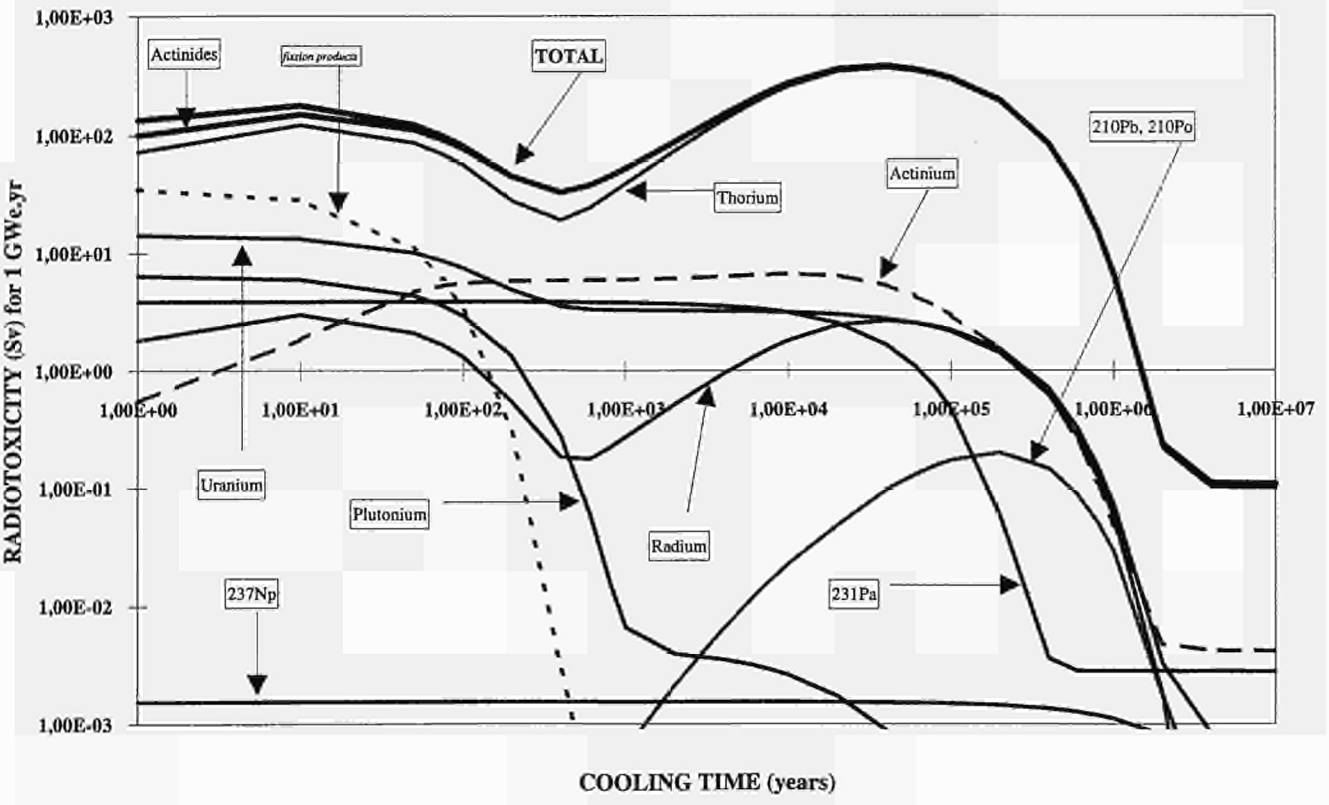

Fig. 5.8(b) The radiotoxicity as a function of cooling time for inhalation: Th-U fuel (3.52% ^{233}U, 60 GWd/t). The contribution of the various actinides and fission products are displayed.

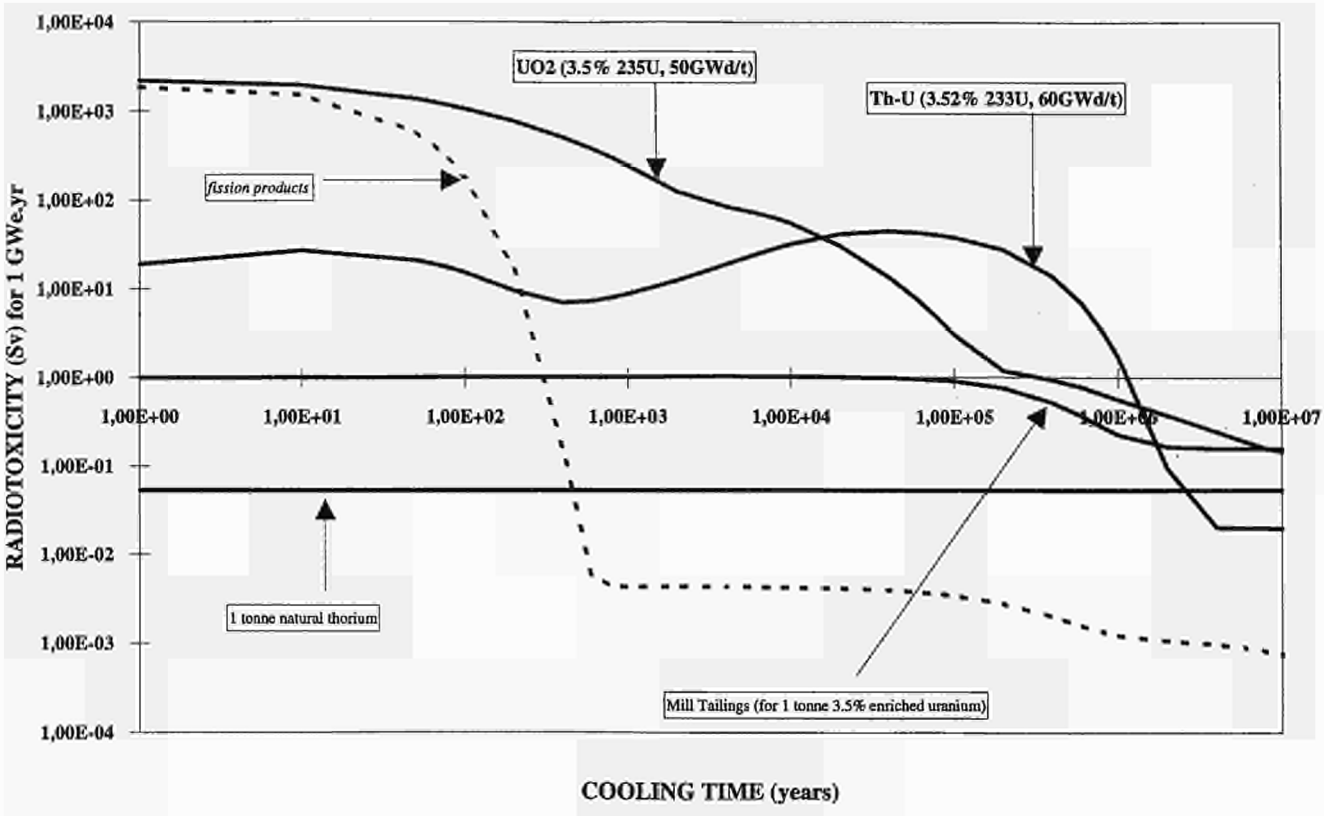

Fig. 5.9(a) The radiotoxicity of actinides as a function of cooling time for ingestion: UO_2 and Th-U fuels. The values for mill tailings from the production of 1 tonne of UO_2 (3.5% enriched) and for 1 tonne of natural thorium are also displayed.

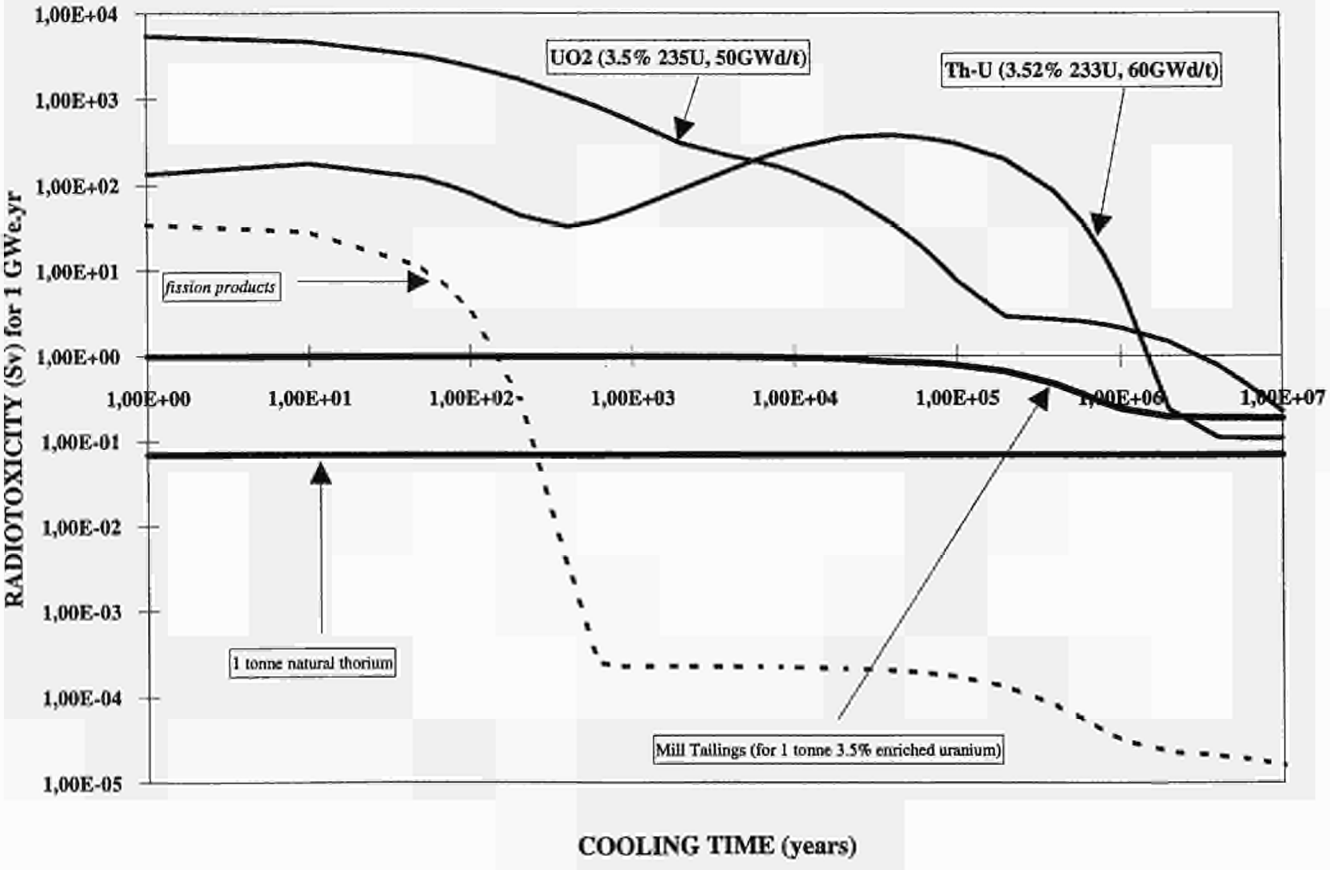

Fig. 5.9(b) The radiotoxicity of actinides as a function of cooling time for inhalation: UO_2 and Th-U fuels. The values for mill tailings from the production of 1 tonne of UO_2 (3.5% enriched) and for 1 tonne of natural thorium are also displayed.

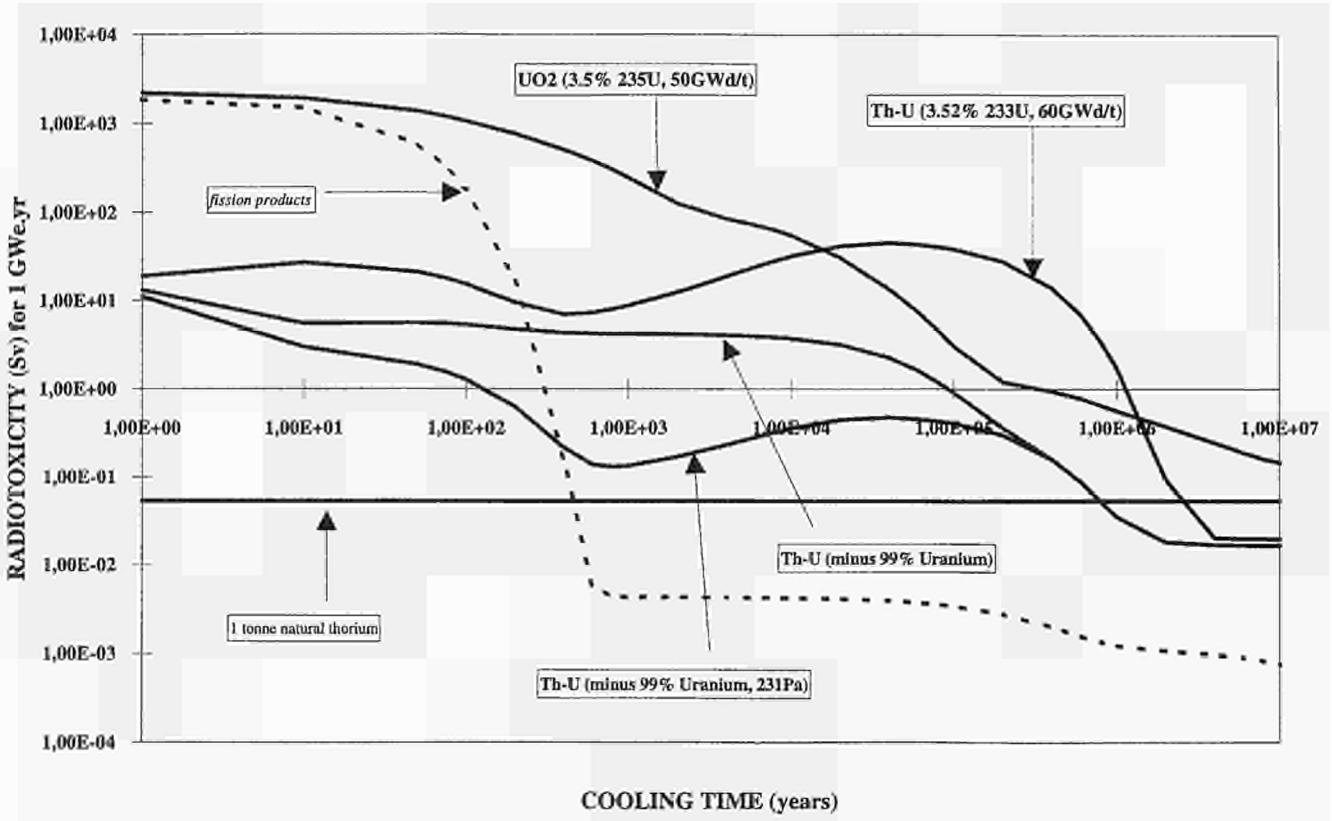

Fig. 5.10(a) The radiotoxicity as a function of cooling time for ingestion: UO_2 and Th-U fuels. Results for the recovery of 99% uranium and 99% protactinium in the Th-U cycle are included.

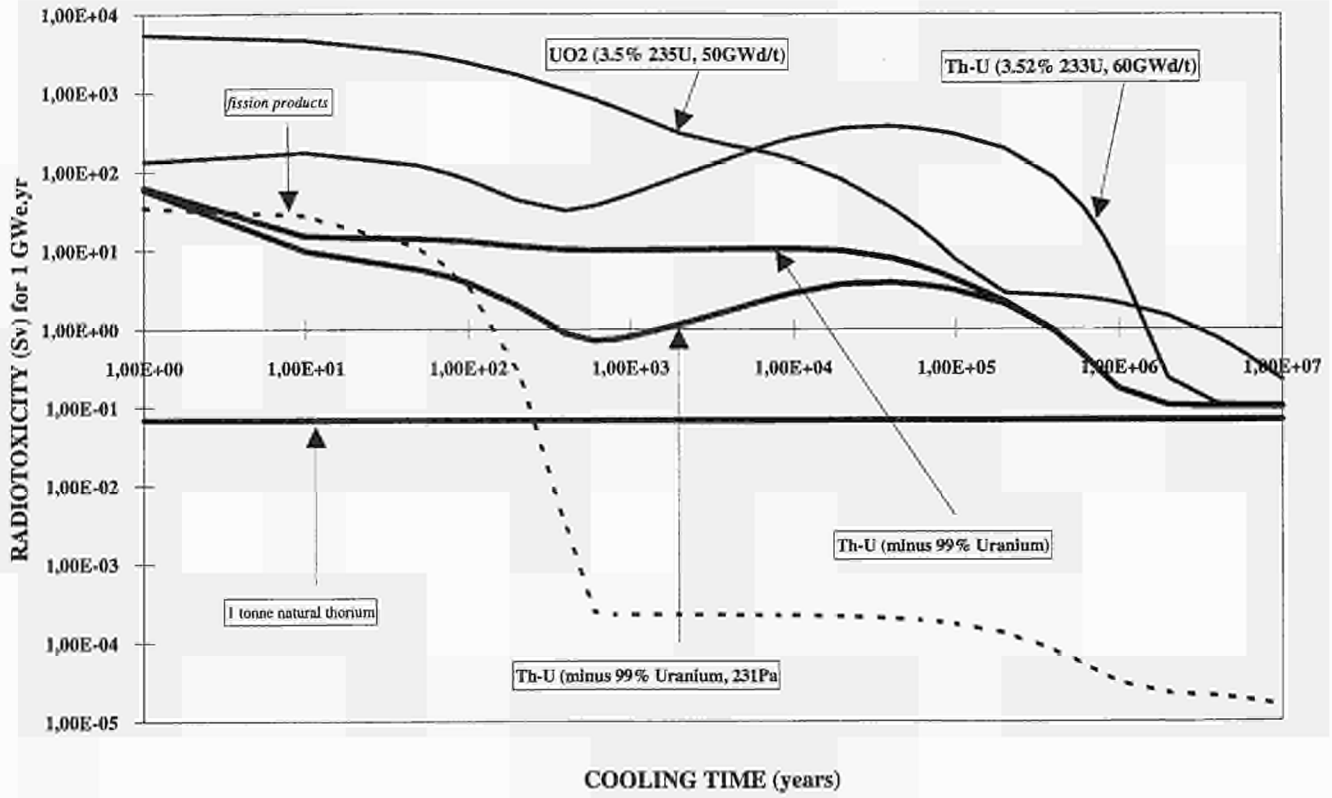

Fig. 5.10(b) The radiotoxicity as a function of cooling time for inhalation: UO_2 and Th-U fuels. Results for the recovery of 99% uranium and 99% protactinium in the Th-U cycle are included.

5.4 Property Studies with U-Al Cermets

Introduction

During the reporting period a new MTR fuel, based on uranium nitride, with a maximum uranium loading of 7 g U/cm^3 was developed in collaboration with the Compagnie pour l'Etude et la Réalisation de Combustibles Atomiques (CERCA/Romans) with the Institute.

The results of this work were presented at the international meeting on Reduced Enrichment for Research and Test Reactors (RERTR) in Williamsburg, VA/USA, Sept. 1994 [1].

Development of a new high density MTR-fuel

Since the very beginning of MTR fuel production, about 30 years ago, there has been a constant need for an increase in the uranium loading per plate. With the conversion to low enriched uranium in order to support non-proliferation policies, the increase in uranium loading has become more important.

CERCA has been an active member in this development and investigated together with our Institute the fabrication parameters of MTR fuel plates based on nitride fuels.

By using the denser fuel UN, instead of U_3Si_2, the theoretical load of a MTR fuel plate can be increased from 4.8 - 5.8 g U/cm^3 to 6.0 - 7.3 g U/cm^3 depending on the volume fraction of the fuel - Al powder mixture.

Before manufacturing plates the metallurgical compatibility of UN and aluminium was investigated in the temperature range of 25 - 600 °C under argon atmosphere.

A dilatometric analysis was carried out on a sandwich made of a pellet of UN between two discs of aluminium. Fig. 5.11 shows the dilatometric graph obtained. A slow expansion of the sample until about 550 °C was observed. Thereafter a fast interaction begins and the sandwich collapses at 620 °C (melting).

As a metallurgical reaction seems to occur at about 550 °C, compacts made of UN powder mixed with Al powder were heated at 480, 550 and 580 °C for a 5, 15 and 20 hour period under argon atmosphere.

Optical micrographs, X-ray analysis and Scanning Electron Microscopy (SEM) gave the following information:

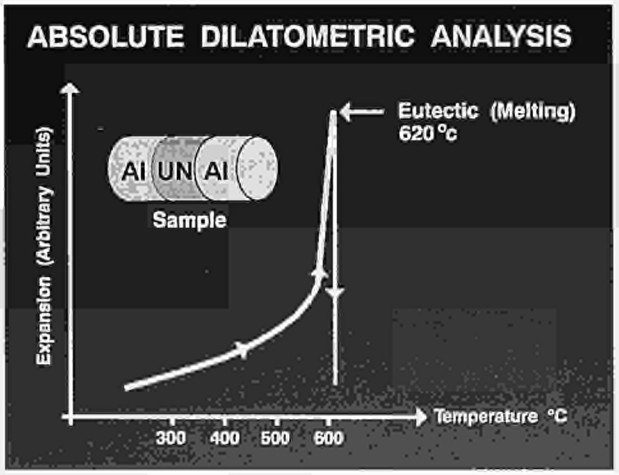

Fig. 5.11 Compatibility of uranium nitride and aluminium.

- 480 °C: no diffusion detected
- 550 °C: a slight swelling at the interface between UN and Al but no new phase is detected by X-ray analysis
- 580 °C: a new phase, mainly UAl_3, is detected at the grain boundaries

By comparison U_3Si_2 reacts rather rapidly with aluminium above 600 °C to produce $U(Al,Si)_3$. At 500 °C no reaction zone can be seen in the optical micrograph.

Uranium nitride does not seem to be more reactive with aluminium than U_3Si_2 fuel.

As these studies carried out in the Institute prove that there is no incompatibility between UN and Al below 500 °C, the logical continuation was to set up a preliminary manufacturing test of MTR plates.

ITU fabricated for CERCA depleted uranium mononitride powder and CERCA manufactured a few plates applying the advanced process developed for high volume fraction of fuel particles. As the main advantage of the uranium nitride is its high uranium content, the aim of this test was to manufacture plates containing about 7 g U/cm^3.

The most interesting results of this manufacturing test on a laboratory scale are given by the Scanning Electron Micrographs. A comparison between an uranium nitride and a U_3Si_2 plate is shown in Fig. 5.12.

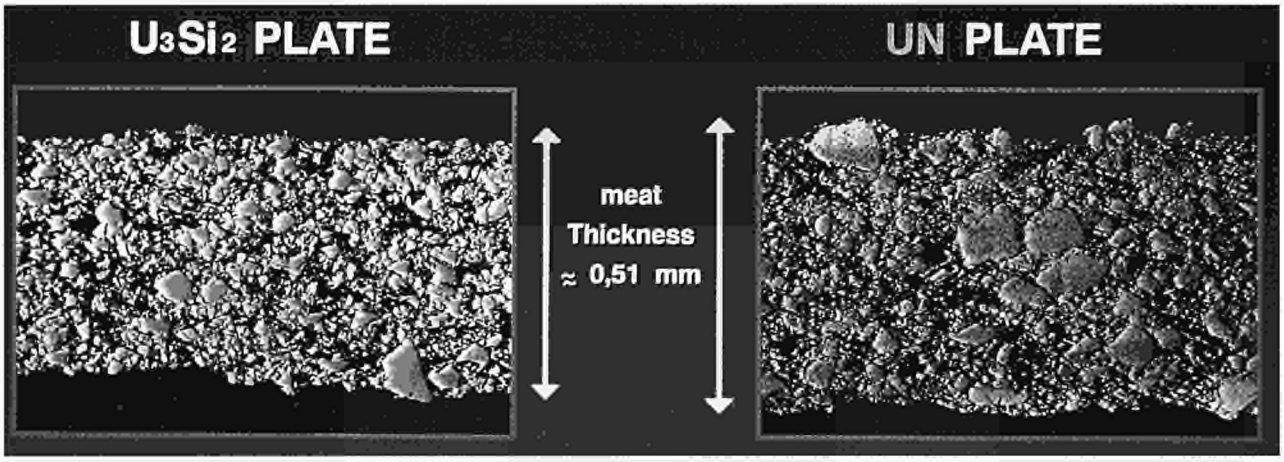

Fig. 5.12 Comparison between U_3Si_2 and UN plates (Scanning Electron microscopy)

On a first comparison, the plates look very similar. A good metallurgical cohesion is found between the meat and cladding and no lack of bonding was revealed by a Blister test.

The overall porosity of the UN plate is about 16%. Less than an half of this is due to internal porosity of UN particles. This porosity leads to a plate with an uranium density close to 7 g U/cm^3.

These results confirm the information gained by the studies of ITU which showed a good compatibility of uranium nitride and aluminium below 500 °C.

The feasibility of manufacturing mononitride plates on a laboratory scale has been demonstrated at CERCA. It was confirmed that:

- no metallurgical reactions occurred.
- The cohesion of the meat was good.
- No lack of bonding between the cladding and the meat was detected.
- The use of mononitride could permit to be increased to the maximum uranium loading to 7 g U/cm^3.

In order to qualify this new fuel an international consensus on its acceptance and irradiation experiments is necessary. Funding seems to be possible by the US-RERTR "high density fuel" programme.

Reference

[1] J.P. Durand, P. Laudamy, K. Richter; Preliminary Developments of MTR Plates with Uranium Nitride, International Meeting on Reduced Enrichment for Research and Test Reactors (RERTR), Williamsburg/USA, Sept. 1994

5.5 Two-Dimensional Heat Transfer Mapping

Development of the Fast Transient Thermography (FATT) method

In the last annual report (TUAR-93, p. 56) new methods were described to investigate the feasibility of carrying out thermal diffusivity measurements under non-conventional conditions. A first set-up was constructed where the sample is placed in a small chamber with a controlled atmosphere, and supported by three ceramic pins. The specimen disk is heated from two sides by a continuous laser, and a Nd-YAG laser pulse is then applied. The thermal diffusivity is then measured as in the case of the usual laser-flash technique. Very high temperatures can be attained both in vacuo and under chemically active atmospheres.

Another advanced technique, called FATT, for the measurement of the heat transport in heterogeneous systems is being developed based on high speed CCD cameras and 2D thermography processing. At the present time it has been found possible to use a CW YAG laser instead of CO_2 laser both for the FATT and conventional laser flash. This will considerably simplify the set-up made for a hot-cell or for a glove-box because at the YAG wavelength use of optical fibres is possible. It is also important, that only one laser head is required with a beam splitting device, so the power ratio in two beams will remain constant even in the presence of small instabilities of the output power. A suitable laser was purchased: this can deliver up to 500 W of CW power to the beam splitter with a continuously adjustable power ratio. The important advantage of CW YAG laser with a fibre optic beam delivery system is that a very homogeneous power density distribution is achieved which helps to minimise temperature gradients across the sample before applying instantaneous probe laser shot. This YAG laser has been tested and a dual beam heating system is being constructed.

6. Scientific-Technical Support to Community Policies

6.1 Support to DG I

6.1.1 Field test of robotized system for the chemical treatment of diluted spent fuel solutions

Introduction

The initial proposal for a field test of the robotized system developed at ITU was made in 1988, calling for the installation of a system at the Gatchina reprocessing facility south of Leningrad in the USSR. Further discussions resulted in a joint task proposal under the European Community Support Programme and the Russia Support Programme to the IAEA.

The objectives of the joint U.S.S.R., EURATOM and IAEA field test of the robot system were:

- To test the reliability of the robot system under routine field operation
- To evaluate the accuracy and precision of the measurement performance obtained by on-site robotized isotope dilution mass-spectrometry (IDMS).
- To check the adequacy of the authentication measures applied for sample preparation for IDMS.
- To serve for inspector training purposes after the field test was completed.

During the field test, the robot was to perform the chemical treatment of diluted spent fuel solution samples up to the loading of filaments.

As originally foreseen, up to 40 batches of spent fuel would be sampled in duplicate, diluted and spiked for isotope dilution analysis of U and Pu by thermal ionisation mass-spectrometry. The robot system, as previously described [1], would carry out all steps associated with sample preparation, including the loading of mass-spectrometer filaments. These filaments would be measured at the Seibersdorf Analytical Laboratory (SAL) and parallel aliquots would be measured at the Khlopin Radium Institute (KRI) and ITU. The "total evaporation" method would be performed at SAL and ITU and compared with measurements using the conventional mass-spectrometric technique at KRI and ITU. A meeting held in Gatchina in October, 1990 between representatives of the three organisations summarised the progress of the field trial at the time of the installation and first use of the robot system.

Ultimately, four batches taken from a single spent fuel solution were treated in duplicate by the robot and measured at SAL, ITU and KRI. Meetings were held in Vienna in September of 1991 and in Gatchina in October of 1991 to discuss the results of the 1st phase and to identify follow-up actions. Based on these recommendations, improvements were made in the equipment and procedures and a follow-up exercise was planned.

The 2nd phase experiment as originally planned would have involved single aliquots and replicate spiking of 24 separate batches of spent fuel. The actual experiment which was carried out involved 4 input solutions from each of which 6 aliquots were taken and diluted to give 24 solutions. Eight of these were sub-sampled, spiked in duplicate and measured at all three institutes. A report of the phase 2 experiment including only the results of the KRI measurements was produced in 1993 [2].

Phase 1

The first phase of the testing of the robot began in October, 1990 using a diluted spent fuel solution ("master solution") containing approximately 500 µg/g U and 5 µg/g Pu. Four batches were sampled from this master solution; from each batch, two sub-samples were spiked and additional aliquots were taken for unspiked measurements. The robot performed the sub-sampling, spiking, isotopic equilibration step, separation using tributyl phosphate (TBP) in CCl_4, and filament loading. A control sample was also processed in parallel with the spent fuel solutions.

The robot-loaded filaments were measured at SAL in April, 1991. Replicate samples loaded from solutions were measured at TUI in the same period and aliquots from

the 4 batches were measured at KRI in the period from October, 1990 to January, 1991.

Several observations can be made from the results:

1. Agreement between the 3 laboratories for the U results is acceptable and in the range of 0.06 to 0.5% relative, except for sample 9956-08 where the SAL and KRI results agree for each of the spikings, but not between the 2 spikings. The ITU result in this case seems to be an average of the 2 spikings.
2. Similar results are seen for the Pu, with the between-laboratory agreement in the range 0.05 to 0.6% relative, except for sample 9956-08.
3. The problem for sample 9956-08 seems to be due to a weighing problem, either of the sample or spike aliquots. This is revealed by the consistency of the Pu/U ratios which agree both within and between laboratories at the 0.5 to 1.0% level, even though the replicate spikings give U and Pu concentrations which differ by 4.5%.
4. Similar weighing problems appear, to a lesser extent, in sample 9956-06 (i.e. between-spiking differences of 2.0 to 2.5%, with differences in the Pu/U ratios of around 0.3%).
5. As a result of the observations above, improvements were made in the robot hardware and operating programme and the analytical balance used by the robot was replaced in May 1992.

Phase 2

An examination of these results yields the following observations:

1. For uranium, there are several cases where the agreement between replicate spikings for the same batch are outside of acceptable limits (1% relative) . These batches are 9655-01 (SAL), 9655-05 (SAL), 9667-04 (SAL) and 9667-02 (KRI). This indicates a problem with spike-sample equilibration or mass-spectrometric measurement.
2. In general, the agreement between laboratories for uranium is good with only two exceptions, 9667-02 (1.4% difference between SAL and KRI) and 9667-04 (10.5% difference between SAL and KRI). For sample 9667-04, there seems to be either a problem of sample identification in the SAL data or else a problem with the mass-spectrometric measurement.
3. For Pu, there are two apparent outliers in the SAL data, 9655-01 and 9655-04, which are probably due to mass-spectrometric measurement problems (too little Pu on the filament for a good measurement). Agreement between replicate spikings of the same batch was generally acceptable, except for 9667-03 (SAL) where the difference is slightly greater than 1% relative.
4. The agreement between laboratories was good, provided that the apparent outliers mentioned in point 3 are ignored. However, for samples 9655-01 and 9655-04 the differences between the SAL and KRI and between ITU and KRI are greater than 1%, relative, indicating a possible problem with the KRI measurements.
5. The differences between the average values for U and Pu in samples 9667-03 and 9667-04 are greater than 1% in the KRI (U and Pu) and SAL (Pu only) data, indicating a possible problem with weighing of the sample or spike. This suggests that problems were still observed with the balance used by the robot, similar to those in Phase 1, but with less serious effects. The nature of the data makes it difficult to separate such effects clearly.
6. Sample 9667-03 was apparently wrongly numbered in case of ITU. Either it is a duplicate of sample 9667-02 or the missing sample 9667-01.

Conclusions

It is possible to draw the following conclusions:

1. The robot system worked well under the actual conditions experienced at a reprocessing facility. There were no major breakdowns of the equipment or delays in processing samples. All sub-systems of the robot worked equally well and mass-spectrometer filaments were loaded successfully.
2. Problems with weighing of samples and spikes inside the glove-box enclosure created poor agreement between replicate spikings, especially in Phase 1, but also to a lesser extent in Phase 2. This problem may be related to electrostatic charging problems or vibration.
3. The chemical separation procedure used in the robot system was the same as used at ITU which does not provide sufficiently clean Pu fractions for measurement at SAL, nor was the Pu recovery sufficiently high. This revealed itself as poor signal strength in the mass-spectrometer and a large ^{238}U interference on the ^{239}Pu peak. The reverse-phase chromatographic procedure using trioctyl phosphine oxide (TOPO) which has already been adapted at SAL to the ITU-designed robot system would be a preferable procedure.
4. The possibility of checking the adequacy of the authentication measures by video cameras proved to be successful.

References

[1] L. Koch, et al.; "Automatic Analysis for Input of Nuclear Fuel Reprocessing", Isotopenpraxis **24** (1988) 229-231

[2] G. A. Akopov, et al.; "Field Test for On-Site Sample Conditioning by Robot", V. G. Khlopin Radium Institute, June 1993.

6.1.2 The ARTINA (Analysis of Radioisotope Traces for the Identification of Nuclear Activities) laboratory

An important contribution to the identification of undeclared nuclear activities is the detection of nuclear signatures by the analysis of environmental samples in the area of the suspected activity. The analysis of such samples is a highly specialised and exacting discipline requiring suitably equipped and designed facilities and a high level of analytical competence. Detection limits for U and Pu should be of the order of 10^7 atoms [1].

A good part of the instrumental capabilities already exist in the Institute but it was realised that a laboratory completely isolated from the contamination zone of the Institute was required, where samples can be received, handled and prepared for measurements without cross-contamination.

The ARTINA (Analysis of Radioisotope Traces for the Identification of Nuclear Activities) laboratory was conceived for this purpose and the design phase has been started. A laboratory external to the Institute will be constructed using prefabricated techniques to arrive at a class 100 environment. The ARTINA design will provide:

- personnel access with appropriate clothing
- transfer and acceptance of samples with preliminary cleaning and removal of the outer packaging
- chemical treatment to concentrate elements of interest. Sample type include water, sediment, soils, vegetation and swipes. High purity spikes may be added to allow subsequent quantification by isotope dilution mass-spectrometry.
- preparation of reference or control samples for internal quality control

The final design concept of ARTINA will be approved in the beginning of 1995 and first operation is expected for October 1995.

Reference

[1] D. Donohue, S. Deron, E. Kuhn; IAEA Bulletin 3 (1994) 20-23

6.1.3 Analysis of radionuclide traces for the identification of nuclear activities

In the framework of the safeguards monitoring for detection of undeclared nuclear activities, we have been asked to analyse radioisotopes at trace levels in environmental-type samples.

As reported previously (TUAR-93, p. 212-214) we have started to adapt the procedures already existing and used for other kind of samples to this type of samples. It was also realised that new procedures needed to be developed in parallel and therefore exploratory researches on new methods have been started as well.

In March 1994 a liquid scintillator counter (LSC) was installed. The instrument has been tested and analytical procedures for tritium determination have been optimised. It has been possible to measure tritium at low levels of activity in different type of samples: natural waters (river and sea water), on surfaces of copper/brass seals typically used in Safeguards inspections, and on filter paper used as wipe tests. Methods for the measurement by LSC of other radioisotopes: $^{129/131}$I, ^{14}C, ^{133}Xe, ^{85}Kr, $^{103/106}$Ru, ^{144}Ce, $^{134/137}$Cs, $^{239/240/241}$Pu, ^{99}Tc, present at low activity levels in environmental samples are under investigation.

Until the planned ARTINA laboratory outside the contamination control zone of the Institute has been completed, exploratory studies concerning the method of dissolution of environmental samples have been started in an existing cold laboratory. In these studies certified environmental samples from the IAEA have been used. These samples consist of soils, sediments and dried grass containing very low activities with different isotopic 'signatures'. The characteristics of one of these samples as an example are reported in Tab. 6.1. The activity level of this sample is very low. As a consequence there is a real possibility of cross-contamination during treatment.

Tab. 6.1 Measurement of IAEA-375 soil sample. The soil (top soil to a depth of 20 cm) was collected on the field of the collective farm "Starvi Vishokov" Novozybkov district Brjansk region, Russia, in July 1990, reference date: 31-12-1991. There is evidence for the presence of small hot particles which can seriously influence the measured activity concentrations of transuranium nuclides.

Nuclide	Bq/Kg	g/Kg
Cs-134	463	9.5×10^{-12}
Cs-137	5280	1.6×10^{-9}
I-129	1.7×10^{-3}	2.6×10^{-10}
K-40	424	
Ra-226	20	5.4×10^{-10}
Ru-106	56	
Sb-125	77	2.0×10^{-12}
Th-232	20.7	5.0×10^{-3}
U-238	22.6	1.8×10^{-3}
Am-241	0.13	

A widespread literature survey has been made concerning sample pre-treatment (grinding, homogenisation, drying) and dissolution methods. For the moment priority is being given to the dissolution. Various methods are under investigation. The aim is to determine the most appropriate in view of the subsequent wet instrumental technique used: liquid scintillation spectrometry, inductive-coupled plasma mass-spectrometry (ICP-MS), thermal ionization mass-spectrometry (TIMS).

For the direct analysis of the solid, the same samples are being investigated by glow-discharge mass-spectrometry (GDMS) and electron micro-probe analysis (EMPA). GDMS, which has detection limits in the ppt-ppb range, is being using for trace elements analysis of the bulk material. A complete survey of each sample is generally performed using a resolution of about 5000. At this resolution it is possible to separate molecular isobaric interferences arising from the complex matrices of the samples, from the analytes of interest. Subsequently, the elements of interest are selected and analysed in repetitive scans. Isotopic analysis is also being carried out directly on the solid samples. In this case the resolution is reduced to 1000 in order to obtain flat peaks.

EMPA is being used to determine different mineral phases in the soil and sediments and to carry out quantitative analysis of the elements present. A combination of energy dispersive and wavelength dispersive analysis is employed. Energy dispersive analysis is used for a rapid overview and quantification with a standard analysis procedure. Wavelength dispersive analysis is employed for quantitative analysis of light elements ($Z< 10$) and of the actinide elements ($Z>92$).

Since the samples must be conductive for both the techniques, various methods of sample preparation are being investigated.

The problem of single particle characterization is being investigated. A micro-manipulator and a microscope have been ordered and will be installed at the end of this reporting period. The aim is to be able to separate single particles from the bulk of the sample and then to characterise them by mass-spectrometric techniques, whereby it is hoped to be able to also apply secondary-ion mass-spectrometry (SIMS). Experimental work on standard particles and real samples will be performed during 1995.

6.2 Support to DG XIII

6.2.1 Acoustic aerosol agglomeration

The main aim of this research has been the development of a process using acoustic waves to treat airborne particles so that they can be separated with higher efficiency by conventional gas cleaning devices. During the year, discussions concerning a project involving the "Vereinigung der Großkraftwerkbetreiber" (VGB) and the "Fachverband Dampfkessel-, Behälter- und Rohrleitungsbau e.V." (FDBR) were pursued. Contacts with KEMA were established and a contract to carry out tests on acoustic agglomeration of aerosols at their coal fired pilot plant in Arnhem has been proposed and is awaiting final signature. Investigations on the influence of inertial particles on the acoustic agglomeration process were continued in the ITU laboratories, and the results are presented below.

Influence of inertial particles on the acoustic agglomeration of a titanium dioxide aerosol

Introduction

Investigations on the acoustic agglomeration of glycol fog have shown that at sufficiently high droplet concentration, the initially monomodal size distribution evolves into a bimodal distribution. It has been shown experimentally [1-3] that the characteristic size dividing the droplet populations corresponds to droplets whose relaxation time, τ, is equal to the wave period, T. The interactions between droplets, which controls the form of the final size distribution, can be grouped qualitatively into two mechanisms which occur simultaneously. Coalescence of the inertialess droplets (τ<T) amongst themselves to produce inertial droplets (τ>T) is related to hydrodynamic interaction [4]. Coagulation by impaction of small droplets on inertial droplets (ortho-kinetic mechanism [5]) is the second effect which occurs in the presence of an acoustic field. When the initial size distribution is such that most of the droplets are inertialess, the first mechanism dominates. When a sufficient quantity of big droplets has been generated impaction between the two populations is favoured. The role of the latter mechanism was evaluated in an earlier investigation on the acoustic agglomeration of glycol fog [1,3]. The studies presented here are concerned with the characterization of the interaction of inertial droplets with small inertialess aggregates of TiO_2. These investigations are an extension of those reported earlier on pure fog [1,3]. The experimental conditions were such, however, that an improved control of both the generation of inertial droplets and the initial aerosol size distribution was possible.

Experimental procedure

All experiments were performed in a cylindrical plexiglas chamber using a 21 kHz source operating at 100 Watts electrical power. Further details on the experimental arrangement are presented elsewhere [1,3]. After an initial injection of fog, inertial droplets are formed by the coagulation of small droplets (τ<T; $\rho \approx 10^3$ kg m^{-3}). Once the inertial droplets were generated, a TiO_2 aerosol was injected into the cavity. The evolution of the number concentration of small particles, N_s, of inertial droplets, N_I, and of the total number of particles, N_T, during a specific experimental run, is plotted in Fig. 6.1. The size distributions at various times are also shown. After injection of the fog, at t = 124 s, the number of inertial droplets increases due to coagulation of small droplets amongst themselves, and reaches a maximum value and then decreases. The exponential decrease of N_I with time is due to the domination of their dynamics by losses to the chamber walls. The characteristic bimodal shape of the size distribution, just before injection of TiO_2 particles (here t_i = 330 s), should be compared with that of the initial fog size distribution. A peak, characteristic of inertial particles, forms at an aerodynamic diameter, d_I, of 2.8 µm. By choosing the time, t_i, of TiO_2 injection, the concentration of inertial droplets in the fog+TiO_2 period can be controlled. Thus each experimental run involved two steps,

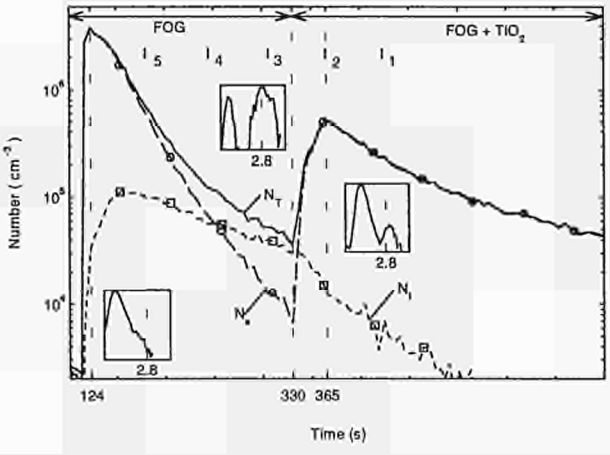

Fig. 6.1 Total number concentration N_T (—), number concentration of small, N_s, (○) and inertial particles, N_I, (□) as a function of time. Size distributions are shown following the injection of fog, and just before and just after the injection of TiO_2. Injection of TiO_2 was made at five different times. The numbers 1 to 5 correspond to the time at which the injection was completed.

the injection of fog and the injection of TiO_2. Three runs were made at each selected value of t_i, and they were then averaged to improve statistics. Five values of t_i were selected; the data of Fig. 6.1 correspond to the second of these (Nr 2; t_i = 330 s).

Discussion

The initial size distributions in the fog+TiO_2 regime, which corresponds to the second maxima in N_T *vs* t, are plotted in Fig. 6.2, for the 5 different values of t_i as indicated in Fig. 6.1. A size distribution corresponding to an experiment with TiO_2 alone is also plotted in Fig. 6.2 for comparison. It can be seen that the small particle mode (d_g = 0.95 µm, σ_g = 1.25), is mostly composed of TiO_2 particles for runs 1 to 3. For run 4, a slight broadening of the fine particle peak indicates that there were remnant fog droplets present in this mode. Due to the early injection time, t_i, (see Fig. 6.1) of run 5, the fine mode is heavily contaminated with fog droplets which are still present, and the size distribution is almost identical to that obtained in the absence of TiO_2 [1,3]. The peak due to the inertial droplets, after injection of TiO_2, is centred on d_I=3.4 µm, which is slightly higher than the value for pure fog before injection (d_I=2.8 µm [1,3]). The maximum of the peak due to the inertial particles increases in magnitude from run 1 to run 5, but its shape is only in similitude for runs 1 to 3.

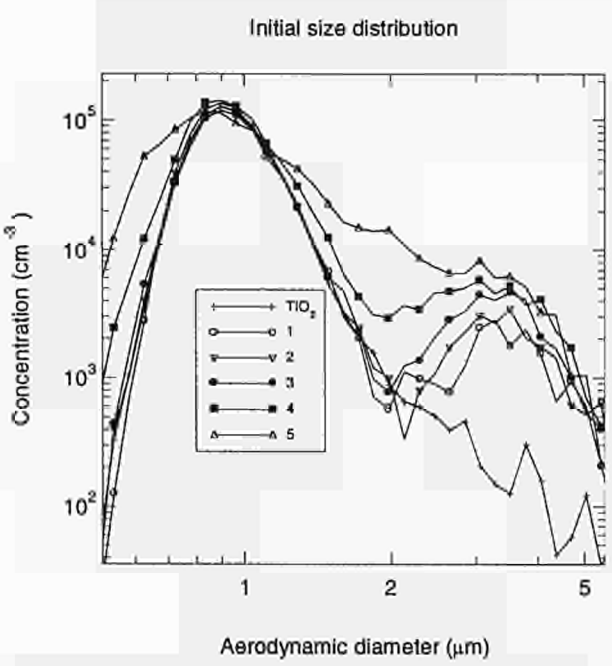

Fig. 6.2 Initial size distributions for TiO_2 alone and following injection of TiO_2 into a fog aerosol treated for 5 different periods of time. The fine particle mode for runs 1 to 4 are almost identical to that of pure TiO_2.

The initial agglomeration coefficient (just after injection) of the TiO_2 aerosol, $K=dN_s/N_s dt$, can be evaluated as a function of the initial concentration of inertial particles. The results, plotted in Fig. 6.3, show that K increases linearly with N_I for runs 1 to 4, and for experiments made with TiO_2 alone. Due to the different initial size distribution (Fig. 6.2), run 5 does not follow the same pattern. As its initial condition is more similar to those with fog alone, however, it is consistent with the previous set of experiments [1,3]. As the experimental point corresponding to acoustic agglomeration of TiO_2 alone is aligned with those corresponding to TiO_2+fog, it would appear that the geometrical factor entering the equations for the agglomeration of small aggregates of TiO_2 with inertial droplets of fog is similar, if not identical, to that for the agglomeration of small aggregates of TiO_2 with inertial aggregates of TiO_2.

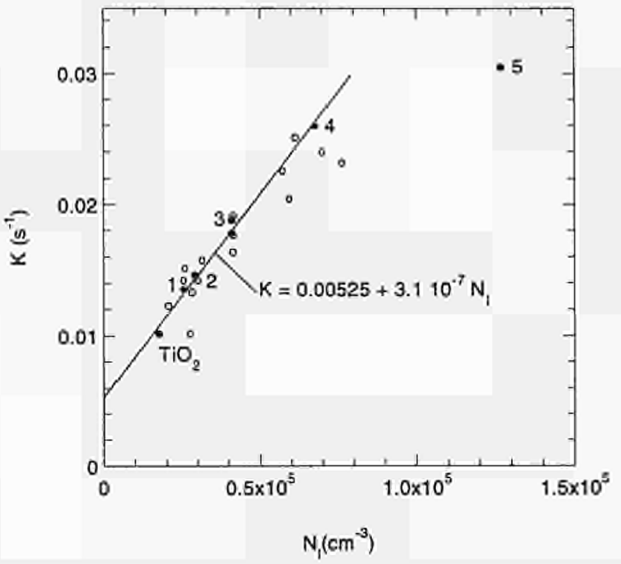

Fig. 6.3 Acoustic agglomeration rate of small particles of TiO_2 as a function of the number of inertial particles. Open symbols correspond to evaluations made on individual experimental runs. The full symbols correspond to the averaged runs made at specific TiO_2 injection times indicated by the numbers 1 - 5 and also in the case of TiO_2 alone.

The linear increase of the initial agglomeration rate with the initial number of inertial particles reflects the increased probability of impaction of small particles on inertial particles. The evolution of the inertial peak with time provides further evidence for this phenomenon. The size distributions of the mixture of fog and TiO_2 have been plotted in Fig. 6.4 at different times after injection of TiO_2. The inertial peak shifts to the right indicating that the aerodynamic diameters of the inertial particles are increasing with time. This effect is due to ingestion of the TiO_2

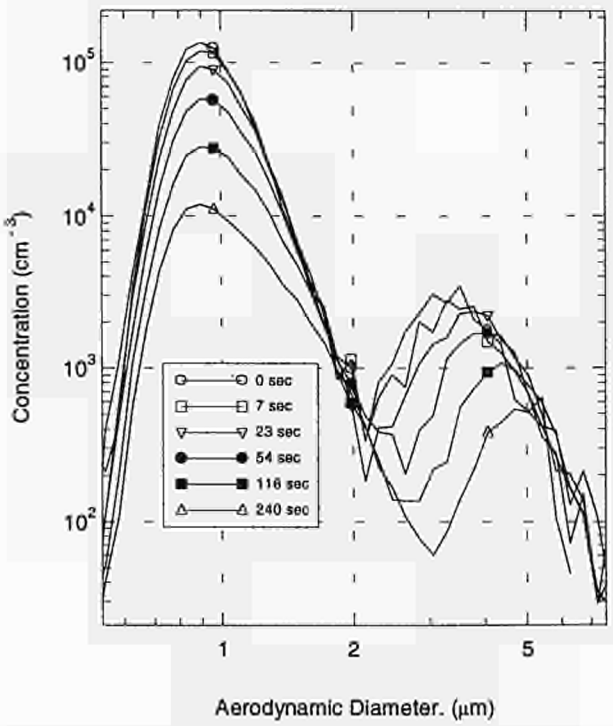

Fig. 6.4 Size distributions at different times following TiO_2 injection for run Nr 2. The peak due to inertial particles shifts to the right, as TiO_2 aggregates are ingested by the inertial droplets.

aggregates by the inertial droplets. As the density of TiO_2 is greater than glycol, the mass of these droplets increases to a greater extent than their geometric volume. Thus the overall density of the droplets increases, and a large increase in aerodynamic diameter is observed. This effect also explains the shift in the peak due to the inertial particles which occurs during injection of TiO_2. The shift in size of the inertial particles is much less apparent in the case of pure fog, as the density remains constant as the geometric diameter increases [1,2]. The increase in aerodynamic diameter of the inertial droplets also causes increased wall losses. This is observed in Fig. 6.1, where the slope of N_1 *vs* t is steeper following injection of TiO_2.

Conclusions

These experiments clearly show that the acoustic agglomeration of TiO_2 aggregates can be enhanced by the addition of inertial droplets of glycol fog. The coagulation of particles with different densities indicates clearly that the TiO_2 aggregates are ingested by the large fog droplets. Furthermore, the shift in the inertial peak corresponds to the total number of primary particles ingested in the inertial droplet which, in a more detailed analysis, permits an evaluation of the mean number of primary particles per TiO_2 aggregate with a given aerodynamic diameter.

References

[1] Ph. Capéran, J. Somers, K. Richter, S. Fourcaudot; Proc. of the '10èmes Journées d'Études sur les Aérosols', Paris, 30 nov.-1 dec. 1993, p. 131-138

[2] TUAR-93, p. 173

[3] TUAR-93, p. 180

[4] N. L. Shirokova; in L. D. Rozenberg (ed), Physical principles of ultrasonic technology, translated from the Russian by J.S.Wood, Plenum, New-York, 1970, 477-541

[5] E. P. Mednikov; Acoustic coagulation and precipitation of aerosols, translated from the Russian by Larrick, C. V., Consultants Bureau, New York (1965)

6.3 Support to DG XVII

6.3.1 European Commission's Safeguards Analytical Measurements (ECSAM)

Qualification of different methods for high accuracy uranium measurements

Introduction

One of the goals of the Euratom Safeguards Directorate is the improvement of the efficiency in safeguarding uranium. This is expected to be achieved gradually through the introduction of improved methods used for item verification, a change in emphasis from destructive to non-destructive analysis techniques and the implementation of an on-site measurement and data management system.

The quality of the measurement system should in general be equal or better than the analytical standards set by the target values proposed by ESARDA (European Safeguards Research and Development Association). Consequently, the analytical laboratory releasing results for nuclear accountability and in particular for verification purposes has to take adequate measures to assure the required quality. One of these measures is to establish a quality assurance system (QA), covering all the steps of the measurement procedure to arrive at reliable results and guaranteed uncertainties for each method used.

Well-documented procedures, training of staff, use of reference materials, regular use of quality control materials, participation in external quality control programmes such as REIMEP (Regular European Interlaboratory Measurement Evaluation Programme) [1] are essential components of a QA scheme. Processing control samples by the same procedures provide essential information on the precision of the analytical technique under investigation. Reference materials are used to determine the bias correction factor of an analytical procedure. These expensive materials may also be used for internal quality control, in which case not only information on the precision will be obtained but also information on the accuracy of the analytical procedure.

Experimental

At present the components for uranium analysis for the on-site laboratory are being tested. For the bulk analysis of uranium in reprocessing output samples (nitrate solutions or oxide powders) the performances of two DA techniques and two NDA methods have been examined:

- titration for quantitative element analysis
- mass-spectrometry for concentrations (IDMS) and isotopic abundances (TIMS) [2]
- K-edge densitometry (KEDG) for quantitative elemental analysis [3]
- Combined Product Uranium Concentrations and Enrichment Assay (COMPUCEA) using a portable compact K-edge instrument [4].

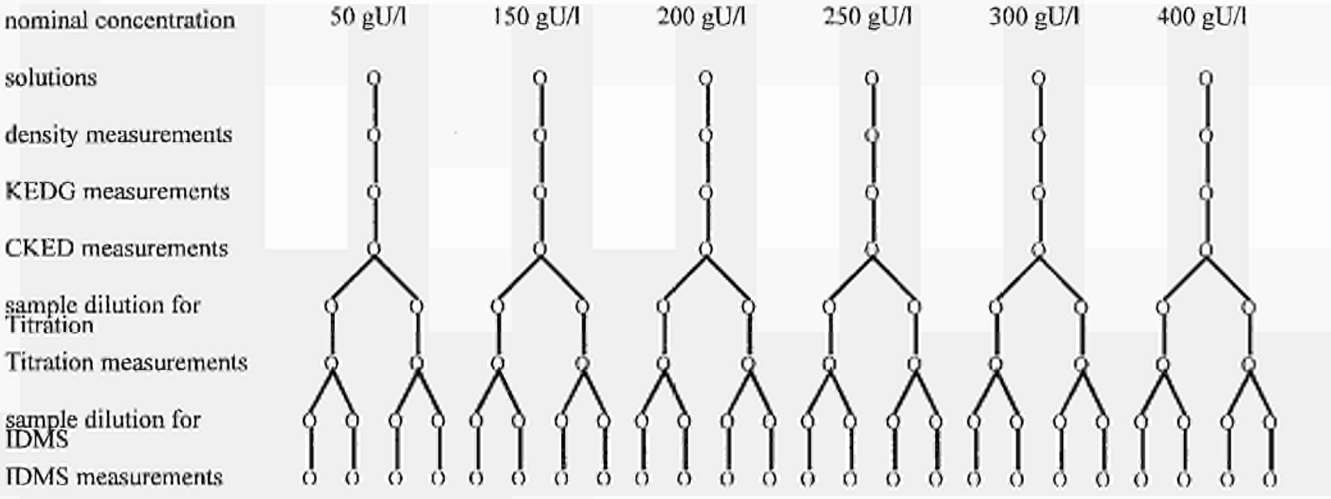

Fig 6.5 Sample preparation and analysis scheme.

Tab. 6.2 Characteristics of the certified uranium solutions.

		uncertainty (2s)
uranium mass fraction:	0.99985	0.00005
molecular mass:	238.02886	0.00000045

nominal concentration gU/l	concentration gU/kg	uncertainty 2s	density g/ml	uncertainty 2s	concentration gU/l	uncertainty 2s
50	43.010	0.004	1.165	0.001	50.110	0.050
150	115.978	0.012	1.295	0.001	150.203	0.150
200	147.379	0.015	1.361	0.001	200.540	0.201
250	176.182	0.018	1.424	0.001	250.886	0.250
300	201.681	0.020	1.487	0.002	299.987	0.300
400	238.683	0.024	1.587	0.002	378.683	0.379

	molar isotope abundance in %	uncertainty 2s
234-U	0.005508	0.00002
235-U	0.721831	0.000290
236-U	0.000015	0.000004
238-U	99.272646	0.000295

A set of reference materials, prepared for calibrating K-edge instrumentation, was also used for internal quality control. The materials, solutions with the same acidity but different uranium concentrations, were used for uranium assay by K-edge densitometry, potentiometric titration and isotope dilution mass spectrometry. The results obtained by these three methods were used to assess the quality of a measurement series, to compare methods, to determine experimental variabilities between different operators and to determine biases in one or other measurement system.

The sample preparation and subsequent analysis were carried out as outlined in the analytical scheme (Fig. 6.5).

The reference solutions were prepared and characterized gravimetrically at IRMM, (Geel) from primary reference material (uranium metal). The isotopic composition was certified at IRMM by mass-spectrometric measurements using gas-source mass-spectrometry ($^{235}U/^{238}U$ ratio, Varian MAT 511) and thermal-ionisation mass-spectrometry (Finnigan MAT 260 and Finnigan MAT 262 RPQ). The reference solutions were delivered to the Institute in sealed glass ampoules, each containing 10 ml of solution. One part of the solution was directly used for K-edge densitometry, another part was diluted by weight to 40 mg U per gram of solution for titration, and a third aliquot was diluted to 800 g U per gram of solution for isotope-dilution mass-spectrometry. The characteristics of the certified uranium solutions are given in Tab. 6.2.

Instrumentation results

K-edge densitometry (KEDG)

Method: K-edge densitometer based on transmission measurements with an X-ray continuum
Source: X-ray tube operated at 145 kV
Sample: 3 ml of liquid filled into glass cuvette with 2 cm pathlength
Equipment: standard spectroscopy instrumentation with 200 mm^2 HPGe detector and industrial 160 kV X-ray unit

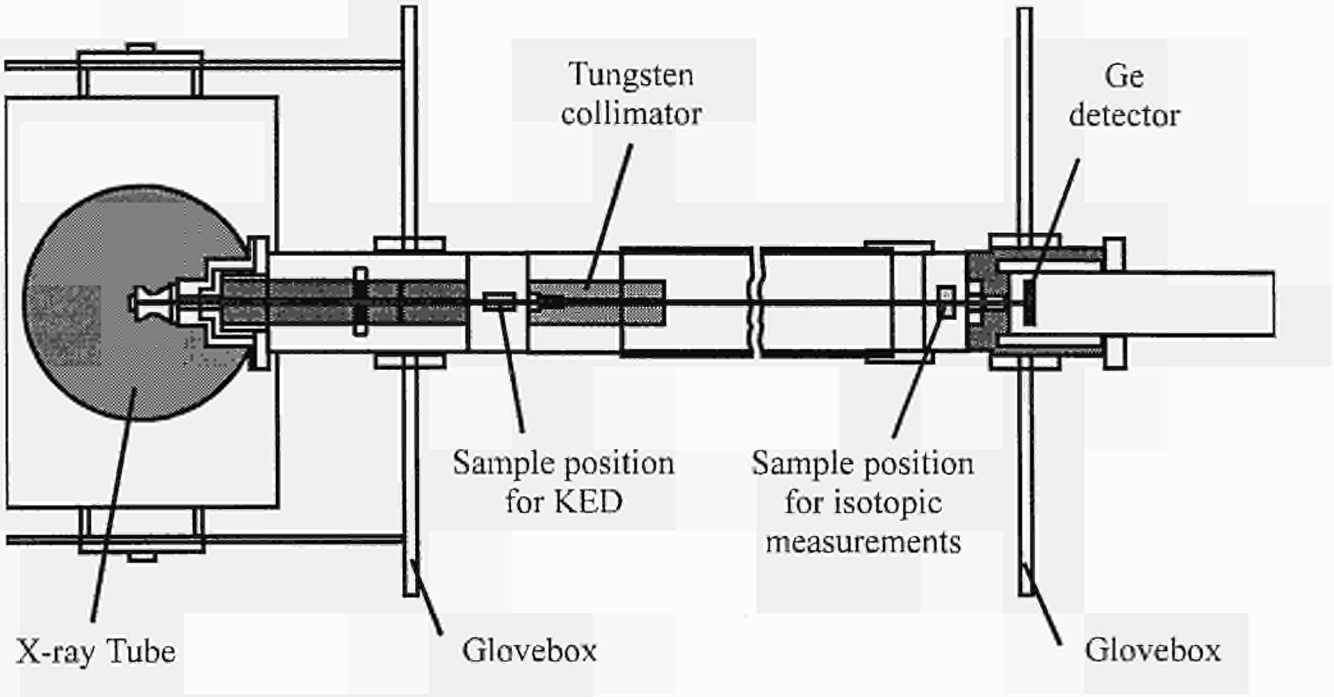

Fig. 6.6 Schematic layout of the KEDG instrument.

Tab. 6.3 Results of the KEDG measurements

number of measurements	n	9	9	9	9	9	9
mean	(gU/l)	49.850	150.280	200.370	250.950	300.000	378.460
standard deviation (2s)	(gU/l)	0.120	0.180	0.200	0.240	0.260	0.340
precision	%	0.24	0.12	0.10	0.10	0.09	0.09
uncertainty (2s)	%	0.36	0.20	0.18	0.18	0.17	0.17
ESARDA Target Value	%	0.28	0.28	0.28	0.28	0.28	0.28
bias	%	-0.52	0.05	-0.08	0.03	0.00	-0.06

CKED

Method:	K-edge densitometer based on multi-energy transmission measurements using a single isotopic source
Source:	^{57}Co (ca. $3 \cdot 10^8$ Bq) with incorporated uranium converter foil
Sample:	3 ml of liquid filled into glass cuvette with 2 cm pathlength
Equipment:	standard spectroscopy instrumentation with 200 mm^2 HpGe detector

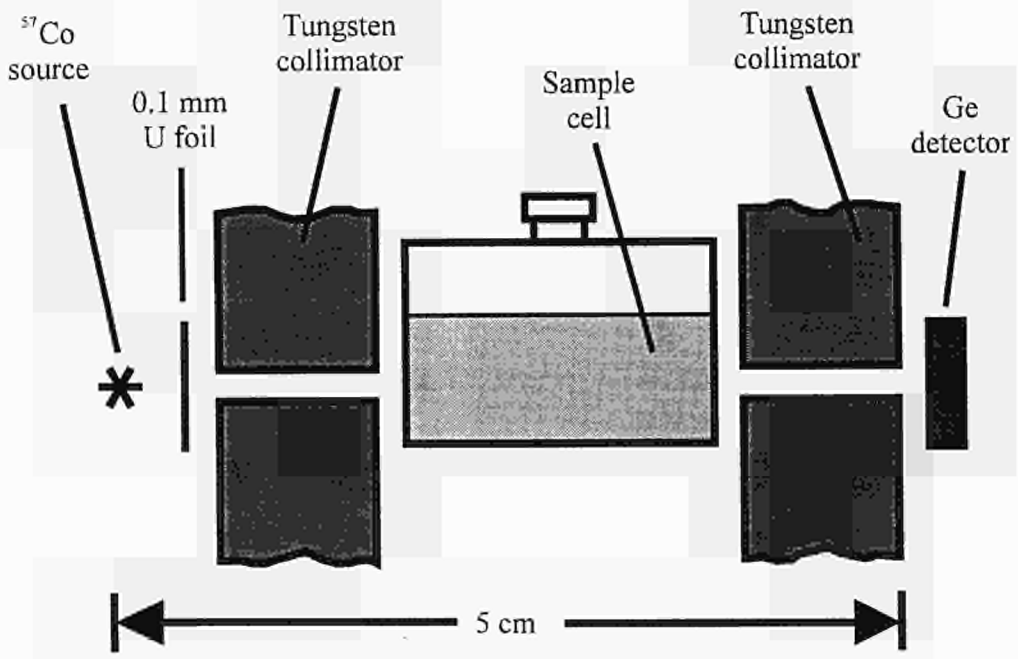

Fig. 6.7 Schematic layout of the COMPUCEA instrument.

Tab. 6.4 Results of the COMPUCEA measurements

number of measurements	n	9	9	9	9	9	9
mean	(gU/l)	49.960	150.350	200.310	251.030	300.120	378.630
standard deviation (2s)	(gU/l)	0.140	0.220	0.240	0.260	0.300	0.380
precision	%	0.28	0.15	0.12	0.10	0.10	0.10
uncertainty (2s)	%	0.41	0.24	0.20	0.18	0.18	0.18
ESARDA Target Value	%	0.28	0.28	0.28	0.28	0.28	0.28
bias	%	-0.30	0.10	-0.11	0.06	0.04	-0.01

Titration

Method: modified Davies and Gray
Sample: 40 mg uranium aliquots
Equipment: Radiometer equipment connected to a PDP-11 computer

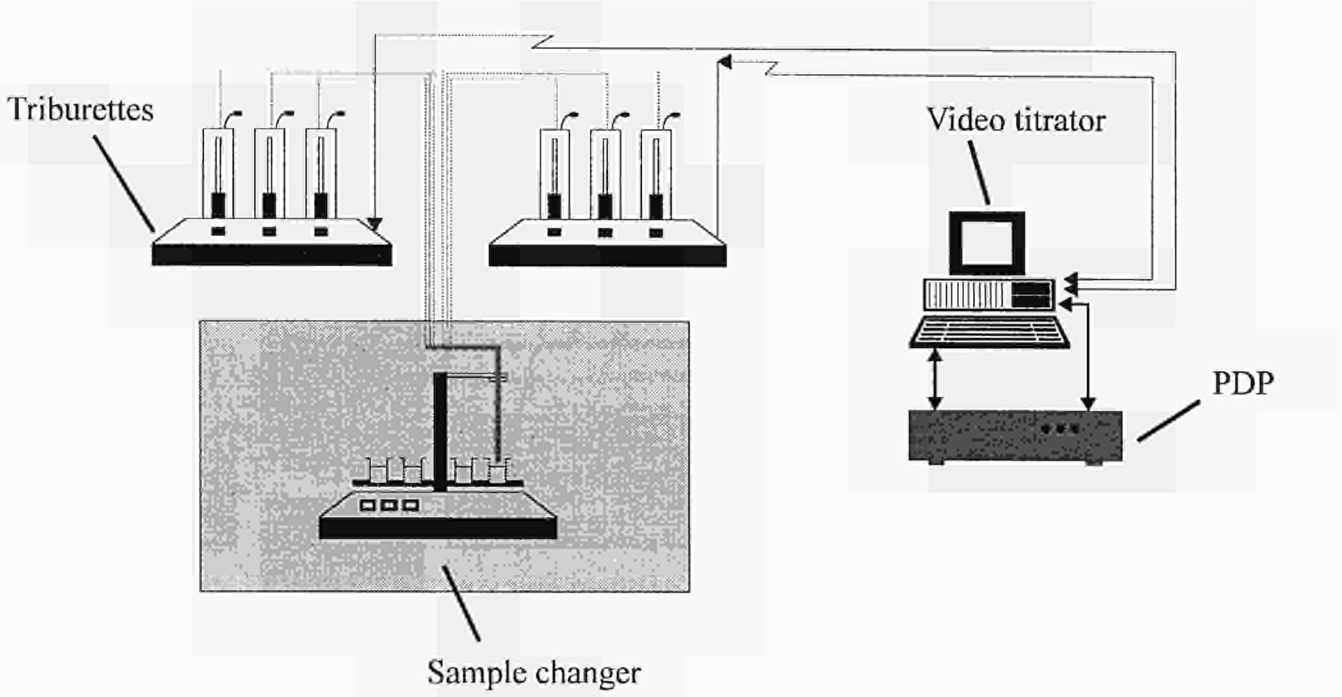

Fig. 6.8 Schematic layout of the titration equipment.

Tab. 6.5 Results of the titration measurements.

number of measurement	n	5	5	6	4	6	5
mean	(mgU/g)	43.012	115.956	147.395	176.217	201.591	238.705
standard deviation (2s)	(mgU/g)	0.03	0.079	0.019	0.095	0.042	0.025
precision	%	0.07	0.07	0.01	0.05	0.02	0.01
uncertainty (2s)	%	0.20	0.16	0.05	0.15	0.07	0.03
ESARDA Target Value	%	0.14	0.14	0.14	0.14	0.14	0.14
bias	%	0.01	-0.02	0.01	0.02	-0.04	0.01

IDMS

Method: total flash evaporation technique
Sample: filaments containing 40 - 50 ng uranium prepared by a Zymark robot
Equipment: Finnigan MAT 261 multicollector instrument

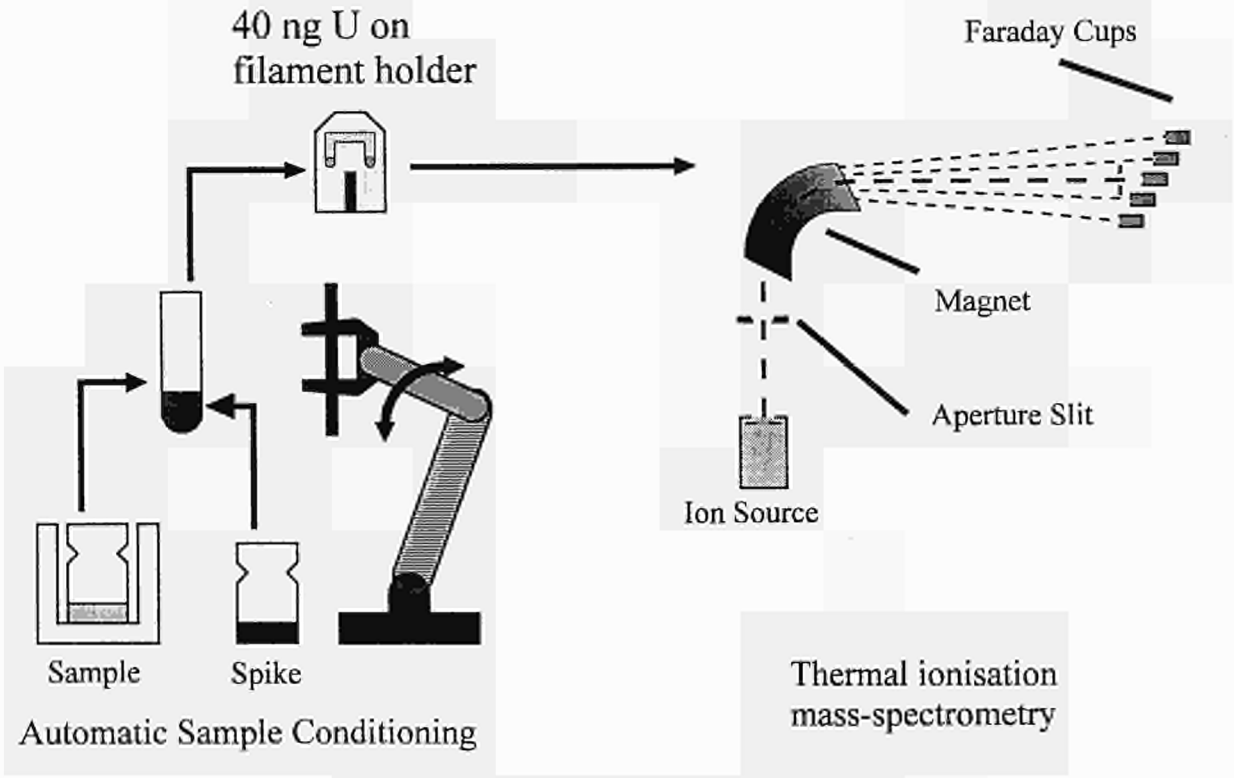

Fig. 6.9 Schematic layout of the IDMS equipment.

Tab. 6.6 Results of the IDMS measurements.

number of measurements	n	9	12	11	11	12	12
mean	(mgU/g)	43.091	116.079	147.495	176.367	201.895	238.866
standard deviation (2s)	(mgU/g)	0.042	0.160	0.152	0.132	0.182	0.228
precision	%	0.10	0.14	0.10	0.08	0.09	0.10
uncertainty (2s)	%	0.15	0.20	0.15	0.12	0.14	0.14
ESARDA Target Value	%	0.28	0.28	0.28	0.28	0.28	0.28
bias	%	0.19	0.09	0.08	0.11	0.11	0.08

isotope abundance ^{235}U

number of measurements	mean	standard deviation (2s)	precision	uncertainty (2s)	ESARDA Target Value	bias
110	0.720340	0.000450	0.06%	0.11%	0.28%	-0.21 %

Conclusions

KEDG and CKED
Both NDA techniques demonstrated accuracies of 0.1% for intermediate concentrations (100 - 300 gU/l) and for a counting time of 1000 s. Systematic deviations of about 0.3% are found at the boundary limits of the measurement range arising from slight non-linearities in the calibration curve.

Titration

The observed differences between the certified and the measured concentrations are randomly distributed and their absolute value (<0.1%) is usually smaller than the standard deviation of the measurements (0.15%), and much smaller than the overall accuracy of the results. Consequently, one may conclude that the method is well under control.

IDMS

The results obtained for the element assay show in general a low standard deviation (0.15%). The biases observed were usually small (< 0.1%) and most often within the measurement uncertainty. However the biases tended to be positive, possibly indicating a small systematic error.

Isotope abundance measurements were carried out over a period of six months. The precision of the isotope abundance measurements on natural uranium was calculated as 0.11% (2 s). However a systematic deviation of -0.21% from the reference value for the isotope 235 was observed. As this bias was highly reproducible and not dependent of the measurement date or dilution factor, reasons such as contamination or operator influence may be excluded. The problem will be examined further and also other uranium isotope reference materials will be measured, in order to investigate the reasons for this bias.

References

[1] K. Mayer, A. Alonso, P. de Bievre; Proceedings of the 15th ESARDA Symposium, Rome, May 11-13, 1993, p. 465-468

[2] M. de Rossi, H. Gerlach, L. Koch, R. Molinet, R. Wellum, Proceedings of the 9th Annual ESARDA Symposium, London, May 12-14, 1987, p. 91-93

[3] H.G. Wagner, H. Ottmar et al.; Proceedings of the 15th ESARDA Symposium, Rome, May 11 - 13, 1993, p. 281-287

[4] P. Matussek, I. Michel-Piper, H.G. Wagner, B. Brandalise, O. Cromboom; Proceedings of the 15th ESARDA Symposium, Rome, May 11-13, 1993, p. 415-422

6.3.2 On-site laboratories

Progress of the on-site laboratory (OSL) project, Sellafield

Introduction

Important steps forward have been taken concerning the organisation of the on-site laboratory (OSL) which will allow the construction of the gloveboxes and equipment to be carried out as well as the necessary infrastructure at Sellafield during the course of next year. The work has included the following areas:

- The hazards of procedures study, part 3 (HAZOP III) was finished and the pre-commencement safety report (PCSR) finalized
- An agreement between DG XVII and the Institute on the construction of the on-site labs was signed
- A quality assurance (QA) system, aimed at reaching ISO 9001 standard, has been started for design, manufacture, testing and maintenance of the equipment and gloveboxes
- The final laboratory design was finished
- Purchasing procedures for the instruments and gloveboxes have been started
- Testing of new non-destructive equipment was carried out
- Training of the OSL operators has continued

During the course of the year the recruitment of the on-site teams continued. The new staff is undergoing extensive training.

Precommencement Safety Report (PCSR)

The HAZOP (TUAR-93, p. 183) studies came to an end early this year and they will be followed by the PCSR. This report was considered and accepted by the Sellafield Research and Development & Analytical Services Management Safety Committee (R&AMSC), an essential step for the progress of the project. Changes to the design required by the HAZOP studies are now integrated in the final design version, which is considered to be frozen as from September 1994.

Construction of the laboratories

The design included in the PCSR is the basis for the laboratories' infrastructure and provision of services from BNFL. It was the subject of several intensive discussions with BNFL engineering department which had been awarded a contract to install the infrastructure by DG XVII.

Quality assurance

The laboratory will be the subject of appropriate quality assurance arrangements for all phases of its life-cycle as required for all undertakings covered by the Site Licence of Sellafield. To comply with this requirements a QA system, which is in compliance with ISO 9001 for design, manufacture, testing and maintenance, has been started in close co-operation with NNC Ltd, Risley, England.
It consists of a quality plan, project procedures and working instructions. The quality plan defines the organisation of the project, the interfaces with external organisations and the quality assurance measures to be taken. The project procedures describe the implementation, responsibility and internal interfaces for each of the twenty quality assurance elements of ISO 9001. Working instructions give detailed information for the performance of special production steps or testing procedures, e.g. welding, use of adhesives, sealing tests for gloveboxes. The laboratory design will be subject to a design plan and safety related software will be produced through a specially written software design plan.

Some of the requirements of the standard are already daily practice but need to be more formalised; a good part is nevertheless totally new. This demands extra effort to make sure we comply with the QA requirements.

Development of components

Status of the NDA equipment

The status of development for the NDA equipment to be installed at the OSL: COMPUCEA, K-edge /gamma counter and neutron/gamma counter (TUAR-93, p. 185) - is well advanced. Tested prototype versions now exist for all 3 systems. In the course of the year these have started to be used for the analysis of actual safeguards samples in order to evaluate their performance. Only minor modifications - mainly with regard to shielding and collimation - had to be made to the previously assembled configurations in order to achieve the desired operating characteristics. The operational experience gained after this optimisation work proved that the final equipment for the OSL can be built according to the existing design and layout of the prototype versions.

Remaining development work to be done for the final OSL equipment mainly concerns the area of software. In agreement with DCS Luxembourg it was decided to choose for the COMPUCEA the Ethernet-based Genie PC-version (Canberra) for data acquisition. This decision implies that the existing software and user-interface for the COMPUCEA will have to be adapted to the OS/2 operating system of this new configuration. The necessary development work will be carried out under a contract between DCS and KfK.

Earlier in the year the new PROCOUNT software developed by Canberra for the neutron/gamma counter was received and implemented into the DEC ALPHA machine, which at the OSL will serve as common host computer for the K-edge gamma/counter and neutron/gamma counter. Some deficiencies of the PROCOUNT software noticed during subsequent test measurements were removed in the revised version, which was received later in the year. Some further modifications were proposed to make the software more flexible in specific areas.

In order to harmonise the user interface for the K-edge and neutron measurements, it is planned to adapt the existing K-edge software to the layout of the PROCOUNT software, which utilises Motif windows for the user dialogue. The new K-edge software will also integrate the Multi Group Analysis (MGA) software for combined K-edge and Pu isotopic measurements.

Data processing upgrades

The automatic data analysis system has been continually improved and modified for new demands, e.g. for the parallel handling of a sample measured with various methods, such as is typically needed for standard materials. The data handling of the results from the non-destructive techniques, K-edge, COMPUCEA and neutron counting has been improved so that the measurement techniques are dealt with individually and not in the form of combined results. The possibility of accepting special samples which do not fall into one of the pre-set analysis schemes into the system has also been implemented.

The use of a ^{242}Pu spike has now been included in the system for Pu by IDMS and the calculations of Nd, Am and Cm by IDMS as well. These latter calculations are needed when for instance the burnup is required to be determined: it is not envisaged, however, that they will be needed for the on-site laboratories. The inclusion of quality control samples in the system, which has also been implemented, is a necessary part of the system for Sellafield and La Hague.

The automatic data processing system runs under VMS on a VAX 3100/90 computer. PC's (personal computers) are connected via TCP/IP for the direct input of results. The central VAX and the VAX workstations (e.g. for the K-edge and gamma spectrometers) are connected via DECNET which allows a quick and automatic transfer of results.

Evaluation of measurement performance

Introduction

The performance evaluation for the NDA instruments was started in the course of the year with first intercomparison measurements for element and isotopic assay on uranium and plutonium safeguards samples.

Prior to their on-site installation the equipment designated for the OSL has to pass a phase of thorough testing and performance evaluation. The main objective of this work is to ensure that the quality of measurements conforms to established international targets for measurement performance. At the same time it may also help to identify possible weaknesses in certain measurement procedures of both the DA and NDA techniques involved, which could be the cause of systematic measurement errors.

Gamma stations for Pu isotopic analysis

The NDA equipment for the OSL incorporates two gamma stations for Pu isotopic measurements: one at the K-edge apparatus for the analysis of Pu nitrate, another in the neutron counter for the analysis of Pu oxide and MOX samples. Both stations utilise the gamma deconvolution code MGA (Multi Group Analysis) for the determination of the Pu isotopic composition. The K-edge gamma counter is presently working with MGA version 7.4, whereas the neutron gamma counter incorporates the later MGA version 9.12.

The performance of the MGA code for the analysis of both types of samples, liquid and solid, was tested from measurements on a set of 12 safeguards samples, which were received at the Institute as gram-sized PuO_2 samples of typical reactor-grade material.

Weighed amounts of about 1g PuO_2 were first measured in the neutron/gamma counter. A total of 6 to 8 different 1 hour runs were performed on each sample. Upon the completion of these measurements the PuO_2 samples were dissolved to prepare Pu nitrate solutions of suitable concentration for the K-Edge and isotopic measurements in the K-edge/gamma counter. The Pu concentration of the solution samples was adjusted to about 130 g Pu/l. For the isotopic measurement each sample was counted 10 times for 4000 s to test the degree of repeatability.

The isotope abundances determined by gamma spectrometry were compared with those from mass spectrometry. A summary of the observed average differences and standard deviations for paired results from gamma and mass spectrometry for the isotopes 238-241, which can be directly measured by gamma spectrometry, is presented in Tab. 6.7. It is evident from the data that the results provided by MGA version 9.12 appear to be significantly biased for all isotopes, whereas the results provided by version 7.4 generally agree to within about 0.1-0.3% of the reference values from mass-spectrometry. The latter data represent about the level of performance that can reasonably be expected at best from gamma-spectrometric isotopic measurements.

The above results were presented and discussed at an international MGA user's workshop held at IRMM, Geel [1]. Reference spectra have been transmitted to R. Gunnink, developer of the MGA code, and to the firm

Tab. 6.7 Average relative difference and standard deviation (%) for the paired comparison of isotope abundances from MGA and mass spectrometry. MGA analysis with declared ^{242}Pu.

Isotope	MGA 7.4		MGA 9.12	
	Pu-Nitrate	PuO_2	Pu-Nitrate	PuO_2
Pu-238	-0.18 ± 0.22	-0.31 ± 0.21	-1.93 ± 0.25	-1.69 ± 0.30
Pu-239	-0.18 ± 0.10	-0.08 ± 0.06	1.11 ± 0.15	0.62 ± 0.15
Pu-240	-0.27 ± 0.20	0.31 ± 0.18	-2.01 ± 0.22	-0.99 ± 0.26
Pu-241	-0.37 ± 0.18	-0.22 ± 0.17	-1.49 ± 0.24	-1.02 ± 0.29

Canberra to resolve the observed inconsistency of results given by different MGA versions.

Isotope correlations for ^{242}Pu

The major drawback of the gamma technique for Pu isotopic measurements results from the lack of a detectable gamma-ray signature from the isotope ^{242}Pu. For this reason the abundance of ^{242}Pu is usually estimated from correlations among the measurable Pu isotopes 238-241. Different types of correlations have been used in the past for this purpose, but none of them has proved to work satisfactorily for all types of Pu materials.

We have therefore started a systematic performance evaluation on correlations for ^{242}Pu. Isotopic calculations using the KORIGEN code available at KfK Karlsruhe are being performed to understand the impact on accuracy by passing from a multi-parameter relation (as in KORIGEN where a large range of possible correlations can be considered) to a two or three parameter description when only the measured Pu isotope data are available. Results from mass-spectrometric analyses made at the Institute have also been investigated.

For a self-consistent algorithm, isotopic ratios which do not depend on the final value for ^{242}Pu will have to be used. Isotopic data have been compiled in a 3D representation, I242 = f(I238, I240), where I238 etc. stands for the corresponding isotopic ratios Pu-238/Pu-239. We have used the fit function $I242 = A*I240^B*I238^C$ [2].

For burnups above 25 GWd/t and with a data set covering different PWR types without further specification of the fuel, I242 has a standard deviation (fit - actual value) of approximately 4%. We have proposed a mathematical pre-test using I238 and I240 values to recognise potential candidates for large deviations. However, the remaining "worst case" in such a data set still shows a deviation of up to 11%.

More detailed studies to investigate the behaviour of the coefficients A, B and C for different types of spent fuel are underway. They will be used to quantify pos-

sible improvements in accuracy by entering specific parameters for different fuel batches. The impact of the ^{242}Pu error on the final accuracy of the neutron coincidence counting foreseen for the OSL will be quantified, too.

Neutron Counter

The present scheme of analysis for the OSL assumes that all solid Pu samples (PuO_2 and MOX) are submitted to the neutron-coincidence counter (NCC) for Pu concentration measurements. From previous tests [3] it has been concluded that accuracies of 0.1-0.2% should be achievable in principle for the determination of Pu element concentration in gram-sized samples by neutron-coincidence counting. However, this level of performance still needs to be verified from measurements on real samples.

To this end we have carried out first exploratory measurements on realistic PuO_2 samples to assess the performance of the neutron counter. The samples used for this study were safeguards PuO_2 materials containing about 1g of typical medium to high-burnup Pu. For this amount and type of Pu the neutron counter provides a net coincidence counting rate of about 30 cps. This means that a counting time of about 3 h at minimum is required to achieve a counting precision of 0.2% or better. The samples were therefore counted for 6-8 h, where the total counting time was split into sub-runs of 1 h duration to investigate the degree of repeatability. In general we found that the precision determined from the individual runs agreed perfectly with the precision calculated from counting statistics, which proves the anticipated degree of stability of about 0.1% for the counter. The same observation was also made from quality control measurements, which were repeatedly carried out on a reference sample over a period of 1 month.

A complete test for the absolute measurement accuracy has not yet been possible because of the lack of suitable calibration standards. The certified reference material available from IRMM with a fissile content of 94 atom % was not well suited for establishing a valid calibration for reactor-grade Pu because of noticeable neutron multiplication effects. Attempts to calibrate the counter with the Standard Material SM2 previously characterised at the Institute (TUAR-93, p. 186) were unsatisfactory. For still unknown reasons the neutron coincidence rate obtained from this material turned out to be about 2% lower than the rate observed for Pu of comparable, reactor-grade isotopic composition.

The very first measurements on real Pu samples have therefore mainly been used for an initial assessement of random errors encountered in small sample assays. This information was deduced from paired comparisons with results from parallel analyses performed by K-edge densitometry (KEDG) and titrimetry (TITR).

The standard deviations for the differences between paired results from different methods are given in Tab. 6.8.

Tab. 6.8 Standard deviations for paired results from measurements on 12 reactor-grade samples.

Methods	NCC/KEDG	NCC/TITR	KEDG/TITR
Stand. Dev.	0.36%	0.44%	0.32%

The data suggest that there are no significant differences in performance for the 3 compared techniques, which show random errors of about 0.2-0.3%. It should be noted that for KEDG and NCC the expected random errors due to counting statistics alone were about 0.15-0.20% for the underlying measurements.

For the neutron measurements a non-negligible error component arises from uncertainties in the relative abundances for the Pu isotopes 238, 240 and 242, which are required for the conversion of the neutron-coincidence counting rate into Pu mass. The uncertainties for the isotope abundance estimation must indeed be as low as 0.5% for ^{238}Pu, 0.1% for ^{240}Pu and 0.25% for ^{242}Pu, if their contribution to the Pu element assay on reactor-grade material is to be kept to 0.2% or below. The indicated accuracy levels for ^{240}Pu and ^{242}Pu should pose no problems for quality-controlled mass-spectrometry (they correspond to international target values). The required accuracy level of 0.5% for ^{238}Pu however represents a real challenge for the alpha spectrometry technique, used at the Institute as routine method for the determination of this isotope. With current practice ^{238}Pu is measured to between 1-3% accuracy only.

Better measurement performance for ^{238}Pu has been obtained from gamma- and mass- spectrometry, which on the average agreed within 0.2-0.3% for the present measurements. We have therefore used the ^{238}Pu abundance values from mass-spectrometry for the interpretation of the neutron measurements.

The availability of suitable and well-characterized calibration standards is a matter of prime importance for the further evaluation of the neutron counter. Work has therefore been started on the preparation of a new PuO_2 reference material of representative isotopic composition. The characterisation and certification of this reference material will be carried out in collaboration with the IRMM, Geel.

COMbined Product-Uranium Concentration and Enrichment Assay (COMPUCEA)

It is planned that the vast majority of uranium nitrate solutions arriving at the OSL will be analysed by COMPUCEA [4]. Early in 1994 two different hardware versions of COMPUCEA were available for testing and performance evaluation at the Institute:

1. An apparatus coupled to a transportable glovebox, manufactured on request of DCS Luxembourg for use as in-field instrument at La Hague. This instrument, which closely resembles in design that of the glovebox version to be installed at the OSL, was transferred in mid 1994 to La Hague for permanent installation.
2. A portable version as initially designed for in-field use during inspections at different installations. This prototype equipment has been utilised during this year for two further field tests at fuel fabrication plants in Germany and the United Kingdom.

Intercomparison measurements for performance evaluation were carried out at the Institute on a set of safeguards samples comprising a total of 29 uranium oxide samples. After dissolution the samples were analysed for U-element content by COMPUCEA (using the 2 systems mentioned above), K-edge densitometry and titrimetry. The calibration for the K-edge densitometers had been established prior to the measurements with a set of certified uranyl solutions provided by IRMM, Geel. The same reference solutions were also used to control the titration analysis.

A plot of the relative differences between the results from the different measurements is shown in Fig. 6.10. The indicated uncertainty limits of ±0.2% correspond to the international target values for random and systematic uncertainty components in U-concentration measurements on solutions by K-edge densitometry. The data prove that this target has been met, although the present performance evaluation was carried out with solid samples and included the necessary additional steps for sample preparation (weighing, dissolution, dilution, density measurement). Only 2 significant outliers were identified among the results, which apparently have to be attributed to erroneous titration results. The evaluated mean differences and standard deviations are summarised in Tab. 6.9.

Future performance tests with COMPUCEA will also include its enrichment measurement station as soon as valid procedures for this measurement have been established and suitable calibration standards have become available.

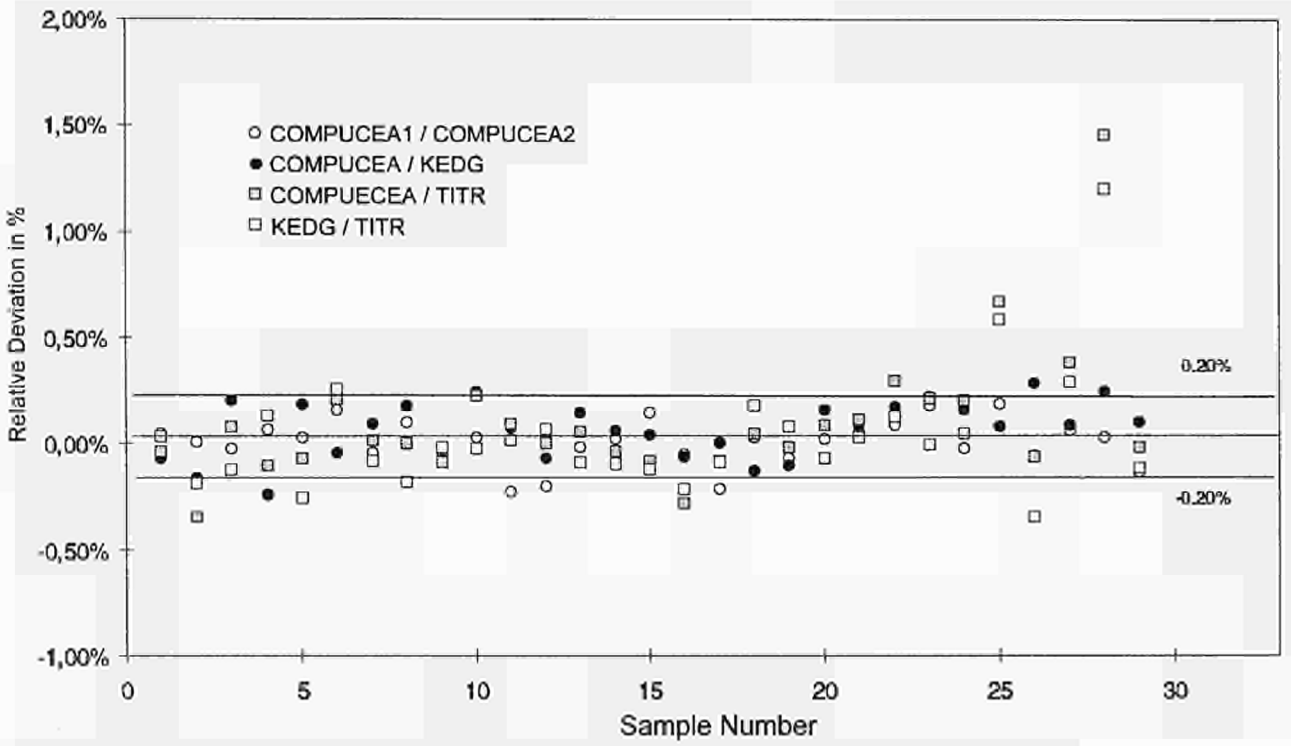

Fig. 6.10 Relative differences between measurement results on U content in UO_2 powder samples.

Tab. 6.9 Performance evaluation of assay techniques and instruments for the determination of the U metal content in U oxide powders.

	COMP1/2	COMP/ KEDG	COMP/ TITR	KEDG/ TITR
Stand. Deviation	0.11%	0.14%	0.16%	0.15%
Mean Difference	0.01%	0.06%	0.06%	-0.02%
No. of Samples	29	29	29	29
No. of Outliers	0	0	2	2

Progress of the Laboratoire sur site (LSS), La Hague

This project was suspended between March and September 1993 because of budgetary problems and reactivated in November 1993. Since this time, DCS Luxembourg has placed two contracts for the'Avant projet' with the Société Générale des Matières Nouvelles (SGN), one for the high active and one for the low active area. The complete 'Avant projet' is to be delivered to DCS by the end of February 1995. It will include an estimated overall cost and a time schedule for the project. The extension to the building UP3, where the LSS will be situated has been constructed and it was visited by representatives from the Institute, SGN and DCS Luxembourg in November 1994. Several technical meetings have taken place between representatives of the Institute, Cogema and SGN in order to define:

- the analytical methods to be employed
- the number of samples to be analyzed
- the distribution of samples between the different locations of the laboratory.
- the storage capacity necessary
- the maximum electrical power needed

The number of samples has significantly increased compared to that declared in the 'Avant projet' of November 1992. This is partly due to the start up of the units URP (Unité de Redissolution de Pu Agé) and in the future the unit UCD (Unité de Conditionnement des Déchets) for which samples will have to be analysed, and partly due to new requests from DCS.

On certain points no agreement could be reached up to now and further discussions will be held to clarify the situation.

References

[1] H. Ottmar, A. Schubert, H. Eberle, H. Van der Vegt; MGA in K-Edge-gamma and neutron-gamma counters, Internat. MGA User's Workshop, IRMM Geel, Oct. 19-20,1994

[2] G. Bignan, W. Ruhter; ,A New Algorithm for ^{242}Pu Content Evaluation', MGA Workshop, IRMM Geel, 19-20 Oct. 1994

[3] H. Menlove, R. Wellum, M. Ougier, K. Mayer; Performance tests of the high-accuracy combined neutron/gamma detector (OSL-counter), Proc. 15th ESARDA Symposium, Rome, May 11-13, 1994, p. 363

[4] P. Matussek, I. Michel-Piper, H. G. Wagner, D. Brandalise, O. Cromboom; First in-field experiences with COMPUCEA, a portable assay system for the combined determination of uranium concentration and ^{235}U abundance in uranium solutions by NDA methods, Proc. 15th ESARDA Symposium, Rome, May 11-13,1994 p. 415

On-site verification measurements

On request from DCS Luxembourg support has been provided for on-site verification measurements with installed and mobile NDA equipment. This work includes the operation of the Hybrid K-edge (HKE) instruments installed at the reprocessing plants in La Hague and Sellafield for input verification measurements, and field tests with the Compact Uranium Concentration and Enrichment Apparatus (COMPUCEA) system in various nuclear facilities.

The involvement of personnel of this Institute in this work has considerably increased during the past year for several reasons:

- Upon a request from DCS Luxembourg , the input verification measurements at La Hague with the HKE instrument are now performed on a 100% basis by ITU personnel.
- The HKE instrument at Sellafield has become operational after the start-up of the THORP plant mid of 1994.
- The participation in the field tests with COMPUCEA is an additional item of support.

The new arrangement for the operation of the HKE instrument at La Hague, which became effective in August 1994, necessitates in practice the weekly presence of ITU personnel at the facility in order to manage the number of measurements to be done. The regime of instrument operations practised since then involved on the average 3-4 days of measurement per week. The steadily increasing flow of samples to be measured soon will require an operating scheme of a 5-days-per-week basis.

The tight schedule of measurements, which pushes the instrument near to the limits of its capacity, causes increasing operational problems in that it leaves only limited time for instrument maintenance and measurement control. Instrument breakdowns which occurred during the past year further exacerbated this situation.

At the Sellafield plant the HKE instrument was brought into a ready-for-use status. An initial calibration was carried out using reference solutions supplied by IRMM Geel. The existing calibration allows the U and Pu analysis in input solutions from LWR and Magnox fuels. Only a limited number of samples have so far been submitted for measurement. Two training courses for safeguards inspectors from the THORP plant were held at the Insti-

tute to familiarize them with the principles and the use of the HKE instrument.

Three field exercises were conducted with the COMPUCEA to gain further experience with this device from different applications under field conditions. Measurements were carried out on uranyl solutions at La Hague, and on uranium oxide samples at the fuel fabrication plants of Siemens, Hanau and BNFL, Springfields. The performance of the measurements was evaluated from a comparison with results obtained from parallel analyses with the mobile titration/mass-spectrometer equipment of DCS Luxembourg. The feedback from the operational experiences gained from these field tests will be used to establish sound measurement procedures for the later official use of COMPUCEA in the verification activities of DCS Luxembourg [1].

References

[1] P. Matussek, I. Michel-Piper, H. G. Wagner, D. Brandalise, O. Cromboom; First in-field experiences with COMPUCEA, a portable assay system for the combined determination of uranium concentration and ^{235}U abundance in uranium solutions by NDA methods, Proc. 15th ESARDA Symp. Rome, May 11-13, 1994, p. 415

6.3.3 Analytical techniques

Application of Glow Discharge Mass-Spectrometry (GDMS) for direct analysis of non-conducting nuclear materials: investigations on uranium oxide specimens

Introduction

The elemental and isotopic analysis of conductive and non-conductive nuclear materials is usually performed, after dissolution of the sample, by Inductively Coupled Plasma Mass Spectrometry (ICP-MS) [1-3] and Thermal Ionisation Mass Spectrometry (TIMS) [4]. Since in some cases, especially in the case of non-conducting material, the dissolution of the sample can be difficult and time-consuming the direct analysis of the solid sample can be the preferable choice.

For the analysis of materials of nuclear origin, mass-spectrometric techniques, because of their sensitivity and multi-isotopic capabilities, offer unique application possibilities. Among the mass-spectrometric techniques directly applicable to solids with the potential for ultratrace analysis, Glow Discharge Mass Spectrometry (GDMS) is now widely accepted as the analytical tool of choice and has been used for the determination of trace level impurities in high purity metals, alloys and semiconducting materials [5,6].

Not only trace elements can be detected but also major components can be measured by GDMS. And applying the secondary cathode method [7] or the use of binders [8], insulators can also be analysed. Similar to other solid-state mass-spectrometric techniques, GDMS allows *in situ* analysis without chemical preparation of the sample. Only techniques such as cutting rods or discs, fracturing pins, or compacting pellets from powders are applied before analysis. Pre-sputtering allows surface contaminants to be removed to a large extent, thus minimizing the problem of contamination.

Thus GDMS is an analytical tool ideally suited for the analysis of solid samples of nuclear origin, requiring minimum sample treatment. The elemental and isotopic capabilities of GDMS can be fully applied to materials having either non-natural or natural isotopic abundances.

Glow discharges provide a steady-state source of excitation and ionisation that is relatively free of matrix effects because of separate atomisation and excitation/ionisation steps. Also, since the cathodic sputtering step is non-thermal in nature, sample atomisation rates for various species are quite uniform. Because of this fact, and aided by the process of steady-state sputtering, the gas-phase concentrations of sputtered species in the negative glow region of the discharge can be generally assumed to be directly representative of the bulk solid concentrations.

All these advantages that characterize the glow discharge itself characterize also the application of the d.c. glow discharge to the direct analysis of non-conducting samples.

Recently a GDMS VG9000 has been adapted to a glove-box for the analysis of solid samples of nuclear origin [9] (TUAR-93, p. 200) and it has been shown that the elemental and isotopic capabilities of glow-discharge mass-spectrometry can be successfully applied to the characterization of samples of unknown isotopic composition. By comparing with other techniques, such as ICP-MS, GDMS has a comparable precision and accuracy with the major advantage of very quick and straightforward sample preparation.

In this investigation two methods, one based on the use of a binder and a second using a secondary cathode for the analysis of solid non-conducting nuclear samples by d.c. glow-discharge mass-spectrometry have been compared. Both these techniques are applied directly to solids and though dilution of the analyte with the host material is necessary in the first, none is necessary in the latter. Results of the application of both techniques for non-conductive uranium oxide samples are reported.

Experimental

Instrumentation

The VG9000 glow discharge mass spectrometer modified and adapted to a glove-box has been previously described [9]. The instrument consists of a d.c. glow- discharge ion source coupled to a double-focusing mass spectrometer of reverse (Nier-Johnson) geometry. This provides high transmission (> 75%) and sensitivity whilst operating at the high resolving power of 5000 with 10% of valley definition.

Ion detection is accomplished by a dual detection system comprised of a Faraday cup for the measurement of large (typically > 10^{-13} A) ion currents and a transverse mounted Daly detector [10] for the detection of lower signals.

Materials

The argon discharge gas (BOC 99.9999%) enters the discharge cell via a heated getter inlet system (SAES GP50). The pressure is regulated using a leak valve (VG - UK) and monitored using an ion gauge situated above the cryogenic pump (Edwards Coolstar 1500 - UK) serving the source housing. The discharge cell is cooled using a flow of liquid nitrogen to reduce background gases such as water vapour.

Uranium oxide reference material NBL95-6 (USA), Morille and Chantarelle (CEA, Paris, France); pure graphite (Ringsdorff-Werre GmbH, Bonn, Germany) and silver powder (99.9995%, 22 mesh, A.D. Mackay, Red Hook NY, USA) were used.

Disc and pin electrode samples were prepared using an automatic hydraulic press (3630 X, SPEX, USA). Uranium oxide pin electrodes with a length of 20 mm and a diameter of 2 mm were prepared by compacting the powder transferred to a 5 ml polyethylene slug with 12 tons for 5 minutes. Uranium oxide disc electrodes with a diameter of 13 mm and 2 mm thick, were directly pressed with 8 tons for 5 minutes.

Silver and graphite, when used as binders, were added both to pins and discs in the amount of 50%. Around 100 mg of U_3O_8 powder were transferred to a 5 ml polyethylene sample bottle and the same amount of graphite or silver was added. The sample bottle was sealed with a polyethylene stopper and machine shaken for two minutes to promote efficient mixing.

The sample electrodes were degreased in acetone. All manipulations were made in a glove-box. Once inside the discharge cell, each sample was pre-sputtered for 15 minutes with a 2 mA discharge current to remove any remaining surface contamination prior to analysis.

Results and discussion

Analysis of non-conducting materials

Non-conducting materials present glow-discharge mass spectrometry with a new set of problems and opportunities compared to metals and have not been fully characterized. Recently, radio-frequency (r.f.) discharges have been used to analyse non-conducting materials [11]. For a direct current glow discharge, the requirement for a conducting matrix is met by mixing the sample with pure powders of materials such as graphite, silver, copper or gold. A sample disc or pin can then be formed from the mixture for the analysis in a glow discharge. In contrast to metals and alloy targets, glow discharge sputtering of compacted powder samples can create complex spectral background and elemental interferences. Because of this, some systematic studies to find suitable matrix materials and optimum discharge conditions have recently been carried out [8].

There are also some disadvantages inherent in the use of binders in the sample preparation to be considered. For example, mixing with an appropriate host material is equivalent to analyte dilution and loss of sensitivity. Furthermore, problems of contamination, loss of analyte, and inhomogeneity may also result.

As well as this, for trace element determination the choice of binder material is related to its level of purity. That is a limitation in the use of this sample preparation technique since the background from the binder might be higher or of the same level of concentration than the sample content. As consequence, the detection limits of the analysis become higher and traces in the range of ng/g cannot be determined any more.

Another approach for the direct analysis of non-conducting materials by d.c. glow discharge is the use of a secondary cathode [7]. Such a system consists of a high purity metal disc, approximately 0.25 mm thickness, containing an orifice, typically of 4 mm in diameter. This disc forms the cathode for the discharge, and is placed directly onto the non-conducting material to be analysed. The discharge is formed as for a normal glow discharge [12], with argon ions being attracted to the metal cathode. Atoms are sputtered from this in the normal manner [13] and diffuse into the discharge. In the discharge, these atoms will suffer collisions with the species present [14]. Some of these collisions will result in the metal atoms being returned to (and redeposited on) the surface of both the metal and the exposed non-conducting material. Any metal atoms redeposited onto the non-conducting mate-

rial will form a thin conducting layer and will consequently attract argon ions causing sputtering in this region. The sputtering process is energetic enough to penetrate the thin metallic film and remove atoms from the underlying non-conducting sample. An equilibrium is soon established between the redeposition of metal atoms and the sputtering of non-conducting atoms, resulting in a steady state discharge comprising ions representative of the insulating material and of the metal cathode.

Analysis of Uranium Oxide

For the analysis of uranium oxide spark-source mass spectrometry has traditionally been used for the determination of impurities to ng/g (ppb) levels, when very pure host material was available. Glow-discharge mass spectrometry offers a faster and more quantitative approach to this requirement without the need for lengthy and skilled interpretation of photographic plates.

Non-conducting uranium oxide powders were analysed after mixing with a binder and also with the use of a secondary cathode to promote sputtering in a d.c. glow discharge.

Use of binders: silver and carbon graphite

Conventional d.c. glow discharge devices can be applied to the direct analysis of electrically non-conductive solids if the sample is first rendered conductive by compaction into a conductive host matrix material. This involves intimately mixing the sample with a conductive host matrix material, both in powder form, and pressing a portion of the resulting mixture to form an overall conductive solid sample that can serve as the cathode in the glow discharge.

A host material with high sputter rates is desirable. Among the most suitable, considering the type of analysis normally required for nuclear materials and the possible isobaric interferences coming from the host matrix materials, silver and graphite appeared the most promising and in this investigation samples of uranium oxide were prepared for the GDMS by mixing with silver or graphite powder as binders.

The compaction of uranium oxide powder with graphite resulted in pin electrode samples which were too fragile to be handled. Since pin samples could be prepared only by mixing with silver, only comparative results obtained for disc electrodes are discussed here.

The results obtained when uranium oxide was analysed using silver and carbon graphite powder as binder are shown in Tabs. 6.10 and 6.11. The maximum intensities

Tab. 6.10 Analysis of uranium oxide disc electrode samples using silver as binders: maximum peak intensity for different discharge current values. (In brackets standard deviation values in A units over 10 measurements are reported).

Discharge current (mA)	U (peak intensity) A x 10^{-11}	Ag (peak intensity) A x 10^{-11}
0.2	5.2 (2.9 x 10^{-12})	1.1 (9.1 x 10^{-13})
0.5	25 (1.7 x 10^{-11})	2.5 (1.5 x 10^{-12})
1.0	84 (1.9 x 10^{-10})	7.8 (2.5 x 10^{-11})
1.8	190 (4.2 x 10^{-11})	30 (1.0 x 10^{-11})

Tab. 6.11 Analysis of uranium oxide disc electrode samples using graphite as binder: maximum peak intensity for different discharge current values. (In brackets standard deviation values in A units over 10 measurements are reported).

Discharge current (mA)	U (peak-intensity) A x 10^{-11}	C (peak-intensity) A x 10^{-11}
0.2	0.41 (4.7 x 10^{-13})	4.3 (1.8 x 10^{-11})
0.5	1.0 (2.2 x 10^{-12})	2.7 (6.4 x 10^{-12})
1.0	4.8 (2.5 x 10^{-12})	55 (1.2 x 10^{-10})
1.8	8.8 (9.8 x 10^{-13})	139 (1.7 x 10^{-10})

for the peaks corresponding to uranium, silver and carbon (expressed in Amperes) along with their standard deviations over 10 different measurements for four applied discharge currents (0.2 - 1.8 mA) are reported. In both cases, when increasing the discharge current from 0.2 to 1.8 mA, the intensity of the uranium peak increased. For values higher than 1.8 mA, the uranium peak was completely quenched.

In Fig. 6.11 the ratios between the maximum intensity peak of uranium/carbon (U/C) and in Fig. 6.12 those of uranium /silver (U/Ag) are shown. Different trends of this ratio with the applied current can be seen. For carbon a maximum of the ratio U/C was found when a discharge current of 0.5 mA was applied (Fig. 6.11).

In the case of silver, the trend of the U/Ag ratio was different. As mentioned previously, the maximum intensity peak of uranium increased when higher discharge cur-

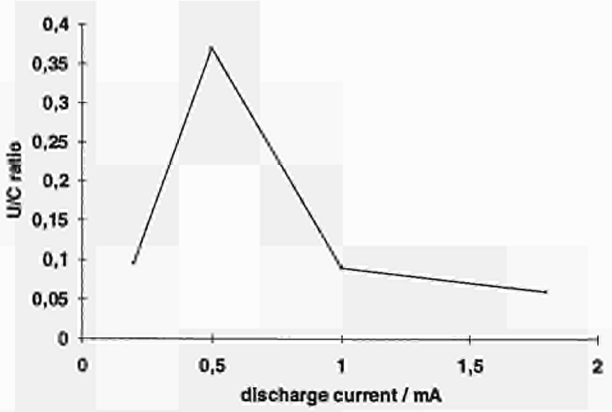

Fig. 6.11 Uranium/carbon ratios

rent values were applied (see Tab. 6.12). But the maximum peak intensity of silver remained almost stable having a maximum for 1 mA of discharge current applied. From Fig. 6.12, it appears that the ratio U/Ag reaches a maximum for a discharge current value of 1 mA, and its value remains almost constant between 0.5 - 1 mA of discharge current applied.

From this point of view, when silver has not to be determined, its use for the analysis of uranium oxide can be advantageous compared with the use of graphite, since the value of discharge current is not so critical and can be fixed between 0.5 - 1 mA.

Use of tantalum secondary cathode

For use as a secondary cathode, tantalum metal can be obtained with a very high purity level and it does not give isobaric interferences in the analysis of uranium oxide. Tantalum has also been observed to produce a stable discharge with good sensitivity for the uranium ion intensity.

The maximum intensity of the uranium and tantalum peaks obtained when different discharge current values

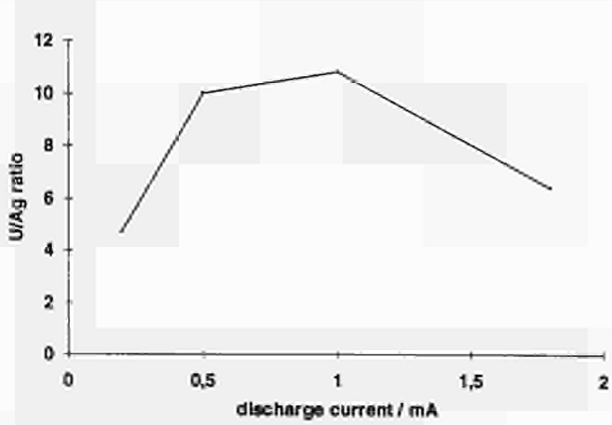

Fig. 6.12 Uranium/silver ratios

were applied are reported in Tab. 6.12 together with the values of the standard deviations over ten measurements. When the discharge current value increases, the maximum intensity of both the uranium and the tantalum peak increased, but the tantalum peak increased faster than the uranium peak. At a discharge current of 2 mA, the uranium peak was completely quenched.

Tab. 6.12 Analysis of uranium oxide disc electrode samples using a tantalum secondary cathode with an orifice of 5 mm: maximum peak intensity for different discharge current values. (In brackets standard deviation values over 10 measurements are reported).

Discharge current (mA)	U (peak-intensity, A) A x 10^{-12}	Ta (peak-intensity, A) A x 10^{-12}
0.2	5.3 (2 x 10^{-12})	13 (3.0 x 10^{-12})
0.5	26 (9.1 x 10^{-13})	23 (2.4 x 10^{-12})
1.0	180 (3.3 x 10^{-11})	330 (3.2 x 10^{-11})
1.8	210 (1.3 x 10^{-10})	1000 (3.9 x 10^{-10})

The ratio between the maximum intensity peak of uranium and tantalum (U/Ta) for different values of discharge currents has been calculated and the U/Ta ratio as function of the discharge current for two secondary cathodes with two different apertures, 5 and 2 mm respectively, is shown in Fig. 6.13. In both the cases a maximum for the U/Ta ratio was obtained when a discharge current of 0.5 mA was applied.

The trend obtained in this case is very similar to that obtained when carbon was used as binder. For a secondary cathode with an orifice of 2 mm the maximum value obtained for the ratio U/Ta is of the same order of magni-

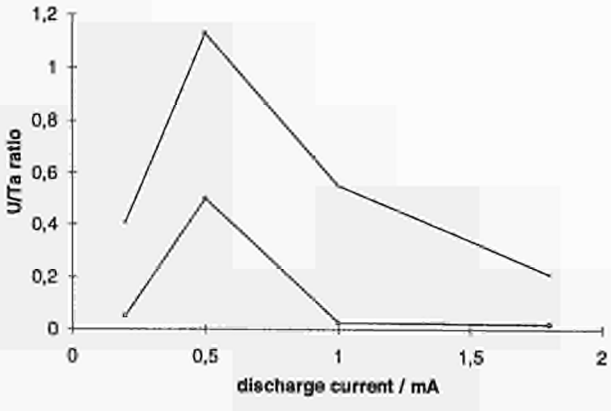

Fig. 6.13 Uranium/tantalum ratios using secondary electrodes with apertures of 2 and 5 mm

tude of that obtained in the case of carbon. When a cathode with a 5 mm orifice was employed, with a discharge current of 0.5 mA the value of the ratio U/Ta doubled but still remained lower than that obtained in the case of silver.

The use of a tantalum secondary cathode with an orifice of 5 mm has a better sputtering efficiency for uranium oxide than when carbon is used as binder. However, silver still remains the more efficient binder even though it has a disadvantage of needing more sample manipulation for the pellet compaction.

Analysis of trace elements in uranium oxide specimens

Analyses of uranium oxide by GDMS have already been made and the results obtained for a series of NBL standards of uranium oxide compacted with carbon graphite powder in the form of pin electrodes have been reported [15]. No external standards were employed since the graphite matrix was used as internal reference element and ion beam ratios, analyte versus carbon were utilised for the quantification.

In our investigation different standards of uranium oxide have been analysed using both silver or carbon graphite powder as host matrix and also with a tantalum secondary cathode.

For the elements which were analysed, the proper ion beam ratio (IBR) is defined as follows:

$$IBR(X)=(Xi/Cxi)/(Ak/Cak)$$

where:
Xi = total ion counts of the selected isotope i, of the element X,
Cxi = isotopic abundance of the isotope i,
Ak = total ion counts of the selected isotope k of the matrix element A
Cak= isotopic abundance of the isotope k.

In this particular case the matrix element considered is uranium and its main isotope with mass 238. The Relative Sensitive Factors (RSF) were then obtained, according to the following equation:

$$RSF(X) = IBR(X)/m(X)$$

where m(X) is the mass concentration of the element X (i.e. mg/Kg).

In order to have information on the accuracy and precision of the method employed, samples of uranium oxide obtained from the reference material "Morille" were analysed by the use of binders and with a tantalum secondary cathode. The best results in terms of precision and accuracy where obtained when a secondary cathode was employed.

For this case, the experimental results along with the certified values are reported (Tab. 6.13). For all analytes, the experimental concentration values have been calculated after tantalum background correction.

Tab. 6.13 Comparison between certified values (± σ) and experimental (± σ) values obtained by GDMS for Morille uranium oxide reference material using a tantalum secondary cathode.

Element	Cert. value/ ppm	Exp.value/ ppm	Bias %
Li	5.0 ± 0.2	4.8 ± 0.9	- 4
Be	5.4 ± 0.6	5.9 ± 0.3	+ 9.25
B	3.8 ± 1.6	3.5 ± 0.1	- 8.6
Mg	19.3 ± 1.5	19.5 ± 1.2	+1
Al	99 ± 6	100 ± 5	+1
Si	100 ± 8	102 ± 5	+2
Ca	93 ± 8	94 ± 7	+1
Ti	49.2 ± 2.6	48.6 ± 5	-1.2
V	48.7 ± 2.8	47 ± 1.1	-3.5
Cr	99 ± 2	101± 4	+2
Mn	24.5 ± 0.5	25 ± 2	+2
Fe	211.6 ± 6.5	204 ± 7	-3.6
Co	9.8 ± 2	11 ± 0.7	+12.2
Ni	147 ± 3	149 ± 2	+1.4
Cu	50.2 ± 1	49.8 ± 3.3	-0.7
Zn	98.6 ± 5.5	112 ± 8.2	+13.6
Zr	59.9 ± 4.1	57 ± 5	-4.8
Mo	147 ± 5	144 ± 8.7	-2
Ag	10.4 ± 1.6	9.9 ± 1.3	-4.8
Cd	4.9 ± 0.7	4.3 ± 0.3	-12.2
In	9.4 ± 1.0	10.4 ± 0.4	+10.6
Sn	18.5 ± 5.6	20.8 ± 2	+12.4
Ba	9.6 ± 0.4	9.3 ± 0.9	-3.1
Sm	0.50 ± 0.12	0.55 ± 0.04	+10
Eu	0.52 ± 0.03	0.50 ± 0.03	-3.8
Gd	0.56 ± 0.06	0.54 ± 0.03	-3.6
Dy	0.50 ± 0.06	0.45 ± 0.04	-10
W	100 ± 9	106 ± 9	+6
Pb	101 ± 3	103 ± 5	+2
Bi	24.4 ± 1.9	23.1 ± 1.4	-5
Th	6.2 ± 0.8	5.7 ± 0.7	-8

In Tab. 6.12 the bias values, calculated according to the equation:

Bias % = [(Exp - Cert)/ (Cert)] x 100

have been also reported, where 'Exp'. is the experimental and 'Cert' the certified values for each analyte. As can be seen from the analyte concentration, good accuracy for all elements considered has been obtained the bias values lying in the range from better than 1% to 14%. When the method of sample compaction with a host matrix was used the bias values varied from 5 to 30% and when using carbon graphite the accuracy and precision were worse than when employing silver powder. This may be due to the fact that the electrodes formed with graphite are less stable than those made using silver. Graphite also has poorer sputtering properties than silver and produces many hydrocarbon and metal carbide interferences.

Conclusions

The analysis of non-conductive nuclear materials which are difficult to dissolve can be performed directly on solid pellets.

The use of a secondary cathode, compared with compaction of samples in a host matrix was shown to have some advantages. Using this method, not only the problem of liquid waste is circumvented, but the material can be reused after the analysis.

In the particular case of uranium oxide, a secondary cathode of pure tantalum was employed and for the analysis of 32 elements at trace level of concentration, accuracy and precision better than the method of using host matrices have been obtained.

References

[1] J. S. Crain, D. L Gallimore; App. Spectrosc. **46** (1992) 547
[2] J. I. Garcia Alonso, D. Thoby-Schultzendorff, B. Giovannone, L. Koch, H. Wiesmann; J. Anal. Atom. Spectrom. **8** (1993) 673
[3] M. Betti, J. I. Garcia Alonso, Ph. Arbore, L. Koch, T. Sato; in Applications of Plasma Source Mass Spectrometry II, eds. G. Holland and A. N. Eaton, Royal Society of Chemistry, Cambridge, 1993, p. 205
[4] T. Adachi, M. Ohnuki, N. Yoshida, T. Sonobe, W. Kawamura, H. Takeishi, K. Gunji, T. Kimura, T. Suzuki, T. Y. Nakahara, T. Mutomura, Y. Kobayashi, H. Okashita, T. Yamamoto; J. Nucl. Mater. **174** (1990) 60
[5] Mei Yuan, R. K. Marcus; Trends in Anal. Chem. **12** (1993) 86
[6] A. P. Mykytiuk, P. Semeniuk, S. Berman; Spectrochimica Acta Rev. **13** (1990) 1
[7] D. M. P. Milton, R. Hutton; Spectrochimica Acta, **48B** (1993) 39
[8] L. Tong, W. W. Harrison; Spectrochimica Acta, **48B** (1993) 1237
[9] M. Betti,G. Rasmussen, T. Hiernaut, L. Koch, D. P. M. Milton, R. Hutton; J. Anal. At. Spectrom. **9** (1994) 385
[10] N. R. Daly; Rev. Sci. Instrum. **31** (1960) 264
[11] M. R. Winchester, C. Lazik, R. K. Marcus, R. K.; Spectrochimica Acta, **46B** (1991) 175
[12] W. W. Harrison, K. R. Hess, R. K. Marcus, F. L. King; Anal. Chem. **58** (1986) 341A
[13] W. D. Westwood; Prog. Surf. Sci. **7** (1976) 71
[14] B. Chapman,Glow Discharge Processes, Wiley, New York, 1980
[15] K. Robinson, E. F. H. Hall; J. Met. **39** (1987) 14

Determination of major elements in nuclear samples by Inductively-Coupled Plasma Mass Spectrometry (ICP-MS)

Introduction

ICP-MS has traditionally been applied for trace and ultratrace elemental analysis in view of its high sensitivity and multielemental capabilities. This came from the basic concept that ICP-MS was a mere "detection improvement" on ICP-AES instruments. The fact that ICP-MS can measure isotopic ratios however allows the use of more sophisticated analytical methods than those possible by measuring only absolute intensities. The method of isotope dilution analysis (for polyisotopic elements), or the method of standard additions with internal standard (for monoisotopic elements) can be applied and provide adequate precision and accuracy for major element analysis. This is particularly important in the nuclear field where the setting up of analytical instrumentation for routine analysis is very expensive and a multielemental technique like ICP-MS could be applied to many elements with minor operating changes. When new type of samples and non-routine elements have to be analysed, the application of ICP-MS could offer advantages over other techniques. The accuracy of major element analysis by ICP-MS will be governed mainly by mass discrimination errors (mass bias) and detector dead time losses. Those factors have to be determined and corrected for. Examples for the determination of Gd, U, Pu and Zr in nuclear samples will be presented.

Experimental

Instrumentation

Two ICP-MS instruments were used, an ELAN 250 and an ELAN 5000 (Sciex, Canada). Both were modified in order to handle radioactive samples in a glove box. The ion lens settings were optimised using Rh for Gd and Zr and using U for the actinides. All measurements were done in scanning mode. Quantitative data were obtained in low resolution mode. Data were transferred to a PC for computation using an electronic spreadsheet.

Reagents and Materials

Enriched isotopes used include ^{91}Zr, ^{154}Gd, ^{233}U and ^{244}Pu. Inactive standards were prepared by simple dilu-

tion in acid-washed volumetric flasks. Radioactive samples and standards were diluted by mass in the glove box or in the hot-cell facility: 10 or 20 ml polyethylene bottles were used for all radioactive material.

Isotope Dilution Analysis.

To an unknown number of atoms of an element of which the isotope abundances are known (or measurable), a known number of atoms of the same element possessing different isotope abundances (also known or measurable) are added and the new isotope abundances are measured in the mixture. From the measured isotope abundances both in the sample, the spike and the mixture, the concentration of the element in the sample can be calculated.

For a polyisotope element, with N_S the number of total atoms in the sample S, and A^a_S and A^b_S the isotope abundances (a/o) of two selected isotopes, **a** and **b**, the isotope ratio R_S in the sample will be

$$R_S = N^a_S/N^b_S = (A^a_S * N_S)/(A^b_S * N_S) = A^a_S/A^b_S$$

where N^a_S and N^b_S are the total number of atoms of isotopes **a** and **b** in the sample respectively. For this study, the isotope **b** will be taken as the main isotope in the sample so that $R_S<1$. If the reference isotope in the spike, **a**, is not present in the sample then $R_S=0$.

For the spike (Sp), the isotope ratio R_{Sp} will be:

$$R_{Sp} = A^b_{Sp}/A^a_{Sp}$$

In this case, the isotope **a** should be the main isotope in the spike or, at least, have an isotope abundance greater than that of isotope **b** for the best results to be obtained. In order that $R_{Sp}<1$ the isotope ratio here is inverted with respect to R_S. In this case, if the isotope **b** is not present in the spike then $R_{Sp}=0$.

$$R_M = (A^b_S * N_S + A^b_{Sp} * N_{Sp})/(A^a_S * N_S + A^a_{Sp} * N_{Sp})$$

The ratio R_M is taken here similarly to that of R_{Sp} (i.e. Isotope **b**/Isotope **a**) and could be greater or less than 1 depending on the isotope abundances and on the number of atoms taken from sample and spike. Rearranging the equation for N_S we obtain

$$N_S = N_{Sp} * \frac{R_M * A^a_{Sp} - A^b_{Sp}}{A^b_S - R_M * A^a_S} \qquad (1)$$

Equation (1) is more conveniently expressed in concentration units (μg/g) rather than in number of atoms:

$$C_S = C_{Sp} * \frac{W_{Sp}}{W_S} * \frac{Aw_S}{Aw_{Sp}} * \frac{A^a_{Sp}}{A^b_S} * \frac{R_M - R_{Sp}}{1 - R_M * R_S} \qquad (2)$$

In the case of analysis of natural elements using a certified enriched spike, only R_M would have to be determined experimentally (except for certain elements which show natural variations in their isotope abundances). For the analysis of fission products and actinides, the parameters Aw_S, A^b_S, R_M and R_S have to be determined experimentally as the isotope abundances in the sample are unknown.

Results and Discussion

Sources of error in isotope dilution analysis with an ICP-MS

If we consider that all parameters in equation (2) are affected by errors, both random and systematic, and that the measurement of isotope abundances and isotope ratios is done by mass spectrometry, then the influence of those parameters on the expected error in C_S can be studied. Random and systematic errors on the concentration of the spike and on the weights of sample and spike will be considered negligible here when compared to the other parameters in equation (2) which have to be determined by ICP-MS.

Systematic errors

Systematic errors in ID-ICP-MS can originate from mass-discrimination errors, non-linearity of the detector at high counting rates, isobaric interferences on the measured isotopes and procedural blanks. In our experience, procedural blanks for the analysis of fission products and actinides in nuclear samples are negligible when cross-contamination between samples is avoided. For this reason systematic errors due to procedural blanks will not be discussed here. Mass-discrimination errors can originate in the ion source (from fractionation, as in TIMS) or in the mass spectrometer. ICP-MS instruments are prone to mass-discrimination errors of the second type because of a mass-dependent transmission of the ions through the ion lens and quadrupole filter. Fortunately, these mass-discrimination errors are time-independent and can be corrected for by the use of isotope reference materials or natural elements with well-defined isotope abundances. The second type of systematic error is also observed in the pulse-counting mode of most ICP-MS instruments at high counting rates and is due to the dead-time of the detector. The third source of systematic errors in isotope dilution analysis is that of the isobaric interference when isotopes of different elements or polyatomic ions are present at the same nominal mass to charge ratio. However, for the analysis of major elements, the problem of isobaric interferences does not exist.

1. Mass-discrimination errors

In absence of detector dead time effects (e.g. for relatively low counting rates), the ion count rate ratio in ICP-

MS would be equivalent to the atomic isotope ratio if there were no mass-discrimination errors. Because of a mass-dependent ion-transmission and/or ion-detection effect in our ELAN 250 and ELAN 5000 this may not be the case.

For the analysis of actinides, the ion lens were optimised using ^{238}U. It was possible to obtain conditions under which no mass discrimination could be measured. The variation of the molar sensitivity with mass for different actinide elements measured using standard solution of various isotopes showed a constant molar response was obtained under those conditions indicating the lack of mass bias. This was further checked by measuring the isotopic ratios of mixtures of ^{233}U and ^{238}U prepared from weighed amounts of the ^{233}U reference material and the depleted U reference material. However, this was not the case for the analysis of fission products. The experimental and theoretical isotope ratios were obtained for natural abundances of Zr, Mo, Ru and Pd. These elements were measured in three different solutions to avoid isobaric interferences, at concentration levels at which no dead-time correction was necessary and using ion lens conditions in the mass spectrometer optimised with ^{103}Rh. The relative systematic error in the isotope ratios was found to be proportional to the mass difference between the two isotopes considered and independent of the element tested for this mass range. A negative error of 2.16% per mass unit of difference between the isotopes used to calculate the isotope ratio was observed. The linear relationship between the relative errors in the isotope ratios and the mass difference between the measured isotopes can be expressed as

$$\frac{R_{exp} - R_{theo}}{R_{theo}} = K * \Delta M \qquad (3)$$

where R_{exp} and R_{theo} are the experimental and theoretical isotope ratios and M is the mass difference between the measured isotopes. The value of K, the mass-discrimination factor, was derived from the slope of the regression line (Fig. 6.14). Once K was computed using natural elements (or certified isotope reference materials), the corrected isotope ratios, R_{corr}, were calculated using

$$R_{corr} = \frac{R_{exp}}{1 + K * \Delta M} \qquad (4)$$

When we applied equation (4) to correct the experimental isotope ratios the relative errors in the corrected ratios now lay within the experimental standard deviation of the measured ratios.

2. Detector dead-time errors

For high counting rates, the measured isotope ratios deviate from the true isotope ratios due to dead-time losses in the detector. The count rate that should be measured

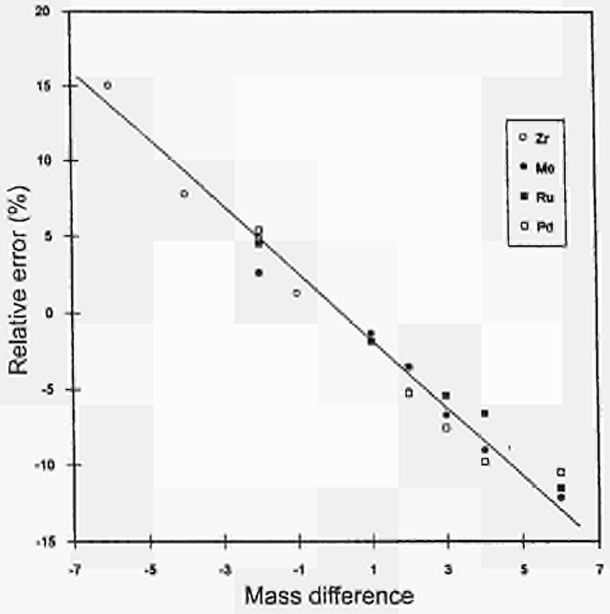

Fig. 6.14 Relative error as a function of mass difference

relates to the experimental count rate and the dead-time, τ, by the expression

$$I_{real} = I_{meas} / (1 - \tau * I_{meas})$$

where I_{meas} is the experimental count rate and I_{real} the count rate that should have been measured if there were no dead-time errors. The isotope ratio R_{real} (I^1_{real}/I^2_{real}) can be expressed as a function of the measured ratio as

$$R_{real} = R_{meas} * \frac{1 - \tau * I^2_{meas}}{1 - \tau * R_{meas} * I^2_{meas}} \qquad (5)$$

In order to evaluate the detector dead-time in the ELAN 250 we have measured 4 solutions containing different concentrations of a Pu standard solution whose isotope abundances were determined previously by TIMS. The ratios 238/239, 240/239, 241/239 and 242/239 were measured using the ion lens optimised on ^{103}Rh in order to have both mass discrimination and detector dead time effects. The isotope ratios measured varied slightly with the concentration of Pu and they were also different from the reference ratios because of mass-discrimination.

We have determined the detector dead-times by making use of both mass-discrimination and dead-time corrections simultaneously. If we combine equations (4) and (5) we arrive at:

$$R_{corr} = \frac{\frac{R_{meas} * (1 - \tau * I^2_{meas})}{1 - \tau * R_{meas} * I^2_{meas}}}{1 + K * \Delta M} \qquad (6)$$

Based on equation (6) the values of K and can be determined by least squares fitting minimising the expresion $\Sigma ((R_{Corr} - R_{Theo})/R_{Theo})^2$ for all data points

measured. The best fit corresponded to a dead time of 56 ns and a mass discrimination factor of 0.0050. Once the values of dead time and mass discrimination are determined, the corrected isotopic ratios can be determined applying equation (6). The agreement with the reference values is then within the standard deviation of the measurements.

The dead time was also determined in the ELAN 250 using natural Gd standards of increasing concentration. The best fit corresponded to a dead time of 33 ns and a mass discrimination factor of -0.0079. It is to be expected that the mass discrimination factor changes for different mass ranges but the detector dead time should be independent of the mass of the measured element. The mean dead time would be 44 ns with a standard deviation of 12 ns (ca. 25% RSD).

The systematic error on R_{meas}, $R/R = (R_{meas} - R_{real})/R_{real}$, for dead time only, will be

$$\frac{\Delta R}{R} = \frac{\tau * I^2_{meas} * (1 - R_{meas})}{1 - \tau * I^2_{meas}} \qquad (7)$$

The systematic error on R will depend on the detector dead-time, the count rate of the second isotope used to measure the ratio, I^2_{meas}, and on the ratio measured itself. From equation (7) it can be demonstrated that for high counting rates, serious systematic errors will occur even for R values close to 1. It is clear that the errors due to detector dead time losses have to be corrected for.

Random error propagation

Evaluation of random errors in the measured isotope ratios

The relative standard deviation in the measurement of ion counts in our modified ELAN 250 has been determined. The data correspond to the measurement of different samples and isotopes of natural Gd as part of its determination by isotope dilution analysis in Gd containing uranium oxide. The relative standard deviation corresponds to 5 measurements of 1 sec integration time each (50 msec dwell time for each integration). The relative standard deviation follows Poisson statistics for low count rates but diverges from that at count rates higher than 10000 ions/sec. Above that level plasma instability is the main source of uncertainty in our instrument and there seems to be no correlation between the RSD and the ion counts actually measured. Above 10000 counts the mean RSD was 1.64% ± 1.15%, (1σ, n=95). It is possible, however, for the plasma instabilities in the measurement of isotope ratios to mutually compensate and that Poisson statistics apply to the measured ratios thanks to the fast scanning performed.

The ion-count rate ratio, R, for two isotopes **i** and **j** will be I^i/I^j. Both I^i and I^j have been obtained by counting N^i and N^j counts during t^i and t^j seconds respectively ($N=I*t$). Applying error propagation and ignoring the variance of the counting time:

$$[s(R)/R]^2 = [s(N^i)/N^i]^2 + [s(N^j)/N^j]^2$$

Following Poisson statistics, $s(N) = \sqrt{N}$ and then

$$\left[\frac{s(R)}{R}\right]^2 = \frac{1}{N^i} + \frac{I}{N^j} = \frac{I}{I^i * t^i} + \frac{1}{I^j * t^j} \qquad (8)$$

Given the counting rates and the counting time, the theoretical relative standard deviation for Poisson statistics can be calculated for different isotope ratios. The comparison between the theoretical (equation (8)) and experimental RSDs obtained for the same Gd samples showed no correlation for different values of R or I^j. It can be concluded that, at least for our instrument and counting conditions, the precision of the isotope ratios was limited by plasma instability and not by counting statistics for a large range of isotope ratios and intensities.

Random error propagation in isotope dilution analysis

The variance in C_S, $s(C_S)^2$, will depend on the variance of the other parameters in equation (2). Following error propagation analysis for the measurement factors:

$$s(C_S)^2 = \left[\frac{\partial C_S}{\partial Aw_S}\right]^2 * s(Aw_S)^2 + \left[\frac{\partial C_S}{\partial Aw_{Sp}}\right]^2 * s(Aw_{Sp})^2 +$$

$$\left[\frac{\partial C_S}{\partial A^a_{Sp}}\right]^2 * s(A^a_{Sp})^2 + \left[\frac{\partial C_S}{\partial A^b_S}\right]^2 * s(A^b_S)^2 + \left[\frac{\partial C_S}{\partial R_M}\right]^2 *$$

$$s(R_M)^2 + \left[\frac{\partial C_S}{\partial R_{Sp}}\right]^2 * s(R_{Sp})^2 + \left[\frac{\partial C_S}{\partial R_S}\right]^2 * s(R_S)^2$$

Taking the partial derivatives, ∂C_S, in equation (2) and reorganising the expression we arrive at:

$$\left[\frac{s(C_S)}{C_S}\right]^2 = \left[\frac{s(Aw_S)}{Aw_S}\right]^2 + \left[\frac{s(Aw_{Sp})}{Aw_{Sp}}\right]^2 + \left[\frac{s(A^a_{Sp})}{A^a_{Sp}}\right]^2 +$$

$$\left[\frac{s(A^b_S)}{A^b_S}\right]^2 + \left[\frac{R_M * (1 - R_{Sp} * R_S)}{(R_M - R_{Sp}) * (1 - R_M * R_S)}\right]^2 * \left[\frac{s(R_M)}{R_M}\right]^2 + \qquad (9)$$

$$\left[\frac{-R_{Sp}}{R_M - R_{Sp}}\right]^2 * \left[\frac{s(R_{Sp})}{R_{Sp}}\right]^2 + \left[\frac{R_M * R_S}{1 - R_M + R_S}\right]^2 * \left[\frac{s(R_S)}{R_S}\right]^2$$

As can be observed in equation (9) the relative error in C_S depends on a series of parameters which have to be minimised. In the case of samples containing natural elements and when a certified enriched isotope is used as the spike, the first four factors in equation (9) can be considered negligible compared to the other three factors which depend only on the isotope ratios measured and their relative errors. Also, in the case of natural elements, only R_M has to be measured experimentally and the errors in R_S and R_{Sp} will be negligible compared to R_M. So, for the analysis of natural elements, equation (9) reduces to

$$\left[\frac{s(C_S)}{C_S}\right]^2 = \left[\frac{R_M*(1-R_{Sp}*R_S)}{(R_M-R_{Sp})*(1-R_M*R_S)}\right]^2 * \left[\frac{s(R_M)}{R_M}\right]^2 \quad (10)$$

The function $[R_M*(1 - R_{Sp}*R_S)/((R_M - R_{Sp})*(1 - R_M*R_S))]$ is the so-called error magnification factor, f(R). The actual value of f(R) depends on R_M, R_S and R_{Sp} in a very complicated manner. As R_S cannot be chosen, only R_M and R_{Sp} can be optimised for minimum f(R). It is well known that for optimum values of R_M and R_{Sp}, error magnification factors close to 1 can be obtained and the relative error in the concentration by isotope dilution analysis will approach the error in the measured isotope ratio.

In the analysis of non-natural elements containing unknown isotope abundances, no simplifications apply and the general equation for the error magnification factor has to be used. For that purpose those parameters in equation (9) which depend on the sample or the spiked sample can be supposed to be determined experimentally by MS and referred finally to errors in isotope ratios measured. We will consider now that the errors in the isotope composition of the spike are negligible, either by the use of a natural element or a certified enriched isotope, and we will study only the random error propagation in the measurement of the sample and the spiked sample. However, for the equations used below, the errors in the spike can be determined in the same way as those in the sample.

The unknown values of the atomic weights and isotope abundances in the sample have to be determined experimentally. The isotope abundance of the reference isotope in the sample A^b_S was calculated as follows:

$$A^b_S = 100\,\Sigma\,(R^i_S) \quad (11)$$

where A^b_S is the isotope abundance of the reference isotope in the sample (a/o) and R^i_S is the isotope ratio for the **i**th isotope of the element containing **n** isotopes.

The elemental atomic weights are then calculated as:

$$Aw_S = (Aw^i * R^i_S)/(\Sigma\, R^i_S) \quad (12)$$

where Aw^i is the atomic weight of the **i**th isotope of the element, A^i_S its isotope abundance and Aw_S the atomic weight of the element in the sample.

For the determination of the error in the isotope abundance of the main isotope in the sample, A^b_S, we can apply error propagation theory and take partial derivatives in equation (11) with respect to the measured ratios. After developing the expression we arrive at:

$$\left[\frac{s(A^b_S)}{A^b_S}\right]^2 = \sum_{i=1}^{n}\left[\left[\frac{R^i_S}{\sum_{i=1}^{n} R^i_S}\right]^2 \left[\frac{s(R^i_S)}{R^i_S}\right]^2\right] \quad (13)$$

where $s(R^i_S)$ is the standard deviation for the **i**th ratio measured (note that for **i=b**, R=1 and s(R)=0 by definition). From equation (13) it can be inferred that the relative error in the isotope abundance of the reference isotope in the sample will decrease for higher isotope abundances where $\Sigma(R^i_S)$ tends to 1 and the R^i_S values tend to 0.

In a similar way, the relative error in the atomic weight can be expressed as

$$\left[\frac{s(Aw_S)}{Aw_S}\right]^2 = \sum_{i=1}^{n}\left[\left[\frac{Aw^i*R^i_S}{\sum_{i=1}^{n}(Aw^i*R^i_S)} - \frac{R^i_S}{\sum_{i=1}^{n}(R^i_S)}\right]^2 * \left[\frac{s(R^i_S)}{R^i_S}\right]^2\right] \quad (14)$$

assuming that the errors in the atomic weights of the isotopes, Aw^i, are negligible. As can be observed, the random error propagation for the elemental atomic weights will be much lower than that for the isotope abundances, especially for heavy elements where the value of $Aw^i/\Sigma(Aw^i*R^i_S)$ is very similar to that of $1/\Sigma(R^i_S)$.

Now, all parameters in equation (9) can be expressed as a function of the experimental errors in the measured isotope ratios, s(R)/R. If we introduce equations (13) and (14) for A^b_S and Aw_S in equation (9), and assuming that the errors in the spike are negligible, then

$$\left[\frac{s(C_S)}{C_S}\right]^2 = \sum_{i=1}^{n}\left[\left[\frac{Aw^i*R^i_S}{\sum_{i=1}^{n}(Aw^i*R^i_S)} - \frac{R^i_S}{\sum_{i=1}^{n}(R^i_S)}\right]^2 * \left[\frac{s(R^i_S)}{R^i_S}\right]^2\right] +$$

$$\sum_{i=1}^{n}\left[\left[\frac{R^i_S}{\sum_{i=1}^{n} R^i_S}\right]^2 \left[\frac{s(R^i_S)}{R^i_S}\right]^2\right] + \left[\frac{R_M*(1-R_{Sp}*R_S)}{(R_M-R_{Sp})*(1-R_M*R_S)}\right]^2 *$$

$$\left[\frac{s(R_M)}{R_M}\right]^2 + \left[\frac{R_M*R_S}{1-R_M*R_S}\right]^2 * \left[\frac{s(R_S)}{R_S}\right]^2 \quad (15)$$

As can be observed, the relative error in the concentration by ID for the analysis of non-natural elements will be a function of the relative errors in the measured isotope ratios both in the sample and in the spiked sample, assuming a certified spike is used. A closer look at equation (15) shows that all the parameters which depend on R^i_S cannot be optimised and will give a constant contribution to the total error when the sample contains non-natural elements whose isotope abundances have to be measured. From equation (15) it can be demonstrated that the parameters depending on R^i_S tend to zero when there is only one enriched isotope of the element present and increases when there are several isotopes with similar isotope abundances: which, unfortunately, is the case for many fission products.

Correction for mass-discrimination

The effect of mass-discrimination correction on error propagation can be developed from equation (4), following the error propagation theory

$$\left[\frac{s(R_{corr})}{R_{corr}}\right]^2 = \left[\frac{s(R_{exp})}{R_{exp}}\right]^2 + \left[\frac{-K*\Delta M}{1+K*\Delta M}\right]^2 * \left[\frac{s(K)}{K}\right]^2 \quad (16)$$

The relative error on the corrected ratio will be higher than the relative error in the experimental ratio by a factor depending on the experimental mass-discrimination factor, the mass difference between the measured isotopes and the relative error in the determination of K, which can be evaluated by the standard deviation of the slope of the linear regression used to calculate K. For every experimentally measured isotope ratio, the expected error after correction for mass-discrimination can be evaluated from equation (16) and later introduced in equation (15).

Correction for dead-time losses

The effect of the dead-time correction on random error propagation can be determined from equation (6) applying the error propagation theory and developing the partial derivatives we arrive, without simplification, to

$$\left[\frac{s(R_{real})}{R_{real}}\right]^2 = \left[\frac{1}{1-\tau*R_{meas}*I^2_{meas}}\right]^2 * \left[\frac{s(R_{meas})}{R_{meas}}\right]^2 + \left[\frac{I^2_{meas}*\tau*(R_{meas}-1)}{(1-\tau*I^2_{meas})*(1-\tau*R_{meas}*I^2_{meas})}\right]^2 * \left[\left[\frac{s(\tau)}{\tau}\right]^2 + \left[\frac{s(I^2_{meas})}{I^2_{meas}}\right]^2\right] \quad (17)$$

As can be observed, the first term in equation (17) tends to 1 for low values of I^2_{meas} or . In this case the error in the corrected ratio will be equivalent to the error in the measured ratio.

Conclusions

As can be observed, ICP-MS can be applied for the determination of major elements in nuclear samples with adequate precission and accuracy when the sources of error in Isotope Dilution ICP-MS are known and corrected for. The flexibility to adapt to new types of samples and different elements is one of the strengths of ICP-MS for the analysis of nuclear materials.

7. Work for Third Parties

7.1 Radiotherapeutical Work: Separation and Purification of ^{229}Th and Daughter Products

Following the initial experiments (TUAR 93,) to optimize columns and separation methods, a large-scale purification of ^{229}Th from the parent material ^{233}U has been carried out under contract with Alphamedical Holdings BV, the Netherlands. Approximately 400g ^{233}U containing material was purchased from Oak Ridge, USA. The material was a slurry containing old residues of ^{233}U together with the daughter products (^{229}Th,..) and also some ^{232}Th. The thorium was separated and purified from the total material using an anion exchange column (DOWEX 1x8), whereby 200 mg ^{229}Th, contaminated with a large amount of ^{232}Th (35g), was obtained from an estimated 9g ^{233}U. The ^{225}Ac was then separated and purified from the Th fraction on a cation exchange column. The ^{225}Ac grows in with a 10 day halflife, allowing a ^{225}Ac ‚cow' to be prepared every 2-3 weeks, depending on the activity required.

Two ^{225}Ac ‚cows' were prepared and sent to the Memorial Sloan Kettering Cancer Center, New York for clinical experiments. The ‚cows' had to meet very stringent requirements to be able to be applied for clinical studies. Investigations have also been carried out into the complex formation of Ac using ^{225}Ac in cooperation with AKZO-Nobel/ORGANON, the Netherlands.

7.2 Transmutation of Minor Actinide-Containing Alloys in PHENIX

The fuel to be irradiated in PHENIX (the METAPHIX irradiation) have been fabricated under contract for the Central Research Institute of the Electric Power Industry (CRIEPI). The UPuZr rods are encapsulated in quartz tubes with the minor-actinide-containing rods being held under vacuum. The filling methods of the pins, the sodium bonding and the welding are presently being tested using steel rods as substitute.The development of the techniques for Na bonding is well advanced: the extent of Na bonding of the pins will be controlled by X-ray and eddy current measurements.

Transportation of the pins to Cadarache is planned for the first half of 1995. The expected pin temperature must be estimated and a packaging selected so that the temperature will not rise above 98 °C, the melting point of sodium, during the transport.

The METAPHIX irradiation experiment in PHENIX is planned to start at cycle 51, August 1995, if there are no further delays in restarting reactor operation. Cycle 51, like cycle 50, will be run at 2/3 nominal full power, i.e. 350 MW, so these cycles will be longer than normal. The position of the METAPHIX pins in the core will be chosen, however, so that the linear rating remains at 400 W/cm as requested by CRIEPI.

7.3 Spent Fuel Characterization for Interim Dry Storage

Under a contract with the Central Research Institute for the Power Industry (CRIEPI), work is being carried out to characterize high burnup UOX and MOX spent fuels in order to assess their interim dry storage behaviour and obtain experimental data for the verification of computer codes used to evaluate the radiation source term for these fuels. The spent fuel characterization is performed by destructive and non-destructive analysis techniques. The study began in 1993 and will continue through to the end of 1996.

The experimental tasks of the project can be grouped under: isotope analyses and radiation measurements for burnup credit, radiation source measurement and distribution, and fuel performance studies (cladding, pellet-cladding interface and fission gas data). As well as this, fuel and fuel assembly information (design, fabrication and irradiation history) is provided. During the second year of the programme the following studies were performed: chemical analyses for actinide and fission product content, radial gamma microscan of fission product distribution, alpha- beta- gamma-autoradiography, ceramography (porosity, optical analyses, grain size, pellet-cladding interaction), metallography (hydrides, optical analyses, corrosion) and Electron Probe Micro Analysis (EPMA).

The preliminary comparison of measured and calculated (by CRIEPI) neutron emission rates indicates that ORIGEN-2 can potentially be used for the evaluation of the radiation source terms of these fuels. Experimental-to-theoretical ratios of 0.98 for the UOX and 1.08 and 1.01 for the two MOX fuels were obtained.

7.4 Passive Neutron Interrogation for Nuclear Material Measurements in the Pilot Conditioning Plant Gorleben

A passive neutron detection device has been developed by GNS (Gesellschaft für Nuklear Service mbH, Hannover), supported by KfK/INR, APA (Anlagen Planung Alzenau GmbH) and MAB (Münchener Apparatebau für Elektronische Geräte GmbH), and is being tested in the hot-cells of the Institute with spent fuel pins (TUAR-92, p. 204) [1]. The device is intended for for safeguards purposes at the Gorleben Pilot Plant where conditioning of spent fuel is planned to be performed prior to long-term intermediate storage and eventual final geological disposal.

The neutron and gamma emissions of a fuel bundle have the potential to be used as a 'signature' for its identification through the plant. It is considered that axial measurements on a fuel bundle could distinguish between BWR and PWR fuel, which have different distributions of burnup and therefore neutron and gamma emmissions along the fuel rods.

The work carried out in 1994 involved the characterisation of BWR spent fuel rods. The aim was twofold: (i) to establish profiles of the neutron and gamma emissions along the active length of the fuel; (ii) to measure the neutron and gamma emissions along a line of the pin axis and hence to determine the effect of these profiles on the radiation emission along the line of the pin axis extended away from its ends. The evaluation of the data obtained is in progress.

Reference

[1] E. Leitner, R. Weh and G. Nicolaou; Proceedings 15th Annual ESARDA Meeting, 11-13 May 1993, Rome, Italy

7.5 In-situ Monitoring Technique for Dissolution Progress of Spent Fuel

Introduction

Direct monitoring by spectrophotometry of the dissolution of spent nuclear fuel in nitric acid at the head-end of a reprocessing process is difficult, because the dissolver solution generally includes many fission products which also absorb in the visible range. Furthermore the presence of insoluble residues disturbs the measurement. The method of measuring the concentration of NO_x or ^{85}Kr in the off-gas has therefore often been used to monitor the dissolution progress of spent fuel indirectly. An alternative method is to measure the concentration of uranyl ions in the dissolver solution after sampling and chemical purification.

However in the dissolver solution of spent fuel U is present as U^{VI} , which has a wide absorption peak at around 400 nm. It should therefore be possible to measure the concentration of U in the solution as an in-situ monitor for the dissolution progress of spent fuel if the interference by fission products can be reduced. This report describes such an in-situ monitoring technique for the dissolution of spent fuel using the measurement of the concentration of the uranyl ion in the dissolved solution directly and continuously. The work was done under contract with CRIEPI and a coworker from Mitsubishi Heavy Industries collaborated in the experiment.

Experimental

The dissolver equipment was installed inside a hot cell. A schematic drawing of the installation is shown in Fig. 7.1. A piece of spent fuel (6.3 g, burn-up ca. 60 000 MWd/

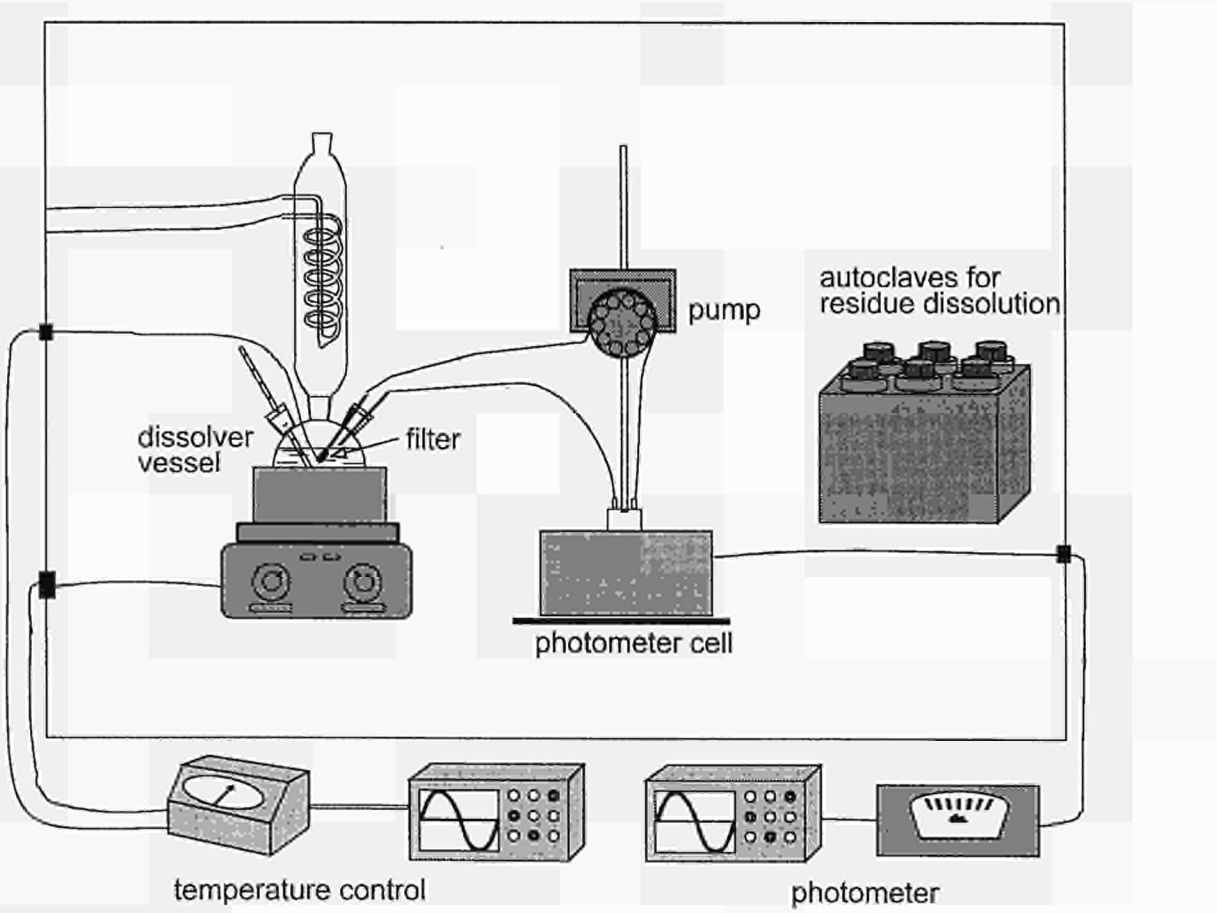

Fig. 7.1 Experimental set-up

t U) was dissolved at about 90 °C in approximatly 30 ml of 3.4 M nitric acid solution. The dissolved solution was continually pumped through a photometer cell. Particles in the circulating solution were removed by filtering at the entrance to the sampling tube. The photometer cell was connected with an optical fiber to the spectrophotometer (CARY 17D), located outside of the hot cell. The concentration of uranyl ions in the solution was measured at 445 nm using a 10 mm absorption length up to a concentration of 50 g U/l and 1 mm for concentrations above this value.

Results and discussion

1. The selected monitoring wavelength was 445 nm for the following reasons:
2. The influence of fission product absorption is comparatively small at this wave-length. For example, the molecular absorption coefficient of the uranyl ion, UO_2^{2+}, at 445 nm is approximatly 2 [1] similar to that of the ruthenium nitrate complex ion - a representative fission product included in dissolved solution - but the molecular ratio of individual fission products to uranium is normally less than 0.01.
3. The absorption of uranyl ion does not vary much at the selected wave-length.
4. The absorption of HNO_3 at this wave-length is very low.

The absorption of the uranyl ion as a function of its concentration is shown in Fig. 7.2. These calibration curves were used to scale the absortion axis of the monitoring curve of a spent fuel dissolution (Fig. 7.3). The time lag in this is due to the change from a 10 mm to 1 mm photometer. These results show, that monitoring of spent fuel dissolution directly by measuring the concentration of uranyl ions in the dissolver solution by optical absorption is a very suitable method. In the present case, the dissolution was completed after 31 min and based on an estimated surface area of the sample (geometrical) of 12.7 cm^2, an initial dissolution rate constant of 84 mg /cm^2.min could be calculated.

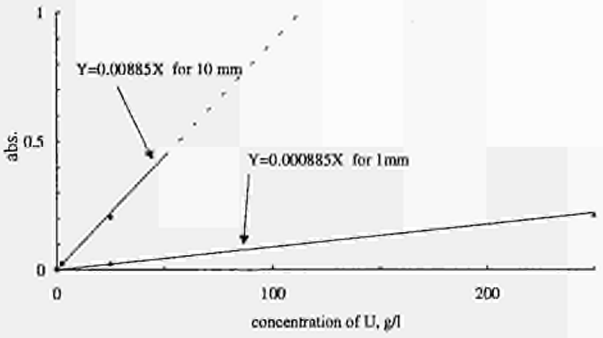

Fig. 7.2 The relation between concentration and absorption ratio of the uranyl ion at 445 nm in 3.4 N HNO_3

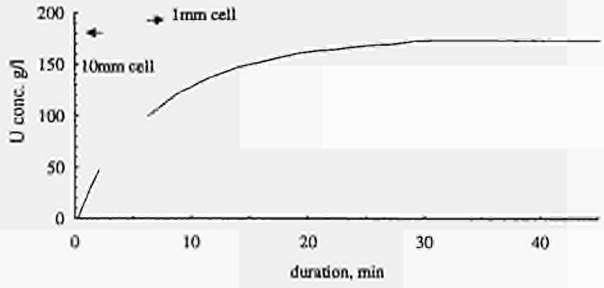

Fig. 7.3 Monitoring curve for the dissolution of a spent fuel (6.3 g) in 3.4 N HNO_3 at 90 °C

Reference

[1] "Gmelin Handbook of Inorganic Chemistry", Uranium Nr. 55, Verlag Chemie (1984).

7.6 Post-Irradiation Examination of Pressurized and Boiling Water Reactor Fuel Rods

In the framework of the contract with Siemens AG - Bereich Energieerzeugung (KWU), non-destructive and destructive examinations of power reactor fuel rods are to be carried out (see TUAR-91, TUAR-92 and TUAR-93).

In 1994, 11 fuel rods from the reactor Krümmel (KKK), a Boiling Water Reactor (BWR) type), were received for the analysis at the Institute, 3 of them corresponding to a failure analysis project. The 5 fuel rods received in 1993 from the reactor ISAR (KKI) were conditioned and transported back to the reactor pool.

A list of the numbers and types of examinations carried out on different fuel rods in 1994 is given in Tab. 7.1.

Tab.7.1 Siemens / KWU contract

Type of Analysis	MTS-6 15.05.91	KKGg-VII 04.05.92	MTS-2 21.05.92	GKN1-III 18.03.93	KKGg-VIII 16.03.93	TEM/Met 10.05.93	MTS-3 04.08.93	KKI2-1 04.08.93	KKK-Def. 04.02.94	KKK-1 04.02.94	KKK-1 10.06.94	TOTAL Exam.
Vis. examination								5	3	8		16
Fuel rod length									1	8		9
Profilometry									1	8		9
Defects									3	8		11
Oxide layer thick.									1	8		9
Gamma Scan.								3	2	8		13
Fission Gas Anal.								2	1	8		11
Free volume								2	1	8		11
Metallography		8			6	3		6		8		31
Ceramography		5		4	4							13
Burn-up					1							1
H2-Determin.		21			5			10				36
SEM-Cladding		3			2			1				6
TEM		3				3		2				8
Weighing												0
ICP-MS								3				3
Re-encapsulation GKN-2												28
Re-encapsulation KK1-2												5
LOCA simulation exper.												1
Re-fabrication for HFR re-irradiation (KKGg)												4
GDMS - cladding												8
ICP-MS - cladding												5

7.7 Phebus pf: BR3 Fuel Characterization

In the previous annual report (TUAR-93, p. 257) the non-destructive and destructive testing of irradiated BR3 rods intended for the Phebus pf project was reported in its current state. In summary each rod of the batch (of 26 rods) was non-destructively tested, by γ-scanning, eddy current defect testing and length measurement (visual inspection). For 3 rods of each batch eddy current oxide thickness and profilometry were additionally measured. One of each batch was taken for filling gas analysis of fission gas and for ceramographic examination of maximum and mean power position as well as a radiochemical analysis of a sample pellet from the maximum power position.

The current status of the examination is that 4 batches of 26 rods have been completed and a report on their examination has been sent (after external editing) to the Phebus pf project who have issued it as a technical report (TG 122) in Oct. 1994. The reporting was done then so as to distribute the BR3 rod data characterization to the project partners in time to do the fission product inventory calculation or modelling of test bundle behaviour and finalise the test protocol for the next test (FPT1) which is planned for May 1995 and will use the fuel rods from batch 2. (The first test FPT0 was successfully carried out on 2-5 Dec. 1993 using non-irradiated fuel.) The final batch (Nr. 5) of 26 BR3 rods will be delivered early next year to ITU from CEN/SCK Mol after the large hot-cell renovations are completed and will be examined in the first half of 1995.

One of the important conclusions from the NDT and destructive testing was that the rods of all four batches are in good condition. Although there was some ovalisation of the rods, no cladding defects were observed and the outer oxide was thin (~ 5 m thick metallographically estimated) and adherent with no inner oxidation and only very occasional pellet cladding interactions (Tab. 7.2a). No grain growth or pore coalescence or diffusion was noted even at the maximum power position. No fission product diffusion (e.g. ^{137}Cs) was observed in the γ-scanning or β-autoradiographs. The filling gas analysis revealed very slight fission gas (Kr and Xe) release estimated at 0.2 % of inventory (Tab. 7.2b). α-autoradiographs revealed a orientation effects in the rods from the BR3 reactor used for the irradiation.

Tab. 7.2a Metallographic fuel and cladding dimensions for batches (Lots) 1-4.

	Nominal Starting Values	PIE Values (% Variation)							
Lot Nr.		1 U119 5 %		2 U627 6.85 %		3 U568 6.85 %		4 U570 6.85 %	
Rod Nr.									
^{235}U Enrichment %									
cut		max.	mean	max.	mean	max.	mean	max.	mean
Position of cut (mm from bottom end)		510 mm	217 mm	497 mm	223 mm	495 mm	225 mm	485 mm	240 mm
local burn-up (GWd/tU)		34.5	26.7	29.5	23.4	30.9	24.5	35.0	27.8
Parameter									
A) CLADDING									
ø ext (mm)	9.485 - 9.493	9.463 ± 0.006 (-0.3 %)	9.470 ± 0.005 (-0.2 %)	9.470 ± 0.01 (-0.4 %)	9.484 ± 0.003 (-0.3 %)	9.461 ± 0.007 (-0.3 %)	9.462 ± 0.005 (-0.3 %)	9.447 ± 0.004 (-0.4 %)	9.451 ± 0.005 (-0.4 %)
ø int (mm)	8.24 (spec.)	8.185 ± 0.006 (-0.7 %)	8.195 ± 0.003 (-0.5 %)	8.19 ± 0.01 (-0.6 %)	8.208 ± 0.003 (-0.4 %)	8.193 ± 0.004 (-0.6 %)	8.201 ± 0.004 (-0.5 %)	8.191 ± 0.005 (-0.6 %)	8.195 ± 0.005 (-0.5 %)
Thickness (mm)	0.58 (spec.)	0.639 (+ 10.2 %)	0.638 (+ 10.0 %)	0.640 (+ 10.3 %)	0.638 (+ 10.0 %)	0.634 ± 0.007 (+ 9.3 %)	0.631 ± 0.004 (+ 8.8 %)	0.627 ± 0.004 (+ 8.1 %)	0.629 ± 0.004 (+ 8.4 %)
outer oxide layer (µm)	-	4.4 ± 0.5	4 ± 0	3 ± 0.4	4 ± 0.4	3.4 ± 0.3	2.8 ± 0.7	4.4 ± 0.3	3.8 ± 0.3
B) FUEL/CLADDING GAP									
width (µm)	98 ± 6	20 ± 3 (-80 %)	34 ± 7 (-65 %)	23 ± 3 (-77 %)	46 ± 5 (-53 %)	16 ± 5 (-84 %)	35 ± 14 (-64 %)	21 ± 5 (-79 %)	22 ± 5 (-78 %)
C) FUEL									
ø mean (mm)	8.039 - 8.051	8.143 ± 0.004 (+ 1.3 %)	8.125 ± 0.007 (+ 1.1 %)	8.14 ± 0.02 (+ 1.2 %)	8.11 ± 0.02 (+ 0.9 %)	8.161 ± 0.006 (+ 1.4 %)	8.130 ± 0.031 (+ 1.1 %)	8.149 ± 0.008 (+ 1.3 %)	8.154 ± 0.004 (+ 1.4 %)

Tab. 7.2b Fission gas releases determined by puncturing from the destructively tested rods from batches (Lots) 1-4.

Mean Burn-up ($GWd.tU^{-1}$)	1 U119 (Lot 1) 26.7	2 U627 (Lot 2) 23.4	3 U568 (Lot 3) 24.5	4 U570 (Lot 4) 27.8	Inventory estimate from codes (1) (cm^3) (NTP)		Release as % of total KORIGEN / MITRA Inventory	
Krypton Isotopes	(cm^3) (NTP)	(cm^3) (NTP)	(cm^3) (NTP)	(cm^3) (NTP)	MITRA U119	KORIGEN U627	MITRA U119	KORIGEN U627
^{83}Kr	0.01	0.01	0.01	0.01	6.5	5.0	0.15	0.20
^{84}Kr	0.02	0.02	0.01	0.02	12.6	10.6	0.16	0.19
^{85}Kr	0.00	0.01	0.00	0.00	1.09	1.9	-	0.50
^{86}Kr	0.03	0.04	0.02	0.03	20.9	19.6	0.14	0.20
Total Kr	**0.07**	**0.08**	**0.04**	**0.05**	**41.1**	**37.1**	**0.17**	**0.21**
Xenon Isotopes								
^{131}Xe	0.05	0.07	0.04	0.04	34.4	27.6	0.15	0.25
^{132}Xe	0.10	0.13	0.07	0.09	59.3	51.7	0.17	0.25
^{134}Xe	0.15	0.18	0.10	0.11	94.4	84.0	0.16	0.21
^{136}Xe	0.21	0.24	0.13	0.15	122.6	116.3	0.17	0.21
Total Xe	**0.52**	**0.62**	**0.33**	**0.39**	**310.7**	**279.6**	**0.17**	**0.22**

Mean Burn-up ($GWd.tU^{-1}$)	1 U119 (Lot 1) 26.7	2 U627 (Lot 2) 23.4	2 U568 (Lot 3) 24.5	3 U570 (Lot 4) 27.8	Inventory estimate from KORIGEN / MITRA codes (1)
Ratio Xe/Kr	7.43	7.75	8.25	7.80	7.55
relative error of vol. meas. (and calibration)	5 %	5 %	< 5 %	< 5 %	
Pin pressure prior to test	25.0 bar	23.6 bar	24.1 bar	24.1 bar	-

(1) Input data:

Code	MITRA [3]	KORIGEN [4]
fuel pin	U119	U627
Initial enrichment ^{235}U %	5	6.85
Burn-up (rod average) GWd/tU	26.7	23.4
Discharge date	30.6.87	30.6.87
Cooling time	5 years	6 years

The radiochemical analysis is given in Tab. 7.3a. A rough estimate of the burn-up was made using the ^{148}Nd concentration as a check of the radiochemical analyses. These are compared in Tab. 7.3a with the estimates given by Belgonucleaire. For 3 of the 4 batches the agreement is to within 2% (the expected accuracy). However for batch (Lot) 2 the agreement was not so good (10% difference) but the reason for this is uncertain. The Pu/U ratio for batch (Lot) 3 is also unexpectedly high considering its similar burn-up to U627.

In Tab. 7.3b the isotopic composition for Pu and U is given. It can be seen with increasing burn-up in going from batch 2 to 4 that there is greater Pu content and with an increasing proportion of the higher Pu isotopes e.g. 240 and 241.

Batch (Lot) 1 has a lower initial enrichment (5 % U-235) than the other batches (6.85% U-235) and shows more higher Pu isotopes since it has a correspondingly higher initial U-238 content from which the Pu-239 and subsequently the higher Pu isotopes (240 and above) are formed by neutron capture. Nevertheless the total Pu content is lower, which is also unexpected. The above differences may be due to local differences of the neutronic spectrum in the reactor that would occurred because of the presence of several fuels during the irradiation.

Concluding Remarks

The NDT and DT analysis of the first 3 batches has made a thorough characterization of the irradiated BR3 fuel rods. It has confirmed their good condition and given their heavy element composition so that 20 rods from each batch of 26 can be selected for the subsequent Phebus pf tests. The analyses also enable the fission product inventories to be calculated and fuel rod behaviour in the Phebus bundle to be modelled in preparation for these tests. The modelling to be carried out at Cadarache will need to take the local neutron spectrum differences in the BR3 reactor into account in order to replicate the inventory found by radiochemistry.

Tab. 7.3a Radiochemical results1: Burn-up analyses (atoms / g conc. sol)

Lot Rod Cut Initial Enrichment (% ^{235}U) local burn-up (BN) (GWd/tU)	1 U119 Max power 5 % 34.5	2 U627 Max power 6.85 % 29.5	3 U568 Max power 6.85 % 30.9	4 U570 Max power 6.85 % 35.0
A) U (%)				
^{234}U	0.02	0.03	0.03	0.03
^{235}U	1.98	3.79	3.68	3.40
^{236}U	0.57	0.63	0.66	0.70
^{238}U	97.43	95.55	95.63	95.86
Total U i) %	100	100	100	100
ii) at/g conc. soln.	$2.1172 + 20$	$1.0537 + 20$	$1.1435 + 20$	$1.0853 + 20$
B) Pu (%)				
^{238}Pu	0.92	0.78	0.89	1.00
^{239}Pu	63.90	72.24	72.12	69.19
^{240}Pu	25.11	19.12	18.75	20.79
^{241}Pu	7.27	6.42	6.64	7.02
^{242}Pu	2.80	1.43	1.59	2.00
Total Pu i) %	100	100	100	100
ii) at/g conc. soln.	$1.1959 + 18$	$6.4860 + 17$	$7.6744 + 17$	$7.2002 + 17$
Total Pu / Total U + Pu	0.56 %	0.61 %	0.67 %	0.66 %

Tab. 7.3b Radiochemical results 2: U and Pu isotopic compositions.

Lot Rod Cut Initial Enrichment (% ^{235}U)	1 U119 Max power 5 %	2 U627 Max power 6.85 %	3 U568 Max power 6.85 %	4 U570 Max power 6.85 %	Technique (accuracy)
A) Total U	2.1172 + 20	1.0537 + 20	1.1435 + 20	1.0853 + 20	chrom / ID-MS
Total Pu	1.1959 + 18	6.4800 + 17	7.6744 + 17	7.2002 + 17	<0.7% accuracy
Total U + Pu	2.1292 + 20	1.0602 + 20	1.1512 + 20	1.0925 + 20	
B) ^{148}Nd	1.188 + 17	5.6948 + 16	6.7518 + 16	6.9162 + 16	chrom / ID-MS 1% accuracy
C)					
i) ^{137}Cs	3.1328 + 17	1.858 + 17	2.1228 + 17	2.1790 + 17	quant. γ-spec. 3 % accuracy
ii) $^{134}Cs/^{137}Cs$ (ratio)	0.0050	0.0067	0.0057	0.0060	γ-spec. ratios 10 % accuracy
Analysis date	20.04.93	10.12.92	20.02.94	20.02.94	
D) Burn-up GWd/tU					~ 2 % accuracy
i) from analysis	31.3	28.9	31.6	34.1	
ii) given by BN	34.5	29.5	30.9	35.0	
iii) % difference in BU estimates	10.2	2.1	-2.2	2.6	

n.b. concentration values between columns can not be directly compared as concentrated solution volume varies slightly with sample.

7.8 Matrix Materials for the Transmutation of Actinides

A new project between the Institute for Transuranium Elements and Electricité de France has been started in 1994 in order to investigate inert matrices for transmutation of minor actinides.

The aim of this project is to obtain a reliable basis for selecting stable matrices and to discard unstable matrices, based on experimental results on radiation damage. Furthermore, information on (acceptably small) damage effects in the selected matrices will be obtained.

The effect of the three main damage sources which are:

- fission
- neutrons
- α-decay (α-particles, recoil atoms)

plus possibly effects of electrons and γ-rays have to be investigated to obtain reliable data.

An extensive literature review was performed to search for new matrix materials with suitable properties. The main physical and technological properties which were considered within this review are melting points, behaviour against water, thermal conductivity, Young's modulus, solubility of actinides and radiation stability.

Experiments with different matrix materials have been started and first results to characterize the radiation damage are expected in the middle of 1995.

7.9 The Rim Effect Irradiation

The irradiation of the UO_2-based fuel discs fabricated in the last reporting period (TUAR-93, p. 227) started in Dec. 1993. It reached a peak burnup of 44 GWd/t in Oct. 1994. As explained in TUAR-93, the High Burnup Rim Project is coordinated by the Central Research Institute of Electric Power Industry (CRIEPI) and the irradiation is performed in the OECD Halden Reactor. The aim is to study the influence of temperature, burnup, pressure and type of fuel on the formation of the RIM-structure, i.e. the grain subdivision process occurring in UO_2 at high burnup. A matrix of 4 temperatures, 4 burnups and 2 pressures is used. Up to the end of 1994, the irradiation proceeded according to the schedule. Temperatures and gas release were controlled and measured [1] and the end of the irradiation is foreseen for early 1996, with the highest burnup being 100 GWd/t U.

References

[1] M. Kinoshita, T. Matsumura, T. Kameyama, S. Kitajima, E. Kolstad, Hj Matzke, Extended Halden Project Meeting, Bolkesjø , Norway, paper F 1.9, Nov. 1994.

7.10 An Investigation of the Intermetallic Precipitates in Irradiated Zircaloy Cladding Samples by Transmission and Scanning Electron Microscopy

A very comprehensive investigation by Transmission Electron Microscopy (TEM) of the density, size distribution, chemical composition and structure of the Fe-Cr-Zr intermetallic precipitates in irradiated samples of Zircaloy cladding was completed during the reporting period, under a contract with Siemens-KWU.

The programme involved the analysis of samples taken from different positions on one pin to investigate the effects of temperature on the behaviour of the intermetallic particles, and samples taken from different pins, which showed different corrosion behaviour. An analysis was also made of the unirradiated materials used in the fabrication of the pins for comparison.

Small pieces of each irradiated cladding material were cut at the appropriate pin positions in the Institute hot-cells. From these pieces discs were prepared with a diameter of 3 mm and a thickness of about 150 µm, which were mechanically dished to give a residual centre thickness of 20 to 50 µm. The discs were finally electropolished to perforation in an electrolyte of 15% perchloric acid / 85% methanol, at a potential of 25 V and a polishing current of 1 to 4 mA.

The electrolyte was maintained within the temperature range -30 to -15 °C by cooling periodically using liquid nitrogen. The time to perforation varied from 40 min. to 2 hr. Fresh electrolyte was used for each of the specimens since water is introduced from the liquid nitrogen and affects the conductivity of the electrolyte. After perforation the specimen surfaces were cleared of any residual oxide film by treatment in an ion beam thinning apparatus for about 30 minutes on each surface.

The thinned specimens were examined in the 200 kV Hitachi H700 HST electron microscope, modified for handling radioactive and contaminated samples. The microscope is equipped with a scanning attachment permitting scanning transmission and secondary electron surface images to be recorded.

Precipitate composition was analysed using Energy Dispersive X-ray analysis (EDX) with a Tracor Northern TN 5500 system attached to the TEM. The different types of precipitate were characterized by EDX measurements of the relative amounts of Fe and Cr, but leaving Zr out of the calculations. The reason for this is that beam scattering and penetration of the small precipitates produces an anomalous Zr signal from the surrounding matrix, leading to a large scatter in the measured compositions. However, the Fe and Cr x-ray signals arise almost exclusively from the individual particles, thus giving a very low scatter in the measured ratios. For this reason the particles are more readily identified from the Fe:Cr ratio. Where detected, Sn and Si were also included in the analysis.

Particle size distributions for each specimen were made based upon measurements of the "Equivalent Diameter" of more than 200 particles, where possible. In some samples it was not possible to find so many particles. The results have been presented in the form of histograms of the logarithmic size distribution.

Particle density measurements were made taking care to cover a representative area of sample, thus where the distribution was inhomogeneous particle-free grains were also photographed and included along with particle-rich grains. In many cases the particle contrast is low, and it was essential to perform extensive tilting operations in the TEM to optimise contrast and thus ensure that all particles were included. Failure to recognise this difficulty is a possible criticism of previous studies which have been made in this field.

Some of the general observations which have been made are summarised here:

1) A strong influence of cladding in-pile temperature on the behaviour of the intermetallic precipitates was found. In the low temperature samples there was a reduction in the particle density, and a change in the particle character. Evidence of apparent particle dissolution was found, and an example is shown in Fig. 7.4 where the precipitates are surrounded by "haloes" of about double the diameter of the remaining particle and approximately reflecting its shape. The EDX spectrum from this particle is shown in Fig. 7.5; the Cu peaks in this spectrum arise from the specimen holder, and are irrelevant to the analysis.

   In the highest temperature sample, however, there was little change in particle density, but a spread of compositions from Fe:Cr = 100:0 through to Fe:Cr = 40:60. The particles with only Fe as alloying element were nearly always spherical and crystalline.

2) In the samples from the different pins, but with approximately the same in-pile temperature, the original particle composition of Fe:Cr = 70:30 converts into a distribution of compositions from pure Fe as

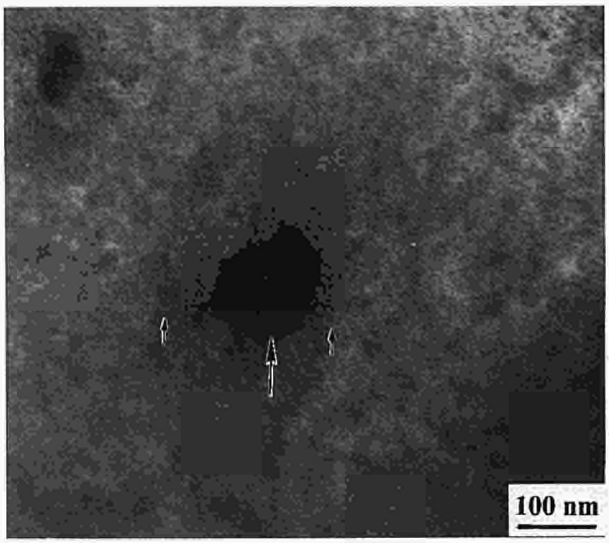

Fig. 7.4 An intermetallic precipitate with the composition ratio Fe:Cr = 17:83, showing a "Haloe" effect suggesting peripheral dissolution of the particle.

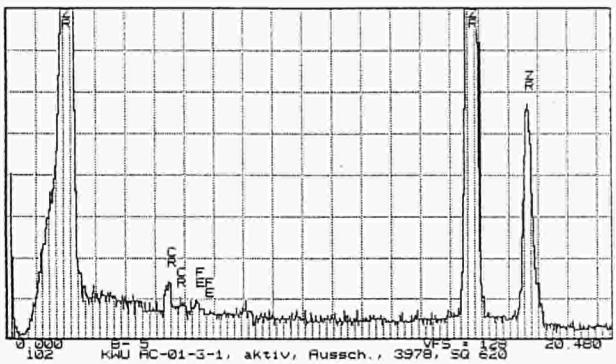

Fig. 7.5 The EDX spectrum from the particle in Fig. 7.4. No detectable levels of Fe or Cr could be obtained from the halo region.

alloying element to pure Cr. The main differences between the different samples lies in the composition distributions of the particles.

The spatial distributions of the particles were usually very inhomogeneous with particles of widely different compositions adjacent to each other in the same grain. An example is shown in Fig. 7.6.

3) Interesting "duplex" particles were often found in which the components had different compositions, and these were often associated with cavities in the specimens. An example is shown in Fig. 7.7. Other particles were found with strong radial composition differences which could be measured using EDX line scan.

The full evaluation of the large quantity of results obtained from all the samples will continue into the next reporting period.

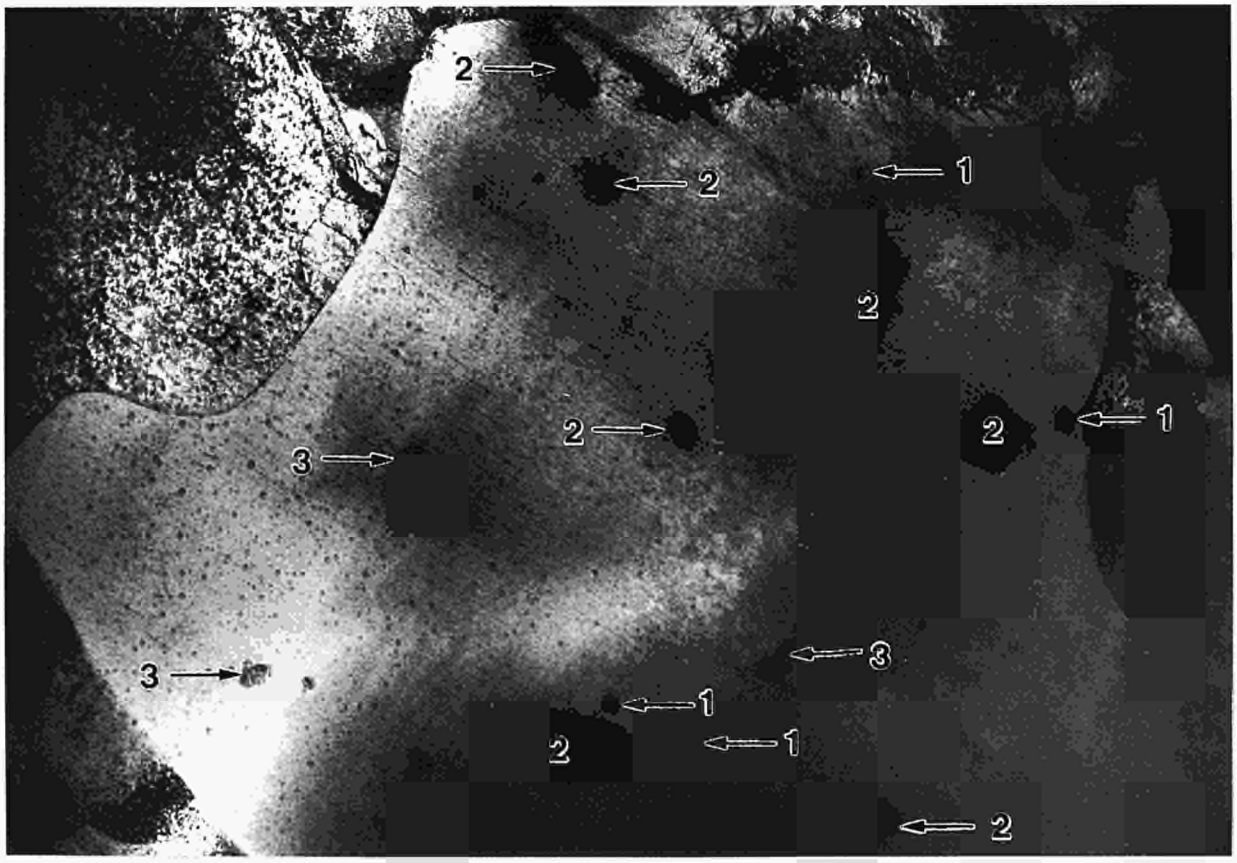

*Fig. 7.6 A low magnification TEM image of a grain showing three different types of particle in close proximity. These are type **A**: Fe:Cr = 100:0, type **B**: Fe:Cr = 50:50 (approx.) and type **C**: Fe:Cr = 20:80.*

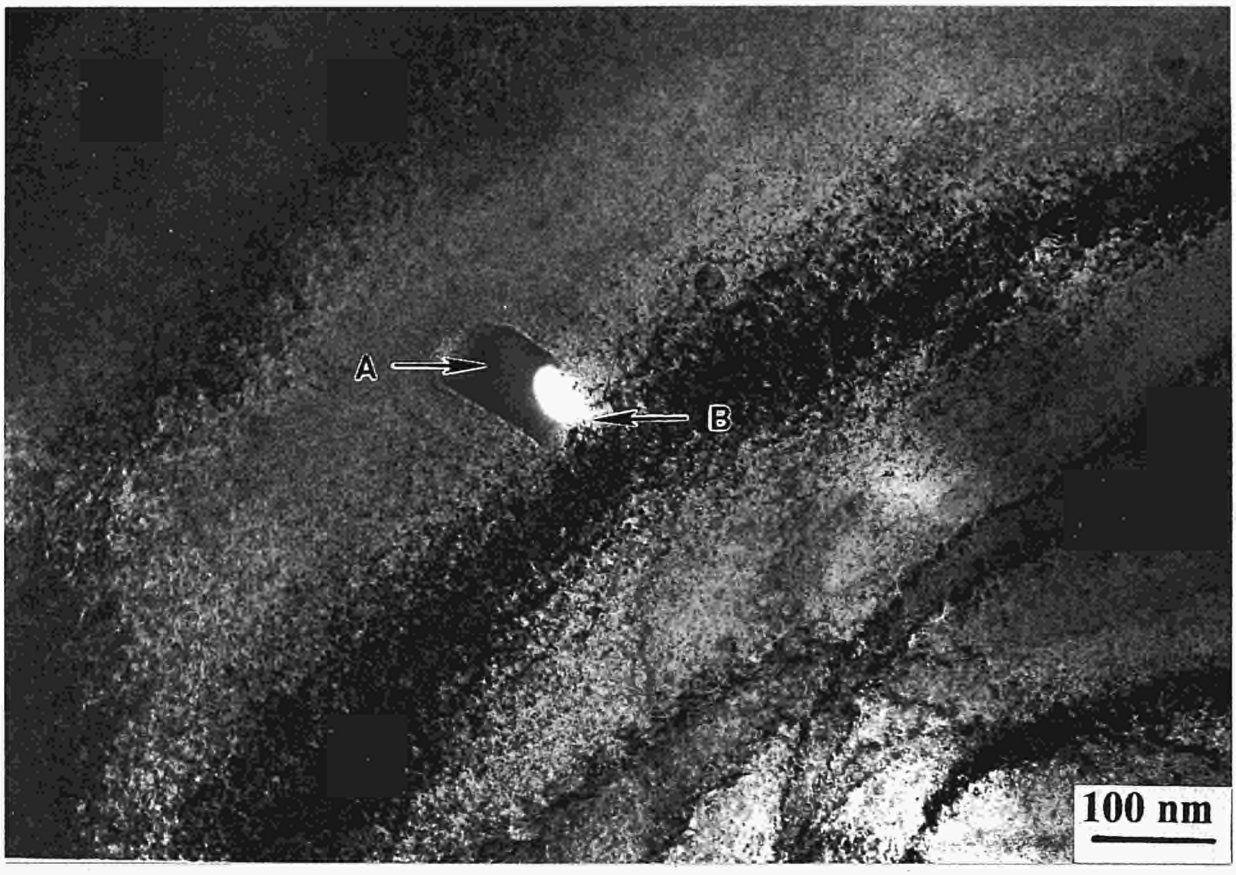

*Fig. 7.7 A duplex particle consisting of two components with different compositions (part **A**: Fe:Cr = 16:84, part **B**: Fe:Cr = 23:77), associated with a cavity in the specimen.*

7.11 An Investigation of the Metal-Oxide Interface in Irradiated Zircaloy Cladding Samples by Transmission Electron Microscopy

The investigation of the oxidation of Zircaloy cladding performed under contract with the Paul Scherrer Institute (PSI), as part of their programme with the NFIR, was continued throughout the reporting period and will be finished in January 1995. A second contract involving the investigation of nine more cladding samples has been requested by the PSI.

Cross sectional samples of the oxide-alloy interface have been prepared from a number of different irradiated cladding samples and thinned for the Transmission Electron Microscope (TEM) by ion etching. In general these specimens were very difficult to observe in the TEM because of the unequal thickness of the oxide and metal at the interface, thus it has been very difficult to photograph the narrow transition zone. However, this has on some samples been achieved, and an analysis made of the width and nature of the transition zone, the neighbouring oxide and the nature of any intermetallic particles found close to the transition zone.

An analysis has also been made of the composition of the intermetallic particles as a function of distance into the metal from the oxide-metal interface. Near to the metal surface particles have been found which have an Fe-rich core, and an example of such a particle is shown in Fig. 7.8. Figs 7.9 and 7.10 show the Energy Dispersive X-ray

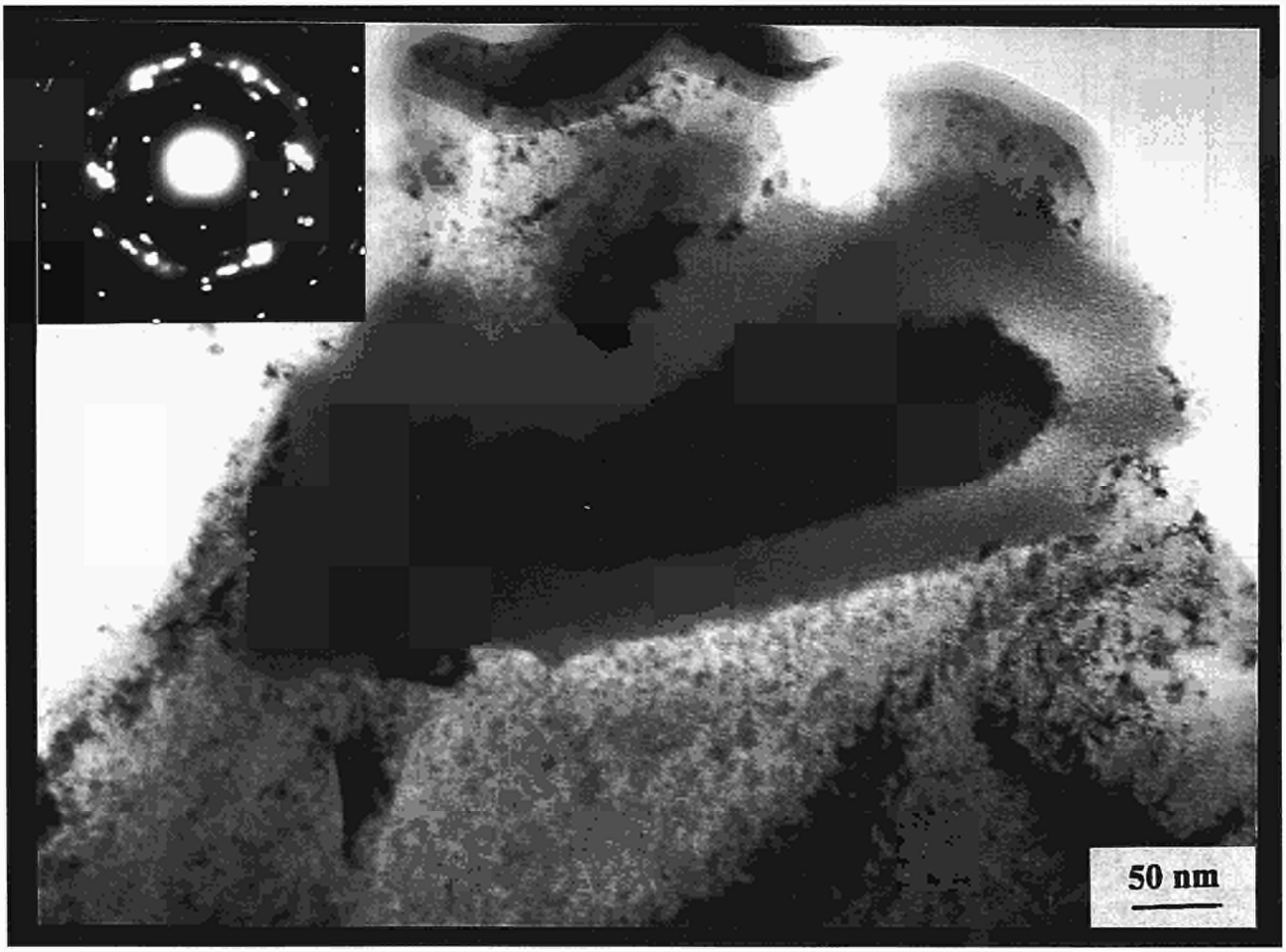

Fig. 7.8 TEM micrograph of a particle with an Fe-rich core, caused by the diffusion of Fe out of the periphery of the particle into the Zr matrix.

(EDX) spectra from the core and from the periphery of this particle respectively, and Fig. 7.11 shows an EDX line scan taken across a particle diameter.

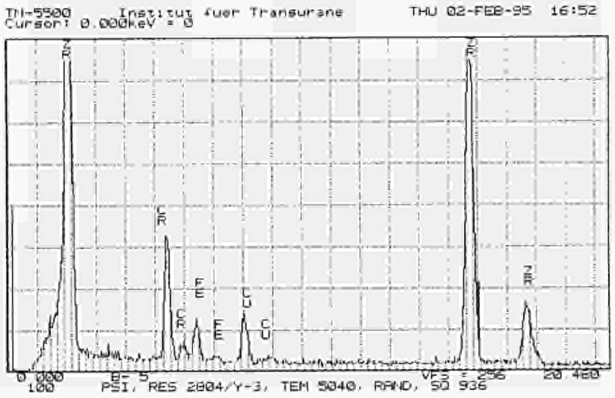

Fig. 7.9 EDX spectrum from the centre of the precipitate imaged in Fig. 7.8, showing the ratio Fe:Cr = 67:33.

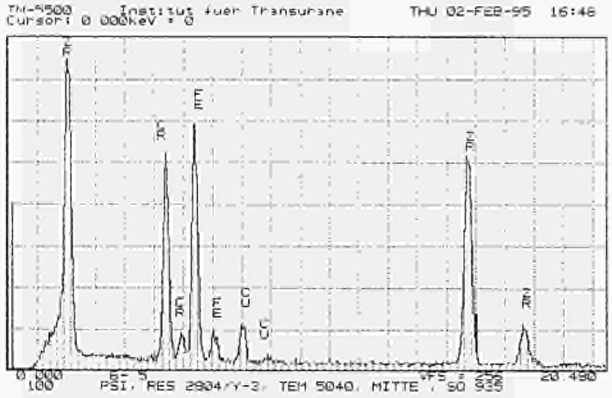

Fig. 7.10 EDX spectrum from the periphery of the precipitate imaged in Fig. 7.8, giving the ratio Fe:Cr = 43:57.

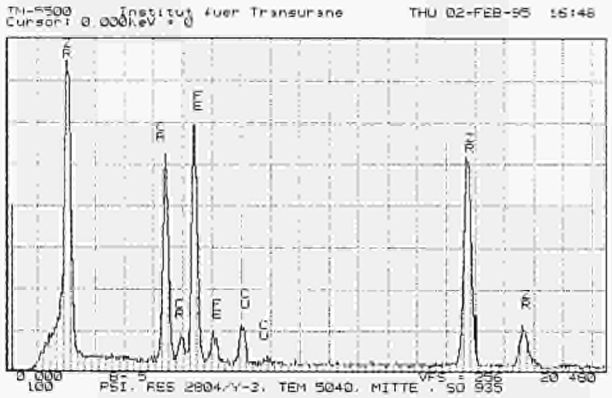

Fig. 7.11 EDX linescan taken across the particle imaged in Fig. 7.8 showing the diametral variation of the Fe (1) and Cr (2) concentrations.

8. Scientific Infrastructure

8.1 Guest Scientists, Visitors, Training Opportunities at ITU

During the year 1994, the Institute has welcomed six new doctoral grantees from France, Ireland, Spain and The Netherlands. In the frame of the Human Capital and Mobility Programme of the European Commission thirteen new postdoctoral grantees started at ITU. They originated from Belgium, France, Germany, Italy, Spain, Sweden, the Netherlands and the United Kingdom.

The Institute hosted two visiting scientists from Germany and Greece.

Two doctoral grantees from the Institute have obtained their Ph. D. in 1994 at the University of their choice:

- Thomas Gasche, "Ground State, Optical and Magneto-Optical Properties from First Principle Theory", at the University of Uppsala (Sweden);

- Maria Theresa Oliveira de Almeida, "Study of Gas Adsorption (O_2, CO_2, CO and C_2H_4) in Pu metal and some actinide intermetallics by Photoelectron Spectroscopy (UPS/XPS)", Technical University of Lisbon (Portugal).

Four "stagiaires visiteurs" came from France and Japan. They were supported by their organization of origin.

Two scientists from Russia stayed at the Institute in the frame of a collaboration with the High Energy Density Research Centre of the Russian Academy of Sciences, in Moscow.

8.2 Quality Management

In 1993 the decision was taken to introduce of a quality management system at the Institute (TUAR-93, p. 231). This introduction is being pursued on two levels:

a) To satisfy immediate needs for quality management arising from requests of customers or to prevent problems of product liability, quality plans or - for less extensive tasks - project specific procedures are drawn up. These documents contain statements to what extent and in which manner each of the twenty elements of EN 29001 (ISO 9001) or other relevant standards are to be considered within the quality management of the specific project.

   During the last year such plans or procedures were established for post-irradiation examination of fuel rods, the installation of an on-site laboratory for safeguards analysis in a reprocessing plant, the production of -sources for cancer treatment and the examination of "Vagabonding Material".

b) On the second level quality measures which are common to all projects or describe the overall management of third-party work (i.e. organization, contract review, quality system, procurement, document control, internal auditing) will be described in procedures and finally summarised in the Institute quality manual.

Annexes

Annex I

Publications 1994

1. Conferences

Conference papers published in 1994 in journals or special conference proceedings volumes may appear also under paragraph 2 (Books and Periodicals)

1994 Winter Conference on Plasma Spectrometry
January 10-15, 1994, San Diego, CA (US)

Betti, M., Rasmussen, G., Koch, L.
Analysis of Solid Nuclear Materials by Glow Discharge Mass Spectrometry

International Symposium on Actinides: Processing and Materials
February 27-March 3, 1994, San Francisco, CA (US)

Bokelund, H., Glatz, J.P.
Trends in Actinide Chemistry as applied to the Nuclear Fuel Cycle

IAEA Symposium on International Safeguards
March 14-18, 1994, Vienna (AT)

Brandalise, B., Ougier, M., Wellum, R., Wagner, H.G., Wojnowski, D., Koch, L.
Robotised Equipment for the On-Site Analysis of Fissile Material
Proceedings IAEA-SM-333/37

Cromboom, O., Koch, L., Mayer, K., de Bièvre, P., Matussek, P., Ottmar, H.
Using Reference Materials for within Laboratory Quality Control

8th Annual Conference of the Aerosol Society
March 21-23, 1994, York (GB)

Somers, J., Magill, J., Richter, K., Fourcaudot, S., Barraux, P., Lajarge, P.
Acoustic Agglomeration of a Mixture of Titanium Dioxide and Glycol Fog Aerosols

American Physical Society Meeting
March 21-25, 1994, Pittsburgh, PA (US)

Gu, G., Vohra, Y.K., Spirlet, J.C., Benedict, U.
High Pressure Phase Transformation in $Ce_{0.5}Th_{0.5}$ Alloy to 253 GPa

Workshop on Photon and Neutron Studies of Magnetic Materials
April 8-10, 1994, Marathon (GR)

Lander, G.H.
Neutrons as a Probe of f-Electron Systems

24èmes Journées des Actinides
April 16-19, 1994, Obergurgl (AT)

Amanowicz, M., Braithwaite, D., Ichas, V., Benedict, U., Rebizant, J., Spirlet, J.C.
The Electrical Resistance of NpSb under High Pressure

Amanowicz, M., Rebizant, J., Spirlet, J.C.
Transport Properties of $PuSb_{1-x}Te_x$

Bednarczyk, E., Kalbusch, J., Lefebvre, P., Moens, A., Rebizant, J., Rijkeboer, C., Spirlet, J.C., Waerenborgh, J.C., Walker, C.T., Wastin, F., Zwirner, S.
Advances in Preparation of Actinide Compounds at ITU Karlsruhe

Benedict, U., Abraham, C., Dancausse, J.P., Gu, G., Gerward, L., Hulliger, F., Heathman, S., Mattenberger, K., Staun Olsen J., Spirlet, J.C. et al.
Synchrotron X-Ray Diffraction Study of Actinide Materials at High Pressure

Bourdarot, F., Amanowicz, M., Burlet, P., Jeandey, C., Oddou, J.L., Rebizant, J., Sanchez, J.P., Spirlet, J.C., Vogt, O.
Magnetic Properties of NpP

Bourdarot, F., Zobkalo, I., Ressouche, E., Schweizer, J., Burlet, P., Spirlet, J.C., Rebizant, J.
Magnetic Form Factor of NpTe

Colineau, E., Blaise, A., Burlet, P., Jeandey, C., Oddou, J.L., Sanchez, J.P., Larroque, J., Rebizant, J., Spirlet, J.C.
Magnetic Properties of $NpAl_3$ and $NpIn_3$

Cottenier, S., Toye, A., Rots, M., Spirlet, J.C., Winand, J.M.
Perturbed Angular Correlation Analysis of the Magnetic State in the Pseudo-Binary System $U(In_{1-x}Sn_x)_3$

Goncalves, A.P., Waerenborgh, J.C., Bonfait, G., Almeida, M., Estrela, P., Godinho, M., Spirlet, J.C.
Structural and Magnetic Studies of U-Fe-M (M=Mo, Si) Compounds with $ThMn_{12}$-Type Structure

Havela, L., Sechovsky, V., Svoboda, P., Purwanto, A., Robinson, R.A., Nakotte, H., Seret, A., Winand, J.M., Rebizant, J., Spirlet, J.C.
Magnetic Ordering in U_2Pd_2Sn and U_2Pd_2In

Ichas, V., Braithwaite, D., Benedict, U., Wastin, F., Moens, A., Spirlet, J.C.
Electrical Resistance of NpGa3 under Pressure

Lander, G.H., Felcher, G.P., Tang, C., Brown, S., Haycock, S., Stirling, W.G., Plaskett, T.
Experiments on Multilayers Containing Uranium

Merli, L., Lambert, B., Fuger, J.
Calorimetric Determination of the Molar Enthalpy of Formation of Hydroxides, Carbonates, and Hydroxycarbonates of Lanthanides and Actinides

Oddou, J.L., Colineau, E., Jeandey, C., Sanchez, J.P., Rebizant, J., Spirlet, J.C.
Magnetic Properties of Np_2T_2Sn Compounds

Paolasini, L., Paixao, J.A., Lander, G.H., Delapalme, A., Burlet, P., Sato, N.
Scattering Studies of a Single Crystal of the Heavy Fermion UPd_2Al_3

Pereira, L.C.J., Winand, J.M., Wastin, F., Rebizant, J., Spirlet, J.C.
Syntheses and Crystal Chemistry of Ternary Intermetallic Compounds An_2T_2X (An= U,Np X=In,Sn,Al,Ga T=Co,Fe,Ir,Ni,Pd,Pt,Rh,Ru)

Seret, A., Wastin, F., Bednarczyk, E., Braitwaite, D., Waerenborgh, J.C., Rebizant, J., Spirlet, J.C., Powietzka, B., Kanellakopulos, B., Zwirner, S.
Electrical Resistivity and Magnetic Susceptibility of $NpNi_2Al_3$ and $NpPd_2Al_3$

Spirlet, J.C., Cremer, B., Lebrun, M., Sasahara, A., Inoue, T.
Preparation and Refining of Americium and Curium Metal

Zwirner, S., Waerenborgh, J.C., Potzel, W., Kalvius, G.M., Rebizant, J., Spirlet, J.C., Geibel, C., Steglich, F.
Mössbauer Studies on $NpNi_2Al_3$, $Np_{0.5}U_{0.5}Pd_2Al_3$ and $Np_{0.3}U_{0.7}Pd_2Al_3$

Zwirner, S., Waerenborgh, J.C., Potzel, W., Spirlet, J.C., Rebizant, J., Gal, J., Kalvius, G.M.
Mössbauer High Pressure Studies of NpX_3

International Topical Meeting on Light Water Reactor Fuel Performance
April 17-21, 1994, West Palm Beach, FL (US)

Manzel, R., Coquerelle, M., Billaux, M.R.
Fuel Rod Behaviour at Extended Burnup
Proceedings Amer. Nucl. Soc. (1994) 335-342

RECOD '94, 4th International Conference on Nuclear Fuel Reprocessing and Waste Management
April 24-28, 1994, London (GB)

Glatz, J.P., Koch, L., Pagliosa, G., Garcia Alonso, J.I., Matsumura, T., Tsukada, T.
Characterisation of Residues and Reprecipitation from Dissolver Solution of Highly Burnt LWR Fuel

Song, C., Glatz, J.P., Bokelund, H., Koch, L.
Actinide Partitioning by Means of the TRPO Process

Tsukuda, T., Kameyama, T., Yokoyama, H., Glatz, J.P., Koch, L., Garcia Alonso, J.I.
Dissolution Study of High Burnup WR Fuel and Ceramographic Characterization of Residue

5th Panhellenic Symposium of Nuclear Physics
May 6-7, 1994, Patras (GR)

Ronchi, C.
Recent Developments in High Temperature Thermodynamic Properties of Nuclear Reactor Oxide Fuel

European Aerosol Conference
May 30-June 2, 1994, Blois (FR)

Capéran, Ph., Somers, J., Richter, K., Fourcaudot, S.
Scaling of the Acoustic Agglomeration Rate as a Function of the Wave Energy

Somers, J., Capéran, Ph., Richter, K., Fourcaudot, S.
Agglomeration of a Titanium Dioxide Aerosol in a High Intensity Sound Field

1994 Conference on Magneto-optic Materials
June 16-18, 1994, Los Alamos (US)

Brooks, M.S.S., Gasche, T., Johansson, B.
Calculated Ground State, Optical and Magneto-optical Properties of Uranium Sulphide
Proceedings J. of Phys. Chem. Solids

6th Joint International Conference on Magnetism and Magnetic Materials
June 20-23, 1994, Albuquerque, NM (US)

Havela, L., Sechovský, V., Svoboda, P., Diviš, M., Nakotte, N., Prokeš, K. , de Boer F.R., Purwanto, A., Robinson, R.A., Seret, A., Winand, J.M., Rebizant, J., Spirlet, J.C., Richter, M., Eschrig, H.
Heavy Fermion Behavior of U_2T_2X Compounds
Proceedings J. Appl. Phys. 76 (1994)

Purwanto, A., Robinson, R.A., Prokeš, K., Nakotte, H., de Boer, F.R., Havela, L., Sechovský, V.,, Kergadallan, Y., Spirlet, J.C., Rebizant, J.
Structure, Transport and Thermal Properties of UCoGa
Proceedings J. Appl. Phys. 76 (1994) 7040-7042

8th World Ceramic Congress (CIMTEC-8)
June 29- July 4, 1994, Florence (IT)

Matzke, Hj.
The RIM-Effect in high Burnup UO_2 Nuclear Fuel

Solid Compounds of Transitions Elements-11 (SCTE-11)
July 5-8, 1994, Wroclaw (PL)

Wastin, F., Spirlet, J.C., Rebizant, J.
Progress on Solid Compounds of Actinides
Proceedings J. Alloys and Comp. 219 (1995) 232-237

INMM Annual Meeting
July 17-22, 1994, Naples, FL (US)

Nicolaou, G., Koch, L.
Radiation Dose Aspects of Fuels used for the Transmutation of Minor Actinides

13th IUPAC Conference Chemical Thermodynamics. - Symposium Nuclear Materials
July 17-22, 1994, Clermont-Ferrand (FR).
(Proceedings; ed. Hj. Matzke)

Chkuaseli, V.F., Matzke. Hj.
Volatile Fission Product Bubble Behaviour in Uranium Dioxide
Proceedings, J. Nucl. Mater. 223 (1995) 61-66

Glatz, J.P., Toscano, E.H., Pagliosa, G., Nicholl, A.
Influence of Granite on the Leaching Behaviour of Different Nuclear Waste Forms
Proceedings, J. Nucl. Mater. 223 (1995) 84-89

Lucuta, P.G., Matzke, Hj., Verrall, R.A.
Microstructural Features and Thermal Properties of Hyperstoichiometric SIMFUEL
Proceedings, J. Nucl. Mater. 223 (1995) 51-60

Matzke, Hj.
Oxygen Potential Measurements in High Burnup LWR UO_2 Fuel
Proceedings, J. Nucl. Mater. 223 (1995) 1-5

1st Workshop on Comparative Science of the f-Elements
July 28-30, 1994 Bühlerhöhe (DE)
Proceedings J. Alloys Comp.

Benedict, U.
Comparative Aspects of the High-pressure Behaviourof Lanthandide and Actinide Compounds

Hiess, A., Boucherle, J.X., Givord, F., Canfield, P.C.
Magnetic Susceptibility and Magnetization Measurements of an YbA_{13} Single Crystal for Groundstate Investigations

49th Calorimetry Conferenence
July 31-August 4, 1994, Santa Fe, NM (US)

Merli, L., Lambert, B., Fuger, J.
Molar Enthalpy of Formation of Carbonates, Hydroxy-carbonates and Hydroxides of Lanthanides

2nd International Conference on f-Elements (ICFE-2)
August 1-5, 1994 Helsinki (FI)

Benedict, U.
Recent Results of High-Pressure Work on f-Metals and Compounds

Spectrum '94 International Topical Meeting on Nuclear and Hazardous Waste Management
August 14-18, 1994, Atlanta, GA (US)

Coquerelle, M., Glatz, J.P.
Characterization of High Burn-Up UO_2 Spent Fuels

International Conference on Strongly Correlated Electron Systems (SCES '94)
August 15-18, 1994, Amsterdam (NL)

Brooks, M.S.S.
Band Structure Calculations for f-Electron Systems
Proceedings, Phys. B 206& 207 (1995) 1-7

Cottenier, S., Toye, A., Rots, M., Spirlet, J.C., Winand, J.M.
Perturbed Angular Correlation Study of the Pseudo-Binary System $U(In_{1-x}Sn_x)_3$
Proceedings, Phys. B 206& 207 (1995) 492-494

Seret, A., Wastin, F., Waerenborgh, J.C., Zwirner, S., Spirlet, J.C., Rebizant, J.
Electrical Resistivity of AnT_2Al_3 (An=Np, Pu; T = Ni, Pd)
Proceedings, Physica B 206 & 207 (1995) 525-527

Sanchez, J.P., Colineau, E., Jeandey, C., Oddou, J.L., Rebizant, J., Seret, A., Spirlet, J.C.
Magnetic Properties of Np_2T_2Sn Compounds
Proceedings, Physica B 206 & 207 (1995) 531-533

International Conference on Magnetics
August 22-26, 1994, Warsaw (PL)
Proceedings J. Magn. Magn. Mater.

Cottenier, S., Toye, A., Rots, M., Spirlet, J.C.
Perturbed Angular Correlation Analysis of the Magnetic State in the Pseudo-Binary System $U(In_{1-x}Sn_x)_3$

Godinho, M., Bonfait, G., Goncalves, A.P., Almeida, M., Spirlet, J.C.
Magnetic Properties of a UFe_4Al_8 Single Crystal

Goncalves, A.P., Bonfait, G., Almeida, M., Estrela, P., Godinho, M., Spirlet, J.C.
Structural and Magnetic Properties of UFe_xM_{12-x} (M=Al, Mo and Si)

Havela, L., Sechovský, V., Svoboda, P., Nakotte, H., Prokeš, K., de Boer, F.R., Seret, A., Winand, J.M., Rebizant, J., Spirlet, J.C. et al.
Magnetism in U_2T_2X Compounds

Kindo, K., Fukushima, T., Kumada, T., de Boer, F.R., Nakotte, N.,Prokeš, K., Havela, L., Sechovský, V., Seret, A.,Winand, J.M.
Spirlet, J.C., Rebizant, J.
Electronic Properties of U_2Ni_2Sn

Lander, G.H., Stirling, W.G., Langridge, S.
Resonant X-ray Scattering in 5f Magnetism

4th International Aerosol Conference
August 28-September 2, 1994, Los Angeles (US)

Capéran, Ph., Somers, J., Richter, K., Fourcaudot, S.
Influence of Inertial Particles on the Acoustic Agglomeration of a Titanium Dioxid Aerosol

Research on Highfield Magnetism
August 29-31, 1994, Nijmegen (NL)

Bonfait, G., Goncalves, A., Spirlet, J.C., Almeida, M.
High Field Magnetoresistance of UFe_4Al_8

Fukushima, T., Matsuyama, S., Kumada, T., Kindo, K., Prokeš, K., Nakotte, H., de Boer, F., Havela, L., Sechovský, V., Winand, J.M., Rebizant, J., Spirlet, J.C.
High-field Magnetization Studies of some U_2T_2X Compounds

4th International Conference on Plasma Source Mass Spectrometry
September 11-16, 1994 Durham (GB)

Garcia Alonso, J.I., Sena, F., Arbore, Ph., Julian Rodriguez, R., Koch, L.
Determination of Major Elements in Nuclear Samples by ICP-MS

IAEA - Research Co-ordination Meeting on Fuel Element Modelling at Extended Burnup (FUMEX)
September 15-16, 1994, Windermere (GB)

O'Caroll, C., van de Laar, J., Lassmann, K.
Report in ITU FUMEX Results

International Meeting on Reduced Enrichment for Research and Test Reactors (REHTR)
September 18-23, 1994, Williamsburg, VA (US)

Durand, J.P., Laudamy, P., Richter, K.
Preliminary Developments of MTR Plates with Uranium Nitride

IAEA Technical Committee Meeting on Water Reactor Fuel Element Modelling at High Burnup and its Experimental Support
September 19-23, 1994, Windermere (GB)

O'Carroll, C., van de Laar, J., Walker, C.T., Ott, C., Restani, R.
Validation of the TUBRNP Model with the Radial Distribution of Plutonium in MOX Fuel Measured by SIMS and EPMA

O'Carroll, C., Lassmann, K., van de Laar, J., Walker, C.T.
First Steps Towards Modelling High Burnup Effects in UO_2 Fuel

Lassmann, K., O'Carroll, C., van de Laar, J.
Probalistic Fuel Rod Analyses using the TRANS-URANUS Code

Lucuta, P.G., Verrall, R.A., Matzke, Hj.
Themal Conductivity of Hyperstoichiometric SIMFUEL

European Nuclear Conference & Exhibition
October 2-6, 1994, Lyon (FR)
Proceedings

Coquerelle, M., Glatz, J.P.
Underground Water Contamination in a Spent Fuel Deposit

Glatz, J.P., Morita, Y., Song, C., Koch, L.
Advanced Reprocessing of Spent Nuclear Fuels

International Symposium on Spent Fuel Storage - Safety, Engineering and Environmental Aspects
October 10-14, 1994, Vienna (AU)

Matsumura, T., Nicolaou, G., Miyahara, K., Homma, C.
Experimental and Computation Analyses Program for Radiation Source Characterization of MOX and High Burnup UOX Spent Fuels
Proceedings IAEA-SM-355/13P

International Conference on Neutron Scattering
October 11-14, 1994, Sendai (JP)
Proceedings Physica B

Lander, G.H., Shapiro, S.M.
Observation of a New Magnetic Phase Transition in USb

Langridge, S., Stirling, W.G., Nuttall, W.J., Lander, G.H., Lebech, B., Vogt, O.
Neutron Scattering Study of the Magnetic Phases of $USb_{0.8}Te_{0.2}$

International MGA User's Workshop
October 19-20, 1994, Geel (BE)

Ottmar, H., Schubert, A., Eberle, H., van der Vegt, H.
MGA in K-Edge-Gamma and Neutron-Gamma Counters

Halden Project Meeting
October 31-November 4, 1994, Bolkesjö (NO)

Kinoshita, M., Matsumara, T., Kameyama, T., Kitajima, S., Kolstad, E., Matzke, Hj.
High Burnup Rim Project: Irradiation Program to Study Rim Structure Formation Enlarged

Technical Committee Meeting IAEA
Unconventional Methods of Pu Disposition
November 7-11, 1994, Obninsk (RU)

Magill, J., O'Carroll, C., Gerontopoulos, P., Richter, K., van Geel, J.
Advantages and Limitations of Thorium Fuelled Energy Amplifiers

WWER Reactors Fuel Performance, Modelling and Experimental Support
November 7-11, 1994 Varna, St. Constantine (BG)
Proceedings of the Conference

Lassmann, K., O'Carroll, C., van de Laar, J., Ott, C.
TRANSURANUS: A Fuel Rod Analysis Code Ready for Use

Lassmann, K., O'Carroll, C., van de Laar, J., Ray, I., Stefanova, S., Chantoin, P.
Main Concepts and Objectives of Fuel Performance Modelling and Code Development

Stefanova, S., Vitkova, M., Simeonova, V., Passage, G., Manolova, M., Haralampieva, Z., Scheglov, A., Proselkov, V., Lassmann, K.
Modelling of the WWER-440 Fuel Rod Behaviour under Operational Conditions with the Codes PIN-MICRO and TRANSURANUS

3rd International Information Exchange Meeting on Actinide and Fission Product Partitioning and Transmutation
December 12-14, 1994, Cadarache (FR)

Babelot, J.F., Gruppelaar, H., Mühling, G., Prunier, C., Rome, M., Salvatores, M.
EFTTRA, A European Collaboration for the Development of Fuels and Targets for the Transmutation

Glatz, J.P., Babelot, J.F., Nicolaou, G., Koch, L.
Theoretically and Experimentally Derived Criteria for Partitioning and Transmutation of Radionuclides in Existing Reactors

2. Books and Periodicals

(including publications which had been submitted or presented at conferences in 1993 and which appeared in print in 1994)

Ahuja, R., Auluck, S., Johansson, B., Brooks, M.S.S.
Electronic Structure, Magnetism and Fermi Surfaces of Gd and Tb
Phys. Rev., B Condens. Matter 50 (1994) 5147-5154

Amanowicz, M., Braithwaite, D., Ichas, V., Benedict, U., Rebizant, J., Spirlet, J.C.
High-Pressure Resistance Study of NpSb up to 23 GPa
Phys. Rev., B Condens. Matter 50 (1994) 6577-6582

Bagger, C., Mogensen, M., Walker, C.T.
Temperature Measurements in High Burnup UO_2 Nuclear Fuel: Implications for Thermal Conductivity, Grain Growth and Gas Release
J. Nucl. Mater. 211 (1994) 11-29

Benedict, U.
Comparative Aspects of the High-pressure Behaviour of Lanthanide and Actinide Compounds
J. Alloys Comp. (submitted)

Betti, M., Rasmussen, G., Hiernaut, T., Koch, L., Milton, D.M.P., Hutton, R.C.
Adaptation of a Glow Discharge Mass Spectrometer in a Glove-box for the Analysis of Nuclear Materials
J. Anal. At. Spectrom. 9 (1994) 385-391

Betti, M., Rasmussen, G., Zierfuss, S., Koch, L.
Analysis of Non-Conducting Nuclear Materials by d.c. Glow Discharge Mass Spectrometry: Investigations of Uranium Oxide Specimens
J. Anal. At. Spectrom. (submitted)

Capéran, Ph., Somers, J., Richter, K., Fourcaudot, S.
Acoustic Agglomeration of a Glycol Fog Aerosol: Influence of Particle Concentration and Intensity of the Sound Field at two Frequencies
J. Aerosol Sci. (submitted)

Colineau, E., Sanchez, J.P., Rebizant. J., Winand, J.M.
Hyperfine Interaction Parameters in $GdPd_2Al_3$ and Ground State of $CePd_2Al_3$ and $NpPd_2Al_3$
Solid State Commun. 92 (1994) 915-919

Dalle Donne, M., Scaffidi, F., Ferrero, C., Ronchi, C.
Modelling of Swelling and Tritium Release in Irradiated Beryllium
J. Nucl. Mater. 212-215 (1994) 954-960

Delapalme, A., Raison, P., Lander, G.H., Rebizant, J. Schweiss, P., Kanellakopulos, B.
Studies of $U(C_5H_5)_3Cl$: II-Temperature Dependence of the Molecular Configurations
Z. Kristallogr. 209 (1994) 727-732

Fischer, E.O., Apostolidis, C., Dornberger, E., Filippou, A.C., Kanellakopulos, B., Lungwitz, B., Müller, J., Powietzka, B., Rebizant, J., Woth, W.
Carben- und Carbin-Komplexe des Technetiums und Rhenium - Synthese, Struktur und Reaktionen
Z. Nat.forsch. (submitted)

Garcia Alonso, J.I., Thoby, D., Giovanonne, B., Glatz, J.P., Pagliosa, G., Koch, L.
Characterization of Spent Nuclear Fuel Dissolver Solutions and Dissolution Residues by Inductively Coupled Plasma Mass Spectrometry
J. Anal. At. Spectrom. 9 (1994) 1209-1215

Garcia Alonso, J.I., Sena, F., Koch, L.
Determination of ^{99}Tc in Nuclear Samples by Inductively Coupled Plasma Spectrometry
J. Anal. At. Spectrom. 9 (1994) 1217-1222

Garcia-Alonso, J.I.
Random and Systematic Errors in the Determination of on-Natural Elements by ICP-MS Using Isotope Dilution Analysis
J. Anal. At. Spectrom. (submitted)

Garcia Alonso, J.I., Sena, F., Arbore, Ph., Betti, M., Koch, L.
Determination of Fission Products and Actinides in Spent Nuclear Fuels by Isotope Dilution Ion Chromatography ICP-MS
J. Anal. At. Spectrom. (submitted)

Goncalves, A.P., Waerenborgh, J.C., Bonfait, G., Amaro, A., Godinho, M.M., Almeida, M., Spirlet, J.C.
UFe_6Ge_6: A New Ternary Magnetic Compound
J. Alloys Comp. 204 (1994) 59-64

Goncalves, A.P., Almeida, M., Walker, C.T., Ray, I.L.F., Spirlet, J.C.
Phase Relations and Single Crystal Growth of U-Fe-M (M=Al, Si) Compounds with $ThMn_{12}$-Type Structure
Mater. Lett. 19 (1994) 13-16

Goncalves, A.P., Estrela, P., Waerenborgh, J.C., Godinho, M., Almeida, M., Spirlet, J.C.
Structural and Physical Properties of $UFe_{10}Mo_2$
Metals and Alloys (submitted)

Gu, G., Vohra, Y.K., Benedict, U., Spirlet, J.C.
Ultrahigh-pressure Phase Transformations in the $Ce_{0.43}Th_{0.57}$ Alloy: Implications for f-electron Behavior under Compression
Phys. Rev., B Condens. Matter 50 (1994) 2751-2753

Holland-Moritz, E., Lander, G.H.
Neutron Inelastic Scattering of Actinides and Anomalous Lanthanides.
"Handbook on the Physics and Chemistry of Rare Earths"
Eds.: Gschneidner, K.A., Eyring, L., Lander, G.H., Choppin, G.R.,
Elsevier Science B.V. Vol. 19 (1994) 1-121

Joachim, J.E., Apostolidis, C., Kanellakopulos, B., Meyer, D. Raptis, C., Rebizant, J., Ziegler, M.L.
Synthese, Charakterisierung und Röntgenstrukturanalyse von η^{5-} Tetramethylazacyclopentadienyl-technetiumtricarbonyl $(Me_4C_4N)Tc(CO)_3.HNC_4Me_4$ und seinen Mn- und Re-Homologen
J. Organomet. Chem. 476 (1994) 77-84

Joachim, J.E., Apostolidis, C., Kanellakopulos, B., Meyer, D., Nuber, B., Raptos, K., Rebizant, J., Ziegler, M.
Metallorganische Chemie des Technetiums: Photolytische CO-Substitutionsrekationen von Technetiumtricarbonylverbindungen
J. Organomet. Chem. (submitted)

Julian Rodriguez, R., Sari, C., Criado Portal, A.J.
Investigation of the Np-Zr and U-Zr-Np Systems
J. Alloys Comp. 209 (1994) 263-268

Kern, S., Hayward, J., Roberts, S., Richardson, J.W., Rotella, F.J., Soderholm, L., Cort, B., Tinkle, M., West, M., Hoisington, D., Lander, G.H.
Temperature Variation of the Structural Parameters in Actinide Tetrafluorides
J. Chem. Phys. 101 (1994) 9333-9337

Kern, S., Lander, G.H., Soderholm, L., Loong, C.K.
Trouw, F., West, M., Doisington, D., Cort, B., Welp, U.
Neutron Inelastic Scattering Studies of UF_4 and NpF_4
J. Chem. Phys. 101 (1994) 9338-9343

Kurata, M., Inoue, T., Sari, C.
Redistribution Behavior of various Constituents in U-Pu-Zr Alloy and U-Pu-Zr Alloy containing Minor Actinides and Rare Earths in a Temperature gradient
J. Nucl. Mater. 208 (1994) 144-158

Lander, G.H., Fisher, E.S., Bader, S.D.
The Solid-State Properties of Uranium - A Historical Perspective and Review
Adv. Phys. 43 No. 1 (1994) 1-111

Lander, G.H., Burlet, P.
On the Magnetic Structure of Actinide Monopnictides
Physica B (submitted)

Langridge, S., Stirling, W.G., Lander, G.H., Rebizant, J., Spirlet, J.C., Gibbs, D., Vogt, O.
X-ray Study of the Critical Magnetic Scattering in NpAs
Europhys. Lett. 25 (1994) 137-142

Langridge, S., Stirling, W.G., Lander, G.H., Rebizant, J.
Resonant Magnetic X-ray-Scattering Studies of NpAs. I. Magnetic and Lattice Structure
Phys. Rev., B Condens. Matter 49 (1994) 12010-12021

Langridge, S., Stirling, W.G., Lander, G.H., Rebizant, J.
Resonant Magnetic X-ray-Scattering Studies of NpAs. II. The Critical Regime
Phys. Rev., B Condens. Matter 49 (1994) 12022-12029

Lassmann, K., O'Carroll, C., van de Laar, J., Walker, C.T.
The Radial Distribution of Plutonium in High Burnup UO_2 Fuels
J. Nucl. Mater. 208 (1994) 223-231

Lucuta, P.G., Matzke, Hj., Verrall, R.A.
Modelling of SIMFUEL Thermal Conductivity - The Effect of the Burnup
J. Nucl. Mater. 217 (1994) 279-286

Matzke, Hj.
Ceramics for Energy Production and Environmental Applications with Emphasis on Nuclear Energy
Ceram. Acta 6 (1994) 31-50

Matzke, Hj.
Oxygen Potential in the Rim Region of High Burnup UO_2 Fuel
J. Nucl. Mater. 208 (1994) 18-26

Matzke, Hj.
Ion Beam Analyses of Ceramics and Glasses in Nuclear Energy
Surf. Interface Anal. 22 (1994) 472-476

Monachesi, P., Domanski, Z., Brooks, M.S.S.
Optical and Magneto-Optical Properties of PrSb
Phys. Rev., B Condens. Matter 50 (1994) 1013-1022

Naegele, J.R.
Actinides and some of their Alloys and Compounds
Chapter 2.8 of the book: Electronic Structure of Solids: Photon Emission Spectra and Related Data. Publ.: Landolt-Börnstein
Springer-Verlag Berlin Vol. 23, Subv. b (1994) 183-327

Naegele, J.R., Cox, L.E., Ward, J.W.
Nature of the 5f Electrons in δ-Pu: A High-Resolution Photoemission Study
Phys. Rev. Lett. (submitted)

Nicoll, S., Matzke,j., Catlow, C.R.A.
The Effect of Gas Concentration on the Behaviour of Xe in UO_2
J. Nucl. Mater. (submitted)

Oddou, J.L., Arons, R.R., Blaise, A., Burlet, P., Colineau, E., Jeandey, C., Ressouche, E., Sanchez, J.P., Rebizant, J., Spirlet, J.C.
Revisited Magnetic Properties of $NpAl_3$-Comparison with other Cubic $AuCu_3$-Type Actinide Compounds
J. Magn. Magn. Mater. 135 (1994) 183-190

Paixao, J.A., Rebizant, J., Blaise, A., Delapalme, A., Sanchez, J.P., Lander, G.H., Nakotte, H., Burlet, P., Bonnet, M.
Magnetism of a New U-Sb Phase: U_5Sb_4
Physica B 203 (1994) 137-146

Paixao, J.A., Delapalme, A., Paulus, W., Brück, E.
Structure of URuAl by Single-Crystal Neutron Diffraction at 120K
Z. Kristallogr. 209 (1994) 594-596

Paolasini, L., Paixao, J.A., Lander, G.H., Burlet, P., Sato, N., Komatsubara, T.
Field Dependence of Magnetic Structure of UPd_2Al_3 in the Normal State
Phys. Rev., B Condens. Matter 49 (1994) 7072-7075

Paolasini, L., Caciuffo, R., Lander, G., Rebizant, J., Keen, D., Sato, N., Komatsubara, T.
Anomalies in the Normal-state Properties of UPd_2Al_3
J. Phys. Chem. Solids (submitted)

Perez, R.A., Dyment, F., Matzke, Hj., Linker, G., Dhers, H.H.
Zr Diffusion in α-Ti measured by RBS and HIRBS
J. Nucl. Mater. 217 (1994) 48-53

Purwanto, A., Robinson, R.A., Havela, L., Sechovský, V., Svoboda, P., Nakotte, N. et al., Seret, A., Winand, J.M., Rebizant, J., Spirlet, J.C.
Magnetic Ordering in U_2Pd_2In and U_2Pd_2Sn
Phys. Rev., B Condens. Matter 50 (1994) 6792-6801

Raison, P., Rebizant, J., Apostolidis, C., Lander, G.H., Delapalme, A., Kiat, J.M., Schweiss, P., Kanellakopulos, B., Gonthier-Vassal, A., Brown, P.J.
Studies of $U(C_5H_5)_3Cl$: I-Evidence for Structural Phase transitions below Room Temperature
Z. Kristallogr. 209 (1994) 720-726

Raison, P., Lander, G.H., Delapalme, A., Williams, J.H., Kahn, R., Carlile, C.J., Kanellakopulos, B.
Studies of $U(C_5H_5)_3Cl$: Reorientational Motions of Cyclopentadienyl Rings
Mol. Phys. 81 (1994) 369-383

Ronchi, C.
On the Thermal Conductivity and Diffusivity of Solid and Liquid Uranium Dioxide
J. Phys., Condens. Matter 6 (1994) L561-L567

Sari, C., Walker, C.T.
Interaction of U-Pu-Zr Alloys Containing Minor Actinide and Rare Earth Elements
J. Nucl. Mater. 208 (1994) 201-210

Scaffidi, F., Dalle Donne, M., Ferrero, C., Ronchi, C.
Helium Induced Swelling and Tritium Trapping Mechanisms in Irradiated Beryllium: A Comprehensive Approach
Nucl. Eng. Des. (submitted)

Wastin, F., Rebizant, J., Sanchez, J.P., Blaise, A., Goffart, J., Spirlet, J.C., Walker, C.T., Fuger, J.
New Actinide Ternary Intermetallic Compounds: Synthesis, Characterization and Physical Properties
J. Alloys Comp. 210 (1994) 83-89

3. Reports

Babelot, J.F., Gueugnon, J.F., McGinley, J., Richter, K., Spirlet, J.C.
Projet EFTTRA Fabrication de 3 capsules Technétium pour irradiation dans HFR
K0294182 (1994)

Lassmann, K., van de Laar, J., O'Carroll, C.
Blind Predictions of FUMEX Cases using the TRANS-URANUS Code
K0294178 (1994)

Nicolaou, G., Koch, L. (eds.)
Proceedings of the Working Group Meeting on Targets and Fuels, Karlsruhe,
Institute for Transuranium Elements, 29 and 30 June 1993
EUR 15774 EN (1994)

Schmidt, H.E., Richter, J., Ruczka, L. (eds.)
Institute for Transuranium Elements Annual Report 1993
EUR 15741 EN (1994), 271 p.

Tasman, H.A.
Ultrasonic Thermometry in the PHEBUS FPTO Test
K0294179 (1994)

Tasman, H.A.
Ultrasonic Thermometer Sensors for PHEBUS FPT1 through FPT5
K0294180 (1994)

Tasman, H.A.
Black Box Mark 3: Control and Evaluation Electronics and Software (Version 2.3) for Ultrasonic Thermometry
K0294181 (1994)

4. Patents

a) Patents granted in 1994

Heinz, W.
Vorrichtung zur optischen Erfassung schneller Vorgänge mit einer Fernsehkamera
Patent Nr.: 0374467, Granting date: 20.04.94, Country: EP
Patent Nr.: 58907510.1.08, Granting date: 20.04.94, Country: DE
Patent Nr.: 2052865, Granting date: 20.04.94, Country: ES

Hiernaut, J.P., Werner, P.
Verfahren und Vorrichtung zum Herstellen eines Pulvers von amorphen Partikeln einer keramischen oder metallischen Substanz
Patent Nr.: 168592, Granting date: 02.05.94, Country: DK

Magill, J.
Vefahren und Vorrichtung zum kontrollierten Abbau einer Aerosolwolke
Patent Nr.: 60858, Granting date: 17-08.94, Country: IE
Patent Nr.: 87576, Granting date: XX.XX.94, Country: PT

Magill, J., McGinley, J., Richter, K.
Akustische Kammer für die Aerosolbehandlung von Abgasen
Patent Nr.: 0488097, Granting date: 14.09.94, Country: EP

Ronchi, C.; Hiernaut, J.P., Beukers, R., Heinz, W., Selfslag, R.
Mehrwellenlängen-Pyrometer
Patent Nr.: 0420108, Granting date: 08.06.94, Country: EP
Patent Nr.: 59006014.7-08, Granting date: 08.06.94, Country: DE
Patent Nr.: 2056328; Granting date: 0806.94, Country: ES

van Geel, J., Fuger, J., Koch, L.
Verfahren zur Erzeugung von Aktinium-225 und Wismut-213
Patent Nr.: 0443479, Granting date: 13.07.94, Country: EP
Patent Nr.: 59102132.3.08, Granting date: 13.07.94, Country: DE
Patent Nr.: 2058951; Granting date: 13.07.94, Country: ES
Patent Nr.: 5355394, Granting date: 11.10.94, Country: US

b) Patent applications in 1994

Magill, J. Werner P.
Maschine zur Abscheidung von Aerosolteilchen
Deposition Nr.: PCTEP94/02472, Deposition date: 27.07.94

Richter, K., Magill, J., Somers, J.
Verfahren zur Entfernung von fein verteilten Stoffen aus einem Gasstrom
Deposition Nr. PCTEP94/03207, Deposition date: 26.09.94
Country: WO

Ronchi, C., Heinz, W.
Vorrichtung zur Erzeugung von mehreren Sekundärlichtstrahlen aus einem Primärstrahl
Deposition Nr. 94101090.2, Deposition date: 25.01.94
Country: EP

Ronchi, C.
A method for evaluating the channel signals of a multichannel pyrometer
Deposition Nr. PCTEP94/03532, Deposition date: 25.01.94
Country: WO (JP, US)

c) Patent proposals in 1994

Ronchi, C., Cheindline, M.
Multipurpose Laser-Laser Setup for Measurement of the Thermal Diffusivity under Remote Manipulation
PP 2464

Koch, L., Babelot, J.F., Niemax, K., Hiddemann, L.
Fernmessung von U(Pu) in Gläsern
PP 2465

Annex II

Collaborations with External Organisations

Argentina

CNEA Buenos Aires: Diffusion in solids (F. Dyment)

Austria

International Atomic Energy Agency, Vienna: Evaluation and automation of techniques for safeguards analysis (K. Lessmon)

Belgium

Belgonucléaire, Brussels: Post irradiation examinations (S. Pilate, M. van den Borck)

University of Leuven: Xe-implantation (H. Pattyn)

University of Liège: Single crystal growth, X-ray diffraction, and analysis (J.F. Desreux, L. Martinot, M.R. Spirlet)

Canada

AECL Chalk River: Gas release, SIMFUEL production and property studies (I. Hastings, P. Lucuta, R. Verrall)

AECL Whiteshell: Behaviour of Rb and Cs in SIMFUEL (W. Hocking)

McMaster University, Hamilton: Synchrotron X-ray scattering (B. Gaulin)

Czech Republic

University of Prague: Magnetic and electrical measurements (V. Sechovsky, L. Havela); Gas release measurements (V. Balek)

Denmark

Risø National Laboratory: Neutron scattering (B. Lebech)

Technical University Lyngby: High-pressure X-ray diffraction (L. Gerward)

University of Copenhagen: High pressure X-ray diffraction (J. Staun-Olsen)

France

CEA, Cadarache: Transmutation of actinides - irradiation experiments: DEC (J.L. Faugère, R. Ginier, Y. Guerin, C. Prunier, D. Warin); DER (A. Lanquille, J. Rouault); DRN (M. Salvatores); TRANSURANUS fuel pin development (J.P. Pages); PHEBUS PF programme: post irradiation examinations (L. Codron, P. von der Hardt)

CEN, Grenoble: Neutron diffraction, magnetic studies, transport properties and Mössbauer studies (P. Burlet, J.P. Sanchez and B. Fåk)

CEN, Saclay: Neutron diffraction (J.M. Mignot)

CERCA, Romans: MTR fuel development (J.P. Durand, B. Lelievre)

CNRS (Lab. de Cristallographie), Grenoble: Crystallography of phase transitions (J.C. Marmeggi)

CNRS, Orsay: Basic studies on spent UO_2 fuel (J.C. Dran)

COGEMA, La Hague: On-site laboratory

EDF/Septen, Lyon: Transmutation of actinides (M. Rome, D. Deydier)

EDF, Paris: TRANSURANUS fuel pin code development (B. Salles); RIM effect (M. Baron); Chemical interactions fuel/cladding (thermal reactor) and determination of mechanical properties of irradiated UO_2 (M. Baron)

ESRF, Grenoble: Synchrotron studies on actinides (C. Vettier, G. Grübel, M. Wulff)

FRAMATOME, Paris: TRANSURANUS fuel pin code development (P. Blanpain)

ILL, Grenoble: Polarized neutron diffraction and neutron inelastic scattering (P.J. Brown, C. Zeyen)

Univ. of Grenoble: Transport measurements (J.M. Fournier)

Germany

Apparatebau Rothemühle, Wenden: Acoustic aerosol scavenging (W. Niggeschmidt, N. Seyfert)

Bundesministerium für Umwelt, Naturschutz und Reaktorsicherheit, Bonn, vagabonding materials (B. Fechner)

Bundesministerium für Bildung, Wissenschaft, Forschung und Technologie (BMBF), Bonn, enviromental monitoring (H.H. Remagen)

GSI, Gesellschaft für Schwerionenforschung, Darmstadt: High energy ion implantation (C. Trautmann, J. Vetter)

Hahn-Meitner-Institut, Berlin: Ranges of ions in solids, B-profiles in leached glasses (D. Fink, J. Biersack)

Hahn-Meitner-Institut, Berlin: High-energy ion implantation (S. Klaumünzer)

TECHNOMAR: Fast multichannel pyrometry (H. Dippelhens)

KfA Jülich, Inst. für Festkörperforschung: Electrical resistivity under pressure (J. Wittig)

KfK, Karlsruhe, Inst. für Technische Chemie: Susceptibility and crystal preparation (B. Kanellakopulos)

KfK, Karlsruhe, INFP: Radiation damage studies, RBS analyses, channeling, ion implantation (O. Meyer, G. Linker)

KfK, Karlsruhe, Institut für Kernphysik III: On-site laboratory training; K-edge densitometry (H. Ottmar, H. Eberle)

KfK Karlsruhe, Institut für Neutronenphysik und Reaktortechnik: Neutron collar development

KfK Karlsruhe, Projekt Nukleare Sicherheitsforschung (PSF): Irradiation experiment CAPRA-TRABANT (G. Heusener, G. Mühling)

Max Planck Institut für Festkörperphysik Stuttgart: High-pressure reflectivity studies (K. Syassen)

Siemens/KWU, Erlangen: Post-irradiation fuel element examination (R. Manzel)

Technischer Überwachungsverein Bayern, München: TRANSURANUS fuel pin code development (G. Sauer)

Technischer Überwachungsverein Hannover/Sachsen-Anhalt: TRANSURANUS fuel pin code development (D. Märtens)

Technischer Überwachungsverein Norddeutschland, Hamburg: TRANSURANUS fuel pin code development (H. Schmidt)

Technischer Überwachungsverein Südwest, Mannheim, Karlsruhe: TRANSURANUS fuel pin code development (I. Brestrich)

Technische Universität München: Mössbauer and μSR studies (M. Kalvius, W. Potzel, L. Asch)

Universität (GH) Paderborn, Experimentalphysik: Actinides under pressure (W.B. Holzapfel)

Universität Stuttgart, IKE: Source term studies (H. Hocke)

Universität Stuttgart, IKE: Data bank system THERSYST (G. Neuer, G. Jaroma-Weiland)

Univ. München, Inst.Anorg.Chem.: Single crystal growth and X-ray diffraction (F. Lux, M. Böhme)

VGB-Forschungsstiftung, Essen: Flue gas cleaning (J.P. Jacobs, H. Krüger)

Israel

Technion, Haifa: Waste glass studies (Y. Eyal)

Italy

Centro Ceramico Bologna: Leaching studies, Indentation techniques (L. Esposito)

Centro Legnaro/Padova: RBS, Ion implantation, H-analysis on leached waste matrices (G. Della Mea, V. Rigato)

University of Padova: Analysis of glass surfaces (P. Mazzoldi)

University of Trento: Indentation techniques (R. DalMaschio)

University of Ancona: Neutron and bulk magnetization studies (R. Caciuffo)

Japan

Central Research Institute of Electricity Producing Industries (CRIEPI), Tokyo: Preparation and characterisation of minor actinide alloys; Dissolution studies on high burn-up fuel (T.Ohe); Spent fuel characterisation

JAERI, Tokai Mura: Basic studies on nitride fuels (T.Ohmichi); DIDPA actinide separation process (Y. Morita); Gas release from oxide fuels (T. Ogawa)

Netherlands

AKZO n.v., Arnhem: Separation of alpha-emitting nuclides (M. Geerlings)

ECN, Petten: Transmutation of fission products (W. Franken, M. Gruppelaar)

Interfaculty Reactor Institute, Delft: Gas release (A. van Veen)

KEMA, Arnhem: Flue gas cleaning (R. Hunik, R. Tanke)

Ministerie van Economische Zaken, Den Haag, environmental monitoring (R. Ackx)

University of Amsterdam: Low temperature magnetization and resistivity (F. R. de Boer, J. Franse, E. Brück)

Poland

Institute for Low Temperature and Structure Research, Wroclaw: Bulk properties and neutron scattering (R. Troc, W. Suski)

Nuclear Institute, Warszawa: Channeling techniques, Radiation damage studies (A. Turos)

Portugal

LNETI, Sacavem: Physical chemistry of actinides (A. Piros de Matos, M. Almeida)

University of Coimbra: Neutron and X-ray studies (J.A. Paixão)

Russia

Academy of Sciences, IVTAN, Moscow: Studies on high-melting materials (A.E. Sheindlin)

International Science and Technology Center, Moscow

Radium Khlopin Institute, St.Petersburg: Field testing of a robotized system for safeguards analysis (N. Shulyak)

Spain

CIEMAT, Madrid: TRANSURANUS fuel pin code development (J. Lopez Jimenez)

Instituto de Acústica, Madrid: Acoustic aerosol scavenging (J.A. Gallego-Juarez)

Sweden

University of Uppsala: Solid state theory of actinides (B. Johansson, O. Eriksson)

Infrasonik AB, Årsta: manufacture of infraphones (M. Olsson)

Switzerland

ETH, Zürich: Single crystal growth, magnetic, optical and transport properties, preparation of U and Th compounds (O. Vogt, P. Wachter, K. Mattenberger)

Paul-Scherrer-Institut, Würenlingen: TRANSURANUS fuel pin code application (C. Ott); Post-irradiation structural investigations by electron microscopy

United Kingdom

Birkbeck College: neutron and magnetization studies (K. McEwen)

BNFL, Sellafield: On-site laboratory

Department for Trade and Industry (DTI), London, environmental monitoring (G. Andrew)

Royal Institute, London: Calculation of fission products in UO_2

University of Birmingham: Preparation of high purity single crystals (D. Fort)

University of Keele: X-ray and neutron scattering (W.G. Stirling, W.J. Nuttall, S. Langridge)

University of Warwick: Compton scattering (M.J. Cooper); Radiative properties at high temperatures (G. Hyland)

USA

Argonne National Laboratory: Neutron scattering (C.K. Loong; L. Soderholm, S. Kern)

Brookhaven National Laboratory: High-resolution and magnetic X-ray scattering (D. Gibbs, J. Axe, G. Watson)

Lawrence Livermore National Laboratory: Surface reactions (C. Colmenares)

Los Alamos National Laboratory: Materials preparation and photoemission (B. Cort, J. Ward, L. Cox)

Oak Ridge National Laboratory: Material preparation, high pressure X-ray and optical studies (R.G. Haire, J.R. Peterson)

University of New Mexico, Albuquerque: High resolution TEM, radiation damage (R. Ewing, L. Wang)

University of W. Virginia, Morgantown, W.-Virginia: Actinide theory (G.J. Hu, B.R. Cooper)

Annex III

Human Resources

1. Institute's Staff

The evolution of the staff situation in 1994 is given for three reference dates on the table below:

Date	A2-A4	A5-A8	B	C	D	total
01.01.	23	23	79	68	1	193
01.07.	20	23	81	66	1	191
31.12.	21	26	86	64	1	198

2. Visiting Scientists and Scientific Fellows

39 graduate sectorial grantees from the following countries spent in 1994 prolonged periods of time at the Institute:

B	(3)	IR	(2)
D	(5)	NL	(3)
ES	(5)	P	(2)
F	(8)	S	(1)
GR	(2)	UK	(4)
I	(4)		

Annex IV

Organisational Chart

Institute Director	Jacques VAN GEEL
Adviser, acting as Institute Deputy Director	Jean FUGER
Adviser (Programmes)	Hans Eberhard SCHMIDT (until 31.3.94) Roland SCHENKEL (since 1.8.94)
Personnel and Administration	Paul BLAES
S/T Services:	
– Technical Physics	Michel COQUERELLE
– Applied Physics	Hansjoachim MATZKE
– Nuclear Technology	Karl RICHTER
– Nuclear Chemistry	Lothar KOCH
– Actinide Research	Ulrich BENEDICT
S/T-Support:	
– Radiation Protection	Klaas BUIJS
– Technical Services	Gérard SAMSEL

Annex V

Glossary of Acronyms and Abbreviations

ADR: Accelerator-Driven Reactor
ADTT: Accelerator-Driven Transmutation Technology
AECL: Atomic Energy of Canada Ltd.
AES: Auger Electron Spectroscopy
ALI: Annual Limits of Intake
amu: atomic mass unit
ANTICORP: Américium, Neptunium, Technétium Incinérés dans les COuvertures Radiales de Phénix
APA: Anlagen Planung Alzenau GmbH (Germany)
APW: Augmented Plane Wave
ATWS: Anticipated Transient Without Scram

BE: Binding Energy
BIBLIS: PWR reactor, Biblis/Rhein (Germany)
BNFL: British Nuclear Fuel plc, Springfields (United Kingdom)

CAPRA: Consommation Accrue de Plutonium dans les RApides
CCD: Charged Coupled Device
CEA: Commissariat à l'Énergie Atomique, France
CEN: Centre d'Etudes Nucléaires, Mol (Belgium)
CERCA: Compagnie pour l'Étude de la Réalisation de Combustibles Atomiques, Romans (France)
CHEMIF: code to calculate the chemical behaviour of high burn-up fuel
CHESS: Cornell High Energy Synchrotron Source, Cornell Univ., NY (USA)
CKED: Compact K-Edge Densitometer
CMPO: Carbonyl-Methyl-Phosphine Oxide
COGEMA: COmpagnie GÉnérale des MAtériès nucléaires, Vélizy (France)
COMPUCEA: COMbined Product-Uranium Concentration and Enrichment Assay
cps: counts per second
CRIEPI: Central Research Instititute of the Electric Power Company, Tokyo (Japan)
CRP: Coordinated Research Programme
CV: Cyclovoltammetry
CW: Continuous Wave

DA: Destructive Assay
DCS: Direction Contrôle de Sécurité
DECNET: Digital Equipment Corporation NETwork
DF: Decontamination Factor
DG XII: Directorate General "Science, Research and Development" of the European Commission, Brussels (Belgium)
DG XVII: Directorate General "Energy" of the European Commission, Brussels (Belgium), Luxembourg (Luxembourg)
DH: Debye-Hückel model
DIDPA: DiisoDecylPhosphoric Acid
DSC: Differential Scanning Calorimeter

ECN: Energie Centrum Nederland, Petten (Netherlands)
ECSAM: European Commission's Safeguards Analytical Measurements
EDF: Électricité de France
EDXD: Energy-Dispersive X-ray Diffraction
EMPA: Electron Micro Probe Analysis (also EPMA)
EOS: Equation Of State
EPMA: Electron Probe Micro Analysis (also EMPA)

ESARDA: European SAfeguard Research and Development Association
ESRF: European Synchrotron Research Facility
EFTTRA: Experimental Feasibility of Targets for TRAnsmutation
EURATOM: EURopean ATOMic energy community

FATT: FAst Transient Thermography
FDBR: Fachverband Dampfkessel-, Behälter- und Rohrleitungsbau e.V., Düsseldorf (Germany)
FP: Fission Products
FR: Fast Reactor
FUMEX: FUel Modelling at EXtended Burnup research programme
FUTURE: code for fuel transient calculations (ITU, Karlsruhe)

GDMS: Glow Discharge Mass Spectrometry (Spectrometer)
GNS: Gesellschaft für Nuklear Service mbH, Hannover (Germany)
GSI: Gesellschaft für SchwerIonenforschung, Darmstadt (Germany)

HAZOP: HAZards of OPeration study
HDEHP: Hexyl Di(2-Ethyl)Phosphoric acid
HFR: High Flux Reactor, Petten (Netherlands)
HIRBS: Hevy Ion Rutherford Backscattering Spectroscopy
HKE: Hybrid K-Edge densitometer
HLW: High Level Waste
HPXRD: High-Pressure X-Ray Diffraction

IAEA: International Atomic Energy Agency, Vienna (Austria)
IBR: Ion Beam Ratio
ICP-AES: Inductively Coupled Plasma Atomic Emission Spectroscopy
ICP-MS: Inductively Coupled Plasma Mass Spectrometry
ICRP: International Commission on Radiological Protection
ID-ICP-MS: Isotope Dilution ICP-MS
IDMS: Isotope Dilution Mass Spectrometry
ILL: Institut Max von Laue - Paul Langevin, Grenoble (France)
INFP: Institut für Nukleare FestkörperPhysik, Forschungszentrum Karlsruhe (Germany)
INR: Institut für Neutronenphysik und Reaktortechnik, KfK, Karlsruhe, (Germany)
IRMM: Institute for Reference Materials and Measurements, Geel (Belgium)
ISIS: ISIS spallation source, Rutherford-Appleton Lab., Rutherford (United Kingdom)
ISO: International Standard Organization
ITU: Institute for Transuranium Elements, Karlsruhe (Germany)

JAERI: Japan Atomic Energy Research Institute
JRC: Joint Research Center

KEDG: K-EDge densitometer
KEMA: N.V. tot Keuring van Electrotechnische Materialien, Arnhem (Netherlands)
KfK: Kernforschungszentrum Karlsruhe (Germany)
KKI: KernKraftwerk Isar, Eschenbach/Isar (Germany)
KKK: KernKraftwerk Krümmel (Germany)
KORIGEN: KfK development of the ORIGEN code
KRI: Khlopin Radium Institute (Russia)
KWU: KraftWerk Union,

LANL: Los Alamos National Laboratory, Los Alamos (NM), (USA)
LSC: Liquid Scintillation Counter
LSQ: Least SQuare
LSS: Laboratoire Sur Site, La Hague (France)
LURE: Laboratoire d'Utilisation du Rayonnement Électro-magnétique, Orsay, (France)
LWR: Light Water Reactor

MA: Minor Actinides (Np, Am, Cm)
MAB: Münchener Apparatebau für Elektronische Geräte GmbH (Germany)
MATINA: MATrices INertes support des Actinides à incinérer
METAPHIX: MEtal Transmutation des Actinides dans PHénIX
MGA: Multi Group Analysis gamma deconvolution code
MIDPA: MonoIsoDecylPhosphoric Acid
MITI: Ministry of International Trade and Industry (Japan)
MITRA: code to calculate the release of radio-nuclides (ITU, Karlsruhe)
MOX: Mixed OXide fuel
MTR: Materials Testing Reactor
MWd/tM: Megawatt day per (metric) ton of (heavy) Metal
MWd/tU: Megawatt day per (metric) ton of Uranium
μ-Sr: Muon Spectroscopy

NCC: Neutron-Coincidence Counter
Nd-YAG: Neodymium-Yttrium Aluminium Garnet laser
NDA: Non-Destructive Assay
NDT: Non-Destructive Testing
NFIR: Nuclear Fuel Industry Research group CEPRI), Palo Alto, CA (USA)
NILOC: Nitride Irradiation with LOw Carbon content
NNC: National Nuclear Corporation Ltd, Risley (United Kingdom)
NSLS: National Synchrotron Light Source, Brookhaven, NY (USA)

OECD: Organization for Economic Cooperation and Development, Paris (France)
ORIGEN: Oak Ridge Isotope GENeration and depletion code
OSL: On-Site Laboratory

PAC: Perturbed Angular Correlation
PADIT: Particle Agglomeration and Deposition In Turbulence
PCMI: Pellet-Cladding Mechanical Interaction
PCSR: Pre Commencement Safety Report
PHEBUS: French test reactor, Cadarache (France)
PHEBUS-FP: Programme to study fission product release and their distribution in the primary circuit
PHENIX: French prototype fast reactor
PIE: Post-Irradiation Examination
POMPEI: POM PEtten Irradiation experiment to study nitride fuel
PSI: Paul Scherrer Institut, Würenlingen, (Switzerland)
PUDOL: Dosimetry computer program
PWR: Pressurized Water Reactor

Q.A: Quality Assurance

R&AMSC: Research and development & Analytical services Management Safety Committee, Sellafield (United Kingdom)
RBS: Rutherford Backscattering Spectroscopy
REIMEP: Regular European Interlaboratory Measurement Evaluation Programme
RERTR: Reduced Enrichment for Research and Test Reactors
RIA: Reactivity Initiated Accident
RPS: Rutherford Backscattering Spectroscopy
RSD: Relative Standard Deviation
RSF: Relative Sensitive Factor

SAL: Seibersdorf Analytical Laboratory, Vienna (Austria)
SAXS: Small Angle X-ray Scattering
SCK: Studie Centrum voor Kernergie, Mol (Belgium)
SEM: Scanning Electron Microscopy
SGN: Société Générale Nucléaire, (France)

SIMFUEL: SIMulated high burnup FUEL (with major non-volatile fission products)
SIMS: Secondary Ion Mass Spectrometry
SSC: Stress-Corrrosion Cracking
SUPERFACT: Minor Actinide Irradiation in Phenix

TBP: Tri-n-Butyl Phosphate
TCP/IP: Transmission Control Protocol / Internet Protocol
TD: Theoretical Density
TEM: Transmission Electron Microscopy
TIMS: Thermal Ionization Mass Spectrometry
TITR: TITRimetry
TOPO: Trioctyl Phosphine Oxide
TRABANT: TRAnsmutation and Burning of Actinides in TRIOX
TRABI: project to study the TRAnsport of BIg particles
TRANSURANUS: Fuel behaviour code (ITU, Karlsruhe)
TRIOX: HFR irradiation capsule, Petten (Netherlands)
TRPO: TRialkyl Phosphine Acid
TRUEX: TRansUranium EXtraction
TU: TransUranium nuclides
TUAR: Annual Report, Institute for Transuranium Elements (ITU), Karlsruhe (Germany)
TUBRNP: TransUranus BuRNuP model

UCD: Unité de Conditionnement des Déchets, La Hague (France)
UPS: Ultraviolet Photoelectron Spectroscopy
URP: Unité de Redissolution de Pu Agé, La Hague (France)
U.S.S.R.: Union of Soviet Socialist Republics

VFP: Volatile Fission Products
VMS: Virtual Memory System

XPS: X-ray Photoelectron Spectroscopy
XRD: X-Ray Diffraction

Annex VI

List of Contributors to this Document

1. Safety of Actinides in the Nuclear Fuel Cycle

Safety of Nuclear Fuels at High Burnup
Hj Matzke, J.-P. Hiernaut, K. Lassmann, I. Ray, C. Ronchi

Partitioning and Transmutation
L. Koch, H. Bokelund, J.-P. Glatz, J.-F. Geugnon, G. Nicolaou, K. Richter

Minor Actinides Laboratory
K. Richter, J. F. Babelot, J.F. Gueugnon

Particle agglomeration and Deposition in Turbulence
K. Richter, K. Buijs, B. Chavane

2. Fuel Behaviour under Accident Conditions

Hj. Matzke, C. Ronchi, H. A. Tasman

3. Characterization of Nuclear Waste Forms

M. Coquerelle, D. Bottomley, J.-P. Glatz, E. Toscano, D. H. Wegen

4. Actinide Research

U. Benedict, M. Brooks, G. Lander, J. Naegele, J. Rebizant, J.-C. Spirlet, F. Wastin

5. Exploratory Research

M.S.S. Brooks, P. Capéran, C. O'Carroll, I. Garcia Alonso, J.-F. Gueugnon, G. Nicolaou, K. Richter, C. Ronchi, J. Somers, J.-C. Spirlet

6. Scientific-Technical Support to Community Policies

Support to the Directorate-General for External Relations DG I
L. Koch, M. Betti, R. Wellum

Support to the Directorate-General for Telecommunication,
Information Market and Exploitation of Research DG XIII
K. Richter, P. Capéran, J. Somers

Support to the EURATOM Safeguards, Directorate-General DG XVII
L. Koch, O. Cromboom, M. Betti, I. Garcia Alonso, R. Wellum, A. Schubert

7. Work for Third Parties

C. Apostolidis, J.-F. Babelot, M. Betti, D. Bottomley, M. Coquerelle, J.-P. Glatz, J.F. Gueugnon, L. Koch, Hj. Matzke, G. Nicolaou, I. Ray, J. Rebizant, J.-C. Spirlet, K. Richter, A. Stalios, E. Toscano, C.T. Walker

8. Scientific Infrastructure

J. Fuger, W. Bartscher

Annex VII

Previous Progress Reports of the Institute for Transuranium Elements

TUSR	Period	COM-Nr	EUR-Nr
1	Jan - Jun 1966	1580	
2	Jul - Dec 1966	1522	
3	Jan - Jun 1967	1745	
4	Jul - Dec 1967	2007	
5	Jan - Jun 1968	2172	
6	Jul - Dec 1968	2300	
7	Jan - Jun 1969	2434	
8	Jul - Dec 1969	2576	
9	Jan - Jun 1970	2664	
10	Jul - Dec 1970	2750	
11	Jan - Jun 1971	2833	
12	Jul - Dec 1971	2874	
13	Jan - Jun 1972	2939	
14	Jul - Dec 1972	3014	
15	Jan - Jun 1973	3050	
16	Jul - Dec 1973	3115	
17	Jan - Jun 1974	3161	
18	Jul - Dec 1974	3204	
19	Jan - Jun 1975	3241	
20	Jul - Dec 1975	3289	
21	Jan - Jun 1976	3358	
22	Jul - Dec 1976	3384	
23	Jan - Jun 1977	3438	6475 EN
24	Jul - Dec 1977	3484	7209 EN
25	Jan - Jun 1978	3526	7459 EN
26	Jul - Dec 1978	3582	7227 EN
27	Jan - Jun 1979	3657	7483 EN
28	Jul - Dec 1979	3714	7509 EN
29	Jan - Jun 1980	3822	7857 EN
30	Jul - Dec 1980	3846	8230 EN
31	Jan - Jun 1981	3898	8447 EN
32	Jul - Dec 1981	3927	8777 EN
33	Jan - Jun 1982	3990	9581 EN
34	Jul - Dec 1982	4048	10251 EN
35	Jan - Jun 1983	4094	10266 EN
36	Jul - Dec 1983	4117	10454 EN
37	Jan - Jun 1984	4150	10470 EN
38	Jul - Dec 1984	4165	11013 EN
39	Jan - Jun 1985	4201	11835 EN
40	Jul - Dec 1985	4263	11836 EN

TUAR	Period	COM-Nr	EUR-Nr
86	Jan - Dec 1986	4302	12233 EN
87	Jan - Dec 1987		11783 EN
88	Jan - Dec 1988		12385 EN
89	Jan - Dec 1989		12849 EN
90	Jan - Dec 1990		13815 EN
91	Jan - Dec 1991		14493 EN
92	Jan - Dec 1992		15154 EN
93	Jan - Dec 1993		15741 EN
94	Jan - Dec 1994		16152 EN

Previous Programme Progress Reports were confidential for a period of two years. Since 1977 they are made freely accessible after that period as EUR-Reports. They can be ordered from the Office for Official Publications of the European Communities, 2 rue Mercier, L-2985 Luxembourg, Tel. 499 28-1, Telex 1322 PUBOF LU

European Commission

EUR 16152 - Institute for Transuranium Elements - Annual report 1994

Editors: R. Schenkel, J. Richter, D. Pel, R. Wellum

Luxembourg: Office for Official Publications of the European Communities

1995 - 253 pp., - 21.0 x 29,7 cm

Scientific and Technical Research series

Catalogue number: GC-NA-16152-EN-C

Venta • Salg • Verkauf • Πωλήσεις • Sales • Vente • Vendita • Verkoop • Venda • Myynti • Försäljning

BELGIQUE / BELGIË

Moniteur belge/
Belgisch Staatsblad

Rue de Louvain 42/Leuvenseweg 42
B-1000 Bruxelles/B-1000 Brussel
Tél. (02) 512 00 26
Fax (02) 511 01 84

Jean De Lannoy

Avenue du Roi 202/Koningslaan 202
B-1060 Bruxelles/B-1060 Brussel
Tél. (02) 538 51 69
Fax (02) 538 08 41

Autres distributeurs/
Overige verkooppunten:

Librairie européenne/
Europese boekhandel

Rue de la Loi 244/Wetstraat 244
B-1040 Bruxelles/B-1040 Brussel
Tél. (02) 231 04 35
Fax (02) 735 08 60

Document delivery:

Credoc

Rue de la Montagne 34/Bergstraat 34
Boîte 11/Bus 11
B-1000 Bruxelles/B-1000 Brussel
Tél. (02) 511 69 41
Fax (02) 513 31 95

DANMARK

J. H. Schultz Information A/S

Herstedvang 10-12
DK-2620 Albertslund
Tlf. 43 63 23 00
Fax (Sales) 43 63 19 69
Fax (Management) 43 63 19 49

DEUTSCHLAND

Bundesanzeiger Verlag

Breite Straße 78-80
Postfach 10 05 34
D-50445 Köln
Tel. (02 21) 20 29-0
Fax (02 21) 2 02 92 78

GREECE/ΕΛΛΑΔΑ

G.C. Eleftheroudakis SA

International Bookstore
Nikis Street 4
GR-10563 Athens
Tel. (01) 322 63 23
Telex 219410 ELEF
Fax 323 98 21

ESPAÑA

Boletín Oficial del Estado

Trafalgar, 27-29
E-28071 Madrid
Tel. (91) 538 22 95
Fax (91) 538 23 49

Mundi-Prensa Libros, SA

Castelló, 37
E-28001 Madrid
Tel. (91) 431 33 99 (Libros)
431 32 22 (Suscripciones)
435 36 37 (Dirección)
Télex 49370-MPLI-E
Fax (91) 575 39 98

Sucursal:

Librería Internacional AEDOS

Consejo de Ciento, 391
E-08009 Barcelona
Tel. (93) 488 34 92
Fax (93) 487 76 59

Librería de la Generalitat
de Catalunya

Rambla dels Estudis, 118 (Palau Moja)
E-08002 Barcelona
Tel. (93) 302 68 35
Tel. (93) 302 64 62
Fax (93) 302 12 99

FRANCE

Journal officiel
Service des publications
des Communautés européennes

26, rue Desaix
F-75727 Paris Cedex 15
Tél. (1) 40 58 77 01/31
Fax (1) 40 58 77 00

IRELAND

Government Supplies Agency

4-5 Harcourt Road
Dublin 2
Tel. (1) 66 13 111
Fax (1) 47 80 645

ITALIA

Licosa SpA

Via Duca di Calabria 1/1
Casella postale 552
I-50125 Firenze
Tel. (055) 64 54 15
Fax 64 12 57
Telex 570466 LICOSA I

GRAND-DUCHÉ DE LUXEMBOURG

Messageries du livre

5, rue Raiffeisen
L-2411 Luxembourg
Tél. 40 10 20
Fax 49 06 61

NEDERLAND

SDU Servicecentrum Uitgeverijen

Postbus 20014
2500 EA 's-Gravenhage
Tel. (070) 37 89 880
Fax (070) 37 89 783

ÖSTERREICH

Manz'sche Verlags-
und Universitätsbuchhandlung

Kohlmarkt 16
A-1014 Wien
Tel. (1) 531 610
Telex 112 500 BOX A
Fax (1) 531 61-181

Document delivery:

Wirtschaftskammer

Wiedner Hauptstraße
A-1045 Wien
Tel. (0222) 50105-4356
Fax (0222) 50206-297

PORTUGAL

Imprensa Nacional

Casa da Moeda, EP
Rua D. Francisco Manuel de Melo, 5
P-1092 Lisboa Codex
Tel. (01) 387 30 02/385 83 25
Fax (01) 384 01 32

Distribuidora de Livros
Bertrand, Ld.ª

Grupo Bertrand, SA

Rua das Terras dos Vales, 4-A
Apartado 37
P-2700 Amadora Codex
Tel. (01) 49 59 050
Telex 15798 BERDIS
Fax 49 60 255

SUOMI/FINLAND

Akateeminen Kirjakauppa

Keskuskatu 1
PO Box 218
FIN-00381 Helsinki
Tel. (0) 121 41
Fax (0) 121 44 41

SVERIGE

BTJ AB

Traktorvägen 13
S-22100 Lund
Tel. (046) 18 00 00
Fax (046) 18 01 25
30 79 47

UNITED KINGDOM

HMSO Books (Agency section)

HMSO Publications Centre
51 Nine Elms Lane
London SW8 5DR
Tel. (0171) 873 9090
Fax (0171) 873 8463
Telex 29 71 138

ICELAND

BOKABUD
LARUSAR BLÖNDAL

Skólavördustíg, 2
IS-101 Reykjavik
Tel. 11 56 50
Fax 12 55 60

NORGE

Narvesen Info Center

Bertrand Narvesens vei 2
Postboks 6125 Etterstad
N-0602 Oslo 6
Tel. (22) 57 33 00
Fax (22) 68 19 01

SCHWEIZ/SUISSE/SVIZZERA

OSEC

Stampfenbachstraße 85
CH-8035 Zürich
Tel. (01) 365 54 49
Fax (01) 365 54 11

BĂLGARIJA

Europress Klassica BK Ltd

66, bd Vitosha
1463 Sofia
Tel./Fax (2) 52 74 75

ČESKÁ REPUBLIKA

NIS ČR

Havelkova 22
130 00 Praha 3
Tel./Fax (2) 24 22 94 33

HRVATSKA (CROATIE)

Mediatrade

P. Hatza 1
4100 Zagreb
Tel. (041) 43 03 92
Fax (041) 45 45 22

MAGYARORSZÁG

Euro-Info-Service

Honvéd Európá Ház
Margitsziget
H-1138 Budapest
Tel /Fax (1) 111 60 61, (1) 111 62 16

POLSKA

Business Foundation

ul. Krucza 38/42
00-512 Warszawa
Tel. (2) 621 99 93, 628 28 82
International Fax&Phone (0-39) 12 00 77

ROMÂNIA

Euromedia

65, Strada Dionisie Lupu
RO-70184 Bucuresti
Tel./Fax 1-31 29 646

RUSSIA

CCEC

9,60-letiya Oktyabrya Avenue
117312 Moscow
Tel./Fax (095) 135 52 27

SLOVAKIA

Slovak Technical
Library

Nám. slobody 19
812 23 Bratislava 1
Tel. (7) 52 204 52
Fax : (7) 52 957 85

CYPRUS

Cyprus Chamber of Commerce
and Industry

Chamber Building
38 Grivas Dhigenis Ave
3 Deligiorgis Street
PO Box 1455
Nicosia
Tel. (2) 44 95 00, 46 23 12
Fax (2) 45 86 30

MALTA

Miller Distributors Ltd

PO Box 25
Malta International Airport LQA 05 Malta
Tel. 66 44 88
Fax 67 67 99

TÜRKIYE

Pres AS

Istiklal Caddesi 469
80050 Tünel-Istanbul
Tel. (1) 520 92 96, 528 55 66
Fax (1) 520 64 57

ISRAEL

ROY International

31, Habarzel Street
69710 Tel Aviv
Tel. (3) 49 78 02
Fax (3) 49 78 12

EGYPT/
MIDDLE EAST

Middle East Observer

41 Sherif St.
Cairo
Tel/Fax (2) 393 97 32

UNITED STATES OF AMERICA/
CANADA

UNIPUB

4611-F Assembly Drive
Lanham, MD 20706-4391
Tel. Toll Free (800) 274 48 88
Fax (301) 459 00 56

CANADA

Subscriptions only
Uniquement abonnements

Renouf Publishing Co. Ltd

1294 Algoma Road
Ottawa, Ontario K1B 3W8
Tel. (613) 741 43 33
Fax (613) 741 54 39

AUSTRALIA

Hunter Publications

58A Gipps Street
Collingwood
Victoria 3066
Tel. (3) 417 53 61
Fax (3) 419 71 54

JAPAN

Procurement Services Int. (PSI-Japan)

Koru Dome Postal Code 102
Tokyo Kojimachi Post Office
Tel. (03) 32 34 69 21
Fax (03) 32 34 69 15

Sub-agent

Kinokuniya Company Ltd
Journal Department

PO Box 55 Chitose
Tokyo 156
Tel. (03) 34 39-0124

SOUTH-EAST ASIA

Legal Library Services Ltd

Orchard
PO Box 0523
Singapore 9123
Tel. 243 24 98
Fax 243 24 79

SOUTH AFRICA

Safto

5th Floor, Export House
Cnr Maude & West Streets
Sandton 2146
Tel. (011) 883-3737
Fax (011) 883-6569

ANDERE LÄNDER
OTHER COUNTRIES
AUTRES PAYS

Office des publications officielles
des Communautés européennes

2, rue Mercier
L-2985 Luxembourg
Tél. 29 29-1
Télex PUBOF LU 1324 b
Fax 48 85 73, 48 68 17

15

GC-NA-16152-EN-C

NOTICE TO THE READER

All scientific and technical reports published by the Commission of the European Communities are announced in the monthly periodical **'euro abstracts'.** For subscription (1 year: ECU 63) please write to the address below.

OFFICE FOR OFFICIAL PUBLICATIONS
OF THE EUROPEAN COMMUNITIES

L-2985 Luxembourg

ISBN 92-827-0171-9